Hyperpolarised ^{129}Xe Magnetic Resonance Imaging Techniques for Assessment of Human Lung Function

NEIL JAMES STEWART

August 25, 2016

This thesis is dedicated to my parents

Abstract

Purpose: To contribute to advances in acquisition strategies for hyperpolarised ^{129}Xe MRI of pulmonary function via:

i) optimisation of 3D steady-state pulse sequences for imaging lung ventilation with ^{129}Xe

ii) validation of ^{129}Xe MR metrics of lung ventilation and microstructure against ^{3}He equivalents

iii) experimental verification of the ^{129}Xe chemical shift saturation recovery (CSSR) technique for evaluation of pulmonary gas exchange

iv) assessment of the reproducibility and experimental limitations of the CSSR technique

v) development of geometrical models of the alveoli for numerical analysis of ^{129}Xe exchange dynamics in human lungs and substantiation of CSSR data

Methods:

i) A numerical optimisation procedure for 3D balanced steady-state imaging of ^{129}Xe gas was developed and utilised to acquire lung ventilation images with naturally-abundant xenon

ii) MR-derived ^{129}Xe and ^{3}He ventilation volume percentage (VV%) and apparent diffusion coefficient (ADC) measurements were compared in healthy volunteers, and patients with lung cancer and chronic obstructive pulmonary disease (COPD)

iii) ^{129}Xe CSSR was performed in healthy volunteers, and patients with systemic sclerosis (SSc), idiopathic pulmonary fibrosis (IPF)

iv) CSSR reproducibility studies were performed in patients with COPD and age-matched volunteers

v) Histology and micro-CT images were employed to derive representative models of lung microstructure for finite element analysis of ^{129}Xe gas exchange

Results:

i) High quality images of pulmonary ventilation were obtained with optimised steady-state acquisitions of both 129-enriched and naturally-abundant xenon

ii) ^{3}He and ^{129}Xe MR-derived VV% and ADC metrics were comparable in all subjects, and reproducible in COPD patients

iii) ^{129}Xe CSSR-derived septal thickness measurements were capable of distinguishing patients with IPF and COPD from healthy volunteers

iv) ^{129}Xe CSSR septal thickness values were reproducible in COPD patients and age-matched volunteers

v) 2D/3D image-based models (accounting for heterogeneity of lung microstructure) resulted in qualitatively similar ^{129}Xe exchange dynamics as compared with CSSR data, exhibiting subtle differences with 1D models

Conclusion: Hyperpolarised ^{129}Xe shows promise for replacing ^{3}He as a powerful MR contrast agent for assessment of pulmonary function, and providing unprecedented sensitivity to gas exchange limitation.

Acknowledgements

Firstly, I would have been unable to complete this thesis without the invaluable guidance and support of my principal supervisor, Jim Wild, who has taught me how to survive in an academic research environment. Jim has instilled a good work-life balance in me throughout my PhD by pushing me to generate good research output whilst ensuring that I enjoy my work and have a life outside of it. I am thankful for his encouragement to promote my work and for allowing me to attend a number of academic conferences, write my own publications, and develop into a successful researcher. In addition, my industrial supervisory team of Rolf Schulte and Jan Wolber have provided technical support and advice on many occasions, and have enabled me to gain a good insight into life in industry compared with academia.

Throughout my PhD, my work and personal development has been greatly enhanced by being in close proximity to so many intelligent and congenial people in the Polarised Lung and Respiratory Imaging Systems (POLARIS) team, always approachable and willing to help with matters whether basic or complex. In approximate chronological order, I would like to thank Madhwesha Rao, Juan Parra-Robles, Helen Marshall, General Leung, Graham Norquay, Peggy Xu, Felix Horn, Guilhem Collier, Kerry Hart, Bilal Tahir, Andy Swift, Laura Saunders, Paul Hughes, Fung Chan, Laurie Smith, Nick Weatherley, Chris Johns, Martin Brook, Alberto Biancardi and Adam Maunder for becoming good friends as well as colleagues and for sharing with me their technical knowledge and life experiences.

In the wider Academic Unit of Radiology team, I am grateful to Paul Griffiths for being an admirable and approachable group leader. The radiography team, in particular David Capener and Charlotte Hammerton, have been exceptional in organising and assisting with numerous patient studies, and accommodating and generous with scanner time; often trying to find a few spare minutes for me to jump on the scanner for a quick test. From providing stationery supplies to organising patient scans, the Academic Radiology administrative team have been especially helpful in making everyday PhD life easier. In particular, Yvonne Steel, Leanne Armstrong, and Jen Rodgers have ensured the smooth running of the department and greatly reduced the burden of administrative tasks during my PhD.

I would like to extend special thanks to Atsuomi Kimura and Hideaki Fujiwara at the University of Osaka for hosting me at their institution for 2 months in summer 2015. Kimura-sensei and Fujiwara-sensei welcomed me warmly into their laboratory and their enthusiasm and friendly demeanour created a great work environment away from home. I am especially appreciative of Shota Hodono for introducing me to the Japanese people and way of life, and to Akihiro Shimokawa and Hikari Ueda for exchanging lingual and technical knowledge with me and helping me feel at ease in Japan.

I am thankful of football colleagues from the Departments of Physics, Medical Physics & Bioengineering, and others within the hospital network, who have helped to ensure that football has been a constant feature of the latter half of my PhD, and for giving the POLARIS members a run for their money.

Finally, my family have been a huge driving force throughout my studies and their support has been relentless. My parents and my brothers have been inspirational, and I am extremely lucky that they have only ever been a phone call or a few hours' drive away from Sheffield.

Contents

List of Figures

List of Tables

This page is intentionally blank

Chapter 1

Thesis overview

The principal goal of this thesis is to improve and validate existing techniques, and develop new methodologies for assessment of lung structure and function with hyperpolarised ^{129}Xe MRI.

To set the scene and provide relevant background information for this thesis, **Chapter 2** includes a general overview of techniques for human lung imaging with proton and hyperpolarised gas MRI, along with appropriate clinical applications.

The fundamentals of MRI physics and the requirements and strategies for hyperpolarised gas MRI are presented in **Chapter 3**. The purpose of this chapter is multi-fold: (i) to review the key physical principles underpinning MRI, and to discuss how the implementation of hyperpolarised gas MRI differs to that of conventional ^{1}H MRI; (ii) to establish the theoretical foundations upon which each subsequent chapter of this thesis is based; (iii) along with Chapter 2, to provide an overview of methodology for bringing persons new to the field of hyperpolarised gas MRI "up to speed".

Following the introduction of the essential theory behind hyperpolarised gas MRI, this thesis is divided into five chapters, each of which represent discrete but related pieces of original research.

Chapter 4 reports the optimisation of 3D SSFP acquisition strategies for enabling high quality, full lung coverage imaging of lung ventilation with hyperpolarised ^{129}Xe. Simulations of ^{129}Xe 3D SSFP magnetisation dynamics and SNR are presented, which account for the B_1 distribution of typical RF coils and the intrinsic B_0 homogeneity in the lungs. Images with sufficient quality to identify minor abnormalities of lung function are shown to be obtainable using xenon in its relatively inexpensive naturally-abundant form. The possibility of clinical implementation of same-breath hyperpolarised ^{129}Xe and anatomical ^{1}H MRI is highlighted by the use of compressed sensing with 3D SSFP techniques.

Chapter 5 follows on from Chapter 4 and compares the applicability and sensitivity of ^{129}Xe lung MRI to that of ^{3}He, for the purpose of assessing the feasibility of routine use of ^{129}Xe in place of ^{3}He. A qualitative comparison of ventilation images acquired using the two nuclei is presented, and a statistical analysis of quantitative measurements of lung ventilation and microstructure — namely; ventilated volume percentages, and apparent diffusion coefficients — derived from MRI of the two nuclei in a number of different cohorts is reported, along with an appraisal of the reproducibility of each of these metrics in patients with COPD.

Chapter 6 introduces the ^{129}Xe chemical shift saturation recovery (CSSR) technique, which enables evaluation of pulmonary gas exchange function and quantification of lung microstructural parameters. An overview of the physiology and physics of gas exchange in the lungs is provided in this chapter, including a summary of the existing analytical diffusion models of lung microstructure that have been utilised for measuring lung function with ^{129}Xe CSSR. The clinical potential of the technique is explored in subjects with interstitial lung disease and healthy volunteers over a spectrum of ages. **Chapter 7** explores the the reproducibility of CSSR-derived metrics of lung microstructure and function in COPD patients and age-matched healthy volunteers, and reviews the limitations, assumptions and general methodological

considerations for implementation of the ^{129}Xe CSSR technique in humans.

Following on from these experimental measurements of gas exchange dynamics, **Chapter 8** describes finite element simulations of the gas exchange process, using model gas exchange systems and realistic geometries of lung microstructure derived from imaging methods such as histology and micro-CT. The implications of these simulations for future MR imaging and spectroscopy studies with ^{129}Xe are discussed.

In each of these chapters, the relevance and implications of the strategies established in this work are discussed with respect to the fields of hyperpolarised gas lung MRI, and lung physiology. **Chapter 9** summarises the findings of each of the individual projects, and reiterates the potential applications and opportunities for clinical scalability of hyperpolarised ^{129}Xe techniques. This final chapter also presents some preliminary ongoing work pertaining to the implementation of methods for imaging of gas exchange function with dissolved hyperpolarised ^{129}Xe. The challenges and future perspectives of dissolved ^{129}Xe MR methods are discussed with reference to current clinical gold-standards and their limitations.

Chapter 2

Introduction: ^{1}H and multi-nuclear MRI methods for structural and functional assessment of the lungs

The purpose of this chapter is to provide an overview of existing methodologies for ^{1}H and multi-nuclear MR imaging of the lungs and their applications.

This chapter is based on the following publication: "MRI methods for structural and functional assessment of the lungs: proton and multi-nuclear". **N. J. Stewart**, J. M. Wild. *European Respiratory Society Monograph: Chapter 1*, **70**, 1-19 (2016). Author contributions statement: NJS and JMW; drafting and revision of the manuscript.

Conventional magnetic resonance imaging (MRI) involves non-ionising radiofrequency radiation excitation and detection of the nuclear spin free precession of protons (hydrogen nuclei, ^{1}H) within the lungs. Image contrast is provided by fundamental differences in the properties of tissues of interest, including proton density and MR signal relaxation times. ^{1}H MRI of the lungs is inherently challenging due to the low proton density and the complex magnetic environment posed by the vast numbers of tissue and air interfaces. Nevertheless, a variety of methods — both ^{1}H and multi-nuclear, the latter employing inhaled gases as contrast agents — have been developed to overcome these limitations and establish lung MRI as an important clinical tool for assessment of both lung structure and several aspects of regional pulmonary function, with high spatial and temporal resolutions.

In this chapter, an overview of proton and multi-nuclear MR imaging methodologies for the human lung is presented, ranging from recognised clinical tools to recent technological advances. This work aims to provide respiratory physiologists, imaging scientists and clinicians with an introduction to the fundamental principles of MR methods, and to highlight relevant clinical developments.

2.1   Proton lung MRI methods

The abundance of air-tissue interfaces in the lungs creates a challenging magnetic environment; the large magnetic susceptibility difference between air and tissue gives rise to numerous local magnetic field inhomogeneities. As a result, the transverse relaxation time (T_2^*) of ^{1}H in lung parenchyma and blood is extremely short [1], which makes MR signal acquisition challenging from a hardware perspective. This, along with the presence of unavoidable respiratory and cardiac motions, necessitates rapid image acquisition within a single breath-hold and/or accurate motion-triggering procedures.

Generally, a pulmonary ^{1}H MRI protocol comprises various pulse sequences, each targeted to examine specific aspects of the lung, including; structure or tissue density, ventilation, gas exchange and perfusion. The clinical field strength of 1.5 T has historically been considered as an appropriate choice for lung MRI

[2]; the greater magnetic field inhomogeneity at 3 T leads to faster signal losses [3] and the additional signal-to-noise ratio (SNR) associated with higher field imaging of other organs (such as the brain) is less easily realised in the lungs. Furthermore, whilst low-fields (≤ 0.5 T) offer longer relaxation times, signal averaging is required to achieve sufficient SNR, lengthening the acquisition.
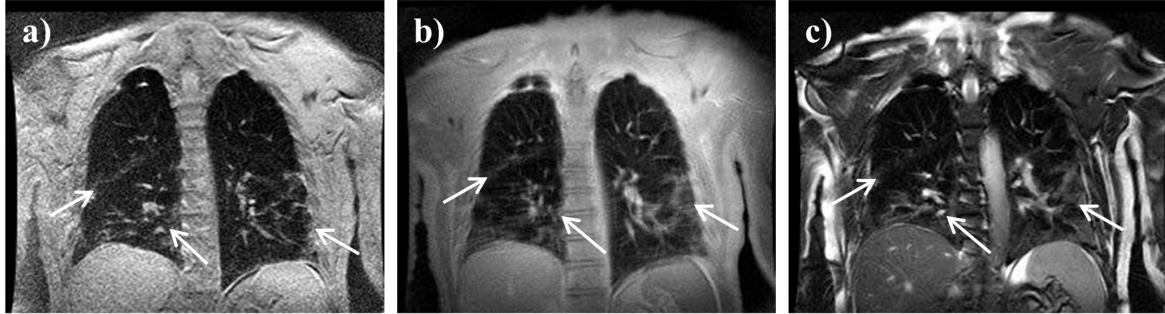
Figure 2.1: Anatomical and structural ^{1}H MR imaging of the lungs of a subject with idiopathic pulmonary fibrosis (IPF). (a) Spoiled gradient echo, (b) ultra-short echo time and (c) steady-state free precession images all highlight peripheral and basal fibrosis in both lungs, and an apparent scar in the middle-right lung, as denoted by arrows.

Spoiled gradient echo (SPGR), single shot and segmented fast spin echo (FSE) and balanced steady-state free precession (bSSFP) pulse sequences are the clinical workhorse methods for anatomical and structural ^{1}H MRI of the thorax, examples of which are illustrated in Figure 2.1. The SPGR sequence comprises a low flip angle radiofrequency (RF) pulse to excite ^{1}H nuclei, followed by a frequency encoding magnetic field gradient with a short echo time to overcome the rapid T_2^* signal decay, and lastly a spoiler gradient, which destroys any residual signal. 3D breath-hold SPGR acquisitions enable whole lung coverage imaging, with image weighting dependent on the T_2^* and a combination of proton density and the longitudinal (T_1) relaxation time. Although the lung parenchyma appears dark on SPGR images, they are suitable for anatomical reference scans, lung volume measurements [4] and assessment of the mediastinum [5]. Furthermore, 3D SPGR sequences are commonly combined with fat saturation methods or gadolinium contrast; the latter which reduces the T_1 of the pulmonary blood vessels enabling identification of enhancement in nodules, inflammation in bronchiectactic airways and delineation of mediastinal tumours [6]. Moreover, when combined with gadolinium contrast, these sequences allow visualisation of the pulmonary blood vessels with MR angiography and perfusion MRI as outlined below.

bSSFP sequences also require short echo time image encoding, however the ^{1}H magnetisation is recycled rather than destroyed at the end of each encoding step, allowing the use of higher flip angles when compared with SPGR, leading to increased SNR at the expense of increased specific absorption rate (SAR) of patient heating by radiofrequency deposition [i]. By virtue of the inherent mixed T_2 and T_1 relaxation time contrast, bSSFP images provide "bright blood" signal, affording a clear depiction of the pulmonary vessels and other long T_2 fluids such as infiltrates and mucous in the lungs. The technique is particularly suited to assessment of central pulmonary emboli (PE) [7] and is a suitable diagnostic alternative to helical computed tomography (CT) [8] in subjects at risk to ionising radiation exposure or MR contrast agents [9]. bSSFP imaging has shown utility for appraisal of bronchiectasis, mucus plugging and atelectasis, with comparable diagnostic value to CT in cystic fibrosis (CF) patients [10], although

---

[i]See Section 3.2.3 for a formal definition of SAR.

currently inferior to CT in interstitial lung disease (ILD) [11]. For diseases characterised by significant tissue loss or reduced blood volume (e.g. chronic obstructive pulmonary disease, COPD), morphological MRI with SPGR or bSSFP sequences is inherently challenging and CT remains the first-line modality [9]. In addition to breath-hold structural imaging, bSSFP sequences are routinely applied for dynamic MRI of free breathing subjects to evaluate respiratory cycle mechanics [12] and for quantitative lung volumetry [4], which has been validated against conventional spirometry tests [13].

Spin echo sequences utilise trains of refocusing RF pulses to recover signal losses from magnetic field inhomogeneities (T_2^* decay), prior to image encoding. FSE images are weighted by the T_2 relaxation time ($\geq T_2^*$) and are well-suited to identification and evaluation of infiltrates, nodules and other fluids with long T_2 [14, 15]. Spin echo acquisitions are lengthier and more SAR intensive than gradient echo acquisitions, and acceleration techniques such as single-shot encoding (e.g. single-shot FSE (SSFSE)), half-Fourier encoding (e.g. half-Fourier single-shot turbo spin echo (HASTE)) or parallel imaging with multiple RF receiver coils, are commonly employed to reduce scan time. SSFSE MRI is sensitive to pulmonary oedema and bronchial wall thickening [16] and exhibits comparable efficacy to CT for detection of pneumonia and pulmonary nodules [15, 17]. In pathologies characterised by fibrotic tissue (e.g. CF), spin echo MRI has been demonstrated as essentially comparable to CT and chest x-ray techniques [18]. High-field respiratory- and cardiac-gated SSFSE MRI has been reported to perform at least comparably to CT for evaluation of ILD [19], and segmented FSE methods employing motion compensation, e.g. respiratory-gating, show great potential for high resolution imaging of multiple pathologies in the lungs [20]. Whilst FSE acquisitions are slower than bSSFP, dynamic SSFSE MRI during free breathing can also be utilised to study respiratory mechanics. Using this approach, abnormal respiratory motion has been observed in emphysema subjects [21], and signal intensity changes between inspiratory and expiratory images have been shown to correlate with pulmonary function testing [22].

Short tau inversion recovery (STIR) preparation sequences, employing an additional RF inversion pulse prior to the standard RF excitation, can be combined with many of the aforementioned techniques to saturate the potentially compounding signal from fat in the thorax, whilst simultaneously affording valuable T_1 and T_2 contrast benefits from the lung parenchyma. Consequently, STIR sequences provide good delineation of fluid-filled regions, in particular, lymph nodes [23], for which the method performs comparably to fludeoxyglucose positron emission tomography (FDG-PET)/CT [24]. In a recent study, a combination of STIR MRI and FDG-PET/CT was demonstrated to improve diagnostic capability for N-staging in cancer patients [25]. Furthermore, turbo inversion recovery magnitude MRI has been shown to be sensitive to segmental inflammatory lung oedema, corresponding to the severity of the regional allergic reaction, as determined by the percentage of eosinophils in broncho-alveolar lavage fluid 24 hours after segmental allergen challenge in patients with asthma [26].

To overcome the low MR signal from lung parenchyma and enhance the functionality of lung MRI, exogenous contrast agents are often introduced. Inhaled oxygen acts to decrease the parenchymal and pulmonary blood T_1, boosting the available MR signal and improving the delineation of ventilated lung tissue. Oxygen-enhanced (OE) MRI is typically implemented via one of two methods: (i) acquisition of IR-prepared, T_1-weighted HASTE images at a number of different inversion times (TI — the time between inversion and acquisition) [27, 28]; (ii) dynamic T_1 mapping with a Look-Locker sequence [29],
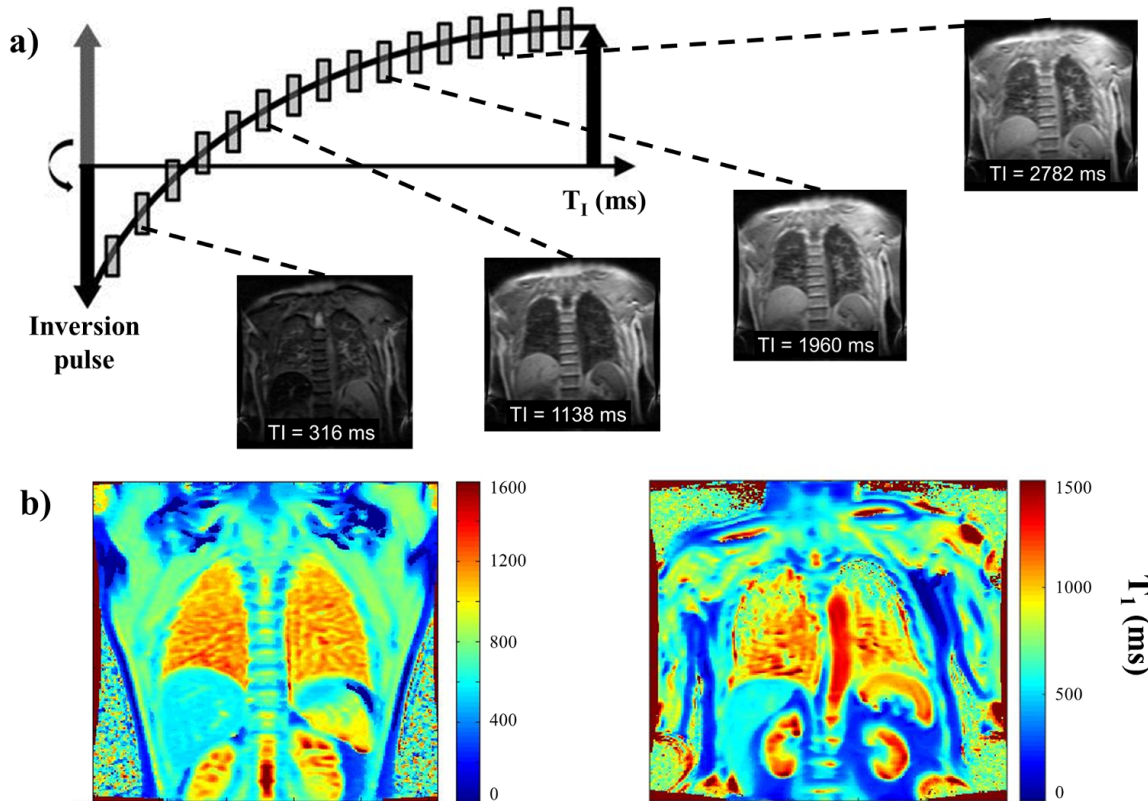
Figure 2.2: Oxygen-enhanced MRI of the lung parenchyma. a) Look-Locker inversion recovery acquisition strategy for obtaining a series of T_1-weighted gradient echo images at different inversion times. This acquisition scheme is repeated for the subject breathing normal air (21% oxygen) compared with pure (100%) oxygen. b) OE proton T_1 maps of the lungs of a healthy subject (left) and a COPD subject (right). The healthy subject exhibits a generally uniform T_1 in the lungs, whilst abnormalities in the emphysematous lungs are highlighted by regions of reduced T_1 (diminished oxygen uptake).

wherein a series of fast, low flip angle gradient echo images are acquired in quick succession after a global inversion pulse [30] (as illustrated in Figure 2.2). In both cases, acquisitions are performed alternately, with the subject breathing room air (21% oxygen) or pure 100% oxygen. Data can be presented as O_2 signal-enhancement maps or image intensities can be fitted on a pixel-wise basis to derive a lung T_1 map. The functional information afforded by OE-MRI comprises a combination of ventilation, gas exchange and perfusion weighting. Assuming that signal enhancement maps predominantly reflect changes in pulmonary ventilation [31, 32] allows for regional depiction of ventilation defects and quantification of fractional ventilation (the fraction of gas turned over in one breathing cycle) from oxygen wash-in and wash-out [33]. In comparison with quantitative CT, MR mapping of oxygen enhancement has been shown to be capable of evaluating pulmonary functional loss in COPD [34]. Following oxygen's diffusive exchange across the air-blood barrier, OE-MRI can be used to assess gas exchange limitation (e.g. in ILD [35, 36]). OE-MRI transfer metrics have been shown to provide comparable information to the whole lung transfer factor of carbon monoxide ($T_{L,CO}$), but on a regional basis, in subjects with emphysema and ILD [37, 38]. Furthermore, areas of reduced T_1-enhancement on OE-MRI ("ventilation defects") have been observed to correspond with perfusion defects in CF patients [39].

Although functionally sensitive, inherently safe and non-invasive, OE-MRI is limited by long scan times, relatively poor spatial resolution and volume coverage and its relatively small T_1 shortening / signal enhancement effect. Gadolinium chelates are routinely employed as MR contrast agents to induce T_1 shortening and signal enhancement in the pulmonary system and other organs [40, 41]. Dynamic contrast-enhanced (DCE)-MRI of the lung typically refers to the process of tracking the first passage of gadolinium through the pulmonary vascular circuit after intravenous contrast injection, providing unique information about pulmonary perfusion with excellent spatial and temporal resolution [28]. Moreover, with timing of the bolus, the arterial and venous enhancement of the pulmonary vessels can be separated to produce high resolution MR angiograms [42] (examples shown in Figure 2.3). For these applications, a rapid 3D gradient echo sequence is typically employed in combination with acceleration techniques such as parallel imaging [43] and view sharing (e.g. time-resolved imaging of contrast kinetics (TRICKS) [44]). DCE perfusion imaging and MR angiography offer increased sensitivity compared with non-CE techniques, which has been exploited for appraisal of pulmonary embolism [7, 42], where DCE-MRI and MR angiography exhibit comparable or superior sensitivity versus nuclear scintigraphy [45, 46]. Additionally, regional DCE-MRI perfusion abnormalities in emphysema patients have been observed to correlate with alveolar destruction on CT [47]. The technique is appropriate for assessment of post-operative lung function, and has been reported as a feasible non-ionising radiation alternative to the current clinical standard means of evaluation of cancer resection surgery (nuclear scintigraphy) [48]. DCE-MRI is also pertinent for studying perfusion impairment in vascular disease, for example pulmonary (arterial) hypertension (P(A)H) [49, 50], and MR angiography screening for chronic thrombo-embolic PH (CTEPH) [51] presents an equally sensitive technique to nuclear scintigraphy. In addition, MR angiograms are routinely used as replacements for catheter pulmonary angiography in the diagnosis of PAH in selected specialised centres.

The dynamics of contrast uptake can be determined by placing regions of interest (ROIs) in different areas of the lung and analysing the full time series of images, in order to yield quantitative perfusion data from signal enhancement versus time curves (see Figure 2.4). Typically, one ROI is positioned at the pulmonary artery to derive the arterial input function, by which to normalise the derived uptake dynamics. Quantitative parametric maps of perfusion parameters can also be generated for regional quantification of pulmonary blood volume (PBV), blood flow (PBF) and mean transit time (MTT) of blood through the pulmonary circuit (MTT=PBV/PBF). A significant relationship has been observed between MTT (and PBF) values and mean pulmonary arterial pressure (mPAP) and pulmonary vascular resistance (PVR) from right heart catheter measurements, the clinical gold-standard metric for assessment of PAH [52]. Quantitative DCE perfusion MRI offers diagnostic value in patients with PAH, where a decreased PBF, PBV and prolonged MTT have been measured in comparison to healthy subjects [49, 53]. Furthermore, in patients with COPD, DCE-MRI parameters appear to correlate with global pulmonary function including $T_{L,CO}$ [54], and in subjects with combined pulmonary fibrosis and emphysema, prolongation of MTT exhibits a correlation with mPAP and PVR [55].

Proton MRI encompasses an array of methods for probing various aspects of pulmonary structure and function that are now routinely used in clinical practice in specialist centres, focusing specifically on high morbidity / high treatment cost diseases such as CF and PH, as a non-ionising radiation alternative to CT. Development of the field of ^{1}H lung MRI continues to be fruitful, with recent advances in ultra-short
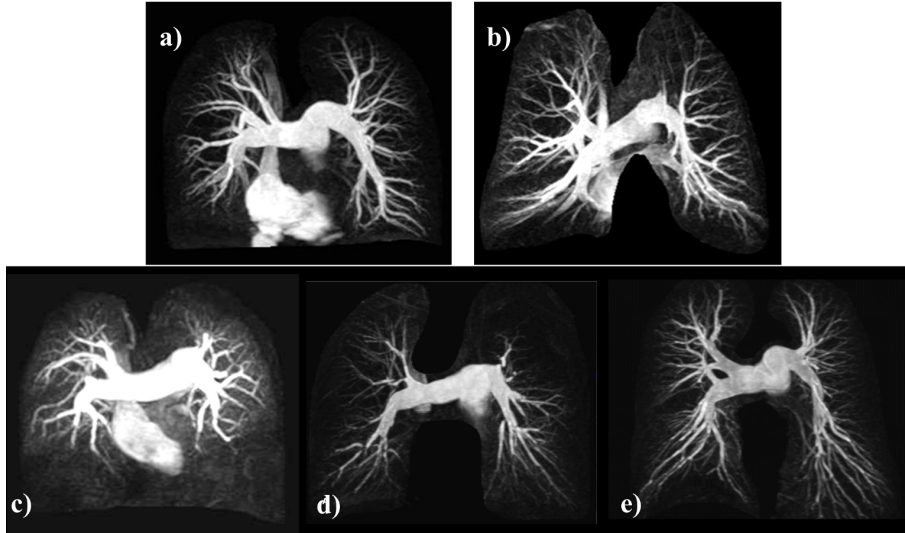
Figure 2.3: Contrast-enhanced MR angiograms of the pulmonary arteries of patients with different sub-types of pulmonary hypertension: a) idiopathic PAH; b) PH with co-existing emphysema / COPD; c) PH in ILD; d) thrombo-embolic PH; e) normal. Figure courtesy of Scott Nagle, University of Wisconsin.
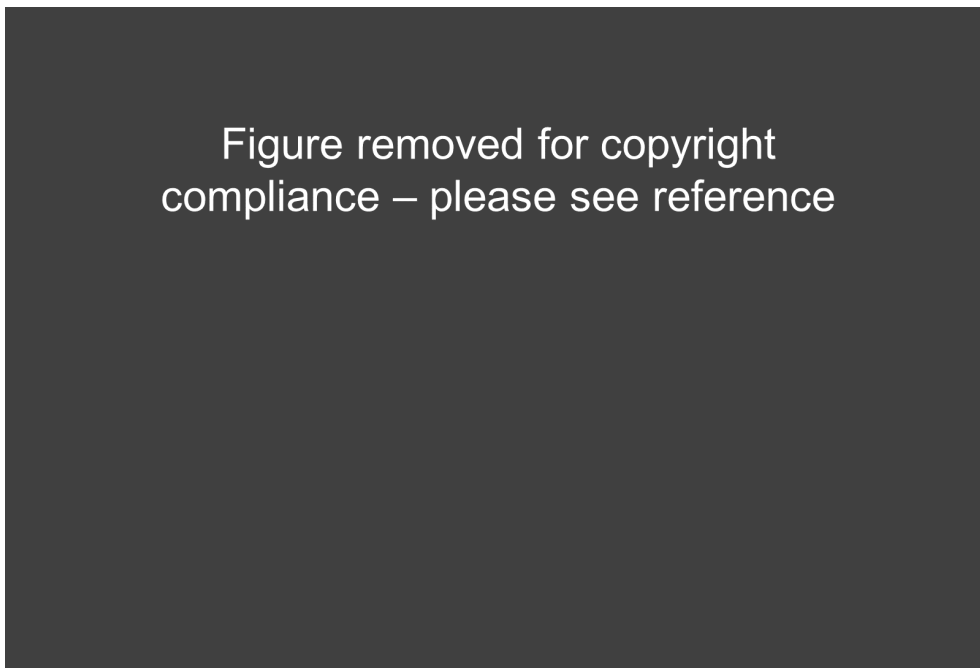
Figure 2.4: a) Time series of DCE-MR images showing gadolinium bolus passage through the pulmonary vasculature (reproduced with permission from [56]). b) contrast-enhanced MR signal vs time curves for regions of interest placed at the position of the pulmonary artery and the left atrium (reproduced with permission from [53]; note PTT equates to MTT, the mean pulmonary transit time of the contrast bolus). c) Two example slices of peak DCE-MR signal (peak gadolinium concentration) maps acquired from the lungs of a subject with idiopathic pulmonary fibrosis (same subject as in Figure 2.1).

echo time (UTE) sequences for accelerated imaging with improved visualisation of the lung parenchyma and airway delineation [57]. The clinical potential of UTE in humans is promising; comparable efficacy to CT for parenchymal assessment of patients with CF, lung cancer, ILD and emphysema has been recently

reported [58]. In addition, Fourier decomposition (FD) MRI, where dynamic analysis of free breathing imaging can be used to generate maps of lung regions modulated by ventilation and cardiac pulsatility, thus providing surrogate maps of ventilation and perfusion from a single slice of the lung [59]. Like OE-MRI, FD-MRI must be shown to be reproducible across centres and capable of providing volumetric lung coverage in order to be considered diagnostically beneficial in a clinical setting [60].

2.2 Multi-nuclear lung MRI methods

Alongside the development of ^{1}H lung MRI methods, MRI with the inhaled hyperpolarised noble gases helium-3 (^{3}He) and xenon-129 (^{129}Xe) has become established as a versatile means of functional assessment of pulmonary ventilation, structure and gas exchange. ^{3}He and ^{129}Xe are intrinsically biologically safe and non-reactive, and possess similar nuclear spin properties to protons. Typical properties of these isotopes relevant to lung MRI are summarised in Table 2.1, in comparison to ^{1}H. Due to the low density of the gases, signal enhancement is necessary to achieve sufficient SNR for in vivo MR applications. Hyperpolarisation of these nuclei, affording a factor of 10^5-10^6 increase in available MR signal, is possible via collisional spin-exchange optical pumping [61] (or metastability-exchange optical pumping [62], ^{3}He only). A number of high-throughput commercial systems are available for polarisation of ^{3}He (e.g. Polarean Inc, Durham, NC) and ^{129}Xe [63], and home-built ^{129}Xe systems with low-cost components can now attain comparable polarisation levels [64, 65].

Since the acquisition of the first images of pulmonary ventilation in human lungs with hyperpolarised ^{3}He in 1996 [66, 67] and ^{129}Xe in 1997 [68], inhaled noble gas MRI has rapidly evolved as a means to provide excellent depiction of pulmonary ventilation and quantification of pulmonary function that is not afforded by other methods [69, 70]. Ventilation MR imaging is typically performed under breath-hold after inhalation of ≤ 1 L of hyperpolarised gas, using fast gradient echo or bSSFP sequences to acquire a stack of 2D slices or a 3D volume [71], providing high resolution visualisation of the gas distribution in the lungs, with image intensity proportional to gas density. In addition to breath-hold time constraints to avoid respiratory motion, rapid acquisition and low excitation flip angles are imposed by the non-renewable nature of the laser-induced hyperpolarisation.

Isotope	^{1}H	^{3}He	^{129}Xe
Isotopic abundance (%)	99.99	1.4×10^{-4}	26.44 [NA] 80 − 90 [EN]
Gyromagnetic ratio (MHz/T)	42.58	−32.44	−11.78
Self-diffusion coefficient (cm^2.s^{-1})	2×10^{-5}	2.05	0.06
Cost (£/L)	N/A	∼ 500	∼ 20 [NA] ∼ 150 [EN]

Table 2.1: Properties of ^{1}H, ^{3}He and ^{129}Xe relevant to lung MRI. ([NA] = natural-abundance xenon; [EN] = xenon enriched with the 129 isotope.)

The majority of clinically-relevant lung imaging research with hyperpolarised gases to date has been performed with ^{3}He, exploiting its intrinsically higher gyromagnetic ratio compared with ^{129}Xe (see Table 2.1) and the fact that it has been historically easier to polarise to levels prerequisite for in vivo MRI. ^{3}He ventilation MRI has been implemented in multi-centre studies [72], is feasible at the clinical field strengths

of both 1.5 T [73] and 3 T [74], and has shown clinical utility in a number of pulmonary pathologies, particularly obstructive lung diseases in which ventilation heterogeneity presents as signal voids in the image. Ventilation defect distribution has been comprehensively studied in patients with asthma [75, 76], chronic obstructive pulmonary disease (COPD) [72, 77] and cystic fibrosis (CF) [78, 79]. Furthermore, the technique has exhibited sensitivity to ventilation abnormalities in pulmonary embolism [80] and chronic rejection of lung transplantation [81]. Dynamic ventilation MRI of inspiration has been facilitated by rapid spiral [82] and radial [83] image encoding schemes to track the passage of gas through the major airways and further evaluate flow restrictions in obstructive disease.

The availability of helium-3 is becoming increasingly regulated, as it is not naturally-abundant and is solely generated as a by-product of tritium decay in the nuclear industry [84]. Xenon is considerably cheaper and more readily-available; it is naturally-abundant in air (87 ppb), of which 26% comprises the ^{129}Xe isotope, and the ^{129}Xe fraction can be enriched to up to 80-90% by employing gas centrifuge techniques. Hyperpolarised ^{129}Xe is also a promising contrast agent for pulmonary ventilation imaging, with little or no apparent loss in functional information compared with ^{3}He [85–87]. A side-by-side comparison of ^{3}He and ^{129}Xe ventilation images acquired from normal and abnormal lungs is presented in Figure 2.5. Abnormalities in pulmonary ventilation in COPD have been observed on ^{3}He and ^{129}Xe MRI in a similar manner [85, 86], and preliminary evidence suggests that ^{129}Xe may be sensitive to smaller scale defects [85, 88] by virtue of its low diffusion coefficient, which could be beneficial in early-stage disease detection. Fuelled by recent advancements in polarisation technology [63–65] and pulse sequences, high-quality ventilation imaging has now been realised using natural-abundance xenon [89] and low dosages of enriched xenon [90], highlighting ^{129}Xe as a commercially-scalable contrast agent for routine clinical studies.

The non-ionising radiation nature of hyperpolarised gas MRI is suitable for longitudinal studies of disease progression or treatment response. For example, the increase in prevalence of ventilation defects in asthma patients after exercise and methacholine challenge [91], and the ventilation response to bronchodilator application in COPD and CF [92, 93], has been studied via multiple time-point ^{3}He ventilation imaging. Although xenon possesses anaesthetic properties [94], the low dosages used for lung MRI have been reported to be safe and tolerable over several breath-holds in humans [95, 96], which is promising for low-cost longitudinal screening of patients.

Hyperpolarised gas ventilation imaging can be combined with ^{1}H DCE perfusion MRI in order to evaluate regional ventilation-perfusion matching [97]. The potential for pooled assessment of ventilation and perfusion abnormalities is important in pulmonary embolism [80, 98], and the alteration of ventilation-perfusion relationships has been studied with hyperpolarised ^{3}He and ^{1}H MRI in patients with PE and post-lung transplant [97]. Furthermore, techniques and RF hardware for same-breath acquisition of hyperpolarised gas ventilation images and ^{1}H anatomical images [99, 100] have been recently developed that allow inherently co-registered, complementary structural and functional MR images to be obtained.

In addition to the visualisation of pulmonary ventilation, hyperpolarised gas MRI with ^{3}He and ^{129}Xe permits quantitative evaluation of alveolar microstructure. Diffusion-weighted MRI enables measurement of the apparent diffusion coefficient (ADC) of the hyperpolarised gas in the lungs. The ^{3}He ADC is reduced when compared to its free diffusion coefficient due to the restricting alveolar walls, however, in the presence of tissue destruction (e.g. in emphysema), the ADC increases because the gas diffusion is

10
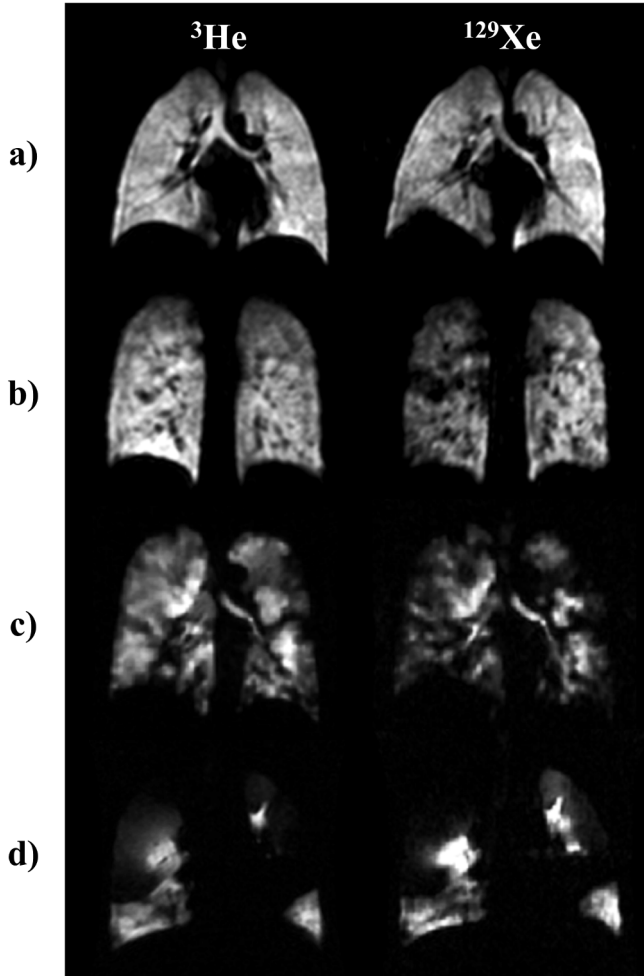
Figure 2.5: Comparison of ^{3}He and ^{129}Xe MR ventilation images of the lungs of a healthy never-smoker (a), a healthy smoker (b), a patient with asthma (c) and a patient with COPD (d). Progressively worse ventilation abnormalities can be seen from b) to d), with mild, patchy abnormalities in the smoker, more severe obstruction in the asthma subject and large regions of completely unventilated lung in the COPD subject. All images were acquired with an optimised 3D SSFP sequence [89]. The slice thickness and resolution for acquisitions a) and b) were identical. ^{3}He images for the asthma and COPD subjects were acquired with a lower slice thickness than ^{129}Xe images, however, for comparison, the ^{3}He images in c) and d) represent reconstructions that mimic the same slice thickness as the ^{129}Xe images.

less restricted [101]. Various geometrical [102, 103] and phenomenological [104, 105] models have been developed to relate observed ADC changes to quantitative physiological alterations in alveolar dimension or surface-area-to-volume ratio. Comprehensive ^{3}He diffusion-weighted MRI studies of emphysema patients [72, 106], asymptomatic smokers [107, 108] and asthma patients [109] have been performed to assess regional variations in diffusion restriction across the lungs, and good correlations with both spirometry [106, 110] and histology [111] have been reported. In addition, alterations in ^{3}He ADC have been mapped in the developing paediatric lung [112] and have been used as evidence of lung development post-pneumonectomy treatment of adenocarcinoma [113] and alveolarisation in young adults [114].

Again, despite the predominant use of ^{3}He in patient studies, hyperpolarised ^{129}Xe ADC mapping is likewise effective for assessment of COPD [115], and direct comparisons between diffusion-weighted MRI of the two nuclei have highlighted agreement in the spatial distribution of ADC values, and correlations in mean ADC values, in healthy volunteers, COPD patients and ex-smokers [85, 116]. Moreover, mean ADC values were observed to correlate with $T_{L,CO}$ and mean Hounsfield units from CT [85, 116]. Figure 2.6 presents a comparison of ^{3}He and ^{129}Xe ADC maps acquired from healthy volunteers and COPD patients.

Although ventilation imaging and ADC mapping are undoubtedly the most well-established and widely-applied hyperpolarised gas MRI techniques in a clinical setting, a number of additional experimental

^{3}He   **^{129}Xe**

a)

b)

ADC [cm^{2}s^{-1}]   ADC [cm^{2}s^{-1}]
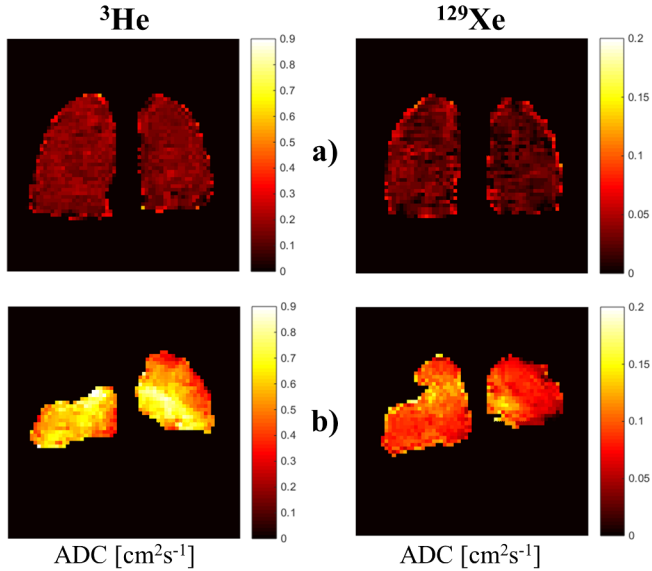
Figure 2.6: Example regional maps of the apparent diffusion coefficient (ADC) of helium (left) and xenon (right) in the lungs, derived from diffusion-weighted hyperpolarised gas MRI, using a 2D spoiled gradient echo sequence. a) One slice acquired from a healthy subject — the mean global ADC values ($\pm$ standard deviation) were 0.166 ± 0.064 cm^{2}s^{-1} and 0.032 ± 0.018 cm^{2}s^{-1} for ^{3}He and ^{129}Xe, respectively. b) One slice acquired from a patient with severe COPD, in which clear unventilated regions of the lung can be observed. The mean ADCs were significantly increased to 0.594 ± 0.131 cm^{2}s^{-1} and 0.090 ± 0.025 cm^{2}s^{-1} for ^{3}He and ^{129}Xe, respectively.

techniques have been developed to further investigate specific aspects of lung function.

Multiple-breath ventilation imaging methods have been implemented to quantify lung ventilation via metrics of ventilation heterogeneity or fractional ventilation (gas turnover per respiratory cycle). Originally demonstrated using multiple sequential imaging acquisitions after a variable number of inhalations of hyperpolarised ^{3}He to study gas wash-in in small animals [117, 118], the technique has subsequently been modified to measure regional gas wash-out in humans to characterise ventilation heterogeneity [119, 120] by acquiring multiple images after sequential exhalation-inspiration cycles of ^{3}He. This technique provides analogous quantitative information to the nitrogen wash-out pulmonary function test, but on a regional rather than global scale, and preliminary evidence suggests its potential utility in the assessment of CF [121]. In comparison to fractional ventilation imaging with ^{1}H OE-MRI (e.g. [33]), multiple-breath hyperpolarised gas imaging is potentially advantageous as a direct, quantitative regional measure of ventilation rather than a measure that is only proportional to lung ventilation.

Following a similar acquisition strategy of repeated ventilation images separated by a specified time gap, delayed ventilation of the small airways can be investigated [77, 122]; where apparently obstructed regions of the lung start to fill during the breath-hold period and present as ventilated regions in images acquired at a later time-point. The technique has been used to assess collateral ventilation pathways in COPD [77]. Although delayed ventilation effects can also be highlighted indirectly by long-range MR diffusion measurements [109], direct imaging methods may be preferred.

The dependence of the ^{3}He longitudinal relaxation time (T_1) on alveolar oxygen tension (i.e. partial pressure, pO$_2$) [123] can be exploited to infer alveolar pO$_2$ from T_1 changes over multiple MR acquisitions during a breath-hold [124, 125]. The alveolar pO$_2$ comprises information about ventilation, perfusion and gas exchange, and hyperpolarised gas pO$_2$ mapping MRI permits non-invasive regional quantification of oxygen uptake. Substantial delays between acquired MR images are required to induce sufficient ^{3}He signal decay, necessitating long breath-holds, which can be partially overcome with 3D sequences [126] or variable flip angle strategies and conservative image encoding schemes [127, 128]. To date, preliminary studies in patients with COPD [122, 127] and post-lung transplant [128, 129] have shown that regional pathological abnormalities in pO$_2$ can be effectively detected. Nevertheless, the application of this method

to obstructive lung disease is limited by collateral ventilation [122].

Phase contrast velocimetry (PCV) MRI offers a means to study gas flow in the lungs and major airways by sensitising the MR acquisition to the hyperpolarised gas velocity [130, 131]. The method has been validated via computational fluid dynamics modelling of the airways [132] and has important clinical implications for particle deposition and drug delivery in the respiratory system. PCV MRI was recently applied to examine gas flow oscillations in the human lungs induced by cardiac motion [133], and shows potential for evaluation of pathological flow abnormalities in patients with obstructive lung disease.

Current developments of ^{129}Xe lung MRI techniques utilise xenon's diffusivity, solubility and MR properties to target the detection of dissolved ^{129}Xe in the parenchyma and blood for the non-invasive assessment of pulmonary gas exchange [134]. Xenon is mildly soluble in somatic tissues and blood [135], and the ^{129}Xe isotope displays unique NMR chemical shift signatures when dissolved in lung tissues and plasma (T/P), and red blood cells (RBCs) [136, 137] (as illustrated in Figure 2.7a). As such, this "dissolved-phase" ^{129}Xe can be detected separately from "gaseous-phase" ^{129}Xe in the alveoli.

Dynamic ^{129}Xe NMR spectroscopy, for example the chemical shift saturation recovery (CSSR) technique, permits studies of gas exchange dynamics [138], which can be analysed using mathematical models of diffusion [138, 139] to quantify global changes in lung microstructure [140], e.g. in COPD [141], and to detect alveolar septal thickening in ILD [142] (Figure 2.7b), both of which have been reported to correlate significantly with the $T_{L,CO}$ metric [141, 142].

Direct imaging of dissolved-phase ^{129}Xe in the lungs is challenging due to the very short T_2^* relaxation times and low concentration of dissolved xenon. One proposed method to separately image dissolved and gaseous ^{129}Xe is to exploit the large NMR chemical shift difference in their resonances to resolve the two compartments in a single image [143]. Although a promising surrogate of ventilation (gaseous ^{129}Xe) and perfusion (dissolved ^{129}Xe) in humans [143], this technique does not permit distinction of the T/P and RBC components, and as such, the dissolved ^{129}Xe signal is only partially comprised of signal from ^{129}Xe in the blood (i.e. it represents only a *pseudo*-perfusion measurement). A number of rapid acquisition techniques with non-Cartesian image encoding schemes [144] have been introduced that exploit different echo times [145, 146] to distinguish the dissolved ^{129}Xe components, and yield RBC images that delineate only ^{129}Xe that has traversed the air-blood barrier into the pulmonary capillaries. These methods have been employed to regionally visualise gas exchange impairment in patients with COPD and asthma [141, 147] (e.g. Figure 2.7c) and regions of low ^{129}Xe RBC signal have been reported to correlate visually with fibrosis on CT in IPF patients [148].

In contrast to direct imaging of dissolved-phase ^{129}Xe, an alternative technique has been proposed to indirectly probe gas exchange function by studying the decay in the ^{129}Xe gas signal following the application of exchange-weighted radiofrequency pulses [149]. Entitled xenon polarisation transfer contrast (XTC) MRI [149, 150], this method has been applied to map the alveolar surface-area-to-volume ratio in the human lungs [151] and regionally depict gas exchange efficiency in the lungs of healthy volunteers and COPD subjects, in attempt to quantify tissue loss due to emphysema [152, 153].

Exposure of hyperpolarised gas MRI to a broad clinical audience has historically been hindered by the limited commercial availability of specialised hardware and the relative expense of the isotopes when compared to other contrast agents. In recent years, fluorinated gas MRI, which exploits the non-zero
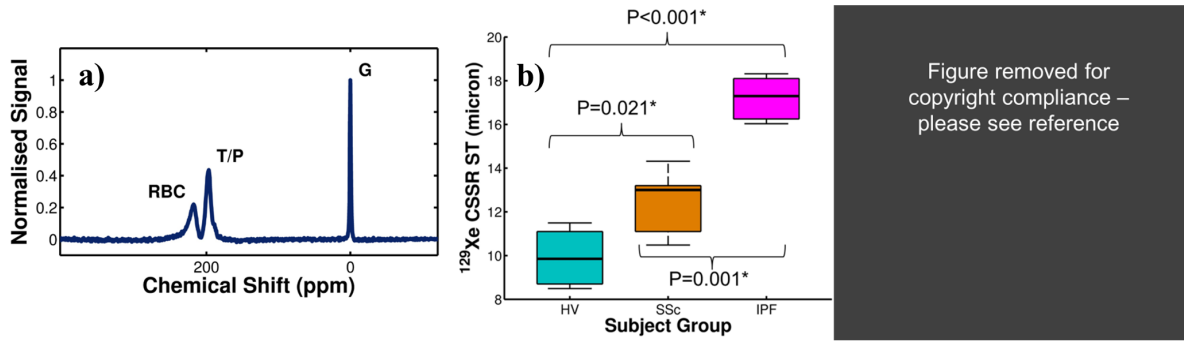
Figure 2.7: MR of pulmonary gas exchange with hyperpolarised ^{129}Xe. a) ^{129}Xe NMR spectrum acquired from the human lungs, exhibiting distinct peaks from ^{129}Xe gas in the alveoli (G), ^{129}Xe dissolved in tissues and blood plasma (T/P) and in red blood cells (RBC). b) Alveolar septal thickness (ST) values estimated from ^{129}Xe chemical shift saturation recovery (CSSR) MR in healthy volunteers (HV, light blue), scleroderma patients (SSc, yellow) and idiopathic pulmonary fibrosis patients (IPF, pink) (adapted from data in [142]). ^{129}Xe CSSR is sufficiently sensitive to detect interstitial tissue thickening in both diseases. c) Chemical shift imaging (CSI) of ^{129}Xe in the lungs of a healthy subject (H6), two patients with COPD (C3,4) and two with asthma (A2,4), depicted in the form of maps of the ratio of signal intensities from each of the NMR peaks (reproduced with permission from [141]). In patients, the gas exchange maps (RBC-to-GP and RBC-to-TP) were considerably more heterogeneous than in healthy subjects, and the mean ratios were reduced in subjects with severe COPD.

nuclear spin of ^{19}F, has emerged as a prospective alternative means to visualise pulmonary ventilation. Fluorinated gases do not require hyperpolarisation, however the innate MR signal is typically low, necessitating continuous breathing of a fluorinated gas mixture prior to breath-hold imaging for adequate SNR to be realised (see e.g. [154]). Although the SNR and resolution of ^{19}F lung MRI is presently inferior to that of hyperpolarised ^{3}He or ^{129}Xe, the possibility of human application has been demonstrated in healthy volunteers and patients with a variety of lung diseases using gradient echo sequences with an inhaled perfluoropropane-oxygen mix [155], and subsequently UTE sequences have been reported to offer enhanced SNR in healthy volunteers [156]. However, ^{19}F gases are not soluble in biological substances and thus cannot be utilised to probe pulmonary gas exchange.

The advent of low-cost ^{129}Xe polarisers constructed from widely-available components, in combination with reductions in gas cost (afforded by naturally-abundant xenon [89] and unpolarised fluorine-19 [154] for example), are paving the way for improved dissemination of multi-nuclear MR methods in the clinic. In particular, hyperpolarised ^{129}Xe is emerging as a cost-effective contrast agent for high-quality MR imaging of pulmonary ventilation. In Sheffield, we have recently established the technique as part of clinical diagnostic referrals with a regulatory licence for manufacture of hyperpolarised ^{3}He and ^{129}Xe gas for routine clinical lung imaging.

2.3   Conclusion

^{1}H lung MRI is now an established non-ionising radiation alternative to CT for structural imaging of the lung, and offers a range of techniques for quantitative investigation of diversified aspects of pulmonary function that have considerable clinical value. MRI with hyperpolarised noble gases provides exquisite depiction of lung ventilation and presents a quantitative functional tool for assessment of lung microstructure and gas exchange. Recent advances in MR pulse sequence acquisition strategies, polarisation technology and image processing algorithms are promising for routine diagnostic lung imaging and clinical translation

of these sensitive multi-nuclear lung MR imaging techniques.

Chapter 3

Theory

This chapter provides an overview of the necessary background required to understand some of the concepts introduced in the experimental chapters of this thesis. The chapter is divided into two main sections; the first covering the morphometry and physiology of the lungs, and the second reviewing the fundamental physics of magnetic resonance imaging and the specifics of hyperpolarised gas MRI.

3.1 Introduction to lung anatomy and physiology

This section describes the basic morphology of the lungs and the physiological basis of ventilation and gas exchange. The content of this section approximately follows that of "What Makes a Good Lung?", E. R. Weibel, *Swiss Med Weekly*, (2009) [157], and the first three chapters of "Respiratory Physiology: The Essentials (Ninth Edition)", J. B. West, *Lippincott Williams & Wilkins*, (2012) [158].

3.1.1 Lung structure and function
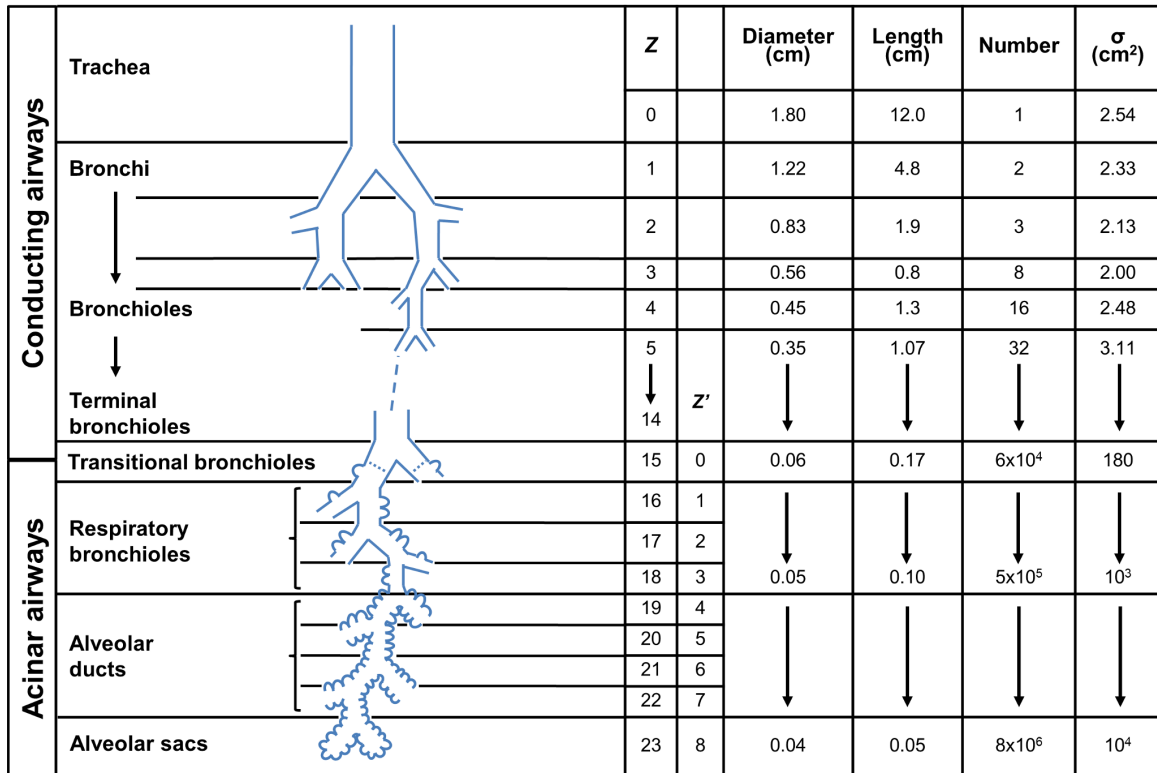
The lungs are ideally suited to their primary function of facilitating exchange of oxygen from the air into the bloodstream. There are three critical anatomical features of the lung for facilitating this gas exchange: (i) the pulmonary airways (which transport inspired air to the alveoli); (ii) the gas exchange surface of the alveoli (where inspired air traverses the blood-gas barrier from the alveoli into the pulmonary capillaries); (iii) the pulmonary vascular system (which perfuses the alveoli and carries away the transferred gas). This subsection provides an introduction to the morphometry of these three main features.

(i) The normal adult human tracheo-bronchial tract can be divided into 23 generations, which become progressively smaller the deeper into the lung they penetrate. A resin cast of these airways is presented in Figure 3.1, and approximate values for relevant morphological parameters as a function of depth are shown in Figure 3.2. The trachea bifurcates into the left and right main bronchi, which in turn bifurcate, and their products bifurcate, and so on and so forth. The first 14 generations from the trachea to the terminal bronchioles — the deepest generation without alveoli — are known as the "conducting airways" ($Z = 0$-14, Figure 3.2), whose function is to "conduct" the inspired gas to the alveolar regions for gas exchange. Beyond the terminal bronchioles, the transitional bronchioles represent the bridge between the conducting airways and the "acinar airways" ($Z' \neq 0$, Figure 3.2), which span the region from the respiratory bronchioles (where the first alveoli form), to the alveolar ducts and sacs (that have a complete lining of alveoli).

(ii) There are approximately 480 million alveoli in the human lungs (range: 274-790 million; coefficient of variation: 37%) [161]. The geometry of the alveoli is tailored to maximise the available surface area for gas exchange, resulting in a total surface area twice the size of a squash court. Each alveolar airspace spans a diameter of approximately 250 microns and is lined with an extremely thin (~ 1 μm) tissue barrier to the pulmonary capillaries. Relevant morphometric data is summarised in Table 3.1.

Figure 3.1: Resin cast of the human airway tree and pulmonary blood vessels. Left: airways only; right: airways, pulmonary arteries (red) and veins (blue). Reproduced with permission from [157].

			Z	Z'	Diameter (cm)	Length (cm)	Number	σ (cm²)
Conducting airways	Trachea		0		1.80	12.0	1	2.54
	Bronchi		1		1.22	4.8	2	2.33
			2		0.83	1.9	3	2.13
			3		0.56	0.8	8	2.00
	Bronchioles		4		0.45	1.3	16	2.48
			5		0.35	1.07	32	3.11
	Terminal bronchioles		14	Z'				
Acinar airways	Transitional bronchioles		15	0	0.06	0.17	6x10⁴	180
	Respiratory bronchioles		16	1				
			17	2				
			18	3	0.05	0.10	5x10⁵	10³
	Alveolar ducts		19	4				
			20	5				
			21	6				
			22	7				
	Alveolar sacs		23	8	0.04	0.05	8x10⁶	10⁴

Figure 3.2: Diagram of the airway generations in the Weibel model, with associated morphometric parameters. Adapted with permission from [159], using data based on [160]. (σ denotes the typical cross-sectional area of airways in a particular generation.)

The blood-gas barrier (i.e. tissue barrier) is composed of epithelial and endothelial layers separated by an interstitial space and supported by basement membranes. 95% of the alveolar epithelium is comprised of specialised, flat, Type I pneumocyte cells embedded in an elastin-collagen mesh, with the remaining 5% made up by cuboidal, Type II pneumocytes which secrete surfactants to modify the compliance of the lung. On the other hand, the endothelium is principally composed of squamous cells. An electron microscope image of a pulmonary capillary, showing high magnification of the blood-gas barrier, is shown in Figure 3.3. It can be seen that the pulmonary capillaries are just wide enough to permit the passage of red blood cells (approximately 7-10 microns in diameter [158]).

(iii) As a consequence of their extreme thinness, the pulmonary capillaries are inherently very fragile. The

Morphometric Parameter	Mean $\pm$ standard error
Alveolar surface area	130 ± 12 m^2
Capillary surface area	115 ± 12 m^2
Capillary volume	194 ± 30 mL
Alveolar diameter	~ 250 μm
Tissue barrier harmonic thickness	0.62 ± 0.04 μm
Total barrier harmonic thickness	1.11 ± 0.1 μm

Table 3.1: Summary of lung morphometric data. Adapted with permission from [157], using data compiled from [162], [163] and [164].
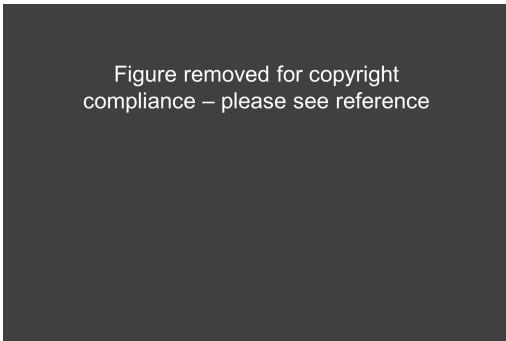
Figure 3.3: Electron microscope image of the pulmonary capillary and blood-gas barrier in the normal human lung. A: alveolus; C: capillary; EP: epithelium; IS: interstitial space; EN: endothelium; RBC: red blood cell. Reproduced and annotated with permission from [165] (originally taken from [162]).

output of the right ventricle must be re-distributed from the pulmonary artery across the dense network of capillaries that line the alveoli; hence, small changes in the pulmonary capillary blood pressure can impact adversely on the alveolar microstructure. As quoted in Table 3.1, the capillary blood volume is of the order of 200 mL, and on average, each RBC spends approximately 0.75 seconds in the pulmonary capillaries (this is known as the RBC transit time). Capillary units are perfused in parallel, such that blood of the same oxygen content is distributed to each unit.

3.1.2 Lung volumes and spirometry

The volume of inspired, expired and residual gas in the lungs at different points during normal (tidal) breathing, and at the extremes of inspiration and expiration, is crucial information for describing the lung structure and function, and provides reference points for quantitative measurements, for example from pulmonary function tests and imaging examinations. Table 3.2 and Figure 3.4 give written and pictorial descriptions, respectively, of the lung volumes that are important in routine clinical practice, and also pertinent to the content of this thesis.

The term pulmonary function tests (PFTs) encompasses a range of measurement techniques that typically involve patients breathing air or specific tracer gases in order to probe particular aspects of lung physiology. Spirometry denotes the most commonly performed subset of PFTs, and includes the measurement of FEV_1, FVC, and the ratio of these two parameters, FEV_1/FVC. In addition, spirometry can provide information about VC and thus FEV_1/VC. FEV_1 and FVC are determined by measuring the volume of gas exhaled by a patient as a function of time after forced exhalation from maximum inspiration. The subject is instructed to inhale to maximum inspiration after a period of steady tidal breathing, then

Lung volume / capacity	Description
Tidal volume (TV)	The peak-to-peak inspiratory-to-expiratory air volume during normal tidal breathing.
Inspiratory reserve volume (IRV)	The additional volume of air beyond TV that can be inspired when a subject inhales to their total lung capacity.
Expiratory reserve volume (ERV)	The volume of air beyond TV that can be expired when a subject exhales to their maximum capacity.
Residual volume (RV)	The volume of the lungs remaining after a subject has exhaled to their maximum capacity.
Forced expiratory volume in 1 second (FEV_1)	The volume of air that can be forcibly expired in 1 second *.
Total lung capacity (TLC)	The total volume of air that can be contained in the lungs.
Inspiratory capacity (IC)	The total volume of air that can be inspired from tidal exhalation.
Vital capacity (VC)	The total volume of inspired air when TLC is achieved. (VC = ERV + TV + IRV)
Forced vital capacity (FVC)	The amount of air that can be forcibly exhaled from TLC *.
Functional residual capacity (FRC)	The volume of air remaining in the lungs after normal tidal exhalation.

Table 3.2: Lung volume (top half) and capacity (bottom half) acronyms and their descriptions relevant for spirometry applications. *: all volumes and capacities except FEV_1 and FVC are shown graphically in Figure 3.4.

forcibly exhale to their full capacity, and then return to normal tidal breathing (this process is shown diagrammatically in Figure 3.4). These fundamental measurements are used routinely in the diagnosis of different pulmonary disorders (in particular COPD) and in distinguishing obstructive airway disease and restrictive disease [i].

The results of PFTs are generally reported in comparison to "predicted" values for a given patient, which are derived from empirical reference equations for normal, healthy subjects with equivalent antrhopometric characteristics to the patient (e.g. sex, age, height, race). For example, COPD is typically classified in terms of %-predicted spirometry values as follows: mild (FEV_1/FVC < 70% and FEV_1 $\geq$ 80%-predicted); moderate (FEV_1/FVC < 70% and FEV_1 < 80%-predicted); severe (FEV_1 < 50%-predicted) [166].

3.1.3 Ventilation and gas exchange

Ventilation defines the process by which air enters the lungs and fills the alveolar airspaces. The total ventilation is the volume of gas inspired or expired from the lung per a certain time interval, or equivalently, the product of the volume of inhaled or exhaled gas and the respiration frequency. This can be divided into contributions from the conducting airways (also known as anatomic "dead space" because they do not contribute to gas exchange) and from the acinar airways:

---

[i]Measurements of additional lung volumes such as TLC, FRC and RV require the use of techniques other than spirometry, for example body plethysmography, which will not be covered in this thesis.
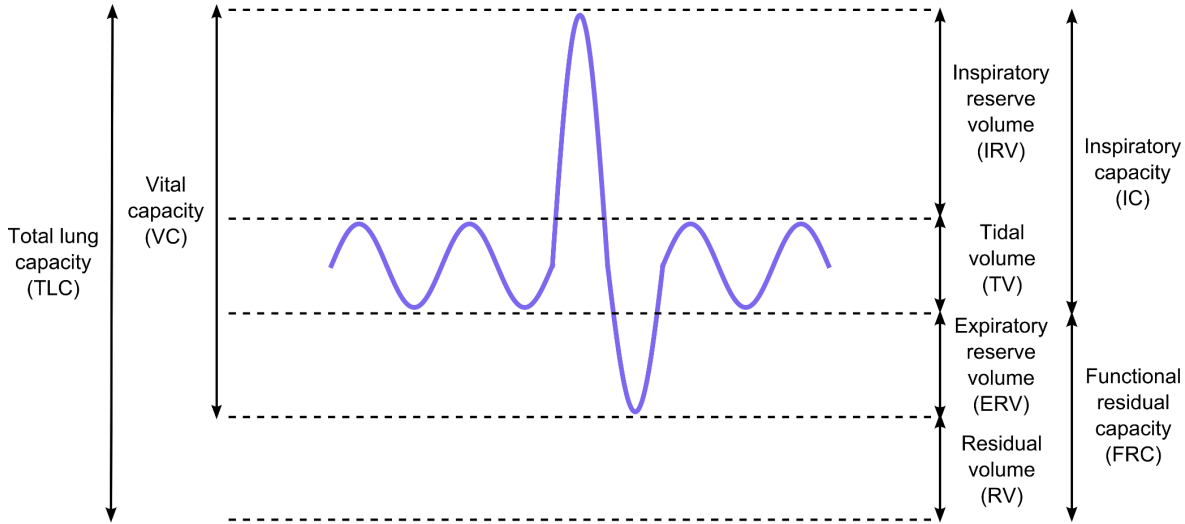
Figure 3.4: Diagram of lung volumes achieved during steady tidal breathing followed by forced inhalation and exhalation, as would be measured by spirometry apparatus.

$$\dot{V}_T = V_T n = \dot{V}_D + \dot{V}_A \tag{3.1}$$

where $\dot{V}_T$, $\dot{V}_D$ and $\dot{V}_A$ are the total, dead space and alveolar ventilations, respectively, V_T is the total volume of expired gas, and n is the breathing frequency (e.g. number of breaths per minute). It is worth noting that the anatomic dead space considers only the volume of the conducting airways; however in practice, there is additional "alveolar" dead space in the lungs resulting from non-perfused alveoli. The anatomical and "physiological" dead space is approximately equivalent in normal subjects (since the alveolar dead space is negligible; physiological = anatomical + alveolar), however in subjects with severe disease, the physiological dead space can become significantly greater than the anatomical dead space. The alveolar ventilation can be determined by re-arranging Equation 3.1 to $\dot{V}_A = \dot{V}_E - \dot{V}_D$ and measuring the expired ventilation, $\dot{V}_E$ and appropriate dead space volumes.

Gas exchange defines the transfer of gas, typically oxygen, from the alveolar airspaces, across the blood-gas barrier and into the pulmonary capillaries. This occurs by passive diffusion of the gas along a partial pressure gradient through the barrier membrane. Efficient gas exchange is facilitated by *matching* the alveolar ventilation and capillary perfusion, such that the optimum partial pressure gradient is created.

Exchange of oxygen across the alveolar-capillary membrane in normal, healthy subjects is limited by the capillary perfusion; i.e. the rate at which oxygen transfers into the capillaries is constrained by the rate at which oxygen is extracted from the capillary bed by blood flow (since the diffusion of oxygen across the membrane itself is relatively fast). On the other hand, the uptake of gases such as carbon monoxide is governed by the rate of diffusion of the gas across the membrane; i.e. the capillary perfusion is sufficiently fast that the capillaries are not saturated with CO on the scale of the RBC transit time, because the diffusion of the gas through the membrane is slow in comparison. The concept of diffusion-limited and perfusion-limited gas exchange is introduced pictorially in Figure 3.5.

Figure 3.5: Pulmonary capillary partial pressure of N_2O, O_2 and CO through the course of a capillary. Transfer of N_2O and O_2 (in normal subjects) is perfusion-limited, whilst transfer of CO is diffusion-limited. Reproduced with permission from [158].

The ability of the lungs to exchange gas in this manner can be quantified by performing a pulmonary function test to determine what is known as the diffusing capacity of the lung for carbon monoxide ($D_{L,CO}$) in the US, or the transfer factor of the lung for carbon monoxide ($T_{L,CO}$) in Europe. Both terms have the same physiological meaning, but the measurement units are different: $D_{L,CO}$ is measured in mL/min/mmHg, whilst $T_{L,CO}$ is measured in mmol/min/kPa [ii]. Carbon monoxide is chosen because its uptake in the pulmonary capillaries is highly diffusion-limited, as illustrated in Figure 3.5. The physiological basis of the measurement is described in the following.

From Fick's law, the rate of diffusion of gas across the membrane separating the alveoli from the capillaries, $\dot{V}$, is dependent on the surface area, A, and thickness, x, of the membrane, the diffusion coefficient of the gas in that medium, D, and difference in partial pressure of the gas between the two media:

$$\dot{V} = \frac{AD\left(P_A - P_c\right)}{x} \tag{3.2}$$

where P_A and P_c are the gas pressures in the alveoli and capillaries, respectively. It can be therefore seen that the rate of gas exchange in the lungs is controlled principally by the alveolar morphometry. The diffusing capacity of the gas across the alveolar-capillary membrane, D_L, is defined as:

$$D_L = \frac{AD}{x} = \frac{\dot{V}}{P_A - P_c} \tag{3.3}$$

For CO, the partial pressure in the capillary is regarded as negligible, because CO transfer across the alveolar-capillary membrane is diffusion-limited, and as such, the associated partial pressure increase in the capillary over time is small. Thus, the diffusion capacity of the lung for carbon monoxide is related by:

[ii]The following conversion can be applied between the two sets of units: $D_{L,CO} \approx 2.986\times\ T_{L,CO}$.

$$D_{L,CO} = \frac{\dot{V}_{CO}}{P_{A,CO}} \qquad (3.4)$$

$D_{L,CO}$ is generally expressed as the product of two quantities, namely the CO transfer coefficient (K_{CO}) and the alveolar volume of the lung containing CO (V_A), which are the output of the standard PFT for deriving $D_{L,CO}$, as discussed below:

$$D_{L,CO} = K_{CO}V_A \qquad (3.5)$$

where K_{CO} is the CO uptake (change in concentration [CO]) per unit time, t, per unit volume, per unit driving pressure:

$$K_{CO} = \frac{\Delta[CO]}{P_{A,CO}\Delta t} \qquad (3.6)$$

These equations are only valid during breath-hold, and can be used to infer $D_{L,CO}$ with a single breath technique [167], by recording the CO concentration decay over time. A volume of gas containing a non-negligible concentration of CO is inhaled until TLC is reached, breath-hold is maintained for a period of a few seconds whilst CO transfers into the bloodstream, and then the gas is expired. The concentration of CO in the inspired and expired gas is recorded by an infrared analyser, and V_A is inferred from the concentration of the tracer gas with which the CO is mixed (usually helium):

$$V_A = V_I \frac{F_{I,He}}{F_{A,He}} \qquad (3.7)$$

where V_I is the inspired volume of helium, and $F_{I,He}$ and $F_{A,He}$ are the fractional concentrations of helium in inspired and expired gas, respectively.

In the above, the diffusion capacity is only considered to be governed by diffusive transport of CO across the alveolar-capillary membrane. However, in practice, it is also influenced by the finite reaction rate of CO with haemoglobin. As formulated by Roughton and Forster [168], these two contributions can be separated by analogy with two conductances in series:

$$\frac{1}{D_{L,CO}} = \frac{1}{D_{M,CO}} + \frac{1}{\theta_{CO}V_c} \qquad (3.8)$$

where $D_{M,CO}$ is the "membrane conductivity", θ_{CO} is the rate of reaction between CO and haemoglobin,

and V_c is the volume of haemoglobin in the capillary blood.

Whilst both these factors must be considered in the explanation of pathological alterations to $D_{L,CO}$, it is notable for the later sections of this thesis that xenon does not react with haemoglobin and hence in an equivalent analysis of the xenon diffusion capacity, the second term in Equation 3.8 is not required [169, 170]. Furthermore, xenon is perfusion-limited [171], and therefore exhibits similar behaviour to N_2O as shown in Figure 3.5. This behaviour is discussed further in reference to techniques for quantifying diffusion limitation with hyperpolarised ^{129}Xe MRI in Chapter 6.

3.2 Fundamentals of magnetic resonance imaging

This section describes the fundamental physics of MRI, providing the required theoretical basis for understanding the spectroscopy and imaging techniques employed in the subsequent sections of this thesis. The content of this section is derived from a number of seminal MRI textbooks and adopts a combination of semi-classical and quantum approaches for describing the motion of spins. For further information, we refer the reader to [172–180].

3.2.1 Nuclear spins in a magnetic field

Quantum mechanical introduction

Spin angular momentum is an intrinsic property of protons, neutrons, electrons and whole nuclei. Spin is quantised, with fermions such as protons, neutrons and electrons each possessing a spin of $\frac{1}{2}$. Nuclei with an even number of neutrons and an even number of protons have zero total nuclear spin, and are unsuitable for NMR. Odd-odd nuclei (nuclei with an odd number of neutrons and odd number of protons) have a positive integer value of nuclear spin, and both odd-even and even-odd nuclei have half integral spin. Conventional MRI exploits the endogenous spin-$\frac{1}{2}$ ^{1}H nuclei in the human body, which consist of a single proton.

An electron possesses both spin angular momentum $\boldsymbol{S}$ and orbital angular momentum $\boldsymbol{L}$, with a total angular momentum $\boldsymbol{J} = \boldsymbol{L} + \boldsymbol{S}$. On the other hand, the orbital angular momentum of a nucleus is negligible, and only the nuclear spin, $\boldsymbol{I}$, contributes to its total angular momentum. Nuclei with non-zero spin have an associated magnetic moment, $\boldsymbol{\mu}$, defined by:

$$\boldsymbol{\mu} = \gamma \boldsymbol{I} \tag{3.9}$$

where the constant of proportionality, γ, is a scalar quantity known as the gyromagnetic ratio [iii]. The nuclear spin $\boldsymbol{I}$ is not just a vector quantity, but a quantum mechanical operator. As such, the nuclear spin can be "observed" by considering its component, m, along a particular axis. For convenience, here we choose to project the spin angular momentum along the z axis, and denote $m \equiv m_z$. Generally termed the spin angular momentum quantum number, m can take $2I + 1$ values (where I is the absolute value of the nuclear spin) in the range: $-I, -I+1, \cdots, I-1, I$, corresponding to $2I+1$ different quantum mechan-

---

[iii] $\boldsymbol{\mu}$ and $\boldsymbol{I}$ are co-linear by definition. It is worth noting that nuclei can have a negative γ, resulting in an oppositely-orientated magnetic moment and spin.

ical states, which are degenerate in energy in the absence of a magnetic field. In practice, a nucleus does not inhabit one specific state; rather it exists in a linear superposition of all $2I+1$ states, $|\psi\rangle$, described by:

$$|\psi\rangle = \sum_m a_m |m\rangle \tag{3.10}$$

where a_m are the amplitudes associated with the $2I+1$ "basis states", $|m\rangle$. When observing the spin angular momentum along the z axis, the spin angular momentum quantum number is an eigenvalue of the eigenstates $|m\rangle$, which adhere to the following equation:

$$\boldsymbol{I_z} |m\rangle = m |m\rangle \tag{3.11}$$

where $\boldsymbol{I_z}$ is the nuclear spin angular momentum operator for the z axis.

When placed in a magnetic field, $\boldsymbol{B_0}$, the degeneracy between the nuclear states is lifted; the states become divided in energy according to the Zeeman Hamiltonian, $\boldsymbol{H}$:

$$\boldsymbol{H} = -\gamma \hbar \boldsymbol{B_0} \boldsymbol{I_z} \tag{3.12}$$

which has "eigen-energies":

$$E = \gamma \hbar B_0 m \tag{3.13}$$

where $B_0 = |\boldsymbol{B_0}|$. These equations arise from the definition of the interaction energy of a magnetic moment in a magnetic field, $\boldsymbol{E} = -\boldsymbol{\mu} \cdot \boldsymbol{B_0}$. The reduced Plank's constant, $\hbar$, is the fundamental unit of energy for a quantised system. The energy level diagram for the most simplistic spin-$\frac{1}{2}$ system is shown in Figure 3.6. The two energy states correspond, for a nucleus with positive gyromagnetic ratio, to $\left|-\frac{1}{2}\right\rangle$, at an energy of $\gamma \hbar B_0/2$, and $\left|\frac{1}{2}\right\rangle$, at an energy of $-\gamma \hbar B_0/2$, with an energy difference of $\Delta E = \gamma \hbar B_0$. By convention, $\left|-\frac{1}{2}\right\rangle$ is usually referred to as the "spin-down state", and $\left|\frac{1}{2}\right\rangle$ as the "spin-up state", corresponding to spins being aligned anti-parallel and parallel to the magnetic field, respectively. (Note: for a nucleus with negative gyromagnetic ratio, the states are reversed in energy, i.e. the spin-up ($\left|\frac{1}{2}\right\rangle$) state is at higher energy.) From this point onwards, we will consider only spin-$\frac{1}{2}$ systems.

Although it has been noted above that the wave function of a fundamental particle or nucleus comprises a linear combination of its basis states, it is helpful for the description of the nuclear magnetic resonance phenomenon to consider that each particle or nucleus can inhabit one of the two states at any given time;
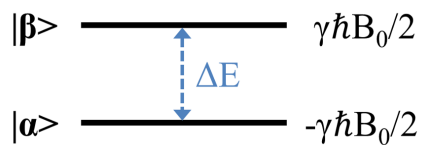
Figure 3.6: Energy level diagram for a spin-$\frac{1}{2}$ (two spin-state) nucleus in a magnetic field. For a nucleus with positive gyromagnetic ratio, $|\beta\rangle \equiv \left|-\frac{1}{2}\right\rangle$; $|\alpha\rangle \equiv \left|\frac{1}{2}\right\rangle$. $\Delta E = \gamma\hbar B_0$, and $\hbar = \frac{h}{2\pi}$, where $h = 6.63 \times 10^{-34}$ Js is Planck's constant.

indeed, when a spin is "observed", it exhibits distinct energies corresponding to one of the two states, rather than a continuum of energies in between. The NMR phenomenon then relies upon inducing transitions between the two nuclear states, which is possible by applying a time-dependent "perturbation" with an angular frequency of ω_0, and an energy described by the Planck equation:

$$\Delta E = \hbar\omega_0 \tag{3.14}$$

In NMR, this time-dependent perturbation is an alternating magnetic field, which can be related by a perturbation Hamiltonian, $\boldsymbol{H_p}$, for example along the x axis:

$$\boldsymbol{H_{p,x}} = -\gamma\hbar\boldsymbol{B_{1,x}}\boldsymbol{I_x}\cos\left(\omega_0 t\right) \tag{3.15}$$

where $\boldsymbol{I_x}$ and $\boldsymbol{B_{1,x}}$ are the x components of the spin angular momentum operator and applied alternating field, respectively, and t is time. As a consequence of the construction of $\boldsymbol{I_x}$, this perturbation Hamiltonian can only induce transitions between states m and m' where $m' = m \pm 1$, i.e. two states that are adjacent in energy. Thus, by combining Equations 3.13 and 3.14, we arrive at:

$$\omega_0 = -\gamma B_0 \tag{3.16}$$

This is the Larmor equation that underpins the angular frequency of a perturbation required to induce a resonant transition between the two ground states of a spin-$\frac{1}{2}$ nucleus, as a function of γ, an intrinsic property of the nucleus, and B_0, a fundamental property of the NMR system. By convention, the negative sign in Equation 3.16 indicates that positive-γ nuclei will exhibit a negative Larmor frequency and a negative-γ species will have a positive Larmor frequency. The same equation results from a classical treatment of the motion of spins in a magnetic field, as discussed in the following subsection.

Semi-Classical description of spins in a magnetic field

In order to move from a description of the energy levels of a single nuclear spin to arrive at a macroscopic description of magnetisation, we must consider an ensemble of spins, and their propensity to inhabit one

of the two spin states. In the presence of a magnetic field, spins exhibit a slight preference to align with the field rather than against it, i.e. to inhabit the slightly lower energy $\left|\frac{1}{2}\right\rangle$ state as shown in Figure 3.6. The relative populations of the two states, $P_{\left|\pm\frac{1}{2}\right\rangle}$ (which can also be thought of as the relative probabilities of inhabiting either state), are well defined by the Boltzmann distribution:

$$P_{\left|\pm\frac{1}{2}\right\rangle} = \frac{N_{\left|\pm\frac{1}{2}\right\rangle}}{N} = \frac{\exp\left(\pm\gamma\hbar B_0/2k_BT\right)}{\exp\left(-\gamma\hbar B_0/2k_BT\right) + \exp\left(\gamma\hbar B_0/2k_BT\right)} \tag{3.17}$$

where $N_{\left|\pm\frac{1}{2}\right\rangle}$ is the number of nuclei in a given state and N is the total number of nuclei in the system; $k_B = 1.38 \times 10^{-23}$ J.K^{-1}, the Boltzmann constant, T is the temperature of the system. The population difference between the two states is known as the polarisation, P, of the sample:

$$P = P_{\left|\frac{1}{2}\right\rangle} - P_{\left|-\frac{1}{2}\right\rangle} = \tanh\left(\frac{\Delta E}{2k_BT}\right) \approx \frac{\gamma\hbar B_0}{2k_BT} \tag{3.18}$$

where the approximation $\tanh(x) \approx x$ at small x is justified by the fact that in general, the thermal energy of a spin system is far greater than the energy difference between the two spin states. As an example, for ^{1}H at 1.5 T and room temperature (293 K), the polarisation $P \approx 5 \times 10^{-6}$. From this result, the macroscopic magnetisation (per unit volume) of a spin ensemble in a magnetic field of strength B_0, caused by the population difference between the two states, can be determined by:

$$M_0 = \mathcal{N}\left(P_{\left|\frac{1}{2}\right\rangle} - P_{\left|-\frac{1}{2}\right\rangle}\right)\mu \approx \mathcal{N}\frac{\gamma^2\hbar^2 B_0}{4k_BT} \tag{3.19}$$

where $\mathcal{N}$ is the number of spins per unit volume, and the magnetic moment operator $\boldsymbol{\mu} = \gamma\hbar\boldsymbol{I}$, such that $\mu = \gamma\hbar/2$.

Continuing the semi-classical treatment, the following concerns the semi-classical approach of describing the motion of spins in a static magnetic field, $\boldsymbol{B_0}$, which for simplicity, we can consider to be pointing in the z direction, i.e. $\boldsymbol{B_0} = B_0\hat{\mathbf{k}}$, where $\hat{\mathbf{k}}$ is the unit vector of the z axis. In many textbooks $\boldsymbol{H_0} = H_0\hat{\mathbf{k}}$ is used to define the applied magnetic field. However, when considering a macroscopic sample of spins, the magnetic susceptibility becomes important, and hence is it appropriate to consider the magnetic induction, $\boldsymbol{B_0}$ rather than the applied magnetic field:

$$\boldsymbol{B_0} = \mu_0\left(1 + \chi\right)\boldsymbol{H_0} \tag{3.20}$$

Here, $\mu_0 = 4\pi \times 10^{-7}$N.A^{-2} is the permeability of free space and χ is the magnetic susceptibility of the

sample (i.e. the propensity of the material to develop a magnetic moment [iv]).

In the presence of a magnetic field, a nuclear spin will experience a torque, $\boldsymbol{\tau}$, governed by the cross product of its magnetic moment and the applied magnetic field, which acts to align the spin with the magnetic field:

$$\boldsymbol{\tau} = \frac{\mathrm{d}\boldsymbol{I}}{\mathrm{d}t} = \boldsymbol{\mu} \times \boldsymbol{B_0} \tag{3.21}$$

where the definition of torque is the rate of change of angular momentum. Equivalently, for a spin ensemble, the net magnetisation vector, $\boldsymbol{M}$, resulting from the average of the individual magnetisation vectors associated with the spins in the ensemble, experiences a torque. Since $\boldsymbol{\mu} = \gamma \boldsymbol{I}$, and the magnetisation is the magnetic moment per unit volume, we can write:

$$\frac{\mathrm{d}\boldsymbol{M}}{\mathrm{d}t} = \gamma \boldsymbol{M} \times \boldsymbol{B_0} \tag{3.22}$$

which, for $\boldsymbol{B_0} = B_0 \hat{\mathbf{k}}$, can be decomposed into the following:

$$\frac{\mathrm{d}M_x}{\mathrm{d}t} = \gamma M_y B_0 \tag{3.23}$$

$$\frac{\mathrm{d}M_y}{\mathrm{d}t} = -\gamma M_x B_0 \tag{3.24}$$

$$\frac{\mathrm{d}M_z}{\mathrm{d}t} = 0 \tag{3.25}$$

In its "equilibrium state", the net magnetisation vector points along z with an initial magnitude of M_0, given by Equation 3.19. However, if the magnetisation is displaced from the z axis by an angle of α in the direction of the y axis, the above equations can be solved with the initial condition $\boldsymbol{M}(t = 0) = 0\hat{\mathbf{i}} + M_0 \sin(\alpha)\hat{\mathbf{j}} + M_0 \cos(\alpha)\hat{\mathbf{k}}$, to yield:

$$M_x(t) = M_0 \sin(\alpha) \sin(\omega_0 t) \tag{3.26}$$

$$M_y(t) = M_0 \sin(\alpha) \cos(\omega_0 t) \tag{3.27}$$

$$M_z(t) = M_0 \cos(\alpha) \tag{3.28}$$

[iv] On a macroscopic scale, most materials do not naturally exhibit a magnetic moment; instead $\boldsymbol{\mu}$ is typically induced according to $\boldsymbol{\mu_{ind}} = \frac{1}{\mu_0} V \chi \boldsymbol{B_0}$, where V is the volume of the object.

These equations describe the precessional motion of the net magnetisation vector with angular frequency ω_0 about the z axis after being perturbed by an angle of α in the direction of the y axis, as shown pictorially in Figure 3.7a. The Larmor equation (Equation 3.16) is typically written with a negative sign, such that the direction of precession is "negative" for positive-γ nuclei, i.e. *clockwise* if the spin is observed in a direction opposite to the magnetic field, and "positive" for negative-γ nuclei, i.e. *anti-clockwise*. The displacement angle α is known as the flip angle in NMR.
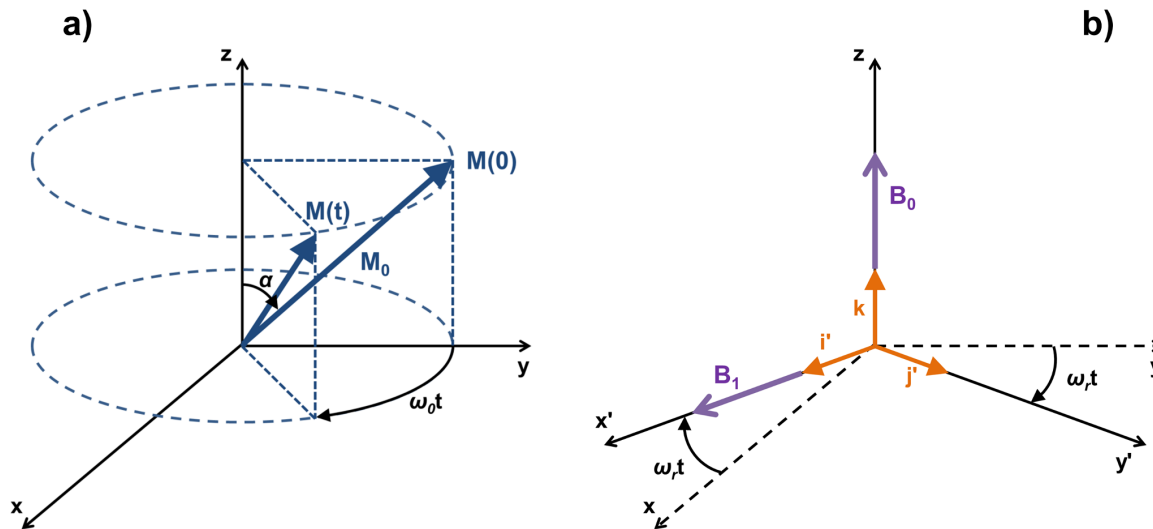
Figure 3.7: Coordinate representations of spin excitation and precession (a), and the rotating reference frame (b). In both cases, the static magnetic field is applied along the z axis. In a), α denotes the angle by which spins are displaced from the z axis towards the y axis. After time t, the net magnetisation vector has precessed by an angular distance of $\omega_0 t$ with respect to its position at $t = 0$. (Note: a chemical species with a negative gyromagnetic ratio exhibits precessional motion in the *opposite* direction with respect to $\boldsymbol{B_0}$ compared to that of a positive gyromagnetic ratio species.) In b), the coordinate system x', y', z is shown to be rotating about the z axis at a frequency of $-\omega_r$. In this rotating frame, both the $\boldsymbol{B_1}$ and $\boldsymbol{B_0}$ fields are stationary, and are aligned along the x' and z axes, respectively. Both diagrams are adapted with permission from [176].

In practice, the perturbation of the magnetisation vector from its rest position is typically achieved by applying an oscillating magnetic field, $\boldsymbol{B_1}$, in a direction perpendicular to the $\boldsymbol{B_0}$ field, and which is rotating with an angular frequency ω_r:

$$\boldsymbol{B_1}(t) = B_1 \cos\left(\omega_r t\right) \hat{\mathbf{i}} - B_1 \sin\left(\omega_r t\right) \hat{\mathbf{j}} \tag{3.29}$$

By substituting $\boldsymbol{B} = \boldsymbol{B_0} + \boldsymbol{B_1}$ for $\boldsymbol{B_0}$ in Equation 3.22, the following expressions can be obtained for the three components of magnetisation:

$$\frac{\mathrm{d}M_x}{\mathrm{d}t} = \gamma \left[M_y B_0 + M_z B_1 \sin\left(\omega_r t\right) \right] \tag{3.30}$$

28

$$\frac{\mathrm{d}M_y}{\mathrm{d}t} = \gamma \left[M_z B_1 \cos\left(\omega_r t\right) - M_x B_0 \right] \tag{3.31}$$

$$\frac{\mathrm{d}M_z}{\mathrm{d}t} = -\gamma \left[M_x B_1 \sin\left(\omega_r t\right) + M_y B_1 \cos\left(\omega_r t\right) \right] \tag{3.32}$$

which can be solved by inspection to yield:

$$M_x\left(t\right) = M_0 \sin\left(\omega_r t\right) \sin\left(\omega_0 t\right) \tag{3.33}$$

$$M_y\left(t\right) = M_0 \sin\left(\omega_r t\right) \cos\left(\omega_0 t\right) \tag{3.34}$$

$$M_z\left(t\right) = M_0 \cos\left(\omega_r t\right) \tag{3.35}$$

where $\omega_r = \gamma B_1$ is the angular frequency associated with the rotating magnetic field. Comparing to Equations 3.26 to 3.28, we arrive at an expression for the flip angle in terms of the $\boldsymbol{B_1}$ field:

$$\alpha = \omega_r t = \gamma B_1 t \tag{3.36}$$

Equations 3.33 to 3.35 dictate that in the presence of both static and rotating magnetic fields, the magnetisation simultaneously precesses about both. Visualisation of this motion is complicated in the conventional laboratory frame, and therefore it is appropriate to transform the problem to a coordinate system that rotates with an angular frequency of $-\omega_r$ about the z axis, such that both the $\boldsymbol{B_1}$ and $\boldsymbol{B_0}$ fields appear stationary. This coordinate system, designated by x', y' and z, is known as the rotating frame, and is illustrated in Figure 3.7b.

Writing the full form of the angular frequency of the rotating frame as $\boldsymbol{\Omega} = 0\hat{\mathbf{i}} + 0\hat{\mathbf{j}} - \omega_r \hat{\mathbf{k}}$, the time derivative of the magnetisation can be separated into two components:

$$\frac{\mathrm{d}\boldsymbol{M}}{\mathrm{d}t} = \frac{\delta \boldsymbol{M}}{\delta t} + \boldsymbol{\Omega} \times \boldsymbol{M} \tag{3.37}$$

where $\frac{\delta \boldsymbol{M}}{\delta t}$ is the rate of change of $\boldsymbol{M}$ with time as viewed from the rotating frame. Combining this with Equation 3.22, we obtain:

$$\frac{\delta \boldsymbol{M}}{\delta t} = \gamma \boldsymbol{M} \times \left(\boldsymbol{B} + \frac{\boldsymbol{\Omega}}{\gamma} \right) \tag{3.38}$$

where the term in brackets can be denoted as the effective field, $\boldsymbol{B_{eff}} = B_1\hat{\mathbf{i}} + \left(B_0 - \frac{\omega_r}{\gamma}\right)\hat{\mathbf{k}}$. If $\frac{\omega_r}{\gamma} = B_0$, $\boldsymbol{B_{eff}} = B_1\hat{\mathbf{i}}$, and the net magnetisation vector precesses around the $\boldsymbol{B_1}$ field. Otherwise, the effective longitudinal (z) field is non-zero, and Equation 3.38 dictates that the magnetisation will precess about an effective field that is offset from the $\boldsymbol{B_1}$ axis.

3.2.2 Relaxation and the Bloch equations

After perturbation from equilibrium — e.g. caused by the application of an oscillating magnetic field — the net nuclear magnetisation vector does not precess indefinitely around the effective field, but instead is restored to its equilibrium state (parallel to the direction of $\boldsymbol{B_0}$) over time by the process of "spin-lattice" (or "longitudinal") relaxation. This process is analogous to the damping of a pendulum caused by air resistance or friction, and represents the energy lost by the spin system via collisional, rotational or electromagnetic interactions with the "lattice" of surrounding nuclei, atoms and molecules. Spin-lattice relaxation denotes the growth/re-growth of magnetisation in the longitudinal (z) direction according to the following expression:

$$\frac{\mathrm{d}M_z}{\mathrm{d}t} = -\frac{(M_z - M_0)}{T_1} \tag{3.39}$$

where $M_z = M_z(t)$ and T_1, the spin-lattice relaxation time, represents the characteristic time-scale of spin-lattice relaxation. This equation has a solution of the form of an exponential growth function, with T_1 as the exponential time constant:

$$M_z(t) = M_z(0)\exp\left(-\frac{t}{T_1}\right) + M_0\left(1 - \exp\left(-\frac{t}{T_1}\right)\right) \tag{3.40}$$

As such, for an initial longitudinal magnetisation $M_z(0) = 0$, e.g. resulting from a perturbation of flip angle 90°, the T_1 represents the time after which approximately 63% of M_0 is recovered along the z direction.

Whenever spin-lattice relaxation is present in a system, an accompanying relaxation process describing the damping of the transverse (x and y) components of magnetisation is also present. This process is known as "spin-spin" or "transverse" relaxation and arises from a combination of indirect energy exchange with the lattice (as in T_1 decay), and additional direct mechanisms, which cause the characteristic relaxation time for spin-spin relaxation, T_2 to be less than or equal to T_1. Spin-spin relaxation is governed by the rate equation:

$$\frac{\mathrm{d}M_{xy}}{\mathrm{d}t} = \frac{-M_{xy}}{T_2} \tag{3.41}$$

which has a solution of the form of a decaying exponential, where the exponential time constant T_2 in this case defines the time after which the transverse magnetisation has decayed to approximately 37% of its initial value.

$$M_{xy}(t) = M_{xy}(0) \exp\left(-\frac{t}{T_2}\right) \tag{3.42}$$

Equations 3.39 and 3.41 can be combined with the equation for torque in the rotating frame (Equation 3.38) in order to derive the Bloch equations in the rotating frame:

$$\frac{dM_x}{dt} = \gamma M_y\left(B_0 - \frac{\omega_r}{\gamma}\right) - \frac{M_x}{T_2} \tag{3.43}$$

$$\frac{dM_y}{dt} = \gamma M_z B_1 - \gamma M_x\left(B_0 - \frac{\omega_r}{\gamma}\right) - \frac{M_y}{T_2} \tag{3.44}$$

$$\frac{dM_z}{dt} = -\gamma M_y B_1 - \frac{M_z - M_0}{T_1} \tag{3.45}$$

These relationships describe the general form of the dynamics of a spin system in the presence of a static magnetic field $\boldsymbol{B_0}$ and an oscillating magnetic field $\boldsymbol{B_1}$ along the x axis, and are a critical reference point for many NMR applications. An example solution to these equations can be derived for the most simple case where the magnetisation has been perturbed by $90°$ from the z axis and lies entirely along the y axis at time $t = 0$ (i.e. $M_z(0) = M_x(0) = 0$, $M_y = M_0$). Also assuming that there is no oscillating field applied after this initial displacement, i.e. $B_1 = 0$, the Bloch equations can be solved by the following functions:

$$M_x(t) = M_0 \exp\left(\frac{-t}{T_2}\right)\sin(\omega't) \tag{3.46}$$

$$M_y(t) = M_0 \exp\left(\frac{-t}{T_2}\right)\cos(\omega't) \tag{3.47}$$

$$M_z(t) = M_0\left[1 - \exp\left(\frac{-t}{T_1}\right)\right] \tag{3.48}$$

where $\omega' = \omega_0 - \omega_r$.

Mechanisms of relaxation and Chemical shift

As mentioned in the previous subsection, spin-lattice relaxation is not only responsible for the return of the net magnetisation vector to thermal equilibrium, but also for the establishment of the net magneti-

sation vector, or net magnetic moment, in the first place. Consider a spin ensemble with an isotropic distribution of spin, and hence magnetic moment, orientations. Instantaneously switching on a magnetic field will cause the spins to precess about the magnetic field direction. Molecular motions, including translations and rotations, cause rapid fluctuations of the local magnetic fields associated with each nucleus and electron. The field experienced by a given nucleus at a particular time is the summed effect of the applied field and the neighbouring fields, thus, each nucleus experiences a field with a slightly different magnitude and orientation at any given instant. These fluctuating fields break the isotropy of the distribution of nuclear spin orientations.

In other words, over time, each nucleus experiences many different microscopic fields, which cause the angle between the spin and the external field to change. This process is not isotropic because the thermal dynamics of the system dictate that the spins have a slight preference to align with the external field, as this is the state of lowest energy. Eventually, the spin ensemble establishes a thermal equilibrium with a net distribution of spins aligned parallel to the external field [v]. The exact same processes act to re-establish a thermal equilibrium magnetisation if the net magnetisation is perturbed, e.g. by the application of a rotating magnetic field as discussed earlier.

In thermal equilibrium, the summation over all spins with different precession angles averages to yield zero transverse component of the net magnetisation vector. Then, on perturbation from equilibrium, the transverse component becomes non-zero and the net magnetisation precesses about the z axis in the same manner as the individual spins. However, the resulting transverse component of the net magnetisation vector decays to zero over time because small fluctuations in the magnetic fields experienced by each nucleus lead to differences in phase between the precession of different nuclei. Hence, the spins in the ensemble lose coherence with each other and the net magnetisation diminishes to zero. This process is known as spin-spin relaxation.

As stated in the previous section, it is often written that $T_2 \leq T_1$ since all processes that induce spin-lattice relaxation will also lead to spin-spin relaxation (and additional mechanisms can induce the latter whilst not influencing the former) [vi]. Before summarising the exact mechanisms of relaxation, since many relaxation processes are driven by molecular motion, it is appropriate to introduce the concept of molecular correlation time τ_c, which is the average time taken for a given molecule to rotate by one radian. This parameter is a characteristic of a particular type of molecule, and exhibits a strong influence on the relaxation times, as shown in Figure 3.8.

Slow motion (i.e. long correlation time) is typical of large, complex molecules such as polymers or proteins. On the other hand, small molecules exhibit fast molecular "tumbling" (τ_c is sometimes called the molecular tumbling rate), and for these molecules, T_1 and T_2 values can be of a similar magnitude. The x-axis in Figure 3.8 can be interpreted as the molecular size or the resistance to motion / viscosity. The minimum T_1 for a given nucleus, i.e. the fastest rate of recovery of longitudinal magnetisation, occurs at a correlation time $\tau_c = \frac{1}{\omega_0}$. In other words, molecular motions are most effective at inducing longitudinal

---

[v]Though this equilibrium state is stable, the thermal motions continue and the orientation of individual spins continues to change, whilst the established net magnetisation remains fixed.

[vi]Although this is often the case, the theoretical limit is actually $T_2 \leq 2T_1$ [174, 181], and experimental evidence has shown that T_2 can indeed be greater than T_1 in certain situations [182].
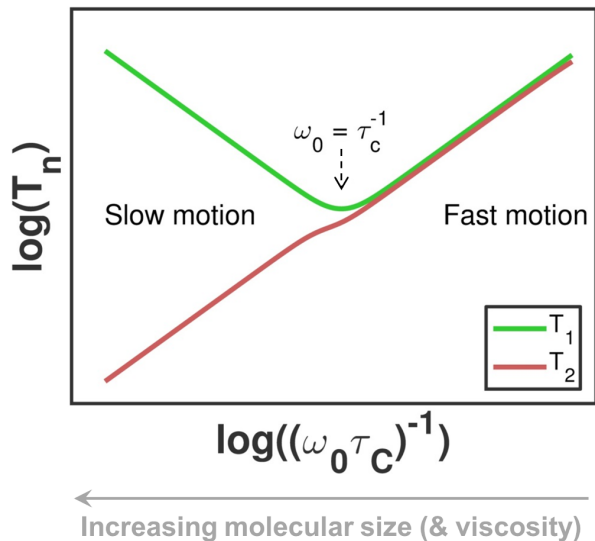
Figure 3.8: Logarithmic plot of the relationship between T_1 and T_2 relaxation times and the molecular correlation time, τ_C. Adapted with permission from [172].

relaxation when they occur at a rate equal to that of the Larmor frequency.

Relaxation can result from a number of different mechanisms, some of which are briefly listed in the following:

i) Dipole-dipole: this is the direct coupling between the dipole of a nucleus and another dipole, either on the same molecule, or on a different molecule. This can occur between any two dipoles, including those generated by an isolated electron or proton, or a nucleus with non-zero spin. Molecular tumbling induces fluctuating fields at each dipole, and both spin-lattice and spin-spin relaxation can occur to differing degrees depending on the rate of molecular tumbling compared to the Larmor frequency. The magnitude of the dipole-dipole effect on the relaxation rate is inversely proportional to the distance between the dipoles raised to the power of six, and thus, dipole-dipole coupling is most effective at relaxing nuclei that are bonded together.

ii) Chemical shift anisotropy: as discussed in the *Aside* below, the external applied field induces currents in the electron clouds of the molecules containing the nuclear spins. These currents in-turn generate an additional magnetic field, which alters the magnetic field experienced by a given nucleus. This process is known as the chemical shift effect. When anisotropy in chemical shift is present, local differences in the induced magnetic fields lead to relaxation. Molecular tumbling causes the orientation and magnitude of these induced magnetic fields to change as a function of time; however, if the tumbling rate is rapid, asymmetries can average out and hence relaxation by chemical shift anisotropy can be alleviated. The magnitude of this effect is proportional to the square of the magnetic field strength.

iii) Scalar (J)-coupling: the indirect interaction of two nuclei lying on the same molecule, mediated by shared bonding electrons. This effect is independent of magnetic field strength.

33

iv) Spin rotation: the interaction of nuclear spins with the local magnetic fields generated by the circular motion of electrons in a rotating molecule. The magnitude of this effect is dependent on the frequency of molecular collisions. This mechanism typically governs the observed relaxation behaviour of gases at high temperatures.

v) Electric quadrupole coupling: for nuclei with spin $> \frac{1}{2}$, which have a non-spherical (oblate/prolate) nuclear charge distributions, this is the interaction between nuclei and local electric field gradients in the surrounding electron clouds. This process does not occur for spin-$\frac{1}{2}$ nuclei which exhibit a spherically-symmetric nuclear charge distribution.

vi) Molecular translation: the movement of nuclear spins from one environment to another on the time-scale of the NMR experiment, e.g. by flow or diffusion, can cause a precessional phase shift between nuclei, and consequentially, a loss of transverse magnetisation coherence, i.e. spin-spin relaxation. This typically occurs when spins pass through susceptibility gradients, and the magnitude of this effect is dependent on the square of the field gradient and the time required for the spin to pass through the gradient.

vii) Chemical exchange: the movement of a spin from one chemical / molecular environment to another with a different chemical shift (and hence Larmor frequency). This process causes spin-spin relaxation via a loss in transverse magnetisation coherence. The magnitude of this effect is proportional to the square of the applied magnetic field and is strongly influenced by the exchange rate, which varies between molecules.

Most of these mechanisms pertain to interactions between the internal electric and magnetic fields of the spin sample. When analysing the internal energy of the spin system, it is appropriate to consider the contribution of each of these mechanisms to the internal Hamiltonian of the system, $\boldsymbol{H_{int}}$. Figure 3.9 provides an overview of the approximate relative contribution of each mechanism to the internal Hamiltonian, and hence its propensity for inducing relaxation, and furthermore summarises the organisation of the interactions - i.e. whether they can occur for a single spin, or two or more spins.

Aside: Chemical Shift

In order to understand the chemical shift anisotropy effect, it is necessary to introduce the concept of chemical shift. In addition, this concept is pre-requisite knowledge for the understanding of ^{129}Xe NMR of pulmonary gas exchange, as presented in Chapter 6.

The magnetic field experienced by a particular nucleus is dependent on its chemical environment. The action of an applied magnetic field tends to produce currents in the electron cloud of each molecule, and in response, the electron cloud generates an "induced" magnetic field that acts to oppose the applied field (by virtue of Lenz's law), and "shield" the nucleus, such that it experiences a local field:
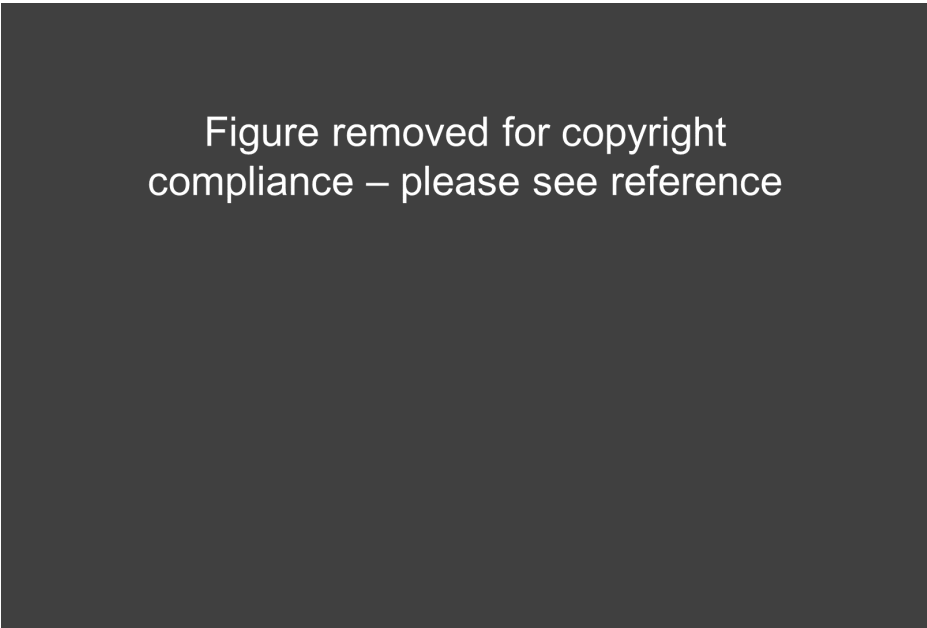
Figure 3.9: Organisation and relative magnitude of internal spin interaction terms, i.e. contributions to the internal Hamiltonian $\boldsymbol{H_{int}}$. (Electric quadrupolar moments are not present in spin-$\frac{1}{2}$ nuclei.) Reproduced with permission from [179].

$$\boldsymbol{B_{loc}} = \boldsymbol{B_0} + \boldsymbol{B_{induced}} = \boldsymbol{B_0}\left(1 - \boldsymbol{\sigma}\right) \tag{3.49}$$

where the induced field $\boldsymbol{B_{induced}}$ is linearly-dependent on the applied field, and $\boldsymbol{\sigma}$ is the shielding tensor. The shielding tensor is a 3×3 matrix, representing the fact that the orientation of the induced field may differ from that of the applied field, depending on the orientation of the molecule in question. In general, a set of axes can be found such that the shielding tensor, and the corresponding chemical shift tensor $\boldsymbol{\delta} = -\boldsymbol{\sigma}$, can be diagonalised such that all off-diagonal elements become zero. The chemical shift can be then reported as a single number, δ_{iso}, which represents the average value over all different orientations of the induced field:

$$\delta_{iso} = \frac{1}{3}\left(\delta_{xx} + \delta_{yy} + \delta_{zz}\right) \tag{3.50}$$

where $\delta_{xx,yy,zz}$ are the three diagonal elements of the diagonalised chemical shift tensor. From the above relationships, it can be seen that an increase in shielding, or a corresponding decrease in chemical shift, implies a reduction of the local magnetic field strength and hence a corresponding reduction in the Larmor frequency of a given nucleus.

In actuality, for a solute nucleus within a solvent, a number of mechanisms contribute to the shielding of the nucleus, and hence the resulting chemical shift, including: the bulk susceptibility of the medium, the anisotropy of the molecular susceptibility, van der Waals forces between the solute and solvent, and polar effects caused by the interaction of solvent and solute electron clouds (see e.g. [183]). This discus-

sion is beyond the scope of this thesis, but is an important consideration when analysing the origin of a measured chemical shift.

Note: chemical shift values are conventionally quoted in parts per million with respect to the resonance frequency of the nuclei of interest in a standard chemical environment. For ^{1}H nuclei, this reference point is either tetramethylsilane (TMS) in organic solvents or sodium 2,2-dimethyl-2-silapentane-5-sulfonic acid (DSS) in aqueous solutions. As encountered in later chapters, ^{129}Xe chemical shifts are conventionally quoted with respect to the Larmor frequency of ^{129}Xe in the gaseous-phase.

3.2.3 Free induction decay, and spin and gradient echoes: Principles of NMR detection

Description of a free induction decay

This subsection concerns the detection of an NMR signal. As introduced in previous subsections, energy must be input to a spin system in order to perturb its thermal equilibrium state, i.e. to displace the net magnetisation vector from alignment with the external magnetic field. In NMR, this perturbation is achieved by applying a secondary, smaller, magnetic field that is rotating with a frequency equal to the Larmor frequency of spins precessing about the static magnetic field. This Larmor frequency lies in the radiofrequency (RF) part of the electromagnetic spectrum, and the application of the rotating magnetic field is often termed as RF excitation. It may therefore be thought that it would be possible to detect the RF energy subsequently emitted by a nucleus. However, the RF energy released by a single nucleus is insufficient for detection, and furthermore, nuclei within a sample emit RF energy in all directions. Various theories exist to explain NMR detection using a quantum mechanical framework; the most popular paradigm being that NMR detection relies on coherent spontaneous emission from a sample of nuclei [184], whilst opposition to this paradigm includes the explanation of NMR detection by the exchange of virtual photons [185]. These theories are beyond the scope of this work, and for simplicity, the detection of an NMR signal is considered as follows by adopting a semi-classical approach.

The precession of magnetisation in the plane transverse to that of the external field will induce an oscillating current in a coil of wire that has its winding axis also positioned transverse to that of the external field. This is a consequence of Faraday's law of induction, which states that the electromotive force, $\mathcal{E}$ induced in a coil of wire with N turns is directly proportional to the rate of change of magnetic flux Φ_B:

$$\mathcal{E} = -N\frac{\mathrm{d}\Phi_B}{\mathrm{d}t} \tag{3.51}$$

where the negative sign arises from Lenz's law that the direction of the induced electromotive force opposes that of the changing magnetic flux. The magnetic flux through a surface is defined as the integral of the magnetic field (a.k.a. flux density) normal to the surface: $\Phi_B = \iint_S \boldsymbol{B} \cdot \hat{\mathbf{n}}\mathrm{d}A$. The electromotive force is the line integral of the electric field over the boundary of the surface: $\mathcal{E} = \oint \boldsymbol{E} \cdot \mathrm{d}\boldsymbol{l}$. These relationships can be used in combination with Stokes' theorem — that the line integral of a function $\boldsymbol{F}$ along the boundary of a surface is equivalent to the surface integral of the curl of that function normal to the

surface — to relate Equation 3.51 to the following Maxwell equation:

$$\boldsymbol{\nabla} \times \boldsymbol{E} = -\frac{\partial \boldsymbol{B}}{\partial t} \tag{3.52}$$

This fundamental equation states that an electric field is always associated with an alternating magnetic field; it is this electric field that induces motion of the electrons within the wiring of the coil. The current induced in the coil oscillates with a frequency equal to the Larmor frequency, and has a decaying amplitude. This signal is known as the free induction decay (FID), and has a rate of decay governed by the T_2 and the effects of spatial inhomogeneity of the external magnetic field $\boldsymbol{B_0}$; two contributions which are combined in the definition of the T_2^* relaxation time:

$$\frac{1}{T_2^*} = \frac{1}{T_2} + \frac{1}{T_2'} \tag{3.53}$$

where T_2' is the relaxation time associated with $\boldsymbol{B_0}$ inhomogeneity ($\frac{1}{T_2'} = \gamma \Delta B_{0,i}$, where $\Delta B_{0,i}$ expresses the spatial variation in the amplitude of the external field).

Typical Larmor frequencies in MRI at standard clinical field strengths are of the order of tens of MHz and above, too high for accurate conversion of the analogue current signal into digital form. Instead, the oscillation frequency is down-converted with respect to a reference frequency, ω_{ref}, such that the resulting FID oscillates with a frequency $\Delta\omega = \omega_0 - \omega_{ref}$. Two output signals are generated by the NMR receiver, chosen to be 90° out of phase with each other in order to represent orthogonal phases of the magnetisation, i.e. the real and imaginary components of a complex FID. (In effect, this is equivalent to detecting M_x and M_y.) This procedure allows the distinction of Larmor frequencies that are greater than and lower than ω_{ref}, which would not be possible by analysis of a single output signal [vii]. Note: if $\Delta\omega = 0$, there is no oscillatory component to the FID.

Following RF excitation [viii] of a certain flip angle (as introduced in Section 3.2.1), the complex FID signal (as discussed in the *Aside* below, this is directly proportional to the net magnetisation) can be written as follows:

$$S\left(t\right) = S_0 \exp\left(i\Delta\omega t\right) \exp\left(-\frac{1}{T_2^*}\right) \tag{3.54}$$

which can be decomposed into its real and imaginary components by expanding the exponential:

[vii]This can be understood by considering the Fourier transform of the cosine and sine functions; the cosine function is even, and its Fourier transform gives two peaks of equal amplitude in the frequency domain at $\pm\omega$, whilst the sine function is odd, such that its Fourier transform gives two peaks at $\pm\omega$ but with oppositely-signed amplitudes. The two signals must be summed together to leave only one single peak at $+\omega$ (separate analysis of one signal or the other would not permit distinction of the peak at $+\omega$ from that at $-\omega$).

[viii]From this point onwards, "RF excitation" will be used interchangeably with the term "RF pulse", which corresponds to a displacement of the net magnetisation vector by the application of a magnetic field rotating at a frequency in the RF range of the electromagnetic spectrum.

$$S_{real}(t) = S_0 \cos(\Delta\omega t) \exp\left(-\frac{1}{T_2^*}\right) \tag{3.55}$$

$$S_{imag}(t) = S_0 \sin(\Delta\omega t) \exp\left(-\frac{1}{T_2^*}\right) \tag{3.56}$$

where S_0 is the signal at time $t = 0$, and $i = \sqrt{-1}$. In practice, there will be an additional $\exp(i\phi_r)$ term in Equation 3.54 to account for the absolute receiver phase, ϕ_r (which means that S_{real} and S_{imag} do not correspond exactly to S_y and S_x), however, for the present analysis, we can consider that the receiver phase is zero or has been accounted for in post-processing of the FID signal. The time domain FID can be converted into the frequency domain by a Fourier transformation:

$$\mathcal{F}[f(t)] = F(\omega) = \int_{-\infty}^{\infty} f(t) \exp(-i\omega t)\, \mathrm{d}t \tag{3.57}$$

where $\mathcal{F}$ is the Fourier transform operation, $f(t)$ and $F(\omega)$ are the time-domain and frequency-domain representations of a signal, respectively. The underlying principle of the Fourier transform is that any time-domain signal can be decomposed into a summation of a series of sinusoidal waveforms, each with different frequencies and amplitudes. The operation in Equation 3.57 thus links the two representations of a given signal. Taking the Fourier transform of the complex time-domain signal in Equation 3.54, we can obtain the real and imaginary components of the NMR spectrum, which is the frequency domain representation of the FID and exhibits the fundamental frequency of the oscillating signal ($\Delta\omega$):

$$Re\{\mathcal{F}[S(t)]\} = \frac{S_0 T_2^*}{1 + (\omega - \Delta\omega)^2 T_2^{*2}} \tag{3.58}$$

$$Im\{\mathcal{F}[S(t)]\} = -\frac{S_0(\omega - \Delta\omega)T_2^{*2}}{1 + (\omega - \Delta\omega)^2 T_2^{*2}} \tag{3.59}$$

These functions describe the *absorption* Lorentzian (real) and *dispersion* Lorentzian (imaginary), respectively. The maximum height of the absorption spectrum occurs at $\Delta\omega = 0$, and its full width at half maximum (FWHM) in units of Hz is $\frac{1}{\pi T_2^*}$. The real and imaginary parts of an FID and the corresponding NMR spectrum are illustrated graphically in Figure 3.10.

Note: in practice, the NMR signal may comprise a number of different components with different frequencies. A general FID consisting of m components, with corresponding amplitudes a_m, transverse relaxation times, $T_{2,m}^*$, and frequencies $\Delta\omega_m$ can be written as follows:

$$S(t) = \sum_m a_m \exp(i\Delta\omega_m t) \exp\left(-\frac{1}{T_{2,m}^*}\right) \tag{3.60}$$

where the amplitudes a_m can be considered to encompass a phase offset ϕ_m for each component: $a_m = |a_m| \exp\{i\phi_m\}$. The same procedure applies for analysing the individual components of the frequency representation of an NMR spectrum; i.e. a signal with multiple components is comprised of a summation of complex Lorentzian terms.
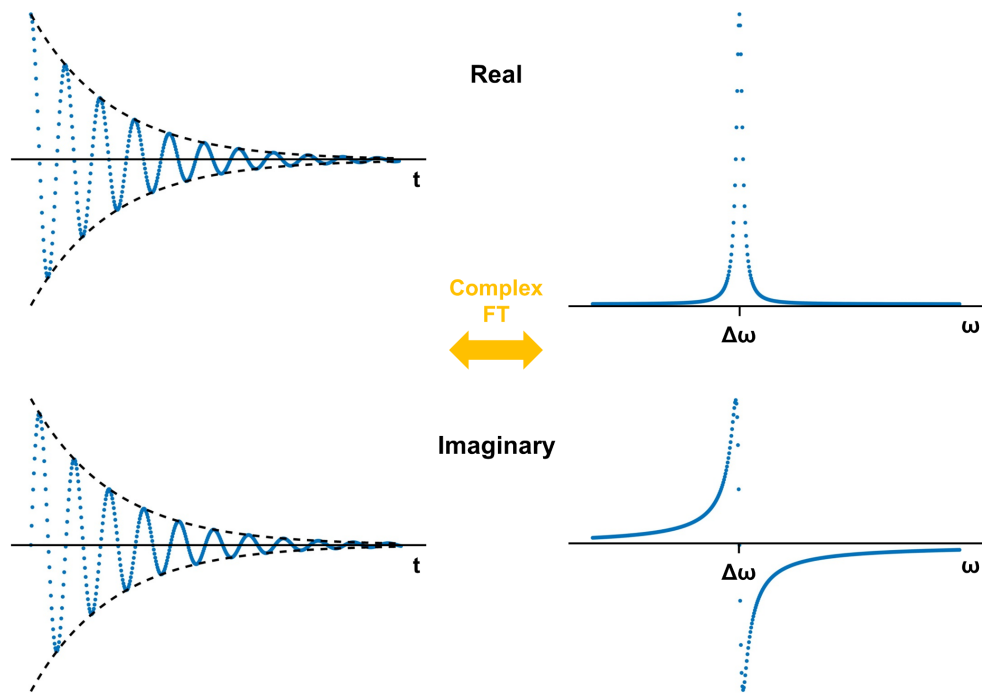
Figure 3.10: Left: real and imaginary parts of the free induction decay (FID), and right: the corresponding real (absorption) and imaginary (dispersion) parts of the complex NMR spectrum resulting from a complex Fourier transformation of the FID. The FWHM of the absorption and positive and negative peak separation of the dispersion spectrum are both equal to $\frac{1}{\pi T_2^*}$.

Aside: SNR of an NMR experiment

In the above discussion, the direct proportionality of S_0 and M_0 was introduced. The origin for this, and consideration of the experimental factors governing the available NMR signal, and also the noise associated with NMR measurements, was reported by Hoult and Richards [186]. Here, we review the salient points of their work, to provide an expression for the signal to noise ratio of an NMR experiment.

From Equation 3.51, it is known that the electromotive force induced in a receiver coil is governed by the rate of change of magnetic field in a direction perpendicular to the surface of a sample. Equivalently, the field produced by a coil through which a current is flowing is given by the same equation. For a sample of magnetisation $\boldsymbol{M}$ within the effective region of the coil, the infinitesimal magnetic moment normal to an area dA of the sample, $d\boldsymbol{\mu} = I\hat{\mathbf{n}}dA$, for current I, can be combined with the definition of magnetisation $\boldsymbol{M} = \frac{d\boldsymbol{\mu}}{dV}$ to yield, for a coil with one turn:

$$\mathcal{E} = -\frac{\mathrm{d}\Phi_B}{\mathrm{d}t} = -\iint_S \frac{\mathrm{d}\boldsymbol{B_1}}{\mathrm{d}t} \cdot \hat{\mathbf{n}} dA = \int_{sample} \frac{\partial}{\partial t} \left\{ \frac{\boldsymbol{B_1}}{I} \cdot \boldsymbol{M} \right\} dV \tag{3.61}$$

which shows that the electromotive force induced in the coil can be derived if the $\boldsymbol{B_1}$ of the coil is known at all points in the sample. Assuming that the magnetisation of the sample has been excited by a flip angle of 90° such that all magnetisation lies in the transverse plane:

$$\mathcal{E} = \omega_0 K \left(\frac{B_1}{I} \right)_{xy} M_0 V_S \cos\left(\omega_0 t \right) \tag{3.62}$$

where V_S is the volume of the sample, and K is an integration constant incorporating the inhomogeneity of the $\boldsymbol{B_1}$ field. The magnetisation M_0 is given by the earlier Equation 3.19. The noise of an NMR measurement can be estimated by the thermal (Johnson) noise associated with the resistance, R, of the coil:

$$V_{rms} = \sqrt{4k_B T_c R \Delta f} \tag{3.63}$$

where k_B is Boltzmann's constant, T_c is the temperature of the coil and Δf is the bandwidth over which the noise is measured. (Note: in practice, the thermal noise associated with a human subject in MRI can sometimes be greater than the thermal noise of the coil, so it is not always appropriate to model the noise in this way.)

Equations 3.62 and 3.63 can be combined with an analytical expression for the coil resistance to arrive at a relationship for the signal-to-noise ratio as a function of experimental parameters and constants (this equation is not derived in full here, see e.g. [186] or [172]). Interestingly, the resulting equation shows that the only experimentally variable quantities governing the SNR are those of the coil geometry, temperature and material properties, and also the noise figure of the electronics used to amplify the signal. (The design of coils for radiofrequency transmission and detection is not covered in this thesis; the reader is referred to [187].) Additionally, the SNR is found to be dependent on the gyromagnetic ratio (i.e. Larmor frequency) raised to the power of $\frac{7}{4}$.

This relationship is applicable for situations where the Johnson noise of the coil is the dominant source of noise. However, at clinical field strengths, the noise of the NMR experiment is typically dominated by the thermal noise of the sample rather than coil noise [188]. In this case, the SNR is found to be *directly* proportional to the gyromagnetic ratio [189]. Note however, for the case of a hyperpolarised sample, the magnetisation is not governed by the Boltzmann distribution (Equations 3.18 and 3.19) [190].

Chemical exchange broadening of an NMR spectrum

Chemical exchange was briefly introduced in Section 3.2.2 as a mechanism for inducing spin-spin relaxation. It pertains to the exchange of nuclear spins between two or more different chemical environments which have a distinct chemical shift associated with them. The corresponding frequency difference induces

a phase difference between spins that results in a loss of coherence and hence a decay in the transverse component of the net magnetisation. As described above, the width of the absorption peak of an NMR spectrum is inversely proportional to the T_2^* relaxation time. Therefore, an increase in the rate of chemical exchange of a given nuclear species will lead to a reduction of the effective T_2^* and a concomitant broadening of the absorption spectrum.

This fact becomes important when attempting to distinguish two or more components of an NMR spectrum pertaining to the Larmor frequency of a given species in two or more chemical environments that are undergoing chemical exchange. The simplest situation that can be considered is two pools of spins a and b with angular frequencies ω_a and ω_b and chemical shifts δ_a and δ_b, with an equal probability for a spin to inhabit each pool. The rate of exchange k between pools is equivalent in the forward and backward directions:

$$a \underset{k}{\overset{k}{\rightleftharpoons}} b \tag{3.64}$$

The appearance of the NMR spectrum depends upon the exchange rate k in comparison to the chemical shift (or frequency) difference between the two pools $\delta_a - \delta_b$. If $k = 0$, there is no exchange between the two pools and the NMR spectrum exhibits two peaks at δ_a and δ_b with a width defined by the T_2^* in the absence of exchange. As the rate of chemical exchange is increased, the peaks begin to broaden (termed "slow exchange") and then merge together when $k \sim \delta_a - \delta_b$ ("intermediate exchange" or "coalescence"). If the exchange rate is increased past the coalescence point — where only a single resonance peak, centred at the average frequency of the two compartments, is observed — the single peak becomes narrower, because the spins exchange so quickly that they inhabit each pool for an insufficient time to develop a significant phase difference (termed as "fast exchange" and "motional narrowing" of the spectrum). A summary of example NMR spectra that would be produced in each of these situations is presented in Figure 3.11.

No exchange: $k = 0$ **Slow exchange:** $k \ll \delta_a - \delta_b$ **Intermediate:** $k \lesssim \delta_a - \delta_b$ **Coalescence:** $k \sim \delta_a - \delta_b$ **Fast exchange:** $k \gg \delta_a - \delta_b$
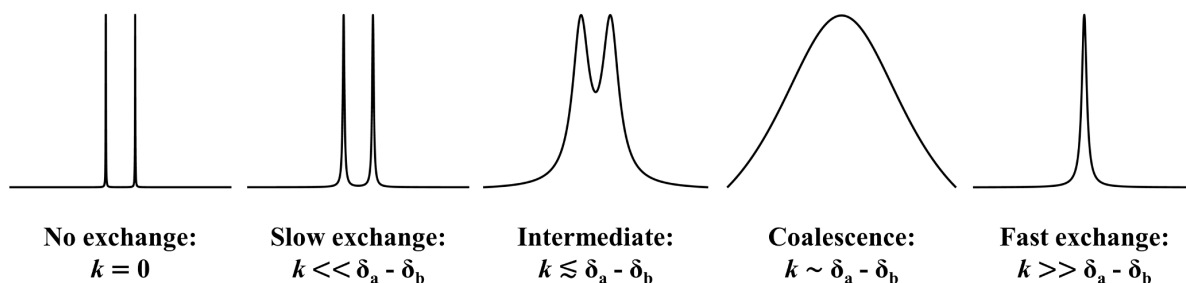
Figure 3.11: The NMR appearance of chemical exchange between two equally-populated pools of nuclear spins, as a function of exchange rate, k (increasing k from left to right).

In many cases, the rates of the forward and backward reactions may be unequal, for example due to an asymmetric energy barrier pertaining to the occurrence of the chemical reaction. In this case:

$$a \underset{k_b}{\overset{k_a}{\rightleftharpoons}} b \qquad (3.65)$$

where k_a and k_b describe the rates of the forward and backward reaction, respectively, and the fractional populations of the two pools will be given by:

$$P_a = \frac{k_b}{k_a + k_b} \qquad (3.66)$$

$$P_b = \frac{k_a}{k_a + k_b} \qquad (3.67)$$

As for the case of a symmetric reaction, the exchange dynamics for an asymmetric reaction can be classified into slow, intermediate and fast regimes, which are defined by $k \ll \delta_a - \delta_b$, $k \sim \delta_a - \delta_b$ and $k \gg \delta_a - \delta_b$, respectively, where $k = k_a + k_b$. The peak shapes are broadened in a similar manner to the symmetric reaction, and furthermore, in the intermediate and fast regimes, the peaks coalesce to a single peak at a chemical shift that is the average of the individual chemical shifts, weighted by the fractional populations of the two pools:

$$\delta_{obs} = P_a \delta_a + P_b \delta_b \equiv \frac{\delta_a + K\delta_b}{1 + K} \qquad (3.68)$$

where $K = \frac{k_a}{k_b}$, the equilibrium rate constant. Although it will not be covered further in this thesis, the reader is referred to the work of McConnell [191], who combined the rate equations for two-site chemical exchange with the Bloch equations in order to describe the influence of chemical exchange processes on the magnetisation dynamics.

Formation of spin and gradient echoes

In practice, the FID introduced in the previous subsection is rarely detected for use in the formation of MR images [ix]. Instead, "echoes" are generated by means of radiofrequency pulses or magnetic field gradients; these echoes appear as additional NMR signals after the FID. It is these signal echoes that are most commonly detected and used to construct MR images.

A "spin echo" (SE) can be formed by the application of a 180° RF "inversion" pulse, some time after an initial 90° RF excitation pulse. After the 90° pulse, spins dephase according to T_2^* relaxation. The 180° pulse inverts (i.e. reverses) the phase angles of the individual spins, and as such the spin ensemble returns to phase synchrony after a total time equal to twice the separation of the two RF pulses, generating an echo signal. The time between the centre of the 90° RF pulse and the centre of the echo is termed the "echo time" or TE. The process of forming a spin echo is illustrated in Figure 3.12.

It is worth noting that spin echoes can be formed with flip angle combinations other than 90° and

---

[ix] However, FID detection is routinely employed in a number of NMR spectroscopic techniques, and in rapid imaging techniques where the species of interest exhibits a very short transverse relaxation time.

180°, although this combination provides the maximum attainable echo signal intensity. In addition, we note that it is possible to apply multiple 180° inversion pulses arranged in a "train" after the original RF pulse (i.e. with a constant time spacing between them) in order to produce a train of echoes of diminishing intensity. This procedure is advantageous for rapid imaging applications, as discussed further in Section 3.2.5.
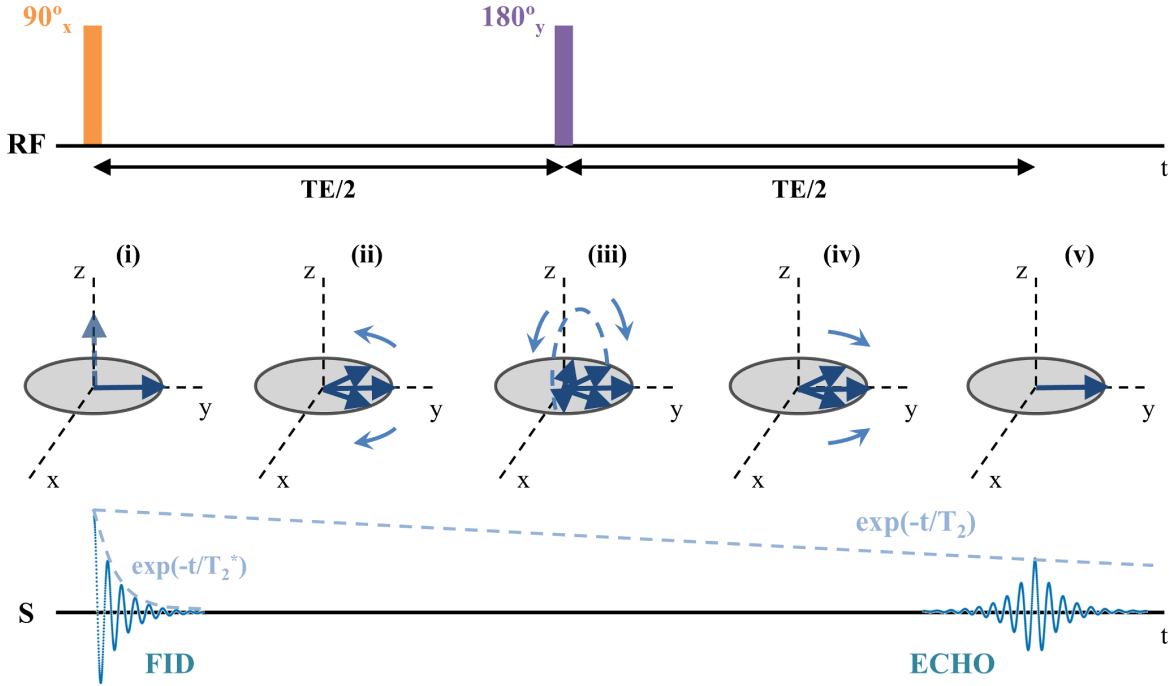
Figure 3.12: Pictorial description of the formation of a spin echo. Initially the net magnetisation vector lies along the positive z direction. (i) The application of a 90° radiofrequency pulse along the x axis tips the magnetisation into the x-y plane such that it instantaneously lies along the y axis. A free induction decay (FID) is generated by precession of the magnetisation in the transverse plane. (ii) Spins precess at different frequencies and lose phase coherence (the amplitude of the FID decays according to T_2^*). (iii) The application of a 180° radiofrequency pulse along the y axis inverts the phase of the individual magnetisation vectors about the y axis. (iv) As such, the original phase dispersion is reversed. (v) After a time equal to twice the separation of the two RF pulses, an echo signal is formed as the spins return to perfect phase. (Note: the rate of decay of the FID and echo have been accentuated with respect to the magnetisation dynamics for illustration purposes.) Adapted with permission from [172].

The intensity of an FID is diminished over time according to the rate of transverse relaxation including inhomogeneities in the static magnetic field T_2^*. Since the inhomogeneity of the $\boldsymbol{B_0}$ field may be assumed to be static in time, the associated induced decay (at a rate $\frac{1}{T_2'}$) is reversible. The application of the 180° pulse to invert the phase of the spins effectively reverses the effects of the static magnetic field inhomogeneity, such that the intensity of the echo signal is governed by the T_2 relaxation time rather than the T_2^*. The spin-spin relaxation mechanisms encompassed in T_2 are intrinsic to the nuclei of interest in a given molecular environment, and cannot be reversed. Furthermore, any diffusional motion of the spins in the time between the two RF pulses will lead to additional dephasing due to spins sampling different magnetic field environments that cannot be reversed by the spin echo procedure. These effects can be summarised to describe the signal of a spin echo, S_{SE} with respect to the initial signal at time $t = 0$, S_0,

in the following equation:

$$S_{SE} = S_0 \exp\left[-\frac{TE}{T_2} - \frac{2}{3}\gamma^2 \Delta B_{0,i}^2 D \left(\frac{TE}{2}\right)^3 \right] \approx S_0 \exp\left(-\frac{TE}{T_2}\right) \tag{3.69}$$

where, D is the apparent diffusion coefficient of the nuclei of interest and, as before, $\Delta B_{0,i}$ represents the gradient (in T.m^{-1}) of the external magnetic field associated with inhomogeneities. Generally, the influence of diffusion on spin dephasing is described by the b-value equation: $S_t = S_0 \exp(-bD)$, where b is a term depending on the square of the gyromagnetic ratio, and the nature of the gradient in magnetic field through which a spin is diffusing. The behaviour of diffusion within magnetic field gradients will be discussed further in Section 3.2.5. For now, it is sufficient to note that the expression in Equation 3.69 represents a simplification of the form of b for a perfect linear gradient. For the purposes of this discussion, we note that if the diffusion coefficient is sufficiently small, and $TE \ll T_2$, the second term can be safely neglected such that the signal dependence is solely governed by the initial signal at time $t = 0$ and the T_2 relaxation time.

A "gradient echo" (sometimes "gradient-recalled echo", GRE) relies on the application of magnetic field gradients in place of a 180° RF pulse in order to generate an echo signal. A simple linear gradient in magnetic field as a function of position causes phase dispersion because spins at different spatial positions along the direction of the gradient experience a different effective magnetic field, and hence acquire a different Larmor frequency. The phase dispersion in the presence of a magnetic field gradient occurs on a much faster timescale than would occur by conventional transverse relaxation processes, thus, rapid signal loss results. A gradient echo can be generated by switching on two magnetic field gradients in quick succession on the same axis but with opposite polarity, following an initial RF excitation of flip angle α (typically less than 90°, as discussed in Section 3.2.5). Firstly, after the RF pulse, a negative polarity gradient is employed to rapidly induce a phase dispersion. Then, a second gradient with positive polarity is used to reverse the phase dispersion caused by the first gradient. As a result, a gradient echo is produced at a time TE when the area of the second gradient is equal to the area of the first gradient. Note: the first gradient is often termed the "dephasing gradient" and the second gradient the "rephasing gradient". (Note: an equivalent result is obtained by applying a positive gradient followed by a negative gradient.) The process of forming a gradient echo is illustrated in Figure 3.13.

The positive and negative gradient lobes do not reverse the loss in phase coherence due to magnetic field inhomogeneities, and, as such, the signal intensity of a gradient echo is governed by T_2^* rather than T_2. In other words, only the spin dephasing that was induced by the first gradient is accounted for by the second gradient; all other dephasing effects occur as normal. Thus, the GRE signal intensity is described by:

$$S_{GRE} = S_0 \exp\left(-\frac{t}{T_2^*}\right) \tag{3.70}$$
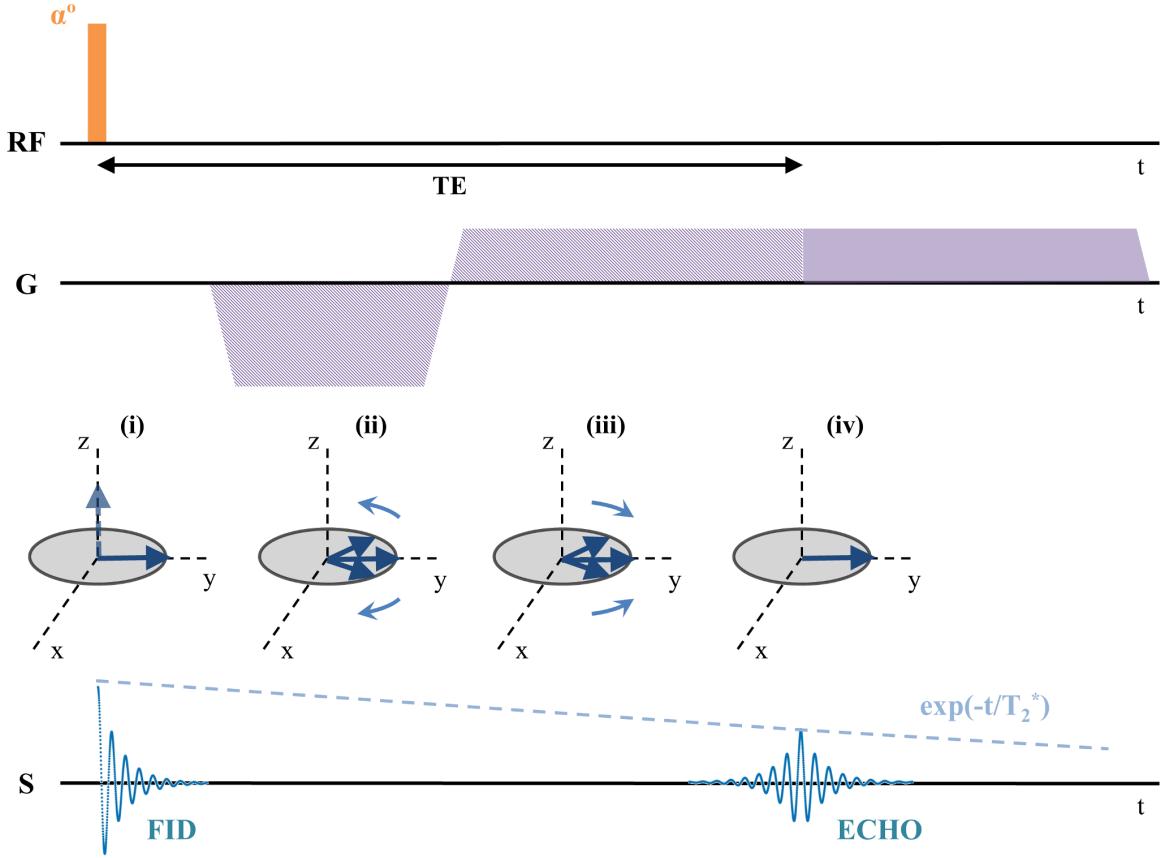
Figure 3.13: Pictorial description of the formation of a gradient echo. Initially the net magnetisation vector lies along the positive z direction. (i) The application of a radiofrequency pulse of flip angle α along the x axis tips the magnetisation into the x-y plane such that it instantaneously lies along the y axis. A free induction decay (FID) is generated by precession of the magnetisation in the transverse plane. (ii) A negative magnetic field gradient is applied to rapidly create a phase dispersion between spins. (iii) The magnetic field gradient direction is reversed, and the phase dispersion created by the first gradient is reversed. (iv) After a time such that the total area of the applied negative and positive gradients is equal (hatched regions), an echo signal is formed as the spins return to perfect phase. (Note: the rate of decay of the FID and echo have been accentuated with respect to the magnetisation dynamics for illustration purposes.)

Due to the inherent rapid forced dephasing of spins by the magnetic field gradients, and the lack of requirement for a second RF pulse, the process of generation of a gradient echo can be significantly faster than that of a spin echo. In addition, if the flip angle used in a gradient echo sequence is significantly less than 90°, the time between subsequent iterations of the simple gradient echo "pulse sequence" shown in Figure 3.13 can be considerably shorter than that of the SE pulse sequence [x]. (Note: pulse sequences will be introduced in the next subsection.) As a result, the time associated with the complete acquisition of a GRE image can be far less than that of a SE image.

---

[x]For high flip angles, a short inter-pulse repetition time may be unfeasible due to: (i) the T_1 of the nuclei; (ii) the high amount of radiofrequency power deposited in the sample (typically a patient) at a fast rate. The limits of safe RF power deposition are set by the specific absorption rate (SAR), which is the rate of energy absorption by a tissue measured in W.kg^{-1}, defined mathematically as: $SAR = \frac{1}{V} \int_{tissue} \frac{\sigma(\boldsymbol{r})|\boldsymbol{E}(\boldsymbol{r})|^2}{\rho(\boldsymbol{r})} \, \mathrm{d}\boldsymbol{r}$, where V is the volume of the tissue sample, $\sigma(\boldsymbol{r})$, $\rho(\boldsymbol{r})$ and $\boldsymbol{E}(\boldsymbol{r})$ are the electrical conductivity, density of the sample and the electric field in the sample as a function of position, $\boldsymbol{r}$. In practice, the SAR can be related to the magnetic field strength, flip angle and RF duty cycle (i.e. repetition time) as follows: $SAR \propto B_0^2 \alpha^2 TR$.

3.2.4 k-space and spatial encoding

Magnetic field gradients

Until this point, this chapter has focussed on the treatment of individual spins or spin systems, and the acquisition of single NMR signals from a sample. This subsection is concerned with the processes of "encoding" acquired NMR signals in order to attribute the origin of different signals to different spatial locations, and the "reconstruction" of this encoded information in order to form an image. Image encoding is typically implemented through a combination of three techniques: "frequency encoding" (or "read-out"), "phase encoding", and "slice selection". Each of these methods will be considered individually in the following discussion. In the following, and the remainder of this thesis, the convention of x as the frequency encoding gradient direction, y as the phase encoding gradient direction and z as the slice selection gradient direction (or the second phase encoding gradient direction for 3D sequences) will be adopted.

Each of these three processes requires the application of magnetic field gradients, which have been introduced in the previous subsection, but have not been described mathematically as yet. For the following discussion, it is appropriate to define a magnetic field gradient in one of the x, y or z directions, $G_{x,y,z}$, typically measured in mT.m^{-1}, by:

$$G_{x,y,z} = \frac{\partial B_z}{\partial x, y, z} \tag{3.71}$$

Thus, each gradient corresponds to a variation in magnetic field as a function of position in x, y or z which adds to (or subtracts from) the external (static) magnetic field, chosen here to lie in the z direction, $\boldsymbol{B_0} = B_0 \hat{\mathbf{k}}$. Taking the x direction as an example, the magnetic field experienced by a nucleus in the presence of a constant amplitude gradient G_x varies linearly with x, according to:

$$B_z(x) = B_0 + G_x x \tag{3.72}$$

and correspondingly, the Larmor frequency will vary with position according to:

$$\omega_0(x) = \gamma(B_0 + G_x x) \tag{3.73}$$

A pictorial description of the effects of a linear magnetic field gradient is presented in Figure 3.14.

In principle, magnetic field gradients cannot be instantaneously switched on or off. When turning on a gradient, a finite "ramp time" is required, during which the gradient increases in amplitude from zero until its target maximum amplitude. An equivalent ramp period is necessitated when the gradient is switching
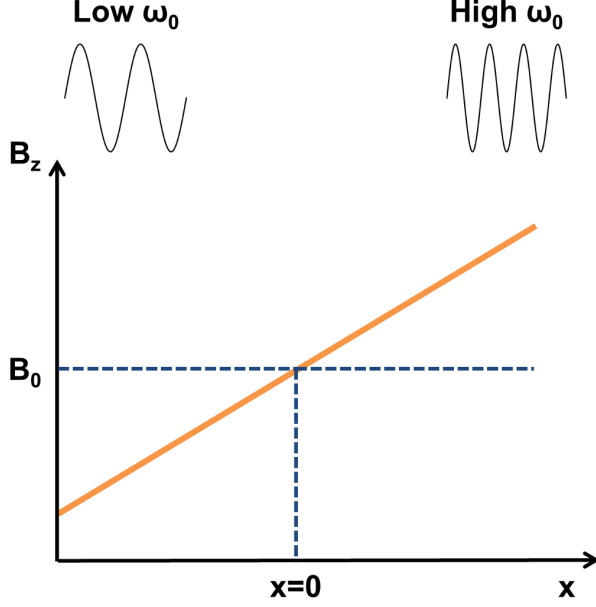
Figure 3.14: The effect of a magnetic field gradient on the magnetic field experienced by a nucleus, and hence on the Larmor frequency it exhibits. Adapted with permission from [175].

off. Hence, the strength of a magnetic field gradient as a function of time traces out a trapezoidal shape; thus, in the following subsections, gradients will be represented by trapezoidal shapes on pulse sequence timing diagrams.

k-space formalism and discrete sampling

In order to establish a mathematical basis upon which to explain methods for encoding the spatial locations of spins by the application of magnetic field gradients, it is appropriate to return to the Bloch equation description of the magnetisation as a function of time, in the presence of an arbitrary magnetic field gradient $\boldsymbol{G}\left(t\right) = G_x\left(t\right)\hat{\mathbf{i}} + G_y\left(t\right)\hat{\mathbf{j}} + G_z\left(t\right)\hat{\mathbf{k}}$. The vector Bloch equation in the rotating frame can be written:

$$\frac{\mathrm{d}\boldsymbol{M}}{\mathrm{d}t} = \gamma\boldsymbol{M} \times \boldsymbol{B} - \frac{\left(M_x\hat{\mathbf{i}} + M_y\hat{\mathbf{j}}\right)}{T_2} - \frac{(M_z - M_0)}{T_1}\hat{\mathbf{k}} \tag{3.74}$$

where $\boldsymbol{B} = B_{1,x}\hat{\mathbf{i}} + B_{1,y}\hat{\mathbf{j}} + \left[\left(B_0 - \frac{\omega_r}{\gamma}\right) + \boldsymbol{G}\left(t\right)\cdot\boldsymbol{r}\right]\hat{\mathbf{k}}$. Assuming that the transmission frequency ω_r is equal to the Larmor frequency associated with the $\boldsymbol{B_0}$ field, the Bloch equations can be written in matrix form, and separated into components associated with precession, relaxation and recovery as follows:

$$\begin{bmatrix} \dot{M_x} \\ \dot{M_y} \\ \dot{M_z} \end{bmatrix} = \underbrace{\begin{bmatrix} 0 & \gamma\boldsymbol{G}\cdot\boldsymbol{r} & -\gamma B_{1,y} \\ -\gamma\boldsymbol{G}\cdot\boldsymbol{r} & 0 & \gamma B_{1,x} \\ \gamma B_{1,y} & -\gamma B_{1,x} & 0 \end{bmatrix}}_{\text{Precession}}\begin{bmatrix} M_x \\ M_y \\ M_z \end{bmatrix} + \underbrace{\begin{bmatrix} -\frac{1}{T_2} & 0 & 0 \\ 0 & -\frac{1}{T_2} & 0 \\ 0 & 0 & -\frac{1}{T_1} \end{bmatrix}}_{\text{Relaxation}}\begin{bmatrix} M_x \\ M_y \\ M_z \end{bmatrix} + \underbrace{\begin{bmatrix} 0 \\ 0 \\ \frac{1}{T_1} \end{bmatrix}}_{\text{Recovery}}M_0 \tag{3.75}$$

where $\dot{M}_{x,y,z} = \frac{\mathrm{d}M_{x,y,z}}{\mathrm{d}t}$. If we consider the situation immediately after the initial RF excitation pulse, $B_{1,x,y} = 0$, the precession and relaxation terms can be combined as follows:

$$
\begin{bmatrix} \dot{M}_x \\ \dot{M}_y \\ \dot{M}_z \end{bmatrix} = \underbrace{\begin{bmatrix} -\frac{1}{T_2} & \gamma \boldsymbol{G} \cdot \boldsymbol{r} & 0 \\ -\gamma \boldsymbol{G} \cdot \boldsymbol{r} & -\frac{1}{T_2} & 0 \\ 0 & 0 & -\frac{1}{T_1} \end{bmatrix} \begin{bmatrix} M_x \\ M_y \\ M_z \end{bmatrix}}_{\text{Precession \& Relaxation}} + \underbrace{\begin{bmatrix} 0 \\ 0 \\ \frac{1}{T_1} \end{bmatrix} M_0}_{\text{Recovery}}
\tag{3.76}
$$

This equation can be decoupled into two equations describing the rate of change of the longitudinal, M_z, and transverse, $M_{xy} = M_x + iM_y$, magnetisations. The M_z part of the equation does not contain a $\boldsymbol{G} \cdot \boldsymbol{r}$ term, and hence has already been solved (see Equation 3.40). The Bloch equation for the rate of change of transverse magnetisation becomes:

$$
\dot{M}_{xy} = \left(-\frac{1}{T_2} - i\gamma \boldsymbol{G} \cdot \boldsymbol{r} \right) M_{xy}
\tag{3.77}
$$

which is a homogeneous differential equation that can be solved with an integrating factor $I(t) = \exp \left[\int_0^t \frac{1}{T_2} + (i\gamma \boldsymbol{G} \cdot \boldsymbol{r}) \, \mathrm{d}t' \right]$ to yield:

$$
M_{xy}(\boldsymbol{r}, t) = \underbrace{M_{xy}(\boldsymbol{r}, 0)}_{\text{Sample}} \underbrace{\exp \left(-\frac{t}{T_2} \right)}_{\text{Relaxation}} \underbrace{\exp \left(-i\gamma \boldsymbol{r} \cdot \int_0^t \boldsymbol{G}(t') \, \mathrm{d}t' \right)}_{\text{Spatial Encoding}}
\tag{3.78}
$$

The spatial encoding component is conventionally described using a three dimensional "spatial frequency vector", or "k-space vector", $\boldsymbol{k}$, which has units of inverse metres:

$$
\boldsymbol{k}(t) = \frac{\gamma}{2\pi} \int_0^t \boldsymbol{G}(t') \, \mathrm{d}t'
\tag{3.79}
$$

such that the transverse magnetisation can be written:

$$
M_{xy}(\boldsymbol{r}, t) = M_{xy}(\boldsymbol{r}, 0) \exp \left(-\frac{t}{T_2} \right) \exp \left(-i2\pi \boldsymbol{k}(t) \cdot \boldsymbol{r} \right)
\tag{3.80}
$$

The MR signal is directly proportional to the volume integral of the transverse magnetisation across the sample as introduced in the previous subsection, and hence we can write:

$$S(t) = \int_{sample} M_{xy}(\boldsymbol{r}, 0) \exp\left(-\frac{t}{T_2}\right) \exp\left(-i2\pi\boldsymbol{k}(t) \cdot \boldsymbol{r}\right) \mathrm{d}^3\boldsymbol{r} \tag{3.81}$$

Finally, this equation can be re-written by noticing that the signal $S(t)$ is exactly equivalent to the Fourier transform of $M_{xy}(\boldsymbol{r}, 0)$, evaluated at $\boldsymbol{k}(t)$ in the limit $T_2 \to \infty$:

$$S(t) = \mathcal{F}\{M_{xy}(\boldsymbol{r}, 0)\}|_{\boldsymbol{k}=\boldsymbol{k}(t)} = F[\boldsymbol{k}(t)] \tag{3.82}$$

These equations are fundamental to understanding the principles of spatial encoding in MRI. From Equation 3.82, it can be seen that the distribution of the initial transverse magnetisation as a function of position (i.e. the target object) can be determined by acquiring MR signals as a function of spatial frequency, $\boldsymbol{k}(t)$, and taking an inverse Fourier transform of the result. As discussed previously (c.f. Equation 3.57) we recall that any signal can be represented by a summation of a series of sinusoidal waveforms with different frequencies. Whilst Equation 3.57 considers the decomposition of a time-domain signal into its respective frequency components, here the spatial frequency vector $\boldsymbol{k}(t)$ has been introduced as a frequency representation of a signal in the spatial domain. $\boldsymbol{k}(t)$ has units of m^{-1} and effectively describes the number (or energy) of spatial frequencies which compose the target image $M_{xy}(\boldsymbol{r}, 0)$. A spatial frequency can be understood as the frequency with which the brightness of an image varies with position; the "DC" spatial frequency $\boldsymbol{k} = \boldsymbol{0}$ describes the average brightness of the overall image. Thus, any image can be decomposed into a summation of signals with different spatial frequencies and amplitudes.

This leads to the concept of "k-space", or spatial frequency space. Any two-dimensional image with spatial axes x and y can be described by a two-dimensional k-space comprising the two spatial frequency dimensions k_x and k_y, as illustrated in Figure 3.15.
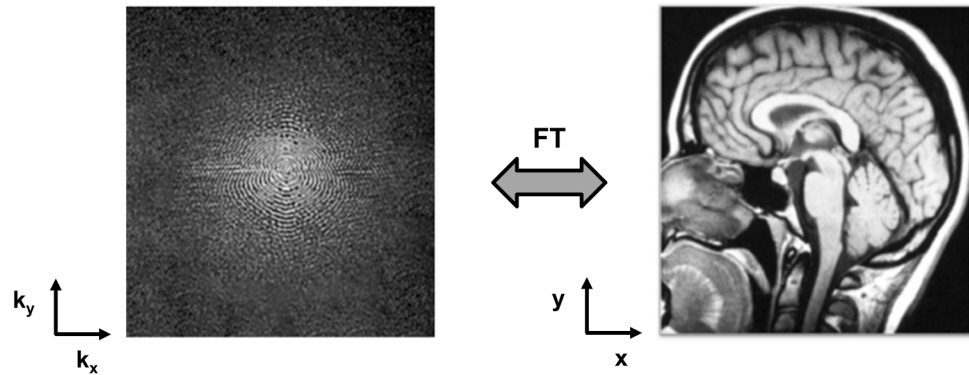
Figure 3.15: Example two-dimensional k-space (left) and corresponding MR image (right). It can be clearly seen that the majority of the energy in k-space is concentrated at the origin, where $\boldsymbol{k}$ is close to zero. Adapted with permission from [180].

The relative brightness of a particular pixel in this two-dimensional k-space denotes the relative contribution of the (2D) spatial frequency vector defined by that pixel ($\boldsymbol{k} = k_x\hat{\boldsymbol{i}} + k_y\hat{\boldsymbol{j}}$) to the overall image. The

2D k-space and image representations of a signal are related by the 2D Fourier transform:

$$F(k_x, k_y) = \int_{-\infty}^{\infty} \int_{-\infty}^{\infty} f(x, y) \exp\left[-i2\pi(k_x x + k_y y)\right] \mathrm{d}x\mathrm{d}y \tag{3.83}$$

thus, comparing to Equation 3.82:

$$S(t) = \int_{-\infty}^{\infty} \int_{-\infty}^{\infty} M_{xy}(x, y, t = 0) \exp\left[-i2\pi(k_x x + k_y y)\right] \mathrm{d}x\mathrm{d}y \tag{3.84}$$

The k-space vector, $\boldsymbol{k}(t)$ relates the trajectory through k-space that is traced out when magnetic field gradients are switched on. The rate of change of the k-space vector, $\dot{\boldsymbol{k}}$, describes the velocity with which k-space is traversed, which is governed by the amplitude of the applied gradients. The double time derivative of the k-space vector, $\ddot{\boldsymbol{k}}$, is the acceleration associated with the k-space traversal, determined by $\dot{\boldsymbol{G}}$, the rate of change of the gradient field. $\dot{\boldsymbol{G}}$ is also known as the "slew rate", and defines the minimum ramp time required for a gradient to reach its maximum amplitude. It is worth noting that, by definition of Equation 3.79, for nuclei with positive and negative values of γ, the direction of k-space traversal is opposite.

In the following subsections, the various strategies for traversing k-space and obtaining spatial frequency information in order to reconstruct an image of the magnetisation distribution of an object of interest are introduced. Firstly, however, the concept of *discrete sampling* of k-space will be discussed.

$F[\boldsymbol{k}(t)]$ in Equation 3.82 (or $F(k)$, assuming k is one-dimensional for simplicity) is a smooth, continuous function. Measurement of a purely continuous function would in principle require an infinite number of measurements to be taken along the variable dimension of that function (i.e. k). In practice, the function can only be sampled with a finite number of measurement points, with a discretised "sampling interval" (Δk) in between sampling points.

Discrete sampling in k-space can be considered by multiplying $F(k)$ with the comb function:

$$\mathrm{comb}(k) = \sum_{n=-\infty}^{\infty} \delta(k - n\Delta k) \equiv \frac{1}{\Delta k}\mathrm{comb}\left(\frac{k}{\Delta k}\right) \tag{3.85}$$

where δ represents the Dirac delta function, which is defined by:

$$\int_{-\infty}^{\infty} F(k)\,\delta(x - a)\,\mathrm{d}x = F(a) \tag{3.86}$$

The sampling process can thus be described by a sampling function $Q(k)$:

$$Q(k) = \frac{1}{\Delta k} \text{comb}\left(\frac{k}{\Delta k}\right) F(k) \tag{3.87}$$

This process is shown diagrammatically in Figure 3.16a, where $Q(k)$ precisely defines the values of $F(k)$ at a finite number of points with spacing Δk.

In k-space, samples are acquired symmetrically about $(k_x, k_y) = (0, 0)$. There exists a minimum sampling rate, (proposed separately by Shannon and Nyquist) in order to ensure that $F(k)$ is correctly represented by the discrete function $Q(k)$, equal to two times the maximum frequency contained within the continuous function of interest. This condition is depicted in Figure 3.16b for an example of a single frequency sinusoidal function. In the top plot, the sine wave is sampled at a sampling rate $R_Q \gg N_S$, where N_S is the Shannon / Nyquist sampling rate, whilst in the bottom plot, the function is sampled at a rate $R_Q \ll N_S$. As a result, the top sampling function gives a correct representation of the signal $F(k)$, whilst the bottom sampling function gives an incorrect ("aliased") representation of the sine wave $F(k)$ as a constant (dashed line). The origin of the Shannon / Nyquist criterion can be understood by realising that adding one additional sampling point to the bottom sampling function (in the middle of the negative lobe of the sine function) will allow a correct representation of $F(k)$ to be obtained with $Q(k)$; if this additional point was added, the sampling rate would be twice the frequency of the sine wave.
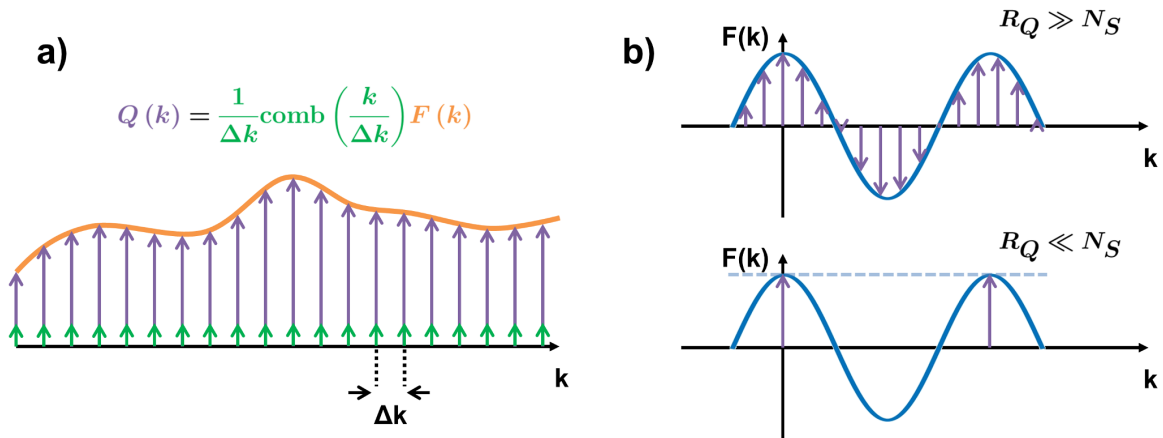
Figure 3.16: a) Pictorial representation of the discrete sampling of an arbitrary k-space function, $F(k)$, with a sampling function $Q(k)$, as described mathematically by Equation 3.87. b) Illustration of the Shannon / Nyquist sampling criterion, and how sampling at an insufficient rate can lead to an incorrect representation of the measured signal.

At this point, it is useful to think about the two-dimensional representation of a discretised k-space. It is important to note that by definition, the Fourier transform operates on continuous functions, but a discretised form can be derived in order to numerically relate the discretised k-space and image space representations of a signal, in which the continuous integrals are replaced with discrete summations over a finite number of values. Conventionally the fast Fourier transform (FFT) (see e.g. [192]), an algorithm for computing the discrete Fourier transform (DFT), is employed for rapid reconstruction of images from acquired k-space data. A pictorial representation of a two-dimensional discretised k-space and corresponding image space is shown in Figure 3.17.
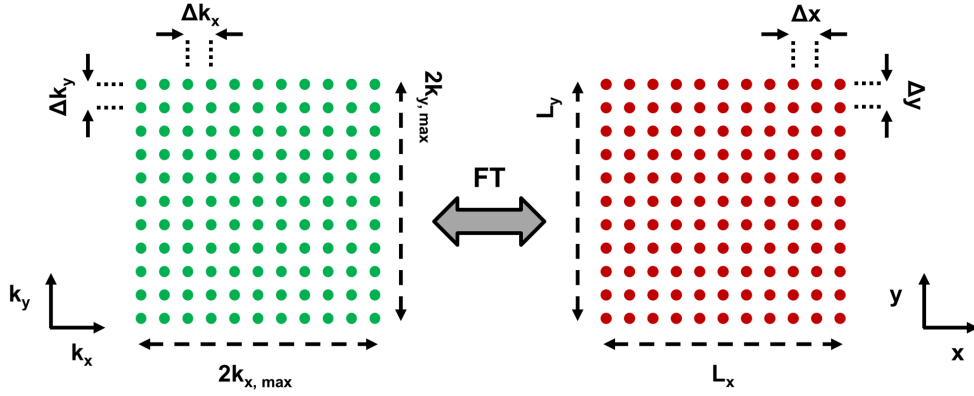
Figure 3.17: Discretised representation of a 2D k-space (left) and 2D image space (right), linked by the two-dimensional Fourier transform (FT). $k_{x,y,max}$ is the maximum k-space vector in the x or y directions for a k-space centred at the origin. $L_{x,y}$ is the maximum spatial extent in the x or y direction, also known as the field-of-view (FOV) of the image. $\Delta k_{x,y}$ and $\Delta x, y$ are the spacings between discretised sampling points in k-space and image space, respectively.

The properties of the FT provide some important relationships between the quantities defined in Figure 3.17. Firstly, the spatial separation between sampling points in the spatial domain, $\Delta x, y$, also known as the resolution of the image, is inversely related to the maximal extent of k-space sampled. In the x direction:

$$\Delta x = \frac{1}{2k_{x,max}} = \frac{1}{N_{k,x}\Delta k_x} \tag{3.88}$$

where the number of sampling points in the k_x direction, $N_{k,x} = \frac{2k_{x,max}}{\Delta k_x}$. Reciprocally, the separation between adjacent k-space sampling points is inversely proportional to the maximum spatial extent in image space (the FOV):

$$\Delta k_x = \frac{1}{L_x} = \frac{1}{N_x \Delta x} \tag{3.89}$$

where the number of sampling points in the x direction of image space, $N_x = \frac{L_x}{\Delta x}$. Equivalent equations exist for y and k_y. It can therefore be seen that the spatial resolution and field-of-view of the image are controlled by the maximum k-space extent and k-space sampling rate, respectively.

In practice, if the function describing the object extends beyond L_x or L_y, then the portion of the function that overlaps is aliased (or "wrapped") back on to the opposite end of the field-of-view. In an image, this is equivalent to a portion of the object extending past the field-of-view in one direction being mapped back on to the other side of the image. This artefact can be understood by considering the scaling properties of the Fourier transform, and employing the convolution theorem, to derive the sampling function in image space (x in 1D) from Equation 3.87. The result is that the sampling function in image space is defined

by the convolution of a comb function and the spatial function to be sampled $f(x) = \mathcal{F}[F(k)]$:

$$q(x) = 2k_{x,max}\text{comb}(\Delta k_x x) * f(x) \tag{3.90}$$

where $*$ is the convolution operator. Thus, by consequence of the convolution with the comb function, the function $f(x)$ is replicated in image space, with consecutive occurrences of $f(x)$ separated by $\frac{1}{\Delta k}$. Therefore, if $\Delta k_x \leq \frac{1}{R_x}$ (where R_x is the extent of $f(x)$), consecutive occurrences of $f(x)$ do not interfere with each other, and only one occurrence is contained within L_x. However, if $\Delta k_x > \frac{1}{R_x}$, the adjacent occurrences of $f(x)$ will overlap to some degree [xi], producing an aliased signal within the field-of-view.

Note: another artefact that should be considered when applying a Fourier transform to a sampling function is the Gibbs' or truncation artefact. That is, it is impossible to sample an infinite extent of k-space and hence certain high spatial frequency data cannot be acquired. Sampling therefore effectively results in "chopping off" the ends of an infinite k-space, which presents as a "ringing" (alternation of bright and dark bands) in image space, most prominently at high-contrast boundaries in the image (which require a large number of spatial frequencies to be represented correctly).

Frequency encoding (read-out)

The following subsections explain the processes employed for spatial encoding in three dimensions. As mentioned at the beginning of Section 3.2.4, frequency and phase encoding will be introduced to describe spatial encoding within a 2D plane — with the convention of frequency encoding for traversing in the k_x direction and phase encoding for traversing in k_y — and slice selection will be introduced for the purpose of localisation of signals to a given slice in the z direction.

Frequency encoding is the general term denoting the association of a particular Larmor frequency with a certain spatial location by the application of a magnetic field gradient, where the frequency is linearly proportional to the spin location along the gradient direction. If the transverse magnetisation of an object is sampled as a function of time during the application of a constant amplitude gradient, the resulting sampled data traces out equally-spaced points in k_x. This is the process of acquiring frequency-encoded data.

In practice, a magnetic field gradient is not just instantaneously switched on as soon as an FID has been generated by an RF pulse. In standard, Cartesian sampling with a gradient echo sequence (as described later), a negative gradient is first applied, which, according to Equation 3.79, is associated with a negative k-space vector. Typically, this "prewinder" or "prephasing" gradient is associated with a k-space vector $\boldsymbol{k} = -k_{x,max}$, and, as discussed in Section 3.2.3, serves a dual purpose of dephasing spins in order to generate an echo when the subsequent positive gradient is applied [xii]. After the negative gradient, a positive "read-out" gradient is applied which leads to the traversal of k_x from $-k_{x,max}$ to $+k_{x,max}$. The generated echo exhibits peak signal intensity where the total area under the read-out gradient is equal

---

[xi] The left part of the immediate right copy of $f(x)$ will be included into the right hand side of the field-of-view, and vice-versa.

[xii] For SE sequences, the prephasing gradient has positive polarity and is positioned prior to the 180° inversion pulse.
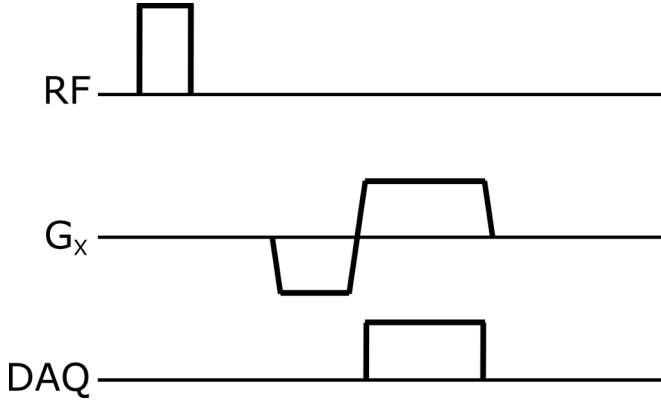
Figure 3.18: Depiction of a frequency encoding gradient on the pulse sequence timing diagram. The RF axis shows a rectangular radiofrequency pulse used to generate transverse magnetisation M_{xy}. G_x represents the amplitude of the frequency encoding gradient as a function of time, which is played out after the initial RF pulse. DAQ denotes the position of the data acquisition window.

to that of the prephasing gradient. Hence, the echo is conventionally centred at $k_x = 0$. Normally, data is only acquired during the plateau region of the positive gradient, such that k_x is traversed with an equal spacing between sampling points. An inverse Fourier transform of the frequency-encoded k-space data thus yields the spatial distribution of signal along the x direction. The typical implementation of a frequency encoding gradient as a function of time is shown on a pulse sequence timing diagram, along with the corresponding data acquisition positioning, in Figure 3.18.

Equation 3.73 relates the angular frequency as a function of position x, in the presence of a gradient G_x. In the rotating frame, the γB_0 term can be removed to yield:

$$\omega\left(x\right) = \gamma G_x x \tag{3.91}$$

The phase accumulated by a precessing spin in the presence of a magnetic field gradient G_x between time $t' = 0$ and $t' = t$ is therefore:

$$\phi\left(x\right) = \int_0^t \omega \mathrm{d}t' = \gamma \int_0^t G_x\left(t'\right) x\left(t'\right) \mathrm{d}t' = 2\pi x k_x \tag{3.92}$$

where k_x is the one-dimensional k-space vector. From Equation 3.81, it can be seen that in one dimension, the NMR signal in the presence of a gradient G_x as above can be written as a summation over all spin isochromats j [xiii], in terms of their acquired phase $\phi_{x,j}$ and weighted by their spin density $\rho_{x,j}$:

$$S\left(t\right) = \sum_{j=1}^{n} \rho_{x,j} \exp\left(-i\phi_{x,j}\right) \approx \int_{-\infty}^{\infty} \rho\left(x\right) \exp\left(-i\phi\left(x\right)\right) \mathrm{d}x \tag{3.93}$$

In order to mathematically describe the effects of the prephasing and read-out gradients, we can define the duration of the prephasing gradient as t_p and the timing of the echo relative to the start of the

---

[xiii] A spin isochromat is a group of spins exhibiting the same precessional frequency.

read-out gradient as t_e, and introduce the corresponding k-space vectors $k_{x,p}$ and $k_{x,r}$, and phases ϕ_p and ϕ_r. Then, since the direction of the phase dispersion created by the two gradients is opposite, we can write:

$$S\left(t\right) = \int_{-\infty}^{\infty} \rho\left(x\right)\exp\left[-i\left(\phi_r\left(x\right) - \phi_p\left(x\right)\right)\right]\mathrm{d}x \tag{3.94}$$

where $-i\left(\phi_r\left(x\right) - \phi_p\left(x\right)\right) = -i2\pi x\left(k_{x,r}\left(t\right) - k_{x,p}\left(t\right)\right)$. At a time t_e from the start of the read-out gradient, $k_{x,p} = k_{x,r}$, the phase dispersion term is zero and an echo is formed. At this point, the areas of the two gradients $G_{x,r}$ and $G_{x,p}$ are equal, i.e.:

$$\int_0^{t_e} G_{x,r}\mathrm{d}t' = \pm\int_0^{t_p} G_{x,p}\mathrm{d}t' \tag{3.95}$$

where the $\pm$ indicates that the prephasing gradient may be of positive or negative amplitude for SE or GRE sequences, respectively.

The total read-out gradient duration is determined by the ramp time and the acquisition time, T_{acq}, which is equal to the length of the gradient plateau. In order to symmetrically sample k-space, $t_e = \frac{T_{acq}}{2}$ (for a hypothetical ramp time of zero). T_{acq} is the product of the number of sampling points N_x and the sampling time (a.k.a. dwell time, Δt):

$$T_{acq} = N_x\Delta t = \frac{N_x}{2\Delta\nu} \tag{3.96}$$

where the bandwidth of the receiver is $\pm\Delta\nu$. By definition of the k-space vector for a constant gradient, the spacing in k_x corresponding to a dwell time Δt is:

$$\Delta k_x = \frac{\gamma}{2\pi}G_x\Delta t \tag{3.97}$$

Thus, comparing to Equation 3.89, $\Delta k_x = \frac{1}{N_x\Delta x}$, the amplitude of the read-out gradient, G_x, is found to be inversely related to the field-of-view $L_x = N_x\Delta x$, as follows:

$$G_x = \frac{4\pi\Delta\nu}{\gamma L_x} \tag{3.98}$$

Hence, at fixed receiver bandwidth, stronger gradients are required to achieve a smaller field-of-view. Furthermore, Equation 3.98 dictates that nuclei with low γ require the use of more powerful gradients to achieve a given field-of-view compared with high γ nuclei.

In order to reduce the echo time (e.g. for species with short T_2 or T_2^* values, or for alleviating susceptibility artefacts), k_x can be sampled asymmetrically. Practically, the area of the prephasing gradient can be reduced such that fewer values in the negative k_x direction are sampled, and correspondingly, the position of the echo is shifted earlier in the data acquisition read-out. This is known as a partial-echo read-out. Utilising the symmetry of the Fourier transform (conjugate symmetry) to synthesize the missing data in the $-k_x$ direction, it is possible to reconstruct images as if a complete data-set was acquired. Note: in principle, in the absence of phase errors (i.e. introduced due to variations in precession frequency across the object of interest), MR images would be real-valued and could be reconstructed from exactly half the number of k-space samples required for complete symmetric sampling of k_x. However, in reality, algorithms such as the homodyne reconstruction algorithm [193] require a small portion of k-space in the $-k_x$ direction to be acquired such that the resulting small amount of symmetrical k-space data can be used to evaluate phase errors prior to synthesizing the missing data.

It is worth noting that frequency encoding can be implemented along any of the three principal axes, and also at arbitrary angles from the k_x axis, e.g. by simultaneously playing out magnetic field gradients in the x and y directions with amplitudes of $G_x = G_{max} \cos(\beta)$ and $G_y = G_{max} \sin(\beta)$. As such, radial "spokes" can be traversed through the k-space centre, as discussed briefly in Section 3.2.5.

Slice selection

Slice selection pertains to the localised RF excitation of a specific section of the sample of interest, as opposed to the sample as a whole. Slice selection is a special case of frequency encoding in which a frequency-selective RF pulse is applied at the same time as a magnetic field gradient (termed the "slice selection gradient").

The simplest example of a frequency-selective RF pulse is a sinc-shaped pulse; a B_1 field with an amplitude that varies according to $\text{sinc}(t) = \frac{\sin(t)}{t}$. This pulse has a rectangular-shaped frequency profile; $\mathcal{F}\left[\text{sinc}\left(\frac{t}{2}\right)\right] = \text{rect}(\omega)$, where $\text{rect}(\omega) = \begin{cases} 1, & \text{if } |\omega| \leq \frac{1}{2} \\ 0, & \text{otherwise} \end{cases}$. It has been introduced that a magnetic field gradient can be used to assign a frequency variation as a function of spatial position. Thus, if a sinc RF pulse is played out at the same instant as a magnetic field gradient, then the range of frequencies excited by the RF pulse, Δf, will correspond to a certain spatial extent, Δz. This spatial extent is known as the thickness of the "slice".

The direction along which the slice selection gradient is applied is the normal to the plane of the resulting slice [xiv]. For example, if we assume that the slice selection gradient is applied along the z axis, and that this axis corresponds to the cranial-caudal axis of a subject, then an axial slice of the body would be excited by the RF pulse.

A pictorial description of the slice selection process is provided in Figure 3.19, and the positioning of the slice selection gradient with respect to the pulse sequence timing diagram is shown in Figure 3.20.

The selective RF pulse is only played out during the plateau of the slice selection gradient [xv], and hence

---

[xiv]This originates from the fact that the frequency shift associated with a given gradient is proportional to the dot product of the gradient and the spin position.

[xv]Because of this, the z component of $\boldsymbol{G}$ in Equation 3.81 can be taken out of the k-space vector integral, and as such,

Time domain

Frequency / Spatial domain
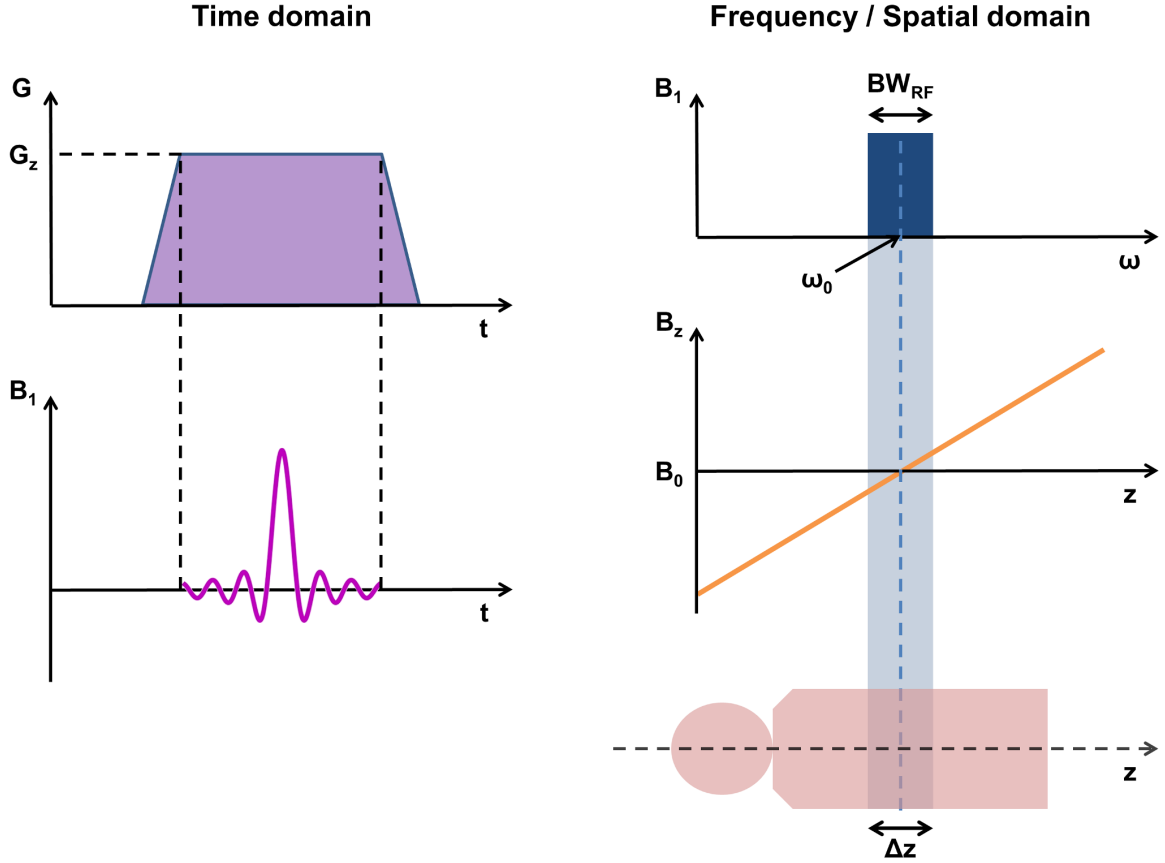
Figure 3.19: Left: time domain representation of a slice selection gradient of amplitude G_z along the z axis, and corresponding frequency-selective (sinc) radiofrequency pulse. Right: frequency domain representation of the radiofrequency excitation and the accompanying magnetic field gradient. Right bottom: the spatial domain depicting the resulting slice of thickness Δz. Adapted with permission from [178] and [175].

the change in Larmor frequency with position is given by (c.f. Equation 3.91):

$$f(z) = \frac{\gamma}{2\pi} G_z z \tag{3.99}$$

If the desired slice is centred at the isocentre of the $\boldsymbol{B_0}$ field, then the slice must span a frequency range Δf with frequencies at the edge of the slice given by $f_0 \pm \frac{\Delta f}{2}$. Depending on the strength of the gradient, this range of frequencies is associated with a spatial extent Δz:

$$\Delta z = \frac{2\pi \Delta f}{\gamma G_z} \tag{3.100}$$

Δz thus describes the thickness of a slice excited by an RF pulse with a bandwidth $BW_{RF} = \Delta f$. There-

---

the Fourier transformation reduces to a two-dimensional problem in x and y, as shown in Figure 3.15.
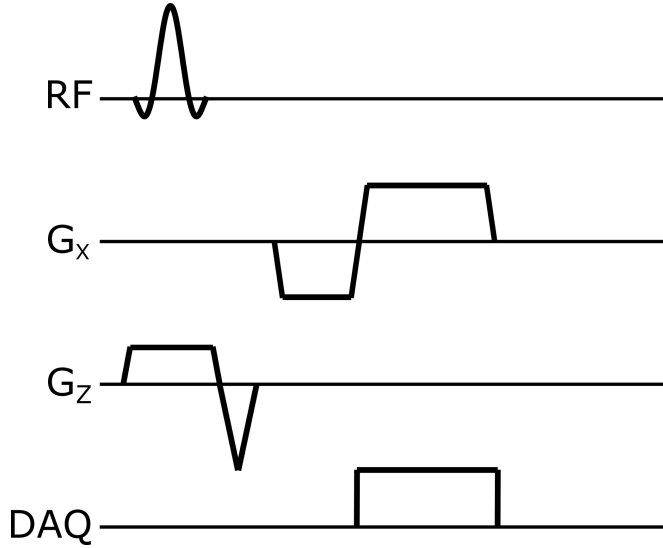
Figure 3.20: Depiction of a slice selection gradient on the pulse sequence timing diagram. The RF axis depicts a truncated sinc pulse, played out at the same time as the slice selection gradient on the G_z axis. G_x represents the frequency encoding gradient, and DAQ denotes the position of the data acquisition window.

fore, the slice thickness can be controlled by the strength of the slice selection gradient and the bandwidth of the radiofrequency pulse.

In order to excite a slice of spins situated at a position δz away from the isocentre, the transmission frequency of the RF pulse must be shifted from f_0 by a factor δf:

$$\delta f = \frac{\gamma}{2\pi} G_z \delta z \tag{3.101}$$

where the gradient amplitude G_z remains unchanged from a slice located at isocentre. In practice, most MR imaging scans acquire a set of slices (at a number of frequency offsets) in a given gradient direction in order to obtain a set of images over a particular volume of the sample. Slices are either acquired sequentially (i.e. k-space is encoded in its entirety for one slice, then the next slice, and so on) or in an interleaved fashion (for each encoded point in k-space, all slices are acquired before moving to the next point in k-space).

Slice selection gradients can be applied on axes other than z in order to localise the RF excitation to slices in one of the other anatomical planes (sagittal or coronal). Furthermore, it is possible to apply two or more slice selection gradients on different axes in order to localise excitations to slices at an oblique angle to one of the principal axes. For example, gradients of amplitude $G_x = G_{SS}\cos(\xi)$ and $G_y = G_{SS}\sin(\xi)$ can be employed to obtain a slice at an angle ξ from the x axis (where G_{SS} is the amplitude of the slice selection gradient defined by the desired slice thickness in Equation 3.100).

It is not practically feasible to obtain a perfectly rectangular slice profile. A true sinc function has limits that extend to $\pm\infty$, however, practicality, safety and time constraints enforce that sinc pulses be truncated / apodised for realistic MRI applications, such that the number of sidelobes of the pulse is restricted. The Fourier transform of the truncated sinc function is not a perfect rect function; instead there is some rippling and fall-off of the excitation profile at the edges of the slice, and hence excitation of some spins outside of the desired slice profile results. For many in vivo MR imaging applications, sinc pulses are

not used; instead, tailored Shinnar La Roux [194] or Gaussian pulses are commonly employed to achieve better excitation profiles, although trade-offs between the RF pulse width, SAR, and desired slice profile are still required. Shinnar La Roux algorithms offer a means to solve the Bloch equations numerically, which become non-linear for $B_{1,xy} > 0$ (i.e. the problem has no general analytical solution unlike in the previous subsection).

In addition to inadequacies in the RF excitation profile, inhomogeneity or non-uniformity of the slice selection gradient itself could result in a modulation of the slice profile from the ideal rectangular shape. Furthermore, if the sample of interest comprises spins with different chemical shifts, the slice positions of these chemically-different species will be offset from each other, causing potential misinterpretation of the spatial position of a given species.

Note: the action of the slice selection gradient produces some phase dispersion along the gradient axis during the application of the RF pulse. In order to reverse this phase dispersion, the slice selection gradient is usually immediately followed by a slice rephasing gradient, which has opposite polarity to the slice selection gradient (shown as a negative triangle after the slice selection trapezoid in Figure 3.20). Conventionally, the slice rephasing gradient has a total area equal to half the area of the slice selection gradient, assuming that the centres of the RF pulse and the slice selection gradient are aligned. Conceptually, it can be imagined that the RF pulse acts instantaneously at the centre of the slice selection gradient, such that excited spins accumulate a position-dependent phase in the second half of the slice selection gradient, which must be corrected by the rephasing gradient.

Phase encoding

It is not possible to assign a unique frequency to every point in a two dimensional slice by simultaneously applying frequency encoding gradients in two dimensions (there will always be two or more points that have the same assigned frequency). In order to encode spatial signals in y (or spatial frequencies in k_y), an alternative technique known as phase encoding can be employed.

As shown by Equation 3.92, spins accrue a phase according to their spatial location in the presence of a magnetic field gradient. Where frequency and phase encoding differ is that when the magnetic field gradient is switched off, the spins return to precessing with a common resonance frequency (i.e. frequency encoding is turned off); however, the phase differences induced by the gradient remain. In other words, the phase dispersion induced by the gradient is permanent (or, until it is reversed by another gradient), whilst the frequency dispersion is transient and only occurs during the time when the gradient is non-zero. Phase encoding is implemented in practice by switching on a phase encoding gradient (e.g. along the k_y direction) for a certain length of time following the RF pulse, and then switching it off, and subsequently playing out the normal frequency encoding gradient to resolve the spatial distribution of signals in x.

However, one phase encoding gradient can only be used to resolve one phase component (i.e. one step in k_y), rather than the full range of k_x probed by a single frequency encoding gradient amplitude. This is because, whilst the Fourier transform can distinguish between individual frequency components, it cannot distinguish between different phase shifts for spins resonating at the same fundamental frequency [xvi]. This problem is resolved by repeating the acquisition for a number of different amplitudes of the

---

[xvi]This can be understood by taking an example of the summation of two sinusoids oscillating at the same frequency but with different phase offsets; the summation results in a sinusoid that oscillates at the same basic frequency as the individual
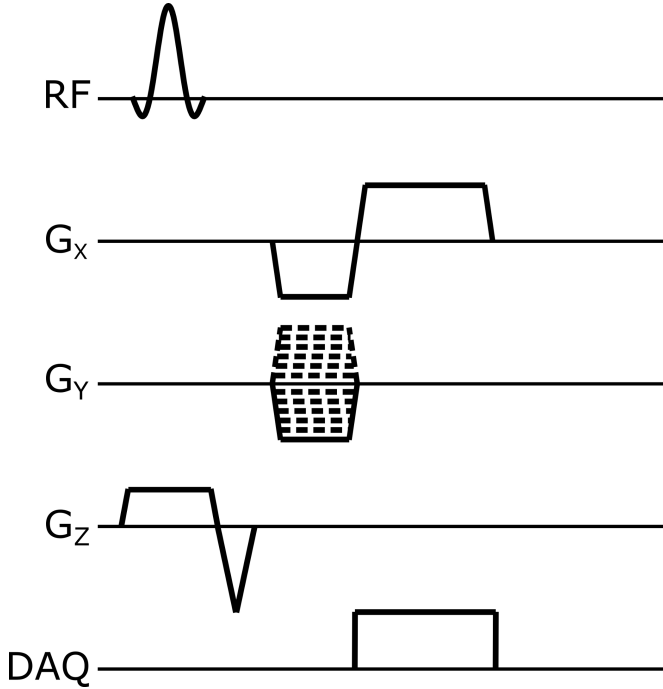
Figure 3.21: Depiction of a phase encoding gradient on the pulse sequence timing diagram. The RF axis depicts a truncated sinc pulse, simultaneously applied with the slice selection gradient on the G_z axis. G_x represents the frequency encoding gradient, and DAQ denotes the position of the data acquisition window. G_y depicts the conventional means of displaying a phase encoding gradient as a number of different gradient amplitudes on top of each other. This depiction is chosen to represent the fact that acquisition of the whole of the 2D k-space k_{xy} requires the sampling of a number of different phase encode gradient amplitudes. For each new phase encoding gradient (each new "repetition" of the sequence), the slice selection and frequency encoding gradient amplitudes remain constant.

phase encoding gradient; each different amplitude introduces a distinct relative phase shift. As such, N_y phase encoding gradient amplitudes can be used to distinguish N_y phase components (i.e. N_y steps in the k_y direction). The total time required to encode a complete 2D k-space is therefore defined by the product $N_y TR$, where TR represents the "repetition time"; the time required for acquisition of one line of k-space.

The resulting phase encoded signals in k_y can be converted into a corresponding spatial distribution in y by a 1D Fourier transform. In practice, frequency encoding and phase encoding are unravelled simultaneously by the 2D Fourier transform (Equation 3.83). The relative positioning of the phase encoding gradient is shown in the pulse sequence timing diagram in Figure 3.21.

The mathematical basis for describing the phase accrued during a gradient has already been introduced; a phase encoding gradient in the y direction can be considered by transforming $x \rightarrow y$ in Equation 3.92. The maximum area of the phase encoding gradient — required to acquire the k-space line corresponding to $k_{y,max}$ — can be derived as follows.

Usually, N_y phase encodes are acquired symmetrically about $k_y = 0$, with one acquisition corresponding to $k_y = 0$, such that $k_{y,max} = \frac{1}{2}(N_y - 1)\Delta k_y$. According to Equation 3.89, the spacing of subsequent phase encoding steps in k-space is given by $\Delta k_y = \frac{1}{L_y} = \frac{1}{N_y \Delta y}$. Thus, the maximum area of the phase encoding gradient is:

$$A_{y,max} = \int_0^t G_y(t')\,\mathrm{d}t' = \frac{2\pi}{\gamma}k_{y,max} = \frac{\pi(N_y - 1)}{\gamma L_y} \tag{3.102}$$

---

sinusoids, but with a single phase shift that is the average of the two individual phase shifts. Hence, the two phases cannot be resolved by a Fourier transform; only one averaged phase value would be apparent.

The duration of the phase encoding gradients is typically minimised in order to reduce the time required for one repetition of the pulse sequence; as such, the maximum phase encoding gradient area $A_{y,max}$ will generally result from applying a gradient of maximum amplitude and slew rate.

Similar principles to those discussed previously for asymmetric / partial echo sampling in the frequency encoding direction can be applied in the phase encoding direction. By exploiting the conjugate symmetry of the Fourier transform in the k_y direction, it is possible to reconstruct an image from data acquired with just over half the number of phase encodes required to obtain a fully-sampled, symmetric k-space (where the "just over" lines are required to correct for phase errors). This technique is termed "half-Fourier" encoding. The major advantage of reducing the number of acquired phase encoding samples is that the overall scan time required to encode the entire k-space reduces by the same factor. Note: partial echo sampling cannot be combined with half Fourier encoding, because only acquiring only $\sim \frac{1}{4}$ of the fully-sampled k-space data is insufficient to exploit conjugate symmetry properties to synthesize the missing data.

Phase encoding can in principle be applied in any number of spatial dimensions. In fact, the frequency encoding gradient could be replaced by a series of phase encoding gradients, although in practice this is rarely done as it necessitates that the total scan time increases by a factor of N_x. However, for certain applications, phase encoding can be applied in the z direction to replace slice selection (known as "slice encoding"). Pulse sequences with phase encoding in two dimensions (y and z) are generally classified as 3D sequences, because they require the introduction of a third k-space dimension, k_z. On the other hand, pulse sequences with one-dimensional phase encoding in y and slice selection in z are termed 2D slice-selective sequences, because the k-space representation is two-dimensional.

Acquisition of a 3D volume with a 3D sequence requires a lengthier scan time by a factor of N_z in comparison to the acquisition of each 2D slice. If 2D slices are acquired sequentially, then the number of acquisitions required to obtain N_z slices is equal to N_z, and hence if the TR is the same for the 2D and 3D sequences, the total scan time is the same. However, in practice, multiple slices can often be acquired in an interleaved manner within one TR, such that the number of acquisitions required to sample all slices is $< N_z$, and therefore a 2D sequence would be completed faster than a corresponding 3D sequence with equal TR.

In addition, the SNR of 2D and 3D acquisitions can be compared. The SNR of an MR acquisition is proportional to the product of the three pixel dimensions and the square root of the total time required to sample the complete data-set. Hence, for a 3D sequence:

$$SNR_{3D} \propto \Delta x \Delta y \Delta z \sqrt{N_y N_z \mathrm{NSA} T_{acq}} \tag{3.103}$$

where NSA represents the number of spectral averages, which is the number of times that each k-space point (or image pixel) is sampled, and T_{acq} is length of time for which the data acquisition window is open. The SNR of a 2D slice-selective sequence is similarly related by:

$$SNR_{2D} \propto \Delta x \Delta y \Delta z \sqrt{N_y \text{NSA} T_{acq}} \tag{3.104}$$

Thus $\frac{SNR_{3D}}{SNR_{2D}} = \sqrt{N_z}$. However, if interleaved acquisition of 2D slices is possible, this permits a comparable or equivalent SNR to an analogous 3D sequence to be obtained.

Finally, 2D slice-selective acquisitions are limited by imperfect slice profiles as discussed in the previous subsection; generally, 3D phase-encoded acquisitions produce better-resolved "slices". Furthermore, the minimum resolution (i.e. slice thickness) that can be obtained in 3D acquisitions in typically lower than that of 2D acquisitions within standard hardware and timing limitations; as shown by Equation 3.100, 2D slice thicknesses are limited by the maximum achievable gradient amplitude and RF bandwidth. Nevertheless, 3D sequences introduce the possibility of Gibbs' artefacts in the z direction which are not encountered in 2D slice-selective acquisitions. Since Gibbs' artefacts are alleviated by reducing the slice thickness, in reality, 3D sequences are only used in place of 2D sequences when the desired slice thickness is less than a certain threshold value.

3.2.5 MR imaging sequences

Gradient echo and subclasses

The most basic gradient echo imaging sequence is composed of each of the individual spatial encoding components discussed above: an RF pulse with simultaneously-applied slice selection gradient; a phase encoding gradient; and a frequency encoding gradient. The relevant pulse sequence timing diagram has been presented in Figure 3.21.

Gradient echo sequences employ small flip angle RF pulses ($\alpha < 90°$), allowing a short repetition time (TR) between subsequent phase encoding steps. By virtue of the fact that the TR of a GRE sequence is usually much less than the spin-lattice relaxation time, T_1, there is insufficient time within one repetition for the longitudinal magnetisation to fully recover. After a few RF pulses have been applied to the system with a fixed repetition time between them, a "steady-state" or "dynamic equilibrium" is reached; as such, the proportion of longitudinal magnetisation excited per repetition is equivalent to the proportion recovered by spin-lattice relaxation in one repetition.

In addition, if $TR < T_2$, some transverse magnetisation remains at the end of each repetition. This *residual* transverse magnetisation is conventionally dealt with in one of two ways: "spoiling" (i.e. eliminating) the residual transverse magnetisation; or "rewinding" (i.e. preserving) it for use in the next iteration of the sequence.

Firstly, spoiled gradient echo (SPGR, a.k.a fast low angle shot (FLASH)) sequences denote a classification of pulse sequence in which the transverse magnetisation is destroyed at the end of each sequence repetition. This magnetisation spoiling can be implemented by: a) selecting $TR \gtrsim 5T_2$, such that the transverse magnetisation has naturally decayed away to zero by the end of the repetition; b) applying "spoiler" magnetic field gradients after the frequency encoding gradient in order to dephase residual magnetisation; c) varying the phase of the RF excitation pulse between acquisitions in order to accentuate the natural dephasing process. In practice, the first method is not routinely used because it negates the speed advantage of SPGR sequences as compared to other approaches. The most effective technique for spoiling

Figure 3.22: Pulse sequence timing diagram for a typical two-dimensional spoiled gradient echo (SPGR) pulse sequence. RF: radiofrequency excitation axis; G_x: frequency encoding gradient axis; G_y: phase encoding gradient axis; G_z: slice selection (and spoiler) gradient axis; DAQ: data acquisition axis. One instance of this timing diagram (with one phase encoding gradient amplitude) represents one repetition, of length TR.

with magnetic field gradients is to use a spoiler gradient amplitude that varies in a pseudo-random fashion from acquisition to acquisition. However, gradient spoiling is inherently spatially-nonuniform, and RF spoiling, by varying the phase of each RF pulse in a pseudo-random manner (or according to a specific cyclical schedule) often provides better, spatially-uniform results [xvii]. The pulse sequence timing diagram for a typical 2D SPGR sequence is shown in Figure 3.22.

By considering the propagation of longitudinal and transverse magnetisation between successive sequence repetitions after steady-state has been reached, an expression for the steady-state signal of a perfectly-spoiled SPGR sequence can be derived as:

$$S_{SPGR} \propto \frac{\sin\left(\alpha\right)\left(1 - \exp\left(-\frac{TR}{T_1}\right)\right)\exp\left(-\frac{TE}{T_2^*}\right)}{1 - \cos\left(\alpha\right)\exp\left(-\frac{TR}{T_1}\right)} \tag{3.105}$$

where the constant of proportionality will be related to the spin density, ρ. The RF excitation flip angle that provides the maximum signal intensity can hence be derived by differentiating Equation 3.105 with respect to α, to obtain the result:

$$\alpha_E = \arccos\left[\exp\left(-\frac{TR}{T_1}\right)\right] \tag{3.106}$$

[xvii]A spatially-uniform result is only achieved if a phase encoding rewinder gradient is used to ensure that the total gradient area on each axis does not vary between repetitions.

where α_E is often termed the *Ernst* angle (see [195]). Note: in the limit that $TR \gg T_1$, $\alpha_E \to 90°$, however, in most applications, $TR < T_1$, so the Ernst angle will be less than $90°$.

Equation 3.105 can be analysed to determine the conditions required for different image contrast to be obtained. The contrast of an SPGR image will depend upon a combination of the T_1, T_2^*, and spin density, according to the flip angle and pulse sequence timing settings. At long echo times, the image contrast is dominated by T_2^* relaxation (the image is said to be "T_2^*-weighted"). At low flip angles, $\cos(\alpha) \to 1$, such that the $1 - \exp\left(-\frac{TR}{T_1}\right)$ terms in the numerator and denominator of Equation 3.105 cancel and the image contrast is dominated by the spin density. T_1-weighted images can be obtained by increasing the flip angle and/or decreasing the TR.

The second approach to dealing with residual transverse magnetisation present at the end of a given acquisition is to recycle it and utilise it in subsequent acquisitions. "Rewound" GRE sequences (such as gradient recalled acquisition in the steady-state (GRASS), a.k.a. fast imaging with steady precession (FISP)) have an additional phase "rewinder" gradient at the end of the repetition to re-phase the transverse magnetisation and enforce consistency in the phase gradient area between repetitions; this ensures that spins are phase coherent. As a result, this leads to the formation of a steady-state *transverse* magnetisation after a few repetitions, in addition to an analogous steady-state *longitudinal* magnetisation that is observed with SPGR sequences. This concept is illustrated in Figure 3.23.
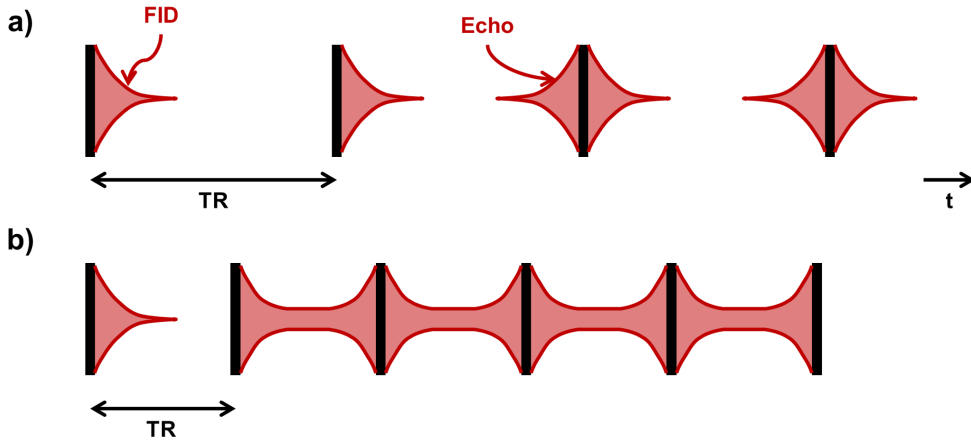
Figure 3.23: Formation of a steady-state transverse magnetisation. a) Any two successive RF pulses with an inter-pulse spacing TR produce an echo at a time $2TR$. Thus, each subsequent RF pulse in a train will be immediately preceded by the formation of an echo from the previous RF pulse pair, and immediately succeeded by the FID generated by the current pulse itself. If $TR \gg T_2$, the transverse magnetisation decays to zero between successive RF pulses. b) However, if $TR < T_2$, the subsequent FID and echo signals will overlap, such that a steady-state transverse magnetisation is generated for each acquisition. Adapted with permission from [180].

The development of a steady-state transverse magnetisation requires a number of conditions to be met: (i) fundamentally, TR must be less than T_2, otherwise the transverse magnetisation would die away naturally before the next RF pulse; (ii) gradient-induced phase shifts must be consistent between cycles (i.e. a phase rewinder gradient is needed); (iii) field inhomogeneities (causing a variation of phase across the object) must be constant (i.e. static) throughout the complete acquisition.
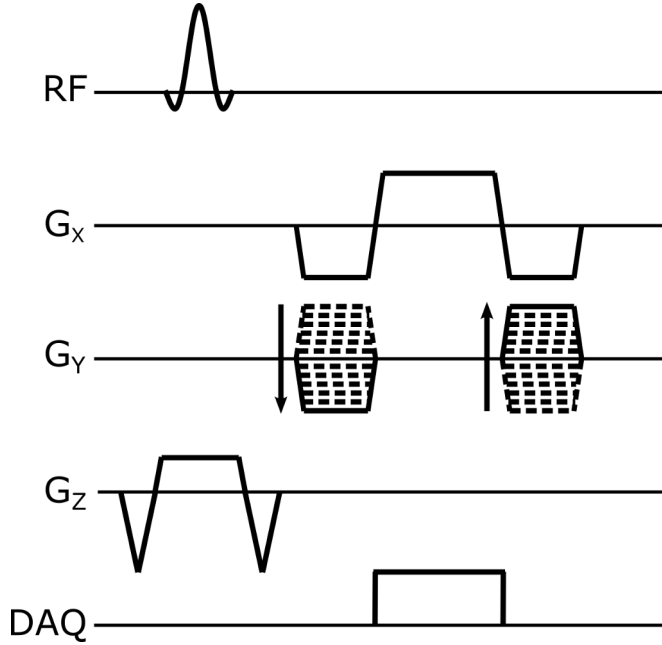
Figure 3.24: Pulse sequence timing diagram of a typical two-dimensional balanced steady-state free precession (bSSFP) pulse sequence. RF: radiofrequency excitation axis; G_x: frequency encoding gradient axis; G_y: phase encoding gradient axis; G_z: slice selection gradient axis; DAQ: data acquisition axis.

As shown in Figure 3.23, after steady-state is reached, the transverse magnetisation is made up of an FID-like signal that forms immediately after each RF pulse, and an echo-like signal that forms immediately prior to that RF pulse, resulting from previous combination(s) of RF pulses [xviii]. In most steady-state pulse sequences, the phase of the RF pulse is alternated, because this leads to more efficient restoration of longitudinal magnetisation and hence a higher steady-state signal than if the RF pulse was always applied in the same direction.

Balanced steady-state free precession (bSSFP, a.k.a True FISP) sequences are rewound GRE sequences in which the gradients on all three axes are completely balanced, such that the time integral of the gradients along each axis is zero. As a result, the peaks of the FID- and echo-like signals occur at exactly the same instance in time (the centre of the TR). As with conventional rewound GRE sequences, alternation of the sign of the RF pulse (changing the phase of the pulse by $\pm180°$ each repetition) is routinely implemented to yield an optimum steady-state signal.

The signal dependence of a bSSFP sequence can be derived in the same manner as that of a spoiled GRE sequence, and leads to the following result (assuming that the sign of the RF pulse alternates each repetition):

$$S_{SSFP} \propto \frac{\sin\left(\alpha\right)\left[1 - \exp\left(-\frac{TR}{T_1}\right)\right]\exp\left(-\frac{TE}{T_2}\right)}{1 - \cos\left(\alpha\right)\exp\left(-\frac{TR}{T_1}\right) - \exp\left(-\frac{TR}{T_2}\right)\left[\exp\left(-\frac{TR}{T_1}\right) - \cos\left(\alpha\right)\right]} \tag{3.107}$$

where again, there will be a constant of proportionality related to the spin density, ρ. T_2^* is replaced with T_2 to represent the transverse magnetisation decay prior to the echo time, which is valid if $TE = \frac{TR}{2}$

[xviii]FISP acquisitions sample the FID-like signal, and an equivalent and opposite acquisition-type (known as PSIF) exists which samples the echo-like signal.

(otherwise, if the echo position is shifted from the centre of the repetition, the signal will be influenced somewhat by T_2'). This T_2 dependence can be thought of as originating from the fact that the echo-like signals arise from a combination of spin echo- and stimulated echo-type contributions [xix]. For further details, the reader is referred to [196].

bSSFP sequences are acutely sensitive to inhomogeneity in the main magnetic field $\boldsymbol{B_0}$. If the phase accumulated per TR due to field inhomogeneities is equivalent to $180°$, then the effect of RF phase alternation is completely opposed. Associated signal losses appear as dark bands in the image, characteristically associated with regions of high susceptibility difference, or poor $\boldsymbol{B_0}$ homogeneity. Since the phase accrued in a given repetition depends upon the sequence TR, very short TR values are typically chosen for bSSFP sequences in order to minimise the prevalence of these "banding" artefacts. Equation 3.107 can be simplified for $TR \ll T_1, T_2$ by expanding the exponentials as a Taylor series (i.e. $\exp\left(-\frac{TR}{T_{1,2}}\right) \approx 1 - \frac{TR}{T_{1,2}}$), to yield:

$$S_{SSFP} \propto \frac{\sin(\alpha)\exp\left(-\frac{TE}{T_2}\right)}{\left(\frac{T_1}{T_2}\right)[1 - \cos(\alpha)] + 1 + \cos(\alpha)} \tag{3.108}$$

which has a maximum signal at $\alpha_E = \arccos\left(\frac{T_1 - T_2}{T_1 + T_2}\right)$. This equation dictates that the bSSFP signal is essentially independent of TR if TR is short; the signal varies only as a function of flip angle and the ratio $\frac{T_2}{T_1}$. In particular, for a flip angle of $90°$, Equation 3.108 simplifies further to:

$$S_{SSFP} \propto \frac{T_2\exp\left(-\frac{TE}{T_2}\right)}{T_1 + T_2} \tag{3.109}$$

which becomes $\frac{1}{2}\exp\left(-\frac{TE}{T_2}\right)$ if $T_2 \approx T_1$, and $\frac{T_2}{T_1}\exp\left(-\frac{TE}{T_2}\right)$ if $T_2 \ll T_1$.

In most cases, bSSFP images exhibit a mixture of T_1 and T_2 weighting; as seen in Equation 3.108, the bSSFP contrast can be defined by the ratio $\frac{T_2}{T_1}$, particularly for the case of high flip angles (c.f. GRASS sequences, which inherently exhibit some T_2^* weighting). As such, fluids, which have long T_2 values, appear bright on bSSFP images. Although not routinely employed, the use of low flip angles leads to increased spin density weighting. In addition to magnetic field inhomogeneities, bSSFP sequences are particularly sensitive to motion and flow which can destroy the coherence in transverse magnetisation built up between subsequent acquisitions.

3D balanced steady-state sequences, and the process of simulating the magnetisation dynamics for 3D bSSFP imaging with hyperpolarised gases, form the substance of Chapter 4 of this thesis.

Spin echo and subclasses

Standard single-echo spin echo (SE) sequences employ a $90°$ RF excitation pulse, followed by a $180°$ refocusing pulse, and the aforementioned spatial encoding gradients, as illustrated in Figure 3.25. Whilst for

---

[xix]Stimulated echoes form from three consecutively-applied RF pulses; the first pulse generates transverse magnetisation, which is converted to longitudinal magnetisation by the second pulse, and then refocussed by the third to generate an echo signal.
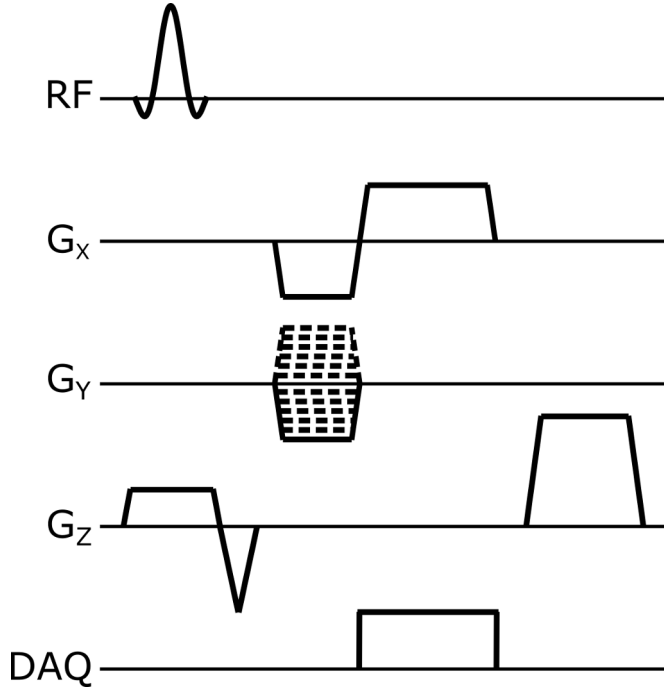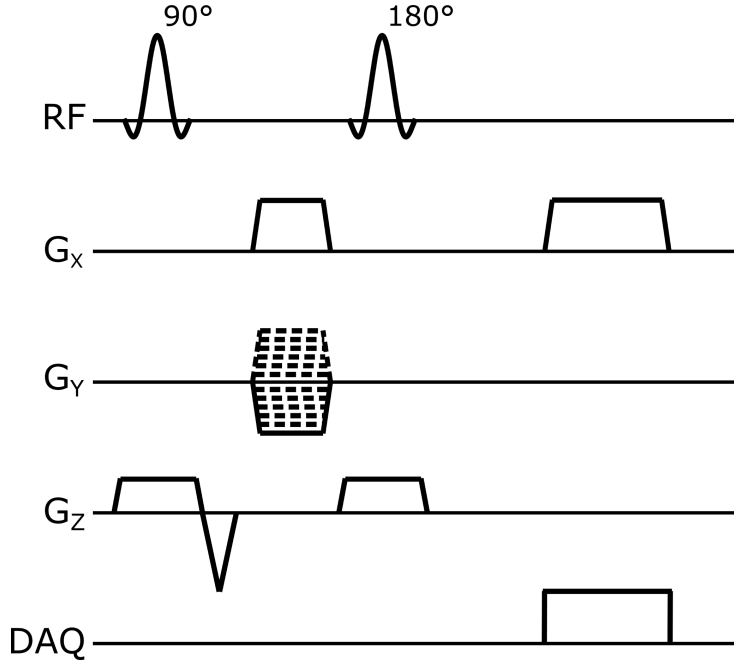
Figure 3.25: Pulse sequence timing diagram for a typical two-dimensional spin echo (SE) pulse sequence. RF: radiofrequency excitation axis; G_x: frequency encoding gradient axis; G_y: phase encoding gradient axis; G_z: slice selection gradient axis; DAQ: data acquisition axis.

gradient echo sequences, the prephasing lobe of the frequency encoding gradient has a negative polarity and is positioned immediately before the part of the frequency encoding gradient where data acquisition is performed, in spin echo sequences, the prephasing lobe has positive polarity and is positioned prior to the 180° pulse, because the echo is RF-induced rather than gradient-induced. The position of the resulting echo is determined by when the area under the frequency encoding lobe is equal to that of the prephasing lobe. Conventionally, the time at which the gradient areas are equal is designed to be the same as the time at which the RF spin echo would be formed in the absence of imaging gradients; if these two times are not equivalent the echo intensity will be reduced by a factor $\exp\left(-\frac{t_{off}}{T_2^*}\right)$, where t_{off} is the time difference between the position of the RF- and gradient-induced echoes.

By considering the propagation of longitudinal and transverse magnetisation during one instance of a spin echo sequence, an expression for the signal of a SE sequence (assuming flip angles of 90° and 180°) can be obtained:

$$SNR_{SE} \propto \left[1 - 2\exp\left(-\frac{(TR - \frac{TE}{2})}{T_1}\right) + \exp\left(-\frac{TR}{T_1}\right)\right]\exp\left(-\frac{TE}{T_2}\right) \qquad (3.110)$$

where all symbols have their previously-defined meanings. In the case $TE \ll TR$, this equation simplifies to:

$$SNR_{SE} \propto \left[1 - \exp\left(-\frac{TR}{T_1}\right)\right]\exp\left(-\frac{TE}{T_2}\right) \qquad (3.111)$$

A full form of Equation 3.110 can be derived for arbitrary flip angles of the excitation and inversion RF

pulses; indeed, it is readily seen from the full form that the maximum signal is obtained with flip angles of 90° and 180° for the two pulses, respectively.

The timing parameters of a spin echo sequence can be tailored to produce image weighting dominated by T_2, T_1 or spin density, depending on the desired application. As can be seen from Equations 3.110 and 3.111, at short echo and repetition times, T_1-weighted images will be obtained, whilst long TE and TR values lead to T_2-weighted images. Spin density weighting can be achieved at an intermediate situation of long TR and short TE (note: as before, the proportionality constant in Equations 3.110 and 3.111 is directly related to the spin density).

Provided that sufficient transverse magnetisation remains at the end of each sequence repetition, one or more additional echoes may be generated by subsequent 180° RF pulses. As such, additional images can be acquired, each with a different T_2 weighting [xx]. Of particular interest, dual-echo sequences usually involve the acquisition of one image with a short TE and one with a long TE, which will be weighted by proton density and T_2, respectively.

SE sequences are characteristically slower than GRE sequences, especially when T_2 or spin density contrast is needed. In practice, normally both the excitation pulse and refocusing pulse are slice selective, such that multiple slices can be excited in an interleaved manner within one repetition time. In addition, species with sufficiently long T_2 relaxation times afford the possibility of multiple k-space lines to be acquired within a single TR, by generating multiple echoes with different phase encodings.

Fast spin echo (FSE, a.k.a. turbo spin echo, TSE, or rapid acquisition with relaxation enhancement, RARE) sequences involve the acquisition of multiple phase encoding lines per TR by acquiring multiple echoes with different phase encoding gradients applied just prior to each echo. In order to preserve signal coherence and traverse k in the same direction for each consecutive echo, a phase rewinding gradient must be applied after each acquisition. The phase of the 180° RF pulses is typically shifted by 90° with respect to the initial excitation pulse in order to correct for phase errors that can be introduced by diffusion effects, imperfect 180° pulses and/or inhomogeneity of the $\boldsymbol{B_1}$ field. A schematic of a typical FSE pulse sequence is shown in Figure 3.26.

The major benefit of FSE-based approaches is that the total scan time required for a FSE sequence is reduced by a factor equal to the echo train length (ETL; the number of echoes acquired per TR) as compared with a conventional SE sequence. These time saving benefits are often crucial for practical applications where T_2-weighted images are desired (long TR, long TE needed). In addition, as with standard SE sequences, 2D FSE approaches permit interleaving of multiple slice acquisitions per TR, whilst 3D FSE sequences involve phase encoding along one dimension using the echo train and phase encoding in the other dimension is conventionally performed step-wise after each TR.

In a similar manner to standard SE sequences, FSE sequences can be designed to obtain images with T_1, T_2 or spin density contrast by accordingly altering the TE and TR. However, the definition of TE must be considered differently in a FSE sequence as compared to a conventional SE sequence. As a result of the different phase encoding steps being applied for different echoes, different lines of k-space are acquired at distinct values of TE (where TE is the time difference between the initial excitation pulse and the

---

[xx]In these multi-echo sequences, the same phase encoding gradient applies to all subsequent echoes, unlike in the case of FSE sequences, as discussed below.
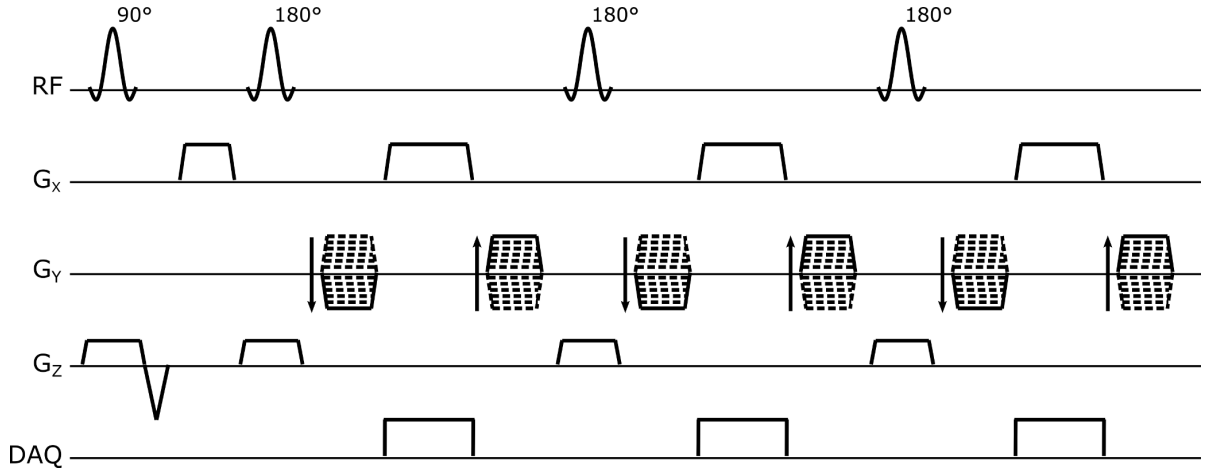
Figure 3.26: Pulse sequence timing diagram of a typical two-dimensional fast spin echo (FSE) pulse sequence. RF: radiofrequency excitation axis; G_x: frequency encoding gradient axis; G_y: phase encoding gradient axis; G_z: slice selection gradient axis; DAQ: data acquisition axis.

centre of each echo). In practice, the *effective* echo time defining the overall image contrast is the time associated with the acquisition of the central line(s) of k-space. Therefore, a cluster of central k-space lines acquired with TE values close to the TE of a conventional SE sequence chosen for a specific image contrast weighting will yield a FSE image with comparable contrast to that SE image. Note: in addition to the effective echo time, the ETL is a critical determinant of FSE image contrast. For example, increasing the ETL will lead to stronger T_2 weighting.

Furthermore, dual-echo FSE sequences can be employed to obtain two images at different effective echo times, weighted by spin density and T_2. A common means of implementing dual-echo FSE is view-sharing, where the central lines of k-space are acquired at both early and late effective TE values in the echo train; the k-space lines associated with higher spatial frequencies are shared between the two images, whilst the differing central lines provide a distinct contrast.

Trajectories for traversing k-space

In addition to the choice of pulse sequence and associated pulse sequence parameters, the manner in which k-space is traversed is an important factor that has a bearing on acquisition speed, image contrast and SNR. A number of both simple and complex k-space traversal approaches have been developed for specific applications, as briefly introduced below. A summary of some of the most common k-space acquisition trajectories is presented in Figure 3.27.

Conventionally, spin echo and gradient echo sequences employ a sequential (a.k.a. linear) trajectory for filling k-space points on a Cartesian grid. In sequential sampling, k-space lines are acquired in order from one edge ($k_{y,max}$) to the opposite edge ($-k_{y,max}$) or vice-versa, such that the central line ($k = 0$) is acquired approximately halfway through the scan. In single echo sequences, one line is acquired per RF excitation pulse, whilst in multi-echo sequences, a number of k-space lines can be acquired after only one RF excitation.

It is sometimes advantageous to acquire the central line of k-space at the beginning of the acquisition rather than halfway through. Centric encoding is a Cartesian sampling method similar to sequential

sampling, in which the order of acquired k-space lines is altered such that k-space is filled from the centre-out, rather than from one end to the other. This is achieved by consecutively switching between positive and negative phase encoding gradient amplitudes. Centric ordering is often employed in dynamic contrast-enhanced MRI with gadolinium contrast injection, to exploit the fact that the majority of the image contrast is dominated by the central k-space lines. Additionally, signals arising late in the scan can be suppressed using centric encoding schemes, because only the extremities of k-space will be sampled at that stage.

Echo planar imaging is an extreme example of fast encoding of k-space in which the entire k-space is encoded after one RF pulse. Typically, EPI follows a sequential Cartesian-type pattern, but the frequency encode gradient switches from positive to negative amplitudes such that each subsequent k-space line is acquired in the opposite direction. "Blipped" phase encoding gradients are typically applied after each line of k-space has been acquired, in order to add to the phase dispersion of the previous phase encoding gradient and therefore advance to the next k-space line. This results in a snake-like trajectory across k-space.
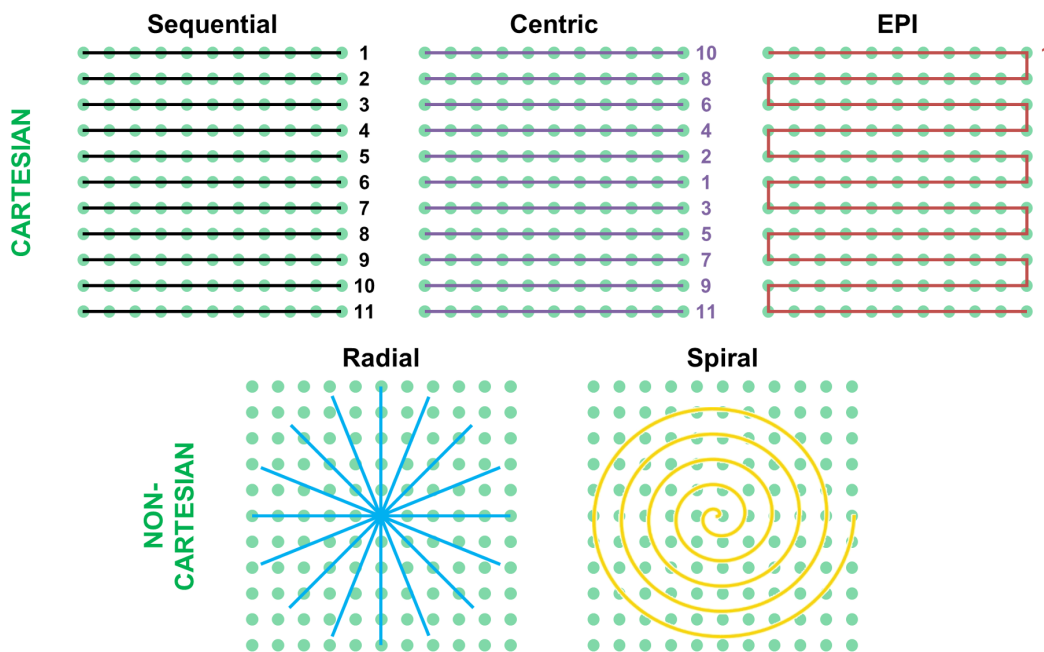
Figure 3.27: Summary of typical Cartesian and non-Cartesian trajectories for k-space traversal. (For Cartesian acquisitions, numbers indicate the order in which the k-space lines are acquired.)

Non-Cartesian methods of k-space sampling are classified as those which acquire points that do not lie on the standard Cartesian grid of equally-spaced points in k_x and k_y. A variety of techniques exist for encoding k-space by tracing different shapes in two or three dimensions. Although other methods are available, images are commonly reconstructed by a procedure is known as "gridding", which involves considering the contribution of each acquired data-point to each point on a standard Cartesian grid, and then mapping the non-Cartesian data-points onto the Cartesian grid such that a regular Fourier transform can be performed to obtain the desired image.

One of the most popular non-Cartesian sampling methods is radial encoding, where frequency encoding (read-out) gradients are simultaneously applied in the x and y (and z) directions with amplitudes governed by the trigonometric functions, in order to encode points tracing a circle (or sphere) in two-dimensional (or three-dimensional) k-space by sampling along radial "spokes" passing through the k-space origin. Radial acquisitions negate the need for phase encoding gradients and thus allow minimisation of the echo time, either by rapidly forming an echo with two gradients of opposite polarity, or by directly sampling the free induction decay with a unipolar gradient immediately after the RF excitation pulse. This permits imaging of species with extremely short T_2 values, such as protons in bone or tendons. Additionally, radial sequences are intrinsically robust to motion artefacts because the centre of k-space is sampled by all radial spokes; though the relatively reduced sampling density of the periphery of k-space can lead to image blurring.

An alternative non-Cartesian k-space sampling method is spiral encoding, which involves the application of time-oscillating gradients along x and y in order to trace a spiral pattern through k-space. As with radial acquisition strategies, spiral k-space trajectories remove the need for phase encoding gradients by simultaneously encoding multiple points in k_x and k_y. Spiral trajectories are typically implemented in a single-shot or multiple-interleaved manner, and afford considerably improved efficiency for encoding the whole of k-space as compared to Cartesian sequences. Nevertheless, any variations in Larmor frequency (off-resonance) across the sample due to $\boldsymbol{B_0}$ inhomogeneity and/or susceptibility artefacts can severely impact the application of spiral trajectories by inducing image blurring.

Motion encoding sequences: Diffusion and flow

Standard spin echo and gradient echo sequences can be modified to provided contrast weighting governed by the diffusion behaviour of the species of interest. This is achieved by the addition of two magnetic field gradients of equal area (known as "diffusion gradients") to the standard sequence. SE sequences achieve diffusion weighting by applying both diffusion gradients with positive polarity in between the slice selection pulse and the data acquisition, at either side of the 180° inversion pulse. The simplest implementation is sometimes referred to as a Stejskal-Tanner sequence [197]. In the case of GRE sequences, the two diffusion gradients have opposite polarity and do not straddle any other pulses or gradients. A characteristic pulse sequence timing diagram for a diffusion weighted (DW)-SPGR sequence is presented in Figure 3.28.

According to Equation 3.92, spins precessing in the transverse plane accrue a certain phase in the presence of any magnetic field gradient. The spatial position of a diffusing spin changes over time in a random fashion; as such, a random phase is accrued. The principle of the two diffusion gradients is such that, for spatially-fixed spins, the phase dispersion induced by the first gradient is reversed by the second gradient (which has an equivalent area), whilst the spins that have diffused in a random manner during the gradients will not be re-phased. Thus, MR signal is lost as a result of diffusion in the presence of these gradients. As shown below, this signal loss presents itself in a similar manner to standard transverse relaxation processes; therefore, the applied diffusion weighting must be sufficient for diffusion-related signal losses to dominate the MR signal behaviour over T_2 or T_2^* relaxation in the case of SE or GRE sequences, respectively.

The Einstein relationship for the mean square displacement of a spin diffusing for a time, t in one direc-
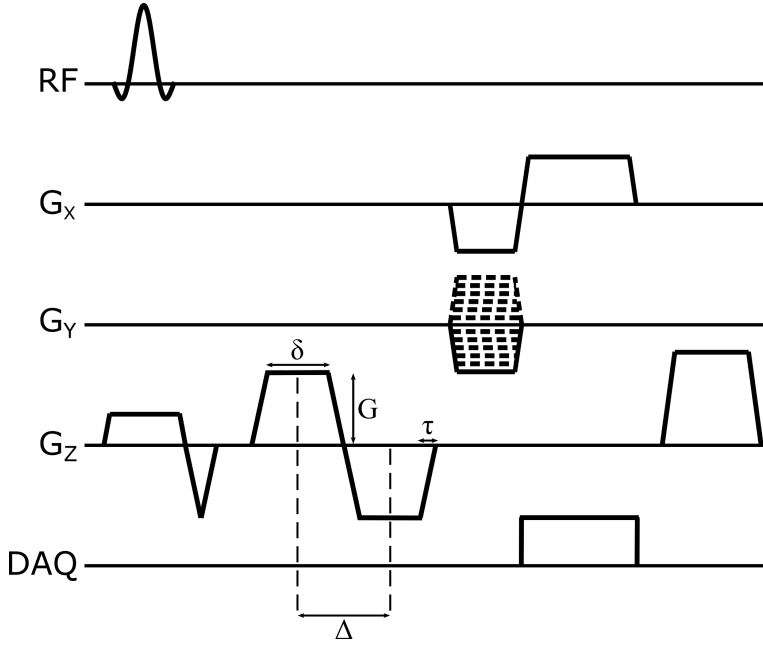
Figure 3.28: Pulse sequence timing diagram of a 2D spoiled gradient echo (SPGR) pulse sequence with bi-polar diffusion gradients added to the slice (G_z) axis for diffusion sensitisation. RF: radiofrequency excitation axis; G_x: frequency encoding gradient axis; G_y: phase encoding gradient axis; G_z: slice selection gradient axis; DAQ: data acquisition axis.

tion, x is given by $\langle x^2 \rangle = 2Dt$, where D is the diffusion coefficient. In three dimensions, this becomes $\langle |\boldsymbol{r}|^2 \rangle = 6Dt$ (assuming the diffusion coefficient is isotropic). In this subsection, diffusion gradients are considered to be applied on one direction only (chosen to be the z axis by convention), and hence diffusion along this axis only will contribute to measured MR signal losses.

For the sake of clarity, we note again that the phase accrued in the presence of an arbitrary magnetic field gradient (originally described in Equation 3.92 for a gradient in the x direction) is:

$$\Delta\phi\left(\boldsymbol{r}\right) = \int_0^t \omega\left(t'\right) \mathrm{d}t' = \gamma \int_0^t \boldsymbol{G}\left(t'\right) \cdot \boldsymbol{r}\left(t'\right) \mathrm{d}t' \tag{3.112}$$

where, in the case of a diffusing spin, $\boldsymbol{r}\left(t'\right)$ is not constant in time. The ensemble average of the phase modulation of transverse magnetisation induced by diffusion in the presence of an arbitrary magnetic field gradient is given by:

$$\langle \exp\left(i\Delta\phi\left(\boldsymbol{r}\right)\right)\rangle = \int_{-\infty}^{\infty} P\left(\Delta\phi\right) \exp\left(i\Delta\phi\right) \mathrm{d}\Delta\phi \tag{3.113}$$

where $\Delta\phi$ is as defined in Equation 3.112, and $P\left(\Delta\phi\right)$ is the probability density function describing the spread of $\Delta\phi$ values. In most diffusion-weighted MRI applications, $P\left(\Delta\phi\right)$ is assumed to follow a Gaussian / normal distribution, which yields $\langle \exp\left(i\Delta\phi\left(\boldsymbol{r}\right)\right)\rangle = \exp\left(-\langle\Delta\phi\rangle^2\right)$. This dictates that the loss in MR signal according to molecular diffusion follows an exponential relationship with diffusion coefficient, such that:

72

$$S = S_0 \exp\left(-\langle\Delta\phi\rangle^2\right) = S_0 \exp\left(-bD\right) \tag{3.114}$$

where b is defined as the *b-value* of a pair of diffusion gradients, measured in s.m^{-2}, and S_0 is the MR signal in the absence of diffusion. The b-value is governed by the properties of the applied diffusion gradients, and controls the strength of the diffusion weighting (i.e. it is analogous to TE determining the T_2 contrast of an image). Assuming a Gaussian phase distribution, the b value can be formally defined as:

$$b = \gamma^2 \int_0^{TE} \left[\int_0^t \boldsymbol{G}\left(t'\right) \mathrm{d}t'\right]^2 \mathrm{d}t = (2\pi)^2 \int_0^{TE} \boldsymbol{k}\left(t\right) \cdot \boldsymbol{k}\left(t\right) \mathrm{d}t \tag{3.115}$$

where the second equality defines b in terms of the k-space vector (c.f. Equation 3.79). The b-value is thus solely determined by the diffusion gradient waveforms and the gyromagnetic ratio of the species of interest. For many standard gradient waveform designs, the b-value can be analytically derived in terms of parameters describing the timing and amplitude of the diffusion gradients. As an example, for a gradient echo sequence, assuming perfectly rectangular diffusion gradients (i.e. $\tau = 0$ in Figure 3.28, which is practically impossible), the b-value is given by:

$$b = 2\gamma^2 G^2 \frac{\delta^2}{3} \tag{3.116}$$

It can therefore be seen that the degree of diffusion weighting can be controlled by: the amplitude of the diffusion gradients (G); the length of the plateau region of each diffusion lobe (δ); the length of the ramp region of each diffusion lobe (τ, assumed to be zero in this simplified case); and the separation of the two lobes ($\Delta = \delta + \tau$, measured from centre-to-centre or from leading edge to leading edge is the "effective" diffusion time), as defined pictorially in Figure 3.28.

It is worth noting that the diffusion-weighted signal equation (Equation 3.114) can be equivalently derived from a modified version of the Bloch equations that include a term for the diffusion coefficient, D. For completeness, in one dimension:

$$\frac{\mathrm{d}M_x}{\mathrm{d}t} = \gamma M_y \left(B_0 - \frac{\omega_r}{\gamma}\right) - \frac{M_x}{T_2} + \nabla \cdot \boldsymbol{D} \cdot \nabla M_x \tag{3.117}$$

where the term containing the diffusion coefficient is of exactly the same form as that of the standard diffusion equation; a fundamental result of Fick's laws, this conventionally describes the time-dependent concentration of a diffusing species. Equation 3.117 is known as the Bloch-Torrey equation and its generalised, 3D form is relevant for more complex situations of three-dimensional diffusion-weighted imaging, e.g. diffusion tensor imaging (DTI), where the diffusion behaviour is directionally-dependent (i.e. $\boldsymbol{D}$ is a

3D matrix).

In practice, the apparent diffusion coefficient, ADC, is used in place of D in the above analysis. The ADC is the measured or effective diffusion coefficient of the species of interest in a particular medium, which is often less than the "free" or "self" diffusion coefficient of the species. For instance, in the lungs, the diffusion of gas is restricted by the walls of the alveoli, and as such, the MR-observed diffusion coefficient of gases such as helium and xenon, the nuclei of interest in the experimental sections of this thesis, is significantly reduced as compared to the free diffusion coefficient, as introduced in Section 2.2.

Whilst any diffusion-weighted SE or GRE sequence can be utilised to obtain diffusion-weighted images, two or more acquisitions with different diffusion weightings offers the possibility of quantifying the ADC of a particular species in each voxel (in this case, the ADC can be defined as the mean diffusion coefficient observed in a given voxel). Typically, *maps* of the ADC parameter can be derived by interleaving the acquisition of k-space lines with the application of diffusion gradients associated with at least two different b-values (usually including $b = 0$). On a voxel-by-voxel basis, the ADC can be determined by fitting the natural logarithm of the signal intensities of images associated with different b values according to Equation 3.114. Measuring the apparent diffusion coefficient is a powerful means of assessing molecular motion in a particular environment, and hence gleaning information about the length scales by which diffusion is restricted (e.g. the dimensions of the alveoli which confine gas molecules, as discussed in Section 2.2).

In a similar manner to diffusion sensitisation of MR sequences, bi-polar gradients can also be utilised to encode information about the *velocity* of spins that are *flowing* in a particular direction. Again, motion in each direction is considered separately by applying gradients along each of the three principal axes. Whilst diffusional motion is spatially-random by nature, flow motion is regarded as coherent motion of particles along a single direction. Thus, constant velocity flow in the x direction can be treated by replacing $\boldsymbol{r}(t') \rightarrow x(t') = x'_0 + v_x t'$ in Equation 3.112, which results in a total accumulated phase after the bi-polar gradients that is linearly proportional to the flow velocity v_x in the gradient direction.

Analogous to the b-value of diffusion-weighted imaging, the "strength" of velocity encoding of an image can be defined by a parameter v_{enc}, which is the flow velocity that would result in an accumulated phase shift of π. Although its exact mathematical formalism is beyond the scope of this review, v_{enc} is related to the strength and separation of the bi-polar gradients, and determines the range of flow velocities that will be highlighted in a given velocity-encoded acquisition. It is worth noting that in principle, information about higher orders of motion, including acceleration, can be revealed by applying particular combinations of gradients (with more than two lobes) prior to the acquisition.

Finally, it should be noted that whilst flow encoding schemes are designed to reveal specific aspects of flow motion, there are a number of ways in which flow motion can affect standard MR imaging sequences (that do not possess flow encoding gradients). For example, flow enhancement can be observed in images where a slow-flowing component enters the imaging volume during the acquisition; the spins in this component are excited by fewer MR pulses and are hence associated with a higher signal than the spins localised to the imaging volume. This principle, known as time-of-flight, can be exploited to obtain non-contrast-enhanced MR angiograms. Similarly, signal losses in SE sequences can result from fast-flowing species that are subjected to the initial RF excitation but then flow out of the imaging volume before the inversion pulse is applied. Furthermore, phase errors will be introduced by flow motion during imaging

gradients, or in the presence of an inhomogeneous $\boldsymbol{B_0}$ field (since a phase difference will be accrued by moving spins according to the same principles applied for velocity encoding).

3.2.6   Specifics of hyperpolarised gas lung MRI

Many of the customised approaches employed for optimised hyperpolarised gas imaging of the lungs were introduced in Chapter 2. In this subsection, considerations for hyperpolarised gas MR implementation from the perspectives of polarisation hardware and pulse sequence design are discussed with reference to the aforementioned acquisition techniques. Additionally, a summary of the NMR-relevant properties of ^{129}Xe — the nucleus which is the focus of the experimental chapters of this thesis — is presented.

Spin-exchange optical pumping

Due to the intrinsically low spin density of gases as compared to protons in the body, the bulk magnetisation produced by the spin-$\frac{1}{2}$ gaseous isotopes ^{3}He and ^{129}Xe according to the Boltzmann equation (see Equations 3.17 to 3.19) at standard clinical field strengths is insufficient for MR imaging applications. For example, Figure 3.29a shows the averaged NMR spectrum produced after 25 acquisitions from a ^{129}Xe thermal phantom consisting of 18 mL 129-enriched xenon (86% ^{129}Xe at Boltzmann polarisation) and 10 mL oxygen (for T_1 shortening as discussed in the following subsection), with a flip angle of 90° and $TR \gtrsim 5T_1$ to allow full recovery of longitudinal magnetisation between subsequent excitations.

"Hyperpolarised" describes the status of a species in which the effective nuclear polarisation has been increased far beyond the thermal equilibrium conditions set out by Equations 3.17 and 3.18. In other words, it can be imagined that the probability of a nucleus inhabiting the lower energy state (for a spin-$\frac{1}{2}$ system) greatly exceeds that of inhabiting the higher energy state. Attainable polarisation values are typically many orders of magnitude greater than the equivalent thermal (Boltzmann) polarisation; in fact, the techniques discussed below can be used to obtain polarisation values of tens of percent (i.e. $P \sim 10^{-1}$; c.f. the estimate of $P \approx 5 \times 10^{-6}$ for the ^{1}H Boltzmann polarisation at 1.5 T and 298 K presented in Section 3.2.1).

Figure 3.29b shows a single NMR spectrum acquired from a 10 mL sample comprising 3% 129-enriched (hyperpolarised) xenon, with a flip angle of 10°.

In order to quantify the observed polarisation, $P_{obs,Xe}$, of a sample of hyperpolarised ^{129}Xe gas, the signal intensities of NMR acquisitions from a hyperpolarised sample (S_{hp}) and a thermally-polarised sample (S_t) can be compared, as follows [65]:

$$P_{obs,Xe} = \frac{S_{hp}}{S_t} \frac{\sin(\alpha_t)}{\sin(\alpha_{hp})} \frac{A_t}{A_{hp}} \frac{V_t}{V_{hp}} P_B \tag{3.118}$$

where α denotes the flip angle, A is the relative fraction of the ^{129}Xe isotope within each sample, and V is the volume of xenon gas within the coil active volume. P_B is the Boltzmann polarisation (see Equation 3.17).
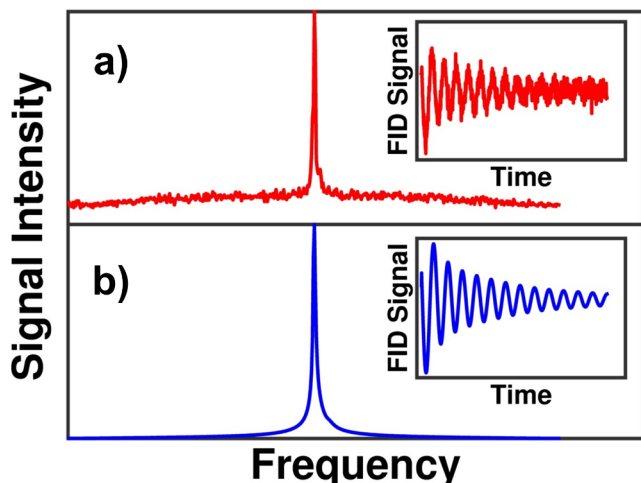
Figure 3.29: Representative ^{129}Xe gas NMR spectra and corresponding FIDs (insets) obtained from a) 25 averaged acquisitions of a thermally-polarised sample and b) a single acquisition of a hyperpolarised sample.

The most-commonly employed technique for generating hyperpolarised ^{3}He and ^{129}Xe is spin-exchange optical pumping (SEOP) [61]. Others methods have been demonstrated for ^{129}Xe, such as low temperature "brute force" approaches [198] and Dynamic Nuclear Polarisation (DNP) [199, 200]. Metastability-exchange optical pumping (MEOP) [62] has been employed in a number of applications for hyperpolarisation of ^{3}He, but is not practically feasible for ^{129}Xe. The fundamentals of SEOP only are reviewed in this subsection, with a focus on special considerations for ^{129}Xe.

SEOP is fundamentally a two-stage process, comprising an optical pumping (OP) stage and a spin-exchange (SE) stage. In summary: firstly, alkali metal atoms (typically rubidium) are optically pumped with resonant laser light in order to polarise the valence electron spins; second, the induced polarisation is transferred between the alkali metal electrons and the noble gas nuclei by spin-exchange processes.

Alkali metals are suited to acting as an intermediate in the SEOP process, by virtue of their simplified electronic structure and efficient absorption of laser light. In its ground state, the single valence electron of an alkali metal atom occupies the ^{2}S$_{\frac{1}{2}}$ sublevel. In the presence of a magnetic field, Zeeman splitting of the ground and excited (^{2}P$_{\frac{1}{2}}$) states produces two states with spin angular momentum quantum number $m = \pm\frac{1}{2}$ in each sublevel, and two states in $m = \pm\frac{3}{2}$ in the P sublevel [xxi]. A valence electron in one of the ground states can be excited by light at a wavelength equal to the energy of separation between the ground and excited states. Then, the excited state electron can relax into one of the ground states. By tuning the polarisation of the laser light, an ensemble-averaged accumulation of electrons in a desired ground state quantum level (i.e. an electron polarisation) can be achieved.

For the case of rubidium, a laser wavelength of 794.77 nm corresponds to the D$_1$ resonance (transition between the $5^2S_{\frac{1}{2}}$ and $5^2P_{\frac{1}{2}}$ states). Driving this transition with left-circularly polarised photons (σ^+) at 794.77 nm results in the transfer of +1 unit of angular momentum to the electron, inducing a change in the spin angular momentum quantum number of the electron by one unit, $\Delta m = +1$. A schematic of this process is shown in Figure 3.30.

Sometimes termed "collisional" spin-exchange, the process of transferring polarisation from alkali metal

---

[xxi]The S sublevel corresponds to states with orbital angular momentum of the electron $l = 0$, whilst the P sublevel corresponds to $l = 1$.

Collisional mixing

$^2P_{1/2}$ m = -½   m = +½

50%   50%

$\sigma+$
(794.77 nm)

$^2S_{1/2}$ m = -½   m = +½
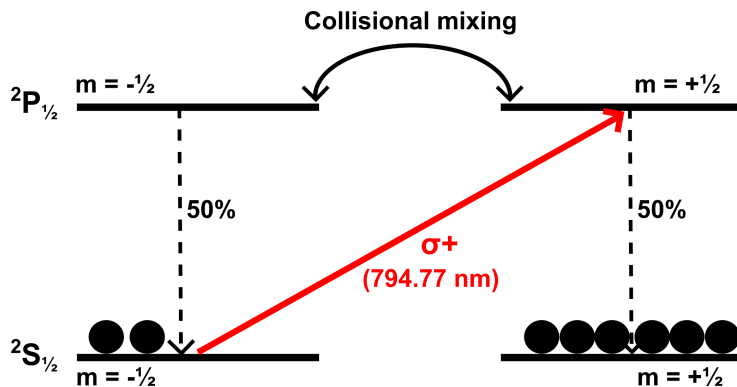
Figure 3.30: Diagram of optical pumping of the electronic states of rubidium by interaction with resonant σ^+ laser light. "Collisional mixing" denotes the process by which the rate of de-excitation from excited state to either ground state is equalised. Adapted with permission from [61]. Copyrighted by the American Physical Society.

electrons to noble gas nuclei fundamentally involves collisions between the two species. Spin-exchange of ^{3}He occurs predominantly via binary collisions between rubidium and helium atoms. The helium electron cloud is tightly-bound, and characteristically unreactive; hence the probability of spin-exchange interactions is relatively low and necessitates that SEOP be performed over the order of many hours [201] to attain saturation of the nuclear polarisation.

In the case of ^{129}Xe, the electron cloud is much larger and consequently the probability of spin-exchange is increased. However, correspondingly, the probability of Rb-Xe collisions that can destroy the induced rubidium polarisation (a process known as "spin destruction") is also increased. For these reasons, optical pumping cells — in which the noble gas of interest is contained along with a few mg of rubidium (which is vaporised prior to optical pumping) — comprise different gas concentrations for helium and xenon experiments. For helium, OP cells are usually filled with 100% ^{3}He, whilst for ^{129}Xe, a gas mixture containing approximately $1-3\%$ xenon is typically used in order to ameliorate the destruction of Rb polarisation via Rb-Xe collisions [202]. The gas mixture in the xenon OP cell is balanced by "buffer" gases (typically a mixture of N_2 and ^{4}He). In addition to simply making up the gas concentration in the cell, nitrogen also serves the purpose of quenching potential radiative transitions of excited-state Rb electrons; the excess energy is instead converted to rotational and vibrational motion of the nitrogen molecules.

In most cases, both ^{3}He and ^{129}Xe OP cells are pressurised to more than one atmosphere, in order to broaden the intrinsically narrow Rb D_1 resonance. For xenon, the operating pressure becomes important in terms of the mechanism governing the spin-exchange interaction: at high pressures, spin-exchange is dominated by Rb-Xe binary collisions, whereas at low pressures, the formation of temporary Rb-Xe van der Waals molecules is significant [xxii].

In the high cell pressure, low xenon concentration regime, the $\sim$ litre quantities of polarised ^{129}Xe required for lung imaging are typically obtained by operating the polariser in "continuous flow" over a period of minutes to hours [xxiii]. This process involves continuously flowing the OP cell gas mixture through the cell at a sufficiently low flow rate that the ^{129}Xe nuclei are adequately polarised during the time in which they reside in the cell. Upon exiting the OP cell, xenon is cryogenically separated from the

---

[xxii]It is beneficial to operate ^{129}Xe polarisers at low pressures in order to suppress collisional destruction of Rb polarisation; however, this necessitates the use of extremely narrow-linewidth lasers and large, complex optical pumping cells in order to counteract the lack of pressure-broadening of the Rb D_1 resonance, and overcome the low xenon concentration, respectively [63, 203].

[xxiii]Since for SEOP of ^{3}He, the ^{3}He itself usually constitutes $\sim$ 100% of the gas mixture contained within the optical cell, no continuous flow accumulation process is required; instead, batches of hyperpolarised ^{3}He can be extracted directly from the OP cell after a saturation polarisation has been reached.

buffer gases as it passes through glassware submersed in liquid nitrogen and housed within a permanent magnetic field (to preserve the ^{129}Xe polarisation). Xenon solidifies within the glassware at liquid nitrogen temperatures (see Section 3.2.6), whilst the buffer gases do not and can be safely extracted and discarded.

The gas flow persists over a period of tens of minutes and, once a sufficient quantity of xenon has been accumulated in the frozen state, the xenon "ice" can be sublimated into gaseous form by immersing the glassware in warm water. The resulting hyperpolarised xenon gas is typically transferred to a plastic (Tedlar) bag, to which a mouthpiece can be affixed in order to administer the gas to a patient. The freezing and subsequent thawing of xenon does not result in significant ^{129}Xe polarisation losses [204], and as such, litre quantities of ^{129}Xe gas with nuclear polarisations of the order of tens of percent can be routinely obtained using this method [65, 202, 205].

The ^{129}Xe continuous flow SEOP process can be described mathematically as follows. Upon exiting the OP cell, the polarisation of ^{129}Xe, P_{Xe}^{cell}, is governed by [65, 202]:

$$P_{Xe}^{cell}\left(t_{res}\right) = \frac{\gamma_{SE}}{\gamma_{SE} + \Gamma_{Xe}} \left\langle P_{Rb}\right\rangle \left(1 - \exp\left(-\left(\gamma_{SE} + \Gamma_{Xe}\right)t_{res}\right)\right) \tag{3.119}$$

where γ_{SE} is the spin-exchange rate dictating the transfer of spin polarisation between rubidium electrons and ^{129}Xe nuclei, Γ_{Xe} is the rate constant of ^{129}Xe polarisation loss (by a number of relaxation mechanisms as discussed in the following subsection), and $\left\langle P_{Rb}\right\rangle$ is the ensemble-averaged rubidium polarisation in the OP cell. During passage through the cell, the xenon polarisation builds-up according to an exponential relationship as a function of residency time in the cell, t_{res}. The rubidium polarisation as a function of position along the laser axis z, can be written:

$$P_{Rb}\left(z\right) = \frac{\gamma_{opt}\left(z\right)}{\gamma_{opt}\left(z\right) + \Gamma_{Rb}} \tag{3.120}$$

where $\gamma_{opt}\left(z\right)$ is the position-dependent optical pumping rate for rubidium electrons, and Γ_{Rb} is the rate of rubidium spin polarisation destruction, governed by the rate of binary collisions and van der Waals molecule formation with xenon. The optical pumping rate can be defined as a function of frequency, ν, as the integral of the product of laser photon flux, $\Phi\left(\nu, z\right)$, and the photon absorption cross section, $\sigma_s\left(\nu\right)$:

$$\gamma_{opt}\left(\nu, z\right) = \int \Phi\left(\nu, z\right)\sigma_s\left(\nu\right)\mathrm{d}\nu \tag{3.121}$$

Finally, the theoretical spin-exchange rate γ_{SE}^{theory} can be decomposed into a summation of terms related to van der Waals (vdW) molecule formation and binary collisions (BC):

$$\gamma_{SE}^{theory} = \gamma_{SE}^{vdW} + \gamma_{SE}^{BC} = \left(\kappa_{SE}^{vdW} + \kappa_{SE}^{BC}\right)[\text{Rb}] \tag{3.122}$$

78
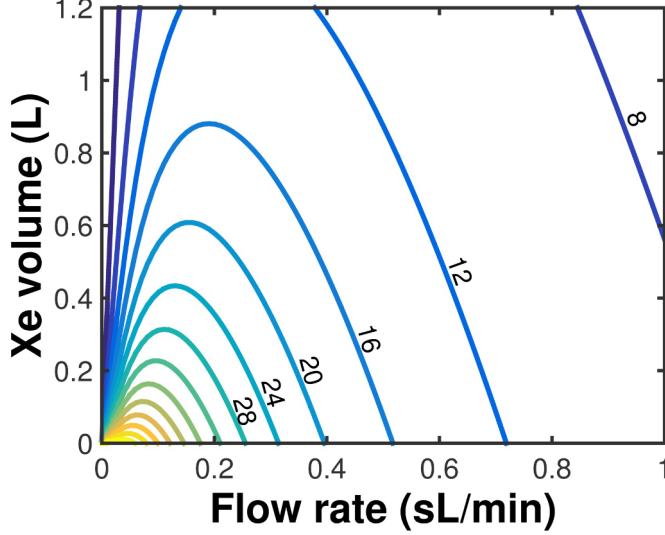
Figure 3.31: Contour plot of ^{129}Xe polarisation as a function of gas flow rate and total accumulated volume (for an upgraded version of the polariser presented in [65], and employed in Chapter 4 of this thesis).

where the κ_{SE} terms represent spin-exchange cross sections related to van der Waals molecule formation and binary collisions, and [Rb] is the concentration of rubidium in the OP cell.

Although Equation 3.119 provides a theoretical prediction of the polarisation of ^{129}Xe immediately after it exits the OP cell, the polarisation of ^{129}Xe after cryogenic accumulation, $P_{Xe}^{acc}(t_{res}, t_a)$, is affected by spin-lattice relaxation of ^{129}Xe in the frozen state, which occurs with a characteristic time constant $T_{1,f}$:

$$P_{Xe}^{acc}(t_{res}, t_a) = P_{Xe}^{cell}(t_{res}) \frac{T_{1,f}}{t_a} \left(1 - \exp\left(-\frac{t_a}{T_{1,f}} \right) \right) \tag{3.123}$$

where t_a is the length of time for which xenon is accumulated in the cryogenic glassware. These equations relate that for a fixed experimental set-up (including gas and rubidium concentrations, OP cell volume, laser flux, etc.) the polarisation of ^{129}Xe in the gaseous form at the end of the polarisation procedure is determined by the ^{129}Xe residency time t_{res} in the OP cell, and the accumulation time in the cryogenic glassware, t_a. The former is inversely proportional to the gas flow rate, and the latter depends on the flow rate and the intended gas volume. Therefore, experimental parameters should be chosen accordingly to achieve the best compromise between the desired ^{129}Xe polarisation, total xenon volume, and the total accumulation time. Figure 3.31 shows a contour plot of some of these parameters for the upgraded version of the polariser in [65] (and also described in Chapter 4 of this thesis).

The polariser utilised in the experimental chapters of this thesis has been previously described in [206] and [65] and is shown schematically in Figure 3.32a. The apparatus consists of: a glass OP cell housed within a ceramic oven (for vaporisation of rubidium); a Helmholtz coil pair, for producing the static $\boldsymbol{B_0}$ field (i.e. for Zeeman splitting of electronic and nuclear energy states); spiral glassware submerged in liquid nitrogen (for accumulation of frozen hyperpolarised xenon). In all experiments, the OP cell was filled with a gas mixture of 3% Xe, 10% N$_2$ and 87% ^{4}He, at a cell temperature of 100°C and pressurised

to 2 bars.

During the course of this work, improvements were made to the laser hardware used to generate the circularly polarised light for Rb optical pumping (see details in Section 4.4.1); hence, certain experiments were performed with different laser characteristics and resulting ^{129}Xe polarisations. The original form of the laser hardware, comprising an external cavity diode laser and a number of optical elements to shape the laser beam onto the cell, is shown in Figure 3.32. In each chapter of this thesis, the type of laser hardware employed is detailed explicitly, and any modifications to the above operating scheme are discussed.
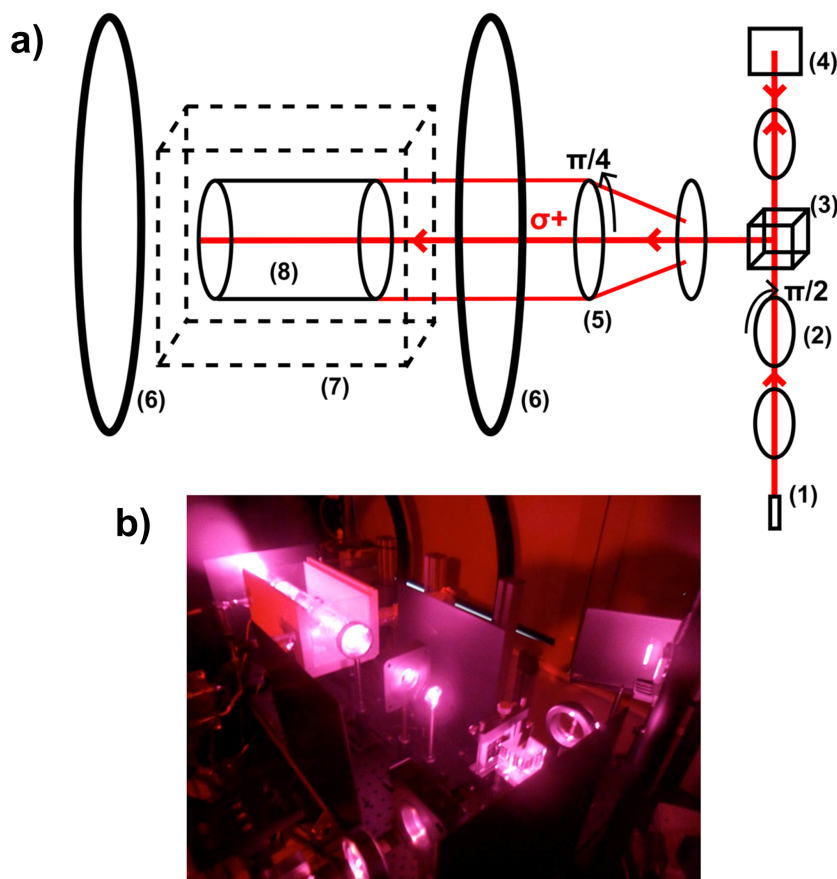
Figure 3.32: a) Schematic diagram of the "continuous flow" ^{129}Xe polariser used in this thesis, including the original laser hardware and optical apparatus: (1) laser diode array; (2) half-wave plate, for rotation of the plane of linear polarisation from the laser; (3) polarisation beam splitter, with $\frac{1}{3}$ transmission down the laser axis, and $\frac{2}{3}$ reflection down the cell axis; (4) holographic grating, for narrowing of the laser beam and tuning of the operating wavelength; (5) quarter-wave plate, for conversion of linear to circular light polarisation; (6) Helmholtz $\boldsymbol{B_0}$ coils; (7) temperature-controlled oven; (8) glass OP cell. b) Photograph of the polariser.

Considerations for hyperpolarised gas MRI

This subsection concerns the unique properties of hyperpolarised gases that govern their NMR behaviour. These properties therefore dictate the applicable MR acquisition strategies for ^{3}He and ^{129}Xe, and are considered on a point-by-point basis in the below discussion.

(i) *The induced hyperpolarisation is non-renewable.* Upon excitation by a radiofrequency pulse, the longitudinal magnetisation of hyperpolarised gas nuclei recovers by spin-lattice relaxation to the thermal (Boltzmann) polarisation. As discussed in the previous subsection, the Boltzmann polarisation is normally many orders of magnitude lower than the induced hyperpolarisation, and is insufficient for MRI applications. Thus, the induced hyperpolarisation of a nuclear spin ensemble can be considered to decay according to its spin-lattice relaxation time. As such, high flip angles are impractical for hyperpolarised gas MR imaging (e.g. whilst a 90° RF pulse will lead to a high initial transverse magnetisation, it will leave no longitudinal magnetisation remaining for subsequent excitations) [xxiv].

In practice, hyperpolarised gas MR images of the lungs are typically acquired using low flip angle SPGR pulse sequences, as discussed in Section 2.2. By considering the propagation of transverse and longitudinal magnetisation at different points in a spoiled gradient echo sequence — and considering the spin-lattice relaxation term to be represented by an exponential decay rather than an exponential recovery term — the transverse magnetisation of a hyperpolarised species as a function of RF pulse number, n, can be written as (see e.g. [207]):

$$M_{xy}(n) = M_0 \exp\left[-(n-1)\frac{TR}{T_1}\right] \sin(\alpha_n) \prod_{j=1}^{n-1} \cos(\alpha_j) \tag{3.124}$$

where α is the RF excitation flip angle, M_0 is the initial longitudinal magnetisation at the start of the sequence, TR is the repetition time between RF pulses, and T_1 is the longitudinal relaxation time. This equation permits the flip angle to vary in an arbitrary fashion during the acquisition; however, in most regular applications, a constant flip angle is used, such that the above equation reduces to:

$$M_{xy}(n) = M_0 \sin(\alpha) \cos^{n-1}(\alpha) \exp\left[-(n-1)\frac{TR}{T_1}\right] \tag{3.125}$$

Thus, the rate of decay of hyperpolarised gas magnetisation during an SPGR acquisition is governed solely by the excitation flip angle and the number of RF pulses required to encode the image (for a fixed TR and T_1). For a 2D sequence with no image acceleration, the required number of RF pulses is equal to the number of phase encodes in the k_y direction, N_y. In order to maximise the signal in a sequentially-ordered 2D SPGR hyperpolarised gas acquisition, the transverse magnetisation for $n = \frac{N_y}{2}$ should be maximised. Thus, the optimum flip angle can be derived by differentiating Equation 3.125 with respect to α [208]:

$$\alpha_{opt} = \arctan\left(\frac{1}{\sqrt{\frac{N_y}{2} - 1}}\right) \tag{3.126}$$

The decay in longitudinal magnetisation of a hyperpolarised species as a function of the RF pulse number

---

[xxiv] High flip angles are also difficult to achieve in the thorax, particularly for ^{129}Xe, which has an almost four-fold lower gyromagnetic ratio than ^{1}H. Consequently, fast spin echo techniques are impractical for hyperpolarised gas lung MR imaging.

is known as the "k-space filter". Compared to MR imaging of thermally-polarised nuclei such as ^{1}H —
where constant flip angle RF excitation results in a steady-state longitudinal magnetisation being reached
after a few RF pulses, leading to a flat k-space filter — constant flip angle, sequential MR acquisitions
of hyperpolarised nuclei magnetisation result in a smoothly decaying k-space filter, which leads to image
blurring according to the distinct signal weightings associated with different k-space lines. Centrically-
ordered k-space acquisitions can be utilised to obtain images with a greater signal-to-noise ratio at the
expense of increased blurring due to the high weighting of the centre of k-space and relatively low weight-
ing of points at large k_y values; in this case, the k-space filter is approximately symmetric about $\frac{N_y}{2}$.
Optimal image sharpness can be obtained by varying the flip angle throughout the acquisition procedure
according to [207]:

$$\alpha_n = \arctan\left(\frac{1}{\sqrt{N_y - n}}\right) \tag{3.127}$$

where $\alpha_{N_y} = 90°$. As mentioned in the previous footnote, limitations imposed by RF coil hardware
constrain the use of high flip angles, which is one reason for the lack of widespread uptake of variable flip
angle SPGR imaging of hyperpolarised gases. In practice, a good compromise between complexity of im-
plementation, and sharpness and SNR of the resulting image, can be achieved by employing a constant flip
angle approach that results in a longitudinal magnetisation at the end of the acquisition of $\approx 0.2 - 0.3 M_0$.

(ii) *The effective flip angle of customised RF coil designs is not typically known in advance.* The excitation
flip angle in standard ^{1}H MR applications is typically calibrated and optimised by built-in software for
most MRI scanners. However, for hyperpolarised MRI with custom-built radiofrequency coils, the flip
angle must be characterised when the coil is loaded by the subject of interest. The mean flip angle of an
RF coil can be calculated by measuring the MR signal decay during the course of an imaging acquisition
in which the phase encoding gradients are nulled; i.e. a sequence comprising an RF pulse, a frequency
encoding gradient and a spoiler gradient only. The decay in echo signal intensity then follows the form
of Equation 3.125 as a function of RF pulse number. Unless the T_1 of the hyperpolarised species is well-
known, it is appropriate to use a sequence with a short TR such that T_1 relaxation can be considered
negligible. Therefore, the average flip angle can be determined by fitting the signal decay with a function
$\propto \cos^{n-1}(\alpha)$.

Whilst this procedure yields the average flip angle of a given RF coil across the whole of the thorax, it
is possible to extend this approach to an imaging experiment in order to obtain a quantitative map of the
flip angle distribution, as described in Section 4.3.3. The design of customised RF coils for hyperpolarised
gas lung imaging applications requires a compromise to be made between: the flexibility and filling factor
of the coil for imaging subjects of variable size; the range of achievable flip angles necessitated by particu-
lar pulse sequences / applications; the required homogeneity of the resulting flip angle across the thorax.

(iii) *Spin-lattice relaxation of hyperpolarised gas nuclei is dominated by paramagnetic molecular oxygen.*
As introduced briefly in Section 2.2, the T_1 of hyperpolarised gas nuclei changes with the molecular oxygen
content of the gas mixture. In fact, the inverse of the relaxation time (i.e. the relaxation rate) is directly

proportional to the partial pressure of molecular oxygen, $p\mathrm{O}_2$ [123, 209]:

$$\frac{1}{T_1} = B\left(T\right) p\mathrm{O}_2 \tag{3.128}$$

where $B(T)$ is a temperature-dependent coefficient. Molecular oxygen is paramagnetic by virtue of possessing a free-radical pair and hence a permanent dipole. In the lungs, the dipole-dipole coupling interaction with residual O_2 typically dominates the relaxation behaviour of ^{3}He or ^{129}Xe, resulting in a T_1 of ~ 20 s for both nuclei. This places strict limits on the MR acquisition time and necessitates that the hyperpolarised gas be inhaled only immediately before the scan is commenced.

Furthermore, all stages of the process prior to the patient inhaling the hyperpolarised gas — including the SEOP procedure and the transfer of gas to the patient — must be performed under controlled, low-oxygen conditions [xxv].

Although minimisation of the spin-lattice relaxation induced by molecular oxygen is of utmost importance, there are additional factors to consider that contribute to the relaxation rate of hyperpolarised gas nuclei both during and after the SEOP process (Γ_{Xe} in Equation 3.119), as follows.

(a) During SEOP: intermolecular dipole-dipole collisions in ^{3}He [210]; spin-rotation interactions between ^{129}Xe molecules [211]; cross-relaxation of ^{129}Xe with the isotope ^{131}Xe [212]; binary collisions [213]; and the formation of Xe-Xe van der Waals molecules [214], all contribute to longitudinal relaxation.

(b): During and post-SEOP: surface ("wall") relaxation is often the ultimate limiting factor for longitudinal relaxation, although T_1 values of the order of hours can be achieved for hyperpolarised ^{129}Xe in a Tedlar bag in a homogeneous storage field [215]; relaxation in the presence of field gradients, e.g. the fringe-field of the polariser and scanner magnets, can reduce T_1 values from hours to minutes [216].

(iv) *Respiratory motion necessitates MRI at breath-hold.* Respiratory motion occurs over a time-period of the order of seconds and can severely affect MR images that are acquired on this time-scale. Although a number of MR motion recording and correction strategies have been developed, the most feasible practical solution for minimisation of respiratory motion effects is to perform hyperpolarised gas imaging whilst the subject maintains a breath-hold manoeuvre. In addition, breath-holding ensures that only a nominal amount of molecular oxygen can enter the lungs during the scan process. Conventionally, the procedure of preparing for a hyperpolarised gas scan involves instructing a patient to inhale a bag containing hyperpolarised gas from a given lung inflation level, e.g. FRC, after a period of relaxed, tidal breathing.

Coincidentally, the typical breath-hold time achievable by human subjects is similar to the T_1 of ^{3}He and ^{129}Xe in the lungs, and therefore both place a comparable constraint on total scan duration.

(v) *Gases are highly diffusive.* Both helium and xenon gas exhibit a free diffusion coefficient many orders of magnitude larger than the mean diffusion coefficient of protons in bodily tissues: $D_{0,He} \sim 2$ cm^2.s^{-1} [217]; $D_{0,Xe} \sim 0.06$ cm^2.s^{-1} [218]; $D_{0,water} \sim 2 \times 10^{-5}$ cm^2.s^{-1} [219]. In healthy lungs, the apparent

---

[xxv]The entire SEOP system must be free of paramagnetic impurities, and also water vapour, with which rubidium reacts violently. In practice, optical cells are prepared under closed vacuum and pressurised using an inert-gas glove box.

diffusion coefficient of helium is reduced compared to the free diffusion value, whilst the xenon ADC is comparable to its free diffusion coefficient (due to a combination of effects from dilution of the gas in air and diffusion restriction by the alveolar walls): $D_{He} \sim 0.2$ cm^2.s^{-1} [101, 106] and $D_{Xe} \sim 0.04$ cm^2.s^{-1} [115, 220]. Under these conditions, gas diffusion during imaging gradients induces transverse relaxation in a similar manner to T_2 relaxation as described previously; according to Equation 3.114 for diffusion-weighted MRI. Thus, the effective b-value of the phase encoding, slice selection and frequency encoding gradients must be considered when designing a hyperpolarised gas imaging pulse sequence and assessing the apparent T_2^* of the gas. In 2D SPGR applications, diffusion effects are slight, but non-negligible, and frequency encoding gradients usually exhibit the largest b-values for concern [208]. However, in bSSFP acquisitions, diffusion during imaging gradients can lead to appreciable reductions in the effective T_2. This issue is discussed further in Chapter 4.

(vi) *The magnetic field is inhomogeneous across the thorax.* The susceptibility difference between the lung parenchymal tissue (which is diamagnetic) and the air (containing residual molecular oxygen which is paramagnetic) means that fluctuations in the static magnetic field $\boldsymbol{B_0}$ experienced by each nucleus can be prominent in the lungs due to the presence of numerous air-tissue interfaces. The associated variation in Larmor frequency presents as phase errors and extremely low T_2^* values in the lung tissue ($\sim$ 1-2 ms for ^{1}H, as introduced in Chapter 2). As a result, ^{1}H MR imaging of the lungs results in images with poor signal-to-noise, where the lungs appear dark against the rest of the anatomy of the thorax. Nevertheless, the transverse relaxation times of ^{3}He and ^{129}Xe gas ($\gtrsim 25$ ms) are sufficient for SNR advantages to be gleaned with balanced steady-state acquisition strategies, as discussed in Chapter 4.

Despite the reasonable T_2^* values of hyperpolarised gases, the complexity of the lung anatomy — particularly in close proximity to the vessels, and at the boundaries between air and tissue at the lung periphery and notably at the diaphragm — can lead to significant susceptibility artefacts on GRE images [82, 221], and the possibility of banding artefacts in balanced sequences [222]. Careful consideration of the mean Larmor frequency across the chest, in addition to knowledge of the 3D $\boldsymbol{B_0}$ distribution in the imaging volume of interest, is critical to minimising the effects of these variations in magnetic susceptibility. (The latter can be calculated from an interleaved imaging acquisition with two or more TE values, according to the procedure explained in Section 4.3.3.)

Fundamental properties of ^{129}Xe

Xenon is a noble gas atom with atomic number $Z = 54$ and a molecular weight of 131 a.m.u. Chemically inert, it exists monatomically, with nine stable isotopes, of which only ^{129}Xe and ^{131}Xe have a non-zero nuclear spin quantum number, as required for NMR detection. Table 3.3 lists some of the NMR-relevant properties for ^{129}Xe and ^{131}Xe, in comparison with ^{3}He and ^{1}H (see also Table 2.1 in Section 2.2).

As illustrated in Table 3.3, the gyromagnetic ratios of both ^{129}Xe and ^{131}Xe nuclei nuclei are significantly smaller than those of ^{3}He and ^{1}H. As a result of its relatively larger gyromagnetic ratio (and historically greater attainable SEOP-induced polarisation), ^{3}He has typically been employed as the noble gas nucleus of choice for human lung MR imaging applications. However, the availability of ^{3}He is diminishing and its cost has greatly increased since the advent of its regulation by the US government [84]. On the other hand, xenon occurs naturally in air, at a concentration of 0.087 ppm [227]. Also, ^{129}Xe possesses

Property	^{1}H	^{3}He	^{129}Xe	^{131}Xe
Nuclear spin, I	$\frac{1}{2}$	$\frac{1}{2}$	$\frac{1}{2}$	$\frac{3}{2}$
Magnetic moment, $\frac{\mu}{\mu_N}$	4.84	-3.69	-0.78	0.69
Quadrupole moment, Q (barn)	0	0	0	-0.114
Gyromagnetic ratio, γ (MHz.T^{-1})	42.58	-32.44	-11.78	3.49
Self diffusion coefficient, D_0 (cm^2.s^{-1})	2×10^{-5}	2.00	0.06	
Diffusion coefficient in air, D_a (cm^2.s^{-1})		0.86	0.14	

Table 3.3: Table of NMR-relevant properties of ^{129}Xe and ^{131}Xe, in comparison to ^{3}He and ^{1}H. Data from [223, 224], except the quadrupole moment of ^{131}Xe [225], self diffusion coefficients (see references in the previous subsection) and diffusion coefficients in air [226]. (See previous subsection for values of the ^{3}He and ^{129}Xe diffusion coefficients in human lungs.) The relative natural abundances of the isotopes ^{129}Xe and ^{131}Xe are 26.44% and 21.18%, respectively. μ_N is the nuclear (Bohr) magneton.
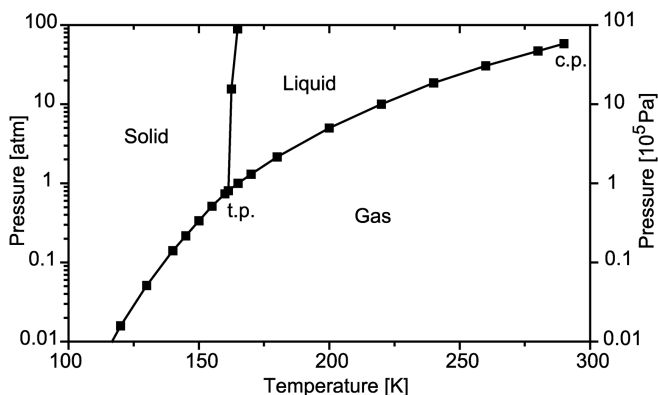
Figure 3.33: The phase diagram of xenon, reproduced from [230], based upon data from [231]. The triple point (t.p.) at 161.3 K and 81.6 kPa is clearly identifiable.

additional properties — including a non-negligible solubility in various compounds, and a chemical shift modulation dependent upon its molecular environment — that can be exploited in a number of ways to enable functional NMR studies that cannot be performed with ^{3}He (see e.g. Chapters 6 to 8).

As discussed in the previous subsection, both ^{3}He and ^{129}Xe are highly diffusive, which permits quantification of lung microstructural dimensions by diffusion-weighted MR acquisitions (see Sections 2.2, 3.2.5 and 5.2). Of note, the xenon self diffusion coefficient and diffusion coefficient in air are substantially smaller that the matching helium diffusion coefficients, which offers the possibility of probing smaller length-scale structures with ^{129}Xe as opposed to ^{3}He diffusion-weighted MRI.

The non-zero quadrupole moment (see Section 3.2.2) of the ^{131}Xe nucleus gives rise to rapid spin-lattice relaxation, with a relaxation time constant on the same timescale as typical NMR experiments (even in perfectly evacuated systems, T_1 values are of the order of seconds to minutes [228]). Nevertheless, additional sensitivity to surface interactions and high magnetic fields is obtainable with NMR of spin-$\frac{3}{2}$ ^{131}Xe versus spin-$\frac{1}{2}$ ^{129}Xe (see e.g. [229]).

Figure 3.33 depicts the xenon phase diagram, which highlights the fact that all three physical states are accessible under moderate physical conditions, and hence NMR experiments can be performed on ^{129}Xe or ^{131}Xe in any of those phases. Of particular relevance for SEOP (see Section 3.2.6), xenon will readily deposit or solidify at pressures of ≤ 1 bar and liquid nitrogen temperatures (77 K).

The large electron cloud of xenon (108 pm, calculated [232]) is easily distorted / "polarised" by neigh-

bouring molecules. As such, xenon is a highly sensitive probe of its local chemical environment, and is readily soluble in a number of polar and non-polar solvents. Xenon's ready solubility in *somatic* solvents has facilitated its routine clinical use as a general anaesthetic for many years [233, 234]; inhaled concentrations of 71% xenon yield general anesthesia in 50% of patients [235].

The acute sensitivity of the xenon atom to its chemical environment is highlighted by the broad NMR chemical shift range exhibited by ^{129}Xe; ~ 250 ppm when dissolved in various liquids [236] (and up to 7500 ppm when present in molecules with electronegative fluorine or oxygen partners [227]), in comparison to only 0.8 ppm for ^{3}He [237] [xxvi]. Table 3.4 provides a summary of values of the Ostwald solubility of xenon in a number of biologically-relevant substances, and the corresponding NMR chemical shift of ^{129}Xe (in comparison to the gaseous-phase ^{129}Xe resonance at 0 ppm). (For a review of the chemical shifts of xenon dissolved in liquid hydrocarbons, see e.g. [238].)

Solvent	Ostwald Solubility Coefficient		Chemical Shift (ppm)	
Distilled Water	0.083	[239]	190	[240]
	0.083	[241]		
Saline (0.9% NaCl)	0.093	[242]	194	[243]
	0.078	[239]		
Olive Oil	1.83	[244]	198	[236]
	1.79	[241]		
Adipose Tissue	1.715	[244]	191[†]	[245]
Blood Plasma	0.103	[242]	194	[240]
	0.091	[241]	192	[136]
	0.094	[244]	197	[246]
Erythrocytes (RBCs)	0.20	[242]	216	[240]
	0.19	[241]	216	[136]
	0.27	[244]	222	[246]
PFOB	1.20	[247]	106	[247]

Table 3.4: Xenon Ostwald solubility coefficients and corresponding ^{129}Xe chemical shifts in somatic substances. Chemical shift data is expressed in parts per million (ppm) offset from the gaseous-phase ^{129}Xe resonance (0 ppm). PFOB: perfluorooctyl bromide emulsion, a substance employed as a blood substitute. [†]: rat adipose tissue.

Upon inhalation, xenon gas fills the alveolar airspaces and diffuses through the lung parenchymal tissue and into the capillary bed. As shown in Table 3.4, ^{129}Xe exhibits two distinct resonances when dissolved in blood; pertaining to ^{129}Xe dissolved in blood plasma (P) and red blood cells (RBCs), which are shifted downfield by ~ 196 ppm and 218 ppm on average, respectively from the position of the gaseous-phase ^{129}Xe resonance. The chemical shift of ^{129}Xe dissolved in lung parenchymal tissue is identical to that of blood plasma, and hence the two environments contribute to a single, combined resonance in vivo (known as the tissue/plasma, or T/P resonance).

The large frequency separation of dissolved- and gaseous-phase ^{129}Xe allows selective RF excitation, and hence independent investigation, of the two phases, even at fields as low as 0.2 T [248]. However, the available MR signal from ^{129}Xe dissolved in the T/P and RBC compartments in vivo is significantly reduced compared with the gaseous-phase ^{129}Xe signal, by virtue of the relatively low solubility of xenon

---

[xxvi]Helium is also characteristically insoluble in most substances.

in parenchymal tissues and blood, and the small fraction of the total lung volume that is occupied by the dissolved-phase compartments.

Figure 3.34 depicts an example NMR spectrum of hyperpolarised ^{129}Xe obtained from the human lungs, exhibiting all three resonances.
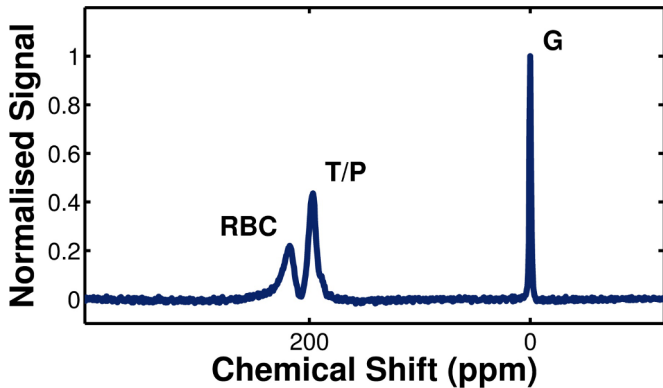
Figure 3.34: NMR spectrum of hyperpolarised ^{129}Xe in the human lungs. The resonance of ^{129}Xe in the gaseous-phase (G) is conventionally placed at 0 ppm. Two spectrally-separated resonances arising from ^{129}Xe dissolved in parenchymal tissues and blood plasma (T/P) and red blood cells (RBCs) can be observed at approximately 196 ppm and 218 ppm downfield from the gas resonance, respectively. This spectrum was obtained by applying a 90° Gaussian RF pulse centred in between the two dissolved-phase resonances, which produced an off-resonant $\lesssim$ 1° excitation of the gaseous-phase ^{129}Xe magnetisation.

Xenon atoms dissolved in whole blood undergo continuous chemical exchange between the plasma and RBCs; i.e. rather than permanently binding to RBCs, xenon atoms tend to "hop" on and off. The rate of chemical exchange of xenon between the two compartments is quantified by an exchange constant of approximately 12 ms [136]. In addition, passive diffusive exchange of xenon between the airspaces, parenchymal tissues and capillaries, occurs on a similar timescale (see Chapters 6 and 8). As a result, the dissolved-phase ^{129}Xe resonances are exchange-broadened, and the effective transverse relaxation time constant, T_2^*, of ^{129}Xe in these dissolved-phase compartments is very short ($\sim$ 1-2 ms [249, 250] ^{xxvii}).

As discussed in Section 2.2, these short relaxation times constrain the feasibility of MR imaging of ^{129}Xe dissolved in the lung tissues and blood. Nevertheless, provided that the gaseous ^{129}Xe magnetisation is not strongly excited by selective RF pulses applied to dissolved ^{129}Xe, there exists a large reservoir of available magnetisation in the gaseous-phase, from which ^{129}Xe spins continuously diffuse into the blood and tissues during the imaging TR to replenish the dissolved-phase ^{129}Xe signal.

The longitudinal relaxation time constant, T_1, of ^{129}Xe gas is of the order of hours when stored in a polymeric Tedlar bag [215]; however, upon inhalation into the lungs, it is reduced to approximately 20-30 s [134, 252] (due to the presence of residual paramagnetic oxygen molecules, as mentioned in the previous subsection).

When dissolved in whole blood, the ^{129}Xe T_1 relaxation time is of the order of a few seconds, and has been observed to increase in a non-linear manner with the oxygenation of the blood. Average T_1 values for ^{129}Xe in whole blood have been reported as follows: $\sim$ 3-4 s in deoxygenated blood [246, 253, 254] and a wide range of values in oxygenated blood, from 5.7 s [246] to 13 s [254]. The most up-to-date report has been recently published by our group, which quotes a T_1 of 2.2 s in deoxygenated blood (oxygen saturation, sO$_2$=0.06) and 7.8 s in completely oxygenated blood (sO$_2$=1.00) [255].

Thus, the T_1 relaxation times of ^{129}Xe dissolved in arterial blood are comparable to the blood circula-

---

^{xxvii}By comparison, the T_2^* of ^{129}Xe gas in the lungs has been reported to be 50 and 25 ms, in fully-inflated and partially-inflated lungs, respectively at 1.5 T [251].

tion time from the lungs to the brain in humans [256], and are hence sufficient for detection of ^{129}Xe NMR signal in tissues distal to the lungs, such as the heart [257], kidneys [258] and brain [68, 259]. Furthermore, the T_1 relaxation times of ^{129}Xe dissolved in the brain are adequate for further preservation of ^{129}Xe MR signal; $T_1 \approx 14$ s and 8 s in grey and white matter, respectively [260].

In addition, blood oxygenation has a significant impact on the chemical shift of the ^{129}Xe RBC resonance (whilst the plasma resonance is unaffected). In a similar manner to the relaxation time, the ^{129}Xe RBC chemical shift has been observed to increase in a non-linear fashion as a function of blood oxygenation [261]. The most recent measurements of this effect, reported by our group, suggest a ~ 5 ppm change in ^{129}Xe RBC chemical shift can be observed over the full range of blood oxygenation values [262].

It is currently believed that the physical mechanisms underpinning the relaxation and chemical shift behaviour with blood oxygenation are the same [262]; they are thought to be governed by changes in the conformational state and xenon binding site locations of haemoglobin with oxygenation. In light of these observations, hyperpolarised ^{129}Xe has excellent potential as a non-invasive probe of blood oxygenation in the pulmonary system, and possibly also other, distal tissues.

The rate of exchange of xenon between lung tissue and blood is governed by the diffusion coefficient of xenon in those environments. The diffusion coefficient of xenon dissolved in human blood and tissues is not well known (see Section 7.4), and NMR measurements with standard diffusion-sensitising pulse sequences are challenging, due to the inherently short, exchange-weighted, transverse relaxation times of ^{129}Xe dissolved in these media as discussed above. Wolber et al have presented a spin echo train spectroscopic technique for quantification of the diffusion constant of xenon in vitro in water, PFOB and benzene samples using hyperpolarised ^{129}Xe [263], yielding values of $D_{Xe,PFOB} = (4.5 \pm 0.6) \times 10^{-5}$ cm^2.s^{-1} and $D_{Xe,water} = (2.2 \pm 0.4) \times 10^{-5}$ cm^2.s^{-1}. However, in blood, the rapid chemical exchange between plasma and RBCs means that the echo trains cannot be refocused. To this end, pulsed-gradient spin echo techniques have been employed to study the diffusion of ^{129}Xe in plasma ($D_{Xe,plasma} = 1.0 \times 10^{-5}$ cm^2.s^{-1}) [264]. As reviewed in Section 7.4, only one in vivo measurement of the average xenon diffusion coefficient in lung tissues and blood has been performed to date; Ruppert et al presented a combined dissolved-phase ^{129}Xe diffusion coefficient derived from exchange-weighted spectroscopic measurements in rabbits of 3.3×10^{-6} cm^2.s^{-1} [265]. Determining distinct xenon diffusion constants for human tissues and RBCs in vivo is experimentally challenging, as is the preparation and measurement of tissue or RBC samples in vitro that adequately mimic the in vivo functional status. Hence, no reports of the xenon diffusion constant in tissue samples or RBCs have been published to date.

Chapter 4

^{129}Xe ventilation imaging with 3D balanced steady-state free precession (bSSFP)

4.1 Introduction

As described in previous chapters, hyperpolarised noble gas lung MRI with ^{3}He and ^{129}Xe can overcome many of the constraints of existing clinical gold-standard methods for diagnosing pulmonary disease, including: the lack of regional information offered by pulmonary function testing; the ionising radiation associated with computed tomography; and the low spatial resolution of nuclear scintigraphy. ^{3}He has made the initial impact in clinical lung imaging research [69], most likely due to two factors; firstly it has historically been easier to polarise ^{3}He to higher levels in the volumes required for lung MRI, and secondly the larger gyromagnetic ratio of ^{3}He when compared with ^{129}Xe (see Section 3.2.3 for details on the relationship between signal-to-noise ratio and gyromagnetic ratio). ^{3}He MRI has been implemented in multi-centre studies [72] and has demonstrated clinical utility, with sensitivity to early disease processes, in numerous pulmonary pathologies [75, 77, 78]. Preliminary studies have shown that hyperpolarised ^{129}Xe is also promising for pulmonary ventilation imaging, with image quality similar to that of ^{3}He [85, 86, 100]. Furthermore, ^{129}Xe possesses additional functional sensitivity [134] as a tracer of gas exchange and lung perfusion, based on its non-negligible solubility and broad range of NMR chemical shift in tissue and blood.

Although ^{3}He enjoys intrinsic MR signal advantages over ^{129}Xe, it is generated exclusively as a by-product of tritium decay and is difficult to obtain in the quantities needed for widespread clinical dissemination [84]. On the other hand, xenon is naturally-abundant in air (87 ppb, of which 26% comprises spin-$\frac{1}{2}$ ^{129}Xe). The proportion of ^{129}Xe can be enriched to $\sim$80-90% by gas centrifuge techniques, however this requires significant additional investment. Although xenon is substantially cheaper than ^{3}He, gas doses delivered to patients for inhalation have typically been ≥ 3 times higher for enriched xenon (hereafter denoted EN^{129}Xe) (i.e. up to 1 L [95]) than for ^{3}He (up to $\sim$300-400 mL [86]), in order to obtain lung images of sufficient SNR for clinical interpretation. The reason for this is two-fold: the achievable polarisation of ^{129}Xe has historically been lower; and the gyromagnetic ratio is only $\frac{1}{3}$ that of ^{3}He. Naturally-abundant xenon gas (26% ^{129}Xe, hereafter denoted NAXe) is significantly cheaper than both EN^{129}Xe and ^{3}He, but has not been well-explored for imaging in humans due to SNR limitations imposed by the 3-fold lower proportion of spin-$\frac{1}{2}$ ^{129}Xe nuclei [248]. However, with recent developments in gas polarisation technology, promoting the utilisation of high power, narrow-linewidth lasers and mid-low cell pressures [63–65], polarisation of ^{129}Xe to levels previously achieved with ^{3}He can now be realised. Furthermore, continued advances in pulse sequence optimisation have shown that improved image SNR can be obtained in hyperpolarised gas lung imaging by using steady-state free precession (SSFP) [222, 266, 267] rather

than conventional spoiled gradient echo (SPGR) sequences [71, 207].

In this chapter, the application of 3D SSFP sequences for high-quality MR imaging of pulmonary ventilation with ^{129}Xe is presented. The theoretical background of this acquisition method is introduced, and the results of an optimisation of sequence parameters by numerical simulations of the 3D SSFP signal, and in vivo measurement of k-space filters, is reported. The possibility of clinical translation of the technique is assessed by evaluating the feasibility of lung MR imaging with NAXe at 1.5 T and 3 T. Further image acceleration with compressed sensing techniques is reported for the purpose of enabling same-breath acquisition of ^{129}Xe ventilation images and ^{1}H anatomical images. The quality of ^{129}Xe images produced highlights the potential of xenon as a cost-effective contrast agent for clinical MR imaging of pulmonary ventilation.

Part of this chapter is based on the following publication: "Feasibility of Human Lung Ventilation Imaging using Highly Polarized Naturally-Abundant Xenon and Optimized 3D SSFP". **N. J. Stewart**, G. Norquay, P. D. Griffiths, J. M. Wild. *Magnetic Resonance in Medicine*, **74**, 346-352 (2015). Author contributions statement (for all parts of the chapter other than Section 4.5): study design, NJS, GN, JMW; acquisition of data, NJS, GN; analysis of data, NJS; preparation of manuscript, NJS, GN, PDG, JMW. Author contributions statement for Section 4.5: this section of work was completed in collaboration with Guilhem Collier, who performed all CS simulations, and contributed to all stages of study design, data acquisition and analysis.

4.2   Theory: 2D SPGR vs 3D SSFP

The purpose of this section is to review the fundamental theoretical description of 2D SPGR and 3D SSFP pulse sequences, and the manner in which the dynamics of the hyperpolarised gas magnetisation differs between the two approaches.

4.2.1   2D SPGR

As discussed in Section 2.2, 2D spoiled gradient echo (SPGR) sequences have been typically employed as the workhorse approach for lung ventilation imaging with hyperpolarised gases, with reproducible results demonstrated at a number of different centres [68, 71, 86, 87]. In Sheffield, after establishing effective protocols for ^{3}He ventilation imaging with SPGR sequences, the first in vivo ^{129}Xe images were reported using 2D, slice-selective SPGR sequences [251].

Replicating the results shown in Section 3.2.6, the dynamics of the magnetisation of hyperpolarised gas nuclei during an SPGR acquisition is expressed by the following equation (see Equation 3.124):

$$M_{xy}(n) = M_0 \exp\left[-(n-1)\frac{TR}{T_1}\right] \sin(\alpha_n) \prod_{j=1}^{n-1} \cos(\alpha_j) \tag{4.1}$$

where α is the radiofrequency excitation flip angle, M_0 is the initial magnetisation at the start of the

sequence, n is the RF pulse number, TR is the repetition time and T_1 is the longitudinal relaxation time for the nuclei of interest. This equation intrinsically accounts for a variable excitation flip angle during the acquisition. However, for the case of a constant flip angle, and assuming that $TR \ll T_1$, Equation 4.1 reduces to (c.f. Equation 3.125):

$$M_{xy}(n) = M_0 \sin(\alpha) \cos^{n-1}(\alpha) \tag{4.2}$$

As explained previously, the magnetisation of hyperpolarised gas is non-renewable; once excited, it recovers to its thermal equilibrium value. Thus the rate of decay of magnetisation during an SPGR acquisition is dictated by the excitation flip angle and the number of RF pulses required to encode the image, the latter which is equal to the number of phase encodes for a 2D slice-selective sequence, or the product of the number of y and z phase encodes ($N_y \times N_z$) for a 3D sequence.

A diagram of a typical SPGR sequence is depicted in Figure 3.22. The presence of a spoiler gradient destroys residual magnetisation after the read-out, minimising the sequence TR and enabling rapid acquisition of many slices during a single breath-hold. A relatively low flip angle $\lesssim 10°$ is used for 2D slice-selective imaging in order to preserve magnetisation throughout the full acquisition process. As such, these sequences are often referred to as "fast low-angle shot" (or "FLASH") sequences.

3D SPGR sequences, with phase-encoding on the z-axis as opposed to slice-encoding, afford full coverage images of the lungs to be obtained. It has been demonstrated that 3D SPGR sequences can offer a SNR benefit over 2D SPGR sequences of a factor of ~1.5 for hyperpolarised ^{3}He applications [71]. Intrinsically, each spin receives an increased number of RF pulses in a 3D sequence due to the additional z phase-encoding. This results in a SNR increase by a factor of $\sqrt{N_z}$, where N_z is the number of z phase encodes, although in practice, much of this SNR discrepancy can be recovered by interleaving of 2D multi-slice sequences. Note: by virtue of the increase in total number of RF pulses, the excitation flip angle in a 3D sequence must be considerably reduced compared with that of a 2D sequence.

4.2.2 3D SSFP

Due to the absence of refocusing RF pulses or balanced gradients, SPGR sequences are constrained by T_2^* decay and associated susceptibility artefacts. However, as a consequence of the relatively long T_2^* values of ^{129}Xe and ^{3}He when compared with the sequence repetition time — at 1.5 T, $T_{2,Xe}^* \sim 25$ and 52 ms (in partially- and fully-inflated lungs, respectively) [251] and $T_{2,He}^* \sim 27$ ms [268] [i] — a significant proportion of hyperpolarised noble gas magnetisation remains at the end of each encoding step that is destroyed by the spoiling process and hence cannot contribute to the signal in subsequent encoding steps. The utilisation of steady-state free precession (SSFP) sequences enables this magnetisation to be recycled, resulting in an overall improvement in SNR compared with SPGR sequences for hyperpolarised gas applications [222].

A schematic of a 2D balanced SSFP sequence is depicted in Figure 3.24. The 3D form of the sequence offers a minimal echo time by permitting removing of the slice selection gradient, using of a hard

---

[i]At 3 T, $T_{2,Xe}^* \sim 18$ and 24 ms in partially- and fully-inflated lungs, respectively.

radiofrequency pulse of short duration, and implementing phase encoding along the z direction for three-dimensional imaging. Balancing the phase encoding gradients ensures that the magnetisation coherence is preserved between excitations.

For SSFP of thermally-polarised ^{1}H nuclei, a true steady-state magnetisation is achieved and the transverse relaxation time can be approximated by the Carr-Purcell-Meiboom-Gill (CPMG) T_2 [269].

In the absence of imaging gradients, it has been shown that a *pseudo* steady-state can be achieved in a ^{3}He gas phantom with an effective $T_2 \sim 1$ s (see Figure 4.1). However, in the presence of magnetic field gradients, gas diffusion during the acquisition causes dephasing of spins, which reduces the effective T_2. As such, the MR signal continuously decays over the course of the image acquisition, as presented in Section 4.3.1 (see e.g. Figure 4.2). For a 3D SSFP sequence with a hard radiofrequency (RF) pulse, the dominant gradient in terms of diffusional attenuation of MR signal is the read-out gradient. The effective T_2, $T_{2,eff}$, is modified as follows:

$$T_{2,eff}(\tau) = \frac{\tau}{b(\tau)D + \frac{\tau}{T_{2,CPMG}}} \qquad (4.3)$$

where τ is the time for which diffusion occurs (in the case of the read-out gradient this becomes the echo time, TE); $b(\tau)$ is the b-value of the read gradient; D is the hyperpolarised gas diffusion coefficient, taken to be $D_0 = 0.062$ cm^2.s^{-1} [226], the xenon self-diffusion coefficient, in the following work.
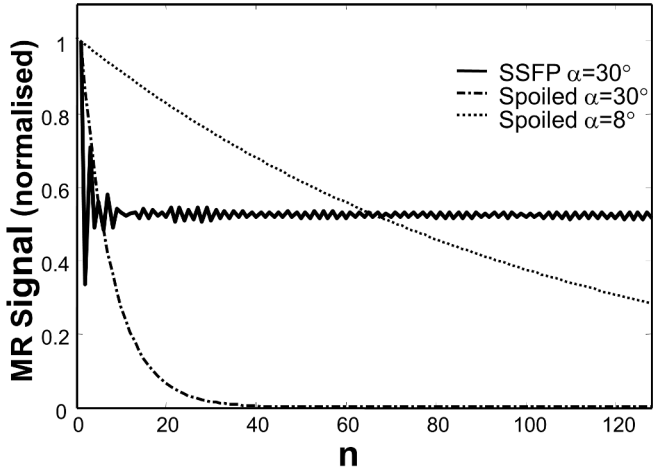
Figure 4.1: Normalised MR signal decay in the absence of imaging gradients for a 2D SSFP experiment (128 phase encodes) compared with 2D SPGR equivalents for a ^{3}He gas syringe phantom ($D = 0.9 \times 10^{-4}$ cm^2.s^{-1}). Figure reproduced from Figure 2 of reference [222], with permission from the publisher.

The gradual rate of signal decay in SSFP compared with SPGR sequences permits the use of considerably higher flip angles in the former. Higher flip angles, in combination with the low TR, and associated high RF duty cycle, may however place restrictions on the flip angle and repetition time in order to maintain safe RF deposition to human subjects. This is a particularly important consideration for SSFP sequences with ^{129}Xe because its relatively low gyromagnetic ratio necessitates increased RF power to achieve the same flip angle as for a nucleus with a greater gyromagnetic ratio (see Equation 3.36).

Furthermore, steady-state sequences are acutely sensitive to B_0 field inhomogeneity, manifesting as banding artefacts (regions of low signal) where the resonance frequency is significantly offset from the

Larmor frequency. This issue is discussed in detail in Section 4.3.3. Finally, by virtue of the excitation of the entire 3D volume of spins for each phase-encoding step, and the associated longer image acquisition times, 3D sequences are less robust to motion artefacts than 2D sequences. Since hyperpolarised gas images are typically acquired at breath-hold, respiratory motion can often be mitigated, however, cardiac motion can induce artefacts such as ghosting. Nevertheless, resulting "ghosts" usually appear outside the lungs and thus can be removed by careful masking of the lung cavity, for example with the aid of simultaneously-acquired ^{1}H anatomical scans.

4.3 3D SSFP sequence optimisation: Simulation of signal dynamics

The purpose of this section was to optimise the 3D SSFP pulse sequence for hyperpolarised ^{129}Xe lung imaging applications, in order to evaluate ^{129}Xe as a cost-effective alternative to ^{3}He for clinical applications in humans.

4.3.1 Theoretical background

The signal-to-noise ratio of a 3D SSFP experiment depends fundamentally on sequence parameters, including: echo/repetition time (TE/TR); read-out bandwidth (BW); the associated b-value of the read gradient; the (sine of the) flip angle (α); the voxel size or resolution in three-dimensions; the field-of-view (FOV). In addition, the following factors *external* to the sequence must be considered: B_0 inhomogeneity and the resulting distribution of off-resonance frequencies across the chest; the diffusion coefficient of the gas of interest in the alveolar spaces, D; the transverse and longitudinal relaxation times, T_1, T_2, T_2^*; the polarisation of the hyperpolarised gas, i.e. P_{Xe}.

With this knowledge, it is possible to simulate the ^{129}Xe magnetisation during the course of a 3D SSFP acquisition using a matrix product operator approach. This involves the propagation of the matrix form of the Bloch equations for each encoding step in the acquisition. The theory underpinning this approach has been detailed previously for ^{1}H [270] and ^{3}He [222, 266] applications, and considers the combined effects of excitation flip angle, off-resonance (B_0) inhomogeneity, and pulse sequence parameters, as follows.

The magnetisation at encoding step $n+1$, M_{n+1}, can be described by the multiplication of the magnetisation at the previous encoding step, M_n, by a propagation matrix, A:

$$M_{n+1} = AM_n + B \tag{4.4}$$

The term B is related to the recovery of magnetisation and is hence zero for hyperpolarised gas nuclei, because the T_1 decay acts to return the polarisation to its thermal equilibrium state, in which detection by in vivo imaging methods is not feasible. The propagation matrix comprises the product of a series of matrices describing the rotation, free precession and relaxation of magnetisation during a single encoding step:

$$A = P_{TE}C_{TE}R_{\pi}(n) R_{\alpha}P_{TR-TE}C_{TR-TE} \qquad (4.5)$$

where P_{τ} represents the free precession of magnetisation:

$$P_{\tau} = \begin{bmatrix} \cos{(2\pi\Delta f_0\tau)} & \sin{(2\pi\Delta f_0\tau)} & 0 \\ -\sin{(2\pi\Delta f_0\tau)} & \cos{(2\pi\Delta f_0\tau)} & 0 \\ 0 & 0 & 1 \end{bmatrix} \qquad (4.6)$$

Here, τ is the time for which free precession occurs and Δf_0 is the difference between the resonance frequency and the ^{129}Xe gas Larmor frequency. This matrix becomes the identity matrix if spins are assumed to be resonating at the Larmor frequency.

The matrix C_{τ} accounts for relaxation in the transverse and longitudinal planes:

$$C_{\tau} = \begin{bmatrix} \exp{(-\tau/T_2(\tau))} & 0 & 0 \\ 0 & \exp{(-\tau/T_2(\tau))} & 0 \\ 0 & 0 & \exp{(-\tau/T_1)} \end{bmatrix} \qquad (4.7)$$

where T_2 and T_1 are the transverse and longitudinal relaxation rates, respectively. As shown in Equation 4.5, one instance of the sequence can be divided into two periods of free precession and relaxation where τ takes the values TE and $TR - TE$, respectively.

R_{α} is the 3D rotation matrix, shown below for the case of excitation by a flip angle α about the x-axis.

$$R_{\alpha} = \begin{bmatrix} 1 & 0 & 0 \\ 0 & \cos(\alpha) & \sin(\alpha) \\ 0 & -\sin(\alpha) & \cos(\alpha) \end{bmatrix} \qquad (4.8)$$

Finally, R_{π} represents the rotation matrix evaluated at a flip angle of π or $-\pi$ radians, depending on the RF pulse number n. This accounts for magnetisation phase cycling between successive excitations.

4.3.2   Methods

Full details of the hardware relating to the MR scanner, radiofrequency coils, and ^{129}Xe polarisation apparatus employed in this work are described in Section 4.4.1.

To maximise the available SNR from a 3D SSFP experiment, the global ^{129}Xe magnetisation vector was simulated using the matrix form of the Bloch equations for different experimental conditions. The matrix product operator approach was utilised to predict the longitudinal magnetisation dynamics (so-called "k-

space filters") imposed by the 3D SSFP ^{129}Xe magnetisation evolution, for various receiver bandwidths and flip angle settings, in order to compare with in vivo experiments. The 3D SSFP image SNR was modelled as a function of bandwidth and flip angle, by normalising the simulated transverse magnetisation, M_{xy}, at the centre of k-space (i.e. signal) by the square root of the bandwidth (i.e. noise).

In these initial simulations, a range of $T_{2,CPMG}$ values between 300 ms and 25 ms (the ^{129}Xe T_2^* in partially-inflated human lungs at 1.5 T [251]) was used. The $T_{2,CPMG}$ of ^{129}Xe at 1.5 T or 3 T has not been reported, though measurements at low-field (0.2 T) in humans [248], and high-field (4.7 T) in rats [271] have suggested a value of ~ 300 ms in the lungs. However, the field dependence of $T_{2,CPMG}$ is not known, and measurement of this parameter is challenging in the lungs with xenon due to the finite inter-echo times attainable and diffusion of the gas causing incomplete magnetisation refocusing. Thus, it is appropriate to perform simulations over a range of $T_{2,CPMG}$ values and assess the value at which optimum agreement is observed between simulated and experimental data.

The longitudinal relaxation time of ^{129}Xe in human lungs was taken to be $T_1 = 20$ s [134]. It is worth noting that the effect of diffusional dephasing due to applied imaging gradients on the $T_{2,eff}$ is lesser for ^{129}Xe compared with ^{3}He [222], due to the ~ 10-fold lower diffusion coefficient, and the fact that the gradient b-value scales with the square of the gyromagnetic ratio (see Equations 3.115 and 3.116).

To provide a measured reference with which to compare simulated magnetisation responses, k-space filters were acquired from the lungs of a healthy smoker (male, 28 years) in vivo at 1.5 T. This was done by nulling the y and z phase-encoding gradients of a 3D SSFP sequence and recording the ^{129}Xe frequency-encoded read-out as a function of RF pulse number, for different flip angle and bandwidth settings, using the experimental set-up described in Section 4.4.1. For each flip angle or bandwidth setting, the subject inhaled 200 mL of a 50:50 EN^{129}Xe:N$_2$ mixture from a 1 L bag and maintained breath-hold for 8-22 seconds, whilst k-space filters were acquired [ii].

The effect of off-resonance due to inaccurate centre frequency estimation or local B_0 inhomogeneity upon the 3D SSFP k-space filters and SNR was also simulated. Typically, the mean (global) resonance frequency of ^{129}Xe gas in the lungs is calibrated prior to imaging in order to maximise the available signal throughout the acquisition. However, local variations in resonance frequency, due to susceptibility differences and/or B_0 inhomogeneity, can cause variability in signal intensity across the image. In order to simulate this effect for 3D SSFP acquisitions, maps of Δf_0, the off-resonance frequency, were acquired in a healthy subject (male, 33 years). A dual-interleaved 3D SPGR sequence with two different echo times was employed with the following parameters: field-of-view (FOV), 40 cm; phase FOV, 1; 16 effective coronal slices (z phase encodes) with no slice gap; in-plane resolution, 32×32 (12.5 mm in-plane pixel dimension); effective slice thickness, 18 mm in the anterior-posterior direction; flip angle, $\sim 3°$; hard RF pulse; $TE_1/TR_1 = 1.4/3.2$ ms; $TE_2/TR_2 = 4.6/6.4$ ms; bandwidth, ± 8 kHz; breath-hold, 5 s. The subject exhaled to functional residual capacity and inhaled 500 mL of hyperpolarised EN^{129}Xe gas, mixed with 500 mL nitrogen gas, from a 1 L Tedlar bag prior to image acquisition.

From the resulting Δf_0 maps, assuming a constant flip angle and a number of RF pulses corresponding to the target image dimensions for an in vivo imaging experiment (see Section 4.4.1), the 3D SSFP SNR

[ii]The lowest achievable bandwidth for the experimental set-up described in Section 4.4.1 was ± 2 kHz, however this required an unfeasibly long breath-hold of ≈ 39 s, and as such this data-set could not be acquired.

was modelled on a regional basis for each resonance frequency of each pixel within the lung mask. Thus, a 3D map of the effects of off-resonance on 3D SSFP SNR was generated.

In a similar fashion, to predict the spatial variations in 3D SSFP signal resulting from flip angle ($\boldsymbol{B_1}$) inhomogeneity across the lungs generated by the flexible transmit-receive coil used for ^{129}Xe ventilation imaging (see Section 4.4.1), B_1 maps were obtained from the same healthy volunteer. Three successive 3D SPGR acquisitions with minimal time-gap between were acquired with the following sequence parameters: FOV and resolution as above; flip angle, $\sim 4°$; hard RF pulse; $TE/TR = 1.4/3.2$ ms; bandwidth, ± 8 kHz; breath-hold, ~ 5 s. Gas delivery was performed as above.

From the resulting flip angle (α) maps, the B_1 amplitude was scaled up to achieve the target flip angle for an in vivo imaging experiment (see Section 4.4.1), assuming a linear performance of the RF hardware with current in the coil. Assuming that all spins were on resonance, and a number of RF pulses corresponding to the target image dimensions, the 3D SSFP SNR was modelled on a regional basis for each flip angle of each pixel within the lung mask. Thus, a 3D map of the effects of flip angle on 3D SSFP SNR was generated.

4.3.3 Results

Experimentally-measured k-space filters
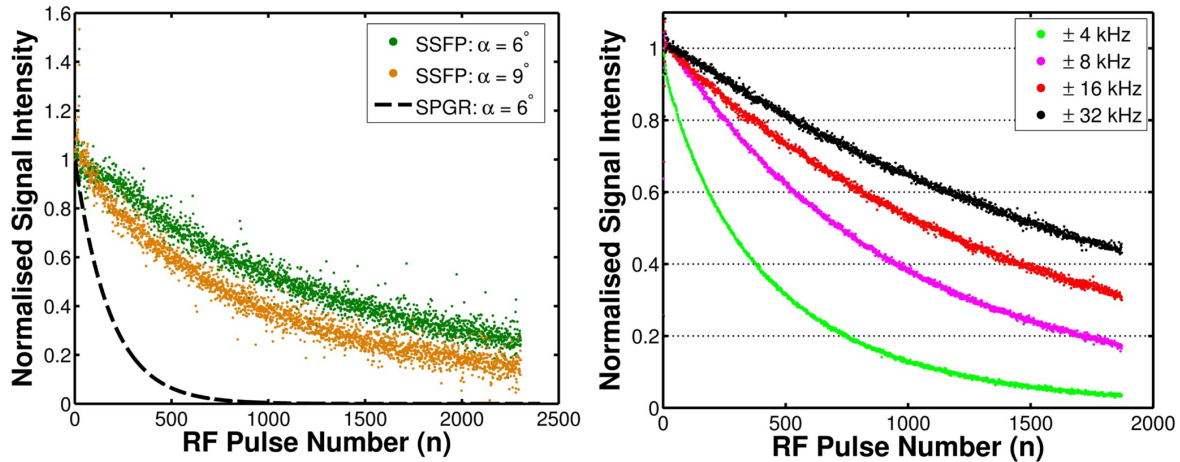
Figure 4.2: In vivo measured k-space filters for 3D SSFP with ^{129}Xe at different flip angle and bandwidth settings at 1.5 T. The normalised ^{129}Xe MR signal intensity — during the course of a sequence in which the y and z phase encoding gradients have been nulled — is plotted for 3D matrix sizes of 96×24 and 78×24 ($N_y \times N_z$) in the left and right graphs, respectively. (The right-hand graph shows k-space filters acquired with $\alpha = 10°$. The left-hand plot shows k-space filters acquired at a fixed bandwidth of ± 8 kHz, and includes a simulated k-space filter for a 3D SPGR experiment of the same matrix size, derived using Equation 4.2.)

Figure 4.2 depicts experimentally-measured k-space filters for a 3D SSFP sequence with pixel dimensions as implemented in Section 4.4.1. In all cases, the signal decay was considerably more gradual than that of a SPGR acquisition with an equivalent flip angle. As expected, the decay in hyperpolarised ^{129}Xe signal over the course of the experiment was steeper for low bandwidths, due to increased dephasing of magnetisation in the presence of lengthier read-out gradients. These data can be utilised to determine suitable bandwidth and flip angle settings for a 3D SSFP imaging experiment. A typical guideline adopted in

hyperpolarised gas ventilation imaging in order to attain reasonable SNR without introducing significant image blurring is to choose a k-space filter that results in a final magnetisation value of $\approx \frac{1}{3} M_0$ (see Section 3.2.6).

Global signal simulations (assuming on-resonance)

Simulated ^{129}Xe 3D SSFP k-space filters (for various bandwidths at a fixed flip angle of $\alpha = 10°$) are presented in Figure 4.3. The measured in vivo decay of ^{129}Xe longitudinal magnetisation (Figure 4.2) was considerably faster than the simulated decay using $T_{2,CPMG} = 300$ ms (which was measured previously under different experimental conditions [248, 271]); in fact, the best agreement between simulation and experiment (at 1.5 T) was found at a value of $T_{2,CPMG} = 80$ ms [iii], for which case the simulated k-space filters are plotted in Figure 4.3.

Figure 4.3: Simulated k-space filters depicting the decay in longitudinal magnetisation, M_z, of hyperpolarised ^{129}Xe during a 3D SSFP acquisition at 1.5 T, for different imaging bandwidths at a fixed flip angle of $\alpha = 10°$, assuming that all spins resonate at the same (Larmor) frequency.

Simulation results for 3D SSFP SNR (as a function of imaging bandwidth and flip angle) for 78 and 24 phase encodes in the y and z dimensions, respectively, and $T_{2,CPMG} = 80$ ms, are shown in Figure 4.4. The available MR signal increases with bandwidth, however, the Johnson (shot) noise also scales as the square root of the bandwidth, resulting in a simulated optimum SNR at a bandwidth of ± 8 kHz. These SNR simulations highlight that for 3D SSFP of ^{129}Xe, the SNR is relatively robust and tolerant to variations in flip angle setting; with an optimum flip angle of $9.5°$ and a predicted SNR penalty of 20-25% for using flip angles of $5°$ or $15°$.

Global signal simulations (of off-resonance effects)

Steady-state acquisition strategies are acutely sensitive to off-resonance, which presents as characteristic "banding" artefacts in the image; periodic nulls in the SSFP signal as a function of Δf_0 result in dark bands of low signal intensity that can obscure the image interpretation and potentially be misdiagnosed as ventilation defects (see e.g. [272]). The B_0 field exhibits considerable inhomogeneity across the lungs, which is hampered by the large susceptibility differences at the air-tissue interfaces [221], as discussed

---

[iii] It was assumed that the more rapid magnetisation decay measured in vivo resulted from a $T_{2,CPMG}$ value of 300 ms being inappropriate under these experimental conditions. However, in practice, other factors may contribute to this discrepancy; for example inhomogeneity in flip angle or B_0, as is discussed in subsequent subsections.
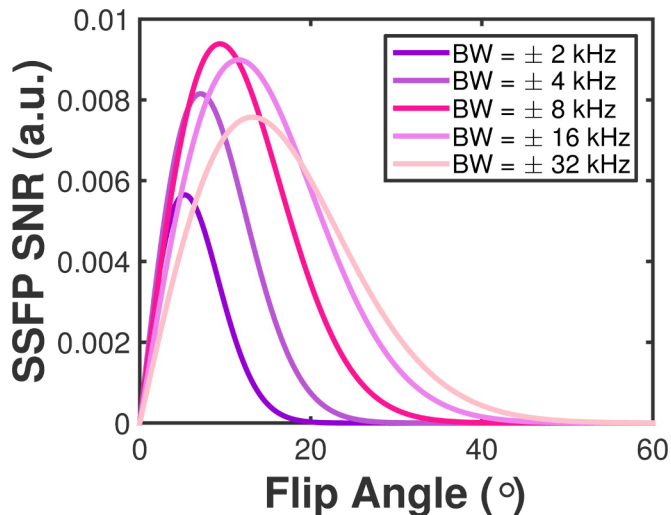
Figure 4.4: Simulated SNR for hyperpolarised ^{129}Xe 3D SSFP, normalised to the maximum predicted value (at a bandwidth of $\pm$ 8 kHz), as a function of excitation flip angle and imaging bandwidth, assuming that all spins resonate at the same (Larmor) frequency.

in Chapter 2. In particular, this can lead to substantial signal drop-off, distortion or blurring near the diaphragm in hyperpolarised gas images [82, 221]. Furthermore, B_0 inhomogeneity is elevated at increased field strength, as evidenced by the reduction in T_2^* measured for ^{129}Xe at 3 T compared with 1.5 T [251], which implies that increased artefact severity may be observed at 3 T compared with 1.5 T.
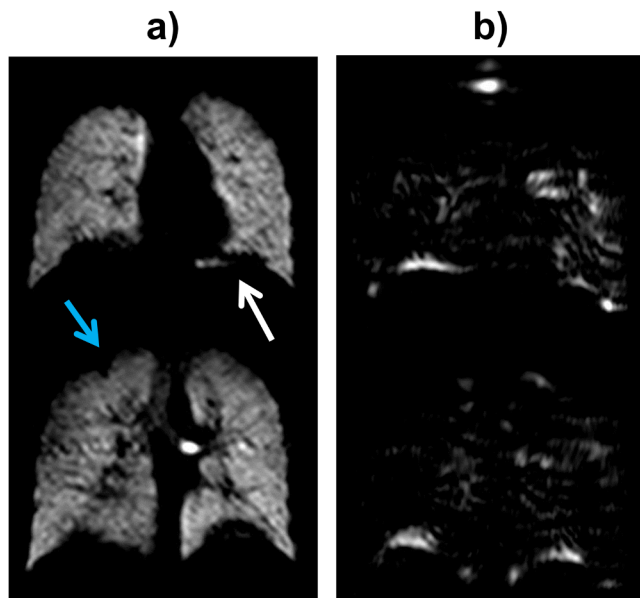
Figure 4.5: a) Example banding artefact (white arrow) due to significant off-resonance near the diaphragm in a selected ^{129}Xe 3D SSFP lung image slice. In certain cases, these artefacts could potentially be misinterpreted as true ventilation abnormalities (e.g. the blue arrow shows an artefact caused due to a bifid rib in another example slice). Images in a) were acquired after calibrating the transmit and receive frequencies to the average (global) measured resonance frequency in the lungs. b) Images obtained without calibrating the mean transmit and receive frequencies. In this extreme case, the receive frequency was $\approx$ 70 Hz different from the average measured resonance frequency.

As illustrated in Figure 4.5a, non-negligible signal nulling due to off-resonance can often be seen in certain slices of a ^{129}Xe 3D SSFP acquisition, even when the global resonance frequency is well-calibrated. Although banding artefacts are typically most-prevalent in a similar position in each scan — at the base of the lungs, close to the diaphragm (see the following subsection) — it is possible that these defects could be confused for actual abnormalities in pulmonary ventilation function. Poor estimation or calibration of the mean (global) resonance frequency of the target nucleus can result in almost complete loss of the available signal across the whole of the lungs; as illustrated in Figure 4.5b, where the regions of high and

low intensity are reversed with respect to Figure 4.5a.

Figure 4.6 demonstrates how imperfect calibration of the transmit and receive frequency with respect to the measured resonance frequency of ^{129}Xe in the lungs can severely impact on the available signal during a 3D SSFP acquisition. Increasing the degree of off-resonance results in more rapid signal decay and an amplification and elongation of the oscillatory behaviour of the longitudinal magnetisation at the beginning of the acquisition [iv]. However, further increasing Δf_0 past a certain value leads to the opposite behaviour, i.e. less steep k-space filtering and a smoothing of the oscillatory behaviour, such that for $\Delta f_0 \approx 160$ Hz, an approximately equivalent k-space filter to that for $\Delta f_0 = 0$ Hz can be observed. Indeed, the effects of off-resonance on magnetisation are periodic, as shown in Figure 4.7, and hence in Figure 4.6 the appearance of the k-space filter for $\Delta f_0 = 240$ Hz appears similar to that for $\Delta f_0 = 80$ Hz.
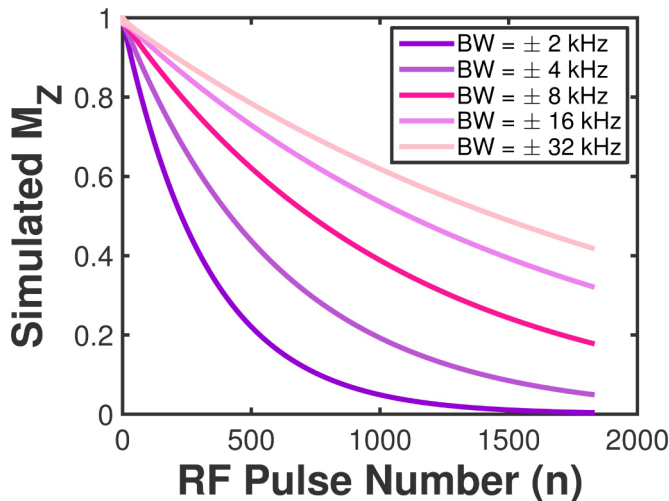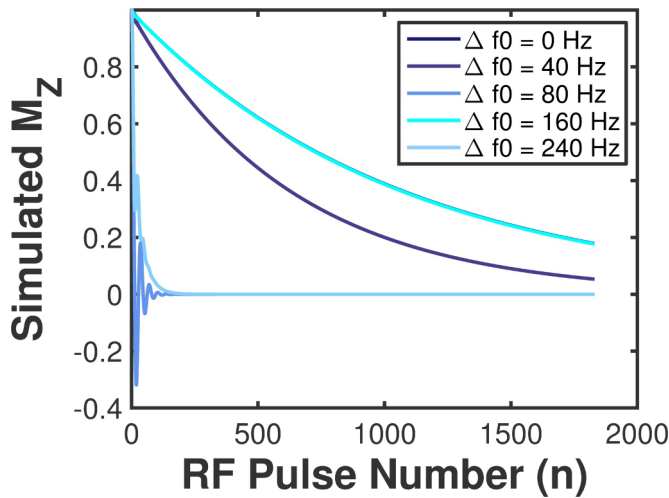

Figure 4.6: Simulated k-space filters depicting the decay in longitudinal magnetisation, M_z, of hyperpolarised ^{129}Xe during a 3D SSFP acquisition, for a fixed flip angle of $\alpha = 10°$ and a fixed bandwidth of ± 8 kHz, with variable frequency offsets (Δf_0).

These observations hence suggest that there should be an off-resonance frequency value between 0 and 160 Hz that induces a maximal rate of signal decay and most severe initial oscillatory behaviour. This is confirmed by the SNR simulations depicted in Figure 4.7, where periodic nulls in the 3D SSFP signal can be observed as a function of off-resonance frequency in the voxel of interest. The null position is common to signal simulations for different flip angle settings, although the width of the null region, and the amplitude of the predicted signal at non-null frequencies is significantly influenced by the choice of α. In particular, it is noteworthy that the maximum on-resonance ($\Delta f_0 = 0$ Hz) signal is greater for a flip angle close to the optimum value (10°) as compared to that at a setting of 5°.

Regional signal simulations with B_0 and B_1 mapping

To further characterise the effects of flip angle and off-resonance on the 3D SSFP signal on a regional basis, B_1 and B_0 maps were obtained using the acquisition strategies described in Section 4.3.2.

Firstly, B_1 / flip angle maps were calculated using the first two of three successive 3D SPGR acquisitions. For each pixel in the image domain, the signal intensities from the two acquisitions $S_{1,2}$ and the number of RF pulses between the two acquisitions were utilised to derive the effective flip angle at that

---

[iv]Some oscillatory behaviour was present in all simulated and measured k-space filters, representing the regime prior to reaching steady-state.
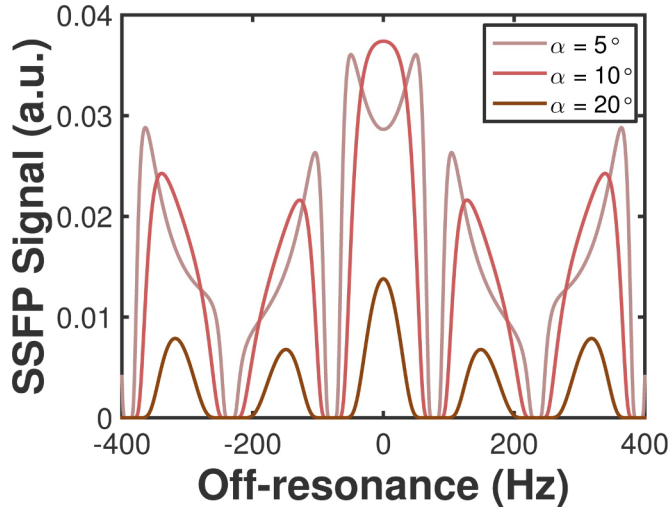
Figure 4.7: Simulated SNR for hyperpolarised ^{129}Xe 3D SSFP, for a fixed bandwidth of ± 8 kHz at different flip angles, as a function of frequency offset (Δf_0).

particular pixel location:

$$\alpha = \arccos\left(\frac{S_2}{S_1}\right)^{\frac{1}{N_y N_z}} \tag{4.9}$$

where α is the flip angle and N_y and N_z are the number of phase encodes in the y and z directions, respectively. The SPGR acquisitions must be performed with a high-enough target flip angle such that sufficient signal decay is induced between successive acquisitions; for very low flip angles, inaccuracies in the derived flip angle map can arise from relatively small differences in S_2 and S_1. Nevertheless, the maximum flip angle is also constrained by the need to retain signal for a minimum of two complete acquisitions. These considerations are especially important in 3D flip angle mapping when compared with 2D mapping, because all image voxels are excited by each RF pulse.

The flip angle for the flexible transmit-receive vest coil used for ^{129}Xe ventilation imaging at 1.5 T (described in Section 4.4.1) was found to be generally homogeneous across the 3D volume of the lungs, as shown in Figure 4.8. In the most posterior slices, a higher flip angle was observed in the left lung, particularly the inferior region. In addition, the flip angle in the apex of the lungs was slightly lower than that of the central and inferior lungs, especially in the central slices in the anterior-posterior direction. However, overall, the inhomogeneity was less than 50%, with differences of $\sim$ 2-3° across the lungs in the central slices and $\sim$ 5° in the most anterior and posterior slices, for an input flip angle of 10°. The mean $\pm$ standard deviation of the flip angle over the whole 3D volume was $\alpha = (4.29 \pm 0.68)°$ for the input flip angle of 4°, which was scaled up to an input of 10°, resulting in a mean $\pm$ standard deviation of $(10.74 \pm 1.7)°$, assuming linearity of the RF hardware chain.

Resulting simulations of the distribution of ^{129}Xe 3D SSFP SNR using these flip angle maps indicated that the 3D SSFP acquisition is robust to variations in flip angle of the order of a few degrees (supporting the simulations presented in Figure 4.4). As illustrated in Figure 4.9, the 3D SSFP signal was found to be largely uniform across central and anterior slices, with a small degree of drop-off in regions of particularly high flip angle in the most posterior slices.
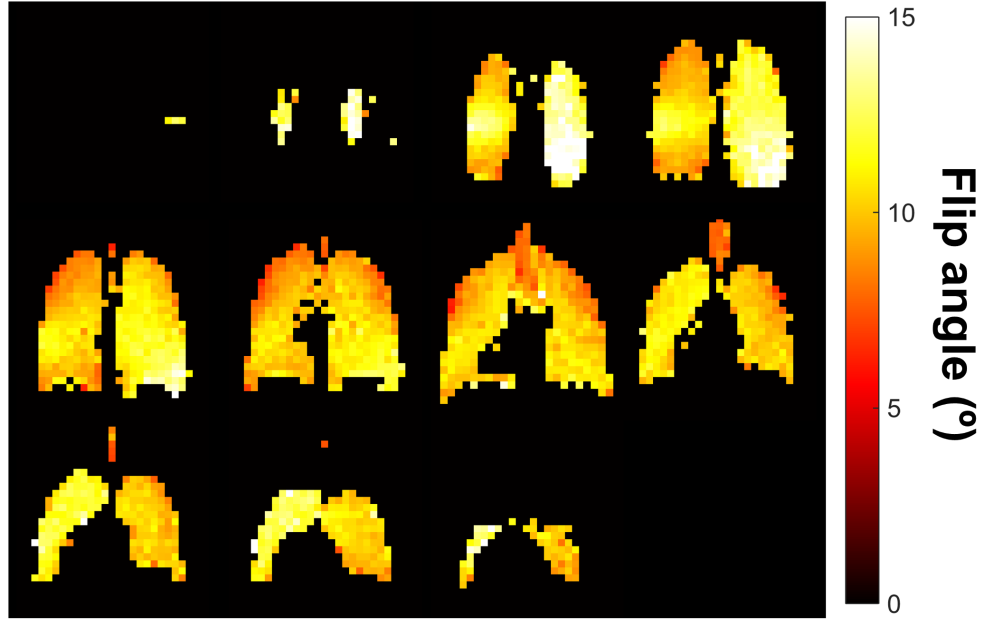
Figure 4.8: 3D flip angle maps for a flexible transmit-receive RF coil tuned to the hyperpolarised ^{129}Xe resonance frequency at 1.5 T. Original maps were acquired with an input flip angle of $4°$, as calibrated from the measurement of the rate of global signal decay from a pulse-acquire-spoil sequence with short TR, as introduced in Section 3.2.6. Displayed maps have been scaled to an input value of flip angle of $10°$, assuming linearity of the RF hardware chain. The mean $\pm$ standard deviation of α from these maps was $(10.74 \pm 1.7)°$.

Figure 4.9: Simulated distribution of 3D SSFP SNR for a matrix size of 78×24 phase encoding steps in the y and z directions, respectively, derived using the 3D flip angle maps for ^{129}Xe at 1.5 T shown in Figure 4.8.

B_0 / Δf_0 maps were determined from a two-interleaved 3D SPGR sequence with different TE settings for each interleave. For each voxel, of location $\boldsymbol{r}$, the accumulated phase difference between the two in-

terleaves can be related as follows:

$$\Delta\phi\left(\boldsymbol{r}\right) = \phi_{TE_2}\left(\boldsymbol{r}\right) - \phi_{TE_1}\left(\boldsymbol{r}\right) = -\gamma\Delta B_0\left(\chi\left(\boldsymbol{r}\right)\right)\Delta TE \tag{4.10}$$

where $\phi_{TE_m}\left(\boldsymbol{r}\right)$ is the phase of the particular voxel for interleave m and $\chi\left(\boldsymbol{r}\right)$ is the local magnetic susceptibility in the voxel at position $\boldsymbol{r}$. This equation can be derived using the Larmor equation $\omega = 2\pi\gamma B_0$ and the definition of angular frequency as the rate of change of phase with time, $\Delta\omega = \frac{\Delta\phi}{\Delta TE}$, and can be rearranged to yield:

$$\Delta f_0\left(\boldsymbol{r}\right) = -\gamma\Delta B_0\left(\chi\left(\boldsymbol{r}\right)\right) = \frac{\Delta\phi\left(\boldsymbol{r}\right)}{2\pi\Delta TE} \tag{4.11}$$

This equation can be utilised to derive the off-resonance frequency for each pixel in a 3D multi-interleave acquisition by evaluating the phase angles of each voxel in the two interleaves.
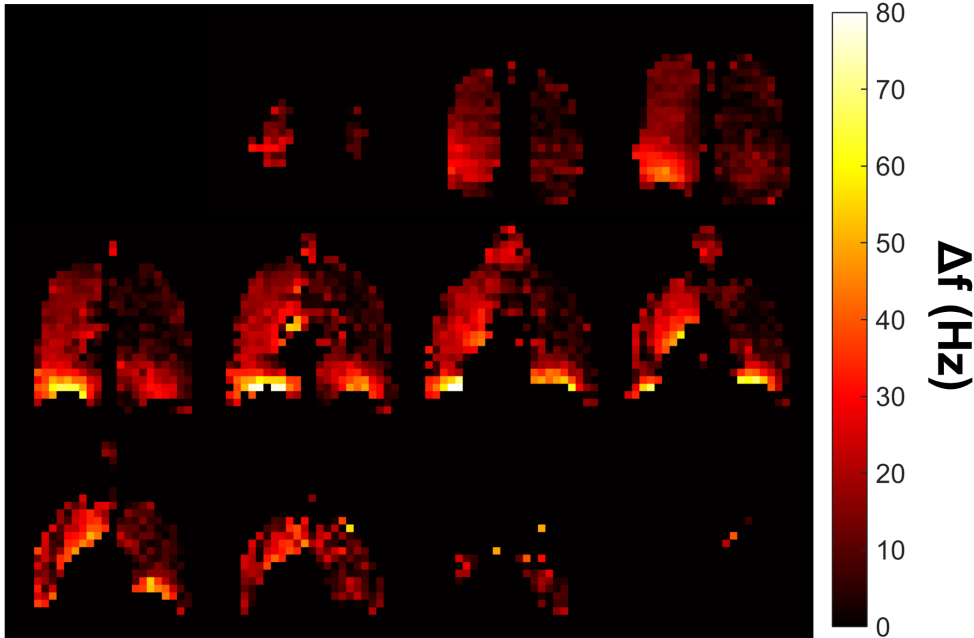
Figure 4.10: 3D Δf_0 maps obtained using hyperpolarised ^{129}Xe at 1.5 T. The mean $\pm$ standard deviation of Δf_0 from these maps was (15.15 ± 13.26) Hz.

The off-resonance frequency, Δf_0, was observed to be homogeneously distributed across the lungs, with slightly higher values in the right lung compared to the left lung, as illustrated in Figure 4.10. The exception to this observed homogeneity was that high values of Δf_0 of up to 80 Hz were detected localised to the basal region of the lungs, near the diaphragm. The mean $\pm$ standard deviation of the off-resonance frequency over the whole 3D volume was $\Delta f_0 = (15.15 \pm 13.26)$ Hz.

Resulting simulations of the distribution of ^{129}Xe 3D SSFP SNR using acquired Δf_0 maps exhibited a relatively uniform distribution of signal across the majority of the lungs, with no significant deviations between anterior or posterior slices and central slices or between left and right lungs, as shown in Figure 4.11. However, regions of significantly lower signal intensity near the diaphragm (corresponding spatially to regions of high off-resonance in Figure 4.10) were noticeable in a non-negligible number of slices. Moreover, these regions of low signal intensity correspond to the locations of the banding artefacts typically detected in ^{129}Xe ventilation imaging, as shown in Figure 4.5.
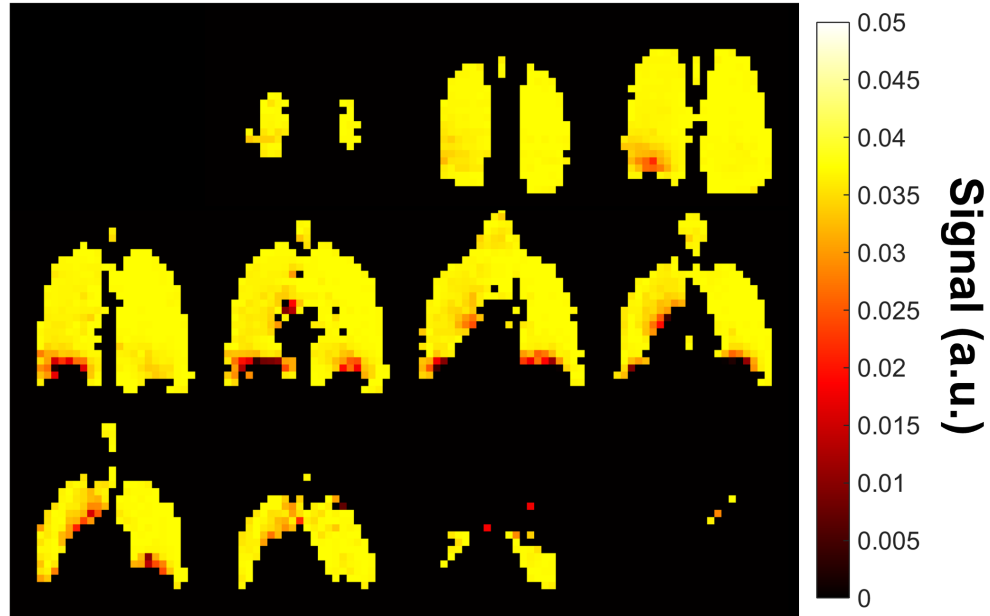
Figure 4.11: Simulated distribution of 3D SSFP SNR for a matrix size of 78×24 phase encoding steps in the y and z directions, respectively, derived using the 3D Δf_0 maps for ^{129}Xe at 1.5 T shown in Figure 4.10.

4.4 Feasibility of human lung ventilation imaging using highly polarised naturally-abundant xenon

The purpose of this section was to evaluate the potential for high quality MRI of pulmonary ventilation using naturally-abundant xenon (NAXe) gas with 3D SSFP pulse sequences optimised according to the methods and findings presented in Section 4.3.

4.4.1 Methods

Study subjects

Three volunteers were recruited for ventilation imaging with naturally-abundant xenon (NAXe): (a) healthy smoker, male, 28 years (HS); (b) healthy never-smoker, female, 32 years (HN1); (c) healthy never-smoker, male, 28 years (HN2). All subjects showed normal spirometry and $\geq 95\%$ oxygen saturation on room air. Each volunteer provided written informed consent for this study, which was approved by the UK National Research Ethics Committee.

Hardware requirements

MR ventilation imaging of NAXe, EN^{129}Xe and ^{3}He was performed on a 1.5 T clinical whole-body MRI scanner — GE Signa HDx (60 cm bore, GE Healthcare, Milwaukee, WI). NAXe MRI was also performed at 3 T — Philips Ingenia (70 cm bore, Philips, Best, The Netherlands). Custom-built, flexible, quadrature vest coils (CMRS, Brookfield, WI) were used to transmit and receive MR signals at the Larmor frequency of ^{129}Xe; 17.7 MHz (1.5 T) and 35.3 MHz (3 T), and of ^{3}He; 48.6 MHz (1.5 T). Xenon gas (The Linde Group, UK) was supplied in pre-mixed cylinders of 3% Xe, 10% N$_2$ and 87% He, with a ^{129}Xe content of 26% (NAXe) or 86% (EN^{129}Xe). Helium-3 gas (Linde) was supplied in high purity (99.99% ^{3}He).

^{129}Xe was polarised by Rb-^{129}Xe collisional spin-exchange optical pumping [61] using a home-built (UK regulatory-approved) polariser constructed from widely-available components. In prior work, this polariser was fitted with an external-cavity diode laser (ECDL), comprising a 30 W, 795 nm laser diode bar externally-tuned by a holographic Bragg grating (2400 lines/mm), and enabled attainment of ^{129}Xe polarisations of the order of 10-15% under "continuous-flow" operation [65]. This system was recently upgraded by fitting a 795 nm laser diode array with integrated volume holographic grating (BrightLase®-Ultra-200™; QPC, Sylmar, CA) providing 50 W of power incident on the optical cell containing the Rb and Xe. An optical train with solid fibre (see e.g. [64]) was coupled to the diode to minimize light loss and improve beam homogeneity along the length of the optical cell compared to the ECDL. These factors have facilitated routine attainment of high ^{129}Xe polarisations ($\sim$ 25% for doses $\leq$ 1 L) under continuous-flow operation [273]. For all ^{129}Xe imaging experiments subsequently reported in this chapter, the 3% Xe gas mixture was continuously flowed, at 0.35-0.4 sL/min, through the optical cell in a direction counter to the incident laser light. Polarised xenon was cryogenically separated from the helium and nitrogen buffer gases via a liquid nitrogen trap at the cell output. Accumulation of a 1 L dose of pure xenon required a total flow time of $\sim$ 80 minutes (flow time $\approx$ dosage / (flow rate $\times$ Xe fraction)).

^{3}He was polarised in an optical cell containing 99.99% ^{3}He by Rb-^{3}He collisional spin-exchange under batch-mode operation, using a prototype commercial system (MITI, Durham, NC) over a period of $\sim$ 14 hours. Doses of pure polarised ^{3}He were extracted directly from the optical cell, with no cryogenic accumulation required.

Image acquisition

Prior to all image acquisitions, the Larmor frequency and effective flip angle of ^{129}Xe nuclei were calibrated. For centre frequency calibration, a high resolution ^{129}Xe spectrum was acquired from the lungs of each subject after inhalation of a 3% xenon mixture from a 1 L Tedlar bag (Jensen Inert Products, Coral Springs, FL). Subjects maintained breath-hold for $\sim$ 5 s, and the excitation flip angle was determined by fitting the decay of the hyperpolarised ^{129}Xe signal from a series of pulse-acquire-spoil acquisitions from the whole lungs with an inter-pulse TR of 50 ms. An equivalent procedure was carried out for ^{3}He using a 5% ^{3}He:95% N$_2$ gas mixture.

The following optimised 3D SSFP sequence parameters (see Section 4.3) were used for ventilation imaging with NAXe at 1.5 T: field-of-view (FOV), 40 cm; phase FOV, 0.8 or 1.0; 20-24 effective coronal slices

with no gap; in-plane resolution, 96×96 (4.2 mm pixel dimension); effective slice thickness, 10 mm in the anterior-posterior direction; flip angle, 10°; hard RF pulse; $TE/TR = 2.1/6.4$ ms ("balanced" SSFP with asymmetric echo); bandwidth, ± 8 kHz; breath-hold, 11-15 sec. Each subject exhaled to functional residual capacity and inhaled 1 L of NAXe gas ($\sim 25\%$ polarisation) from a Tedlar bag prior to image acquisition.

In one subject (HN2), same-breath (back-to-back) NAXe and ^{1}H structural MR was performed at 1.5 T, similar to previous work performed with ^{3}He or EN^{129}Xe [100, 274]. The subject maintained breath-hold for ~ 16 sec after inhalation of 1 L NAXe; a 12 sec NAXe acquisition was followed by a 2 sec ^{1}H scan, with a small time delay in between due to software limitations. The structural ^{1}H scan covered the entire thorax (phase FOV, 1): 3D spoiled gradient echo sequence; $TE/TR = 0.6/1.9$ ms; bandwidth, ± 83.3 kHz; flip angle $= 5°$; identical pixel geometry as NAXe scan.

For comparison with NAXe imaging results, the same 3D SSFP imaging was performed on subjects HN1 and HS at 1.5 T using 400 mL EN^{129}Xe mixed with 600 mL nitrogen, and identical imaging parameters as above. In addition, hyperpolarised ^{3}He 3D SSFP was performed at 1.5 T using a gas mixture of 200 mL ^{3}He (25% polarisation) and 800 mL nitrogen. The following imaging parameters were modified for ^{3}He scans: $TE/TR = 0.6/1.9$ ms; bandwidth, ± 83.3 kHz; breath-hold, 5 sec. EN^{129}Xe and ^{3}He images were acquired subsequent to NAXe images, however, subjects exited the MR scanner for ~ 1 hour between scans to allow for continuous-flow accumulation of hyperpolarised ^{129}Xe and switching of RF hardware, respectively. Subjects were instructed to exhale to the same lung inflation level prior to inhalation of each gas dose, to ensure comparable lung volumes for each data-set.

Lastly, to evaluate the feasibility of naturally-abundant xenon MRI at 3 T, subject HN2 was scanned using a 3D SSFP pulse sequence with the following parameters: voxel size, $4.2 \times 4.2 \times 8$ mm^3, the latter corresponding to the anterior-posterior direction; flip angle, 12°; $TE/TR = 1.5/4.7$ ms; bandwidth, ± 8.5 kHz; breath-hold, 8 sec. As above, the subject inhaled 1 L of NAXe prior to image acquisition.

For comparison of SNR between MR acquisitions with NAXe, EN^{129}Xe and ^{3}He, regions of interest (ROIs) were placed in the upper right lobe of the lung and at the base of the image (outside the lungs) for each slice. SNR was calculated as the ratio of mean signal in the first ROI to the standard deviation of the signal in the second ROI.

4.4.2   Results

All of the NAXe images acquired from the three subjects at 1.5 T were of high quality, with mean SNRs of between 25 and 40 (examples shown in Figure 4.12). The spatial resolution and SNR achieved permitted identification of minor ventilation abnormalities in the healthy smoker's lungs (white arrows, Figure 4.12). A direct comparison of lung MR imaging with 200 mL ^{3}He, 400 mL EN^{129}Xe and 1 L NAXe is depicted for subject HS in Figure 4.13. The average SNR values over all acquired slices were 40 ± 8, 36 ± 4 and 31 ± 5, respectively for the three doses.

At 3 T, the NAXe image SNR was considerably improved for subject HN2 when compared with 1.5 T, even with the reduced voxel size (see Figure 4.14). The average slice SNR at 3 T was 40 ± 10 compared
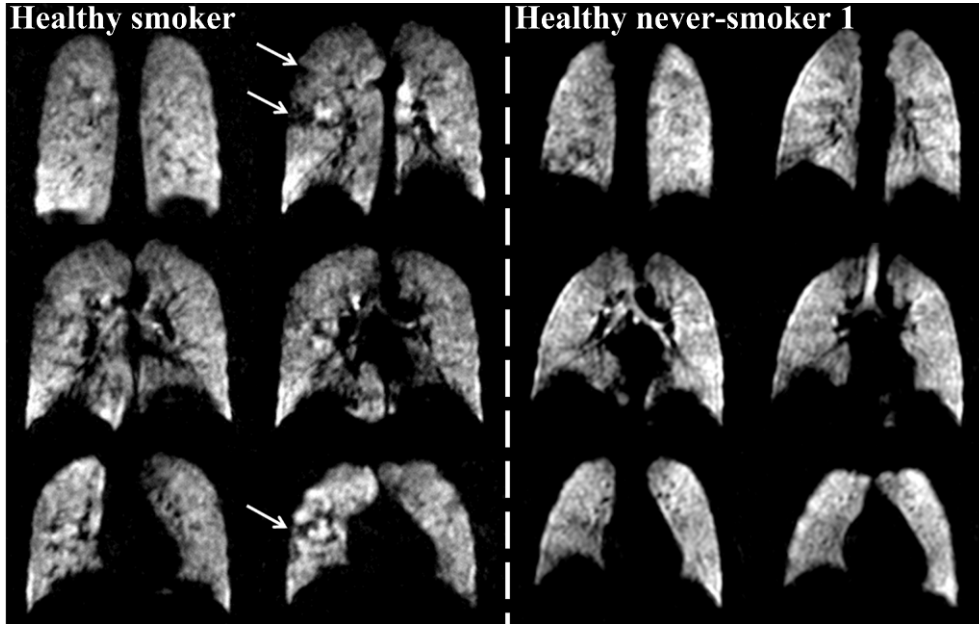
Figure 4.12: Selected coronal 3D SSFP image slices (10 mm thick) acquired from a healthy smoker (HS) and a healthy never-smoker (HN1) after inhalation of 1 L of naturally-abundant hyperpolarised xenon at 1.5 T. White arrows indicate minor ventilation defects (signal voids) identifiable in the lungs of the healthy smoker. The mean SNR (average over all acquired slices) was 31 ± 5 and 33 ± 2 for subjects HS and HN1, respectively.

with 26 ± 6 at 1.5 T for this subject (c.f. $T_2^* \sim 18$ ms and 25 ms in partially-inflated lungs at 3 T and 1.5 T, respectively [251]). A small abnormality in the NAXe images was identified in the upper right lung of this subject (white oval, Figure 4.14). This was previously associated with the impingement of a bifid rib prior to carrying out this work. The NAXe image SNR at 1.5 T was also sufficient to identify this defect. The results of same-breath ^{1}H and NAXe MR at 1.5 T, depicted in Figure 4.15, confirmed that this void in the hyperpolarised gas images was indeed recognisable from the co-registered proton images as a bifid rib.

Particularly noticeable in Figure 4.15, pertaining to the false colour scale, it can be observed that in a number of central and posterior slices, the NAXe signal intensity is lower in the apices of the lungs. This effect can also be identified in Figures 4.12 and 4.14 for NAXe (or EN^{129}Xe), although to a lesser extent than in Figure 4.15. This finding is in agreement with the ^{129}Xe flip angle maps presented in Figure 4.8, and may result from the radiofrequency coil being placed in a more inferior position on subject HN2 compared with HS, HN1, or the subject for which the flip angle maps were acquired.

4.5 Compressed sensing for same-breath 3D ^{129}Xe ventilation imaging and ^{1}H anatomical imaging

The purpose of this section was to assess the applicability of compressed sensing for acceleration of ^{129}Xe 3D SSFP image acquisition, in order to reduce the required breath-hold duration for volumetric imaging of patients with lung disease, and to facilitate same-breath acquisition of ^{129}Xe ventilation images and ^{1}H anatomical images. Author contribution statement: this work was completed in collaboration with

106
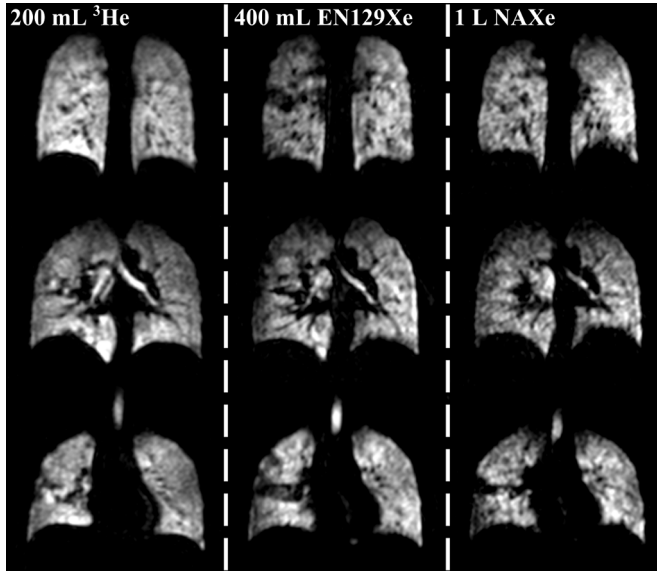
Figure 4.13: Comparative coronal MR image slices from a healthy smoker (HS) after inhalation of a) 200 mL hyperpolarised ^{3}He, b) 400 mL enriched xenon (86% hyperpolarised ^{129}Xe) and c) 1 L naturally-abundant xenon (26% hyperpolarised ^{129}Xe), acquired at 1.5 T using an optimised 3D SSFP sequence. The mean SNR of ^{3}He, EN^{129}Xe and NAXe images attained from this subject was 41 ± 8, 36 ± 4 and 31 ± 5, respectively. Slice locations were not perfectly identical due to the fact that the three scans were not performed in a single session (see Section 4.4.1).
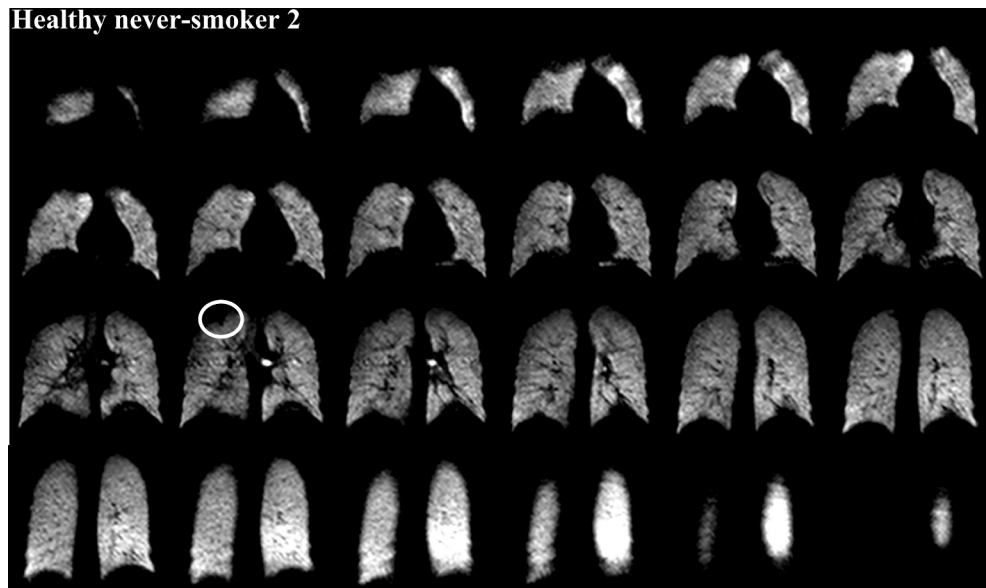
Figure 4.14: 3D SSFP data-set from a healthy never-smoker subject (HN2), acquired using 1 L of naturally-abundant xenon at 3 T. The average SNR over all acquired slices was 40 ± 10. The white oval indicates a small "ventilation abnormality" that was identified for this subject, which is believed to be present due to a bifid rib, rather than impaired ventilation function.

Guilhem Collier, who performed all CS simulations, and contributed to all stages of study design, data acquisition and analysis.

4.5.1 Theoretical background

Image compression algorithms rely on the fact that images contain a considerable amount of redundant information that can be removed in order to minimise the file size of the image whilst preserving image quality and features. Compressed sensing (CS) has been developed as a means to acquire *only* the necessary (non-redundant) information and reconstruct signals from data that would otherwise remain from
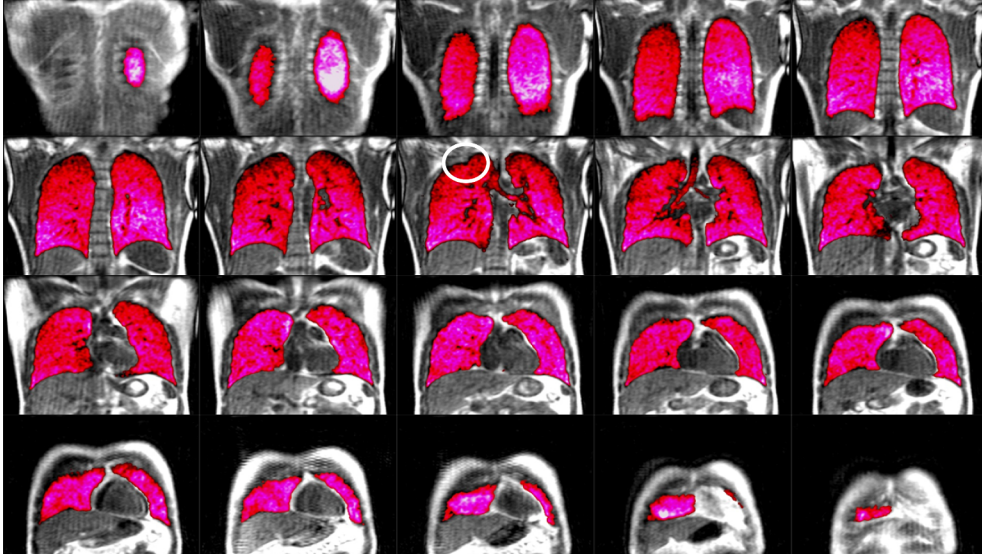
Figure 4.15: Example images from same-breath proton and naturally-abundant xenon MR acquisition for a healthy never-smoker (HN2) at 1.5 T. NAXe ventilation images (magenta) are overlaid directly on ^{1}H (greyscale) structural images; no image registration was performed. The mean SNR of the NAXe ventilation images was 26 ± 6. The white oval indicates a bifid rib, which is clearly confirmed by the ^{1}H image as a structural abnormality in the thorax, external to the lung itself.

the compression process [275, 276]. The CS approach has been adapted for MRI applications by exploiting the intrinsic sparsity of MR images [277]. CS implementation requires that three fundamental conditions be fulfilled: (i) the target image must be sparse / compressible (i.e. should have a large number of zero coefficients) in a given "transform domain"; (ii) data must be undersampled in a random, variable density manner in order to ensure that artefacts in the transform domain are incoherent ("noise-like") whilst preserving the energy distribution of MR images in k-space; (iii) reconstruction must be performed by a non-linear method, in order to ensure both sparsity of the image, and consistency between reconstructed and acquired data. The first condition is intrinsically satisfied in MRI, and the second condition can be implemented by careful choice of undersampling patterns as illustrated in Figure 4.16. Hence, randomly undersampled images can be reconstructed by solving the following non-linear optimisation:

$$\underset{I}{\mathrm{argmin}} \left\{ \|F_u I - y\|_{l_2}^2 + \lambda \|\psi I\|_{l_1} + \lambda_{TV} TV(I) \right\} \tag{4.12}$$

where: F_u is the undersampled Fourier transform (i.e. the Fourier transform evaluated at only the spatial frequencies defined by the undersampling pattern); I is the image to be reconstructed; y is the acquired undersampled data; ψ is the sparsifying transform that translates the original data to the chosen sparse transform domain; λ and λ_{TV} are regularisation parameters that weight the optimisation in order to balance sparsity and data consistency. TV represents the total variation, which is the sum (l_1 norm) of the variations between neighbouring pixels over the image, and aids the reconstruction process by imposing sparsity in finite differences simultaneously to sparsity in the transform domain. The l_p norm is defined as:

$$\|x\|_{l_p} = \sqrt[p]{\sum_i |x_i|^p} \quad \text{where} \quad p \in \mathbb{R} \tag{4.13}$$

Hyperpolarised gas MR images are intrinsically sparse, and CS-based approaches have been tailored for hyperpolarised gas applications in order to reduce acquisition times and facilitate the attainment of multiple aspects of pulmonary function within a single breath-hold; for example, to enable high resolution ventilation imaging and apparent diffusion coefficient (ADC) mapping with [3]He [278] and multiple-interleaved acquisition of [3]He ADC maps, B_1 maps and T_2^* maps in a single breath-hold [279]. Recently, same-breath acquisition of isotropic resolution 3D SSFP [3]He images and anatomical ^{1}H data-sets has been demonstrated using compressed sensing [280]. In addition, a CS-based technique has been implemented to permit phase contrast velocimetry MRI of the upper airways in order to quantify [3]He and [129]Xe gas flow during free breathing [131].

4.5.2 Methodology and preliminary results

In order to simulate the effects of random undersampling and compressed sensing reconstruction, a fully-sampled EN[129]Xe 3D SSFP data-set was acquired from a healthy smoker using sequence parameters slightly modified from the 3D SSFP implementation described in Section 4.4.1. The number of phase encodes in the z direction was increased from 24 to 32, in order to improve the reliability of random undersampling in that dimension. Correspondingly, the pixel dimension in the z direction was reduced to 7.5 mm, such that the voxel resolution was $4.2 \times 4.2 \times 7.5$ mm^3 in three dimensions. Additional sequence parameters were as follows: FOV and flip angle as in Section 4.4.1; phase FOV, 0.8; $TE/TR = 3.6/7.9$ ms; bandwidth, ± 8 kHz; breath-hold, 18 sec. The subject exhaled to functional residual capacity and inhaled a gas mixture of 500 mL EN[129]Xe and 500 mL N$_2$ from a 1 L Tedlar bag prior to image acquisition.
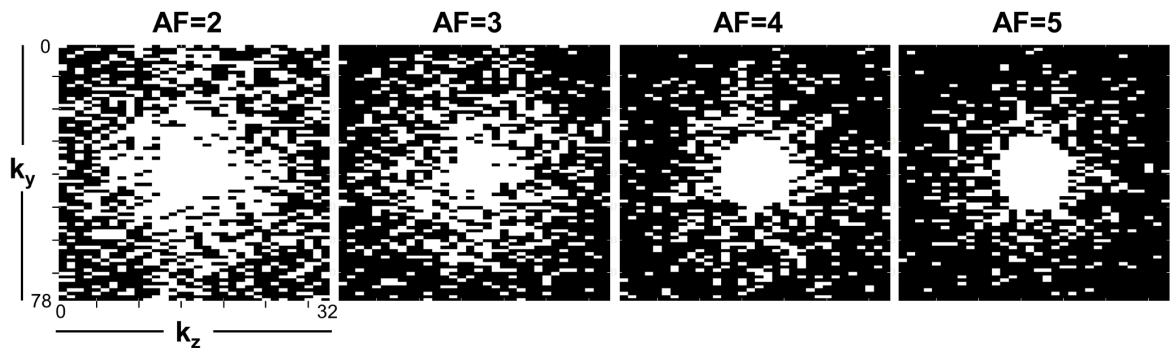
Figure 4.16: Undersampling patterns for 3D SSFP compressed sensing acquisition with [129]Xe, for acceleration factors (AF) of between 2 and 5. (White pixel: data-point will be acquired; dark pixel: data-point will not be acquired.)

"Undersampling patterns" were generated by selecting points, in a pseudo-random fashion, in the y and z phase encoding directions that should not be acquired, whilst ensuring that the central region of k-space was not severely undersampled as to compromise consistency of undersampled and fully-sampled data. This so-called variable density random undersampling was implemented by employing a sampling density

that scales as a power law with the distance of each pixel from the k-space origin [v].

Figure 4.16 depicts optimised sampling patterns for different acceleration factors (AF) between 2 and 5, indicating the factor by which the total number of phase encodes to be acquired is reduced (or equivalently, the factor by which the total scan time is shortened). As illustrated in Figure 4.16, increasing the degree of undersampling leads to the acquisition of significantly fewer high spatial frequency components (or correspondingly, less acquired k-space points near the periphery of k-space), whilst almost all low frequency components (data-points in the central regions of k-space) would still be acquired.
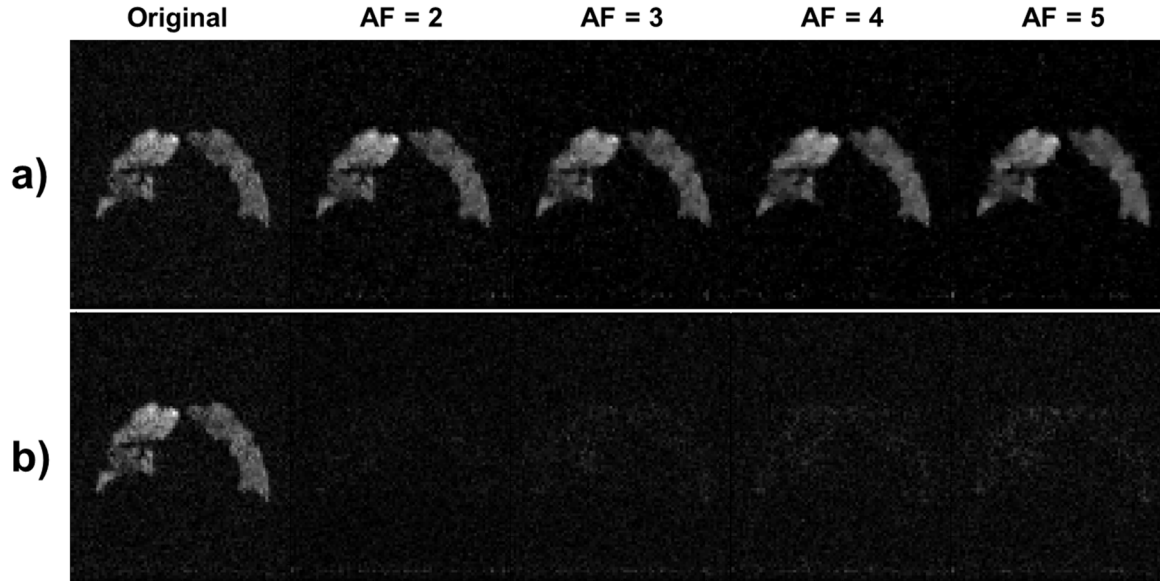
Figure 4.17: a) Representative slice from CS-reconstructed images obtained from retrospective undersampling of the k-space of the original fully-sampled data-set, using the sampling patterns depicted in Figure 4.16, for acceleration factors (AF) of between 2 and 5. b) Difference images representing the pixel intensity difference between the original image and each of the simulated CS-reconstructed images (for AF = 2 to 5; first panel of b) shows the original image).

The k-space of the acquired fully-sampled data-set was retrospectively undersampled in order to simulate the effects of the undersampling patterns. For each designed pattern, retrospectively-undersampled images were reconstructed using the non-linear optimisation in Equation 4.12. Figure 4.17 shows an example slice from the original fully-sampled data-set (reconstructed by the conventional discrete Fourier transform), and the equivalent slice reconstructed from retrospectively-undersampled images at each acceleration factor between 2 and 5, for the optimum sampling patterns shown in Figure 4.16. The effect of the CS reconstruction was noticeable as additional blurring and smoothing of small details in the images, which intensified with increasing AF.

In order to quantify the differences between the original images and the CS-reconstructions of the retrospectively-undersampled k-spaces, the mean absolute error (MAE) metric was evaluated on a pixel-by-pixel basis for a region of interest covering the full lungs.

---

[v]Undersampling patterns were generated for a number of different parameters by varying the order of the power law and also the effective radius of the central disk of fully-sampled points in k-space. For each case, a number of randomly-ordered patterns were generated, and the closest representation of a truly random pattern was used in subsequent simulations.

$$MAE = \frac{\sum_{j=1}^{N_y} \sum_{k=1}^{N_z} |CS_{j,k} - FS_{j,k}|}{N_y N_z} \qquad (4.14)$$

where CS and FS denote CS-reconstructed and original (fully-sampled) images, respectively, and N_y and N_z are the number of phase encodes in the y and z directions, respectively. MAE analysis was performed for all generated undersampling patterns, and the optimum patterns (displayed in Figure 4.16) were chosen as those which provided the minimum MAE value. The MAE for the chosen undersampling patterns is plotted as a function of AF in Figure 4.18. The MAE is 0 by definition for the fully-sampled image, and was observed to steadily increase with AF, appearing to approach a plateau value at the highest AF values.
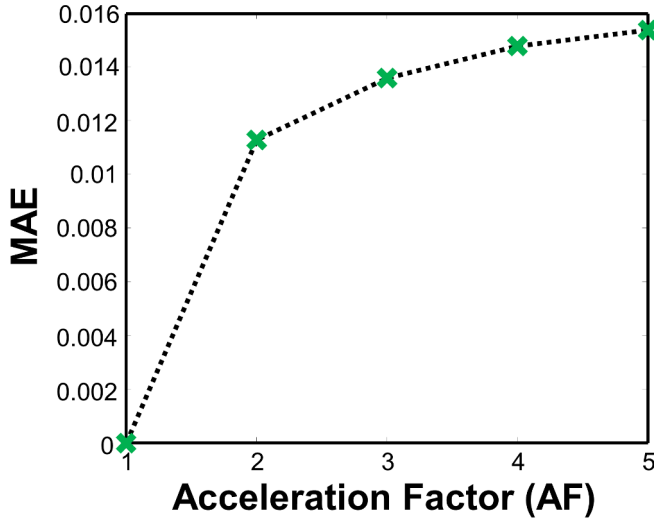
Figure 4.18: Mean absolute error (MAE) as a function of acceleration factor (AF) for CS simulations of the fully-sampled ^{129}Xe 3D SSFP acquisition, as shown in Figure 4.17.

Considering the data presented in Figures 4.17 and 4.18, an acceleration factor of 3 was chosen as a suitable compromise for CS-based acquisitions; affording a significant reduction in scan time whilst preserving the major details of the image, and adding only an acceptably low level of blurring during the reconstruction process. The associated AF = 3 undersampling pattern was employed to obtain prospective CS 3D SSFP data-sets in two healthy subjects (one healthy smoker, HS, as above; one healthy never-smoker, male, 45 years, HN3). Sequence parameters were equivalent to those of the fully-sampled acquisition, except: the flip angle was increased to 11° (the optimum value resulting from SSFP signal simulations, reflecting the 3-fold reduction in number of RF pulses); breath-hold time was reduced to 6 sec; EN^{129}Xe volume, 600 mL (mixed with 400 mL nitrogen).

Reconstructed undersampled images were of a good quality, with high SNR and no significant identifiable losses in image details due to excessive blurring. The complete CS-reconstructed data-set from HN3 is shown in Figure 4.19.
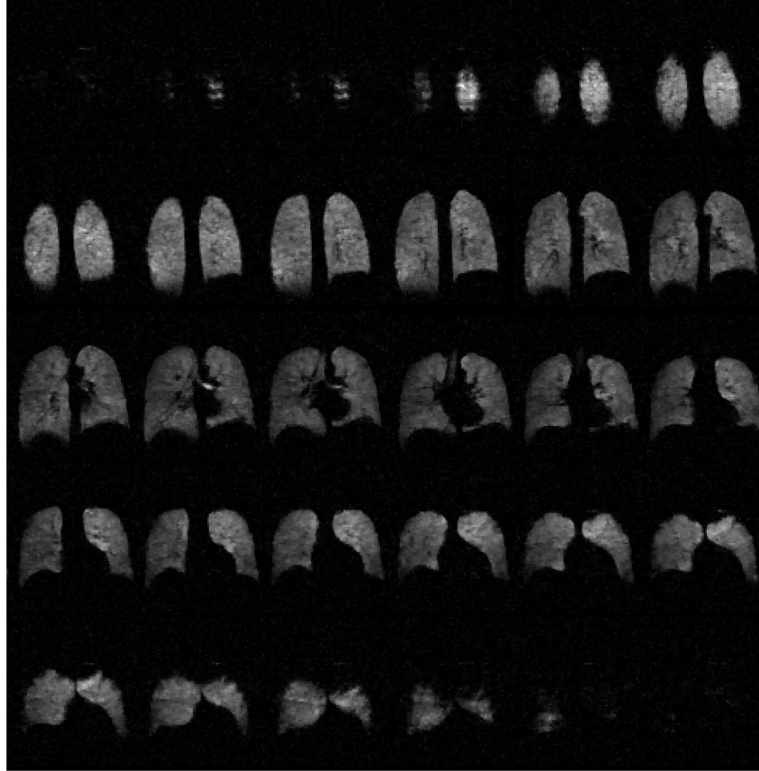
Figure 4.19: Prospective CS data-set obtained using 3D SSFP with 600 mL EN^{129}Xe in a healthy subject (HN3). Acceleration factor = 3; voxel size = $4.2 \times 4.2 \times 7.5$ mm^3, the latter corresponding to the anterior-posterior dimension.

4.6 Discussion & Conclusions

3D SSFP simulations

This work highlights the benefits of 3D SSFP-based acquisition strategies for full-lung coverage, high quality lung ventilation imaging with hyperpolarised ^{129}Xe. The ideal bandwidth and flip angle settings for a target resolution of $4.2 \times 4.2 \times 10$ mm^3 at 1.5 T have been derived by comparing in vivo measured and numerically-simulated k-space filters in order to estimate the $T_{2,CPMG}$ of ^{129}Xe at 1.5 T. Both global and regional simulations, the latter utilising the measured spatial flip angle maps of a flexible transmit-receive vest coil, have demonstrated that 3D SSFP approaches are robust to imperfect calibration of RF excitation flip angle, and minor variations in the flip angle across the lungs, respectively.

The constraints imposed on 3D SSFP imaging by off-resonance and associated banding artefacts have been explored by numerical simulations of the SNR on a global and regional basis, the latter using B_0 maps measured for ^{129}Xe in the lungs. Regions of high off-resonance frequency, and associated banding artefacts, have been observed to be localised to the diaphragm region. Recognition of these artefacts may be improved in future by communicating their prevalence and typical appearance to the image analyst. Unlike the excitation flip angle, it is crucial to ensure that the transmit/receive frequency is carefully calibrated to be equivalent to the Larmor frequency of ^{129}Xe in the lungs of each subject to be scanned; it has been shown here that poor images may result if this condition is not precisely met.

The simulation strategies developed in this work permit the "correction" of 3D SSFP signal intensity using B_1 and B_0 maps. Same-breath acquisition of B_1 and B_0 maps is feasible within a single breath-hold using interleaved sequences, which can be accelerated by the implementation of techniques such as compressed sensing [279]. In future work, it may be feasible to obtain B_1 and B_0 maps in a separate breath to 3D SSFP images, simulate the expected SNR from these maps, and then retrospectively correct the signal distribution of the 3D SSFP data-set. This method would intrinsically account for flip angle and off-resonance frequency variations across the lungs and result in an image weighted predominantly by the ^{129}Xe gas distribution (i.e. ventilation), however would be limited by the accuracy of the image registration techniques used to compare and analyse the separate-breath images.

Since the publication of the paper regarding some of the preliminary work described here, an additional factor associated with the simulation procedure has been identified. The current simulation strategy fundamentally assumes that the SSFP sequence is fully balanced and that the generated echo is positioned in the centre of the acquisition window. Although the gradients employed in Sections 4.3 and 4.4 were balanced such that the total gradient area along each axis was zero, a minimum TE, asymmetric read-out echo was used to enable the shortest possible scan time. As introduced in Section 3.2.5, the SSFP MR signal is governed by T_2 (with little T_2^* contribution) *only* if the echo is positioned at the centre of the acquisition window; i.e. the use of an asymmetric echo leads to some weighting according to T_2^* [vi].

The effect of employing a symmetric echo as opposed to an asymmetric echo is presently under investigation, in order to evaluate the possibility of further improving the image quality with the use of a perfectly symmetric echo, and to determine to what extent our estimate of $T_{2,CPMG}$ is affected by dephasing due to background B_0 inhomogeneity. As a preliminary experiment, following the procedures described in Section 4.3.2, k-space filters were acquired from the lungs of a healthy smoker in vivo using a modified 3D SSFP sequence with an asymmetric echo ($TE = 2.1$ ms) and a symmetric echo ($TE = 3.6$ ms) (other parameters: 8 kHz bandwidth, 10° flip angle). The resulting k-space filters are depicted in Figure 4.20.
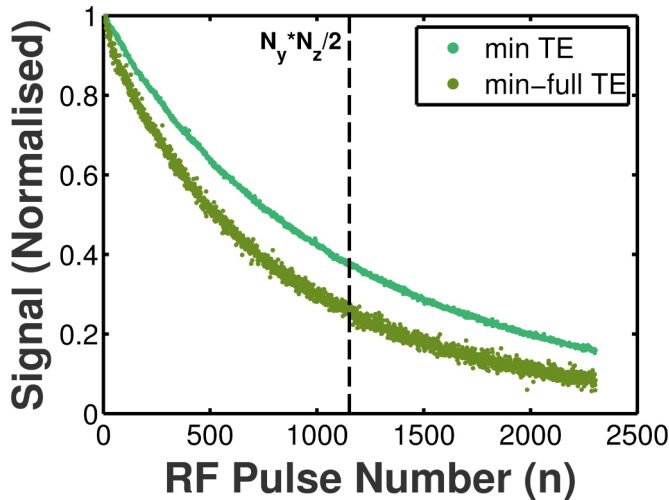
Figure 4.20: Measured k-space filters depicting the decay in longitudinal magnetisation, M_z, of hyperpolarised ^{129}Xe during 3D SSFP with asymmetric (min TE) and symmetric (min-full TE) echoes.

[vi]Nevertheless, in practice, for a spin ensemble in which random (Brownian) diffusion is present, magnetic field inhomogeneities will induce additional signal decay even for a symmetric echo, because the phase losses associated with the random diffusion of spins through an inhomogeneous field cannot be refocussed within the finite inter-echo time.

The observed difference in signal decay behaviour between the two echo types is non-negligible, but appears to be less than the differences seen between bandwidth settings (as shown in Figure 4.3). Therefore, from Figure 4.4, it can be concluded that the difference in optimum flip angle and achievable SNR associated with using symmetric versus asymmetric echoes is relatively minor. Nevertheless, in future work, the simulations presented in Figures 4.3 and 4.4 will be repeated for the case of a perfectly symmetric echo, in order to further investigate the achievable image SNR, and to derive a more accurate estimate of the intrinsic $T_{2,CPMG}$. This will be coupled with the employment of a variable flip angle 3D SSFP scheme for ^{129}Xe, as demonstrated previously in 2D with ^{3}He [266], in order to further improve image SNR and reduce blurring associated with k_y and k_z filtering.

3D SSFP imaging

With improved ^{129}Xe polarisations and pulse sequence optimisation procedures, we have demonstrated full-lung coverage MRI with naturally-abundant hyperpolarised xenon using 3D SSFP, of a similar quality to recent studies with EN^{129}Xe [86, 87, 281]. Scans were completed within a moderate breath-hold ($\leq$ 16 sec), with sufficient resolution ($4.2 \times 4.2 \times 8/10$ mm^3) to allow recognition of subtle abnormalities in pulmonary ventilation, comparable to those expected in early-stage lung disease. At 1.5 T, the mean 3D SSFP image SNR for NAXe was moderately variable between subjects, likely due to differences in lung size, completeness of exhalation to functional residual capacity (and residual oxygen content in the lungs [209]), and fluctuations in ^{129}Xe polarisation. Nevertheless, the SNR for any individual slice over all subjects was $\geq$ 18.5, which should be sufficient for radiological interpretation and automated segmentation. A minor ventilation defect in the right middle lobe of the healthy smoker's lungs was clearly depicted on both EN^{129}Xe and NAXe scans, although arguably less noticeable on ^{3}He images (Figure 4.13). This can be attributed to the different diffusion coefficients of the two gases; we note that Kirby et al. observed a higher ventilation defect percentage for ^{129}Xe than ^{3}He in subjects with chronic obstructive pulmonary disease [85]. Although the xenon diffusion coefficient will be partially increased in the presence of nitrogen, there is no current literature evidence that ^{129}Xe ventilation defect presentation is significantly altered by the concentration of xenon within the inhaled mixture. Despite accurate calibration of the ^{129}Xe Larmor frequency, slight banding artefacts associated with B_0 inhomogeneity were observed in $\leq$ 5 slices per subject, typically appearing as dark bands near the diaphragm. These artefacts were easily identified and did not inhibit the identification of true ventilation defects. Although the magnetic susceptibility and correspondingly B_0 inhomogeneity increases with field strength, there was no observation of more prominent banding at 3 T compared with 1.5 T.

NAXe MR is particularly promising at 3 T, wherein the increased SNR compared with 1.5 T — likely arising from a combination of differences in Larmor frequency, field inhomogeneity, coil sensitivity and the "system" (e.g. the transmission line and receiver noise figure) at the two field strengths — reflects previous observations with spoiled gradient echo imaging [251]. This SNR benefit, coupled with the possibility of using receiver array coils rather than standard transmit-receive designs as employed here, may facilitate NAXe lung imaging with 3D isotropic resolutions in future. In addition, the feasibility of same-breath ^{1}H and NAXe MRI is encouraging for obtaining complementary structure-function information from the lungs without necessitating multiple scans crossing different modalities. However, the breath-hold of $\sim$ 16

sec could be shortened for clinical purposes, e.g. via compressed sensing techniques, as introduced in Section 4.5.2.

Preliminary results of compressed sensing with EN^{129}Xe have demonstrated the feasibility of three-fold undersampling for high quality ^{129}Xe ventilation imaging in a breath-hold $\ll$ 10 sec, with superior resolution in the anterior-posterior direction compared with the NAXe and EN^{129}Xe images presented at 1.5 T in Section 4.4.2. Simulations of the undersampling effects and CS reconstruction, in combination with prospectively-acquired images in healthy volunteers, highlight the promise of rapid ventilation imaging in a clinically-achievable breath-hold with ^{129}Xe. Expected additional blurring introduced during the CS reconstruction was not easily noticed in images obtained at an acceleration factor of 3, and no other ancillary artefacts could be observed on prospectively-acquired undersampled images. The advancement of CS acquisition and reconstruction strategies is ongoing work; for example, current work focusses on the implementation of elliptical encoding with undersampling in the y and z phase encoding dimensions to enhance achievable image SNR and support the CS reconstruction process. These improvements should enable routine implementation of ^{129}Xe 3D SSFP with CS in clinical studies with same-breath ^{1}H scans to provide complementary anatomical information. Same-breath acquisition provides better-matched ^{1}H and hyperpolarised gas lung volumes than separate-breath acquisition [282], simplifying or mitigating image registration and improving the fidelity of quantitative assessment of ventilation defects, e.g. by calculation of ventilated volume.

Perspectives of NAXe MRI

The comparable SNR of lung images acquired with 200 mL ^{3}He, 400 mL EN^{129}Xe and 1 L NAXe is promising for more widespread viable diagnostic lung MRI with naturally-abundant xenon, or reduced doses of enriched xenon. Taking recent cost estimates provided to our group and others, the relative cost of gas for the scans in Figure 4.13 could range from approximately 6:2.5:1 to as high as 20:8:1 for ^{3}He, EN^{129}Xe and NAXe, respectively (assuming that ^{3}He is purchased under controlled release). For many groups the cost benefits of NAXe could be considerably greater; for example, recently, other institutions have delivered 300-400 mL of ^{3}He [86] or up to 1 L of EN^{129}Xe [87, 95] for lung imaging purposes, compared to the modest doses we have shown to be sufficient for high SNR, though the pulse sequences and attainable gas polarisations used in those studies differed from this study.

The implications of the achievable economic benefits with naturally-abundant xenon MRI are multi-fold: not only in the realisation of repeated screening of patients with lung disease, but also for longitudinal studies of disease progression and treatment efficacy. Although litre doses of NAXe may not be sufficient for performing techniques with a particularly high SNR requirement — such as dissolved ^{129}Xe MR spectroscopy [140] or chemical shift imaging [147] where T_2^* decay is rapid [249, 250] and available signal is severely constrained — one can envisage the potential of NAXe as the mainstay gas for future routine clinical ventilation imaging applications. Our findings are encouraging for NAXe fulfilling the requirements imposed by the increasingly limited availability of ^{3}He, and are timely and relevant to the hyperpolarised gas MRI field as a whole. In particular, NAXe should provide an inexpensive testing platform for development of hyperpolarised gas MR methods and offer additional opportunities for exposure of these techniques to the wider clinical audience.

In addition, further technological developments are permitting the production of hyperpolarised ^{129}Xe in large concentrations for "on-demand" delivery [65, 283]. Although this polarisation technology is currently only in-place at a few sites globally, the advent of lower-cost polarisers utilising high power lasers [64] is likely to attract attention from lung clinicians and MR scientists and promote increased application of hyperpolarised ^{129}Xe MRI. Indeed, our group in Sheffield is now undertaking clinical radiology referrals for diagnostic hyperpolarised gas imaging with ^{3}He and ^{129}Xe, made feasible in part due to the technical advancements and economic benefits demonstrated in this work.

Conclusions

In this work, the potential of high quality clinical imaging of pulmonary ventilation with naturally-abundant and enriched ^{129}Xe at both of the clinically-relevant MRI field strengths (1.5 T and 3 T) has been demonstrated.

3D steady-state acquisition strategies have been optimised for full-lung coverage ventilation imaging with ^{129}Xe by simulating the SNR for different combinations of sequence parameters and accounting for the B_1 and B_0 distributions across the thorax. These results should improve the distinction of banding artefacts and true ventilation abnormalities in ^{129}Xe ventilation images, and may permit the correction of the signal distribution of acquired 3D SSFP images in future.

By exploiting these optimisations in pulse sequence acquisition strategy, in combination with recent advances in polarisation technology, high quality lung MR images with litre quantities of inhaled NAXe gas have been acquired using standard transmit-receive RF coil designs, with no loss of functional information compared to hyperpolarised ^{3}He MRI. At a fraction of the cost per scan of ^{3}He, commercially-realistic diagnostic, longitudinal and treatment efficacy studies may now be envisaged.

Furthermore, the applicability of compressed sensing reconstruction techniques for rapid undersampled acquisition of ^{129}Xe ventilation images should expedite the routine attainment of co-registered functional and structural information via facilitating same-breath hyperpolarised gas and proton MR imaging. Continued improvements in this field should allow ^{129}Xe to fill the gaps imposed by the decline in availability of ^{3}He.

Chapter 5

Comparison of ^{3}He and ^{129}Xe MRI for evaluation of lung microstructure and ventilation at 1.5 T

5.1 Introduction

To date, a large proportion of hyperpolarised gas lung MRI methodological development studies and clinically-relevant patient examinations have been performed using ^{3}He gas. Despite this, recent years have seen an upsurge in the application of ^{129}Xe for lung MRI [284], encouraging an increased number of patient studies of both lung ventilation [85, 87, 89, 95] and microstructure [115, 116] with this naturally-abundant isotope. The resurgence in the use of ^{129}Xe for lung imaging purposes is attributable to both the decline in availability and consequentially rising cost of ^{3}He [84], and developments in the field of gas polarisation technology [63–65], which are helping to bridge the gap in image quality imposed by the difference in gyromagnetic ratio between ^{129}Xe and ^{3}He and its contribution to image SNR.

In the past few years, a number of comparative studies of the relative sensitivity of ^{3}He and ^{129}Xe methods for assessment of lung ventilation function and microstructural changes have been reported — particularly by the group at Robarts Research Institute — in healthy subjects and patients with chronic obstructive pulmonary disease [85, 88], asthma [86] and former smokers [116]. Generally, pulmonary ventilation and microstructural information of similar quality and equivalent pathological significance has been obtained from MRI of the two nuclei. In addition, small animal studies have been performed to evaluate quantitative measurements of ventilated lung volume with ^{3}He and ^{129}Xe [285], and to compare apparent diffusion coefficient measurements derived from both nuclei to histological results [286], with promising results in both cases for the use of ^{129}Xe as an alternative to ^{3}He.

To date, studies comparing ^{3}He and ^{129}Xe ventilation and diffusion-weighted MRI of the lungs in humans have been carried out at the field strength of 3 T (by the Robarts group). As such, possible differences in the implementation of, and quantitative information resulting from, these methods at the more clinically-relevant field strength of 1.5 T have not been examined.

In previous work, the most often presented quantitative metric of hyperpolarised gas ventilation imaging has been the ventilation volume percentage (VV%), or conversely, the ventilation defect percentage (VDP), which represents the total percentage of the lung volume that is ventilated by the hyperpolarised gas, or the volume that is not ventilated, respectively. The ^{3}He VV% metric has been demonstrated to be highly reproducible at 3 T in COPD patients [74, 287], although the one-week variability was found to be considerably higher than the same-day reproducibility. Additionally, good same-day reproducibility in ^{3}He VV% has been reported in a potentially challenging population of paediatric cystic fibrosis patients [288], whilst preliminary evidence has suggested that one-week changes in pulmonary function in adult

CF patients could be identified by the high precision of ^{3}He VDP compared with PFT results [289]. Moreover, the results of a multiple-site study of ventilation defect prevalence in subjects with exercise-induced bronchoconstriction are promising for translation of hyperpolarised ^{3}He ventilation imaging to a wider clinical audience [290].

However, the same-day or week-to-week variability in quantitative measurements of lung ventilation volume or defect prevalence derived from ^{129}Xe MRI has not been determined. Driehuys et al. [95] and Shukla et al. [96] have both reported the successful delivery of multiple doses of ^{129}Xe for ventilation imaging on the same day or on repeated days to subjects with a variety of pulmonary conditions, however, the purpose of those studies was to assess the safety and tolerability of repeated ^{129}Xe MRI, and as such, quantitative evaluation of lung ventilation and its reproducibility was not achieved.

In a similar manner to the VV% or VDP indices, clinical hyperpolarised gas diffusion-weighted MRI studies to date have typically reported the global mean ^{3}He or ^{129}Xe ADC value as a biomarker of overall change in lung microstructure due to disease. Comprehensive investigations of the same-session [291] and multiple-day [292] reproducibility of derived global mean ^{3}He ADC values have revealed a high intra-individual reproducibility in healthy subjects and patients with emphysema, and in addition, an acute sensitivity of ^{3}He ADC to changes in lung volume. Furthermore, investigations at 3 T have highlighted a superior reproducibility of ^{3}He ADC values when compared to VDP values in patients with COPD [74, 287].

To the best of our knowledge, same- or multiple-day variability in ^{129}Xe ADC measurements has not been adequately assessed in healthy subjects or patient cohorts. Furthermore, to date, comparisons of ^{3}He and ^{129}Xe ventilation imaging and ADC mapping in humans have been limited to single session scan results with no ^{129}Xe reproducibility data available. Thus, the relative sensitivity of the two gases to pulmonary functional changes probed by the two different techniques has not been fully explored.

The purpose of this chapter is to evaluate the sensitivity and reproducibility of ^{129}Xe quantitative ventilation imaging and ADC mapping MRI of the lungs relative to ^{3}He-based methods. This work presents the results of a study at 1.5 T in which ^{3}He and ^{129}Xe MR images of lung ventilation were obtained from patients with lung cancer and COPD, and ADC mapping with both nuclei was performed in healthy volunteers and COPD patients. The multiple time-point reproducibility of the derived ^{3}He and ^{129}Xe ventilation volume percentages and global mean ADC values is assessed in comparison to the same-day and weekly variability of pulmonary function test results in COPD patients. Thus, the potential for ^{129}Xe fulfilling the role of ^{3}He as a clinically scalable inhaled contrast agent for functional and structural assessment of the lungs is discussed.

Although the contents of this chapter have not been prepared as a manuscript, preliminary results have been published in the form of a conference abstract (see Section 11.1), and it is planned that a publication based on this chapter will be written in the near future. The co-authors of this chapter are: HF. Chan, P. J. C. Hughes, G. J. Collier, F. C. Horn, G. Norquay, J. Parra-Robles, D. P. Yates, P. Collini, R. Lawson, H. Marshall, and J. M. Wild. Author contributions statement: study design, DPY, PC, RL, HM, JMW; acquisition of data, NJS, HFC, PJCH, GJC, FCH, GN, JPR, HM; analysis of data, NJS, HFC, PJCH, GJC, JPR; drafting of chapter, NJS, JMW.

5.2 Methods

Ten healthy volunteers with no history of smoking or respiratory disorders (6 male, 4 female; mean age $= 42 \pm 4$ years), five patients with COPD (2 male, 3 female; mean age $= 67 \pm 7$ years), and six patients with non-small cell lung cancer (2 male, 4 female; mean age $= 69 \pm 6$ years) were recruited for this study, which was approved by the National Research Ethics Committee. Patient characteristics and pulmonary function test results are summarised in Table 5.1. Subjects with a resting oxygen saturation of $< 90\%$, unstable cardiac disease, or — in the case of lung cancer patients — co-morbid conditions that precluded radiotherapy treatment, were excluded from the recruitment process.

All subjects underwent MRI at 1.5 T (GE HDx, GE Healthcare, Milwaukee, WI). Flexible radiofrequency coils were employed for transmission and reception of MR signals at the Larmor frequencies of ^{3}He and ^{129}Xe, as described in the previous chapter (see Section 4.4.1). Similarly, identical procedures to those outlined in Section 4.4.1 were used for spin-exchange optical pumping of the two gases. In the case of both nuclei, the polarisation achieved prior to inhalation of the gas dose was $\sim 25\%$.

Demographics		PFT Parameters					
Patient	Age (Sex)	FEV_1 (%-pred)	CV (%)	FEV_1/FVC (%-pred)	CV (%)	TL_{CO} (%-pred)	CV (%)
HV1	49 (M)	94	—	78.5	—	102	—
HV2	36 (F)	98	—	82.3	—	—†	—
HV3	43 (M)	103	—	79.45	—	85	—
HV4	51 (M)	106	—	77.97	—	—†	—
HV5	43 (M)	107	—	79.49	—	102	—
HV6	48 (F)	123	—	80.01	—	110	—
HV7	42 (M)	111	—	79.61	—	103	—
HV8	44 (F)	98	—	80.75	—	67	—
HV9	32 (F)	89	—	82.94	—	72	—
HV10	35 (M)	107	—	80.91	—	101	—
LC1	68 (F)	—	—	—	—	—	—
LC2	76 (M)	—	—	—	—	—	—
LC3	62 (M)	—	—	—	—	—	—
LC4	72 (F)	—	—	—	—	—	—
LC5	72 (F)	—	—	—	—	—	—
LC6	62 (F)	—	—	—	—	—	—
COPD1	64 (F)	31.5 ± 0.7	2	33.2 ± 0.6	2	33.2 ± 2.1	6
COPD2	67 (F)	45.4 ± 1.6	4	49.8 ± 0.7	1	98.4 ± 3.8	4
COPD3	71 (M)	31.0 ± 1.3	4	27.6 ± 1.1	4	13.6 ± 2.2	16
COPD4	76 (M)	43.5 ± 2.1	5	32.5 ± 0.8	3	29.6 ± 2.0	7
COPD5	59 (F)	38.6 ± 2.5	6	42.8 ± 0.8	2	38.0 ± 4.1	11

Table 5.1: Patient demographics and pulmonary function test (PFT) results for the ^{3}He-^{129}Xe VV% and ADC comparison study. HV: healthy volunteer; LC: lung cancer patient; COPD: chronic obstructive pulmonary disease patient. FEV_1 = forced expiratory volume in one second; FVC = forced vital capacity; TL_{CO} = diffusing capacity of carbon monoxide; CV = coefficient of variation (i.e. the ratio of the standard deviation to the mean of repeated measurements, expressed as a percentage); %-pred = PFTs expressed as a percentage of a predicted value, based on the subject's age, height, and other demographic factors. †: TL_{CO} data was unavailable from two subjects of the healthy volunteer cohort.

Patients with lung cancer and COPD underwent 3D steady-state free precession (SSFP) imaging of lung ventilation at breath-hold with both ^{3}He and ^{129}Xe. ^{1}H images of the thorax were acquired for anatomical reference and lung volumetry in the same-breath as ^{3}He scans, and in a separate breath-hold to ^{129}Xe scans. Ventilation volume percentages (VV%) were calculated from the resulting hyperpolarised gas and corresponding ^{1}H anatomical images as described previously [282].

Immediately prior to 3D SSFP imaging, the Larmor frequencies of ^{3}He or ^{129}Xe were calibrated in the lungs of each subject, in order to minimise off-resonance effects associated with the steady-state pulse sequence. As outlined in Section 4.4.1, a small dose of either ^{3}He or ^{129}Xe was mixed with medical grade nitrogen and inhaled by the subject, and the Larmor frequency in the lungs of the subject was calibrated from a high resolution spectral acquisition. Unlike in Section 4.4.1, calculation of the RF excitation flip angle setting by NMR was not required; the flip angle for each nucleus was derived from the patient's weight based on look-up plots of RF power values obtained from previous subjects shown in Figure 5.1.
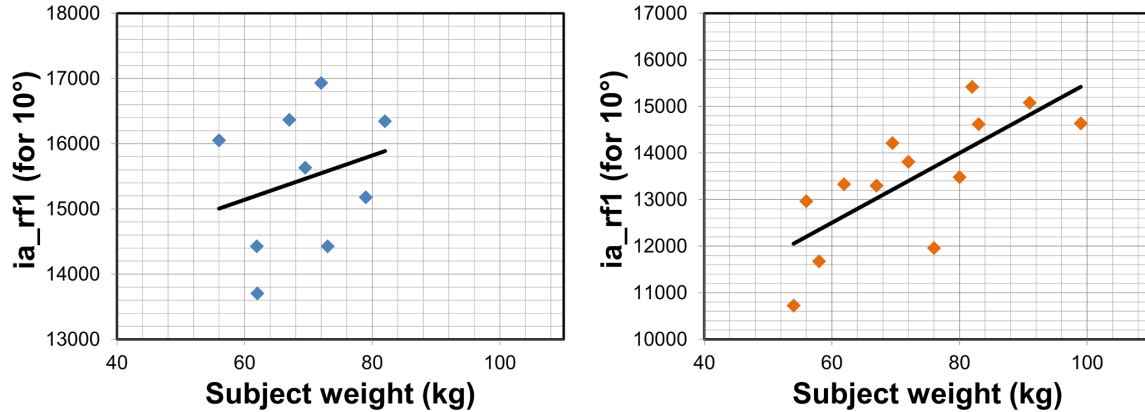
Figure 5.1: Calibration graphs for estimating the instruction amplitude (ia_rf1) required for achieving a 10° flip angle for 3D SSFP ventilation imaging with ^{129}Xe (left) and ^{3}He (right) from the patient's weight. The instruction amplitude is a GE scanner operator parameter that, to a good approximation, scales linearly with the excitation flip angle induced by the coil.

3D SSFP sequence parameters were similar to those detailed in [282] and [89] for ^{3}He and ^{129}Xe, respectively. For ^{3}He: field-of-view (FOV), 40 cm; phase FOV, 0.8; $\approx$ 48 effective coronal slices with no gap; in-plane matrix, 100×100 (4.0 mm pixel dimension); effective slice thickness, 5 mm in the anterior-posterior direction; flip angle, 9°; hard RF pulse; $TE/TR = 0.6/1.9$ ms; bandwidth, ± 83.3 kHz; breath-hold, 9 sec. Each subject exhaled to functional residual capacity and inhaled a mixture of 200 mL ^{3}He gas and 800 mL N_2 from a 1 L Tedlar bag prior to image acquisition.

For ^{129}Xe, sequence parameters were comparable to those described in Section 4.4.1: FOV, 40 cm; phase FOV, 0.8; $\approx$ 24 effective coronal slices with no gap; in-plane matrix, 100×100 (4.0 mm pixel dimension); effective slice thickness, 10 mm in the anterior-posterior direction; flip angle, 9°; hard RF pulse; $TE/TR = 2.2/6.7$ ms; bandwidth, ± 8 kHz; breath-hold, 14 sec. Each subject exhaled to functional residual capacity and inhaled a mixture of 600 mL of EN^{129}Xe gas and 400 mL N_2 from a 1 L Tedlar bag prior to image acquisition. Note: the ^{129}Xe polariser apparatus used was the "upgraded" system described in Section 4.4.1.

In both cases, ^{1}H anatomical images were designed to have exactly the same positioning and resolution
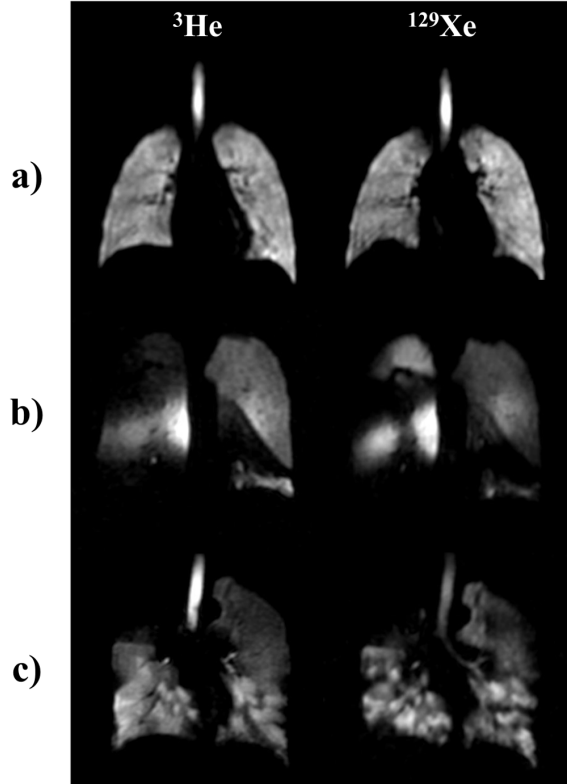
Figure 5.2: Representative ^{3}He and ^{129}Xe MR ventilation images of the lungs of a healthy never-smoker (a), a patient with COPD (b) and a patient with lung cancer (c). The slice thickness and in-plane resolution for the ^{3}He and ^{129}Xe acquisitions in a) was identical, whilst ^{3}He images in b) and c) were acquired with half the slice thickness of the ^{129}Xe images (see body text).

as the matching hyperpolarised gas images in three dimensions, but with a phase FOV of 1.0, and the following prescription: 3D spoiled gradient echo sequence; $TE/TR = 0.6/1.9$ ms; bandwidth, ± 83.3 kHz; flip angle $= 5°$. Example ^{3}He and ^{129}Xe images from the two patient cohorts are shown in Figure 5.2, along with images previously obtained from a healthy subject for visual comparison.

Healthy volunteers and COPD patients underwent multi-slice 2D ^{3}He and ^{129}Xe diffusion-weighted lung MRI. Maps of the apparent diffusion coefficient (ADC) of each gas in the lungs were generated by evaluating the mono-exponential diffusion-weighted signal equation (Equation 3.114) on a pixel-wise basis, using the pixel intensities from the first two interleaves of a multiple b-value acquisition.

2D spoiled gradient echo pulse sequences with diffusion weighting on the z (slice) axis were employed in both cases. Parameters for ^{3}He acquisitions were comparable to those described in [293]: FOV, 40 cm; phase FOV, 0.75; 5 coronal slices with thickness, 15 mm and inter-slice gap, 10 mm; in-plane matrix, 64×64 (6.25 mm pixel dimension); flip angle, $4.8°$; sinc RF pulse; $TE/TR = 4.8/10.0$ ms; bandwidth, ± 31.25 kHz; breath-hold, 16 sec. Diffusion weighting was applied using bi-polar gradient waveforms as follows: diffusion time $\Delta = 1.6$ ms, ramp time $\tau = 0.3$ ms, plateau time $\delta = 1.0$ ms (see Figure 3.28); separation of lobes $= 0$ ms; number of diffusion-weighted interleaves, 6; maximum gradient amplitude, 31.6 mT.m^{-1}; first two interleaves, $b = 0$ and $b = 1.6$ s.cm^{-2}. Each subject exhaled to functional residual capacity and inhaled a mixture of 300 mL ^{3}He gas and 700 mL N$_2$ from a 1 L Tedlar bag prior to image acquisition.

^{129}Xe scans were performed with equivalent FOV, slice thickness and slice gap, but one less slice was
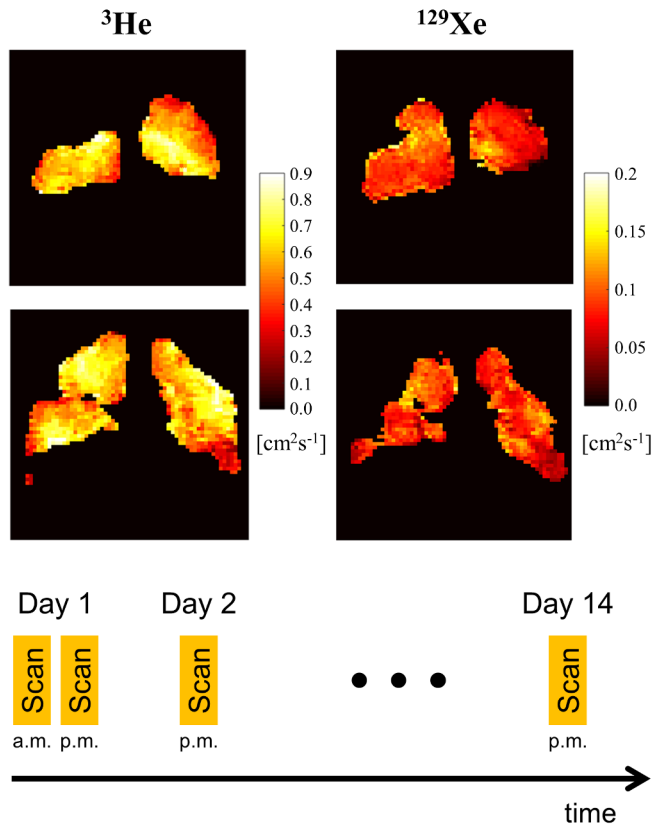
Figure 5.3: Representative example ^{3}He and ^{129}Xe single slice ADC maps obtained from a COPD patient. The slice thickness and slice gap for the ^{3}He and ^{129}Xe ADC acquisitions was equivalent, but the in-plane phase-encoding pixel dimension of the two acquisitions was slightly different (see main body text).
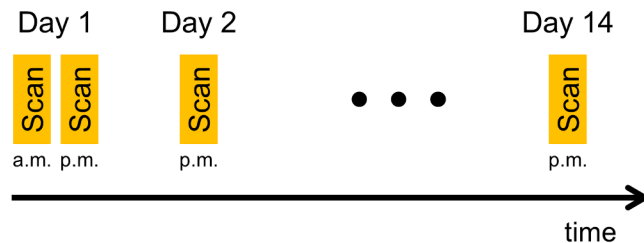
Figure 5.4: Scan schedule for assessment of reproducibility of ^{3}He and ^{129}Xe MR-derived VV% and ADC values. Two scans were performed on the first day, one on the second day, and one two weeks after the first scan date.

acquired overall (totally 4 slices), other parameters were as follows: in-plane matrix, 64×48 (6.25×8.33 mm^2 pixel dimensions); flip angle, 6.7°; sinc RF pulse; $TE/TR = 12.5/27.0$ ms; bandwidth, ± 2 kHz; breath-hold, 16 sec. In order to achieve approximately equivalent diffusion weighting as for ^{3}He within a reasonable breath-hold (i.e. a similar degree of signal attenuation), bi-polar gradient waveforms were applied as follows: diffusion time $\Delta = 5.0$ ms (ramp time $\tau = 0.3$ ms, plateau time $= 3.0$ ms); separation of lobes $= 1.4$ ms; number of diffusion-weighted interleaves, 4; maximum gradient amplitude, 32.2 mT.m^{-1}; first two interleaves, $b = 0$ and $b = 8.0$ s.cm^{-2}. Each subject exhaled to functional residual capacity and inhaled a mixture of 600 mL ^{129}Xe gas and 400 mL N$_2$ from a 1 L Tedlar bag prior to image acquisition.

Examples of ^{3}He and ^{129}Xe ADC maps acquired from a COPD subject are depicted in Figure 5.3. One of these examples is shown side-by-side with ADC maps obtained from a healthy subject in Figure 2.6.

The complete imaging protocol (^{3}He and ^{129}Xe ventilation and diffusion-weighted MR imaging) was repeated in the COPD patients on three additional scan sessions (1: on the same day as the first session (session 0), 2: on the following day, 3: two weeks after session 0, as illustrated in Figure 5.4) in order to assess the reproducibility of ^{3}He and ^{129}Xe MR-derived metrics of ventilated volume percentage and apparent diffusion coefficient.

Pulmonary function tests (PFTs) — including the diffusing capacity of carbon monoxide (TL$_{CO}$), forced expiratory volume in 1 second (FEV$_1$), and the ratio of FEV$_1$ to forced vital capacity (FVC) (FEV$_1$/FVC) — were performed by each COPD patient, once on the same day as each MR scan session (i.e. three times in total). Healthy volunteers carried out equivalent PFTs on the same day as diffusion-weighted MRI scans. Lung cancer patients did not undergo pulmonary function testing as a part of this

study.

Estimates of VV% and ADC derived from ^{3}He and ^{129}Xe MRI were compared in order to appraise the relative functional sensitivity of the two gases to ventilation abnormalities associated with pulmonary tumours and/or obstructive lung disease, and microstructural changes associated with emphysematous tissue destruction or otherwise. MRI-derived measurements were also compared and correlated against PFT results [i]. Where reproducibility data was available, the coefficient of variation (CV) of each MR or PFT parameter was calculated as the ratio of the standard deviation to the mean of the repeated measurements, expressed as a percentage.

5.3 Results & Discussion

In one healthy subject (HV9), the signal-to-noise ratio (SNR) of the obtained ^{129}Xe diffusion-weighted images exhibited insufficient SNR for accurate calculation of the xenon ADC across the lungs. From the COPD patient cohort, one ^{3}He ADC data-set, one ^{129}Xe ADC data-set, one ^{3}He VV% data-set and two ^{129}Xe VV% data-sets (each out of a total of 20 data-sets for each nucleus) were either not acquired successfully or the image SNR was not satisfactory. Aside from these instances, all recorded data was of sufficient SNR for quantitative VV% or ADC analysis (i.e. for ^{3}He, 95% of both ADC and VV% data was acceptable, and for ^{129}Xe, 95% of ADC data, and 90% of VV% data, was acceptable).
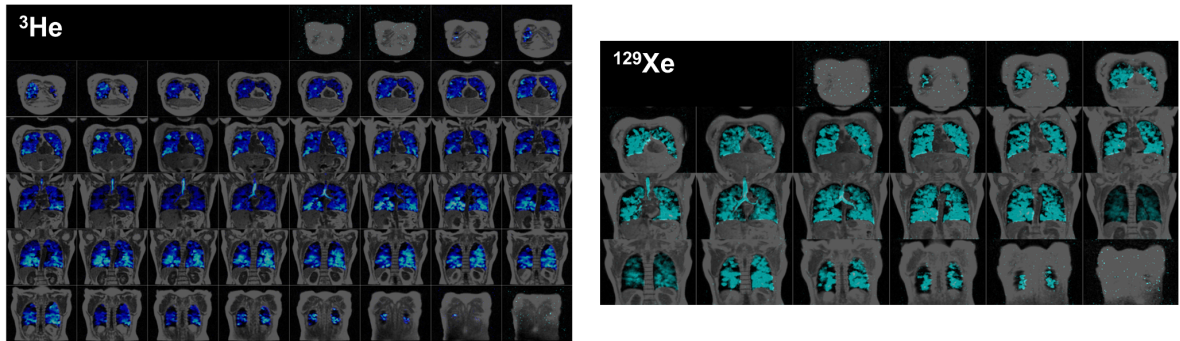
Figure 5.5: Full data-set of ^{3}He and ^{129}Xe MR ventilation images overlaid on anatomical ^{1}H images for a lung cancer patient.

Considerable ventilation abnormalities were observed in patients with lung cancer, with most patients exhibiting a patchy distribution of ventilated airspaces and typically one or more large defect(s) which corresponded visually to the location of a malignancy on structural ^{1}H lung MR images. In COPD subjects, severe ventilation defects were detected, and in some cases, entire lobes of the lungs were seen to be completely unventilated. The mean ^{3}He VV% in lung cancer patients ($84.0 \pm 7.9\%$) was significantly larger than that of COPD patients ($71.8 \pm 8.2\%$) at the $P < 0.05$ level. Whilst the ^{129}Xe VV% appeared to also suggest a trend of higher values in lung cancer patients ($74.6 \pm 15.2\%$) when compared to COPD patients ($59.8 \pm 10.4\%$), there was no statistically-significant difference in the mean values ($P = 0.099$). Example ^{3}He and ^{129}Xe ventilation images of the lungs of a patient with lung cancer and a patient with

---

[i]For the purpose of correlations between parameters derived from the two gases, the mean values ($\pm$ standard deviation) of repeated measurements in COPD patients were used to represent a single data-point for each patient.
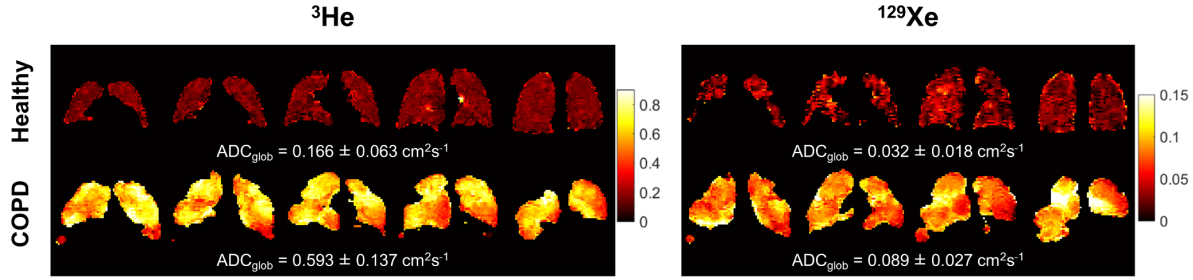
Figure 5.6: Full ^{3}He and ^{129}Xe ADC data-sets obtained from a healthy subject and a COPD patient.

COPD are shown in Figure 5.2, in comparison to corresponding images obtained from a healthy subject. Representative data-sets of all acquired ^{3}He and ^{129}Xe ventilation images overlaid on anatomical ^{1}H images for a subject with lung cancer are depicted in Figure 5.5. It is worth noting that the signal-to-noise ratio of individual ^{3}He and ^{129}Xe images was comparable in most subjects, which results from a balance of factors, including: the 3-fold larger ^{129}Xe dosage; the approximately 3-fold smaller ^{129}Xe gyromagnetic ratio (see Section 3.2.3); and differences in acquisition parameters (e.g. bandwidth, slice thickness), gas polarisation and scanner noise.

Derived VV% values were observed to be larger on average for ^{3}He than ^{129}Xe ($P = 0.001$) images, as calculated by comparing the mean values across all subjects. Similarly, assessing values within the patient groups of COPD patients and lung cancer patients, significant differences between VV% values derived from ^{3}He and ^{129}Xe MRI were found ($P = 0.004$ and $P = 0.050$, respectively). The overall greater ventilated volume percentages resulting from ^{3}He compared to ^{129}Xe scans may be explained by the significantly lower diffusion coefficient of ^{129}Xe, and therefore its reduced ability to penetrate partial obstructions. As reported previously at 3 T [85, 86], and mentioned in Section 4.6, an increased proportion of ventilation defects, or correspondingly, a reduction in ventilated volume, is not unexpected due to the Brownian diffusion behaviour of xenon as compared to helium. This effect was noticeable on a regional basis in a number of patients studied here, where a slightly patchier presentation of ventilation defects, or, conversely, marginally larger defects, were observed on ^{129}Xe images (e.g. Figure 5.2c). Rather than a limitation, situations can be envisaged in which this trend is useful; for example, in the assessment of early-stage obstructive disease, ^{129}Xe may exhibit a greater sensitivity to obstructions on a smaller length scale than can be detected with ^{3}He. Further validation of quantitative ventilation imaging of ^{129}Xe compared with ^{3}He in patients with different forms of lung disease over multiple centres and at multiple time-points is the next step in clinical evaluation of ^{129}Xe MR.

Representative example slice ^{3}He and ^{129}Xe ADC maps obtained from a COPD patient are depicted in Figure 5.3, and examples of all slices acquired from ^{3}He and ^{129}Xe ADC acquisitions of a healthy subject and a COPD patient are shown in Figure 5.6. Mean ADC values derived from both nuclei were significantly elevated in COPD patients when compared to healthy volunteers ($P = 0.013$ in both cases): mean $\pm$ standard deviation of ^{3}He ADC was 0.43 ± 0.13 cm^2.s^{-1} in COPD patients, and 0.19 ± 0.02 cm^2.s^{-1} in healthy volunteers; mean $\pm$ standard deviation of ^{129}Xe ADC was 0.072 ± 0.019 cm^2.s^{-1} in COPD patients, and 0.038 ± 0.003 cm^2.s^{-1} in healthy volunteers. (Note: in the case of the COPD patients, the mean $\pm$ standard deviation represents the mean and standard deviation of the intra-subject mean values.)

124

This observation is in agreement with previous reports of emphysematous tissue destruction leading to less restricted diffusion, as measured with both [3]He [101, 108] and [129]Xe [85, 115].

The diffusion coefficient of xenon in air is almost an order of magnitude lower than that of helium in air, and as such, the ADCs of the two gases as measured in the alveoli are significantly different. As discussed above, the reduced diffusion coefficient of [129]Xe could offer the possibility of investigating smaller microstructural changes than is possible with [3]He. However, the low diffusion coefficient of xenon also constrains the maximum achievable diffusion length scales within a given breath-hold (mean diffusion length in 1D: $\langle \bar{x} \rangle = \sqrt{2Dt}$). As such, "long-range" diffusion measurements (based on mass transport and longitudinal magnetisation, rather than phase dispersion of transverse magnetisation) for the evaluation of complex diffusion pathways in the peripheral airways (see e.g. [109, 294]), may be unfeasible with [129]Xe in pure xenon or xenon-nitrogen mixtures. On the other hand, longer effective [129]Xe diffusion lengths may be enabled by mixing xenon with lighter gases such as [4]He.

Comparison	Spearman's correlation coefficient (r)	P-value
[3]He ADC vs [129]Xe ADC	0.982	< 0.001**
[3]He ADC vs TL_{CO}	−0.967	< 0.001**
[3]He ADC vs FEV_1	−0.883	< 0.001**
[3]He ADC vs FEV_1/FVC	−0.851	< 0.001**
[129]Xe ADC vs TL_{CO}	−0.942	< 0.001**
[129]Xe ADC vs FEV_1	−0.833	< 0.001**
[129]Xe ADC vs FEV_1/FVC	−0.859	< 0.001**
[3]He VV vs [129]Xe VV	0.845	0.001*
[3]He VV vs TL_{CO}	0.700	0.188
[3]He VV vs FEV_1	0.800	0.104
[3]He VV vs FEV_1/FVC	0.900	0.037*
[129]Xe VV vs TL_{CO}	0.300	0.624
[129]Xe VV vs FEV_1	0.500	0.391
[129]Xe VV vs FEV_1/FVC	0.600	0.285

Table 5.2: Summary of correlations between MRI-derived [3]He and [129]Xe VV% and ADC measurements and PFTs in a population of healthy volunteers and patients with lung cancer and COPD. * indicates correlations at the statistical significance level of $P < 0.05$, and ** indicates correlations at the statistical significance level of $P < 0.001$. (Correlations of VV% with PFTs are quoted for COPD patients only.)

A summary of the correlation statistics between MR metrics and pulmonary function tests is presented in Table 5.2. A statistically-significant positive correlation between [3]He and [129]Xe VV% values was identified (Figure 5.7a: Spearman's correlation coefficient r = 0.845, $P = 0.001$). Thus, although the mean derived VV% was characteristically higher for [3]He than [129]Xe, the measurements were clearly related, implying that equivalent functional information was probed in both cases. This finding was corroborated by a Bland-Altman plot (see Figure 5.7b), which exhibits data scattered around a positively-biased mean difference between VV% values extracted from MRI of the two nuclei. Although the data appears scattered, there is preliminary evidence of a trend toward better-matched [3]He and [129]Xe VV% values at mean VV%s of close to 100%. The VV% correlation statistics could be further investigated by recruiting additional

subjects; in particular, the inclusion of healthy volunteer data would widen the range of data-points in Figure 5.7a, since most healthy volunteers would be expected to exhibit VV% values $\approx 100\%$.

Statistical comparisons and correlations between ^{3}He or ^{129}Xe VV% values and PFT results were limited by the fact that PFTs were not performed by the lung cancer patients; as such, correlations were determined for COPD subjects only. When evaluating the correlation of the intra-subject mean VV% values and mean PFTs, only ^{3}He VV% presented a statistically-significant correlation with FEV_1/FVC at the $P < 0.05$ level. The lack of correlation between ^{3}He or ^{129}Xe VV% and other PFTs is attributable to the low number of data-points (n=5) and the absence of comparative data from another subject group, e.g. healthy volunteers.

In prior work, the ventilation defect count per slice from ^{3}He MRI was found to correlate significantly with FEV_1/FVC [295], and in a number of recent studies, VV% values or VDPs associated with both ^{3}He and ^{129}Xe have been reported to correlate significantly with both FEV_1 [85, 110] and FEV_1/FVC [296].
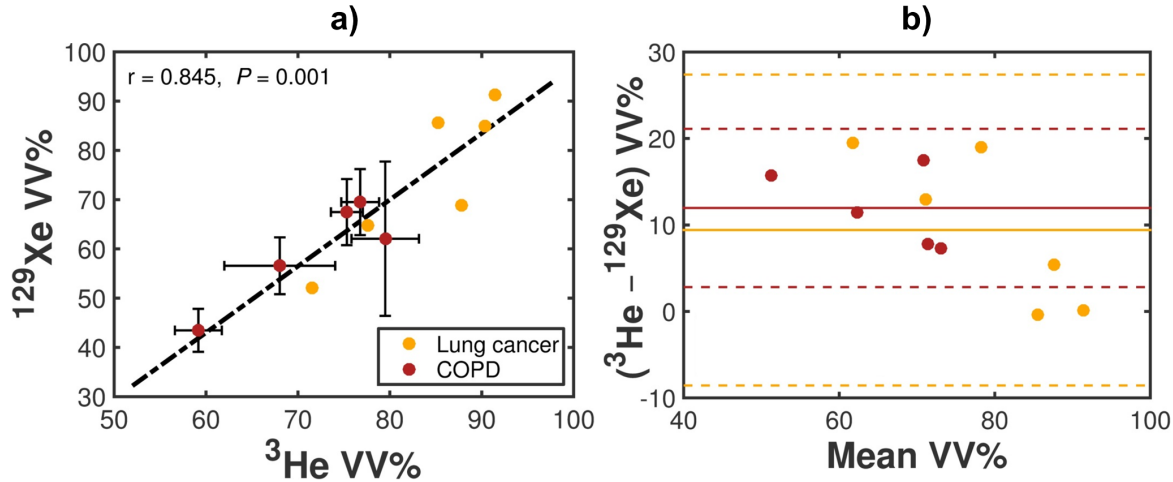
Figure 5.7: a) Correlation between ^{3}He and ^{129}Xe VV% values in patients with lung cancer and COPD, with associated Spearman's correlation coefficient (r) and P value of statistical significance. The solid line represents a linear fit to the data and error bars represent the standard deviation of all repeated scans for each COPD patient. b) Bland-Altman analysis of the differences between ^{3}He and ^{129}Xe VV% values in these patients. Solid lines indicate the mean difference between ^{3}He and ^{129}Xe VV%, and dashed lines represent plus and minus two standard deviations from the mean difference, for each cohort.

A strong positive correlation between mean ^{3}He and ^{129}Xe ADC values was determined in healthy volunteers and COPD patients (Figure 5.8: Spearman's r = 0.982, $P < 0.001$). As expected, by virtue of the difference in diffusion coefficient between the two gases, the mean ADC values were almost an order of magnitude lower for ^{129}Xe than ^{3}He, and hence Bland-Altman analysis was not appropriate.

On a regional basis, the effect of the reduced diffusion coefficient and lower overall ventilated volume was typically noticeable as correspondingly larger defects on ^{129}Xe ADC maps. However, as depicted in Figures 5.3 and 5.6, slight discrepancies in slice position between ^{3}He and ^{129}Xe slice ADC maps were observed, presumably arising due to the replacement of RF hardware and re-positioning of the patients between scans. This suggested that the defect presentation was similar in some slices for the two nuclei, or even that less significant defects were identifiable in ^{129}Xe images (i.e. opposite to the general trend in VV%). Whilst the 3D SSFP ventilation imaging acquisition was immediately followed by a separate- or
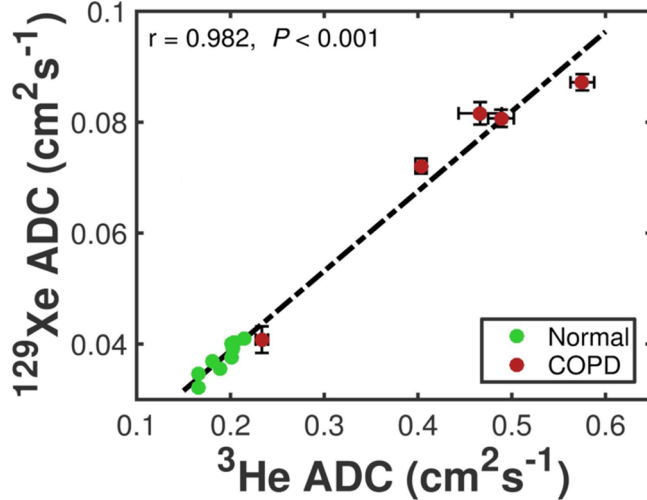
Figure 5.8: Correlation between mean [3]He and [129]Xe ADC values in healthy volunteers and patients with COPD, with associated Spearman's correlation coefficient (r) and P value of statistical significance. The solid line represents a linear fit to the data and error bars represent the standard deviation of all repeated scans for each COPD subject.

same-breath ^{1}H anatomical image, the DW-MR images were not obtained with accompanying ^{1}H images, which may limit the regional assessment of ADC maps, in terms of matching slice positions between nuclei. In future work, the application of compressed sensing for acceleration of DW-MRI [297] may permit the acquisition of same-breath diffusion-weighted hyperpolarised gas images and ^{1}H images in order to mitigate these potential issues.

Mean ADC values derived from both nuclei exhibited significant correlations with PFTs, as summarised in Table 5.2. In particular, correlations with the diffusing capacity of the lung for carbon monoxide, TL_{CO}, were highly significant, with Spearman's r and P values of r = -0.967 and $P < 0.001$, and r = -0.942 and $P < 0.001$ for [3]He and [129]Xe respectively. The TL_{CO} metric has previously been reported by a number of groups to be the most appropriate pulmonary function test against which to compare ADC values [85, 107, 115, 298]. This is likely because, although the TL_{CO} metric quantifies gas exchange function whilst the ADC probes gas diffusion within the alveoli, both measurements fundamentally depend on the surface-area-to-volume ratio of the alveolar airspace.

In COPD patients, a good visual agreement in the presentation of both [3]He and [129]Xe ADC maps was observed as a function of scan time-point, as illustrated in Figure 5.9. Mean [3]He and [129]Xe ADC values were found to be highly reproducible, with mean coefficient of variation (CV) values of less than 3% in both cases. These CV values are comparable to those of FEV_1 and FEV_1/FVC, and considerably less than those of the TL_{CO} parameter, as measured in the COPD patient cohort (summarised in Table 5.3). In addition, the CVs of both [3]He and [129]Xe ADCs were less than the previously reported same-session / same-day variability in FEV_1 [299] and TL_{CO} [300], and furthermore, were substantially lower than measured long-term variability in TL_{CO} ($\sim$ 9% [301]). Moreover, the multi-day CV values of both [3]He and [129]Xe ADC values presented in Table 5.3 were less than those reported by Diaz et al. in healthy subjects, COPD patients and patients with alpha-1 antitrypsin deficiency at 1.5 T [292], and comparable to CV values quoted by Parraga and colleagues for volunteers and COPD patients at 3 T [74].

Likewise, both [3]He and [129]Xe ventilation images appeared visually similar at each of the four scan time-points, as shown in Figure5.10. However, CV values of [3]He and [129]Xe VV% measures were noticeably greater than those of the corresponding ADC values. In particular, the mean CV of [129]Xe VV% was

13.01%, which is larger than that derived for TL_{CO}. The more than two-fold lower mean CV of ^{3}He VV% when compared with ^{129}Xe VV% is likely attributable to difficulties associated with the manual segmentation of ^{129}Xe ventilation images and registration to the anatomical ^{1}H images, which were acquired in a separate breath (rather than the same breath in the case of ^{3}He). Nevertheless, the CV of ^{129}Xe VV% is severely biased by the fact that one subject exhibited an outlying CV of 25%, whilst the CV value in all other subjects was of the order of 10%. As mentioned in Section 4.5, it is hoped that improvement in compressed sensing based acquisition strategies will help to facilitate same-breath ^{129}Xe ventilation and anatomical ^{1}H imaging to alleviate potential issues with image processing, which in turn should lead to a reduction in the CV of derived ^{129}Xe VV% values. Nevertheless, the ^{3}He and ^{129}Xe VV% CV values in COPD patients presented here were of a similar order to the week-to-week variability in FEV_1 and TL_{CO} as reported earlier [299]. In addition, ^{3}He VV% and ^{129}Xe VV% reproducibility was comparable to that previously reported in paediatric CF patients between two sessions on the same day [288], and the mean ^{3}He (but not ^{129}Xe) VV% CV was comparable to that of earlier studies in elderly healthy volunteers [302]. Finally, it is worth noting that an improved reproducibility between same-day scans when compared to scans separated by one-week has been observed for ^{3}He VDP by other groups in healthy volunteers and COPD patients [74, 287]. Although the subject numbers in the present study are limited, in future work it may be statistically feasible to distinguish same-day from two-week reproducibility and therefore better identify the potential sources of variability between the different scan sessions. Data regarding day-to-day and week-to-week reproducibility is critical for understanding the natural physiological variability in VV% and ADC values in patients, and is necessary to further validate these metrics as outcome measures in longitudinal studies (e.g. for assessment of disease progression or treatment response).
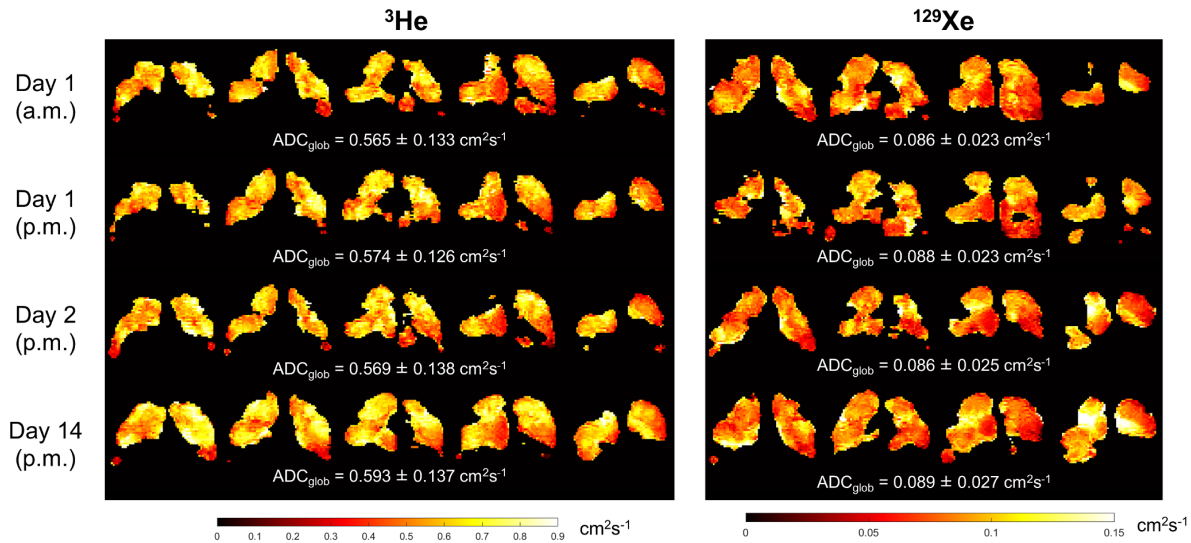
Figure 5.9: Representative ^{3}He and ^{129}Xe ADC maps acquired at each of the four scan time-points from a COPD patient. Global mean ADC values (ADC_{glob}) are quoted underneath each respective set of maps.

To our knowledge, this study presents the first comparative results of ^{3}He and ^{129}Xe MR ventilation imaging in subjects with lung cancer. The analogous functional information attainable with ^{129}Xe may facilitate its use as a cost-effective alternative to ^{3}He for radiation therapy planning applications [303].
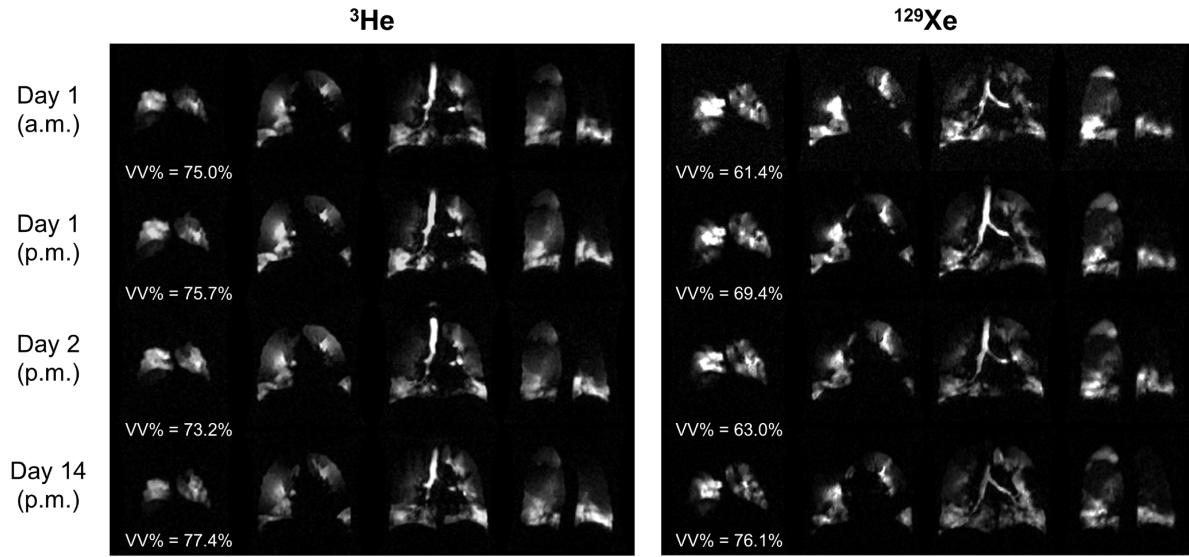
Figure 5.10: Selected ^{3}He and ^{129}Xe ventilation image slices acquired at each of the four scan time-points from a COPD patient. Calculated ventilated volume percentages (VV%) are quoted underneath each respective set of maps.

The lack of ionising radiation dosage associated with hyperpolarised ^{129}Xe MRI may thus present a suitable substitute for 4D-CT in subjects with lung function dominated by the presence of a tumour [304]. This work also details the first comprehensive study of the relative sensitivity of ^{3}He and ^{129}Xe ventilation and diffusion-weighted MR imaging at 1.5 T, indicating that ^{129}Xe-based techniques should be feasible for implementation at most clinical sites globally, with the requirements of only specialised RF and polariser hardware. The findings reported herein support the growing extent of literature demonstrating that ^{129}Xe is close to readiness for replacing ^{3}He for functional lung imaging applications in patients.

Further work is currently in progress to evaluate compressed sensing reconstruction techniques for acquiring undersampled ^{129}Xe ventilation images and facilitating routine same-breath ^{1}H imaging for improving the accuracy of ventilation volumetry. Analysis of the multiple b-value diffusion-weighted data acquired in the present work is also underway to quantify alveolar microstructural dimensions from both ^{3}He and ^{129}Xe data. 3D multiple b-value diffusion-weighted acquisition strategies with CS are under development for whole lung morphometric analysis using diffusion models of lung microstructural dimensions [297]. If successfully implemented with ^{129}Xe, multiple b-value acquisitions can be tailored to provide equivalent information about acinar airway geometry as has been previously presented with ^{3}He [305].

Furthermore, dynamic assessment of hyperpolarised gas wash-out over multiple breath-holds for quantification of fractional ventilation (the volume of gas turned-over per breath) has been recently explored with ^{129}Xe, with promising results exploiting the additional SNR available from SSFP acquisitions strategies [306]. Additionally, Collier et al. have reported sufficient SNR for phase-contrast flow velocimetry of the upper airways with ^{129}Xe in addition to ^{3}He gas [131]. In summary, previously unfeasible acquisition methods are becoming readily translatable to ^{129}Xe, and the potential for novel functional applications to be realised is exciting for the hyperpolarised gas MRI community [134].

Parameter	CV (mean %)	CV (range %)
^{3}He ADC	2.98	$1.48 - 5.61$
^{129}Xe ADC	2.77	$1.68 - 5.88$
^{3}He VV%	4.56	$2.31 - 8.86$
^{129}Xe VV%	13.01	$9.64 - 25.24$
FEV$_1$	4.22	$2.16 - 6.35$
FEV$_1$/FVC	2.35	$1.49 - 3.80$
TL$_{CO}$	8.73	$3.91 - 16.15$

Table 5.3: Reproducibility of MRI-derived ^{3}He and ^{129}Xe VV% and ADC measurements and PFTs in COPD patients, presented as inter-subject means and ranges of coefficient of variation (CV) values.

5.4 Conclusions

Preliminary experimental validation of hyperpolarised ^{3}He and ^{129}Xe MR ventilation imaging and ADC mapping has been demonstrated at 1.5 T in healthy volunteers and patients with lung cancer and COPD. Mean ADC values derived from both nuclei exhibited excellent agreement with each other and significant correlations with pulmonary function test results in volunteers and COPD patients, whilst ^{3}He and ^{129}Xe ventilated volume percentages correlated significantly with each other and showed a positive bias towards increased VV% for ^{3}He compared with ^{129}Xe in lung cancer and COPD patients. ADC and VV% metrics derived from both nuclei showed good reproducibility in the COPD patient cohort. These findings should help pave the way towards increased use of ^{129}Xe as a more readily-available, cost-effective alternative to ^{3}He for future quantitative clinical MR imaging studies of lung ventilation and microstructure.

Chapter 6

Experimental validation of the hyperpolarised ^{129}Xe chemical shift saturation recovery technique

6.1 Introduction

An overview of the background literature underpinning the experimental work in this chapter has been introduced already in Section 2.2. Here, a brief summary is provided, along with further specifics about the ^{129}Xe chemical shift saturation recovery technique.

^{129}Xe possesses attractive properties for in vivo functional studies of the lungs; for example its solubility in somatic substances, including parenchymal tissues and blood [233]. Also, since the xenon electron cloud is highly polarisable, ^{129}Xe exhibits a wide range of NMR chemical shifts in different chemical environments [236]. Of particular importance for lung studies are the resonances of ^{129}Xe dissolved in parenchymal tissues and blood plasma (T/P) and ^{129}Xe dissolved in red blood cells (RBCs) – collectively termed "dissolved-phase" ^{129}Xe. These are well separated from the "gaseous-phase" ^{129}Xe resonance, situated at 197 ppm and 217 ppm downfield, respectively. Since xenon is chemically inert and is not metabolised in the body, the NMR signal measured from this dissolved-phase ^{129}Xe in vivo is governed by diffusive uptake from the lung airspaces and perfusion in the capillaries, allowing quantitative mathematical modelling of the gas exchange process from ^{129}Xe NMR data.

These properties have been explored in several studies of pulmonary gas exchange function with different MR pulse sequence strategies, as follows. Direct imaging techniques [143, 144, 147] have been used, wherein the gaseous and dissolved ^{129}Xe resonances from the lungs are imaged simultaneously to provide complementary information about pulmonary ventilation and perfusion. The xenon polarisation transfer contrast (XTC) method [149–151] uses the relatively weak signal from dissolved-phase ^{129}Xe to modulate (relatively higher SNR) gaseous ^{129}Xe images via diffusional exchange in between image acquisitions. The chemical shift saturation recovery (CSSR) spectroscopy method [248, 265, 307] allows investigation of gas exchange dynamics by monitoring the time-dependent build-up of dissolved ^{129}Xe magnetisation in the T/P and RBC compartments following selective saturation. XTC has been recently extended to allow acquisition of gas exchange contrast images at multiple exchange times (multiple-exchange time XTC, or MXTC) [152, 153], however, unlike CSSR, this method has not been shown to provide separation between the two dissolved-phase ^{129}Xe compartments. The ability of the CSSR spectroscopic technique to yield dynamic information about both dissolved ^{129}Xe compartments simultaneously is thus a unique advantage over alternative techniques. The dynamics of xenon exchange in the lungs measured by ^{129}Xe CSSR can be modelled with standard diffusion equations [138, 307] in order to estimate parameters of lung function and microstructure, including the alveolar septal thickness, the RBC transit time through

the capillary bed, and the alveolar surface-area-to-volume ratio. To date, this methodology has been applied in preliminary studies in humans, where it has been shown to provide clinically-relevant metrics of gas exchange impairment [138, 140], enabling estimation of interstitial (septal) tissue thickening in interstitial lung disease (ILD) [138], and inflammation in chronic obstructive pulmonary disease (COPD) [141]. In addition, it has been utilised to examine lung function in small animals with a number of models of different lung diseases [145, 308–311].

Normal   **IPF**
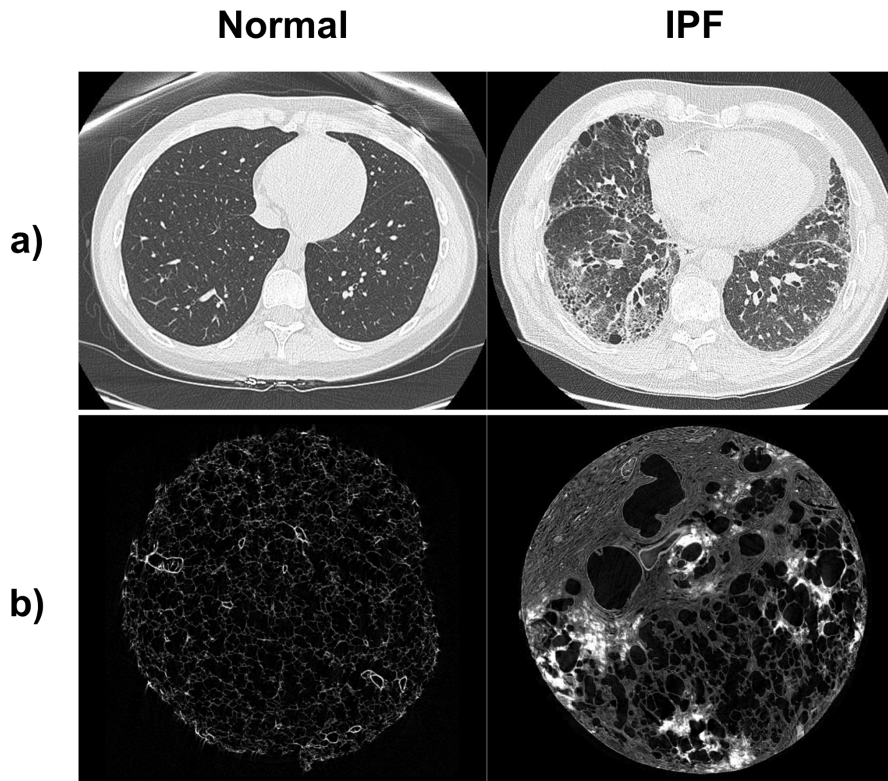
Figure 6.1: Example CT images of normal and IPF lungs. a) Representative slices from whole-lung inspiratory CT of a normal subject and a patient with IPF. b) Representative μ-CT sections from normal and IPF lungs.

The CSSR technique is particularly suited to quantification of gas exchange impairment in interstitial-type lung pathologies, such as idiopathic pulmonary fibrosis (IPF), a condition characterised by fibrosis of parenchymal tissues [312, 313]. IPF is the most prevalent form of ILD and carries a very poor prognosis. Also of significant clinical interest is systemic sclerosis (a.k.a. scleroderma, SSc), a rare connective-tissue disease in which respiratory problems are the most common cause of death; SSc is characterised by a combination of contributions from alveolar, interstitial and pulmonary-vascular components [314, 315]. Assessment of the causes of symptomatic limitation in these patients is challenging: pulmonary function tests including measurement of the diffusing capacity (transfer factor) of carbon monoxide ($T_{L,CO}$) are frequently reduced, but $T_{L,CO}$ provides no information as to the underlying mechanism causing the abnormality of gas exchange. High-resolution CT can be used to assess the extent of structural lung disease but is challenging in IPF; in particular, the derivation of useful quantitative metrics is limited by a multitude of co-factors that contribute to attenuation [316]. Example CT and μ-CT images of IPF lungs are

shown in Figure 6.1, in which key features such as honeycombing, reticulation and traction bronchiectasis can be seen in comparison to normal subjects. The heterogeneity of the disease is also clearly depicted. Interestingly in SSc patients, a reduced $T_{L,CO}$ is frequently observed in patients with apparently normal CT scans. Therefore, the development of novel techniques is required for both disease groups in order to quantify the functional consequences of structural changes in the lung impacting on gas exchange and also to assess the efficacy of potential treatments.

The purpose of this work was to demonstrate the practicality of the ^{129}Xe CSSR method for non-invasive quantification of lung microstructure, gas exchange dynamics and pulmonary-vascular function in healthy normal subjects and patients with SSc and IPF. For ^{129}Xe CSSR to be accepted as a clinical tool for routine application, experimental substantiation with existing gold-standard clinical methods is needed. Here, we compare ^{129}Xe CSSR-derived parameters with $T_{L,CO}$ measurements and quantitative indices derived from dynamic contrast-enhanced (DCE)-MRI [43, 55]. Current quantitative models of diffusive exchange of xenon in the lungs [138, 139, 309] are reviewed and their application to in vivo data is appraised in order to determine the most appropriate and informative model for future clinical use. In addition, the relationship between alterations to inter-alveolar septal structure and intra-alveolar shape and size is assessed by comparing the results of ^{129}Xe CSSR to those of ^{3}He ADC mapping.

Part of this chapter is based on the following publication: "Experimental validation of the hyperpolarized ^{129}Xe chemical shift saturation recovery technique in healthy volunteers and subjects with interstitial lung disease". **N. J. Stewart**, G. Leung, G. Norquay, H. Marshall, J. Parra-Robles, P. S. Murphy, R. F. Schulte, C. Elliot, R. Condliffe, P. D. Griffiths, D. G. Kiely, M. K. Whyte, J. Wolber, J. M. Wild. *Magnetic Resonance in Medicine*, **74**, 196-207 (2015). Author contributions statement: study design, NJS, GL, HM, PSM, CE, RC, DGK, MKW, JMW; acquisition of data, NJS, GL, GN, HM, JPR, RFS; analysis of data, NJS, GL; preparation of manuscript, NJS, GL, GN, HM, JPR, PDG, DGK, MKW, JW, JMW.

6.2 Methods

Study subjects

Four subjects with SSc and four with IPF were recruited for this preliminary study. Inclusion criteria included: patients aged 35-85 years; confirmed diagnosis of IPF or SSc (determined from current clinically-accepted guidelines at the Royal Hallamshire Hospital, Sheffield, UK); resting oxygen saturation of $\geq 90\%$ on room air, as measured by pulse-oximetry. Patients receiving targeted drug therapies were excluded.

Ten healthy volunteers aged 23-74 years, with no history of respiratory or connective-tissue disease, were also recruited. The study protocol and recruitment procedure were approved by the National Research Ethics Committee (UK). Pulmonary function tests (including whole-lung transfer factor, $T_{L,CO}$, forced expiratory volume in one second, FEV_1, and forced vital capacity, FVC) were performed on all subjects and blood samples were taken from all patients by conventional venipuncture. The results of these tests are summarised in Table 6.1.

Parameter		Healthy Volunteers (non-smokers)										SSc Patients				IPF Patients			
	Subject ID	H1	H2	H3	H4	H5	H6	H7	H8	H9	H10	S1	S2	S3	S4	I1	I2	I3	I4
Age		23	28	31	32	42	46	54	60	63	74	38	68	41	62	70	81	64	60
Sex		M	M	M	F	M	M	F	F	F	M	F	F	M	F	M	M	M	M
$T_{L,CO}$ (mmol/min/kPa)		13.70	14.13	10.83	10.22	10.11	11.86	7.13	5.89	6.58	6.45	4.17	2.50	4.81	5.77	1.79	3.32	2.42	2.35
$T_{L,CO}$ (%-pred)		102.8	114.5	88.3	114.4	99.6	110.9	80.3	91.8	73.1	58.2	34.9	45.6	79.9	21.7	41.1	24.5	24.5	23.2
FEV_1 (%-pred)		107.8	107.8	81.5	115.8	97.7	104.4	98.5	99.6	119.7	89.6	91.0	91.0	63.3	116.4	96.6	85.4	46.6	56.3
FVC (%-pred)		111.3	108.7	94.4	131.8	99.2	124.2	111.5	117.1	128.3	109.7	102.8	102.8	63.1	131.1	92.3	85.4	40.1	52.0
FEV_1/FVC (%)		97.5	95.6	82.6	91.9	93.9	95.7	92.0	92.0	101.3	101.1	76.3	73.8	82.1	74.5	83.8	85.1	90.4	85.1
Blood HCT		-	-	-	-	-	-	-	-	-	-	0.38	0.37	0.44	0.45	0.53	0.42	0.42	0.42
ST MOXE (μm)		9.8±1.0	8.0±0.9	9.5±0.6	8.5±0.6	10.5±0.8	9.1±1.0	8.7±0.5	11.1±1.5	12.6±1.0	12.1±0.9	14.8±0.6	13.0±1.1	13.2±0.9	11.1±1.2	15.8±0.8	16.7±1.3	17.9±1.7	18.3±1.7
ST Patz (μm)		9.2±0.8	7.9±0.9	9.3±0.6	8.4±0.5	10.2±0.8	9.0±0.9	8.5±0.5	10.8±1.5	11.7±1.1	11.7±0.9	14.6±0.7	12.4±1.0	12.5±1.0	10.7±1.0	15.4±1.0	16.0±1.4	17.0±0.6	17.4±1.8
ST Månsson (μm)		7.5±0.7	6.1±0.6	7.3±0.6	7.8±0.5	7.8±0.7	7.1±0.7	7.1±0.5	8.4±1.5	8.6±1.1	8.6±0.5	9.4±0.7	9.8±1.0	9.8±0.4	8.6±1.0	11.1±1.0	11.1±1.4	12.9±0.7	11.8±1.1
CTT MOXE (s)		1.6±0.9	1.7±0.1	1.7±0.1	1.9±0.2	4.5±0.7	3.0±0.1	3.0±0.5	1.8±0.3	2.6±0.4	2.8±0.4	3.4±0.6	2.2±0.3	2.0±0.3	2.0±0.3	2.3±0.3	1.0±0.4	2.3±0.2	2.0±0.4
CTT Patz (s)		2.4±0.2	2.4±0.1	2.4±0.1	2.8±0.2	4.1±0.7	3.0±0.1	2.0±0.5	2.0±0.3	2.6±0.4	2.7±0.4	3.6±0.6	2.4±0.3	2.3±0.3	2.4±0.3	2.5±0.4	2.5±0.4	2.4±0.2	2.1±0.4
CTT Månsson (s)		2.1±0.6	1.8±0.2	2.3±0.3	2.7±0.4	0.8±0.8	2.9±0.2	2.9±0.5	2.2±0.4	2.4±0.4	2.4±0.4	2.7±0.6	2.0±0.3	1.8±0.3	1.8±0.3	1.5±0.3	1.6±0.4	1.6±0.2	1.3±0.4
S/V MOXE (cm⁻¹)		190±11	140±10	131±5	150±6	170±7	102±7	96±5	74±7	101±6	122±6	83±2	185±11	168±8	98±6	172±5	87±4	206±3	157±7
S/V Patz (cm⁻¹)		197±13	151±13	137±6	160±6	181±8	107±7	105±5	79±7	107±6	130±7	89±5	196±12	175±9	103±6	187±6	93±7	218±8	165±8
HCT MOXE		0.22±0.05	0.30±0.02	0.26±0.02	0.27±0.01	0.15±0.01	0.27±0.03	0.25±0.01	0.21±0.01	0.18±0.01	0.17±0.01	0.14±0.01	0.15±0.01	0.17±0.01	0.22±0.01	0.13±0.01	0.15±0.01	0.16±0.01	0.16±0.01
HCT Månsson		0.26±0.01	0.30±0.01	0.28±0.02	0.27±0.01	0.14±0.01	0.29±0.03	0.25±0.01	0.24±0.01	0.18±0.01	0.18±0.01	0.14±0.01	0.14±0.01	0.16±0.01	0.16±0.01	0.10±0.01	0.11±0.01	0.12±0.01	0.12±0.01
Global RBC-to-T/P ratio		0.73±0.02	0.60±0.01	0.61±0.02	0.46±0.01	0.28±0.01	0.60±0.06	0.26±0.01	0.29±0.01	0.27±0.02	0.22±0.01	0.18±0.02	0.18±0.05	0.18±0.01	0.22±0.01	0.14±0.05	0.16±0.01	0.08±0.01	0.18±0.04
PTT (s)		-	-	-	-	-	-	-	-	-	-	3.0±0.2	4.4±0.4	5.1±0.6	5.9±1.0	3.9±0.5	7.0±0.5	5.5±0.5	5.5±1.2
FWHM lung (s)		-	-	-	-	-	-	-	-	-	-	4.6±0.2	6.5±1.0	8.6±1.2	7.7±0.3	7.1±1.1	7.8±1.3	7.8±0.9	6.7±2.0

Table 6.1: Subject demographics, pulmonary function test (PFT) results and MRI parameters for the ^{129}Xe CSSR validation study. PFTs include: $T_{L,CO}$ = diffusing capacity of carbon monoxide; FEV_1 = forced expiratory volume in one second; FVC = forced vital capacity; %-pred = PFTs expressed as a percentage of a predicted value, based on the subject's age, height, and other demographic factors; HCT = haematocrit. The following parameters were extracted from fitting models of lung microstructure to CSSR data: ST = septal thickness; CTT = capillary transit time; S/V = surface-area-to-volume ratio; HCT = red blood cell-to-tissue-plasma (RBC-to-T/P) peak ratio. Dynamic contrast-enhanced MRI parameters: PTT = pulmonary transit time; $FWHM$ = full width at half maximum.

CSSR spectroscopy

All hyperpolarised ^{129}Xe spectroscopy experiments were performed on a 1.5 T whole-body MRI scanner (GE Healthcare, Milwaukee, WI), with a flexible transmit-receive vest coil (Clinical MR Solutions, Brookfield, WI) tuned to the ^{129}Xe Larmor frequency (17.66 MHz at 1.5 T). ^{129}Xe was polarised by spin-exchange optical pumping (SEOP), using a "freeze-out" accumulation procedure and a home-built xenon polariser [65] with an external-cavity diode laser (see Section 3.2.6 and the ECDL system described in Section 4.4.1 for further details).

Specially-designed radiofrequency (RF) pulses were employed for excitation of ^{129}Xe nuclei in all experiments. A 14-element, pulse-width modulated, binomial-composite RF pulse (of 1.13 ms duration) was designed according to the procedures described in [317]; this pulse provided extremely selective excitation of dissolved-phase ^{129}Xe. When centred on the ^{129}Xe gas resonance, the excitation profile of the "balanced" form of the binomial pulse (in which the total area of positive and negative elements was equal) yielded an on-resonant excitation of almost zero and a maximum RF power deposition at a frequency ~ 3500 Hz (200 ppm at 1.5 T) downfield from the centre frequency. Thus, for CSSR applications, near-perfect saturation of dissolved-phase ^{129}Xe (flip angle $\approx 90°$) in the lung could be attained whilst a small, repeatable excitation of gaseous ^{129}Xe (flip angle $\sim 1°$) was ensured by adding a single positive element (of length 0.02 ms) to the end of the RF pulse [317].
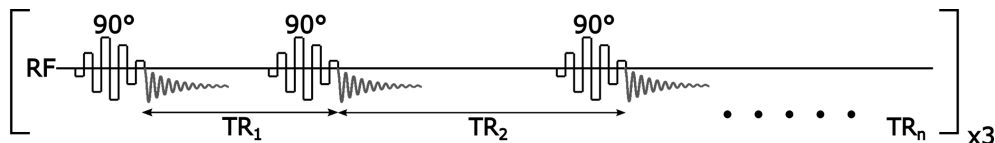
Figure 6.2: The CSSR pulse sequence, as implemented in this work. Pulse-width modulated binomial RF pulses (amplitude modulated pulses shown for display purposes) can produce 90° excitations of dissolved-phase ^{129}Xe with minimal on-resonance excitation of gaseous ^{129}Xe. These RF pulses were used for both saturation and excitation of ^{129}Xe NMR signal (generated free induction decays are shown in grey). The inter-pulse delay time (TR) was varied between values of 20 ms and 1000 ms, in order to quantify the dynamics of xenon exchange in the lungs. Each TR sweep was repeated three times to estimate the same-breath variability in the CSSR measurement.

Prior to CSSR, in order to calibrate the RF excitation flip angle and gaseous ^{129}Xe centre frequency, subjects inhaled 1 L of gas extracted directly from the OP cell of the polariser (3% xenon, $30 - 40\%$ polarisation) from a Tedlar bag (Jensen, Coral Springs, FL). A simple pulse-acquire sequence was utilised for this purpose, with thirty RF pulses and an inter-pulse delay time (TR) of 30 ms ($\ll T_1$ of ^{129}Xe gas in the lungs [134, 252]), leading to a breath-hold of less than one second. The bandwidth was 12 kHz and the centre frequency was chosen such that the RF pulse excitation profile was maximal at the ^{129}Xe gas frequency. The normalised decay in ^{129}Xe gas signal from pulse-to-pulse was fitted to a function of the form $\cos^{n-1}(\alpha)$, where α denotes the flip angle and n the RF pulse number.

The calibrated RF pulse amplitude was then used to determine the settings required for a 90° excitation of dissolved ^{129}Xe for CSSR experiments. Prior to each CSSR acquisition, the subject exhaled to functional residual capacity (FRC) and then inhaled a 50:50 mixture of cryogenically-accumulated, isotopically-enriched xenon gas ($10 - 15\%$ nuclear polarisation) and nitrogen gas from a 1 L Tedlar bag. The saturation recovery technique involves varying the time allowed for gas exchange (in this work, $\equiv TR$) after each successive saturation pulse, in order to sensitise the NMR acquisition to gas exchange, as il-

lustrated in Figure 6.2. 25 different TRs were used in the range 20 ms to 1 s; these were sequentially swept through in three repeated cycles during a single breath-hold to obtain average signal values for each TR and to estimate the uncertainty in each measurement (standard deviation of each point). Additional pulse sequence parameters: 12 kHz receiver bandwidth; 64 spectral points; total breath-hold, 15 s.

CSSR data analysis

CSSR "xenon-uptake curves" were generated by evaluating $F(t)$, the ratio of dissolved ^{129}Xe signal intensity at time $t = TR$ to gaseous ^{129}Xe signal intensity at $t = 0$ (the start of the TR), for each repetition. Signal intensities of each chemical shift compartment were calculated by integration of the respective NMR peaks in the magnitude spectra. The first acquired free induction decay (FID) was discarded since it was associated with an unknown exchange time during inhalation. The signal intensities from each of the three consecutive TR sweeps were first normalised by the ^{129}Xe gas peak and corrected for differences in flip angle experienced by gaseous and dissolved-phase ^{129}Xe and then finally, the signals were averaged to represent the mean result. The combined signal from ^{129}Xe in T/P and RBC compartments (i.e. total dissolved ^{129}Xe) was fitted with the model of Patz et al [138, 248, 307], and individual xenon-uptake curves for ^{129}Xe in T/P and RBCs were fitted with the models of Månsson et al [309], and Chang (also known as MOXE; the model of xenon exchange) [139], using non-linear least squares fitting routines developed in Matlab (MathWorks, Natick, MA).

A complete mathematical description of each model can be found in the respective papers cited above; however, the principal results are reviewed below and a diagrammatic summary of the underlying geometrical model assumed for each is provided in Figure 6.3.

The Patz et al model [138] is based on the solution of the diffusion equation for xenon in the alveolar septum (a slab of thickness d, comprising tissue and capillaries) surrounded by alveolar space on both sides. The boundary conditions for the solution of this problem are defined as follows: at time $t = 0$, the gaseous ^{129}Xe longitudinal magnetisation $M_g(x, 0) = M_0$, and the magnetisation of ^{129}Xe dissolved in the septal compartment $M_d(x, 0) = 0$, since it has been saturated. After a diffusion time, t, for which gas exchange can occur, the gaseous magnetisation is approximately unchanged $M_g(x, t) = M_0$ (due to the relatively low Ostwald solubility of xenon in tissue, λ), and the dissolved ^{129}Xe magnetisation at the boundaries of the septum is $M_d(0, t) = M_d(d, t) = \lambda M_g$ (since it is assumed that there is another airspace situated at the opposite side of the septum). This system is analogous to a heated metal bar with a fixed temperature at either end and has a solution derived via the separation of variables method [318]:

$$M_d(x, t) = \lambda M_g \left\{ 1 - \sum_{n=\text{odd}} \left(\frac{4}{\pi n} \right) \sin \left(\frac{n\pi x}{d} \right) \exp \left(-\left[\frac{n\pi}{d} \right]^2 Dt \right) \right\} \qquad (6.1)$$

where D denotes the dissolved-phase diffusion coefficient of xenon (i.e. the average of D_T and D_B), d is the septal thickness (as defined in Figure 6.3), λ is the Ostwald solubility of xenon in lung tissue, and the summation over n represents the contribution of different diffusion "modes" [i]. The fraction of the

---

[i]As the order of the summation (n) increases, the relative weight of the exponential terms is significantly decreased. Hence, only the first few terms of the summation are considered in practice.
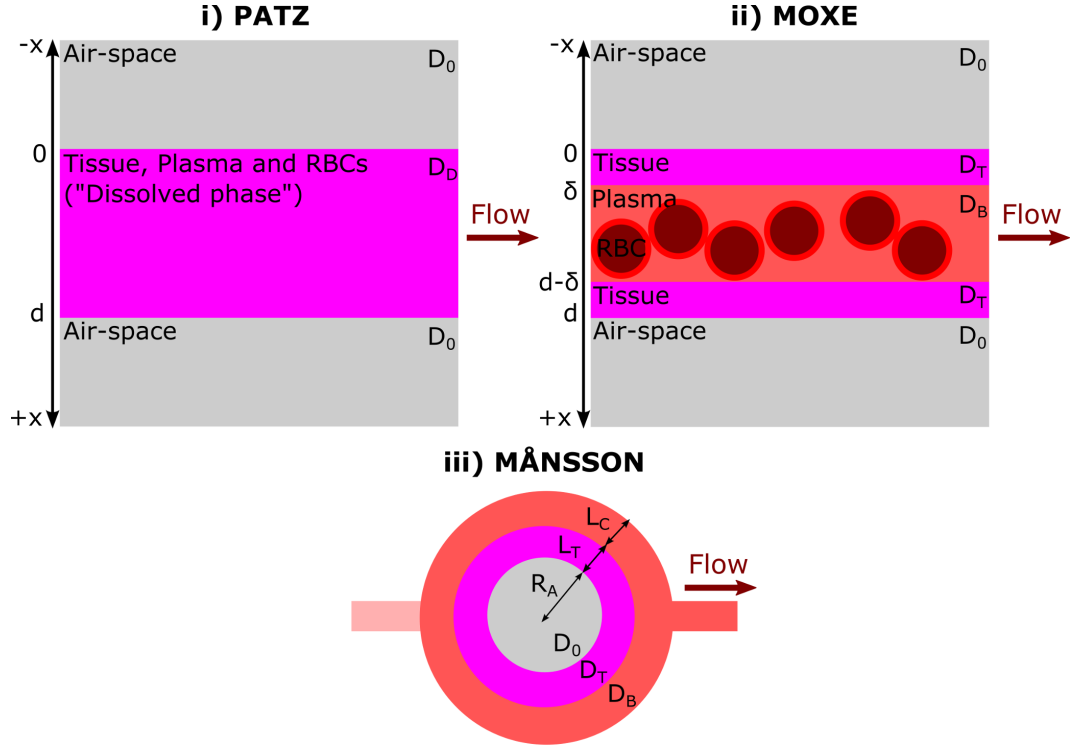
Figure 6.3: Comparison of the geometries adopted for diffusional modelling of xenon uptake in the lungs; from the airspace across the alveolar septum, thickness d. The Patz et al and MOXE models consider solving the diffusion equation with periodic boundary conditions in one dimension, x, created by identical alveolar airspaces on either side of the septum. (i) the model of Patz et al does not distinguish between T/P and RBC compartments; (ii) the model of Chang (MOXE) includes a tissue barrier term (δ) permitting separation of the T/P and RBC compartments, in conjunction with the blood haematocrit (HCT); (iii) the Månsson et al model also considers the two dissolved ^{129}Xe compartments individually, but with a circularly-symmetric geometry, with an alveolar radius (R_A) and tissue and capillary thicknesses L_T and L_C, respectively. In the first two models, blood flow is treated orthogonal to and independent of diffusional gas exchange. In each case D denotes the diffusion coefficient of xenon, in the airspace (D_0, the xenon "self" diffusion coefficient), tissues (D_T), blood (D_B) or combined dissolved-phase (D_D). Note: in the following discussions, D (instead of D_D) is used to represent the dissolved-phase xenon diffusion coefficient, which is fundamentally assumed to be the same for both tissues and blood in all three CSSR models. In practice, these values are likely to be different but are not currently well-known; hence we designate them with different symbols in this figure for completeness.

septum that is occupied with hyperpolarised ^{129}Xe molecules after a diffusion time t is:

$$f(t) = \frac{1}{d} \int_{x=0}^{d} \rho(x,t) \mathrm{d}x = 1 - \sum_{n=\mathrm{odd}} \frac{8}{\pi^2 n^2} \exp\left(-\left[\frac{n\pi}{d}\right]^2 Dt\right) \tag{6.2}$$

where $\rho(x,t)$ is the dimensionless dissolved ^{129}Xe magnetisation density in the septal slab ($\rho(x,t) = \frac{M_d(x,t)}{\lambda M_g}$). In the CSSR experiment, the dissolved-phase ^{129}Xe signal is measured after a diffusion time t and compared with the gas signal at $t=0$; as mentioned above, this ratio is denoted by the quantity $F(t)$:

$$F(t) = \frac{M_d(t \to \infty)}{M_g(t=0)} f(t) = \lambda \frac{V_d}{V_g} f(t) = \frac{\lambda d}{2} \frac{S_A}{V_g} f(t) \tag{6.3}$$

137

where $M_d(t \to \infty)$ denotes the dissolved ^{129}Xe magnetisation when the septal slab is saturated with xenon, $M_g(t = 0)$ denotes the gaseous ^{129}Xe magnetisation at $t = 0$, V_d and V_g are the volumes of the septal compartment and the airspace, respectively. The septal volume is defined to be the product of septal thickness d, and half the alveolar surface area S_A.

As a consequence of blood flow, a given portion of the capillary blood will reside in the gas exchange region for times less than t. To quantify this effect, a simple model of plug flow can be adopted (see Figure 6.3). The Patz et al model assumes that the capillary blood flow is orthogonal to, and independent of, the diffusion of ^{129}Xe. Furthermore, the *entire* capillary septal compartment is considered to flow continuously in a perpendicular direction to the direction of gas exchange (i.e. the thin tissue barrier, δ is ignored in the Patz et al model). The full solution for $F(t)$, including a discretised treatment of blood flow (see [138] for full details) can be written:

$$F(t) = \frac{\lambda d}{2} \frac{S_A}{V_g} \left(\frac{\tau - t}{\tau} \right) f\left(Dt/d^2\right) + \lambda d \frac{S_A}{V_g} \left[\frac{t}{\tau} + \frac{8d^2}{D\pi^4} \frac{1}{\tau} g\left(Dt/d^2\right) \right] \tag{6.4}$$

where τ is the capillary transit time (the average length of time a RBC resides in the gas exchange region) and $f(q)$ and $g(q)$ are functions of the dimensionless parameter $q = Dt/d^2$ and are defined in the following way:

$$f(q) = \left[1 - \sum_{n=\text{odd}} \frac{8}{\pi^2 n^2} \exp\left(-q\pi^2 n^2\right) \right] \tag{6.5}$$

$$g(q) = \left[\sum_{n=\text{odd}} \frac{1}{n^4} \left\{ \exp\left(-q\pi^2 n^2\right) - 1 \right\} \right] \tag{6.6}$$

The model of xenon exchange (MOXE, developed by Chang [139]), is an extension of this methodology in which the septum is separated into its parenchymal tissue and capillary components by the introduction of the parameter δ, the tissue barrier thickness, and the haematocrit (HCT). The relative contributions from ^{129}Xe in plasma and RBCs are distinguished by considering the distinct Ostwald solubilities of xenon in these media (λ_{PL} and λ_{RBC}). Furthermore, the tissue and plasma contributions are combined (since they induce the same NMR chemical shift for ^{129}Xe and are indistinguishable at the B_0 strengths measured to date). Blood flow is treated in an identical manner to that of the Patz et al model, however this time, excluding the tissue barrier regions. Reproducing the result from [139] for the time-dependence of the ^{129}Xe T/P signal:

$$S_{TP}(t) = b \left[\frac{2\delta}{d} - \frac{8}{\pi^2} \sum_{n=\text{odd}} \frac{1}{n^2} \left(1 - \cos\left(\frac{n\pi\delta}{d}\right) \right) \exp\left(-\frac{n^2 t}{T}\right) \right]$$

$$+ b(1-\eta) \left\{ 2 \left[\left(1 - \frac{2\delta}{d}\right) \frac{t}{\tau} - \frac{8T}{\pi^2 \tau} \sum_{n=\text{odd}} \frac{1}{n^4} \cos\left(\frac{n\pi\delta}{d}\right) \left(1 - \exp\left(-\frac{n^2 t}{T}\right)\right) \right] \right. \tag{6.7}$$

$$\left. + \left(1 - \frac{t}{\tau}\right) \left[\left(1 - \frac{2\delta}{d}\right) - \frac{8}{\pi^2} \sum_{n=\text{odd}} \frac{1}{n^2} \cos\left(\frac{n\pi\delta}{d}\right) \exp\left(-\frac{n^2 t}{T}\right) \right] \right\}$$

where $b = \frac{\lambda d}{2} \frac{S_A}{V_g}$, $T = \frac{d^2}{\pi^2 D}$, the latter termed the 'xenon exchange time constant', and η denotes the fraction of ^{129}Xe in RBCs to ^{129}Xe in blood as a whole. The parameter $S_{TP}(t)$ is essentially equivalent to $F(t)$ minus the RBC contribution. Recasting the terms of Equation 6.7 within curly brackets as $S_x(t)$, the time-dependence of the ^{129}Xe RBC signal can be written:

$$S_{RBC}(t) = b\eta S_x(t) \tag{6.8}$$

Equations 6.7 and 6.8 are coupled, such that they can be simultaneously fitted to experimental data, thereby constraining the fit parameters. From these equations, an estimate of the haematocrit, HCT can be derived from the constant η and the Ostwald solubilities of xenon in plasma (λ_{PL}) and RBCs (λ_{RBC}):

$$HCT = \frac{\frac{\eta}{\lambda_{RBC}}}{\frac{\eta}{\lambda_{RBC}} + \frac{(1-\eta)}{\lambda_{PL}}} \tag{6.9}$$

Finally, Månsson et al [309] considered a circularly-symmetric geometry in order to solve the ^{129}Xe septal diffusion problem. In that work, the T/P and RBC signal dynamics were described by the same equation; an exponential growth function on short timescales (where the observed signal dynamics are dominated by diffusional exchange) and a linear increase on longer timescales (where perfusion governs the observed signal):

$$S(t) = S_0 \left(1 - \exp\left(-\frac{t}{T_M}\right)\right) + S_1 t \tag{6.10}$$

where S_0 is the y-intercept of $S(t)$ at $t = 0$, if there was no exponential component; S_1 is the linear slope of $S(t)$ at large t; and T_M is the exponential time constant. These fitting parameters are determined independently for the separate RBC and T/P components. For further details of the relation of these parameters to physiologically meaningful quantities, we refer the reader to [309].

A number of interesting parameters related to lung physiology and microstructure can be derived from the application of these models to ^{129}Xe CSSR data. In particular, the alveolar septal thickness (ST), RBC capillary transit time (CTT) and surface-area-to-volume ratio (S/V) were derived for each subject

in this study. The results extracted from each model were compared in order to assess the suitability of each for interpretation of ^{129}Xe CSSR data. The accuracy of the model fit to the data was evaluated by re-fitting each data-set with different "weightings" – i.e. applying the error function, weighted to specific data points, to the residuals before calculating the sum of squares.

Furthermore, as a semi-quantitative measure of gas exchange efficiency, the ratio of RBC-to-T/P peak integrals was determined from phase-corrected ^{129}Xe CSSR spectra at a TR of 100 ms, consistent with the recent work of Kaushik et al [171]. Lastly, statistical testing was performed using SPSS (IBM SPSS Statistics, V19, Armonk, NY) in order to: (i) identify parameters of lung physiology that were significantly different between subject groups (by a two-tailed, one-way analysis of variance (ANOVA) test with post-hoc contrast); (ii) determine significant correlations between parameters (Pearson's correlation coefficients).

DCE-MRI

For validation of the xenon RBC capillary transit times measured by ^{129}Xe CSSR, two measures of pulmonary-vascular output were determined from DCE-MRI: (i) the full-width at half-maximum (FWHM) of the lung parenchymal signal enhancement and (ii) the pulmonary transit time. Patients were placed in an 8-channel cardiac-array coil and a 0.05 mL.kg^{-1} dose of 1 mmol.mL^{-1} Gd-DPTA solution (Gadovist, Schering, Leverkusen, DE) was injected with a power injector (Spectris, Medrad, Warrendale, PA) at a rate of 4 mL.s^{-1} into the antecubital vein, followed by a 20 mL saline flush. A time-resolved 3D coronal GRE sequence with: 2× phase acceleration and view sharing [44]; 24 slices of thickness 10 mm; bandwidth = ±125 kHz; TE/TR = 0.8/2.3 ms; flip angle = 30°; matrix, 200 × 80; 36 temporal phases at an effective frame rate of 2 volumetric frames per second, was used to image the dynamics of the first pass of gadolinium through the pulmonary vasculature. In order to calculate the pulmonary transit time (PTT) from the time series of images, signal enhancement as a function of time was evaluated for regions of interest (ROIs) placed in the left atrium and pulmonary artery [53, 319]. The PTT was calculated by subtracting the time-to-peak signal of the pulmonary artery from that of the left atrium. For the FWHM of the lung parenchymal enhancement, a ROI was placed on each lung and the FWHMs of the resulting signal enhancement curves were averaged. Due to the positioning of the ROIs, both methods intrinsically provided an estimation of the "whole-lung" gadolinium transit time for comparison to CSSR data.

6.3   Results

As part of a comprehensive pulmonary MRI protocol, hyperpolarised ^{3}He MR imaging of lung ventilation, and conventional structural ^{1}H MRI of the thorax was performed for each recruited IPF and SSc patient. Although no image analysis or quantification was done as a part of this thesis, these images provide good background information about the prevalence of disease in these patients, and form a basis on which to interpret the ^{129}Xe CSSR data. Example images for subject I1 (see Table 6.1) are presented in Figure 6.5. Predominantly peripheral and basal fibrosis is apparent on UTE and bSSFP images, and additional indications of impaired ventilation are present in similar spatial locations on the ^{3}He images (as highlighted by the patchy appearance of ventilation defects / regions of low signal intensity).

^{129}Xe NMR spectra typically highlighted a dominant peak due to ^{129}Xe dissolved in parenchymal tissues
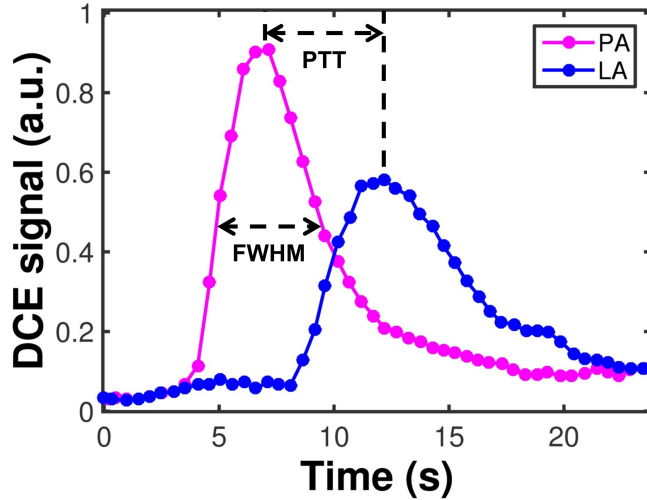
Figure 6.4: Contrast-enhanced signal as a function of time in the pulmonary artery (PA) and left atrium (LA), for derivation of the mean pulmonary transit time (PTT) (see also Figure 2.4). FWHM = full-width at half maximum. (Note: this is the FWHM of the signal-time curve for a ROI placed at the position of the pulmonary artery; in practice, for calculation of the FWHM of lung parenchymal enhancement, the signal intensity is significantly lower.)
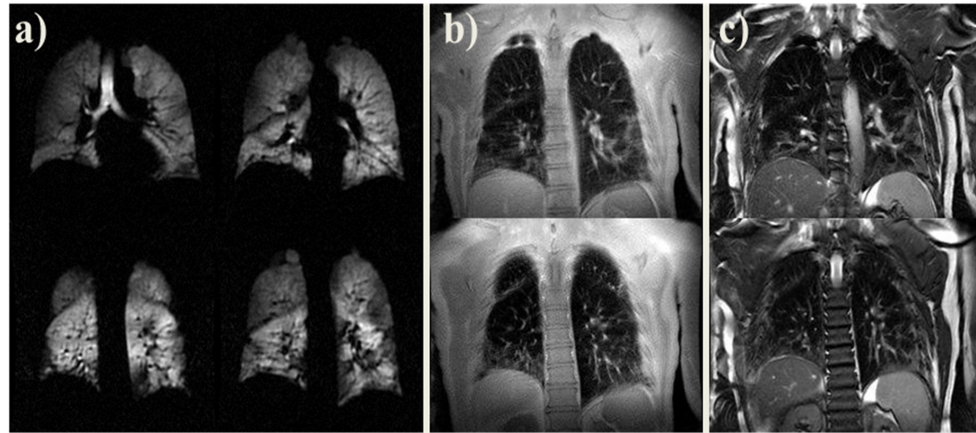
Figure 6.5: Representative hyperpolarised [3]He and structural ^{1}H MR images in an IPF patient. Example slices from a) [3]He ventilation imaging; b) ultra-short echo time (UTE) imaging; c) balanced steady-state free precession (bSSFP) imaging. Additional structural ^{1}H MR images from IPF patients are presented in Figure 2.1.

and blood plasma (T/P) with an accompanying smaller peak from [129]Xe in RBCs, in both SSc and IPF patients when compared with healthy volunteers. At short exchange times, [129]Xe spectra from patients exhibited almost no signal from RBCs, and only a moderate peak was observed at very long TRs ($\sim$ 1 s) (see Figure 6.6, right panel). As illustrated in the left panel of Figure 6.6, [129]Xe uptake curves indicated that gas exchange from the alveoli to capillaries was impaired and delayed in both patient groups compared with healthy volunteers. The exponential, diffusion-dominated part of the curve was visibly prolonged in patients and the T/P component was observed to reach a greater value of $F(TR)$, consistent with the appearance of the individual spectra.

The apparent inhibition of gas exchange in patients suggested thickening of septal tissue, and this was corroborated by fitting the [129]Xe uptake curves with the models of Patz et al (Equations 6.4 to 6.6), Månsson et al (Equation 6.10) and Chang (MOXE) (Equations 6.7 to 6.8). Each model exhibited a considerably increased whole-lung alveolar ST in older healthy volunteers and patients with SSc, and an even greater increase in IPF subjects, when compared to younger ($<$ 50 years) volunteers (see Table 6.1 for a
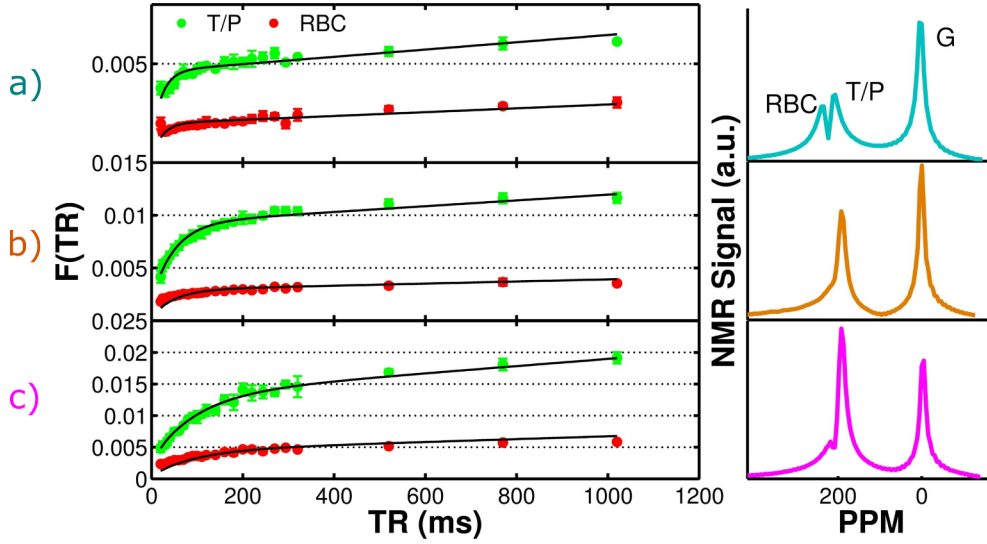
Figure 6.6: Left panel: Dynamics of ^{129}Xe uptake into tissues and blood plasma (T/P), and RBCs, for: a) a typical healthy volunteer; b) a patient with SSc; and c) a patient with IPF. Uptake curves, denoted by $F(TR)$, are displayed with corresponding MOXE model fits (solid black lines, Equations 6.7 to 6.8). Dashed lines indicate increments in $F(TR)$ of 0.005. Right panel: NMR spectra (moderately line-broadened and zero-filled to 128 points) of subjects from the same three groups, acquired at a TR of 1000 ms. The peaks due to ^{129}Xe in RBCs, T/P and the gaseous-phase (G) are clearly indicated.

summary of CSSR-derived parameters and pulmonary function test results). The ST values determined from application of the MOXE model to ^{129}Xe CSSR data are shown as a box plot in Figure 6.7. Using a dissolved-phase ^{129}Xe diffusion coefficient of $D = 3.0 \times 10^{-6}$ cm^2.s^{-1} [138], mean ST values derived from this model were 10.0 ± 1.6 μm for healthy volunteers, 13.0 ± 1.5 μm for subjects with SSc and 17.2 ± 1.1 μm for those with IPF. Statistically significant differences between derived ST values for all three subject groups were found upon fitting each of the three models of lung microstructure to hyperpolarised ^{129}Xe CSSR data. These values are summarised in Table 6.2, along with the P values expressing the statistical significance.

A strong, positive correlation was identified between the CSSR-derived ST and the age of the healthy volunteer cohorts (correlation statistics: $r = 0.74$, $P = 0.015$ using MOXE; $r = 0.77$, $P = 0.010$, Patz et al; $r = 0.75$, $P = 0.012$, Månsson et al), as illustrated in Figure 6.8. This correlation was used to "correct" for the effect of aging in volunteer and patient data; i.e. in attempt to show ST changes that were induced by pathological processes only, and not age-related changes to lung microstructure. With age-correction, a significant increase in ST in IPF patients was still observed ($P < 0.05$) for all models, however none of the three models exhibited a significant difference in ST between volunteers and SSc subjects ($P > 0.05$). The results of the age-correction analysis are presented in Table 6.2.

Furthermore, a statistically significant correlation was observed between the CSSR-derived ST values and $T_{L,CO}$. Results from fitting CSSR data with MOXE are displayed against %-predicted $T_{L,CO}$ in Figure 6.9. Pearson's correlation coefficients (r) and P values for ST versus %-predicted $T_{L,CO}$ were: $r = -0.90$, $P < 0.001$ for data fitted with the Patz et al model; $r = -0.91$, $P < 0.001$, MOXE; $r = -0.92$, $P < 0.001$, Månsson et al. The correlations against $T_{L,CO}$ in standard units (mmol/min/kPa, i.e. not
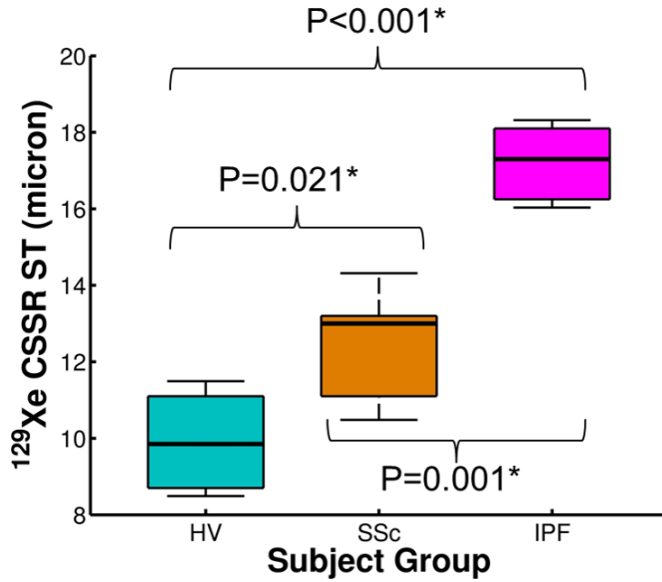
Figure 6.7: Box plot of mean (whole-lung) alveolar septal thickness values for healthy volunteers and patients with SSc and IPF, as derived from fitting the MOXE model to ^{129}Xe CSSR data.
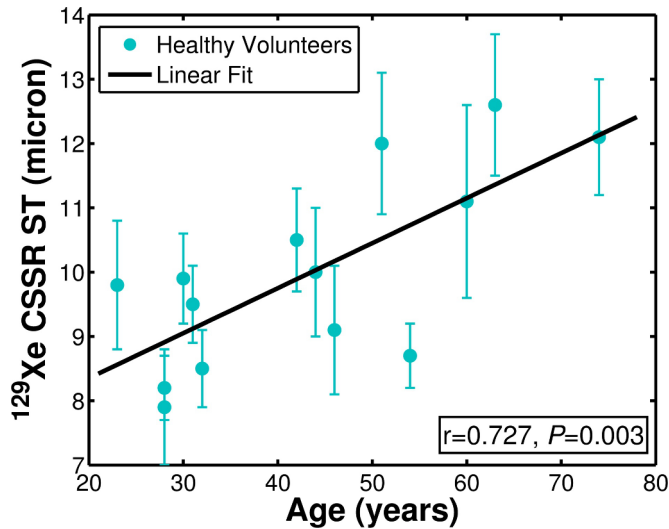
Figure 6.8: Correlation between septal thickness and age of healthy volunteers, with corresponding Pearson's correlation coefficient (r) and P value.

considering subject-wise predictions for height, age, sex) were: $r = -0.85$, $P < 0.001$ for data fitted with the Patz et al model; $r = -0.85$, $P < 0.001$, MOXE; $r = -0.86$, $P < 0.001$, Månsson et al.

Complementary to the CSSR modelling results, the ratio of RBC-to-T/P peak integrals was found to be significantly different between both SSc and IPF patients and healthy volunteers, although, unlike the ST parameter, the ratio did not distinguish between the two patient groups. Mean values (P values) were: 0.42 ± 0.18 in healthy volunteers; 0.18 ± 0.04 in SSc subjects (P(HV-SSc) = 0.040) and 0.13 ± 0.04 in IPF subjects (P(HV-IPF) = 0.009, P(SSc-IPF) > 0.05). Furthermore, the RBC-to-T/P ratio measurements correlated well with ST values from all models ($r = -0.74$, $P < 0.001$, MOXE; $r = -0.74$, $P < 0.001$, Patz et al; $r = -0.77$, $P < 0.001$, Månsson et al).

The mean CSSR CTT was: 2.2 ± 1.0 s, 2.5 ± 0.7 s, 2.5 ± 0.6 s (volunteers); 2.3 ± 0.8 s, 2.5 ± 0.9 s, 2.0 ± 0.5 s (SSc); 2.2 ± 0.2 s, 2.4 ± 0.2 s, 1.5 ± 0.1 s (IPF); respectively for the MOXE, Patz et al and Månsson et al models. This parameter was not significantly different between subject groups ($P > 0.05$).
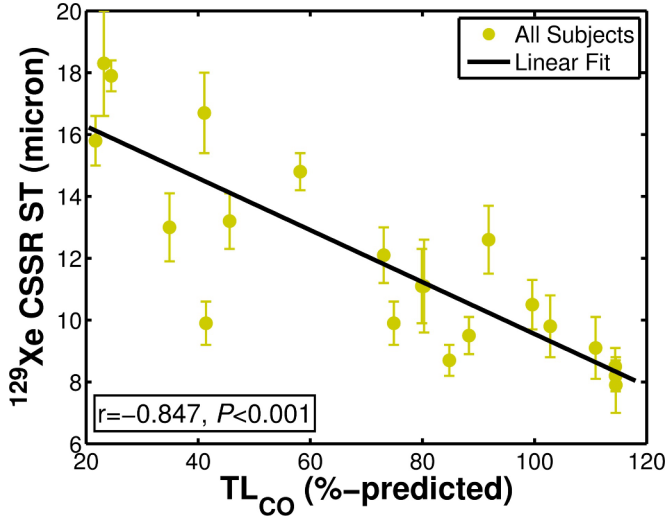
Figure 6.9: Validation of ^{129}Xe CSSR-derived septal thickness values (from the MOXE model) with the clinical gold-standard measure of pulmonary function, the whole-lung transfer factor for carbon monoxide ($T_{L,CO}$). The Pearson's correlation coefficient (r) and corresponding P value are shown. Error bars in ST were estimated by re-fitting the data with different weightings applied to the residuals before taking the sum of squares, as described in Section 6.2. Note: %-predicted $T_{L,CO}$ represents the measured $T_{L,CO}$ value as a percentage of an expected value, based on subject height, sex, age etc.

Group	Mean ST Patz (μm)		Mean ST MOXE (μm)		Mean ST Månsson (μm)	
	Normal	*Age-corrected*	*Normal*	*Age-corrected*	*Normal*	*Age-corrected*
HV	9.7 ± 1.5	8.3 ± 0.8	10.0 ± 1.6	8.5 ± 0.9	7.6 ± 0.9	6.7 ± 0.5
SSc	12.6 ± 1.6	10.4 ± 2.1	13.0 ± 1.5	10.7 ± 2.1	9.4 ± 0.5	8.0 ± 0.9
IPF	16.5 ± 0.9	12.2 ± 1.2	17.2 ± 1.1	12.7 ± 1.4	11.7 ± 0.9	9.3 ± 1.0
P (HV-SSc)	0.001^*	0.274	0.010^*	0.231	0.008^*	0.125
P (SSc-IPF)	0.004^*	0.388	0.004^*	0.332	0.003^*	0.238
P (HV-IPF)	$< 0.001^{**}$	0.009^*	$< 0.001^{**}$	0.011^*	$< 0.001^{**}$	0.020^*

Table 6.2: Summary of mean ^{129}Xe CSSR-derived septal thickness (ST) values calculated using three models of lung microstructure (Patz et al [138], Chang (MOXE) [139], Månsson et al, including values "corrected" for predicted changes due to subject age. [309]). HV: healthy volunteers; SSc: systemic sclerosis patients; IPF: idiopathic pulmonary fibrosis patients. * indicates comparisons that are statistical significant at the level of $P < 0.05$, and ** indicates comparisons that are statistical significant at the level of $P < 0.001$.

The CTTs calculated from CSSR were not found to correlate significantly with the PTT or lung FWHM as determined from DCE-MRI; the highest correlation coefficient was between the CTT (Patz et al) and the lung FWHM ($r = 0.34$, $P = 0.416$).

The derived haematocrit from the MOXE and Månsson et al models was notably lower in IPF patients compared to healthy volunteers, with values of: 0.23 ± 0.05 and 0.24 ± 0.05 (volunteers); 0.17 ± 0.04 and 0.15 ± 0.01 (SSc); 0.15 ± 0.01 and 0.11 ± 0.01 (IPF) for the two models, respectively. The *HCT* was significantly different between healthy volunteers and IPF patients (MOXE) and between volunteers and both patient groups (Månsson et al model) ($P < 0.05$). Finally, as extracted from the MOXE and Patz et al models, the mean alveolar surface-area-to-volume ratio was: 135 ± 37 cm^{-1} and 128 ± 36 cm^{-1} (volunteers); 141 ± 53 cm^{-1} and 134 ± 51 cm^{-1} (SSc); 166 ± 53 cm^{-1} and 156 ± 51 cm^{-1} (IPF); respectively, with P values of significance between groups > 0.05 in all cases.

6.4 Discussion & Conclusions

Clinical findings

Septal thickness values for healthy volunteers calculated from Patz et al and MOXE models agreed well with previously-reported values derived from computerised morphometry of lung samples (~ 10 μm for

normals, see e.g. [320] and the literature review presented in Section 7.4). Thickening of alveolar septa in IPF patients can be attributed to underlying fibrotic changes in lung microstructure that were confirmed by CT scans, which each patient underwent as part of their routine clinical assessment. The significance of apparent septal thickening in SSc subjects is clinically interesting and must be further assessed as these patients had little discernible fibrosis on CT and no evidence of pulmonary hypertension (PH). If validated histologically, septal thickening may help explain the reduced $T_{L,CO}$ frequently observed in patients with SSc in the absence of evident PH and ILD. Nevertheless, since some patients were > 50 years old, the measured thickening may be partially attributable to age-dependent changes in the septal structure, as identified by the measured increase in ST of healthy volunteers with age. In future, with more healthy volunteer data, it may be possible to derive a "%-predicted ST", in accordance with the clinical standard procedures for PFTs (i.e. in order to predict the ST for a particular healthy subject, depending on their height, sex, age, etc.).

Of further potential clinical importance is the fact that the surface-area-to-volume ratio derived from these CSSR models is not significantly different between subject groups. This finding might suggest that the remodelling of the lung parenchyma due to fibrosis is not necessarily associated with emphysematous processes. This result is assessed in relation to preliminary findings from ^{3}He apparent diffusion coefficient mapping MRI in Section 6.4.1. Finally, we re-iterate that the RBC-to-T/P ratios also exhibit significant differences between subject groups. However, since this parameter is only a semi-quantitative measurement of gas exchange that does not distinguish between diffusion- and perfusion-related components of the ^{129}Xe uptake dynamics, it is not possible to derive clinically-relevant parameters of lung microstructure from this method.

The demonstration of a distinct relation between whole-lung transfer factor for carbon monoxide, $T_{L,CO}$, and ^{129}Xe CSSR-derived ST is the first time that the ^{129}Xe CSSR technique has been cross-validated with a clinically-accepted method [ii] and has important implications for clinical application of this technique. For example, if adapted to enable acquisition of regionally-localised spectra (e.g. with receiver-coil arrays or chemical shift imaging based approaches; the latter as postulated in Section 7.4.1), the CSSR method could provide information about gas exchange that is not obtainable by standard pulmonary function testing or CT techniques in ILD patients. However, it should be noted that the value of $T_{L,CO}$ is derived from two measured quantities — the transfer rate of carbon monoxide across the pulmonary septum K_{CO}, and the alveolar volume, V_A, as introduced in Section 3.1.3 — and therefore, in future work it may be more appropriate to compare ST values to K_{CO} only (since we recall that the ST is defined in terms of the xenon exchange time constant, the xenon analogue of K_{CO} for carbon monoxide). The V_A is more relevant for comparisons with the CSSR-derived S/V values, and, if V_A is significantly altered in IPF or SSc patients, it may cloud the interpretation of the measured relationship between $T_{L,CO}$ and ST.

The lack of correlation between ^{129}Xe CSSR CTT values and DCE-MRI parameters suggests that the CTT parameter is not sensitive to small changes in pulmonary-vascular output, or, that its meaning has been obscured by the additional modelling parameters. In all cases, CTT values were significantly lower than the corresponding DCE-MRI PTT values; however, this would be expected due to the different definitions of the parameters. The former describes the average time a RBC resides in the gas exchange region

---

[ii]Since the initial online publication of these results, comparable findings were reported by Qing et al [141] in a cohort of healthy volunteers and COPD patients.

(capillary bed), whilst the latter represents the complete transit time of a gadolinium contrast bolus from the right heart, through the pulmonary-arterial system and lung gas exchange vasculature and back to the left atrium through the pulmonary-venous system. Although the lung FWHM metric potentially provides a closer representation of the CTT measurement, the mean MR signal from the lung ROIs was close to the noise level (even with contrast enhancement) in many patients and thus it was difficult to accurately estimate the FWHM; this may explain the observation of larger FWHM values than PTT values.

The HCT values derived from the MOXE and Månsson et al models were in general lower than results obtained from patient blood samples. The CSSR-HCT was found to be reduced in patients with IPF when compared with healthy volunteers ($P < 0.05$), although blood samples indicated relatively normal values in those patients. As recently highlighted [140], the HCT in the narrow capillaries is reduced (to values as low as 0.28) when compared to the whole-body HCT – due to the Fåhraeus effect [321]. Although this may partially explain the low HCT values for healthy subjects, it does not indicate why the CSSR-derived HCT of IPF patients should be further reduced. However, fixing the HCT to a plausible value in the expected range (0.4-0.5) and repeating the fitting process, tends to yield increased ST values for all subjects. Thus, the apparent reduced HCT values in patients may actually be a further artefact of inhibited gas exchange / septal thickening and the complex, inter-dependent nature of the model parameters. In fact, the HCT was found to correlate with the ST parameter for both models on the $P < 0.01$ level.

Modelling

Based upon the statistical testing, it could be argued that each of the three models assessed are useful for quantification of lung microstructural changes in IPF and SSc. A visual comparison of the application of each of the three models to ^{129}Xe CSSR data from a single healthy volunteer is shown in the left panel of Figure 6.10. It can be seen that each of the three models describes the data reasonably well; the goodness-of-fit as determined from conventional R^2 and χ^2 statistics was typically better for MOXE and Patz et al models than the Månsson et al model, because the latter fails to follow the middle section of the uptake curves as accurately as the other two models, suggesting that it is not appropriate to only consider a single exponential component of diffusive uptake. Also depicted in Figure 6.10 (right panel, (ii)) are Bland-Altman plots highlighting the systematic differences between CSSR parameters extracted from all three models. As expected due to the geometries employed, the Patz et al and MOXE models were found to show similar characteristics, whereas the Månsson et al ST values were consistently lower than those of the MOXE model, with an increased discrepancy in patients. Despite these systematic differences, parameters extracted from all models correlated with each other to the significance level of $P < 0.01$.

Since the MOXE model is an incremental extension of the Patz et al model, providing estimates of additional parameters of lung physiology, it would seem to be the most up-to-date and logical model to use in CSSR studies wherein the dissolved ^{129}Xe resonances can be spectrally resolved. Despite this fact, an increased number of inter-dependent fitting parameters may obscure their interpretation; for example, in this study the tissue-barrier-to-septum ratio parameter ($\frac{\delta}{d}$, could not be compared between subject groups due to the fact that in some cases, the parameter tended towards unrealistically low and even negative values. Hence in all fitting results shown, $\frac{\delta}{d}$ was restricted to lie within a range 0.05-0.30 (note, this restriction had a negligible effect on the values of the other fitting parameters). Therefore, in future work, it may be advantageous to reduce the complexity of the MOXE model, by constraining the fit parameters.

To this end, with further data, we may be able to establish a link between the CTT parameter and DCE-MRI data and could utilise this to yield prior knowledge about the CTT. Similarly, it may be possible to estimate the true tissue-barrier-to-septum ratio from the RBC-to-T/P signal ratio measurements, which provide a representation of the relative fractions of xenon in parenchymal tissues and blood. In combination with knowledge of the HCT (e.g. from blood samples) the MOXE fitting process could be reduced to a 2- or 3-parameter problem, though some correction may be required to account for the Fåhraeus effect.

Experimental limitations

Achievement of precise 90° excitations of dissolved-phase ^{129}Xe magnetisation in vivo can be challenging, as discussed in the following subsection. The design of the flexible transmit-receive coil used in this work does not deliver a uniform flip angle across the whole of the lungs ($\sim 16\%$ variation overall; the ratio of standard deviation to mean flip angle quoted in the caption of Figure 4.8). Of course, the delivered flip angle is dependent upon the position of the flexible coil, and the loading realised by subjects which will be of various shapes and sizes. The coil transmit inhomogeneity has important implications for CSSR measurements. Since the acquired ^{129}Xe spectra represent whole-lung averaged signals, the averaging process takes into account not only the heterogeneity in gas exchange function across the lungs, but also the spatial variation in delivered flip angle. Furthermore, we often observed elevated dissolved ^{129}Xe signal amplitudes at the start of the first TR sweep, which may be associated with $\boldsymbol{B_1}$ inhomogeneity and hence imperfect dissolved ^{129}Xe saturation. Indeed, the early data points may be affected not only by the unknown time for which gas exchange can occur during inhalation, but also by ^{129}Xe signal outside the active region of the coil (this effect was not observed in subsequent TR sweeps). More homogeneous transmitter coils (e.g. of birdcage design [322]) could be utilised; however these would typically be larger and less power-efficient than flexible coils, necessitating increased RF powers to achieve complete saturation of dissolved-phase ^{129}Xe.

Aside: CSSR with incomplete saturation of dissolved-phase ^{129}Xe

90° RF pulses are not readily achievable for ^{129}Xe in the thorax due to a combination of factors, including: the gyromagnetic ratio of ^{129}Xe is almost four times smaller than that of ^{1}H, meaning that the B_1 field strength required to achieve the same excitation flip angle is four times greater; RF amplifiers provided for support of non-^{1}H nuclei typically have a lower power output compared with ^{1}H amplifiers. The compromise solution presented in Section 6.2 is the use of binomial composite pulses, which can be highly frequency-selective whilst maintaining a high power efficiency in terms of B_1 performance [iii].

Nevertheless, some sites / systems may not have the capability for designing and implementing arbitrary RF excitation pulses, and there may be no option for the use of higher-power broadband RF amplifiers capable of delivering a high enough B_1 field in the coil for such pulses. To this end, in this subsection, a model of the expected in vivo dissolved-phase ^{129}Xe magnetisation in a CSSR experiment for excitation flip angles of less than 90° is presented. This derivation assumes a perfectly homogeneous $\boldsymbol{B_1}$ field across the whole of the lungs.

[iii]The SAR associated with these binomial pulses at the flip repetition rates considered in this work is well within safe limits, however rigorous SAR simulations should be carried out before utilising these pulses in a sequence with extremely low repetition rate.
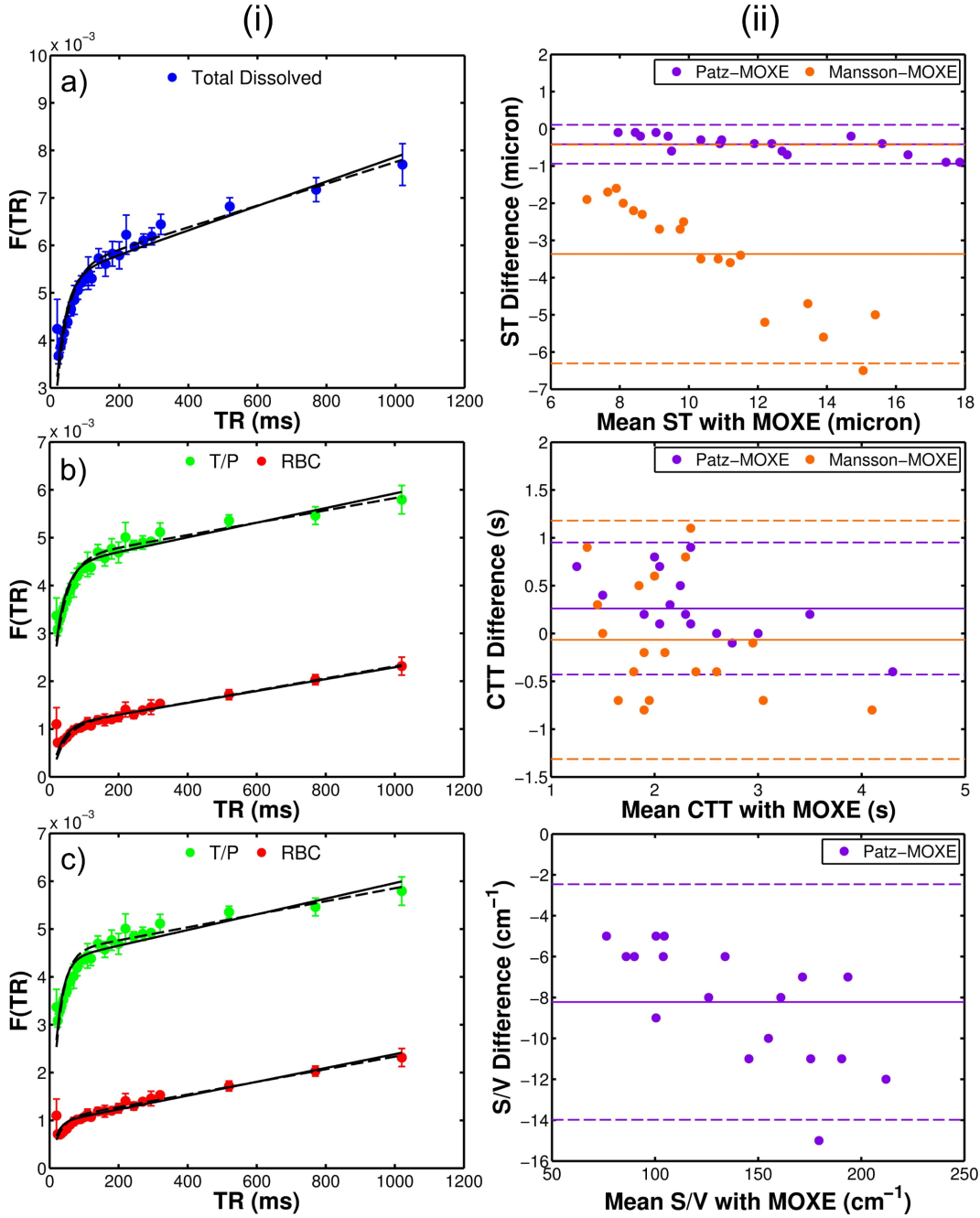
Figure 6.10: (i) Comparison of the accuracy and applicability of the a) Patz et al, b) MOXE and c) Månsson et al models in describing in vivo ^{129}Xe CSSR data from a single healthy volunteer. Blue data points denote the total dissolved ^{129}Xe signal intensities, green the T/P component and red the RBC component. The model fits are shown both with fit-weighting applied to the middle section of each curve (dashed lines), and in the absence of any weighting (solid lines). (ii) Bland-Altman plots of the systematic differences in CSSR-derived parameters (septal thickness (top), capillary transit time (centre) and surface-area-to-volume ratio (bottom)) between models, in each case comparing the Patz et al and Månsson et al model results to those of the MOXE model.

From Equation 3.125 (see Section 3.2.6), it is known that the decay in signal of a hyperpolarised species in a gradient-spoiled pulse sequence is dependent upon the excitation flip angle α, repetition time TR and number of RF pulses n. By considering the propagation of magnetisation at different stages during

the standard CSSR pulse sequence (see Figure 6.2), and using Equation 3.125 as a basis, a model of the expected uptake of ^{129}Xe gas into the bodily tissues and blood during a certain uptake time TR can be derived. In the following, TR is considered to vary in an arbitrary fashion for each RF pulse, such that TR_n denotes the repetition time immediately following the nth RF pulse. This derivation considers only the combined dissolved-phase ^{129}Xe signal, i.e. not separating the signal into its constituent T/P and blood components. Defining $M_{z(0),d}$ and $M_{z(0),g}$ as the dissolved and gaseous ^{129}Xe longitudinal magnetisations at time zero [iv], we can write the following expressions for dissolved and gaseous ^{129}Xe longitudinal magnetisations after the first repetition time, TR_1:

$$M_{z(1),d} = M_{z(0),d}\cos(\alpha_d)\exp\left(-\frac{TR_1}{T_{1,d}}\right) + K_{gd}\left(TR_1\right)M_{z(0),g}\exp\left(-\frac{TR_0}{T_{1,g}}\right) \tag{6.11}$$

$$M_{z(1),g} = M_{z(0),g}\cos(\alpha_g)\exp\left(-\frac{TR_1}{T_{1,g}}\right) + K_{dg}\left(TR_1\right)M_{z(0),d}\exp\left(-\frac{TR_0}{T_{1,d}}\right) \tag{6.12}$$

where, $K_{gd}\left(TR_1\right)$ and $K_{dg}\left(TR_1\right)$ describe the rate of transfer of ^{129}Xe nuclei from the gaseous to dissolved compartments (and vice-versa) respectively, during repetition time TR_1. These terms are essentially equivalent to $F\left(t\right)$ in the Patz et al model, and its associated reverse process (i.e. the transfer of ^{129}Xe nuclei from the tissues and blood into the airspaces), respectively. The transverse magnetisation of either dissolved or gaseous ^{129}Xe can be calculated using:

$$M_{xy(n)} = \sin(\alpha)M_{z(n-1)} \tag{6.13}$$

This model fundamentally assumes that just prior to the point of application of a RF pulse, the transverse magnetisation of the dissolved ^{129}Xe spins, $M_{xy(n-1),d} = 0$. This assumption is valid because all magnetisation is spoiled at the end of each TR, and the dissolved-phase ^{129}Xe T_2^* is intrinsically short (see Section 3.2.6). Furthermore, $M_{xy(n-1),g}$ is considered to be negligible; the excitation flip angle for gaseous ^{129}Xe is typically very small, and additionally, any excited gaseous-phase ^{129}Xe magnetisation that exchanges during the TR will be dephased by the short T_2^* associated with the dissolved-phase.

Extrapolating Equations 6.11 and 6.12 to an arbitrary number of RF pulses, n, the expression for the dissolved-phase ^{129}Xe longitudinal magnetisation immediately after pulse n, $M_{z(n),d}$, is:

$$\begin{aligned} M_{z(n),d} &= M_{z(n-1),d}\cos(\alpha_d)\exp\left(-\frac{TR_n}{T_{1,d}}\right) + K_{gd}\left(TR_n\right)M_{z(n-1),g}\exp\left(-\frac{TR_{n-1}}{T_{1,g}}\right) \\ &\equiv \frac{S_d\left(TR_{n+1}\right)}{\sin\left(\alpha_d\right)} \end{aligned} \tag{6.14}$$

and, for the gaseous ^{129}Xe longitudinal magnetisation, $M_{z(n),g}$:

[iv] Time zero is defined as the time immediately prior to the application of the first RF pulse. There will be an unknown amount of gas exchange prior to the application of this pulse during inhalation of the bag and commencement of the scan.

$$M_{z(n),g} = M_{z(n-1),g}\cos(\alpha_g)\exp\left(-\frac{TR_n}{T_{1,g}}\right) + K_{dg}\left(TR_n\right)M_{z(n-1),d}\exp\left(-\frac{TR_{n-1}}{T_{1,d}}\right)$$
$$\equiv \frac{S_g\left(TR_{n+1}\right)}{\sin\left(\alpha_g\right)}$$

<div align="right">(6.15)</div>

where $S_d\left(TR_n\right)$ and $S_g\left(TR_n\right)$ are the dissolved and gaseous ^{129}Xe MR signals measured in the CSSR experiment (i.e. the signal intensities of each NMR peak). As expected, the dissolved ^{129}Xe longitudinal magnetisation is governed by both the residual (un-excited) dissolved ^{129}Xe longitudinal magnetisation due to a flip angle of less than 90°, and the available longitudinal magnetisation from the gaseous-phase ^{129}Xe at the start of the TR. These relations are recurrence relations, and hence must be solved simultaneously. We note that in the case of $\alpha_d = 90°$, the dissolved ^{129}Xe magnetisation is solely determined by the exchange term, and $M_{z(n),d} \equiv S_d\left(TR_n\right)$.

The flip angles α_d and α_g and spin-lattice relaxation times $T_{1,d}$ and $T_{1,g}$ are either known, can be measured experimentally, or can be included as additional fitting parameters in the CSSR modelling process; although the latter is impractical for reasons discussed in the previous subsection. Since $K_{gd}\left(TR_n\right)$ is the analogue of the $F\left(t\right)$ parameter from the Patz et al model, these recurrence relations should be applicable for determining $F\left(t\right)$ for any arbitrary combination of the flip angles α_d and α_g.

As yet, the applicability of these recurrence relationships to in vivo ^{129}Xe CSSR data has not been properly assessed. Preliminary ^{129}Xe CSSR data in one volunteer acquired at $\alpha_d = 30, 50, 70, 90°$ suggested that the $< 90°$ data can be retrospectively "corrected" such that the uptake curves from each acquisition approximately overlaid each other (data not presented here). However, a thorough study involving many subjects should be carried out before any conclusions about the accuracy of correcting CSSR data with $< 90°$ flip angles, and whether or not the CSSR fitting parameters are adequately preserved at different values of α_d.

Nevertheless, a more pragmatic and relatively straightforward, although costly, solution is to install a higher-power broadband RF amplifier, which we have recently done in Sheffield. With a 4 kW amplifier (double the power output of our previous amplifier), we can readily achieve 90° pulses in a short period of time.

6.4.1 Future perspectives: Linking lung microstructural changes inferred from ^{129}Xe CSSR and ^{3}He ADC mapping

This subsection provides brief details of an ongoing project related to ^{129}Xe CSSR in our laboratory, concerned with the relationship between microstructural changes in the alveoli measured by ^{129}Xe CSSR and ^{3}He apparent diffusion coefficient (ADC) mapping in subjects with interstitial and obstructive lung diseases.

ADC mapping MRI with ^{3}He has demonstrated clinical utility for regional assessment of lung microstructure, and is sensitive to alterations in alveolar dimensions, particular in emphysematous disease (see e.g. [101, 108] and Chapter 5 of this thesis). As demonstrated earlier, the ^{129}Xe CSSR spectroscopy technique is a promising functional tool for pulmonary gas exchange assessment, sensitive to alterations in

septal thickness in interstitial lung disease and COPD / emphysema. However, the relationship between pathology-induced changes to alveolar airspace dimensions and septal wall dimensions measured from these two techniques has not been explored in healthy volunteers or patient populations. Moreover, the functional sensitivity of hyperpolarised ^{3}He ADC mapping has not been investigated in subjects with ILD to date.

The objectives of this work were to evaluate the feasibility of ^{3}He ADC mapping and ^{129}Xe CSSR in patients with ILD and COPD / emphysema, and to appraise the relationship between derived parameters of lung microstructure in order to better characterise the underlying microstructural behaviour in these pathologies.

Subjects recruited for this study included: 10 healthy volunteers from the study presented in Section 6.2, plus 10 additional volunteers (of mean age 42 ± 8 years); 4 patients with idiopathic pulmonary fibrosis (from Section 6.2); 4 patients with systemic sclerosis (from Section 6.2), plus 4 additional SSc patients; 5 patients with COPD (described in more detail in the following chapter, see Section 7.2, and Table 7.1). Note: MR-derived metrics of lung microstructure from COPD patients (in which multiple, repeated scans were performed, see Section 7.2) were averaged to provide a single value for each patient and ensure consistency of inter-group comparisons.

All patients underwent both ^{129}Xe CSSR and diffusion-weighted ^{3}He MRI, however, some volunteers were recruited for specific scan types only; as a result, only 12 volunteers performed both scans. The experimental methodology for ^{129}Xe CSSR spectroscopy has been detailed in Sections 6.2 and 7.2. Experimental details of the ^{3}He ADC mapping acquisition have been described in Section 5.2. Subjects underwent pulmonary function tests including; $T_{L,CO}$, FEV_1 and FVC for comparison to MRI data.

Statistically-significant differences in parameters between subject groups were evaluated according to a two-tailed analysis of variance (ANOVA) with post-hoc contrast, and the relationship between MR-derived metrics and PFTs was assessed using Spearman's correlation coefficient. It was hypothesised that the fundamental differences in underlying microstructural response to disease between interstitial and obstructive pathologies would constrain the interpretation of an inter-group correlation between ^{129}Xe CSSR and ^{3}He ADC values in all subjects. As such, subjects with IPF and SSc were considered separately from subjects with COPD in the correlation analyses.
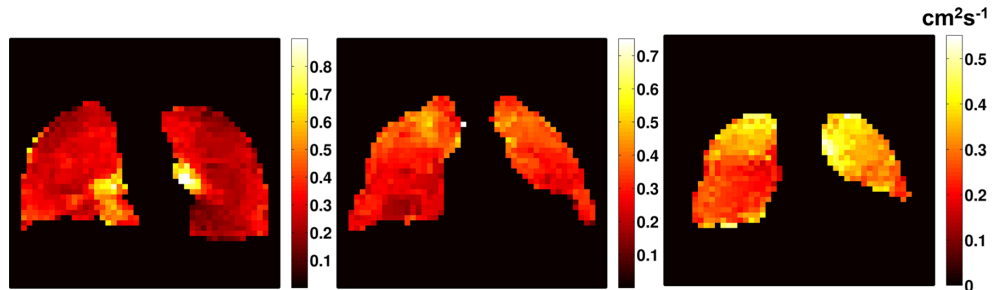
Figure 6.11: Representative single slice ^{3}He ADC maps acquired from an IPF patient.

Example ^{3}He ADC maps from a patient with IPF are depicted in Figure 6.11. This subject was observed to have clear bullous emphysema in the apices of the lungs on accompanying CT scans, particularly in

151

the anterior slices; this was further highlighted by regionally elevated ^{3}He ADC values in those regions. All other IPF and SSc patients did not exhibit co-existing emphysema in addition to their diagnosed interstitial disease, hence this particular patient was excluded from the ^{129}Xe CSSR versus ^{3}He ADC correlation analysis (red circled data-point in Figure 6.13).

Since ^{129}Xe CSSR provides a global mean assessment of lung microstructure, it is appropriate to compare the CSSR-derived septal thickness (ST) with the *global mean* ^{3}He ADC. As has been presented earlier in this chapter, the ST was found to be significantly larger in IPF patients and COPD patients as compared with healthy volunteers. (Although the mean ST difference between healthy volunteers and SSc patients was found to be significant in Section 6.3, the additional subjects included here have led to the statistical significance being reduced above the $P > 0.05$ level.) In addition, global ^{3}He ADC values were elevated in all patient groups compared with healthy volunteers, at the $P < 0.05$ level. In both cases, SSc patients exhibited the next-largest mean ST and ADC parameters after healthy volunteers, and, whilst the ST was greatest in IPF patients, the ADC was greatest in COPD patients, reflecting the intrinsically differing pathological action of these two diseases. Box plots illustrating the group-to-group differences in ^{129}Xe CSSR-derived ST and ^{3}He DW-MRI-derived global ADC are shown in Figure 6.12.
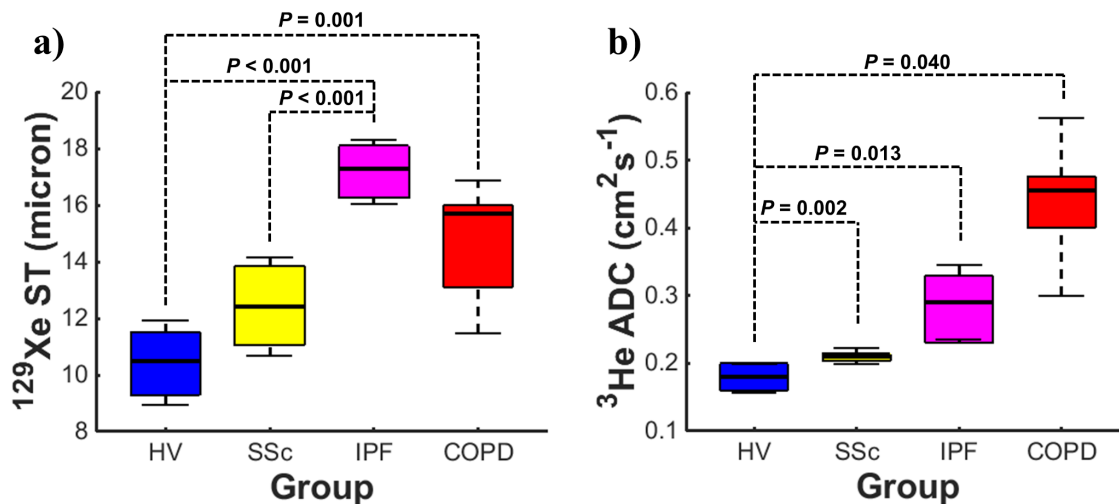
Figure 6.12: Comparison of global alveolar septal thickness values from ^{129}Xe CSSR (a) and global mean ^{3}He ADC values (b) in healthy volunteers (HV), systemic sclerosis (SSc), idiopathic pulmonary fibrosis (IPF) and chronic obstructive pulmonary disease (COPD) patients. Significant differences between groups are indicated by dashed lines and corresponding P values.

The ^{129}Xe CSSR ST and ^{3}He ADC measurements therefore suggest that interstitial lung disease and obstructive / emphysematous lung disease both impact adversely on gas exchange function and cause enlargement of the alveolar airspaces. The correlation between ^{129}Xe ST and ^{3}He global ADC values is shown in Figure 6.13, with separate linear regression lines plotted for healthy volunteers combined with SSc and IPF patients, and healthy volunteers combined with COPD patients. This separate analysis is necessitated by the opposite trend in greatest ST and ADC values in IPF and COPD patients, respectively (as illustrated by Figure 6.12).

In order to further investigate the origin of the functional changes to the septum and the airspace in these diseases, the two MR-derived metrics were compared to standard PFTs. ^{129}Xe CSSR-derived septal

thickness values correlated well with $T_{L,CO}$ and FVC metrics ($r = -0.80$, $P < 0.001$ and $r = -0.55$, $P = 0.003$, respectively in all available subjects) but not with FEV_1 ($P > 0.05$). Global mean ^{3}He ADC values exhibited strong correlations with $T_{L,CO}$ ($r = -0.84$, $P < 0.001$) and FEV_1 ($r = -0.92$, $P < 0.001$), but not FVC ($P > 0.05$). Other groups have reported strong correlations between ^{3}He ADC and $T_{L,CO}$ [85, 298], suggesting that the ADC measurement is inherently influenced by gas exchange function. However, as considered in a previous subsection, the $T_{L,CO}$ is actually defined as the product of the gas exchange rate K_{CO} and the alveolar volume V_A (see Equation 3.5). Thus, it is possible that the correlations of ^{129}Xe ST and ^{3}He ADC with $T_{L,CO}$ are dominated by different components of $T_{L,CO}$ (for example, K_{CO} and V_A, respectively).
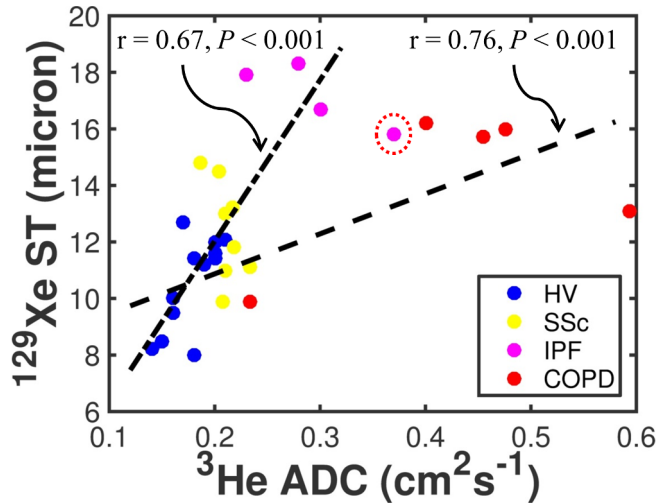
Figure 6.13: Observed correlations between global ^{3}He ADC and ^{129}Xe CSSR septal thickness, including separate linear fits for ILD subjects (small dashes) and COPD subjects (large dashes), with corresponding Spearman's correlation coefficients (r) and P values. Red dashed circle: IPF patient with established emphysema that was excluded from correlation analysis due to the conflicting pathological information contained within the whole-lung average measurements.

This project is ongoing; further investigations are required to fully explore the relationship between ^{129}Xe CSSR- and ^{3}He DW-MRI-derived metrics of lung microstructure in order to determine the fundamental disease mechanisms underpinning lung microstructural remodelling in ILD and COPD. In addition, as presented in Chapter 5, the feasibility of using ^{129}Xe DW-MRI to access the same microstructural information as ^{3}He DW-MRI is currently being assessed. However, an important limitation of the current ^{129}Xe CSSR method in comparison to hyperpolarised gas ADC mapping MRI is the lack of regional specificity afforded by whole-lung spectroscopy. This is particularly crucial in ILD and COPD patients where regional disease heterogeneity is very common. This limitation is addressed in Section 7.4.1.

Conclusions

CSSR spectroscopy with hyperpolarised ^{129}Xe is capable of detecting alterations in whole-lung structure-function in interstitial and obstructive forms of lung disease, via the non-invasive measurement of alveolar septal thickness. Statistically significant septal thickening has been detected in patients with IPF and COPD, and also, preliminary evidence suggests some septal thickening in patients with SSc. Further data may elucidate whether the ^{129}Xe CSSR technique is sensitive to age-dependent changes in lung septal structure. Previously established models of xenon uptake have been reviewed and each has been shown to effectively distinguish between ILD subjects and healthy volunteers to a high level of statistical significance. Additionally, the ^{129}Xe CSSR technique has been compared for the first time against gold-standard

clinical methods, including $T_{L,CO}$ and DCE-MRI. Ongoing work to reconcile the lung microstructural alterations in interstitial lung disease and COPD with ^{129}Xe CSSR in conjunction with ^{3}He ADC mapping MRI has been presented. ^{129}Xe CSSR shows considerable potential for application in a number of novel studies to provide information not readily obtainable by CT or pulmonary function testing. In future, the sensitivity of the technique to fibrosis treatment response, or early changes in ILD, should be assessed to facilitate clinical application.

Chapter 7

Reproducibility and methodological considerations for implementation of the ^{129}Xe CSSR technique

7.1 Introduction

Previous studies with ^{129}Xe CSSR in human subjects have been limited to small patient cohorts, and the reproducibility of the technique has yet to be assessed. The reproducibility of MR-derived functional measures is critical to determining their sensitivity and robustness for future clinical applications as a quantitative outcome measure (see e.g. [323]). For example, though the efficacy of ^{3}He apparent diffusion coefficient mapping for characterisation of emphysema has been well-known for many years [101], the reproducibility of the technique is key to facilitating increased application in a clinical setting [291, 292]. Similarly, ^{129}Xe CSSR-derived measures of pulmonary gas exchange must be demonstrated to be sufficiently reproducible before the sensitivity of the method to disease-related changes in lung structure and function can be adequately assessed.

Building upon the initial experimental validation of the ^{129}Xe CSSR technique presented in Chapter 6, the purpose of this work was to evaluate the intra-subject reproducibility of ^{129}Xe CSSR-derived quantitative parameters of lung microstructure and function in COPD / emphysema patients and age-matched healthy volunteers. Following on from the discussion in Section 6.4, some of the important considerations for implementation of the CSSR method are evaluated by experimental measurements and reviews of previous literature. In particular, the sensitivity of the technique to MR pulse sequence strategy and to lung inflation state is examined by assessing the reproducibility of two existing implementations of the CSSR sequence and performing CSSR experiments at different inflation levels in healthy volunteers, respectively. Furthermore, the fundamental assumptions of the analytical models of CSSR data (introduced in Section 6.2), and the current paucity of literature supporting the choice of xenon physico-chemical constants required as a basis for these models, and the interpretation of the derived estimates of lung microstructure, is discussed in detail. Finally, as a first step towards achieving spatial sensitivity with the CSSR method, a means to obtain regionally-localised, dynamic CSSR data is presented by interleaving the standard CSSR pulse sequence with phase encoding strategies as in chemical shift imaging (CSI), in what we denote a "CSI-CSSR" acquisition.

design, NJS, FCH, DPY, RL, HM, JMW; acquisition of data, NJS, FCH, GN, GJC, HM; analysis of data, NJS; preparation of manuscript, NJS, FCH, GN, GJC, HM, JMW.

7.2 Methods

The reproducibility study was divided into two parts: (i) preliminary investigations of the reproducibility and robustness of performance of two different pulse sequence implementations of the ^{129}Xe CSSR method, and quantification of the effect of lung inflation level on CSSR-derived lung microstructural parameters in healthy volunteers; (ii) reproducibility measurements with one implementation of the CSSR sequence at fixed inflation level in COPD patients and age-matched healthy volunteers.

Preliminary study (i): Five healthy volunteers (mean age $\pm$ standard deviation, 38 ± 14 years) with no history of respiratory disease were recruited (subject demographics shown in Table 7.1). To examine the reproducibility of two different implementations of the CSSR sequence existing in the literature, each subject was scanned on three separate days over a period of 1-3 weeks using the same scanner and experimental set-up as in Section 6.2. The two implementations of the ^{129}Xe CSSR sequence are hereafter defined as the "multi-sweep" and "multi-sat" sequences for the purpose of this preliminary study (see Figure 7.1). The "multi-sweep" sequence is the exact sequence described in Section 6.2, employing the use of single saturation pulses to destroy the magnetisation of ^{129}Xe dissolved in T/P and RBCs, followed by a variable inter-pulse wait period (repetition time, TR), during which alveolar-capillary gas exchange occurs and polarised ^{129}Xe gas diffuses into the T/P and RBC compartments. Multiple repeats of the "TR sweep" are acquired and averaged, as discussed earlier. Sequence parameters were identical to those described in Section 6.2.

The "multi-sat" sequence, as detailed in [140, 141], employs multiple saturation pulses prior to each variable wait period and involves no averaging. This sequence was implemented with the following parameters: RF pulse and bandwidth as for the multi-sweep case; 128 sampling points (increased relative to the multi-sweep implementation because the minimum achievable exchange time is not limited by the read-out duration in the multi-sat sequence); 21 TR values from 20-1000 ms.

In each case, a gas dose of 350-400 mL xenon (86% ^{129}Xe, polarised to $\sim 25\%$ using the "upgraded" polarisation system described in Section 4.4.1), balanced to 1 L with nitrogen, was inhaled from a Tedlar bag from functional residual capacity (FRC) prior to a 10-15 second breath-hold. CSSR data were fitted with the model of Chang (MOXE) [139], using a xenon diffusion coefficient in the dissolved-phase of $D = 3.0 \times 10^{-6}$ cm^2.s^{-1} and an Ostwald solubility coefficient of xenon in tissue of 0.1 [138], to estimate whole-lung alveolar septal thickness (ST) and surface-area-to-volume ratio (S/V).

In order to investigate the change in CSSR-derived parameters with lung inflation level, multi-sweep CSSR data were acquired at three different lung inflation levels from three healthy volunteers (24(M), 28(M) and 31(M) in Table 7.1). Sequence parameters and acquisition strategy were as above. The following inflation levels were attained prior to breath-hold and data acquisition: 1) forced exhalation to residual volume (RV), followed by inhalation of the 1 L xenon-nitrogen mixture; 2) exhalation to FRC, followed by a 1 L inhalation; 3) exhalation to FRC, followed by inhalation of the 1 L dose and additional inhalation of room air to reach total lung capacity (TLC).

156

Demographics				PFT Parameters					MRI Measurements			
Group	Age (Sex)	FEV_1 (%-pred)	CV (%)	FEV_1/FVC (%-pred)	CV (%)	$T_{L,CO}$ (%-pred)	CV (%)	Mean ST (μm)	CV (%)	Mean S/V (cm^{-1})	CV (%)
HV1	24(M)	107.8	-	97.5	-	-	-	11.1 ± 0.3	2	286.7 ± 71.8	25
HV1	32(F)	115.8	-	91.9	-	-	-	10.5 ± 0.5	5	259.9 ± 49.8	19
HV1	42(M)	97.7	-	93.9	-	-	-	12.4 ± 0.7	5	237.7 ± 68.0	29
HV1	63(F)	119.7	-	101.3	-	-	-	12.6 ± 0.6	5	171.8 ± 62.0	36
HV1	28(M)	107.8	-	89.4	-	-	-	11.0 ± 0.4	3	186.3 ± 30.8	17
HV1	31(M)	88.9	-	88.3	-	-	-	11.9	-	145.7	-
HV2	59(F)	100.8	-	97.8	-	-	-	13.5 ± 0.4	3	164.2 ± 44.2	27
HV2	55(M)	92.3	-	96.6	-	-	-	12.6 ± 0.3	3	238.6 ± 29.4	12
HV2	63(M)	100.9	-	93.0	-	-	-	12.3 ± 0.7	6	154.7 ± 41.2	27
HV2	58(M)	105.1	-	98.0	-	-	-	11.4 ± 0.6	5	261.8 ± 39.0	15
HV2	58(F)	79.2	-	105.5	-	-	-	11.4 ± 0.4	4	180.4 ± 9.2	5
HV2	62(M)	97.3	-	93.7	-	-	-	10.5 ± 0.1	1	185.5 ± 24.5	13
HV2	40(F)	110.3	-	101.3	-	-	-	10.9 ± 0.6	5	84.4 ± 5.2	6
HV2	54(M)	101.5	-	106.3	-	-	-	11.5 ± 0.3	3	322.8 ± 24.7	8
HV2	66(M)	90.1	-	101.6	-	-	-	10.6 ± 0.7	7	155.9 ± 21.4	14
COPD	64(F)	31.5 ± 0.7	2	33.2 ± 0.6	2	33.2 ± 2.1	6	14.3 ± 1.8	12	70.9 ± 9.4	13
COPD	67(F)	45.4 ± 1.6	4	49.8 ± 0.7	1	98.4 ± 3.8	4	9.6 ± 0.3	3	215.8 ± 105.8	49
COPD	71(M)	31.0 ± 1.3	4	27.6 ± 1.1	4	13.6 ± 2.2	16	14.1 ± 1.2	9	75.5 ± 1.8	2
COPD	76(M)	43.5 ± 2.1	5	32.5 ± 0.8	3	29.6 ± 2.0	7	16.5 ± 0.3	2	90.5 ± 2.2	2
COPD	59(F)	38.6 ± 2.5	6	42.8 ± 0.8	2	38.0 ± 4.1	11	15.7 ± 0.6	4	130.0 ± 29.9	23

Table 7.1: Subject demographics, pulmonary function test (PFT) results and MRI parameters for the ^{129}Xe CSSR reproducibility study. HV1 = healthy volunteers recruited for preliminary investigations; HV2 = age-matched healthy volunteers recruited for reproducibility tests; COPD = patients with chronic obstructive pulmonary disease recruited for reproducibility tests. PFT = pulmonary function test; FEV_1 = forced expiratory volume in one second; FVC = forced vital capacity; $T_{L,CO}$ = diffusing capacity (transfer factor) of carbon monoxide; ST = septal thickness; S/V = surface-area-to-volume ratio; CV = coefficient of variation. %-pred = pulmonary functional parameters expressed as a percentage of a predicted value, based on demographic factors such as age and height. (All MRI measurements were derived from scans at FRC + 1 L, using the multi-sweep sequence.)
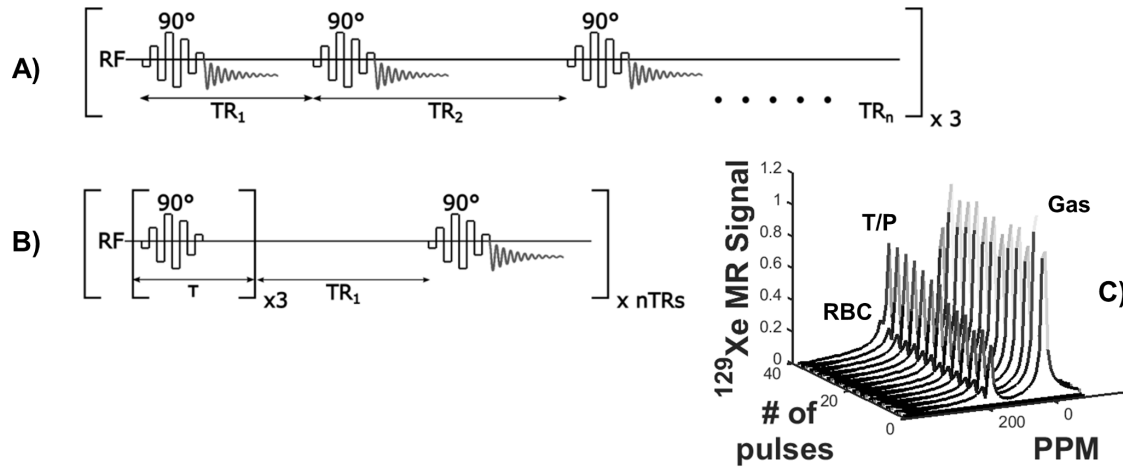
Figure 7.1: Schematic representation of the two implementations of the ^{129}Xe CSSR pulse sequence used in this work: A) 90° RF saturation pulses separated by a variable wait period (equivalent to the inter-pulse repetition time, TR); whole acquisition repeated three times ("multi-sweep" CSSR as in Figure 6.2). B) Multiple RF saturation pulses with a short inter-pulse delay, followed by a variable wait period; whole time-series acquired once ("multi-sat" CSSR). C) Typical time-series of ^{129}Xe NMR spectra acquired using the multi-sweep sequence, normalised to the gas peak. T/P: ^{129}Xe dissolved in tissues and blood plasma; RBC: ^{129}Xe in red blood cells.

Reproducibility measurements (ii): Nine healthy volunteers (59 ± 8 years) with no history of respiratory disease, and five patients with COPD (67 ± 6 years) were recruited (see Table 7.1). To assess the short- and long-term reproducibilities of ^{129}Xe CSSR, COPD patients were scanned on four occasions; twice on the first day, once the following day, and once two weeks later. Volunteers were scanned in three separate sessions on the same day, between which they were repositioned. In all cases, the multi-sweep sequence was employed, with parameters as above and a xenon dosage of 300-350 mL.

For comparison with MR measurements, conventional pulmonary function tests (PFTs) were performed by all subjects (see Table 7.1), including forced expiratory volume in one second (FEV_1) and forced vital capacity (FVC) manoeuvres. In addition, the transfer factor of carbon monoxide ($T_{L,CO}$) test was performed by COPD patients to provide a standard metric of pulmonary gas exchange. For the two healthy volunteer cohorts, PFT data were acquired on only one occasion since the variability of spirometry is well-known in healthy subjects [299], whilst for COPD patients, PFT data were obtained on each of the three scan dates.

To evaluate the reproducibility of each CSSR-derived functional parameter, the intra-subject standard deviation and coefficient of variation (CV; the ratio of the standard deviation (SD) to the mean value, expressed as a percentage) was calculated. A mixed model, repeated measures analysis of variance test was performed for each parameter to determine the significance of any time-dependent variations, according to the F-value (analogous to a conventional statistical t-value) and P value of statistical significance. Reproducibility data are presented as mean, SD and CV values and modified Bland-Altman plots [324] with CV on the y axis. An equivalent analysis was carried out for PFT measurements where applicable.

7.3 Results

In one participant from the age-matched healthy volunteer cohort (62(M) in Table 7.1), the signal-to-noise ratios (SNRs) of spectra obtained from one scan were insufficient to accurately fit the data and derive meaningful estimates of alveolar ST and S/V. Additionally, another participant from this group (59(F)) was unable to maintain breath-hold for the duration of one scan. Hence, only two data-points were used for reproducibility analysis in these subjects. For two COPD patients (64(F) and 67(F)), data were only successfully acquired once on the first day of scanning, and in a third patient (71(M)), spectral SNR was insufficient in one scan from the first day; thus, only three of four proposed acquisitions were available for reproducibility analysis in these patients.

Preliminary study (i): Mean ST values in the five healthy volunteers derived from multi-sweep and multi-sat sequences were 11.5 ± 0.9 μm and 12.6 ± 1.2 μm, and the corresponding mean CV values of ST were $4.1 \pm 1.3\%$ and $10.0 \pm 7.4\%$, respectively. Mean S/V values derived from the multi-sweep and multi-sat sequences were 228 ± 49 cm^{-1} and 195 ± 46 cm^{-1}, and the corresponding mean CV values of S/V were $25.1 \pm 7.8\%$ and $23.7 \pm 13.2\%$, respectively. Figure 7.2 depicts Bland-Altman plots of the intra- and inter-subject variations of ST and S/V parameters derived from the two sequences. (The intra-subject variability (reproducibility) is represented by the CV axis.)
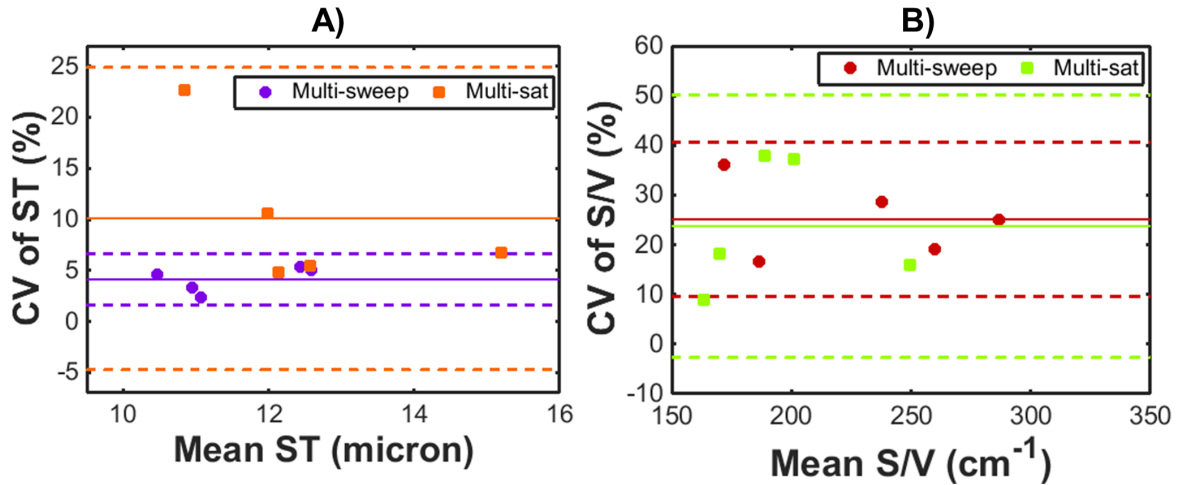
Figure 7.2: Preliminary investigation of the reproducibility of parameters derived from the two different implementations of the ^{129}Xe CSSR sequence, as assessed in five healthy volunteers. The coefficient of variation (CV) of CSSR-derived septal thickness (ST) and surface-area-to-volume ratio (S/V) values are plotted on Bland-Altman charts in A) and B), respectively. Solid lines represent the mean CV and dashed lines denote ± 2 standard deviations from the mean CV.

Mean ST values from the three healthy volunteers were similar at inflation levels of RV + 1 L (11.0 ± 0.1 μm) and FRC + 1 L (11.3 ± 0.5 μm), whilst the ST was significantly reduced ($P < 0.001$) at TLC (7.6 ± 0.5 μm) when compared with both RV + 1 L and FRC + 1 L, as shown in Figure 7.3A. S/V values exhibited a decreasing trend with inflation level (Figure 7.3B), with a significance of $P = 0.057$ between TLC (115 ± 16 cm^{-1}) and RV + 1 L (253 ± 66 cm^{-1}) (S/V at FRC + 1 L was 200 ± 62 cm^{-1}).
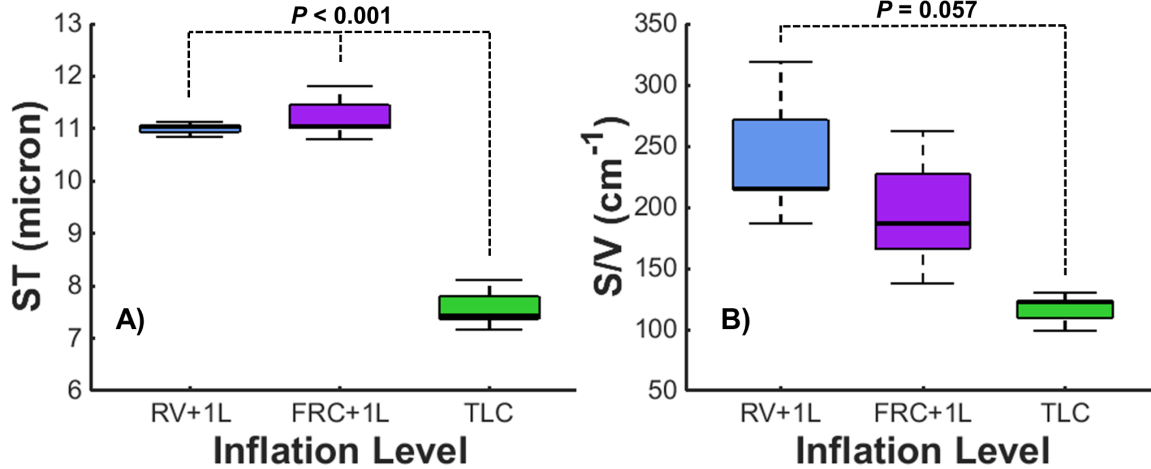
Figure 7.3: Mean ^{129}Xe CSSR-derived A): alveolar septal thickness (ST) and B): alveolar surface-area-to-volume ratio (S/V) measurements as a function of lung inflation level in three healthy volunteers. RV: residual volume; FRC: functional residual capacity; TLC: total lung capacity.

Reproducibility measurements (ii): The average of the mean ST in COPD patients $(14.0 \pm 2.7~\mu\text{m})$ was elevated when compared to age-matched healthy volunteers $(11.6 \pm 1.0~\mu\text{m})$ $(P < 0.05)$. Additionally, evidence of a reduced S/V ratio in COPD patients $(117 \pm 60~\text{cm}^{-1})$ when compared with volunteers $(194 \pm 70~\text{cm}^{-1})$ was observed $(P = 0.055)$. The mixed model analyses showed no significant changes in ST or S/V as a function of scan time-point, with F = 1.32, $P = 0.294$ and F = 2.48, $P = 0.116$ for healthy volunteers; F = 2.08, $P = 0.156$ and F = 0.27, $P = 0.845$ for COPD subjects, concerning ST and S/V, respectively. CV values of ST were $< 8\%$ and $< 13\%$ in volunteers and COPD patients, with a mean $\pm$ standard deviation of $3.9 \pm 1.9\%$ and $6.0 \pm 4.5\%$, respectively (see Figure 7.4A, C). CV values of S/V were $< 28\%$ and $< 50\%$ in volunteers and COPD patients, with a mean $\pm$ standard deviation of $14.1 \pm 8.0\%$ and $18.0 \pm 19.3\%$ (see Figure 7.4B, D).

Average FEV_1 and FEV_1/FVC measurements were significantly reduced in COPD patients when compared to volunteers $(P < 0.001)$ (see Table 7.1). In these patients, the mean CV values associated with pulmonary function tests were: $4.2 \pm 1.5\%$ for FEV_1; $2.4 \pm 1.1\%$ for FEV_1/FVC; $8.8 \pm 4.8\%$ for $\text{T}_{\text{L,CO}}$.

7.4 Discussion & Conclusions

The observation of improved reproducibility (lower CV) of ST for the multi-sweep when compared to the multi-sat implementation of ^{129}Xe CSSR may be a result of the reduction in variance of fitted data points arising from the multiple-averaging process. Nevertheless, upon separate analysis of the individual TR sweeps of the multi-sweep data-sets presented in Figure 7.2, no clear difference in mean CV of ST or S/V values derived from each of the sweeps — when compared with the multi-sweep average — was observed, other than the CV of ST of the first sweep being slightly higher than that of the other two sweeps (mean CV of ST = $4.1 \pm 1.3\%$ for all sweeps, $5.5 \pm 1.3\%$ for sweep 1, $3.5 \pm 2.4\%$ for sweep 2, $3.7 \pm 1.5\%$ for sweep 3, as summarised in Table 7.2). We suspect that the minor increase in CV for the first sweep could have resulted from the fact that this sweep is associated with the highest SNR data-points, and is thus more
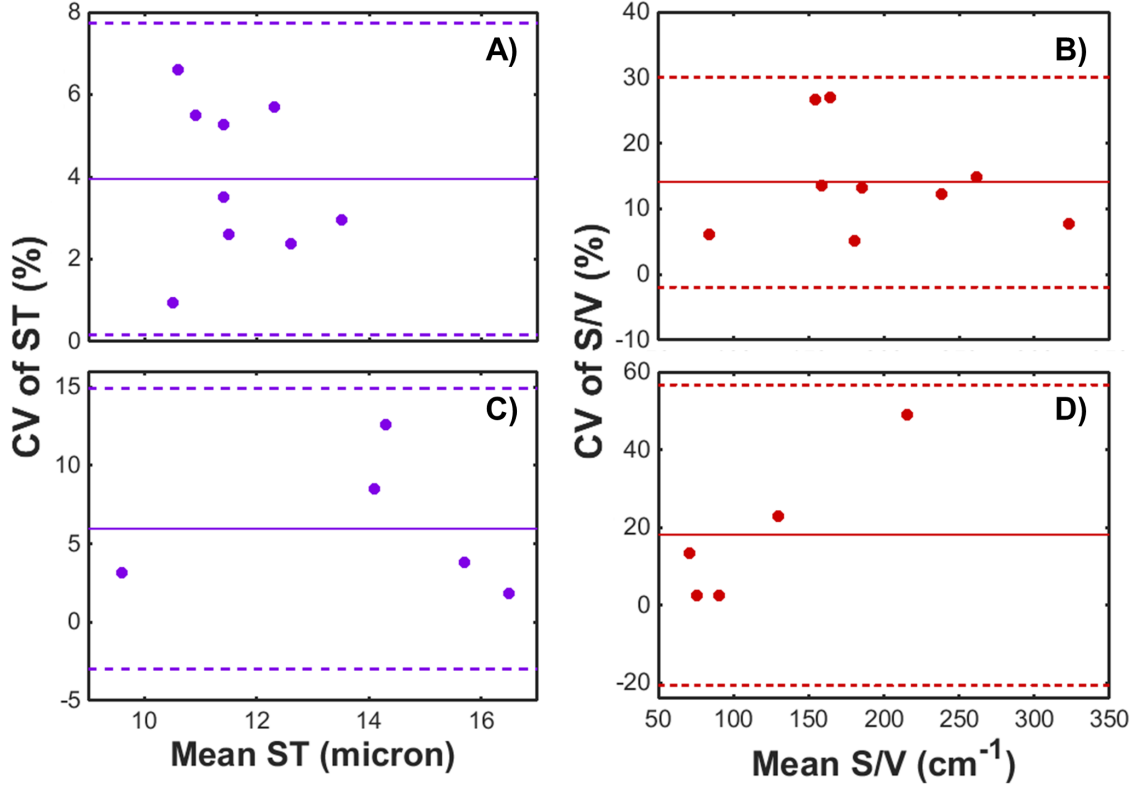
Figure 7.4: Reproducibility of ^{129}Xe CSSR-derived alveolar septal thickness (ST) and surface-area-to-volume ratio (S/V) values in COPD patients and age-matched healthy volunteers. A) and B): ST and SV values in healthy volunteers (mean age $= 59 \pm 8$ years). C) and D): ST and SV values in COPD patients (mean age $= 67 \pm 6$ years). Solid lines represent the mean CV and dashed lines denote ± 2 standard deviations from the mean CV.

sensitive to subtle changes in the shape of the uptake curve between scans. The latter two sweeps have lower SNR, and hence the fitting process results in a curve that approximates a noisier data-set, such that subtle changes between repeated scans may be less apparent. Additionally, it is worth noting that the mean CV for the multi-sat sequence is strongly influenced by an outlying data-point with a CV of ST of 22.7%, resulting from an anomalous ST value in one of the three repeated scans for that subject. In the absence of this outlying data-point, the mean CV between the two CSSR implementations would be considerably closer. Previously, multiple saturation pulses have been required to completely destroy the dissolved-phase ^{129}Xe magnetisation in human subjects [138, 140, 141]. However, the utilisation of a custom binomial-composite pulse design permits highly effective saturation of magnetisation with a single pulse [317]. The observation that the CV of S/V is similar between the two sequence implementations implies that the saturation process itself is reproducible, since the S/V is most strongly influenced by the early time-points of the CSSR experiment, where incomplete saturation could cause significant effects. In light of the apparent improved reproducibility of ST, the multi-sweep implementation was employed for subsequent experiments inflation-level and reproducibility experiments.

Xenon is perfusion limited (see Section 3.1.3) and, at all time-points during an in vivo ^{129}Xe CSSR experiment, it is assumed that the pulmonary capillaries are essentially saturated by xenon. Thus, we would not expect the xenon exchange dynamics to change significantly between subsequent sweeps of a multi-

TR sweep	Mean ST (μm)	Mean CV of ST (%)	SD CV of ST (%)	Mean S/V (cm^{-1})	Mean CV of S/V (%)	SD CV of S/V (%)
Average (all sweeps)	11.50	4.13	1.26	228.5	25.1	7.8
Sweep 1	11.36	5.47	1.29	230.0	25.3	7.7
Sweep 2	11.63	3.53	2.40	225.8	25.6	6.9
Sweep 3	11.58	3.69	1.48	226.6	25.1	8.0
Average (2 & 3)	11.63	3.30	1.63	225.6	25.4	7.5
Multi-sat (from paper)	12.55	10.0	7.4	194.6	23.7	13.2

Table 7.2: Reproducibility of derived ST and S/V parameters from individual sweeps of the multi-sweep CSSR experiment (method comparison study).

sweep CSSR experiment; in fact, it is an important assumption of the method that no change in exchange dynamics occurs over the entire course of the breath-hold. In addition, it is assumed that alterations to associated physiological parameters during the breath-hold (such as capillary oxygen saturation and heart rate) would influence the observed gas exchange behaviour to a negligible degree.

In this study we noticed no clear changes in subject heart rate over the course of the 15 second breath-hold (as recorded by pulse oximetry). However, if the heart rate *was* seen to change over the breath-hold, it may be expected that the rate of extraction of xenon from the capillary bed would be altered, and thus the slope of the perfusion-dominated section of the CSSR uptake curve could be different in the final sweep compared with the first sweep, for example.

In terms of oxygen saturation changes: as stated above, xenon is perfusion limited. Oxygen on the other hand exhibits a mixture of diffusion-limited and perfusion-limited behaviour, particularly in subjects with pathology. It is not thought that the oxygen and xenon binding sites in human deoxy-haemoglobin are the same [262, 325]. However, it may be possible that oxygen acts as an allosteric inhibitor on xenon, such that as the haemoglobin changes conformation (from oxy to deoxy-haemoglobin), the binding sites for xenon and the affinity of the molecule for binding xenon may change. Therefore, it is possible that if the oxygen saturation of the blood were to change considerably during the breath-hold, there may be an alteration of the rate of xenon uptake into the RBCs. However, the principle of the CSSR experiment assumes that the dissolved-phase is already saturated with xenon before starting the experiment – i.e. that the concentration of xenon in the dissolved-phase is roughly constant during the breath-hold, and hence even if this process occurred, its effect should be negligible.

The measured decrease in S/V and ST with lung inflation level can be explained by the expansion of the alveoli and stretching of the lung tissue at high inflation levels, respectively [326]. A reduction in CSSR-derived S/V has been previously reported with lung inflation level [248], and, although a change in CSSR-derived ST with inflation level has not been reported, recent observations of a decline in the ratio of ^{129}Xe T/P- or RBC-to-gas-phase resonances with increasing inflation level [141, 171] indicate a reduced contribution of the dissolved ^{129}Xe MR signal at higher inflation levels due to the lower volume fraction of the dissolved compartment.

Despite our observations, the interpretation of this data must be carefully considered in terms of the meaning of the different inflation levels. Although some recent ^{129}Xe CSSR studies in humans have used the same approach as that described here to achieve a desired inflation level of FRC + 1 L prior to data

acquisition [140], others have employed a procedure of quantifying the subject's TLC prior to MRI, and modifying the inhaled gas dose for each subject in order to achieve an inflation level that equates to a specific fraction of that subject's TLC [138, 141]. The second procedure ensures that the lungs are at an equivalent level of relative inflation in each subject, which should correspond to a comparable alveolar geometry. On the other hand, the inflation level of FRC + 1 L employed in this work may equate to a different fraction of each subject's TLC. In future work, it may be better practice to calculate an inhaled gas dose such that the inflation level is proportionate between subjects (e.g. 50% TLC), making comparisons between subjects more meaningful in terms of viable gas exchange surface. In addition, it may be beneficial to instruct subjects to exhale to RV rather than FRC in all cases prior to inhaling a xenon gas dose, in order to improve the validity of comparisons between different inflation levels. In the current work, whilst the inflation levels of FRC + 1 L and TLC were achieved from an initial state of FRC, the RV + 1 L level was reached from RV, and hence the xenon mixing may have been affected by the differences in residual gas in the lungs prior to inhalation of the xenon dose. On the other hand, it could be argued that the procedure for achieving the RV + 1 L and FRC + 1 L inflation levels should remain as described in Section 7.2 but the TLC level should be achieved by inhaling air up until TLC − 1 L and then inhaling the 1 L xenon dose afterwards. This alternative method ensures that the xenon dose is always the final amount of gas breathed in for each of the three inflation levels.

Assuming that the calculated variation in ST and S/V with lung inflation level cannot be fully explained by inter-subject differences in relative lung inflation level, this observation is an important consideration for future experimental ^{129}Xe CSSR studies; in that, it is crucial to carefully instruct the subject to ensure that the desired inflation level is achieved and that breath-hold is effectively maintained. It might be expected that patients would better-tolerate breath-holds at higher inflation levels than FRC + 1 L. Furthermore, we might also expect the reproducibility of derived ST and S/V metrics at TLC to be improved compared with FRC + 1 L, because TLC represents an extreme limit of lung inflation level, which should be easier to achieve for the patient (whilst the patients' perception of FRC may vary between scans). However, appropriate reproducibility tests must be carried out at TLC before routine ^{129}Xe CSSR studies are possible at this inflation level.

The mean ST and S/V values derived in this work are comparable to estimates obtained from alternative methods: ST $\sim 10 \mu$m from histological methods [327] including computerised morphometry [320, 328]; S/V in healthy volunteers ~ 250 cm^{-1} from histological methods [329] and 200-240 cm^{-1} from hyperpolarised ^{3}He diffusion-weighted MRI [103] (both these articles also reported a reduced S/V of $\sim 50 - 150$ cm^{-1} in a range of patients with severe to mild emphysema). In addition, our results are of the same order as those reported in recent ^{129}Xe CSSR studies with human subjects [138, 140, 141]. However, a direct comparison of the absolute ST and S/V values in this work and other ^{129}Xe CSSR studies in humans requires careful consideration of any discrepancies in the data acquisition and analysis approaches in those works, as discussed below. A thorough review of example literature references for ST and S/V values and a detailed explanation of the challenges in directly comparing our values to those of other ^{129}Xe CSSR studies in humans is provided later in this section.

It is important to consider that the data presented in this study can be analysed using models other than MOXE (see e.g. Section 6.4 and [138, 145, 309]). In Section 6.4, small differences in CSSR-derived lung microstructural parameters resulting from some of these models were highlighted. Furthermore, in

addition to discrepancies in data analysis procedure, most human studies with ^{129}Xe CSSR to date have been performed with slightly different assumptions about the value of critical physical parameters [138–141], such as the diffusion coefficient and Ostwald solubility of xenon in tissue, which have a significant bearing on the absolute derived ST and S/V estimates, respectively. A review of the approaches and assumptions considered in each of these works is presented in the next subsection.

The mean intra-subject standard deviation of CSSR-derived ST values of age-matched healthy volunteers (0.46 ± 0.21 μm)measured in this study is much less than the difference in mean ST between healthy subjects and IPF patients ($\sim 7\mu$m) as quantified in Section 6.3 (mean healthy subject ST = 10.0 ± 1.6 μm; mean IPF patient ST = 17.2 ± 1.1 μm for the MOXE model), and also less than the 2.4 μm mean difference between healthy subjects and COPD patients as presented in Section 7.3. In addition, the Bland-Altman plots in Figure 7.4 illustrate that the CV of ST does not appear to change with the mean value. These factors, coupled with the generally low CV values from volunteers and COPD patients ($< 8\%$ and $< 13\%$, respectively), provide substantive evidence that the CSSR-derived ST is a reproducible parameter. The CV of ST was comparable to that of PFT metrics of gas exchange; mean CV values in COPD patients were comparable to reported long-term variability of $T_{L,CO}$ (9% [301]), whilst the CV in healthy volunteers was of a similar magnitude to that of same-session variability of $T_{L,CO}$ [300].

On the other hand, mean CV values of S/V were above the target value for reproducibility of $T_{L,CO}$. This constrains the interpretation of apparent trends of reduced S/V in COPD patients and changes with lung inflation level. The S/V parameter is derived from the early time-points of the CSSR experiment, where dissolved ^{129}Xe signal-to-noise ratio is lowest [307]. In addition, it would be expected that incomplete saturation of magnetisation would adversely affect the derived S/V more-so than the ST, because the latter is predominantly influenced by later time-points. Furthermore, the complexity of the model of xenon exchange [139] and its multiple interdependent fitting parameters may lead to inaccurate estimates of S/V (whilst by definition of the model, it could be expected that ST values would be less influenced by these interdependencies). A combination of these factors may explain the relatively poor S/V reproducibility.

A further limitation of the reproducibility of the CSSR-derived S/V in patients is the outlying data-point (from subject 67(F)), with 49% CV. This subject exhibited a lower ST than all subjects, and whilst FEV_1 and FEV_1/FVC were $< 50\%$ of the predicted value, $T_{L,CO}$ was 98.1%-predicted; comparable to that of healthy subjects. Further study with larger patient populations and stricter lung inflation level control is necessary to identify these outliers and further validate the S/V reproducibility.

For both ST and S/V metrics, the intra-subject reproducibility was noticeably worse in COPD patients than healthy volunteers, despite similar results obtained from the mixed model analysis. This may be at least partially explained by the fact that patients were scanned on multiple days, whilst volunteers were scanned on a single day. Due to poor-quality or failed scans on the first day of the protocol, there was insufficient data available to accurately separate COPD patient reproducibility data into same-day or multi-day reproducibility data; hence CV values for these patients are dominated by inter-day variations. Additionally, it is worth considering that the reproducibility of the ^{129}Xe CSSR measurement is dependent on a variety of factors, including fluctuations in ^{129}Xe polarisation, reproducibility of lung inflation level, and successful maintenance of breath-hold for the scan duration; the latter two factors depend heavily on

the subject. Patients may have difficulty in inhaling the complete contents of the Tedlar bag, and/or may be less effective in maintaining breath-hold for the scan duration. It is possible to circumvent breath-hold failure in the third sweep by analysing data from the first or second sweeps only. However, factors such as lung inflation level are challenging to control, and it is prudent to carefully instruct the patient on the exact details of the protocol and perform training scans with bags of air prior to the CSSR scan itself, in a similar manner to the repeated procedure employed for pulmonary function testing [330].

Review of literature values of xenon diffusion constants and solubilities used in ^{129}Xe CSSR studies with human subjects

In the existing analytical diffusion models for estimating lung microstructural parameters from ^{129}Xe CSSR data [138, 139, 145, 309], the estimate of septal thickness is directly proportional to the square root of the xenon diffusion coefficient (D) in human lung parenchymal tissue and blood (see the relationship between the CSSR-fitted xenon exchange time constant (T), D and d in Equation 6.7), and the estimate of surface-area-to-volume ratio is inversely related to the septal thickness and the xenon solubility in the lung parenchyma (λ). This review summarises the discrepancies in the choice of values adopted for the xenon diffusion constant and solubility in previous ^{129}Xe CSSR studies in human subjects.

The effect of diffusion coefficient (D)

The diffusion coefficient in human lung tissue used in the present work (including both the studies described in Section 6.2 and 7.2) was $D = 3.0 \times 10^{-6}$ cm^2.s^{-1}, which was taken from the work of Patz et al [138, 248]. The value quoted by Patz et al were assumed to be valid, however, on further inspection, we noticed that Patz et al cited Sta Maria and Eckmann [331] as the origin of this value. In Table 1 of [331], estimated diffusivities of xenon in water, blood, and brain tissue of 1.55×10^{-5} cm^2.s^{-1}, 1.35×10^{-5} cm^2.s^{-1} and 5.4×10^{-6} cm^2.s^{-1}, respectively, are quoted, which were estimated using the methods described in the appendix of that article. The closest value that we can find to 3.0×10^{-6} cm^2.s^{-1} in [331] is 3.8×10^{-6} cm^2.s^{-1}, which is stated as the diffusion coefficient for xenon in rat liver tissue, originally taken from [332]. Thus, we are unsure of the exact origin of the 3.0×10^{-6} cm^2.s^{-1} estimate in [138, 248]; it may be that Patz et al applied some of the methods described in [331] to calculate a diffusivity for xenon in lung tissue, or the value may arise from inaccurate rounding of the value from [332].

Other previous ^{129}Xe CSSR studies in humans [139–141] have quoted a value of the total dissolved-phase xenon diffusion coefficient of $D = 3.3 \times 10^{-6}$ cm^2.s^{-1}. In addition, this value has been adopted in other (non-CSSR-based) ^{129}Xe dissolved-phase MRI studies in humans, e.g. Dregely et al [152] and Cleveland et al [144]. Each of these articles cites a study by Ruppert et al [265] as the source of this value.

Although this value has been accepted in a number of different studies, we believe that the origins of this value and its applicability to human lung tissue should be considered. Ruppert et al [265] derived this value from a ^{129}Xe CSSR-type experiment in rabbits; by fitting the total dissolved-phase ^{129}Xe signal intensity as a function of time post saturation of dissolved-phase ^{129}Xe magnetisation, and assuming a value for the whole-lung average septal thickness in rabbits in order to derive D. (This is essentially the reverse of what has been done in most standard ^{129}Xe CSSR experiments, which is to assume a dissolved-phase xenon diffusion coefficient in order to calculate a septal thickness.)

A key limitation of the validity of this value as the "standard" for D is that it was derived by assuming a global mean septal thickness value in rabbits rather than measuring the ST by other means. Ruppert et al quote a value of 5.5 μm as the average "membrane thickness" which they use to calculate D, citing Kovar et al [333] for this value. In fact, this value is not quoted explicitly in [333], so we must assume that Ruppert et al derived it from Figure 3c of [333], which depicts measurements of alveolar septal wall thickness as a function of rabbit age. Unfortunately, Ruppert et al do not specify the age of the rabbits used in their study, so it is not possible to verify that the assumed value of alveolar septal thickness is indeed determinable from this figure; instead, we must observe Figure 3c of [333] and infer that the age of rabbits in Ruppert et al's study was approximately 20 weeks. (It is worth noting that Figure 3c of [333] has considerable uncertainty associated with the wall thickness values (e.g. error bars $\sim 0.5 \mu$m).)

Ruppert et al [265] do state that there is a wide range of existing literature values for the xenon diffusion coefficient in different tissues and species, although in actuality, the extent of *relevant* literature is quite limited. Ruppert et al cite [334] as a reference that summarises relevant values of the xenon diffusion coefficient in dog and sheep tissue samples, in addition to human blood plasma. Reproducing the values in that article (measured at 37°C): in water, $D \sim 1.9 \times 10^{-5}$ cm^2.s^{-1}; in blood serum $D = 1.61 \times 10^{-5}$ cm^2.s^{-1} and in blood plasma $D = 1.51 \times 10^{-5}$ cm^2.s^{-1}; in sheep liver $D = 2.9 \times 10^{-6}$ cm^2.s^{-1}; in dog muscle, $D = 6.8 \times 10^{-6}$ cm^2.s^{-1}. Thus, it may indeed be expected that there is a wide range of xenon diffusion coefficients in different tissue types of varying compositions and functions.

On a related note, it cannot be assumed that the value of D in blood plasma is identical to that of whole blood – the presence of red blood cells would be expected to cause a significant alteration of xenon's diffusion properties in whole blood. Hence, even if we assume that the diffusion coefficient of xenon in blood plasma and lung parenchyma is the same, it is difficult to infer an average value of the xenon diffusion coefficient in lung tissues and whole blood from the above studies, and moreover, it is likely not appropriate to assume that the diffusion coefficient is the same in tissues and whole blood; an assumption which currently underpins the ^{129}Xe CSSR experiment.

Fundamentally, although Ruppert et al's ($D = 3.3 \times 10^{-6}$ cm^2.s^{-1}) value appears to be the most commonly used to date, it is founded upon several key assumptions:
i) the age of the rabbits in [265], ii) the accuracy of the mean thickness values in [333], iii) the translatability of the situation in rabbit lungs to that in humans, iv) the equality of the diffusion coefficient in lung tissue and whole blood.

For completeness, point ii) can be reviewed further, because importantly, if the assumed tissue thickness value in [265] was slightly different, the value of D would be altered to a non-negligible degree. There is a paucity of literature reference values for rabbit septal tissue thickness, although as an example, here we quote two values that suggest that the mean septal thicknesses could indeed be different to the values reported in [333]: (i) in the same sub-species of rabbits, Mataloun et al [335] determined a mean value of 9.6 ± 2.5 μm in 17 control rabbits on a normal diet and room air at 7 days old, which is larger than the value quoted in [333] (approximately 7.5 μm) for rabbits of the same age; (ii) also for the same breed of rabbits, we can estimate the septal thickness from Birks et al [336] by using the mean radius of curvature of capillaries and blood-gas barrier thickness reported in that work – if we assume that the septal thickness is $\approx$ (2$\times$ capillary radius) + (2$\times$ blood-gas barrier thickness), we obtain $(2 \times 3.63) + (2 \times 0.54) \approx 8.34$ μm. (However, unfortunately the age of the rabbits tested in [336] was not provided and hence this value

cannot be directly compared with those in [333].)

Finally, although not reporting measurements from human subjects, Månsson et al [309], who presented one of the first models with which to analyse ^{129}Xe CSSR data, used a significantly different value of D (1×10^{-5} cm^2.s^{-1}) in their study with lipopolysaccharide-treated rats. This value is sourced from a conference abstract by Wolber et al [264], in which it is stated that this is the measured diffusion coefficient of xenon in plasma, in vitro. Although Ruppert et al's value was derived at 37°C, there is no mention of the temperature at which the diffusion coefficient of 1×10^{-5} cm^2.s^{-1} was derived in Wolber et al's abstract. From [264], we are led to assume that the methods used were the same as those in a previous paper by that group [263], in which values for the xenon diffusion coefficient in water were obtained at 25°C. Thus, we can conclude that the value of 1×10^{-5} cm^2.s^{-1} used in [309] is likely less appropriate for use in human ^{129}Xe CSSR studies than $D = 3.3 \times 10^{-6}$ cm^2.s^{-1}.

In spite of the above discrepancies between studies, we can conclude that the value of $D = 3.3 \times 10^{-6}$ cm^2.s^{-1} from Ruppert et al [265] seems to have been generally accepted by the dissolved ^{129}Xe MRI field, and going forward it may be appropriate to utilise this value until a better estimate becomes available, for example, from new experimental measurements. However, the limitations placed on the validity of this value should be considered in future dissolved-phase ^{129}Xe NMR studies, and further work should be done in attempt to determine accurate estimates for the value of D in human lung tissue.

The effect of solubility coefficient (λ)

There is also some inconsistency in the choice of literature values of xenon solubility in different dissolved-phase compartments (including lung tissue) used in CSSR analysis. For example, Chang et al [140] used a solubility of xenon in lung tissue of $\lambda = 0.2$, citing [241], whilst Patz et al [138, 248] used a solubility of xenon in lung tissue of 0.1, citing [233]. The value of xenon solubility in lung tissue used by Qing et al [141] is not quoted in their paper.

Upon attempting to confirm the source of the values used by Chang et al, we cannot find a quotation of the xenon solubility in (any form of) tissue in [241]. Furthermore, in Chang's earlier article [139], [241] is also cited, however it appears that [333] might also be cited for a value of xenon solubility in tissue (see Figure 4 caption of [139]). There is no mention of a tissue solubility in [333]. Thus, we are unsure as to Chang's motivations and evidence for using a xenon tissue solubility of 0.2, but we note that the discussion of [139] states "the value we used here ($\lambda = 0.2$) was only a highly crude approximation. Approximations of the same nature apply to a few other parameters including the diffusion coefficient D of dissolved xenon."

Although there seems to be "no universally agreed value for λ" (another quote from [139]), we might speculate that Patz et al's estimate of 0.1 is more appropriate than Chang's approximation of 0.2. Eger and Larson [233] (cited by Patz et al [138, 248]) quote values of the xenon water/gas partition coefficient (which is equivalent to the Ostwald solubility of xenon in water if the gas is assumed to be at a pressure of 1 atmosphere) of approximately 0.1 at 37°C. Although [233] refers to unpublished data for the source of this value, we assume that Patz et al considered that parenchymal tissue is predominantly comprised of water, and thus that the value of 0.1 could be directly translated to that of lung tissue.

Further support for using a value of 0.1 is provided by other (non-CSSR) studies in the dissolved

[129]Xe MRI field; for example Dregely et al [152], who stated that the Ostwald solubility of xenon in tissue is approximately equivalent to the blood-gas partition coefficient, which is quoted as ~ 0.1, citing [337], a study which reported a value of 0.115 for the blood-gas partition coefficient of xenon at 37°C. In addition, it is worth noting that Cleveland et al [144] cited Weathersby and Homer [135] as a reference providing values for the solubility of xenon in various tissues. In [135], a summary of xenon Ostwald solubilities and partition coefficients in different media is presented, and, whilst this article does not explicitly report a value of the xenon Ostwald solubility in lung tissue, we can take the quoted values of Ostwald solubility in water and blood plasma as a guideline, which suggest a value in the range $0.09 - 0.11$.

Finally, we review the previously-used values of the Ostwald solubility of xenon in plasma and red blood cells (RBCs); information which is integral to separating the contribution of the T/P and RBC signals and deriving the pulmonary haematocrit according to Equation 6.9. In Chang et al [139, 140], values of 0.091 and 0.19 are used for the xenon solubility in plasma and RBCs, respectively, citing [241] (which requires the assumption that the plasma and RBCs are saturated with air at 37°C). Although we accept the methodology of [241] as valid, we note that it may be more appropriate to use values from Chen et al [244] instead; 0.0939 and 0.271 for xenon solubility in plasma and RBCs, respectively. These values are more up-to-date than those of [241], were determined in a thorough, systematic manner for a number of experimental conditions, and have been adopted previously by other groups in the hyperpolarised [129]Xe MRI field, e.g. [144].

A summary of the above discussion is presented in Table 7.3. In conclusion, although well-accepted estimates of D and λ exist, increased dissemination of results is still required to ensure that all groups in the hyperpolarised [129]Xe MR field adopt the same values, in order to simplify inter-study comparisons. Additionally, further work is needed to obtain more accurate estimates of these parameters. For example, xenon diffusion coefficients in isolated ex vivo tissue and blood samples should be measured, for example by echo train-based diffusion NMR techniques [263], to investigate the differences in D between lung parenchyma and blood. Moreover, the xenon diffusion coefficient and Ostwald solubility should be better characterised in diseased tissue samples in order to identify potential changes induced by structural remodelling / fibrosis.

Paper	D (cm^2.s^{-1})	λ	λ_{PL}	λ_{RBC}	Fitting Model
Patz et al [138, 248]	3.0×10^{-6}	0.1	N/A	N/A	Patz et al (to combined dissolved-phase [129]Xe peak)
Chang et al [140]	3.3×10^{-6}	0.2	0.091	0.19	Chang (MOXE)
Qing et al [141]	3.3×10^{-6}	N/S	N/A	N/A	Patz et al (to T/P peak only)
Study in Section 6.2	3.0×10^{-6}	0.1 (N/S)	0.091 (N/S)	0.19 (N/S)	Chang (MOXE), Patz et al (to combined peaks) and Månsson et al
Present study (Section 7.2)	3.0×10^{-6}	0.1	N/A	N/A	Chang (MOXE)
Most up-to-date / widely-used literature value [+ source]	3.3×10^{-6} [265]	0.1 [337]	0.0939 [244]	0.271 [244]	N/A

Table 7.3: Summary of values of literature constants employed in [129]Xe CSSR studies in human subjects to date. N/A: not applicable; N/S: not specified.

Review of literature values of ^{129}Xe CSSR-derived septal thickness and surface-area-to-volume ratio in previous studies involving human subjects

In light of the discrepancies in the values of literature constants between previous ^{129}Xe CSSR studies as discussed above, the validity of comparing ^{129}Xe CSSR-derived septal thickness and surface-area-to-volume ratio values between different studies is somewhat limited. Firstly, this review introduces values of septal thickness and surface-area-to-volume ratio in human subjects determined from methods other than ^{129}Xe CSSR. Secondly, we discuss the ^{129}Xe CSSR-derived septal thickness and surface-area-to-volume ratio values reported in previous ^{129}Xe CSSR studies in human subjects, and the appropriateness of comparisons between different studies. The following review comprises references for the morphological parameters of human lungs only – there are a number of studies that report ST and S/V in animal lungs, however we do not believe that these values are directly translatable to humans (see e.g. [338]).

(i) *ST and S/V values derived from other (histological) methods*:
A limited number of references are available that quote alveolar septal thickness values in human subjects (where the septal thickness has the same meaning as the parameter derived from ^{129}Xe CSSR):

Gil et al [320] reported septal thickness measurements by interactive computerised morphometry of formalin-instilled single human autopsy lung samples (using an intercept-based method with real-time video of samples). Assessing a range of values from a number of measurements and various experimental procedures, the septal thickness measurements presented in [320] tend to lie between 8.5 and 11 μm.

Kohlhase and Maxeiner [328] used the methods demonstrated in [320] to assess septal thickness in elderly subjects with senile emphysema (aged 71-88 years) who had died either by drowning or cardiac complications. (Note: subjects with serious pathological findings were excluded.) Mean septal thickness values were found to be 10.5 μm and 11.1 μm; 11.3 μm and 11.3 μm in the left and right lungs of drowned and non-drowned subjects, respectively.

Gläser et al [327] obtained lung specimens from subjects who had died some time after a heart transplantation. (Note, patients had no pulmonary complications, and a mean age of 52 ± 14 years.) The average septal wall thickness for 73 patients was 9.9 ± 4.2 μm, although it is worth noting that the authors of [327] suggest that these values are increased compared with what they would consider to be "healthy control" values.

Although the range and standard deviation of literature values for septal thickness is quite large, it can concluded from the above that values of the order of 10 μm should be expected in normal subjects. We may then anticipate that younger subjects would exhibit a lower mean septal thickness, and older or diseased subjects would exhibit higher values.

In the present study, we have reported a mean ST in healthy volunteers (mean age 59 years) of 11.6 ± 1.0 μm and 14.0 ± 2.7 μm in COPD patients, the former of which are comparable to ST values in elderly subjects reported in [328]. However, it should be noted that comparison of in vivo measured ST values with those derived from histological methods is not ideal, because any post-mortem histological analysis will be susceptible to structural changes induced by the treatment procedure (e.g. formalin instillation).

We were unable to find any literature values of septal thickness determined by methods other than ^{129}Xe CSSR in subjects with lung disease, with which to compare with our values obtained in COPD

subjects. We discuss our values in relation to other ^{129}Xe CSSR studies in humans in the second part of this review.

The extent of literature reporting surface-area-to-volume ratio in humans is slightly broader. Here, we note two methods by which S/V can be measured:

The work of Coxson et al [329] stands out as a commonly-referenced report for S/V values determined from fixed human histology samples. Coxson et al reported S/V values of 256 ± 24 cm^2.mL^{-1} in lungs extracted from healthy control subjects, 165 ± 23 cm^2.mL^{-1} in the lungs of mild emphysema patients, and 43 ± 6 cm^2.mL^{-1} in the lungs of severe emphysema patients. (Note: 1 cm^2.mL$^{-1} \equiv 1$ cm^{-1}.)

Also, the alveolar S/V can be estimated from diffusion-weighted MRI of ^{3}He or ^{129}Xe in the gaseous-phase, subject to the constraints of the measured diffusion regime. An example of the derivation of S/V values from ^{3}He diffusion-weighted MRI data is described by Yablonskiy et al [103], who reported the following range of results for healthy volunteers and emphysema patients: S/V $= 200-240$ cm^{-1} in healthy control subjects, $100-140$ cm^{-1} in mild emphysema patients, $50-55$ cm^{-1} in severe emphysema patients.

In the present study, we calculated mean S/V values in healthy volunteers and COPD patients of 194 ± 70 cm^{-1} and 117 ± 60 cm^{-1}, respectively, which are of a similar order to those reported in [103, 329]. We can therefore postulate that our COPD patient data reflects a S/V value of somewhere between that expected for mild and severe emphysema based on [103, 329]. However, the pulmonary function test results in Table 7.1 suggest that emphysema was quite severe in all patients except 67(F).

(ii) *ST and S/V from previous ^{129}Xe CSSR studies in humans (considering each study individually)*:
Qing et al [141] reported median septal thickness values as follows: 7.1 ± 0.9 μm in healthy subjects; 11.9 ± 3.7 μm in COPD patients. In comparison with the values from our study, quoted in (i) above, Qing et al's values are lower in both subject groups. However there are a number of reasons why a direct comparison of our values with those of [141] is challenging.

Firstly, the mean age of subjects was substantially larger in our study (mean age 59 years) compared with [141] (mean age 26 years). As shown in Section 6.3, we believe that there is a non-negligible increase in septal thickness with age.

Secondly, Qing et al used the model of Patz et al [138] to fit CSSR data, rather than MOXE (used in our study). Figure 6.10 clearly shows some slight systematic differences in the absolute values of ST derived using the two models, with a minor bias towards larger values from MOXE. Moreover, Qing et al fitted the Patz et al model to the tissue-plasma (T/P) peak signal only, rather than the combined dissolved-phase signal. As the Patz et al model was designed for use at low field strengths where the two dissolved-phase ^{129}Xe peaks could not be distinguished, the total dissolved-phase signal intensities should be fitted with that model to derive a total septal thickness. We postulate that fitting to only the T/P signal could lead to a slight underestimation of the ST.

Thirdly, the mean values in [141] are quoted at TLC, whilst all our measurements have been conducted at FRC + 1 L. If we compare Qing et al's values with the values derived at TLC in our lung inflation level experiments, the agreement between healthy volunteer data is significantly improved. Although Qing et al did not observe a statistically-significant difference in ST values measured at TLC and 50% FVC or RV, we have found a significant difference between values derived at RV + 1 L and TLC, and FRC + 1

L and TLC, as already presented in Section 7.3.

Finally, Qing et al used a different value of xenon diffusion coefficient in lung tissue to that used in our work, as discussed in the previous subsection. Qing et al do not reference any literature values of ST for comparison with their derived values.

Chang et al [140] reported a mean ST value of 9.2 ± 6.5 μm in healthy volunteers with a mean age of 33.7 years, including results from scans at both 1.5 T and 3 T. Chang [139] did not report fitting results for ST from a human data-set, but instead quoted a value of the "xenon exchange time" of 83 ± 7.5 ms in one "previously-published data-set". This corresponds to a ST value of 16.4 μm, assuming $D = 3.3 \times 10^{-6}$ cm^2.s^{-1} (used in [140]). However, because of the discrepancy in the derived S/V values from human data-sets in [139] and [140] as mentioned below, we do not believe that it is valid to compare our data with that presented in [139].

The mean ST values in our work are comparable to those in [140], though slightly larger, as might be expected since the mean age of subjects was higher in our study. However, even though the same analysis model was used in our work and [140], we note that Chang et al used different values for the diffusion coefficient and Ostwald solubility in lung tissue.

Chang et al [140] compared their ST values to a literature value of 10 μm, citing [320], the results of which are discussed above.

Patz et al [138] reported mean septal thickness values (see Figure 6 of [138]) of approximately 12.5 μm in normal subjects, and 16.5 μm and 22 μm in two patients with interstitial lung disease (we have estimated these values by reading the bar chart in Figure 6). In an earlier paper, [248], Patz et al only presented S/V findings and not ST findings.

Although we have employed the MOXE approach for our CSSR data analysis, the values quoted in [138] may be the most appropriate from other human ^{129}Xe CSSR studies for comparison with our results, because we used the same values of the fundamental constants (xenon diffusion coefficient and solubility in lung tissue) as that work. As mentioned above, we have observed marginally higher septal thickness values with MOXE as compared to the model of Patz et al; mean difference ≈ 0.5 μm (see Figure 6.10). Although the values taken from elderly healthy volunteers in our study are only slightly different to those presented by Patz et al, we are unsure of the age of the subjects in that study; however, we might assume that it is less than that of our reproducibility cohort (see e.g. Table 1 of [248] for supporting evidence for this assumption).

Finally, as discussed in Section 7.4 and below, whilst we have adopted the same approach as Chang et al [140] for achievement of a given inflation level prior to acquiring ^{129}Xe CSSR data, Patz et al used a different procedure; in their work, a number of distinct lung volumes relative to TLC were used, which, as we have shown, might severely impact the derived ST value. Thus, the validity of comparing absolute values between different subjects at different relative inflation levels is limited.

Patz et al [138] did not compare their derived ST results with any literature values from other methods. Qing et al did not present S/V measurements from CSSR.

Chang [139] derived a S/V value of 404 cm^{-1} by fitting a previously-published ^{129}Xe CSSR data-set using MOXE. However, it appears that this value was obtained by assuming that a septal thickness value from

rabbits of 5 μm (cited as originating from [333]) is applicable to human data. Given that Chang et al present significantly lower S/V values in their later paper [140], we may assume that the value of 404 cm^{-1} is not appropriate for comparison with our work.

Chang et al [140] reported a mean S/V of 210 $\pm$ 50 cm^{-1} in healthy subjects with a mean age of 33.7 years, which appears to have been derived from the actual measured septal thickness values (rather than the assumed ST of 5 μm as in [139]). This S/V value is similar to our study measurements (194 $\pm$ 70 cm^{-1} in healthy volunteers). However, we must re-iterate the point that we used a slightly different value of the xenon diffusion coefficient in tissue to that of Chang et al, and crucially, Chang et al employed an Ostwald solubility of xenon in tissues which was a factor of 2 higher than the value we used. (Note: the value we employed is arguably more well-established and supported by literature than that used by Chang et al, as discussed in the previous subsection.) Thus, it may not be appropriate to compare our values of S/V with those in [140].

Chang et al [140] compared their inferred values of S/V to those reported in [329], stating that their values are comparable to those of that study in normal subjects.

In [139], two different literature values of S/V are quoted: a value of 250 cm^{-1}, citing [329], is used to support Chang's initial computational simulations of the CSSR signal; however, later in the article, when Chang presents the results of a CSSR data-set from a healthy volunteer, a literature value of 450 cm^{-1} is quoted instead, the origin of which is unclear to the reader.

Patz et al [138, 248] reported S/V values at different relative lung volumes between 0.25 and 1 $\times$ TLC in each subject. We believe that it would be most appropriate to compare our values of S/V with those measured by Patz et al [138, 248] at volumes of 50% TLC ($\sim$ 120 cm^{-1} in both papers). Nevertheless, in our current work, the % of TLC represented by our chosen inhalation strategy of FRC + 1 L means that the relative inflation level varies between subjects and could correspond to values in a wider range (e.g. 30% to 70% of TLC). Due to the observation of changes in S/V as a function of lung inflation level presented in our current manuscript (and indeed in Patz et al [138, 248]), the validity of comparison of absolute values of S/V between our work and that of Patz et al is limited.

Patz et al compared their inferred values of S/V to those reported in [329], stating that their values are $\sim$ 40% lower than those in [329].

7.4.1 Future perspectives: Chemical shift imaging (CSI)-CSSR

Like Section 6.4.1, this subsection provides initial results of an ongoing project related to ^{129}Xe CSSR in our laboratory, concerning the development of a means to acquire spatially-localised ^{129}Xe CSSR data with an interleaved, phase-encoded CSSR sequence.

^{129}Xe CSSR provides a means of assessment of *whole-lung* average functional changes, allowing estimation of the *mean* alveolar septal thickness and surface-area-to-volume ratio. However, most lung diseases present in a spatially heterogeneous manner; for example, idiopathic pulmonary fibrosis is typically most severe at the base and periphery of the lungs (see e.g. [339] and Figure 6.1). Furthermore, there are well-known gravitational effects in the supine lungs, in terms of tissue density [1] and ventilation-perfusion ratio (V/Q) [340]. Thus, a method for spatial localisation of the dissolved-phase ^{129}Xe signal is required

172

in order to permit regional estimation of lung microstructural parameters.

Whilst Dixon- [145, 148] or "IDEAL"-based chemical shift imaging (CSI) [146, 147] approaches allow the regional depiction of the chemically-distinct resonances of ^{129}Xe dissolved in T/P and RBC compartments, the imaging data is only associated with a single exchange time (TR), such that only semi-quantitative information about gas exchange dynamics and function can be derived. In addition, though the development of multiple exchange time xenon polarisation transfer contrast (MXTC) techniques has permitted regional evaluation of the dynamics of gas exchange for derivation of quantitative maps of parameters related to ST and S/V [152, 153], XTC-based methods do not enable distinction of the signals arising from the T/P and RBC components, and thus do not enable separate assessment of diffusion and perfusion contributions to gas exchange. The relative advantages and disadvantages of each approach are summarised in Table 7.4 and Figure 7.5.

The necessity for multiple repetition times in ^{129}Xe CSSR constrains the spatial resolution achievable within a single breath-hold. Thus, the simultaneous acquisition of regional, spectrally-selective and dynamic/temporal information about gas exchange is challenging, and in practice a compromise is required. Although spiral IDEAL techniques have been recently demonstrated for the acquisition of spatially-localised CSSR uptake curves in rats [341, 342], this involved a multiple-scan approach which is unfeasible for single breath-hold acquisitions in humans at present.

Technique	Advantages	Disadvantages
CSSR (dynamic spectroscopy)	Spectral & dynamic; allows estimation of lung structure	No regional localisation
(M)XTC	Regional (& dynamic)	No spectral selectivity
IDEAL / Dixon CSI	Regional & spectral	No dynamic information; semi-quantitative

Table 7.4: Advantages and disadvantages of currently-adopted ^{129}Xe MRI methods for studying gas exchange.
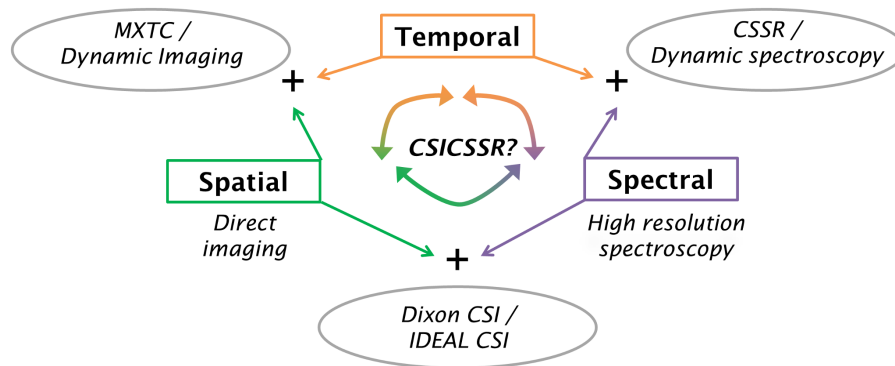
Figure 7.5: Summary of the types of information offered by ^{129}Xe MRI methods for studying gas exchange.

The purpose of this preliminary study was to implement a free induction decay CSI method with multiple spectral acquisitions at different CSSR exchange times for each phase encoding step (which we denote "CSI-CSSR"), in order to study the regional variation in gas exchange dynamics from anterior to posterior, whilst preserving spectral-selectivity of the T/P and RBC components.

A FID-based CSI sequence with a variable repetition time (TR) CSSR acquisition for each phase encode was programmed as shown in Figure 7.6, utilising binomial-composite RF pulses for saturation of dissolved-phase ^{129}Xe (as introduced in Section 6.2). Two healthy subjects were scanned using the same experimental set-up as detailed in previous sections of this thesis. Enriched xenon gas was delivered to subjects in 1 L doses of either 100% hyperpolarised xenon or 50:50 xenon-nitrogen mixtures. Subjects were scanned on two occasions, with one-dimensional phase encoding applied in the right-left (R-L) and anterior-posterior (A-P) anatomical directions.
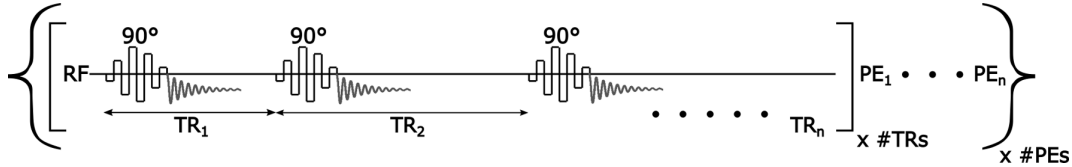
Figure 7.6: Interleaved CSI-CSSR pulse sequence, as implemented in this work. For each CSI phase encoding step (PE), 90° binomial-composite RF pulses were used to saturate the dissolved-phase ^{129}Xe magnetisation and generate FIDs at multiple different inter-pulse delay times (TR values) in order to sensitise the MR acquisition to xenon uptake dynamics for each pixel.

The number of exchange times (TRs) and phase encodes was optimised according to: the available reservoir of gaseous ^{129}Xe magnetisation; the minimum number of TR points required to achieve satisfactory fitting of CSSR uptake curves with diffusion models; and the feasible length of a breath-hold.

In order to assess the first requirement, the decay of gaseous-phase ^{129}Xe signal as a function of RF pulse number was evaluated at a fixed repetition time $TR = 30$ ms ($\ll T_1$ and $\ll$ maximum TR used in ^{129}Xe CSSR). For reference, a Tedlar bag with a 3% hyperpolarised ^{129}Xe gas mixture (balanced with N$_2$ and ^{4}He) was placed in the transmit-receive RF coil (loaded) and subjected to 90° RF pulses centred on the dissolved-phase ^{129}Xe frequency (and separated by spoiler gradients and $TR = 30$ ms). By fitting the decay in gaseous ^{129}Xe signal according to Equation 3.125, the equivalent flip angle for gaseous ^{129}Xe (for a 90° dissolved ^{129}Xe excitation) was found to be 0.85°. The same experiment was performed in three different subjects after inhalation of hyperpolarised ^{129}Xe gas. In this case, the rate of decay was found to be equivalent to that produced by a flip angle of $\sim 10°$ in each subject. This more rapid decay can be attributed to depletion of the gaseous ^{129}Xe reservoir by transfer into the dissolved-phase and saturation by the 90° RF pulse. As illustrated in Figure 7.7A, this implies that the gaseous ^{129}Xe magnetisation will be almost completely diminished after $\sim$ 150-200 RF pulses with $TR = 30$ ms.

A previously-acquired ^{129}Xe CSSR data-set from a healthy volunteer was analysed in order to investigate the effects of reducing the number of temporal data-points sampled during the CSSR uptake curve on the quality of the fit. This was done by fitting the Patz et al model to the combined dissolved-phase ^{129}Xe data after reducing the number of data-points by a factor of 2, 3 and 4, compared to the initial number of 25 (as in Section 6.2). As shown in Figure 7.7B, significant discrepancies in the fit quality were only observed when the number of data-points was decreased by 4× compared with the original number, whilst 2- and 3-fold reductions caused little change in the shape of the curve. ST values derived from the model fitting were 1%, 5% and 19% different to the original values for 2-, 3- and 4-fold reductions, respectively. Hence, 8 TR values were chosen for the CSI-CSSR acquisition, equating to an approximately 3-fold reduction in the sampling density of the CSSR uptake curve as compared with Section 6.2.

Preliminary CSI-CSSR data acquired with 8 or 12 phase encoding samples indicated a non-negligible leakage of signal into neighbouring phase encodes due to insufficient sampling density. However, since it was desired that the maximum number of RF pulses did not exceed 200, a compromise of 16 phase encoding steps was chosen. Thus, the total number of RF pulses was $8 \times 16 = 128$. To limit the sequence duration to that of a realistic breath-hold time (~ 15 sec), it was practically unfeasible to acquire data associated with a TR of 1 s, or even 500 ms; hence, a maximum TR of 320 ms was selected to provide some information about pulmonary perfusion. The minimum TR was 20 ms. Additional sequence parameters were as follows: field-of-view of 26 cm (36 cm) in the A-P (R-L) direction; each phase encode corresponded to ~ 16 (22.5) mm; 128 spectral points were sampled over a bandwidth of 12 kHz.
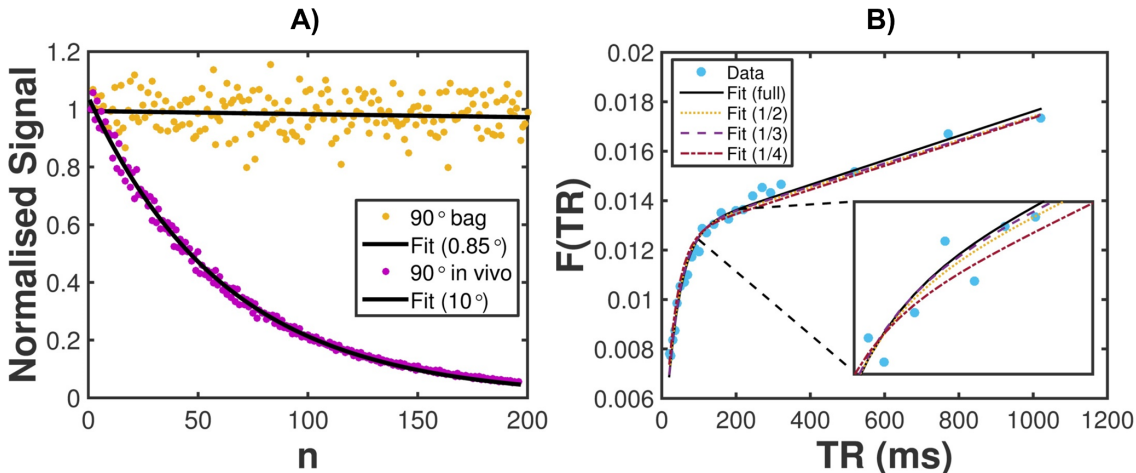
Figure 7.7: Pulse sequence design considerations for ^{129}Xe CSI-CSSR. A) Off-resonant excitation and depolarisation of ^{129}Xe gas signal in a Tedlar bag (orange) and in vivo (pink) upon 90° excitation of dissolved ^{129}Xe. B) Alteration of the quality of the Patz et al model fit to ^{129}Xe CSSR data as the number of data points is reduced to a fraction of the original number (25 points).

In the R-L direction, the dissolved and gaseous ^{129}Xe signal intensities were found to be symmetrically distributed about the trachea at all repetition times, suggesting that there was little R-L variation in ventilation, tissue density, or perfusion. (Spikes in the $F(t)$ parameter in the middle phase encodes were manually excluded; these were attributable to the relatively large gaseous ^{129}Xe signal in the trachea compared with the dissolved ^{129}Xe signal.) An example CSI-CSSR data-set with phase encoding in the R-L direction is shown in Figure 7.8.

CSSR uptake curves associated with each phase encoded region were analysed with the model of Patz et al. In the regions associated with the centres of each lung, the derived septal thickness values were $\leq 13\%$ of previous whole-lung CSSR data in healthy volunteers (see Section 6.3). However, in the extreme right and left locations, the SNR was insufficient to yield high quality data fitting, and as such, meaningful estimates of lung microstructural parameters were not possible in these regions.

Figure 7.9 depicts typical results acquired from one subject in the A-P orientation, highlighting elevated signal from both gaseous and dissolved ^{129}Xe in the posterior regions. At TR values of greater than 50 ms, the total dissolved ^{129}Xe signal from the most posterior regions was greater than that from the anterior regions. Figure 7.9B shows example ^{129}Xe CSSR uptake curves from two posterior positions,
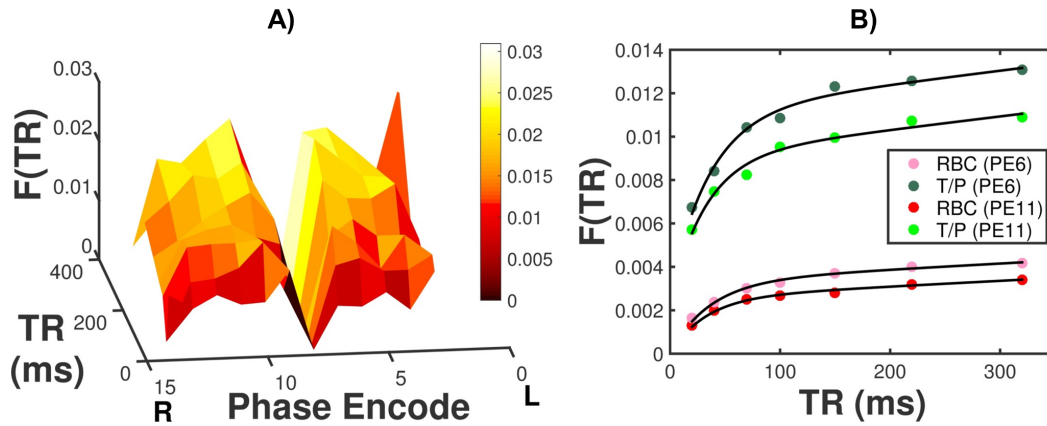
Figure 7.8: A) CSSR data as a function of (CSI-encoded) position in the right-left direction for a healthy subject. B) Example fits to tissue/plasma (T/P) and RBC data for phase encode steps 6 and 11.

fitted with the model of Patz et al, which display a good agreement between the model fit and the data. However, the SNR associated with the dissolved and gaseous [129]Xe signal in the anterior regions was low, constraining the fit quality. As such, reliable estimates of fit parameters, and hence a meaningful estimate of the variation in those parameters as a function of A-P position, could not be derived.

Nevertheless, though ventilation, perfusion and surface-area-to-volume ratio would be expected to differ, we would not necessarily expect to observe an A-P variation in alveolar septal thickness in healthy normal subjects. In order to validate the CSI-CSSR results against a standard clinical observation, the ratio of the integrated signal intensities of gaseous and RBC-dissolved [129]Xe at the longest TR value (320 ms) were calculated for each phase encoding step to provide a surrogate measurement of the ventilation-perfusion ratio (see Figure 7.9C). These findings indicated a marked increase in the signal intensity ratio in the most anterior locations compared with posterior locations, in agreement with previously-published imaging measurements [143] (note: in [143], the dissolved-phase [129]Xe signal was not separated into its constituent components).

The prospect of multiple-interleaved CSI encoding for acquisition of [129]Xe CSSR uptake curves in two or three dimensions in a single breath-hold is desirable, and although challenging, could be realised in future by sparse encoding methods in both the spatial and temporal domains. For example, it may be feasible to apply a compressed sensing type reconstruction (see Section 4.5) and utilise the shape of the [129]Xe CSSR uptake curve from global spectroscopic measurements as prior knowledge to constrain the CS reconstruction (in a similar manner to previous measurements wherein anatomical co-registered ^{1}H MRI data has been used as prior knowledge in the reconstruction of [3]He ventilation images [343]).

There are a number of clinically interesting possibilities for studying regional gas exchange dynamics with CSI-CSSR in future work. In particular, the technique may be applied in its current implementation to measure superior-inferior differences in alveolar septal thickness in fibrotic lung disease with a basal predominance. Additionally, further investigations of gravitational (anterior-posterior) changes in other CSSR-derived lung functional parameters, e.g. perfusion and S/V, are possible.
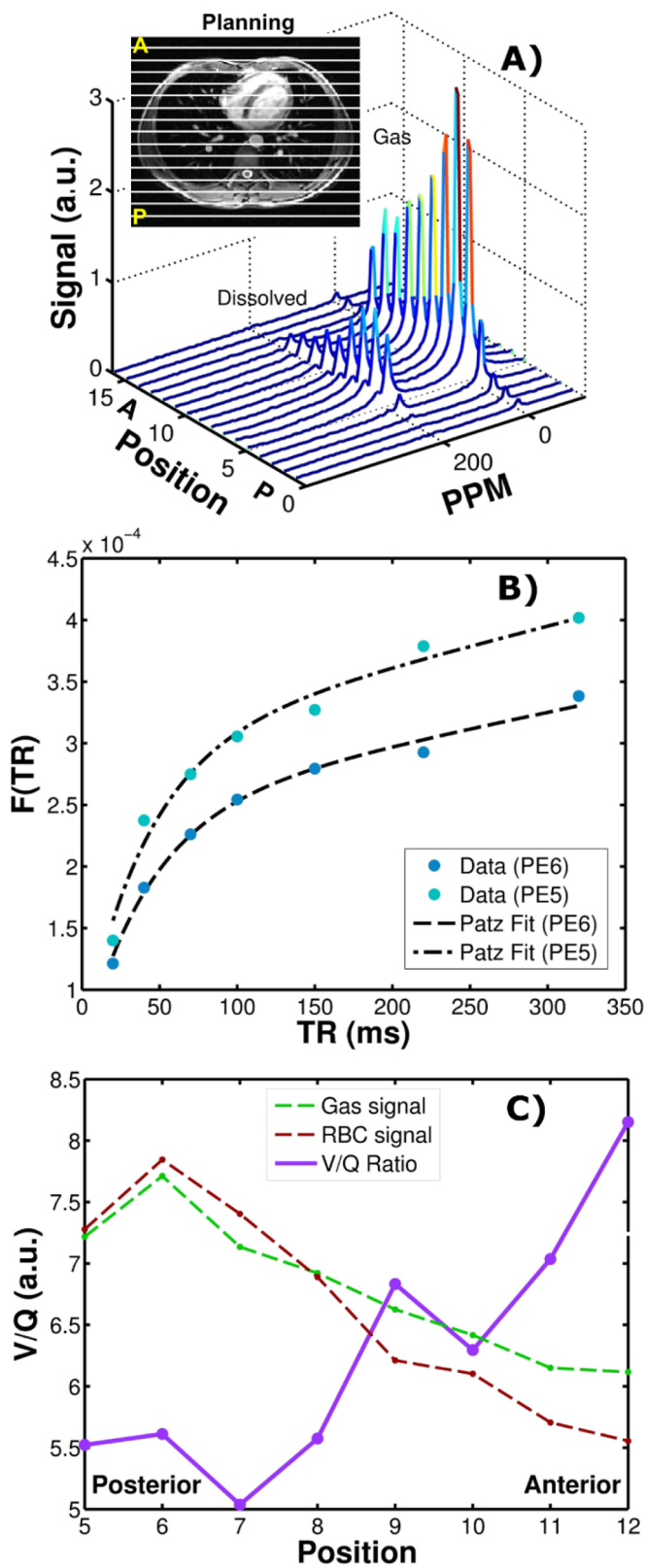
Figure 7.9: CSI-CSSR validation in the anterior-posterior (A-P) direction. A) ^{129}Xe spectra acquired from a healthy subject at a TR of 100 ms, as a function of A-P position (planning shown on anatomical ^{1}H image in the inset). B) Example ^{129}Xe CSSR uptake curves from two posterior sections of the lung (phase encode numbers 5 and 6 in A)), fitted with the model of Patz et al. C) A-P position dependence of signal from gaseous (green) and RBC-dissolved (red) ^{129}Xe at the longest TR of 320 ms, and the corresponding ratio of gas/RBC signal (a surrogate of the ventilation perfusion ratio, "V/Q", plotted in purple). In A) and C), each position step represents an extent of ~ 16 mm.

Conclusions

The ^{129}Xe CSSR technique has been demonstrated to be a reproducible method for the non-invasive quantification of alveolar septal thickness in COPD patients and age-matched healthy volunteers. The reproducibility of the derived ST has been found to be of a similar order to session-to-session variability of conventional pulmonary function tests. Furthermore, the associated mean intra-subject standard deviations of ST were observed to be substantially less than the difference in ST between healthy volunteers and COPD or IPF patients. At present, the CSSR-derived alveolar surface-area-to-volume ratio is not sufficiently reproducible for consideration as a robust clinical biomarker. The limitations of the technique — in terms of fundamental assumptions of the diffusion modelling approach, and the lack of established literature references for the assessment of alveolar septal thickness in humans — have been discussed in detail. In addition, preliminary steps towards regional localisation of ^{129}Xe CSSR data have been taken by employing a CSI-based approach. If some of the factors constraining the clinical applicability of the technique can be overcome, ^{129}Xe CSSR may mature into a beneficial means of early diagnosis and longitudinal assessment in lung diseases characterised by gas exchange limitation.

Chapter 8

Finite element modelling of ^{129}Xe diffusive gas exchange NMR in the human alveolar-capillary bed

8.1 Introduction

The suitability of hyperpolarised ^{129}Xe as a NMR probe of pulmonary gas exchange function has been thoroughly described in Chapters 2, 3 and 6. In particular, the CSSR spectroscopy method has been introduced as a means of assessment of the temporal dynamics of diffusive exchange of xenon from the alveoli to the capillaries during a single breath-hold of inhaled hyperpolarised ^{129}Xe [138, 248]. ^{129}Xe CSSR data can be modelled using analytical solutions of the one-dimensional diffusion equation in order to obtain quantitative information about gas exchange, including estimates of lung microstructural dimensions [138–140, 309]. This has enabled evaluation of alveolar septal thickening in patients with interstitial lung disease and chronic obstructive pulmonary disease (see Chapter 6 and e.g. [138, 141]). The technique has potential clinical impact in interstitial and gas exchange pathologies for which there is no universally-accepted gold-standard metric of gas exchange assessment at present [344].

The most widely-employed analytical model of xenon diffusional exchange in the lungs for interpreting ^{129}Xe CSSR data was developed by considering a simplified 1D description of the acinar regions of the lungs as alveolar spaces separated by septal (interstitial) tissue [138, 248]. This (Patz et al) model was subsequently extended by dividing the interstitial region into tissue and capillary compartments [139] in order to utilise the MR signals arising from the discrete dissolved-phase ^{129}Xe resonances that can be spectrally resolved at sufficiently high B_0 field strengths. Inherent to these approaches is the assumption that the septal thickness separating the alveoli and capillaries is uniform throughout the lungs.

In addition, a 1D radially-symmetric geometry comprising spherical alveoli sheathed by a uniform tissue layer has been considered in order to formulate a comparable model with similar assumptions [309]. In attempt to validate the applicability of these analytical models, preliminary finite difference simulations have been implemented to model ^{129}Xe diffusive exchange in a geometry comprising a single alveolus and a capillary region; however, this model also assumed homogeneity of septal tissue [345]. Fundamentally, these approaches do not utilise realistic representations of the lung microstructure to account for the heterogeneity in alveolar geometry and tissue or capillary thickness that is present in normal lungs [346] and crucially, is accentuated in many lung diseases (see e.g. [347] and example whole-lung and micro-CT images of the lungs of normal subjects and patients with IPF depicted in Figure 6.1 of Section 6.1). Additionally, the efficacy of most analytical methods is constrained by a high number of interrelated fitting parameters that may obscure the quantitative interpretation of metrics of gas exchange and microstructure so-derived (see Section 6.4). Thus, realistic geometrical representations of the alveoli, septa and capillary networks should help to advance the current models of ^{129}Xe diffusional exchange in the human lungs and

strengthen the interpretation of quantitative information about lung microstructure derived from in vivo ^{129}Xe NMR.

In this chapter, ^{129}Xe diffusive exchange between the alveoli and pulmonary capillaries is simulated via finite element analysis, adopting a similar methodology to that previously presented for simulating hyperpolarised gas diffusion MR [348–351]. A number of geometrical approaches are employed, including 3D cylindrical geometries of the pulmonary capillaries (as an initial model system for validation of numerical simulations), and realistic 2D and 3D "image-based" geometries of the alveolar microstructure, derived from histological sections and volumetric μ-CT data of normal human lungs and the lungs of patients with ILD. The implications of these simulations for the analysis of ^{129}Xe CSSR data and the future development of associated analytical models of lung microstructure are discussed.

This chapter is based on the following publication: "Finite Element Modeling of ^{129}Xe Diffusive Gas Exchange NMR in the Human Alveoli". **N. J. Stewart**, J. Parra-Robles, J. M. Wild. *Journal of Magnetic Resonance*, doi:10.1002/mrm.26279 (2016). Author contributions statement: study design, NJS, JMW; acquisition of data, NJS, JPR; analysis of data, NJS; preparation of manuscript, NJS, JMW.

8.2 Methods

Background theory

Although it has been already explained in the previous chapter, this paragraph briefly reviews the formulation of gas exchange "contrast" in ^{129}Xe NMR experiments, which is enabled by the fact that the magnetisation of hyperpolarised ^{129}Xe is non-renewable and can be manipulated by RF pulses. Upon inhalation, xenon rapidly saturates the pulmonary capillaries and its overall concentration in the capillary bed is limited by capillary perfusion. However, the application of spectrally-selective RF saturation pulses that destroy the longitudinal magnetisation of dissolved-phase ^{129}Xe, whilst preserving the polarisation of ^{129}Xe gas in the alveolar spaces, permits the measurement of diffusive exchange of ^{129}Xe from the alveoli to the capillaries [171]. The application of 90° RF pulses effectively "resets" the dissolved-phase ^{129}Xe magnetisation to zero such that the increase in signal during a given NMR repetition time (TR) is governed by the amount of dissolved-phase ^{129}Xe magnetisation that is replenished by diffusive exchange with polarised ^{129}Xe from the reservoir of gaseous-phase ^{129}Xe (in the alveoli) within that time period. The CSSR measurement involves sampling the dissolved-phase ^{129}Xe magnetisation at various delay times (TRs) after the application of selective 90° pulses at the dissolved-phase ^{129}Xe resonance frequency (see Section 6.2 for further information). As such, the dynamics of gas exchange, i.e. a measure of the uptake of ^{129}Xe concentration in the parenchyma and capillaries as a function of time, can be derived, which provides information about "diffusion limitation"; the extent to which a particular disease process (e.g. inflammation or fibrosis) impairs the diffusional exchange of xenon into the capillaries.

Unlike the measurement of hyperpolarised gas ADC values, because diffusion sensitisation is achieved by RF pulses which modulate the longitudinal magnetisation, rather than magnetic field gradients (which modulate the phase of the transverse signal), the dissolved-phase ^{129}Xe magnetisation does not require treatment with the Bloch-Torrey equation. Assuming perfect B_1 and B_0 field homogeneities, and therefore fully on-resonance 90° excitations of the dissolved-phase ^{129}Xe magnetisation in a CSSR experiment, the transport of ^{129}Xe magnetisation into and within the parenchymal tissue and pulmonary capillaries

is governed by the diffusion-convection equation, such that the magnetisation, M_d, can be treated equivalently to a concentration:

$$\frac{\partial M_d}{\partial t} = \boldsymbol{\nabla} \cdot (D\boldsymbol{\nabla} M_d - \boldsymbol{v} M_d) + S \tag{8.1}$$

where D is the diffusion coefficient of xenon, which differs by many orders of magnitude in the alveolar airspace ($D_0 = 0.14$ cm^2.s^{-1} [226]) and in the dissolved-phase (D_t, here assumed to be 3.3^{-6} cm^2.s^{-1} [265], and see Section 7.4) and S represents any additional "sources" or "sinks" of magnetisation. In the following simulations, blood flow in the lungs is assumed to be well-approximated by plug flow [352], thus, the velocity vector, $\boldsymbol{v}$, has constant magnitude in the capillaries, and is zero in the parenchymal tissue.

Boundary conditions

Diffusion-weighted MRI of ^{129}Xe in the alveolar airspaces assumes that xenon gas atoms reflect (i.e. "bounce-off") the alveolar walls rather than transferring into the dissolved-phase; it is this restriction of diffusional motion at the alveolar boundaries that forms the basis of hyperpolarised gas ADC mapping as a probe of alveolar spatial length-scale. This assumption is substantiated by the fact that only a small fraction ($\sim 2\%$) of the total ^{129}Xe MR signal is constituted by xenon dissolved in the pulmonary tissues and blood (as mentioned in the previous chapter, this arises from the relatively low Ostwald solubility of xenon in tissue and the fact that the volume of the pulmonary tissues and blood is a small fraction of the airspace volume).

However, when simulating the diffusion of xenon in both gaseous- and dissolved-phases, the permeation of xenon atoms through the alveolar walls must be considered. Due to the large difference in diffusion coefficient between xenon in the airspace and tissue compartments, and the relatively low Ostwald solubility, the boundary between these two phases is an example of a so-called "stiff" boundary, wherein the xenon concentration exhibits a discontinuity at the boundary itself. In finite element analysis, these discontinuities can be accounted for by applying "stiff" boundary conditions, defined as follows (see e.g. [353]):

$$(-D\boldsymbol{\nabla} M_2 - M_2\boldsymbol{v}) = v_{SS} \left(K_{21} M_1 - M_2 \right) \tag{8.2}$$

where M_i represents the magnetisation in region i, $\hat{\mathbf{n}}$ is the unit vector perpendicular to the boundary between the two regions, K_{ij} is the partition coefficient for the jth medium with respect to the ith medium (equivalent to the ratio of the Ostwald solubility in medium j to that in medium i) and v_{SS} is the "stiff-spring" velocity, a non-physical velocity, the value of which is somewhat arbitrary, but must be sufficiently large to allow a continuous ^{129}Xe flux across the boundaries between the two media, and to permit the concentration (magnetisation) differences in the brackets in Equation 8.2 to approach zero [354].

Here, preliminary investigations were conducted by simulating the diffusion of ^{129}Xe in the airspaces and

dissolved-phase using stiff boundary conditions as applied to 2D histological samples (the implementation and results of which are described below and depicted in Figure 8.4). However, the use of these boundary conditions results in a constantly depleting supply of gaseous ^{129}Xe, and the rate of diffusive uptake of ^{129}Xe depends heavily upon the surface-perimeter-to-area ratio of the alveoli (i.e. the size of the gaseous ^{129}Xe reservoir) contained in the 2D image. As such, this approach does not account for the full 3D extent of the alveolar ducts and sacs. Therefore, in all subsequent simulations, the magnetisation of ^{129}Xe in the gaseous-phase was considered to be constant — in order to represent an infinite reservoir of ^{129}Xe — by applying the Dirichlet boundary condition at the boundary between phases that the ^{129}Xe magnetisation was fixed to a constant, non-zero value. Importantly, this infinite gas reservoir approach is consistent with the assumptions of the CSSR methodology, in which the dissolved-phase ^{129}Xe magnetisation from each acquisition is normalised with respect to the gaseous-phase ^{129}Xe magnetisation to account for sources of gaseous ^{129}Xe signal decay and to treat the ^{129}Xe gas as a constant reservoir supplying hyperpolarised ^{129}Xe to the dissolved-phase.

Geometrical approaches

The 1D model adopted by Patz et al [138] to develop analytical solutions for the dissolved-phase ^{129}Xe signals in a ^{129}Xe CSSR experiment is illustrated in Figure 8.1a. Figure 8.1b shows the Patz et al model applied to a CSSR data-set from a normal subject (same subject as in Figure 6.10 of the previous chapter), reiterating that this analytical approach provides a high quality fit of typical in vivo CSSR data. This three compartment model, comprising a single dissolved-phase ^{129}Xe compartment (septum) separating two adjacent alveoli was extended in [139] in order to divide the septal compartment into two tissue layers with a capillary segment in the middle. This extension is also depicted in Figure 8.1a. A similar one-dimensional analytical solution has been developed by Månsson et al [309] adopting a radially-symmetric capillary model. The fundamental assumption of these models is that the proposed geometrical situation is replicated in a homogeneous manner across the whole of the lungs, and that the alveolar septal thickness is uniform, which is clearly not the case, as illustrated in Figure 6.1 of Section 6.1.
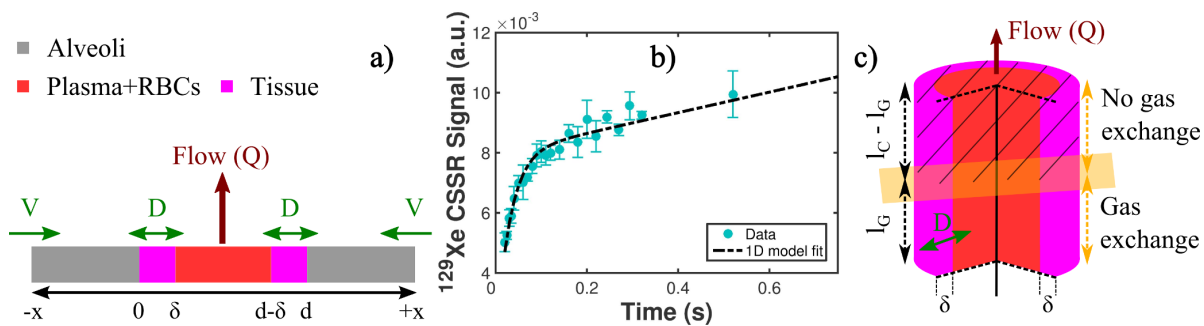
Figure 8.1: Schematics of the design of uniform models of ^{129}Xe gas exchange, with example ^{129}Xe CSSR data. a) One-dimensional geometrical picture of gas exchange employed in [138, 139] to derive analytical expressions for the ^{129}Xe CSSR signal. b) Typical ^{129}Xe CSSR data from a normal subject (see also Figure 6.10), fitted with the equation of Patz et al [138]. c) Design of the uniform, 3D radially-symmetric septal capillary model for numerical simulations of ^{129}Xe diffusive uptake. The cylindrical model is divided into two regions, one in which gas exchange is permitted to occur (un-hatched), and one in which it is not permitted to occur (hatched). [V = ventilation; D = diffusion; Q = perfusion; d = septal thickness; δ = tissue layer thickness; l_G and l_C represent the gas exchange region length and total capillary length, respectively.]

(i) To expand upon these one-dimensional pictures, in this work, a three-dimensional model of a septal compartment was developed by considering a cylindrical capillary surrounded by a cylindrical lumen shell of tissue, as illustrated in Figure 8.1c.

As described in Section 6.2, ^{129}Xe CSSR experiments involve the acquisition of spectroscopic data at a range of time-points from tens of milliseconds to $\sim$ seconds. The early time-points are predominantly governed by diffusive uptake of ^{129}Xe into the pulmonary tissues and the capillary bed, whilst at time-points $\gtrsim$ 100 milliseconds, significant additional increases in dissolved ^{129}Xe signal can be observed due to the detection of dissolved ^{129}Xe down-stream from the gas exchange region in the pulmonary venous system. If signal could only be detected from the region of the lungs where gas exchange occurs, then the signal would be expected to saturate at a time-point related to the size of the capillary septa. However, because the ^{129}Xe lung RF coil excites all of the lungs and not just the alveolar-capillary gas exchange region [i], and the T_1 relaxation time of ^{129}Xe in the blood is sufficient to preserve signal over many seconds [246, 255], additional dissolved ^{129}Xe signal can be detected from ^{129}Xe in the bloodstream that has been carried out of the gas exchange region of the lungs; this leads to an approximately linearly increasing signal at later time-points (see Figure 8.1b). In order to account for the detection of post-capillary bed signal within the cylindrical model developed here, the cylinder was composed of two equal sections, one as described above (with a tissue layer and constant source of alveolar xenon), and one in which the tissue layer and gas source were removed (hatched region in Figure 8.1c), to represent a blood-carrying region whose only source of ^{129}Xe signal was that transported from the first section of the cylinder by perfusion. The signal detected in a CSSR experiment is constituted by the total integrated ^{129}Xe magnetisation in both regions of the cylinder.

The outer perimeter of the tissue layer was assumed to be in contact with gaseous-phase ^{129}Xe (in the alveoli). The diameter of the capillary was chosen based upon previous ^{129}Xe CSSR observations as $d = 10$ μm (see Section 7.4), and the tissue layer thickness was permitted to be a free parameter in the simulations, with values ranging from $\delta = 0.2$-1.0 μm [140]. A Dirichlet boundary condition was implemented at the outer surface of the tissue layer in order to represent a constant source of ^{129}Xe from the gaseous-phase (i.e. ensuring that the cylinder was entirely encompassed by alveoli). The total length of the cylindrical capillary model was determined from estimates of pulmonary blood flow and red blood cell transit time (the latter being the average length of time required for a RBC to traverse through the pulmonary capillary, i.e. the gas exchange region). Taking an approximate value of blood (plasma) velocity in the capillaries as $v_b \approx 0.5$ mm.s^{-1} [355], assuming plug flow as discussed above and an average RBC transit time of $\tau \approx 1.0$ s [356], leads to a gas exchange region length (l_G) of 0.5 mm. This value is identical to that assumed in [355] for the length of a single capillary. For simplicity, here, the two halves of the cylindrical model were chosen to have the same length, such that the total length of the cylinder (l_C) was 1 mm. However, it is worth noting that in principle, the second (post-capillary) section of the model could be chosen to be longer than 0.5 mm, to represent the fact that the T_1 of ^{129}Xe dissolved in blood is > 1 s [255]. Nevertheless, the length of this region only needs to satisfy the requirement of being $\geq$ the distance that blood can travel in the typical CSSR measurement period (i.e. $\sim$ RBC transit time), since there is no mechanism by which ^{129}Xe can be detected further down-stream than this.

---

[i]In reality, the pulmonary vessels and capillaries are regionally inter-mingled and not spatially discrete on the length-scale of MR experiments.

This idealised cylindrical model provides a testing platform for exploring the effects of different geometrical and physical parameters on the resulting ^{129}Xe diffusive uptake behaviour. The influence of different disease-induced microstructural changes upon ^{129}Xe CSSR data can be investigated by varying the following parameters in a certain manner: septal thickness and tissue thickness, d and δ, can be increased, e.g. for simulating interstitial lung disease; blood flow velocity, v_b, can be altered, e.g. for pulmonary hypertension applications; dissolved-phase xenon diffusion coefficient, D, can be modified for diseases in which the tissue structure is remodelled, e.g. fibrotic disease.

(ii) Though the above cylindrical model is a natural 3D extension of the 1D analytical models that provides equivalent information about gas exchange dynamics, and offers a relatively straightforward means of exploring the effect of different ^{129}Xe CSSR fitting parameters on in vivo data, it still requires the assumption of a homogeneous septal geometry across the lungs, which is not representative of the genuine situation (see e.g. Figure 6.1 of Section 6.1). As proposed by Miller et al [350] for simulating the diffusion of hyperpolarised ^{3}He in the alveolar airspaces, a more accurate representation of the alveolar geometry can be obtained by using high resolution histological images. Following the method described in [350], here, 2D histological sections of the alveoli of normal subjects and patients with usual interstitial pneumonia (UIP; the most common form of interstitial lung disease) were segmented — by thresholding and manually revising the resulting segmentations using ScanIP software (Simpleware Ltd., Exeter, UK) — in order to separate the alveoli from the capillaries and thus create two-dimensional models of the alveolar septa (i.e. the "dissolved-phase"). In order to simulate homogeneous tissue thickening and generate comparative models to those derived from UIP histology samples, alveolar septa segmented from normal lung histology samples were artificially-dilated using ball-shaped structuring elements of different sizes between $R = 10$ and 20 pixels. In other words, circles of radius R pixels were placed on each pixel of the septal region, and allowed to overlap such that the edges of the septa were expanded whilst the center of the septa were preserved. The total physical extent of each histology section used was 0.87 mm $\times$ 0.65 mm, with an isotropic pixel dimension of 0.68 μm.

This approach is limited by the fact that it does not permit distinction of the tissue and blood compartments, because they cannot be easily separated using standard histological staining techniques. Furthermore, because the histological samples are two-dimensional, and only comprise alveoli from within the acinar region, the contribution of blood flow and post-capillary bed signal cannot be easily incorporated into the finite element analysis model. Thus, the geometrical situation is directly comparable to the analytical model of Patz et al [138] for the case of static capillary blood, but with the inclusion of geometrical heterogeneity.

We acknowledge the provision of histology samples from Dr William Wallace at the University of Edinburgh.

(iii) In order to implement flowing capillary blood and simulate the effect of post-capillary bed dissolved ^{129}Xe signal for a model with non-uniform septa, models (i) and (ii) were combined. The histology-based models described in (ii) were smoothed and "extruded" into three dimensions; effectively, the model was replicated in a direction perpendicular to the plane of the original image. The resulting 3D model was designed to have the same length as the cylindrical model in (i) (1.0 mm) in the direction of the extrusion, and was divided equally into two regions in the same manner as in that model. As a result, the

model comprised one region in which gas exchange was permitted by considering the magnetisation at the boundaries of the dissolved-phase compartments to be constant, and a second "post-capillary" region in which no gas exchange was permitted. The entire dissolved-phase region was considered to flow with a constant velocity along the direction of the extrusion (i.e. perpendicular to the plane of the original histological image), as described in (i).

The process of segmentation, meshing and extrusion of 2D histological sections to generate 2D and 3D finite element models is illustrated in Figure 8.2.
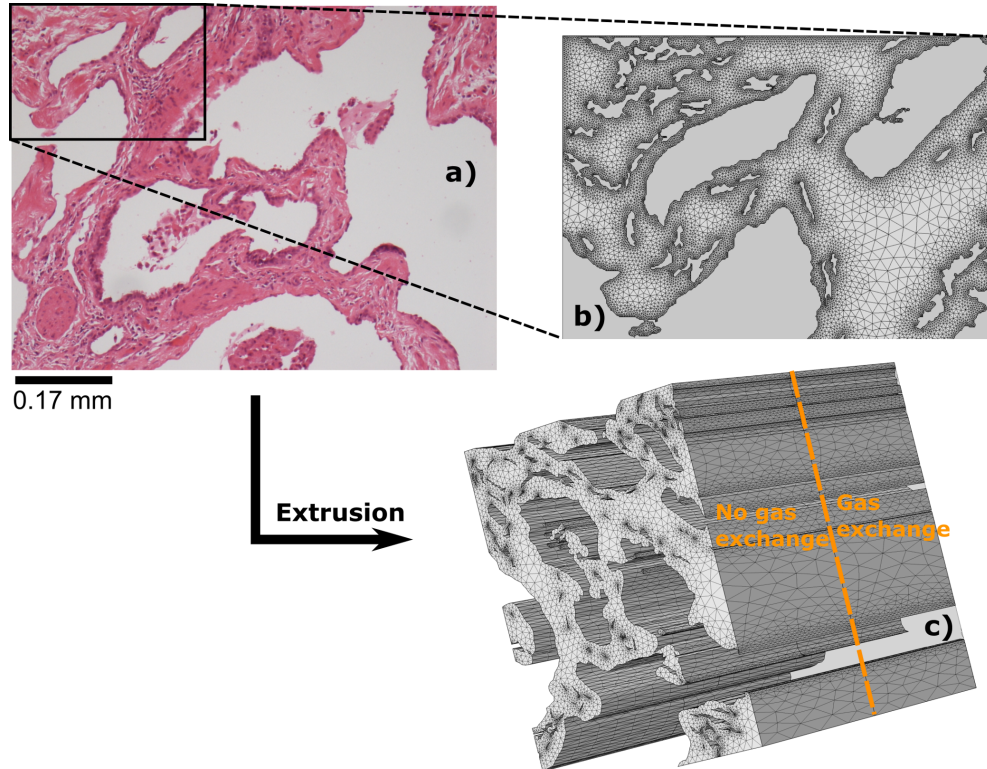
Figure 8.2: Procedure for generation of 2D and 3D finite element models based on lung histology samples. a) Example histology section taken from the lungs of a patient with usual interstitial pneumonia (UIP). Dimensions: 0.87 mm (width) × 0.65 mm (height). b) Magnified view of the resulting 2D mesh in the section of the histology sample highlighted by the black box. c) Resulting 3D extrusion and coarser mesh created by smoothing and extruding the original 2D geometry by 1 mm along the axis perpendicular to the original 2D plane. This 3D geometry is divided into a 0.5 mm region in which gas exchange is permitted and a 0.5 mm region in which no gas exchange is permitted.

(iv) In order to derive a truly representative three-dimensional model of the alveoli (without extrusion of 2D images), sections of volumetric μ-CT images obtained ex vivo from the lungs of normal subjects and patients with IPF were segmented (see [357] for example μ-CT data). Thresholding was applied to the input volumetric images to derive a 3D model of the alveolar septa (dissolved-phase), and subsequent amendment of the model was performed by utilising filters to: (a) "fill in" small gaps in the model, (b) remove "islands" (sections of the model with a volume of less than a certain number of pixels cubed), (c) smooth the resulting model with a Gaussian function. The physical extent of the μ-CT volumes used was 1.68 mm or 1.26 mm in each dimension with isotropic pixel sizes of 8.39 μm or 16.79 μm for normal or

IPF lung samples, respectively. An illustration of the process of converting the volumetric μ-CT images into a 3D model of the alveolar septa is presented in Figure 8.3.

This approach provides a representative 3D model of a section of the alveolar tissue and capillary (dissolved-phase) network. However, the spatial resolution of the μ-CT images used here is significantly lower than that of the histological images, meaning that the number of pixels comprising each septal wall is reduced. Additionally, the implementation of plug flow is not readily achievable with this model, because the model does not provide a means of delineating blood vessels external to the gas exchange region.

We acknowledge the provision of μ-CT samples from Dr Bart Vanaudenaerde and Dr John McDonough of Catholic University Leuven.
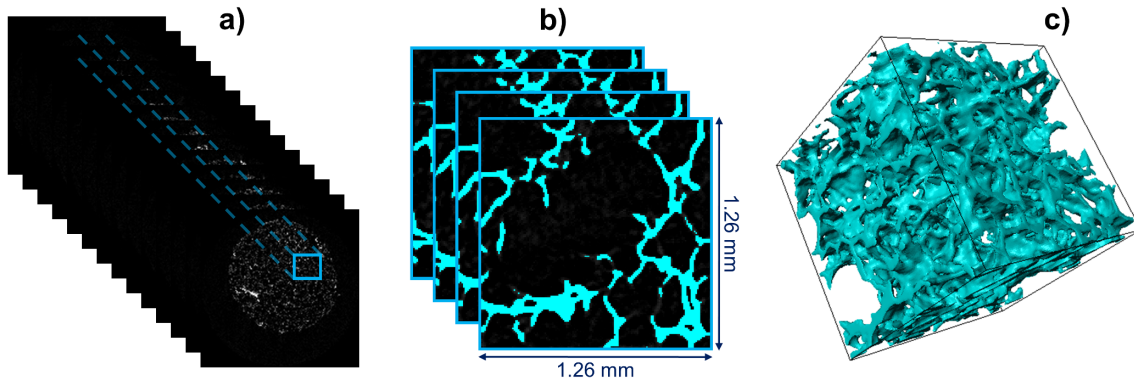
Figure 8.3: Procedure for generation of 3D models of alveolar septa based on volumetric μ-CT images. a) Volumetric stack of μ-CT slices of part of the lungs of a normal subject (slice thickness $\equiv$ in-plane pixel size = 8.39 μm). From this volume, a smaller volume (blue) is extracted that is approximately representative of the overall volume. b) Example slices segmented for the alveolar septa (blue). The selected volume in a) is segmented by thresholding and using morphological filters to fill-in gaps, remove small islands, and smooth the resulting model, as described in the main text. c) Render of the resulting 3D model of the alveolar septal network, generated after manually checking the segmentation in b) in each slice.

Further details of finite element analysis

FEM simulations of ^{129}Xe diffusion and blood flow (using Equation 8.1 with $S = 0$) for each of the four aforementioned models were performed on two desktop PCs (4-core Intel®Core™i7, 3.2 GHz processor, 32 GB RAM; XMA Ltd, St Albans, UK; and 6-core Intel®Xeon®E5-1650 v2, 3.5 GHz processor, 32 GB RAM, Dell, Round Rock, TX), using COMSOL Multiphysics software (versions 4.4 and 5.0; Burlington, MA). The velocity term v_b was set to zero in the tissue compartments of model (i) and the dissolved-phase compartments of models (ii) and (iv), whilst it was permitted to be non-zero in the capillary compartments of model (i) and in all the dissolved-phase compartments of model (iii). In all cases, simulations were performed with an initial ^{129}Xe magnetisation in the tissue and capillary compartments of zero (representing the initial saturation of dissolved-phase ^{129}Xe magnetisation in CSSR), and with boundary conditions as described below. The uptake of ^{129}Xe into the dissolved-phase was initially probed by running simulations from $t = 0$ to $t = 1.0$ s, with a time-step $\Delta t = 0.001$ s. Based on this preliminary data, simulations were repeated for until a longer time-point if required; a time-step of $\Delta t = 0.01$ s was employed for simulations with an end time of > 5 s. For particularly long and computationally-intensive simulations involving three-dimensional geometries, a variable time-step was employed, with Δt taking values between 0.001 s

(for $t < 1.0$ s) and 1.0 s (for $t > 10$ s). Following completion of the FEM simulations, the total dissolved-phase ^{129}Xe signal was computed by integrating the magnetisation across the entire model-space at each time-point. Specific details for each individual model are described below.

(i) To initialise the simulations, the magnetisation of ^{129}Xe in the tissue and capillary compartments was set to zero at all spatial locations. As mentioned before, a Dirichlet boundary condition was implemented at the outer boundary of the tissue lumen layer in order to enforce a constant supply of xenon from the alveoli to the dissolved-phase at all time-points. Stiff boundary conditions were implemented at the interface between the tissue and capillary regions, where the rate of diffusive exchange depends on the xenon partition coefficient between the two compartments. The blood velocity was permitted to be a variable of the simulations, taking values between 0 and 0.5 mm.s^{-1} [355]. Prior to commencing simulations, tetrahedral meshes of the entire geometry were generated in COMSOL.

(ii) Initially, finite element meshes were created for both the airspace (gaseous-) and dissolved-phase ^{129}Xe compartments, and diffusion was simulated using stiff boundary conditions at the interface between the two compartments, with the initial conditions that all gaseous ^{129}Xe possessed a magnetisation of 1 and all dissolved ^{129}Xe had a magnetisation of 0. However, as discussed earlier, the finite extent of the airspaces in the 2D histology sections leads to a depletion of the reservoir of xenon for diffusive exchange (see Figure 8.4). Thus, rather than adopting that approach, all simulations were carried out using an effectively infinite reservoir of gaseous xenon, by implementing a Dirichlet boundary condition of constant magnetisation at the boundary between gaseous and dissolved xenon compartments. Therefore, mixing of ^{129}Xe gas of differing longitudinal magnetisation levels by Brownian diffusion within the alveolar airspaces was not simulated.

Prior to commencing simulations, tetrahedral meshes of the entire geometry were generated in COMSOL. Potential meshing errors arising from inadequate size and number of mesh elements when meshing small regions were circumvented by removing islands (regions of the model comprising less than a threshold number of pixels) prior to meshing.

(iii) Prior to extruding the 2D histological images into three dimensions, a coarse version of the 2D model was generated by removing structures with a total area less than a certain threshold number of pixels (dependent on the exact model, but of the order of tens of pixels) and by specifying the minimum distance between adjacent edge elements to be substantially larger than that of the 2D models. This reduced the memory requirements for the 3D model when running in the COMSOL graphical user interface. As with model (ii), diffusion of ^{129}Xe gas in the alveolar airspaces was ignored, and a Dirichlet boundary condition was implemented at the boundaries of the alveolar septa to enforce a constant source of xenon to the dissolved-phase. Tetrahedral meshes of the entire geometry were generated in COMSOL.

(iv) In order to reduce memory requirements of the COMSOL graphical user interface, finite element meshes comprising tetrahedral elements were generated using the ScanIP $+FE$ module prior to COMSOL import. As above, Dirichlet boundary conditions were implemented at the borders of the alveolar septa to enforce a constant reservoir of xenon to the dissolved-phase.
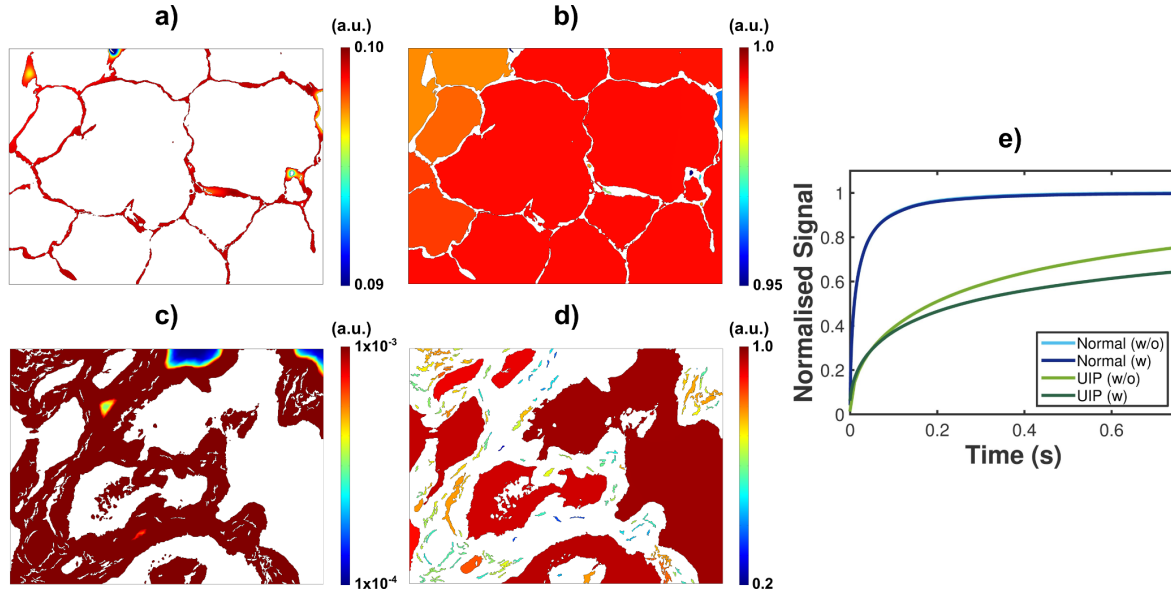
Figure 8.4: Preliminary investigations of the effects of a non-constant gaseous ^{129}Xe reservoir in the alveoli on finite element simulations in 2D histological samples. Distribution of dissolved-phase (a) and gaseous-phase (b) ^{129}Xe in a normal histological sample after $t = 0.75$ s. c) and d) represent equivalent results obtained from a UIP histological sample (denoted UIP #1 in Figures 8.6 and 8.8). In both cases, simulations were initialised with all gaseous-phase ^{129}Xe magnetisation equal to one and all dissolved-phase ^{129}Xe magnetisation equal to zero. Unlike in subsequent simulations, the gaseous-phase ^{129}Xe magnetisation was not fixed at one, and was instead allowed to decrease due to diffusive exchange into the dissolved-phase (i.e. "non-constant gas reservoir"). e) Integrated dissolved ^{129}Xe signal in the two cases (without (w/o) replenishment of the gas reservoir), compared with results obtained from simulations which included a replenishment of the gas reservoir (w). The latter (w) results are presented in full in Figures 8.6 and 8.8. The dissolved-phase ^{129}Xe signal is normalised by that at infinite diffusion time for no blood flow.

8.3 Results

(i) The simulated distribution of ^{129}Xe magnetisation in the uniform 3D cylindrical pulmonary septum model is shown (at different time-points between 5 ms and 330 ms) in the left panel of Figure 8.5. It can be observed that the thin tissue layer ($\delta = 0.5$ μm in the case shown) was saturated with ^{129}Xe from the alveolar reservoir after ~ 10 ms, whilst the xenon in the capillary region was still heterogeneously distributed after 130 ms of exchange. The right panel of Figure 8.5 shows the ^{129}Xe CSSR uptake curves, portraying the dissolved ^{129}Xe signal as a function of time, generated by integrating the total dissolved-phase ^{129}Xe magnetisation over the entire geometry for each time-point, for two different values of δ and v_b. The introduction of non-zero blood velocity leads to an increase in signal at time-points greater than ~ 100 ms, in comparison to the case of zero blood velocity in which a plateau is reached after ~ 300 ms. The increase in signal at later time-points reflects the detection of ^{129}Xe down-stream from the gas exchange region, as measured in vivo via CSSR experiments. The change in tissue layer thickness δ did not induce an obvious difference in uptake behaviour for the case of zero blood flow; in fact, the two curves at $\delta = 0.4$ μm, $v_b = 0$ mm.s^{-1} and $\delta = 2.0$ μm, $v_b = 0$ mm.s^{-1} appear to overlap in Figure 8.5 (right). However, for the case of non-zero blood flow, a marked difference in the rate of uptake and total signal achieved was observed at the different values of δ. As expected, reductions in the dissolved-phase diffusion coefficient D (and/or increases in the total septal thickness d) manifested as longer saturation times (data not shown).
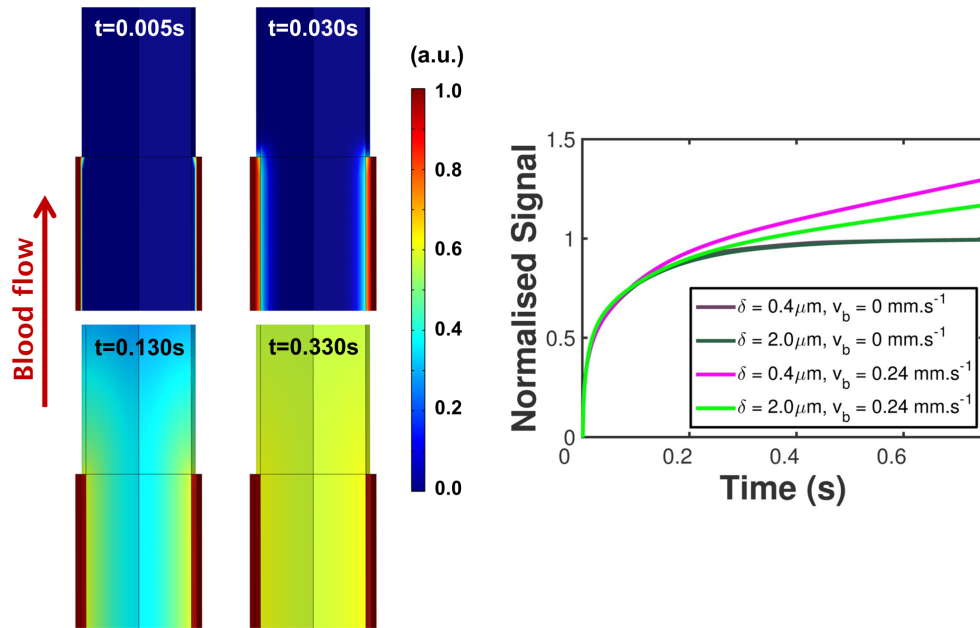
Figure 8.5: Validation of the uniform 3D cylindrical septum model (model (i)). Left: Depiction of the distribution of ^{129}Xe in the cylindrical model at selected time-points. These images are magnified views of the section of the cylinder where the gas exchange region (bottom half) and *no* gas exchange region (top half) intersect. Right: Simulated ^{129}Xe CSSR signal (integral of magnetisation over the entire 3D geometry as a function of time, normalised by that at infinite diffusion time for no blood flow) for two different values of tissue thickness (δ) and blood flow velocity (v_b). In each case, the Ostwald solubility of the tissue compartment was specified as 0.09 and that of the blood was specified as 0.20 [241].

(ii) Figure 8.6 shows the results of finite element simulations of 2D histological samples obtained from the lungs of normal subjects and patients with UIP. The normal histology sample exhibited rapid saturation of the tissue and capillaries with ^{129}Xe in a similar manner to that observed for the cylindrical septum model (i), but with subtle differences in the shape of the curve of uptake dynamics arising from averaging over many unequal septal thickness values. The effect of uniform thickening of alveolar septa by dilation of the model with ball-shaped structural elements is depicted in Figure 8.6B) and C). As expected, artificially-thickened septa required a progressively longer time for the dissolved-phase to completely saturate with increasing degrees of dilation. Simulated uptake curves for the 2D UIP histology samples are depicted in Figure 8.6D) and E), and magnified views of selected sections of the samples (specifically illustrating the ^{129}Xe distribution at $t = 0.03$ s) are shown in panel F). The shapes of these curves appeared qualitatively different to those of the artificially-thickened normal samples. Additionally, when plotted on an x-axis of time raised to the power of $\frac{1}{2}$ [248], whilst the normal and artificially-thickened normal uptake curves exhibited clear linear regions (in agreement with that reported in [248]), the UIP early time-point data exhibited a comparable initial slope to that of the artificially-thickened normal sample (with structuring element size 10 pixels), but relatively quickly deviated from a linear relationship. Although the two UIP histology sections shown in Figure 8.6 were obtained from spatially distinct regions of the lung, and appeared qualitatively different in the snapshots at different time-points, the integrated signal (uptake) curves (normalised by the dissolved-phase ^{129}Xe magnetisation at infinite diffusion time for no blood flow) exhibited comparable time-dependent behaviour, both when plotted against t and plotted against $t^{\frac{1}{2}}$.

189
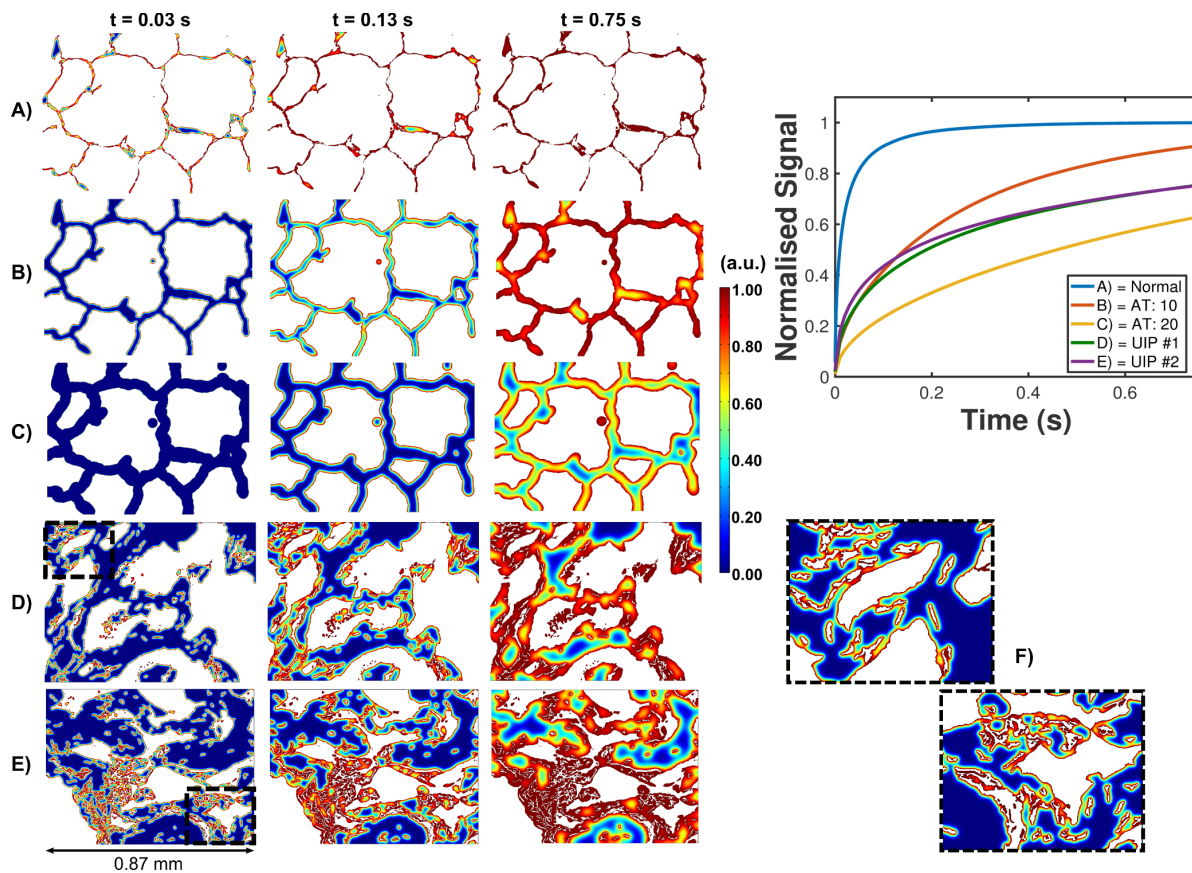
Figure 8.6: 2D FEM simulations in normal, artificially-thickened (AT) normal, and UIP histology samples. A) = normal histology section; B) = section in A) with alveolar septa thickened by a ball-shaped structuring element of 10 pixels in size; C) = section in A) thickened by a 20 pixel structuring element; D) = example UIP histology section; E) = second example UIP section (obtained from a different region of the lung). (In all cases, pixel size = 0.68 μm, and blood is static, i.e. $v_b = 0$ mm.s^{-1}.) Left panels: snapshot images of the distribution of ^{129}Xe in the histology sections at different time-points after initialisation of the simulation. Top right panel: total integrated dissolved ^{129}Xe signal for each case, representing the predicted CSSR uptake curves. The dissolved-phase ^{129}Xe signal is normalised by that at infinite diffusion time for no blood flow. Magnified views of selected regions of the UIP sections (dashed black boxes) at $t = 0.03$ s are shown in the bottom right of the figure, panel F).

(iii) A snapshot of the ^{129}Xe distribution at 0.75 s after commencement of simulations for the 3D model based on an extruded normal histology sample (with non-zero blood flow) is presented in Figure 8.7. The dark red appearance of the boundaries of the alveolar septa reflects the Dirichlet boundary condition of a constant source of ^{129}Xe magnetisation from the airspace (by definition of the model, the boundaries were observed to be dark red at all time-points). However, at the near-edges of the septa, the effect of perfusion is highlighted by the low magnetisation values (blue), which result from blood flow transporting ^{129}Xe away from those regions. Simulated ^{129}Xe CSSR uptake curves, derived from all 3D histology-based geometries, are shown in Figure 8.8a. These uptake dynamics were comparable to the results of the 3D cylindrical model, and qualitatively similar to in vivo CSSR data (see Chapter 6). Discrepancies in the ^{129}Xe diffusive exchange behaviour of models based on normal and UIP histology samples were most significant at early time-points (< 200 ms), indicating that the 0-200 ms behaviour was governed by diffusion, whilst the > 200 ms behaviour was more strongly influenced by perfusion

190
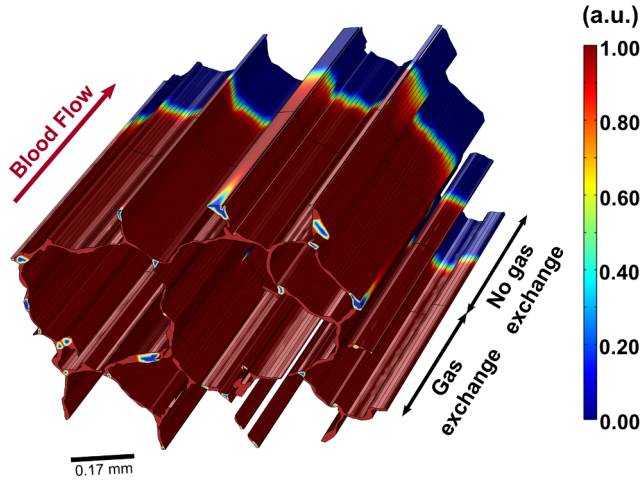
Figure 8.7: Distribution of xenon after $t = 0.75$ s in a 3D model extrusion of a histological section obtained from normal lungs. Blood velocity, $v_b = 0.33$ mm.s^{-1} along the axis indicated by the red arrow.

effects (as expected by definition of plug flow; see Section 8.2). The slope of the perfusion-dominated region, derived by linear regression analysis, correlated significantly with the blood velocity, v_b, as expected.
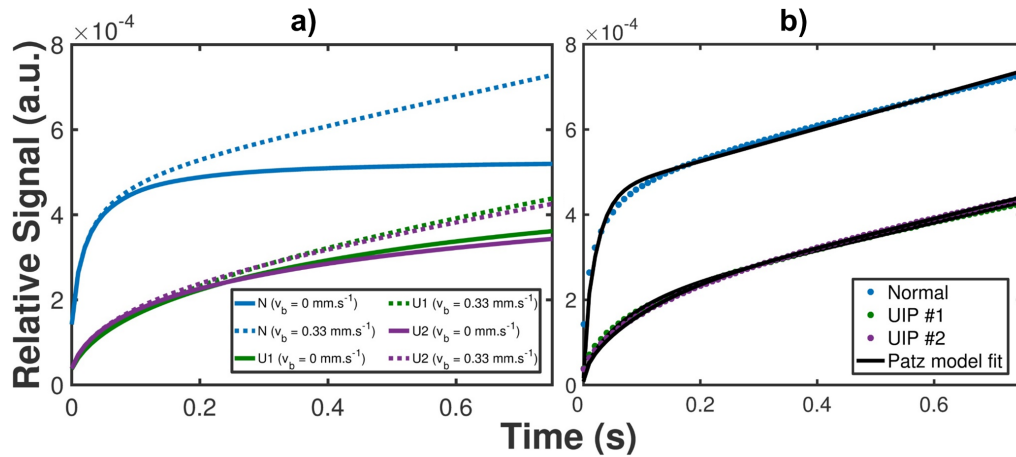
Figure 8.8: a) Integrated dissolved ^{129}Xe magnetisation as a function of time for 3D extrusion models derived from one normal (N) and two UIP (U1, U2) histology samples. In each case, the static case (no blood flow) is compared with the case of blood flow along the axis of extrusion ($v_b = 0.33$ mm.s^{-1}). The signal has been normalised with respect to the dissolved-phase ^{129}Xe signal at infinite diffusion time for no blood flow resulting from the corresponding 2D simulations. b) Simulated normal and UIP ^{129}Xe uptake curves for $v_b = 0.33$ mm.s^{-1} from a) fitted with the 1D analytical model of Patz et al.

(iv) An illustration of the 3D mesh resulting from the segmentation process, and the simulated xenon distribution after $t = 0.33$ s in a geometry derived from volumetric μ-CT data of normal lungs is shown in Figure 8.9a) and b), respectively. Note: the outer surface of the alveolar tissue was saturated at all time-points by definition of the Dirichlet boundary condition. Figure 8.9c) highlights the significantly increased saturation time associated with a geometry derived from a 3D μ-CT volume of IPF lungs compared with that of normal lungs. The saturation time in both cases was longer than that observed for the 2D or 3D histological samples.
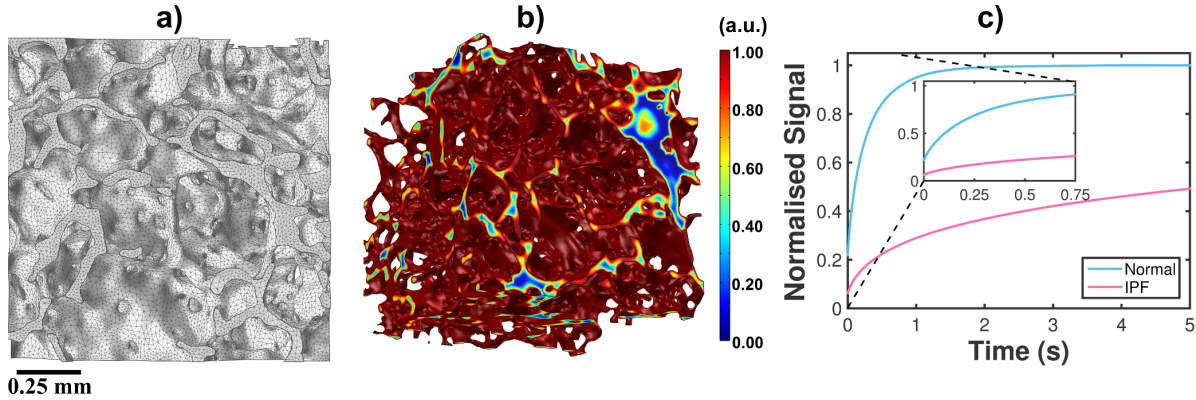
Figure 8.9: 3D FEM simulations for a geometry derived from a section of a 3D μ-CT volume obtained from the lungs of a normal subject. a) Side view of the 3D finite element mesh developed for this image volume. b) Simulated distribution of ^{129}Xe in the dissolved-phase after $t = 0.33$ s. Note: the dark red appearance of the boundaries of the alveolar septa reflects the Dirichlet boundary condition of a constant source of ^{129}Xe magnetisation from the airspace (by definition of the model, the boundaries were observed to be dark red at all time-points). c) Integrated dissolved ^{129}Xe magnetisation as a function of time for geometries derived from μ-CT volumes of normal and IPF lungs. (Inset: magnified view of the $t = 0$ s to $t = 0.75$ s region.) The dissolved-phase ^{129}Xe signal is normalised by that at infinite diffusion time for no blood flow.

8.4   Discussion & Conclusions

This work presents, to our knowledge, the first implementation of a finite element based numerical simulation framework for analysis of ^{129}Xe diffusive exchange in the alveoli and evaluation of the impact of different lung microstructural and physio-chemical parameters on the expected NMR signal behaviour of dissolved ^{129}Xe. In this section, the limitations and implications of the several modelling approaches introduced here are discussed.

Validity and assumptions of geometrical approaches

Of the four geometrical approaches adopted for finite element simulations of ^{129}Xe diffusive exchange in the lungs, no one single model is able to completely fulfil the criteria of accounting for heterogeneity in tissue and capillary thicknesses, whilst still permitting distinction of the ^{129}Xe signals arising from parenchymal tissues and blood plasma as compared with red blood cells. The 3D cylindrical capillary model allows for distinction of the contributions of tissue and blood compartments, but requires assumptions about the pulmonary haematocrit in order to separate the plasma and RBC signal contributions, and does not account for heterogeneity of septal geometry; whilst the image-based models provide an adequate geometrical representation of the heterogeneity of the alveolar geometry, but do not allow the separation of contributions from different septal compartments.

Nevertheless, to date, the primary outcome metric of the ^{129}Xe CSSR experiment that has been presented with most clinical relevance is the whole-lung septal thickness (see e.g. [138, 140, 141] and Section 6.3), which can be derived by treating the entire dissolved-phase as a single compartment [138]. In Sections 6.3 and 6.4, it has been shown that septal thickness values derived from analytical models that treat the dissolved-phase as single or multiple compartments are comparable, with a mean difference in derived ST values of $< 10\%$ between the two implementations. Thus, though there are considerable opportunities for improvement of our geometrical models (as suggested below), we can conclude that our

numerical simulation results can be compared qualitatively with in vivo clinical ^{129}Xe CSSR data in their present state.

However, it is challenging to directly and quantitatively compare in vivo ^{129}Xe CSSR measurements with our simulated data. Full validation of our simulations would require in vivo CSSR of a subject, followed by extraction of a sample of lung tissue and ex vivo CSSR of that sample, further followed by micro-CT and/or histological analysis for generation of finite element geometries. This is an involved procedure, and is highly susceptible to the heterogeneity of the alveolar septa across the lungs, particularly in subjects with lung disease, and is a topic of further work in our laboratory.

As a first step towards semi-quantitative comparison of our simulated data with previous in vivo CSSR data, an existing analytical model of ^{129}Xe diffusive uptake was utilised to fit the simulated ^{129}Xe uptake curves from 3D histological samples and evaluate the derived fitting parameters, namely the alveolar septal thickness. The analytical model presented by Patz et al [138] was chosen for this purpose because it treats the dissolved-phase as a single compartment, and therefore it is appropriate for use with the 3D histological models wherein the tissue and capillary regions cannot be distinguished. In addition, this model has previously been found to be robust in a number of ^{129}Xe CSSR studies involving human subjects (see e.g. [138, 248] and Chapter 6). Fitting the Patz et al model to the simulated signal-time curve (Figure 8.8b, $v_b = 0.33$ mm.s^{-1}) for the 3D normal histology model resulted in a mean septal thickness value of 8.8 μm. In order to validate this value, the septal thickness was also estimated from the original 2D histological image by drawing (~ 60) perpendicular lines on the image across different regions of the septa. The mean septal thickness in the histology section was found to be 9.8 ± 6.3 μm by this method, which is comparable to that derived from fitting the associated uptake curve. In addition, both these septal thickness values are in good agreement with values derived from previous in vivo ^{129}Xe CSSR measurements in healthy human volunteers [138, 140, 141, 248] (and Chapters 6 and 7), which suggest that a value of ~ 10 μm is representative of normal lung.

Septal thickness values derived from fitting 3D UIP histology-based models with the analytical model of Patz et al (Figure 8.8b) were 21.4 μm and 17.2 μm for the two samples (UIP #1 and UIP #2 respectively). These values were significantly lower than the values determined from the original histological images by the line drawing approach (30-40 lines per image resulted in septal thickness values of 62.7 ± 33.5 μm and 79.2 ± 47.1 μm, respectively). However, the fitted-simulated values were in approximate agreement with values reported in the literature for subjects with interstitial lung disease: 15-22 μm [138]; ~ 17 μm (Chapter 6). Discrepancies between in vivo measured values and values obtained from the line drawing approach may be explained by disease heterogeneity; i.e. the fact that the histological samples of UIP lungs were taken from heavily diseased regions of lungs, whilst in reality, UIP lungs are comprised of a mixture of healthy and diseased regions that are distributed heterogeneously (see Figure 6.1 of Section 6.1). However, the differences between the UIP septal thicknesses derived from the fitted-simulated data and the line drawing method are considerable. These differences could result from the fact that the blood flow acts as a "heat-sink" to extract ^{129}Xe from the gas exchange region and create / maintain a concentration gradient to allow a more rapid uptake of ^{129}Xe in the gas exchange region. This increased rate of uptake would then lead to a lower estimated septal thickness. It is likely that this same process contributes to the in vivo measured septal thicknesses being lower than the values derived by line drawing.

One of the principal limitations of the 2D and 3D image-based models is that the resulting geometries reflect the situation in only a relatively small part of the lungs, from which the samples were obtained. Due to the highly heterogeneous nature of the alveolar geometry, particularly so in patients with interstitial lung disease (see again Figure 6.1 of Section 6.1), histological images acquired from different regions of the lungs could result in considerably altered apparent ^{129}Xe CSSR uptake behaviour. Therefore, our current models are biased to provide information about a specific region of the lung parenchyma, whilst the ^{129}Xe CSSR measurement involves acquisition of spectra from the whole of the lungs, corresponding to a global average of the alveolar microstructure. Hence, a better representation of ^{129}Xe CSSR data could be obtained by simulations using a geometry derived from the entire lung volume, for example using 3D volumetric μ-CT images. However, this geometry would be extremely complex and simulations would be practically unfeasible in reasonable timescales on a desktop PC. Furthermore, the resolution of the μ-CT images used in this work is relatively low compared with that of histology images, limiting the number of pixels comprising the dissolved-phase ^{129}Xe regions. If the μ-CT resolution could be improved, finer capillary structures could be identified, and an increased mesh density could be used, allowing for better implementation of the initial saturation conditions at $t = 0$ s [ii]. Nevertheless, increased image resolution would in-turn lead to additional computational complexity. An alternative solution would be to obtain histological samples from specific regions of the lungs to compare with spectral time-series data associated with a comparable spatial location (i.e. obtained by applying additional phase encoding to the CSSR sequence, see e.g. Section 7.4.1).

As mentioned above, the UIP histological samples simulated herein exhibited considerably longer ^{129}Xe saturation times and hence increased diffusive exchange limitation compared with that observed in IPF patients previously studied with ^{129}Xe CSSR (see Section 6.3). This may be partially explained by the highly heterogeneous distribution of tissue fibrosis in IPF lungs; i.e. if the histological samples used in this work were purposely obtained from severely diseased sections of the lungs, the gas exchange process would be expected to be adversely affected to a greater degree than in a whole-lung CSSR measurement that involves averaging over diseased (i.e. structurally altered) and relatively healthy (i.e. not structurally altered) regions of the lungs. Furthermore, histological samples were obtained post-mortem; as such, it may be supposed that they would represent a more severe stage of disease when compared with in vivo ^{129}Xe MR data obtained from live patients. In an ideal situation, histological samples obtained from lung biopsies of ILD patients on, or close to, the date of ^{129}Xe CSSR scanning could be used for direct comparison of simulation results to in vivo data.

Following on from this, it is prudent to discuss the validity of artificial thickening of the alveolar septa of normal histological samples as a means of simulating the effects of interstitial lung disease. As highlighted by the differences in the "static" (2D, no blood flow) uptake curves when comparing UIP samples and artificially-thickened normal samples (Figure 8.6), it is apparent that the derived gas exchange dynamics are significantly disparate. The histological samples obtained from normal lungs exhibit noticeably more homogeneity of septal thickness after dilation than those from UIP lungs, which show a wide range of airspace and capillary sizes. The artificial thickening process was found to increase the mean septal

---

[ii]In the present simulations, the integrated dissolved-phase ^{129}Xe signal is not precisely zero at $t = 0$ since the pixels at the borders of the dissolved-phase are non-zero (due to contact with the gaseous-phase). Improved resolution of the dissolved-phase ^{129}Xe compartments would lead to an initial dissolved-phase ^{129}Xe signal that was closer to zero.

thickness of the histological sample in a linear manner, as quantified by the line drawing method: normal sample, 9.8 ± 6.3 μm; sample dilated by structuring elements of 10 pixels in size, 28.0 ± 7.3 μm; sample dilated by structuring elements of 20 pixels in size, 48.9 ± 8.3 μm. This was also reflected in the time taken for the ^{129}Xe signal in each geometry to saturate (since the saturation time is directly proportional to the square of the septal thickness [138, 139]). Fitting the Patz et al model to the simulated uptake curves derived from normal and artificially-thickened normal samples (data in Figure 8.6) yielded septal thickness estimates of: normal sample, 9.7 μm; sample dilated by structuring elements of 10 pixels in size, 30.2 μm; sample dilated by structuring elements of 20 pixels in size, 52.3 μm. These values are in good agreement with the values calculated using the line drawing method, and further support the uniform thickening induced by the artificial thickening procedure – i.e. that dilation by a structuring element of 10 pixels in size leads to an increase in septal thickness by ~ 20 μm on average. This is not unexpected when the original pixel size is 0.67 μm and the structuring element is ball shaped with a radius equal to either 10 or 20 pixels.

As discussed above, the steep initial section of the ^{129}Xe uptake curve of the UIP samples (and non-linear behaviour when plotted against $t^{\frac{1}{2}}$) can be attributed to the presence of numerous small structures that are saturated on a rapid timescale; these structures were less prominent in artificially-thickened samples. It is also noticeable from observations of the UIP sections that the sizes and shapes of the alveolar airspaces are dissimilar to those of the normal lung sections. These two factors in combination imply that the effects of an alteration to the surface-area-to-volume ratio in addition to the effects of changes in septal thickness may be entwined when fitting the ^{129}Xe uptake dynamics from UIP patients with the aforementioned analytical CSSR models. In future work, it may be beneficial to explore alternative means of artificially thickening the septa of normal histological samples in a more heterogeneous manner, for example by adopting a spatially-random variation in the size of the structuring elements employed for the dilation process.

A final assumption employed herein is that the blood flow in the lungs is well-approximated by linear (plug) flow. Plug flow was assumed previously in the development of the analytical models for simplicity reasons, and here we have adopted the same assumptions for consistency. However, in practice, pulmonary capillary blood flow is weakly pulsatile in nature, and a recent report suggested that oscillations in the ^{129}Xe RBC peak intensity of up to $\sim 20\%$ of the magnitude of the peak can be observed by in vivo NMR spectroscopy methods as a result of the pulsatile blood flow in the capillaries [358]. In our simulations based on 2D and 3D image segmentations, we have considered only a single dissolved-phase ^{129}Xe compartment consisting of lung parenchymal tissue along with plasma and RBCs, thus the pulsatile nature of blood flow would be expected to have a less significant impact on the resulting signal dynamics. We would expect that the oscillatory amplitude of the total dissolved-phase MR signal measured in a ^{129}Xe CSSR experiment would be much less than 20%, and would cause negligible alterations to the derived uptake curve. Therefore, we believe that it is reasonable to assume that blood flow is constant. However, in future work, more complex models of pulmonary blood flow may be implemented relatively straight-forwardly within the existing simulation framework.

Relevance and implications of finite element simulations

The fact that alterations of multiple lung microstructural and physical parameters, such as the septal thickness, air-blood barrier thickness and diffusion coefficient, can present as only subtle changes to the shape of the observed ^{129}Xe uptake dynamics implies that clinically-relevant differences in these parameters may be difficult to uniquely identify from ^{129}Xe CSSR data. Furthermore, under certain experimental conditions, differences in alveolar surface-area-to-volume ratio could be challenging to distinguish from alterations to the tissue geometry or diffusion coefficient.

Thus, in future ^{129}Xe NMR spectroscopy and imaging experiments sensitised to diffusive exchange of xenon in the lungs, care must be taken as to the choice of the acquisition timing post-saturation of the dissolved ^{129}Xe magnetisation with a spectrally-selective 90° RF pulse. If a 90° pulse is used with a fixed repetition time, then the repetition time should be chosen such that it represents a time-point corresponding to the regime where the dissolved ^{129}Xe signal is predominantly governed by diffusive uptake rather than perfusion. In addition, for future ^{129}Xe CSSR experiments, in which a number of exchange times are probed in order to measure the dynamics of the uptake process, we may postulate that the total number of acquired data-points could be reduced by minimising the number of points in the perfusion-dominated region of the curve. In other words, because we have verified that the simulated uptake behaviour after $\sim$ 200 ms exhibits an approximately linear response as a function of time governed by the pulmonary blood flow, only one or two data-points need to be collected in this region, which should help to reduce scan times and facilitate CSSR spectroscopic imaging applications wherein spatial information could be encoded in addition to temporal and spectral information (see e.g. Section 7.4.1 and [341]). As indicated in Figure 8.8, it is critical to acquire a sufficient number of data-points to accurately resolve the short timescale ($<$ 200 ms) behaviour in order to quantify differences in diffusive exchange efficiency between disease states; as can be seen in this figure, the rate of change of the uptake curves of normal and diseased lungs after $\sim$ 200 ms is very similar (because the prescribed blood flow dynamics were equivalent), whilst the short timescale data exhibits significant discrepancies between the normal and the two UIP examples. Thus, to accurately distinguish the different rates of diffusive uptake, acquisition of short timescale data at multiple time-points is necessary.

Due to the relative complexity of the finite element simulations in comparison to calculation of analytical solutions of ^{129}Xe CSSR data, it is impractical to replace typically-employed rapid analytical curve-fitting processes with a least squares optimisation that incorporates a series of time-consuming finite element simulations. However, we propose that the numerical simulations introduced here may be used to validate / verify the analytical solutions, for example, in order to aid decision making about which physical or microstructural parameters may have led to an observed change in the dissolved ^{129}Xe signal behaviour. Unfortunately, due to the multitude of factors contributing to the measured signal, as discussed above, the interpretation of the analytical models may be obscured without numerical validation. Furthermore, by simulating the dissolved ^{129}Xe MR signal for a number of different histology and μ-CT sections from subjects with different forms of lung disease, it may be possible to generate a "library" of data pertaining to the gas exchange behaviour of different disease subtypes and co-pathologies. It may therefore be possible to compare in vivo and simulated data from these subgroups of patients in order to identify and explain subtle alterations to the uptake dynamics.

The numerical simulations performed in this work highlight the importance of considering a representative geometrical picture of the alveolar-parenchymal substrate when investigating ^{129}Xe diffusive uptake via NMR methods. Our findings may be used to improve the existing analytical models of ^{129}Xe diffusive uptake, for example by introducing an additional parameter to quantify the heterogeneity in alveolar septal dimensions. However, the high number of fitting parameters involved in the current analytical models means that the robustness of these models may be approaching the limits of clinical suitability. Thus, it is especially advantageous to maintain a flexible numerical solution to the diffusion problem for validating the results of the analytical models.

The methods introduced here can relatively easily be extended to simulate the ADC of ^{129}Xe in the airspaces, and to quantify to what extent the ADC measurement could be influenced by diffusive exchange of ^{129}Xe between the gaseous- and dissolved-phase compartments. To date, it has been assumed that derived ^{129}Xe ADC values are negligibly affected by the exchange process because only $\sim 2\%$ of the total inhaled ^{129}Xe is taken up into the dissolved-phase, but the validity of this assumption has not been fully explored. Using the approaches described here and elsewhere [348], an end goal of this project would be to generate a full 3D model of the alveolar and airway network and to model the time-course of inhalation, distribution and uptake of ^{129}Xe, allowing simultaneous prediction of the ^{129}Xe ADC in the alveoli and lung microstructural parameters from CSSR spectroscopy. It can be envisaged that representative models of blood flow in the capillary network could be added to the model, accounting for its pulsatile behaviour in order to examine the implications for in vivo NMR experiments [358]. However, it is important to consider that this model would require a means of estimating the contribution from xenon situated outside the gas exchange region to the total dissolved ^{129}Xe signal.

Furthermore, in future experiments, the developed models could be better related to actual in vivo ^{129}Xe spectroscopy data by replacing the absolute magnetisation (employed here as a surrogate for concentration) with the complex form of the measured transverse magnetisation, and conditions could be established to account for the difference in Larmor frequency by applying a different magnetisation phase in the different chemical compartments. This approach would be valid for geometries in which it is possible to accurately separate the parenchymal tissues and blood, and as such, would require distinction of the plasma and red blood cells by visual methods or by making assumptions about the pulmonary haematocrit. Similarly, the gaseous-phase and the dissolved-phases could be isolated by the phase of the magnetisation, such that the ^{129}Xe magnetisation could be more easily simulated in a full 3D model of the alveolar airspace and capillaries, as discussed above.

Conclusions

A model system for simulating the effect of lung microstructural and physical parameters on ^{129}Xe diffusive exchange NMR of the lungs has been developed by implementing a uniform 3D cylindrical model of the alveolar septal compartment. Finite element simulations of ^{129}Xe diffusion have been carried out using this geometry and realistic 2D and 3D geometries of the alveoli derived from histology and micro-CT images of normal and diseased lungs. This work has implications for future MR imaging and spectroscopy studies with dissolved ^{129}Xe in the lungs, in terms of choice of acquisition timing parameters, and in particular, to improve the accuracy of modelling of lung microstructure and gas exchange from ^{129}Xe NMR data.

Chapter 9

Summary and further work

This thesis has been primarily concerned with the development and experimental validation of MR methods for the study of lung function with hyperpolarised ^{129}Xe. This summary chapter reviews the findings of each experimental chapter of this thesis, and summarises the proposed future directions of research in each related area, including some examples of ongoing work. The co-authors of this chapter are: M. R. Rao, G. Norquay and J. M. Wild. Author contributions statement: study design, NJS, MRR, GN, JMW; acquisition of data, NJS, MRR, GN; analysis of data, NJS, MRR; drafting of chapter, NJS, JMW.

The initial impact and historical predominance of clinical studies with both hyperpolarised ^{3}He and ^{129}Xe gas MRI has been realised through direct imaging of pulmonary ventilation, and mapping of the apparent diffusion coefficient of the gases in the alveolar airspaces. **Chapter 4** reports on the optimisation and experimental validation of a 3D steady-state free precession acquisition strategy for high quality lung ventilation imaging with ^{129}Xe, with the goal of improving image SNR to overcome the limitations imposed by the relatively lower gyromagnetic ratio of ^{129}Xe compared with ^{3}He. A method for numerical simulation of the 3D bSSFP signal, including the sensitivity to B_0 and B_1 inhomogeneities, has been demonstrated and utilised to derive the optimum imaging parameters for ^{129}Xe lung imaging. This approach has been employed to acquire high SNR images with relatively cheap and readily-available naturally-abundant xenon. In combination with the development of compressed sensing techniques for attainment of clinically-feasible breath-hold times, this work indicates the potential of ^{129}Xe for replacing ^{3}He in routine ventilation imaging applications, and opens up the possibility of relatively inexpensive longitudinal screening of patients with lung disease without the use of ionising radiation. It is worth noting that the numerical optimisation method and 3D bSSFP pulse sequence is readily applicable to other nuclei, and in fact, variations on the sequence described in Section 4.3.2 are now used routinely in our group for ventilation imaging with hyperpolarised ^{3}He in addition to ^{129}Xe.

   Chapter 5 presents the results of a preliminary study in which two proposed biomarkers of lung function derived from hyperpolarised gas ventilation imaging and ADC mapping with ^{3}He and ^{129}Xe — namely the ventilated volume percentage of the lung and the global mean ADC — are quantitatively compared in healthy subjects, and patients with lung cancer and COPD. Of particular interest, the findings highlight the excellent reproducibility of derived VV% and ADC metrics in a patient cohort, and demonstrate that ^{129}Xe provides almost equivalent functional information to ^{3}He on the whole-lung level. In future work, the relationship between ventilation and ADC data derived from the two gases will be investigated more thoroughly on a regional (slice-by-slice) basis, to appraise the relative sensitivity to spatially-heterogeneous disease. Additionally, whilst the study involving COPD patients has now been completed, recruitment of patients with lung cancer is ongoing, and further data from supplementary cohorts of patients should be collected in order to strengthen the argument for ^{129}Xe being adopted as a more economically-viable alternative to ^{3}He for these applications.

In **Chapters 6**, **7** and **8**, an implementation of the ^{129}Xe chemical shift saturation recovery MR spec-

troscopy method for assessment of pulmonary gas exchange dynamics, an experimental validation and a review of the methodological considerations of the technique, and a finite element modelling framework for further validation and exploration of the limitations of the technique, are presented respectively. A preliminary study in patients with SSc and IPF has been carried out to validate the applicability of the CSSR technique for quantification of pathological alterations to lung microstructural parameters, in particular, the thickness of the alveolar septum. The CSSR-derived septal thickness has been shown to be reproducible in COPD patients and healthy volunteers, and indicates the utility of the method as a complementary functional assessment tool to conventional pulmonary function tests. The applicability of analytical models of gas diffusion in the lung parenchyma and capillaries for estimation of lung microstructural parameters has been evaluated, and a numerical solution to the diffusion equation has been implemented in order to investigate the effects of crucial physico-chemical parameters on diffusive gas exchange in the lungs. Gas exchange simulations have been performed using 2D and 3D image-based models which account for the effects of heterogeneity of lung disease, for the purpose of appraising the robustness of ^{129}Xe CSSR data and permitting better classification of gas exchange behaviour in terms of its underlying causes. These methods exhibit promise for non-invasive quantification of lung microstructural remodelling in lung diseases characterised by gas exchange limitation. Future work will focus on the realisation of acquisition of regional, dynamic information about gas exchange, with selectivity of the signal from ^{129}Xe dissolved in lung tissue and plasma, and RBCs, in a single breath-hold. In addition, further development of geometrical models for numerical simulations of diffusion in the alveolar airspaces, gas exchange, and perfusion in the capillaries in a full three-dimensional network should enable simultaneous prediction of ^{129}Xe ADC mapping and dynamic spectroscopic data.

In light of the successful identification of septal thickening in patients with IPF by ^{129}Xe CSSR, a further study is already underway in our group with the principal aim of assessing longitudinal changes in MR-derived metrics (including ^{129}Xe CSSR-derived septal thickness, and ^{3}He ventilation volume percentage and ADC) in IPF patients at baseline, 6 months and 12 months. The sensitivity of these metrics to early IPF is being investigated by conducting the baseline scans as close as possible to the date of initial diagnosis of the condition. Furthermore, by carrying out two baseline scans on the same scan date, the reproducibility of these metrics in the IPF cohort is under evaluation.

A focus of current experimental work is to establish ultra-short TE pulse sequence acquisition and reconstruction strategies for imaging of dissolved-phase ^{129}Xe in the human lungs for regional evaluation of pulmonary gas exchange. Dixon- [148] and IDEAL-based [147] techniques with radial encoding schemes have been previously demonstrated elsewhere in order to overcome the limitations imposed by the short T_2^* relaxation times and intrinsically low signal associated with dissolved-phase ^{129}Xe in vivo. In combination with existing ^{129}Xe CSSR and high-resolution spectroscopic approaches (see e.g. [171]), these methods have the potential to form a comprehensive dissolved ^{129}Xe MR protocol for the evaluation of multiple aspects of pulmonary gas exchange function.

Preliminary work has been undertaken to design and implement 2D and 3D radial encoding strategies with spectrally-selective radiofrequency excitations of dissolved- and gaseous-phase ^{129}Xe. An example data-set from an isotropic 3D radial acquisition with interleaved excitation of dissolved and gaseous ^{129}Xe in a single breath-hold is shown in Figure 9.1. These initial images clearly depict the challenges associated with imaging ^{129}Xe in the dissolved-phase as compared with the gaseous-phase (in terms of image SNR);

however, the quality of obtained dissolved-phase ^{129}Xe images should be sufficient for the acquisition of distinct images from the two dissolved-phase compartments in the near future.
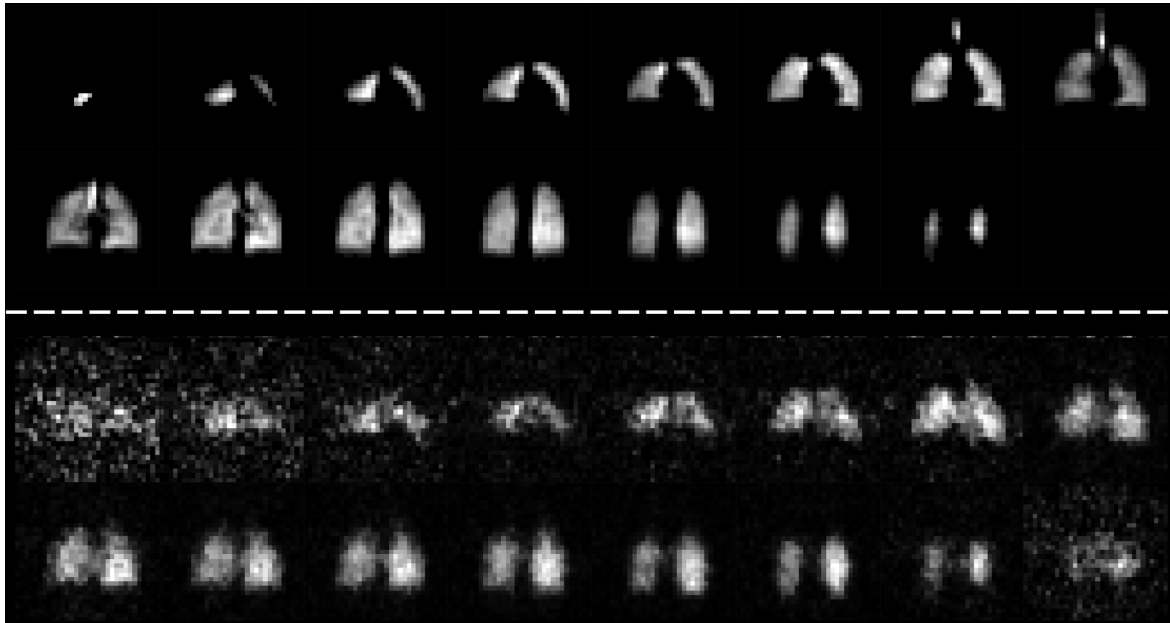
Figure 9.1: 3D radial interleaved acquisition of dissolved- and gaseous-phase ^{129}Xe images from the lungs of a healthy volunteer. Top: coronally-reconstructed gaseous-phase ^{129}Xe images (flip angle $\sim 0.5°$). Bottom: coronally-reconstructed dissolved-phase ^{129}Xe images (flip angle $\sim 18°$). Effective voxel size 12.5 mm^3 in both cases.

One application of 3D (UTE) radial imaging — when used in combination with Dixon or IDEAL CSI for separation of MR signals arising from ^{129}Xe dissolved in T/P and RBC compartments — is the improved visualisation of gas exchange impairment and semi-quantitative assessment of ventilation-perfusion matching, which is particularly of interest in co-pathologies that cause both diffusion and perfusion limitation, for example interstitial lung disease and co-existing pulmonary hypertension.

In addition, work is in progress to optimise acquisition strategies for visualising the distribution of cerebral perfusion via hyperpolarised ^{129}Xe MRI of the brain. In previous work by our group, traditional 2D spoiled gradient echo sequences have been used to obtain preliminary images of ^{129}Xe dissolved in the grey matter in vivo after inhalation by human subjects [359]. However, in light of the low T_2^* of dissolved-phase ^{129}Xe in vivo, ultra-short echo time radial encoding may offer the possibility of improved image SNR. To this end, work is underway to implement and optimise 2D radial acquisition techniques for human brain imaging. Preliminary 2D radial images of ^{129}Xe dissolved in a healthy human brain in the axial and sagittal orientations are depicted in Figure 9.2.

In conclusion, the promise of ^{129}Xe as an alternative to ^{3}He, and for additional functional studies of the lung that are unfeasible with ^{3}He, is considerable. It is hoped that the work presented in this thesis will add to the extensive literature demonstrating the potential of ^{129}Xe MRI techniques, and ultimately, aid in their clinical translation.

As a final note, it has been briefly mentioned in **Chapters 2** and **4** that our group has recently received
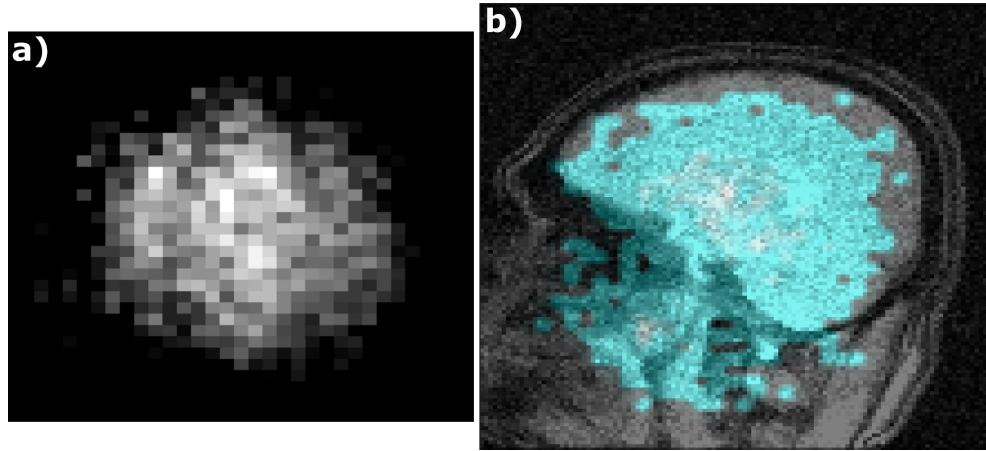
Figure 9.2: 2D radial images of ^{129}Xe dissolved in the human brain. a) Axial image. b) Sagittal image overlaid on a low resolution ^{1}H image (acquired with the ^{129}Xe brain coil in situ). In both cases, the in-plane pixel dimension was 7.5 mm and the slice thickness was either 18 cm (sagittal) or 20 cm (axial). Images were acquired 15 seconds after inhalation of $\approx$ 1 L of pure isotopically-enriched xenon.

a licence for patients to be referred for hyperpolarised gas scans by clinicians. This licence applies to both ^{3}He and ^{129}Xe and represents a vital step towards translation of the technique for diagnostic purposes in a clinical setting. The initial intake of referred patients has been extremely promising, with a current referral frequency of approximately one patient per week. These patients typically undergo a 3D bSSFP imaging sequence for assessment of lung ventilation, and ADC mapping and other more specialised techniques can be requested by the clinician. Although the initial successes of the award of this licence are exciting for the hyperpolarised gas MRI field, a more widespread dissemination of the advantages and possibilities of the techniques is still required to facilitate increased interest from additional centres throughout the UK.

Chapter 10

Bibliography

[1] Hatabu, H., Alsop, D. C., Listerud, J., Bonnet, M., and Gefter, W. B. ≪T2* and proton density measurement of normal human lung parenchyma using submillisecond echo time gradient echo magnetic resonance imaging.≫ European Journal of Radiology, **29**(3):pp. 245–252, 1999.

[2] Puderbach, M., Hintze, C., Ley, S., Eichinger, M., Kauczor, H. U., and Biederer, J. ≪MR imaging of the chest: A practical approach at 1.5 T.≫ European Journal of Radiology, **64**(3):pp. 345–355, 2007.

[3] Bergin, C J, Glover, G H, and Pauly, J M. ≪Lung parenchyma: magnetic susceptibility in MR imaging.≫ Radiology, **180**(3):pp. 845–848, 1991.

[4] Swift, Andy J., Woodhouse, Neil, Fichele, Stan, Siedel, Jochen, Mills, Gary H., van Beek, Edwin J. R., and Wild, Jim M. ≪Rapid Lung Volumetry Using Ultrafast Dynamic Magnetic Resonance Imaging During Forced Vital Capacity Maneuver: Correlation With Spirometry.≫ Investigative Radiolology, **42**(1):pp. 37–41, 2007.

[5] Wielpütz, Mark and Kauczor, Hans-Ulrich. ≪MRI of the lung: state of the art.≫ Diagnostic and Interventional Radiology, **18**(4):pp. 344–353, 2012.

[6] Semelka, Richard C., Balci, N. Cem, Wilber, Kathy P., Fisher, Laurie L., Brown, Mark A., Gomez Caminero, Andres, and Molina, Paul L. ≪Breath-hold 3D gradient-echo MR imaging of the lung parenchyma: Evaluation of reproducibility of image quality in normals and preliminary observations in patients with disease.≫ Journal of Magnetic Resonance Imaging, **11**(2):pp. 195–200, 2000.

[7] Kluge, Alexander, Mueller, Clemens, Strunk, Johannes, Lange, Uwe, and Bachmann, Georg. ≪Experience in 207 Combined MRI Examinations for Acute Pulmonary Embolism and Deep Vein Thrombosis.≫ American Journal of Roentgenology, **186**(6):pp. 1686–1696, 2006.

[8] Stein, Paul D., Fowler, Sarah E., Goodman, Lawrence R., Gottschalk, Alexander, Hales, Charles A., Hull, Russell D., Leeper, Kenneth V., Popovich, John, Quinn, Deborah A., Sos, Thomas A., Sostman, H. Dirk, Tapson, Victor F., Wakefield, Thomas W., Weg, John G., and Woodard, Pamela K. ≪Multidetector Computed Tomography for Acute Pulmonary Embolism.≫ New England Journal of Medicine, **354**(22):pp. 2317–2327, 2006.

[9] Biederer, Jrgen, Mirsadraee, S., Beer, M., Molinari, F., Hintze, C., Bauman, G., Both, M., Van Beek, E. J. R., Wild, J., and Puderbach, M. ≪MRI of the lung (3/3) - current applications and future perspectives.≫ Insights Imaging, **3**(4):pp. 373–386, 2012.

[10] Failo, Riccarda, Wielopolski, Piotr A., Tiddens, Harm A. W. M., Hop, Wim C. J., Pozzi Mucelli, Roberto, and Lequin, Maarten H. ≪Lung morphology assessment using MRI: A robust ultra-short TR/TE 2D steady state free precession sequence used in cystic fibrosis patients.≫ Magnetic Resonance in Medicine, **61**(2):pp. 299–306, 2009.

[11] Rajaram, Smitha, Swift, Andrew J., Capener, David, Telfer, Adam, Davies, Christine, Hill, Catherine, Condliffe, Robin, Elliot, Charles, Hurdman, Judith, Kiely, David G., and Wild, Jim M. ≪Lung Morphology Assessment with Balanced Steady-State Free Precession MR Imaging Compared with CT.≫ Radiology, **263**(2):pp. 569–577, 2012.

[12] Fabel, M., Wintersperger, B. J., Dietrich, O., Eichinger, M., Fink, C., Puderbach, M., Kauczor, H. U., Schoenberg, S. O., and Biederer, J. ≪MRI of respiratory dynamics with 2D steady-state free-precession and 2D gradient echo sequences at 1.5 and 3 Tesla: an observer preference study.≫ European Radiology, **19**(2):pp. 391–399, 2009.

[13] Plathow, Christian, Ley, Sebastian, Fink, Christian, Puderbach, Michael, Heilmann, Melanie, Zuna, Ivan, and Kauczor, Hans-Ulrich. ≪Evaluation of Chest Motion and Volumetry During the Breathing Cycle by Dynamic MRI in Healthy Subjects: Comparison With Pulmonary Function Tests.≫ Investigative Radiolology, **39**(4):pp. 202–209, 2004.

[14] Biederer, J, Busse, I, Grimm, J, Reuter, M, Muhle, C, Freitag, S, and Heller, M. ≪Sensitivity of MRI in detecting alveolar Infiltrates: Experimental studies.≫ RoFo: Fortschritte auf dem Gebiete der Rontgenstrahlen und der Nuklearmedizin, **174**(8):pp. 1033–1039, 2002.

[15] Schroeder, Tobias, Ruehm, Stefan G., Debatin, Jörg F., Ladd, Mark E., Barkhausen, Jörg, and Goehde, Susanne C. ≪Detection of Pulmonary Nodules Using a 2D HASTE MR Sequence: Comparison with MDCT.≫ American Journal of Roentgenology, **185**(4):pp. 979–984, 2005.

[16] Hatabu, Hiroto, Gaa, Jochen, Tadamura, Eiji, Edinburgh, Keith J., Stock, Klaus W., Garpestad, Erik, and Edelman, Robert R. ≪MR imaging of pulmonary parenchyma with a half-Fourier single-shot turbo spin-echo (HASTE) sequence.≫ European Journal of Radiology, **29**(2):pp. 152–159, 1999.

[17] Eibel, Roger, Herzog, Peter, Dietrich, Olaf, Rieger, Christina T., Ostermann, Helmut, Reiser, Maximilian F., and

Schoenberg, Stefan O. ≪Pulmonary Abnormalities in Immunocompromised Patients: Comparative Detection with Parallel Acquisition MR Imaging and Thin-Section Helical CT.≫ Radiology, **241**(3):pp. 880–891, 2006.

[18] Puderbach, Michael, Eichinger, Monika, Haeselbarth, Julie, Ley, Sebastian, Kopp Schneider, Annette, Tuengerthal, Siegfried, Schmaehl, Astrid, Fink, Christian, Plathow, Christian, Wiebel, Matthias, Demirakca, Sueha, Mller, Frank-Michael, and Kauczor, Hans-Ulrich. ≪Assessment of Morphological MRI for Pulmonary Changes in Cystic Fibrosis (CF) Patients: Comparison to Thin-Section CT and Chest X-ray.≫ Investigative Radiolology, **42**(10):pp. 715–724, 2007.

[19] Lutterbey, G., Groh, C., Gieseke, J., von Falkenhausen, M., Morakkabati, N., Wattjes, M. P., Manka, R., Trog, D., and Schild, H. H. ≪Initial experience with lung-MRI at 3.0 T: Comparison with CT and clinical data in the evaluation of interstitial lung disease activity.≫ European Journal of Radiology, **61**(2):pp. 256–261, 2007.

[20] Yi, Chin A., Lee, Kyung Soo, Han, Joungho, Chung, Man Pyo, Chung, Myung Jin, and Shin, Kyung Min. ≪3-T MRI for Differentiating Inflammation- and Fibrosis-Predominant Lesions of Usual and Nonspecific Interstitial Pneumonia: Comparison Study with Pathologic Correlation.≫ American Journal of Roentgenology, **190**(4):pp. 878–885, 2008.

[21] Suga, Kazuyoshi, Tsukuda, Toshinobu, Awaya, Hitomi, Takano, Katsuyuki, Koike, Shinji, Matsunaga, Naofumi, Sugi, Kazuro, and Esato, Kensuke. ≪Impaired respiratory mechanics in pulmonary emphysema: Evaluation with dynamic breathing MRI.≫ Journal of Magnetic Resonance Imaging, **10**(4):pp. 510–520, 1999.

[22] Iwasawa, Tae, Takahashi, Hiroshi, Ogura, Takashi, Asakura, Akira, Gotoh, Toshiyuki, Kagei, Seiichiro, Nishimura, Jun-ichi, Obara, Makoto, and Inoue, Tomio. ≪Correlation of lung parenchymal MR signal intensity with pulmonary function tests and quantitative computed tomography (CT) evaluation: A pilot study.≫ Journal of Magnetic Resonance Imaging, **26**(6):pp. 1530–1536, 2007.

[23] Ohno, Yoshiharu, Hatabu, Hiroto, Takenaka, Daisuke, Higashino, Takanori, Watanabe, Hirokazu, Ohbayashi, Chiho, Yoshimura, Masahiro, Satouchi, Miyako, Nishimura, Yoshihiro, and Sugimura, Kazuro. ≪Metastases in Mediastinal and Hilar Lymph Nodes in Patients with Non-Small Cell Lung Cancer: Quantitative and Qualitative Assessment with STIR Turbo Spin-Echo MR Imaging.≫ Radiology, **231**(3):pp. 872–879, 2004.

[24] Ohno, Yoshiharu, Koyama, Hisanobu, Nogami, Munenobu, Takenaka, Daisuke, Yoshikawa, Takeshi, Yoshimura, Masahiro, Ohbayashi, Chiho, and Sugimura, Kazuro. ≪STIR turbo SE MR imaging vs. coregistered FDG-PET/CT: Quantitative and qualitative assessment of N-stage in non-small-cell lung cancer patients.≫ Journal of Magnetic Resonance Imaging, **26**(4):pp. 1071–1080, 2007.

[25] Morikawa, Miwa, Demura, Yoshiki, Ishizaki, Takeshi, Ameshima, Shingo, Miyamori, Isamu, Sasaki, Masato, Tsuchida, Tatsuro, Kimura, Hirohiko, Fujibayashi, Yasuhisa, and Okazawa, Hidehiko. ≪The Effectiveness of 18F-FDG PET/CT Combined with STIR MRI for Diagnosing Nodal Involvement in the Thorax.≫ Journal of Nuclear Medicine, **50**(1):pp. 81–87, 2009.

[26] Vogel Claussen, Jens, Renne, Julius, Hinrichs, Jan, Schönfeld, Christian, Gutberlet, Marcel, Schaumann, Frank, Winkler, Carla, Faulenbach, Cornelia, Krug, Norbert, Wacker, Frank K, et al. ≪Quantification of pulmonary inflammation after segmental allergen challenge using turbo-inversion recovery-magnitude magnetic resonance imaging.≫ American journal of respiratory and critical care medicine, **189**(6):pp. 650–657, 2014.

[27] Edelman, R. R., Hatabu, H., Tadamura, E., Li, W., and Prasad, P. V. ≪Noninvasive assessment of regional ventilation in the human lung using oxygen-enhanced magnetic resonance imaging.≫ Nature Medicine, **2**(11):pp. 1236–1239, 1996.

[28] Hatabu, Hiroto, Gaa, Jochen, Kim, Ducksoo, Li, Wei, Prasad, Pottumarthi V., and Edelman, Robert R. ≪Pulmonary perfusion: Qualitative assessment with dynamic contrast-enhanced MRI using ultra-short TE and inversion recovery turbo FLASH.≫ Magnetic Resonance in Medicine, **36**(4):pp. 503–508, 1996.

[29] Look, D. C. and Locker, D. R. ≪Time Saving in Measurement of NMR and EPR Relaxation Times.≫ Review of Scientific Instruments, **41**(2):pp. 250–251, 1970.

[30] Jakob, Peter M., Hillenbrand, Claudia M., Wang, Tungte, Schultz, Georg, Hahn, Dietbert, and Haase, Axel. ≪Rapid quantitative lung 1H T1 mapping.≫ Journal of Magnetic Resonance Imaging, **14**(6):pp. 795–799, 2001.

[31] Ohno, Yoshiharu, Hatabu, Hiroto, Takenaka, Daisuke, Adachi, Shuji, Van Cauteren, Marc, and Sugimura, Kazuro. ≪Oxygen-Enhanced MR Ventilation Imaging of the Lung.≫ American Journal of Roentgenology, **177**(1):pp. 185–194, 2001.

[32] Chen, Qun, Jakob, Peter. M, Griswold, Mark. A, Levin, David. L, Hatabu, Hiroto, and Edelman, Robert. R. ≪Oxygen enhanced MR ventilation imaging of the lung.≫ Magnetic Resonance Materials in Physics, Biology and Medicine, **7**(3):pp. 153–161, 1998.

[33] Sá, Rui Carlos, Cronin, Matthew V., Cortney Henderson, A., Holverda, Sebastiaan, Theilmann, Rebecca J., Arai, Tatsuya J., Dubowitz, David J., Hopkins, Susan R., Buxton, Richard B., and Kim Prisk, G. ≪Vertical distribution

of specific ventilation in normal supine humans measured by oxygen-enhanced proton MRI.≫ Journal of Applied Physiology, **109**(6):pp. 1950–1959, 2010.

[34] Ohno, Yoshiharu, Iwasawa, Tae, Seo, Joom Beom, Koyama, Hisanobu, Takahashi, Hiroshi, Oh, Yeon-Mok, Nishimura, Yoshihiro, and Sugimura, Kazuro. ≪Oxygen-enhanced Magnetic Resonance Imaging versus Computed Tomography.≫ American Journal of Respiratory and Critical Care Medicine, **177**(10):pp. 1095–1102, 2008.

[35] Hart, K, Marshall, H., Stewart, N. J., Whyte, Moira K., and Wild, J. M. ≪Quantitative lung T1 mapping and oxygen enhanced MRI in IPF.≫ European Respiratory Journal (Suppl 58), **44**:p. 1727, 2014.

[36] Molinari, Francesco, Eichinger, Monika, Risse, Frank, Plathow, Christian, Puderbach, Michael, Ley, Sebastian, Herth, Felix, Bonomo, Lorenzo, Kauczor, Hans-Ulrich, and Fink, Christian. ≪Navigator-triggered oxygen-enhanced MRI with simultaneous cardiac and respiratory synchronization for the assessment of interstitial lung disease.≫ Journal of Magnetic Resonance Imaging, **26**(6):pp. 1523–1529, 2007.

[37] Müller, Christian J., Schwaiblmair, Martin, Scheidler, Juergen, Deimling, Michael, Weber, Juergen, Löffler, Ralf B., and Reiser, Maximilian F. ≪Pulmonary Diffusing Capacity: Assessment with Oxygen-enhanced Lung MR Imaging - Preliminary Findings.≫ Radiology, **222**(2):pp. 499–506, 2002.

[38] Ohno, Yoshiharu, Hatabu, Hiroto, Takenaka, Daisuke, Van Cauteren, Marc, Fujii, Masahiko, and Sugimura, Kazuro. ≪Dynamic oxygen-enhanced MRI reflects diffusing capacity of the lung.≫ Magnetic Resonance in Medicine, **47**(6):pp. 1139–1144, 2002.

[39] Jakob, Peter M., Wang, Tungte, Schultz, Georg, Hebestreit, Helge, Hebestreit, Alexandra, and Hahn, Dietbert. ≪Assessment of human pulmonary function using oxygen-enhanced T1 imaging in patients with cystic fibrosis.≫ Magnetic Resonance in Medicine, **51**(5):pp. 1009–1016, 2004.

[40] Caravan, Peter, Ellison, Jeffrey J., McMurry, Thomas J., and Lauffer, Randall B. ≪Gadolinium(III) Chelates as MRI Contrast Agents: Structure, Dynamics, and Applications.≫ Chemical Reviews, **99**(9):pp. 2293–2352, 1999.

[41] Kauczor, Hans-Ulrich and Kreitner, Karl-Friedrich. ≪Contrast-enhanced MRI of the lung.≫ European Journal of Radiology, **34**(3):pp. 196–207, 2000.

[42] Meaney, James F.M., Weg, John G., Chenevert, Thomas L., Stafford Johnson, David, Hamilton, Brian H., and Prince, Martin R. ≪Diagnosis of Pulmonary Embolism with Magnetic Resonance Angiography.≫ New England Journal of Medicine, **336**(20):pp. 1422–1427, 1997.

[43] Fink, C., Risse, F., Buhmann, R., Ley, S., Meyer, F. J., Plathow, C., Puderbach, M., and Kauczor, H. U. ≪Quantitative Analysis of Pulmonary Perfusion using Time-Resolved Parallel 3D MRI - Initial results.≫ RoFo Fortschritte auf dem Gebiet der Rontgenstrahlen und der Bildgebenden Verfahren, **176**(2):pp. 170–174, 2004.

[44] Korosec, Frank R., Frayne, Richard, Grist, Thomas M., and Mistretta, Charles A. ≪Time-resolved contrast-enhanced 3D MR angiography.≫ Magnetic Resonance in Medicine, **36**(3):pp. 345–351, 1996.

[45] Ohno, Yoshiharu, Higashino, Takanori, Takenaka, Daisuke, Sugimoto, Kouji, Yoshikawa, Takeshi, Kawai, Hiroya, Fujii, Masahiko, Hatabu, Hiroto, and Sugimura, Kazuro. ≪MR Angiography with Sensitivity Encoding (SENSE) for Suspected Pulmonary Embolism: Comparison with MDCT and Ventilation-Perfusion Scintigraphy.≫ American Journal of Roentgenology, **183**(1):pp. 91–98, 2004.

[46] Amundsen, Tore, Torheim, Geir, Kvistad, Kjell A., Waage, Anders, Bjermer, Leif, Nordlid, Knut K., Johnsen, Harald, sberg, Arne, and Haraldseth, Olav. ≪Perfusion abnormalities in pulmonary embolism studied with perfusion MRI and ventilation-perfusion scintigraphy: An intra-modality and inter-modality agreement study.≫ Journal of Magnetic Resonance Imaging, **15**(4):pp. 386–394, 2002.

[47] Jang, Yu Mi, Oh, Yeon-Mok, Seo, Joon Beom, Kim, Namkug, Chae, Eun Jin, Lee, Young Kyung, and Lee, Sang Do. ≪Quantitatively Assessed Dynamic Contrast-Enhanced Magnetic Resonance Imaging in Patients With Chronic Obstructive Pulmonary Disease: Correlation of Perfusion Parameters With Pulmonary Function Test and Quantitative Computed Tomography.≫ Investigative Radiolology, **43**(6):pp. 403–410, 2008.

[48] Ohno, Yoshiharu, Hatabu, Hiroto, Higashino, Takanori, Takenaka, Daisuke, Watanabe, Hirokazu, Nishimura, Yoshihiro, Yoshimura, Masahiro, and Sugimura, Kazuro. ≪Dynamic Perfusion MRI Versus Perfusion Scintigraphy: Prediction of Postoperative Lung Function in Patients with Lung Cancer.≫ American Journal of Roentgenology, **182**(1):pp. 73–78, 2004.

[49] Ohno, Yoshiharu, Hatabu, Hiroto, Murase, Kenya, Higashino, Takanori, Kawamitsu, Hideaki, Watanabe, Hirokazu, Takenaka, Daisuke, Fujii, Masahiko, and Sugimura, Kazuro. ≪Quantitative assessment of regional pulmonary perfusion in the entire lung using three-dimensional ultrafast dynamic contrast-enhanced magnetic resonance imaging: Preliminary experience in 40 subjects.≫ Journal of Magnetic Resonance Imaging, **20**(3):pp. 353–365, 2004.

[50] Fink, Christian, Bock, Michael, Puderbach, Michael, Schmhl, Astrid, and Delorme, Stefan. ≪Partially Parallel Three-

204

Dimensional Magnetic Resonance Imaging for the Assessment of Lung Perfusion - Initial Results.≫ Investigative Radiolology, **38**(8):pp. 482–488, 2003.

[51] Rajaram, Smitha, Swift, Andrew J, Telfer, Adam, Hurdman, Judith, Marshall, Helen, Lorenz, Eleanor, Capener, David, Davies, Christine, Hill, Catherine, Elliot, Charlie, Condliffe, Robin, Wild, Jim M, and Kiely, David G. ≪3D contrast-enhanced lung perfusion MRI is an effective screening tool for chronic thromboembolic pulmonary hypertension: results from the ASPIRE Registry.≫ Thorax, **68**(7):pp. 677–8, 2013.

[52] Ohno, Yoshiharu, Hatabu, Hiroto, Murase, Kenya, Higashino, Takanori, Nogami, Munenobu, Yoshikawa, Takeshi, and Sugimura, Kazuro. ≪Primary Pulmonary Hypertension: 3D Dynamic Perfusion MRI for Quantitative Analysis of Regional Pulmonary Perfusion.≫ American Journal of Roentgenology, **188**(1):pp. 48–56, 2007.

[53] Swift, Andrew J., Telfer, Adam, Rajaram, Smitha, Condliffe, Robin, Marshall, Helen, Capener, Dave, Hurdman, Judith, Elliot, Charlie, Kiely, David G., and Wild, Jim M. ≪Dynamic contrast-enhanced magnetic resonance imaging in patients with pulmonary arterial hypertension.≫ Pulmonary Circulation, **4**(1):pp. 61–70, 2014.

[54] Hueper, Katja, Parikh, Megha, Prince, Martin R., Schoenfeld, Christian, Liu, Chia, Bluemke, David A., Dashnaw, Stephen M., Goldstein, Thomas A., Hoffman, Eric, Lima, Joao A., Skrok, Jan, Zheng, Jie, Barr, R. Graham, and Vogel Claussen, Jens. ≪Quantitative and Semi-quantitative Measures of Regional Pulmonary Parenchymal Perfusion by Magnetic Resonance Imaging and their Relationships to Global Lung Perfusion and Lung Diffusing Capacity - The MESA COPD Study.≫ Investigative Radiolology, **48**(4):pp. 223–230, 2013.

[55] Sergiacomi, G., Bolacchi, F., Cadioli, M., Angeli, M. L., Fucci, F., Crusco, S., Rogliani, P., Pezzuto, G., Romeo, F., Mariano, E., and Simonetti, G. ≪Combined pulmonary fibrosis and emphysema: 3D time-resolved MR angiographic evaluation of pulmonary arterial mean transit time and time to peak enhancement.≫ Radiology, **254**(2):pp. 601–608, 2010.

[56] Swift, Andrew J., Wild, Jim M., Nagle, Scott K., Roldn Alzate, Alejandro, Franois, Christopher J., Fain, Sean, Johnson, Kevin, Capener, Dave, van Beek, Edwin J. R., Kiely, David G., Wang, Kang, and Schiebler, Mark L. ≪Quantitative MR imaging of pulmonary hypertension: A practical approach to the current state of the art.≫ Journal of thoracic imaging, **29**(2):pp. 68–79, 2014.

[57] Johnson, K. M., Fain, S. B., Schiebler, M. L., and Nagle, S. ≪Optimized 3D ultrashort echo time pulmonary MRI.≫ Magnetic Resonance in Medicine, **70**(5):pp. 1241–1250, 2013.

[58] Ohno, Yoshiharu, Koyama, Hisanobu, Yoshikawa, Takeshi, Seki, Shinichiro, Takenaka, Daisuke, Yui, Masao, Lu, Aiming, Miyazaki, Mitsue, and Sugimura, Kazuro. ≪Pulmonary high-resolution ultrashort TE MR imaging: Comparison with thin-section standard- and low-dose computed tomography for the assessment of pulmonary parenchyma diseases.≫ Journal of Magnetic Resonance Imaging, **43**(2):pp. 512–32, 2016.

[59] Bauman, Grzegorz, Puderbach, Michael, Deimling, Michael, Jellus, Vladimir, Chefd'hotel, Christophe, Dinkel, Julien, Hintze, Christian, Kauczor, Hans-Ulrich, and Schad, Lothar R. ≪Non-contrast-enhanced perfusion and ventilation assessment of the human lung by means of fourier decomposition in proton MRI.≫ Magnetic Resonance in Medicine, **62**(3):pp. 656–664, 2009.

[60] Schönfeld, Christian, Cebotari, Serghei, Voskrebenzev, Andreas, Gutberlet, Marcel, Hinrichs, Jan, Renne, Julius, Hoeper, Marius M., Olsson, Karen M., Welte, Tobias, Wacker, Frank, and Vogel Claussen, Jens. ≪Performance of perfusion-weighted Fourier decomposition MRI for detection of chronic pulmonary emboli.≫ Journal of Magnetic Resonance Imaging, **42**(1):pp. 72–79, 2015.

[61] Walker, T. G. and Happer, W. ≪Spin-exchange optical pumping of noble-gas nuclei.≫ Reviews of Modern Physics, **69**(2):pp. 629–642, 1997.

[62] Colegrove, FD, Schearer, LD, and Walters, GK. ≪Polarization of He^3 Gas by Optical Pumping.≫ Physical Review, **132**(6):p. 2561, 1963.

[63] Hersman, F. W., Ruset, I. C., Ketel, S., Muradian, I., Covrig, S. D., Distelbrink, J., Porter, W., Watt, D., Ketel, J., Brackett, J., Hope, A., and Patz, S. ≪Large production system for hyperpolarized 129Xe for human lung imaging studies.≫ Academic Radiology, **15**(6):pp. 683–92, 2008.

[64] Nikolaou, P., Coffey, A. M., Walkup, L. L., Gust, B. M., Whiting, N., Newton, H., Barcus, S., Muradyan, I., Dabaghyan, M., Moroz, G. D., Rosen, M. S., Patz, S., Barlow, M. J., Chekmenev, E. Y., and Goodson, B. M. ≪Near-unity nuclear polarization with an open-source 129Xe hyperpolarizer for NMR and MRI.≫ Proceedings of the National Academy of Sciences, **110**(35):pp. 14,150–5, 2013.

[65] Norquay, Graham, Parnell, Steven R., Xu, Xiaojun, Parra Robles, Juan, and Wild, Jim M. ≪Optimized production of hyperpolarized 129Xe at 2 bars for in vivo lung magnetic resonance imaging.≫ Journal of Applied Physics, **113**(4):pp. 044,908–9, 2013.

[66] Ebert, M., Grossmann, T., Heil, W., Otten, E. W., Surkau, R., Thelen, M., Leduc, M., Bachert, P., Knopp, M. V., and Schad, L. R. ≪Nuclear magnetic resonance imaging with hyperpolarised helium-3.≫ The Lancet, **347**(9011):pp. 1297–1299, 1996.

[67] MacFall, J. R., Charles, H. C., Black, R. D., Middleton, H., Swartz, J. C., Saam, B., Driehuys, B., Erickson, C., Happer, W., Cates, G. D., Johnson, G. A., and Ravin, C. E. ≪Human lung air spaces: Potential for MR imaging with hyperpolarized He- 3.≫ Radiology, **200**(2):pp. 553–558, 1996.

[68] Mugler, III, J. P., Driehuys, B., Brookeman, J. R., Cates, G. D., Berr, S. S., Bryant, R. G., Daniel, T. M., De Lange, E. E., Downs Iii, J. H., Erickson, C. J., Happer, W., Hinton, D. P., Kassel, N. F., Maier, T., Phillips, C. D., Saam, B. T., and Sauer, K. L. ≪MR imaging and spectroscopy using hyperpolarized 129Xe gas: Preliminary human results.≫ Magnetic Resonance in Medicine, **37**(6):pp. 809–815, 1997.

[69] Fain, S. B., Korosec, F. R., Holmes, J. H., O'Halloran, R., Sorkness, R. L., and Grist, T. M. ≪Functional lung imaging using hyperpolarized gas MRI.≫ Journal of Magnetic Resonance Imaging, **25**(5):pp. 910–923, 2007.

[70] van Beek, Edwin J. R., Wild, Jim M., Kauczor, Hans-Ulrich, Schreiber, Wolfgang, Mugler, John P., and de Lange, Eduard E. ≪Functional MRI of the lung using hyperpolarized 3-helium gas.≫ Journal of Magnetic Resonance Imaging, **20**(4):pp. 540–554, 2004.

[71] Wild, Jim M., Woodhouse, Neil, Paley, Martyn N. J., Fichele, Stan, Said, Zead, Kasuboski, Larry, and van Beek, Edwin J. R. ≪Comparison between 2D and 3D gradient-echo sequences for MRI of human lung ventilation with hyperpolarized 3He.≫ Magnetic Resonance in Medicine, **52**(3):pp. 673–678, 2004.

[72] van Beek, E J R, Dahmen, A. M., Stavngaard, T., Gast, K. K., Heussel, C. P., Krummenauere, F., Schmiedeskamp, J., Wild, J. M., Sgaard, L. V., Morbach, A. E., Schreiber, L. M., and Kauczor, H. U. ≪Hyperpolarised 3He MRI versus HRCT in COPD and normal volunteers: PHIL trial.≫ European Respiratory Journal, **34**(6):pp. 1311–1321, 2009.

[73] Deppe, M. H., Parra Robles, J., Ajraoui, S., Parnell, S. R., Clemence, M., Schulte, R. F., and Wild, J. M. ≪Susceptibility Effects in Hyperpolarized He-3 Lung MRI at 1.5T and 3T.≫ Journal of Magnetic Resonance Imaging, **30**(2):pp. 418–423, 2009.

[74] Parraga, Grace, Ouriadov, Alexei, Evans, Andrea, McKay, Shayna, Lam, Wilfred W., Fenster, Aaron, Etemad Rezai, Roya, McCormack, David, and Santyr, Giles. ≪Hyperpolarized 3He Ventilation Defects and Apparent Diffusion Coefficients in Chronic Obstructive Pulmonary Disease: Preliminary Results at 3.0 Tesla.≫ Investigative Radiolology, **42**(6):pp. 384–391, 2007.

[75] Altes, T. A., Powers, P. L., Knight Scott, J., Rakes, G., Platts Mills, T. A. E., De Lange, E. E., Alford, B. A., Mugler III, J. P., and Brookeman, J. R. ≪Hyperpolarized 3He MR lung ventilation imaging in asthmatics: Preliminary findings.≫ Journal of Magnetic Resonance Imaging, **13**(3):pp. 378–384, 2001.

[76] Tzeng, Yang-Sheng, Lutchen, Kenneth, and Albert, Mitchell. ≪The difference in ventilation heterogeneity between asthmatic and healthy subjects quantified using hyperpolarized 3He MRI.≫ Journal of Applied Physiology, **106**(3):pp. 813–822, 2009.

[77] Marshall, H., Deppe, M. H., Parra Robles, J., Hillis, S., Billings, C. G., Rajaram, S., Swift, A., Miller, S. R., Watson, J. H., Wolber, J., Lipson, D. A., Lawson, R., and Wild, J. M. ≪Direct visualisation of collateral ventilation in COPD with hyperpolarised gas MRI.≫ Thorax, **67**(7):pp. 613–617, 2012.

[78] Bannier, Elise, Cieslar, Katarzyna, Mosbah, Karim, Aubert, Franoise, Duboeuf, Franois, Salhi, Zahir, Gaillard, Sophie, Berthezne, Yves, Crmillieux, Yannick, and Reix, Philippe. ≪Hyperpolarized 3He MR for Sensitive Imaging of Ventilation Function and Treatment Efficiency in Young Cystic Fibrosis Patients with Normal Lung Function.≫ Radiology, **255**(1):pp. 225–232, 2010.

[79] Donnelly, Lane F., MacFall, James R., McAdams, H. Page, Majure, J. Marc, Smith, Jean, Frush, Donald P., Bogonad, Paul, Charles, H. Cecil, and Ravin, Carl E. ≪Cystic Fibrosis: Combined Hyperpolarized 3He-enhanced and Conventional Proton MR Imaging in the Lung - Preliminary Observations.≫ Radiology, **212**(3):pp. 885–889, 1999.

[80] Altes, Talissa A., Mai, Vu M., Munger, Therese Maier, Brookeman, James R., and Hagspiel, Klaus D. ≪Pulmonary Embolism: Comprehensive Evaluation with MR Ventilation and Perfusion Scanning with Hyperpolarized Helium-3, Arterial Spin Tagging, and Contrast-enhanced MRA.≫ Journal of Vascular and Interventional Radiology, **16**(7):pp. 999–1005, 2005.

[81] Gast, K. K., Zaporozhan, J., Ley, S., Biedermann, A., Knitz, F., Eberle, B., Schmiedeskamp, J., Heussel, C. P., Mayer, E., Gnter Schreiber, W., Thelen, M., and Kauczor, H. U. ≪3He-MRI in follow-up of lung transplant recipients.≫ European Radiology, **14**(1):pp. 78–85, 2004.

[82] Salerno, M., Altes, T. A., Brookeman, J. R., De Lange, E. E., and Mugler, III, J. P. ≪Dynamic spiral MRI of pulmonary

gas flow using hyperpolarized 3He: Preliminary studies in healthy and diseased lungs.≫ Magnetic Resonance in Medicine, **46**(4):pp. 667–677, 2001.

[83] Wild, J. M., Paley, M. N. J., Kasuboski, L., Swift, A., Fichele, S., Woodhouse, N., Griffiths, P. D., and Van Beek, E. J. R. ≪Dynamic radial projection MRI of inhaled hyperpolarized 3He gas.≫ Magnetic Resonance in Medicine, **49**(6):pp. 991–997, 2003.

[84] Shea, Dana A and Morgan, Daniel. ≪The Helium-3 Shortage: Supply, Demand, And Options For Congress.≫ Congressional Research Service, Library of Congress, pp. Technical Report: R41,419. 7–5700, 2010.

[85] Kirby, M., Svenningsen, S., Owrangi, A., Wheatley, A., Farag, A., Ouriadov, A., Santyr, G. E., Etemad Rezai, R., Coxson, H. O., McCormack, D. G., and Parraga, G. ≪Hyperpolarized 3He and 129Xe MR Imaging in Healthy Volunteers and Patients with Chronic Obstructive Pulmonary Disease.≫ Radiology, **265**(2):pp. 600–610, 2012.

[86] Svenningsen, Sarah, Kirby, Miranda, Starr, Danielle, Leary, Del, Wheatley, Andrew, Maksym, Geoffrey N., McCormack, David G., and Parraga, Grace. ≪Hyperpolarized 3He and 129Xe MRI: Differences in asthma before bronchodilation.≫ Journal of Magnetic Resonance Imaging, **38**(6):pp. 1521–1530, 2013.

[87] Virgincar, Rohan S., Cleveland, Zackary I., Sivaram Kaushik, S., Freeman, Matthew S., Nouls, John, Cofer, Gary P., Martinez Jimenez, Santiago, He, Mu, Kraft, Monica, Wolber, Jan, Page McAdams, H., and Driehuys, Bastiaan. ≪Quantitative analysis of hyperpolarized 129Xe ventilation imaging in healthy volunteers and subjects with chronic obstructive pulmonary disease.≫ NMR in Biomedicine, **26**(4):pp. 424–435, 2013.

[88] Kirby, M., Svenningsen, S., Kanhere, N., Owrangi, A., Wheatley, A., Coxson, H. O., Santyr, G. E., Paterson, N. A. M., McCormack, D. G., and Parraga, G. ≪Pulmonary ventilation visualized using hyperpolarized helium-3 and xenon-129 magnetic resonance imaging: Differences in COPD and relationship to emphysema.≫ Journal of Applied Physiology, **114**(6):pp. 707–715, 2013.

[89] Stewart, Neil J., Norquay, Graham, Griffiths, Paul D., and Wild, Jim M. ≪Feasibility of human lung ventilation imaging using highly polarized naturally abundant xenon and optimized three-dimensional steady-state free precession.≫ Magnetic Resonance in Medicine, **74**(2):pp. 346–352, 2015.

[90] He, Mu, Robertson, Scott H., Kaushik, S. Sivaram, Freeman, Matthew S., Virgincar, Rohan S., Davies, John, Stiles, Jane, Foster, William M., McAdams, H. Page, and Driehuys, Bastiaan. ≪Dose and pulse sequence considerations for hyperpolarized 129Xe ventilation MRI.≫ Magn Reson Imaging, **33**(7):pp. 877–885, 2015.

[91] Samee, Saba, Altes, Talissa, Powers, Patrick, de Lange, Eduard E., Knight Scott, Jack, Rakes, Gary, Mugler Iii, John P., Ciambotti, Jonathan M., Alford, Bennet A., Brookeman, James R., and Platts Mills, Thomas A. E. ≪Imaging the lungs in asthmatic patients by using hyperpolarized helium-3 magnetic resonance: Assessment of response to methacholine and exercise challenge.≫ Journal of Allergy and Clinical Immunology, **111**(6):pp. 1205–1211, 2003.

[92] Kirby, Miranda, Mathew, Lindsay, Heydarian, Mohammadreza, Etemad Rezai, Roya, McCormack, David G., and Parraga, Grace. ≪Chronic Obstructive Pulmonary Disease: Quantification of Bronchodilator Effects by Using Hyperpolarized He MR Imaging.≫ Radiology, **261**(1):pp. 283–292, 2011.

[93] Mentore, Kimiknu, Froh, Deborah K., de Lange, Eduard E., Brookeman, James R., Paget Brown, Alix O., and Altes, Talissa A. ≪Hyperpolarized He 3 MRI of the Lung in Cystic Fibrosis: Assessment at Baseline and After Bronchodilator and Airway Clearance Treatment.≫ Academic Radiology, **12**(11):pp. 1423–1429, 2005.

[94] Sanders, R. D., Franks, N. P., and Maze, M. ≪Xenon: no stranger to anaesthesia.≫ British Journal of Anaesthesia, **91**(5):pp. 709–717, 2003.

[95] Driehuys, B., Martinez Jimenez, S., Cleveland, Z.I., Metz, G.M., Beaver, D.M., Nouls, J.C., Kaushik, S.S., Firszt, R., Willis, C., and Kelly, K.T. ≪Chronic obstructive pulmonary disease: safety and tolerability of hyperpolarized 129Xe MR imaging in healthy volunteers and patients.≫ Radiology, **262**(1):pp. 279–289, 2012.

[96] Shukla, Yajur, Wheatley, Andrew, Kirby, Miranda, Svenningsen, Sarah, Farag, Adam, Santyr, Giles E., Paterson, Nigel A. M., McCormack, David G., and Parraga, Grace. ≪Hyperpolarized 129Xe Magnetic Resonance Imaging: Tolerability in Healthy Volunteers and Subjects with Pulmonary Disease.≫ Academic Radiology, **19**(8):pp. 941–951, 2012.

[97] Lipson, David A., Roberts, David A., Hansen Flaschen, John, Gentile, Thomas R., Jones, Gordon, Thompson, Alan, Dimitrov, Ivan E., Palevsky, Harold I., Leigh, John S., Schnall, Mitchell, and Rizi, Rahim R. ≪Pulmonary ventilation and perfusion scanning using hyperpolarized helium-3 MRI and arterial spin tagging in healthy normal subjects and in pulmonary embolism and orthotopic lung transplant patients.≫ Magnetic Resonance in Medicine, **47**(6):pp. 1073–1076, 2002.

[98] Hong, Cheng, Leawoods, Jason C., Yablonskiy, Dmitriy A., Leyendecker, John R., Bae, Kyongtae T., Pilgram, Thomas K., Woodard, Pamela K., Conradi, Mark S., and Zheng, Jie. ≪Feasibility of combining MR perfusion,

angiography, and 3He ventilation imaging for evaluation of lung function in a porcine model.≫ Academic Radiology, **12**(2):pp. 202–209, 2005.

[99] Rao, Madhwesha and Wild, Jim M. ≪RF instrumentation for same-breath triple nuclear lung MR imaging of 1H and hyperpolarized 3He and 129Xe at 1.5T.≫ Magnetic Resonance in Medicine, **75**(4):pp. 1841–8, 2016.

[100] Wild, J. M., Marshall, H., Xu, X., Norquay, G., Parnell, S. R., Clemence, M., Griffiths, P. D., and Parra Robles, J. ≪Simultaneous imaging of lung structure and function with triple-nuclear hybrid MR imaging.≫ Radiology, **267**(1):pp. 251–5, 2013.

[101] Saam, B. T., Yablonskiy, D. A., Kodibagkar, V. D., Leawoods, J. C., Gierada, D. S., Cooper, J. D., Lefrak, S. S., and Conradi, M. S. ≪MR imaging of diffusion of 3He gas in healthy and diseased lungs.≫ Magnetic Resonance in Medicine, **44**(2):pp. 174–179, 2000.

[102] Yablonskiy, D. A., Sukstanskii, A. L., Leawoods, J. C., Gierada, D. S., Larry Bretthorst, G., Lefrak, S. S., Cooper, J. D., and Conradi, M. S. ≪Quantitative in vivo assessment of lung microstructure at the alveolar level with hyperpolarized 3He diffusion MRI.≫ Proceedings of the National Academy of Sciences of the United States of America, **99**(5):pp. 3111–3116, 2002.

[103] Yablonskiy, D. A., Sukstanskii, A. L., Woods, J. C., Gierada, D. S., Quirk, J. D., Hogg, J. C., Cooper, J. D., and Conradi, M. S. ≪Quantification of lung microstructure with hyperpolarized 3He diffusion MRI.≫ Journal of Applied Physiology, **107**(4):pp. 1258–1265, 2009.

[104] Parra Robles, J., Marshall, H., and Wild, J. M. ≪Characterization of 3He Diffusion in Lungs Using a Stretched Exponential Model.≫ Proceedings of the 21st Annual Meeting of the International Society for Magnetic Resonance in Medicine, Salt Lake City, Utah, USA, p. Abstract Number: 820, 2013.

[105] Trampel, Robert, Jensen, Jens H., Lee, Ray F., Kamenetskiy, Igor, McGuinness, Georgeann, and Johnson, Glyn. ≪Diffusional kurtosis imaging in the lung using hyperpolarized 3He.≫ Magnetic Resonance in Medicine, **56**(4):pp. 733–737, 2006.

[106] Salerno, Michael, Lange, Eduard E. de, Altes, Talissa A., Truwit, Jonathon D., Brookeman, James R., and John P. Mugler, II. ≪Emphysema: Hyperpolarized Helium 3 Diffusion MR Imaging of the Lungs Compared with Spirometric Indexes - Initial Experience.≫ Radiology, **222**(1):pp. 252–260, 2002.

[107] Fain, Sean B., Panth, Shilpa R., Evans, Michael D., Wentland, Andrew L., Holmes, James H., Korosec, Frank R., O'Brien, Matthew J., Fountaine, Harvey, and Grist, Thomas M. ≪Early Emphysematous Changes in Asymptomatic Smokers: Detection with 3He MR Imaging.≫ Radiology, **239**(3):pp. 875–883, 2006.

[108] Swift, Andrew J., Wild, Jim M., Fichele, Stan, Woodhouse, Neil, Fleming, Sally, Waterhouse, Judith, Lawson, Rod A., Paley, Martyn N. J., and Van Beek, Edwin J. R. ≪Emphysematous changes and normal variation in smokers and COPD patients using diffusion 3He MRI.≫ European Journal of Radiology, **54**(3):pp. 352–358, 2005.

[109] Wang, Chengbo, Altes, Talissa A., Mugler, III, J. P., Miller, G. Wilson, Ruppert, Kai, Mata, Jaime F., Cates, Gordon D., Borish, Larry, and de Lange, Eduard E. ≪Assessment of the lung microstructure in patients with asthma using hyperpolarized 3He diffusion MRI at two time scales: Comparison with healthy subjects and patients with COPD.≫ Journal of Magnetic Resonance Imaging, **28**(1):pp. 80–88, 2008.

[110] Kirby, Miranda, Mathew, Lindsay, Wheatley, Andrew, Santyr, Giles E., McCormack, David G., and Parraga, Grace. ≪Chronic Obstructive Pulmonary Disease: Longitudinal Hyperpolarized 3He MR Imaging.≫ Radiology, **256**(1):pp. 280–289, 2010.

[111] Woods, Jason C., Choong, Cliff K., Yablonskiy, Dmitriy A., Bentley, John, Wong, Jonathan, Pierce, John A., Cooper, Joel D., Macklem, Peter T., Conradi, Mark S., and Hogg, James C. ≪Hyperpolarized 3He diffusion MRI and histology in pulmonary emphysema.≫ Magnetic Resonance in Medicine, **56**(6):pp. 1293–1300, 2006.

[112] Altes, Talissa A., Mata, Jaime, de Lange, Eduard E., Brookeman, James R., and Mugler, John P. ≪Assessment of lung development using hyperpolarized helium-3 diffusion MR imaging.≫ Journal of Magnetic Resonance Imaging, **24**(6):pp. 1277–1283, 2006.

[113] Butler, James P., Loring, Stephen H., Patz, Samuel, Tsuda, Akira, Yablonskiy, Dmitriy A., and Mentzer, Steven J. ≪Evidence for Adult Lung Growth in Humans.≫ New England Journal of Medicine, **367**(3):pp. 244–247, 2012.

[114] Narayanan, Manjith, Owers Bradley, John, Beardsmore, Caroline S., Mada, Marius, Ball, Iain, Garipov, Ruslan, Panesar, Kuldeep S., Kuehni, Claudia E., Spycher, Ben D., Williams, Sian E., and Silverman, Michael. ≪Alveolarization Continues during Childhood and Adolescence.≫ American Journal of Respiratory and Critical Care Medicine, **185**(2):pp. 186–191, 2012.

[115] Kaushik, S. Sivaram, Cleveland, Zackary I., Cofer, Gary P., Metz, Gregory, Beaver, Denise, Nouls, John, Kraft, Monica, Auffermann, William, Wolber, Jan, McAdams, H. Page, and Driehuys, Bastiaan. ≪Diffusion-weighted hyperpolarized

129Xe MRI in healthy volunteers and subjects with chronic obstructive pulmonary disease.≫ Magnetic Resonance in Medicine, **65**(4):pp. 1154–1165, 2011.

[116] Kirby, Miranda, Ouriadov, Alexei, Svenningsen, Sarah, Owrangi, Amir, Wheatley, Andrew, Etemad Rezai, Roya, Santyr, Giles E., McCormack, David G., and Parraga, Grace. ≪Hyperpolarized 3He and 129Xe magnetic resonance imaging apparent diffusion coefficients: physiological relevance in older never- and ex-smokers.≫ Physiological Reports, **2**(7):p. e12,068, 2014.

[117] Deninger, Anselm J., Månsson, Sven, Petersson, J. Stefan, Pettersson, Görran, Magnusson, Peter, Svensson, Jonas, Fridlund, Björn, Hansson, Georg, Erjefeldt, Ingrid, Wollmer, Per, and Golman, Klaes. ≪Quantitative measurement of regional lung ventilation using 3He MRI.≫ Magnetic Resonance in Medicine, **48**(2):pp. 223–232, 2002.

[118] Emami, Kiarash, Kadlecek, Stephen J., Woodburn, John M., Zhu, Jianliang, Yu, Jiangsheng, Vahdat, Vahid, Pickup, Stephen, Ishii, Masaru, and Rizi, Rahim R. ≪Improved technique for measurement of regional fractional ventilation by hyperpolarized 3He MRI.≫ Magnetic Resonance in Medicine, **63**(1):pp. 137–150, 2010.

[119] Deppe, M. H., Parra Robles, J., Ajraoui, S., and Wild, J. M. ≪Combined Measurement of Pulmonary Inert Gas Washout and Regional Ventilation Heterogeneity by MR of a Single Dose of Hyperpolarized He-3.≫ Magnetic Resonance in Medicine, **65**(4):pp. 1076–1084, 2011.

[120] Horn, F. C., Deppe, M. H., Marshall, H., Parra Robles, J., and Wild, J. M. ≪Quantification of regional fractional ventilation in human subjects by measurement of hyperpolarized He-3 washout with 2D and 3D MRI.≫ Journal of Applied Physiology, **116**(2):pp. 129–139, 2014.

[121] Horn, Felix, Horsley, Alex, Smith, Laurie, Tayler, Christopher, Marshall, Helen, Parra Robles, Juan, and Wild, Jim. ≪Visualising regional ventilation heterogeneity by linking multiple breath washout to 3He MRI imaging.≫ European Respiratory Journal (Suppl 58), **44**:p. 546, 2014.

[122] Marshall, Helen, Parra Robles, Juan, Deppe, Martin H., Lipson, David A., Lawson, Rod, and Wild, Jim M. ≪3He pO2 mapping is limited by delayed-ventilation and diffusion in chronic obstructive pulmonary disease.≫ Magnetic Resonance in Medicine, **71**(3):pp. 1172–1178, 2014.

[123] Saam, B., Happer, W., and Middleton, H. ≪Nuclear relaxation of 3He in the presence of O2.≫ Physical Review A, **52**(1):pp. 862–865, 1995.

[124] Deninger, A. J., Eberle, B., Ebert, M., Gromann, T., Heil, W., Kauczor, H. U., Lauer, L., Markstaller, K., Otten, E., Schmiedeskamp, J., Schreiber, W., Surkau, R., Thelen, M., and Weiler, N. ≪Quantification of Regional Intrapulmonary Oxygen Partial Pressure Evolution during Apnea by 3He MRI.≫ Journal of Magnetic Resonance, **141**(2):pp. 207–216, 1999.

[125] Deninger, A. J., Eberle, B., Bermuth, J., Escat, B., Markstaller, K., Schmiedeskamp, J., Schreiber, W. G., Surkau, R., Otten, E., and Kauczor, H. U. ≪Assessment of a single-acquisition imaging sequence for oxygen-sensitive 3He-MRI.≫ Magnetic Resonance in Medicine, **47**(1):pp. 105–114, 2002.

[126] Wild, Jim M., Fichele, Stan, Woodhouse, Neil, Paley, Martyn N. J., Kasuboski, Larry, and van Beek, Edwin J. R. ≪3D volume-localized pO2 measurement in the human lung with 3He MRI.≫ Magnetic Resonance in Medicine, **53**(5):pp. 1055–1064, 2005.

[127] Hamedani, Hooman, Kadlecek, Stephen J., Emami, Kiarash, Kuzma, Nicholas N., Xu, Yinan, Xin, Yi, Mongkolwisetwara, Puttisarn, Rajaei, Jennia, Barulic, Amy, Wilson Miller, G., Rossman, Milton, Ishii, Masaru, and Rizi, Rahim R. ≪A multislice single breath-hold scheme for imaging alveolar oxygen tension in humans.≫ Magnetic Resonance in Medicine, **67**(5):pp. 1332–1345, 2012.

[128] Miller, G. Wilson, Mugler, John P., Altes, Talissa A., Cai, Jing, Mata, Jaime F., de Lange, Eduard E., Tobias, William A., Cates, Gordon D., and Brookeman, James R. ≪A short-breath-hold technique for lung pO2 mapping with 3He MRI.≫ Magnetic Resonance in Medicine, **63**(1):pp. 127–136, 2010.

[129] Gast, KlausKurt, Biedermann, Alexander, Herweling, Annette, Schreiber, WolfgangGnter, Schmiedeskamp, Jörg, Mayer, Eckhard, Heussel, ClausPeter, Markstaller, Klaus, Kauczor, Hans-Ulrich, and Eberle, Balthasar. ≪Oxygen-sensitive 3He-MRI in bronchiolitis obliterans after lung transplantation.≫ European Radiology, **18**(3):pp. 530–537, 2008.

[130] de Rochefort, Ludovic, Matre, Xavier, Fodil, Redouane, Vial, Laurence, Louis, Bruno, Isabey, Daniel, Croce, Cline, Darrasse, Luc, Apiou, Gabriela, Caillibotte, Georges, Bittoun, Jacques, and Durand, Emmanuel. ≪Phase-contrast velocimetry with hyperpolarized 3He for in vitro and in vivo characterization of airflow.≫ Magnetic Resonance in Medicine, **55**(6):pp. 1318–1325, 2006.

[131] Collier, Guilhem J. and Wild, Jim M. ≪In vivo measurement of gas flow in human airways with hyperpolarized gas MRI and compressed sensing.≫ Magnetic Resonance in Medicine, **73**(6):pp. 2255–2261, 2015.

[132] de Rochefort, Ludovic, Vial, Laurence, Fodil, Redouane, Matre, Xavier, Louis, Bruno, Isabey, Daniel, Caillibotte, Georges, Thiriet, Marc, Bittoun, Jacques, Durand, Emmanuel, and Sbirlea Apiou, Gabriela. ≪In vitro validation of computational fluid dynamic simulation in human proximal airways with hyperpolarized 3He magnetic resonance phase-contrast velocimetry.≫ Journal of Applied Physiology, **102**(5):pp. 2012–2023, 2007.

[133] Collier, Guilhem Jean, Marshall, Helen, Rao, Madhwesha, Stewart, Neil J., Capener, David, and Wild, Jim M. ≪Observation of cardiogenic flow oscillations in healthy subjects with hyperpolarized 3He MRI.≫ Journal of Applied Physiology, **119**(9):pp. 1007–1014, 2015.

[134] Mugler, III, J. P. and Altes, Talissa A. ≪Hyperpolarized 129Xe MRI of the human lung.≫ Journal of Magnetic Resonance Imaging, **37**(2):pp. 313–331, 2013.

[135] Weathersby, P. K. and Homer, L. D. ≪Solubility of inert gases in biological fluids and tissue: a review.≫ Undersea Biomedical Research, **7**(4):pp. 277–296, 1980.

[136] Bifone, A., Song, Y. Q., Seydoux, R., Taylor, R. E., Goodson, B. M., Pietrass, T., Budinger, T. F., Navon, G., and Pines, A. ≪NMR of laser-polarized xenon in human blood.≫ Proceedings of the National Academy of Sciences of the United States of America, **93**(23):pp. 12,932–12,936, 1996.

[137] Ruppert, K., Brookeman, J. R., Hagspiel, K. D., Driehuys, B., and Mugler, III, J. P. ≪NMR of hyperpolarized 129Xe in the canine chest: Spectral dynamics during a breath-hold.≫ NMR in Biomedicine, **13**(4):pp. 220–228, 2000.

[138] Patz, S., Muradyan, I., Hrovat, M., Dabaghyan, M., Washko, G., Hatabu, H., and Butler, J. P. ≪Diffusion of hyperpolarized 129 Xe in the lung: a simplified model of 129 Xe septal uptake and experimental results.≫ New Journal of Physics, **13**(1):p. 015,009, 2011.

[139] Chang, Yulin V. ≪MOXE: A model of gas exchange for hyperpolarized 129Xe magnetic resonance of the lung.≫ Magnetic Resonance in Medicine, **69**(3):pp. 884–890, 2013.

[140] Chang, Yulin V., Quirk, James D., Ruset, Iulian C., Atkinson, Jeffrey J., Hersman, F. William, and Woods, Jason C. ≪Quantification of human lung structure and physiology using hyperpolarized 129Xe.≫ Magnetic Resonance in Medicine, **71**(1):pp. 339–344, 2014.

[141] Qing, Kun, Mugler, John P., Altes, Talissa A., Jiang, Yun, Mata, Jaime F., Miller, G. Wilson, Ruset, Iulian C., Hersman, F. William, and Ruppert, Kai. ≪Assessment of lung function in asthma and COPD using hyperpolarized 129Xe chemical shift saturation recovery spectroscopy and dissolved-phase MRI.≫ NMR in Biomedicine, **27**(12):pp. 1490–1501, 2014.

[142] Stewart, Neil J., Leung, General, Norquay, Graham, Marshall, Helen, Parra Robles, Juan, Murphy, Philip S., Schulte, Rolf F., Elliot, Charlie, Condliffe, Robin, Griffiths, Paul D., Kiely, David G., Whyte, Moira K., Wolber, Jan, and Wild, Jim M. ≪Experimental validation of the hyperpolarized 129Xe chemical shift saturation recovery technique in healthy volunteers and subjects with interstitial lung disease.≫ Magnetic Resonance in Medicine, **74**(1):pp. 196–207, 2015.

[143] Mugler, III, J. P., Altes, T. A., Ruset, I. C., Dregely, I. M., Mata, J. F., Miller, G. W., Ketel, S., Ketel, J., Hersman, F. W., and Ruppert, K. ≪Simultaneous magnetic resonance imaging of ventilation distribution and gas uptake in the human lung using hyperpolarized xenon-129.≫ Proceedings of the National Academy of Sciences, **107**(50):pp. 21,707–12, 2010.

[144] Cleveland, Zackary I., Cofer, Gary P., Metz, Gregory, Beaver, Denise, Nouls, John, Kaushik, S. Sivaram, Kraft, Monica, Wolber, Jan, Kelly, Kevin T., McAdams, H. Page, and Driehuys, Bastiaan. ≪Hyperpolarized 129Xe MR Imaging of Alveolar Gas Uptake in Humans.≫ PLoS ONE, **5**(8):p. e12,192, 2010.

[145] Driehuys, B., Cofer, G. P., Pollaro, J., Mackel, J. B., Hedlund, L. W., and Johnson, G. A. ≪Imaging alveolar-capillary gas transfer using hyperpolarized 129Xe MRI.≫ Proceedings of the National Academy of Sciences of the United States of America, **103**(48):pp. 18,278–18,283, 2006.

[146] Reeder, Scott B., Pineda, Angel R., Wen, Zhifei, Shimakawa, Ann, Yu, Huanzhou, Brittain, Jean H., Gold, Garry E., Beaulieu, Christopher H., and Pelc, Norbert J. ≪Iterative decomposition of water and fat with echo asymmetry and least-squares estimation (IDEAL): Application with fast spin-echo imaging.≫ Magnetic Resonance in Medicine, **54**(3):pp. 636–644, 2005.

[147] Qing, Kun, Ruppert, Kai, Jiang, Yun, Mata, Jaime F., Miller, G. Wilson, Shim, Y. Michael, Wang, Chengbo, Ruset, Iulian C., Hersman, F. William, Altes, Talissa A., and Mugler, John P. ≪Regional mapping of gas uptake by blood and tissue in the human lung using hyperpolarized xenon-129 MRI.≫ Journal of Magnetic Resonance Imaging, **39**(2):pp. 346–359, 2014.

[148] Kaushik, S. Sivaram, Robertson, Scott H., Freeman, Matthew S., He, Mu, Kelly, Kevin T., Roos, Justus E., Rackley, Craig R., Foster, W. Michael, McAdams, H. Page, and Driehuys, Bastiaan. ≪Single-breath clinical imaging of

hyperpolarized 129xe in the airspaces, barrier, and red blood cells using an interleaved 3D radial 1-point Dixon acquisition.≫ Magnetic Resonance in Medicine, **75**(4):pp. 1434–43, 2016.

[149] Ruppert, Kai, Brookeman, James R., Hagspiel, Klaus D., and Mugler, III, J. P. ≪Probing lung physiology with xenon polarization transfer contrast (XTC).≫ Magnetic Resonance in Medicine, **44**(3):pp. 349–357, 2000.

[150] Ruppert, K., Mata, J. F., Wang, H. T., Tobias, W. A., Cates, G. D., Brookeman, J. R., Hagspiel, K. D., and Mugler, III, J. P. ≪XTC MRI: sensitivity improvement through parameter optimization.≫ Magnetic Resonance in Medicine, **57**(6):pp. 1099–109, 2007.

[151] Muradyan, Iga, Butler, James P., Dabaghyan, Mikayel, Hrovat, Mirko, Dregely, Isabel, Ruset, Iulian, Topulos, George P., Frederick, Eric, Hatabu, Hiroto, Hersman, William F., and Patz, Samuel. ≪Single-breath xenon polarization transfer contrast (SB-XTC): Implementation and initial results in healthy humans.≫ Journal of Magnetic Resonance Imaging, **37**(2):pp. 457–470, 2013.

[152] Dregely, I., Mugler, III, J. P., Ruset, I. C., Altes, T. A., Mata, J. F., Miller, G. W., Ketel, J., Ketel, S., Distelbrink, J., Hersman, F. W., and Ruppert, K. ≪Hyperpolarized Xenon-129 gas-exchange imaging of lung microstructure: first case studies in subjects with obstructive lung disease.≫ J Magn Reson Imaging, **33**(5):pp. 1052–62, 2011.

[153] Dregely, I., Ruset, I. C., Mata, J. F., Ketel, J., Ketel, S., Distelbrink, J., Altes, T. A., Mugler, III, J. P., Miller, G. W., Hersman, F. W., and Ruppert, K. ≪Multiple-exchange-time xenon polarization transfer contrast (MXTC) MRI: Initial results in animals and healthy volunteers.≫ Magnetic Resonance in Medicine, **67**(4):pp. 943–953, 2012.

[154] Couch, Marcus J., Ball, Iain K., Li, Tao, Fox, Matthew S., Ouriadov, Alexei V., Biman, Birubi, and Albert, Mitchell S. ≪Inert fluorinated gas MRI: a new pulmonary imaging modality.≫ NMR in Biomedicine, **27**(12):pp. 1525–1534, 2014.

[155] Halaweish, Ahmed F., Moon, Richard E., Foster, W. Michael, Soher, Brian J., McAdams, H. Page, MacFall, James R., Ainslie, Maureen D., MacIntyre, Neil R., and Charles, H. Cecil. ≪Perfluoropropane gas as a magnetic resonance lung imaging contrast agent in humans.≫ Chest, **144**(4):pp. 1300–1310, 2013.

[156] Couch, Marcus J., Ball, Iain K., Li, Tao, Fox, Matthew S., Littlefield, Shalyn L., Biman, Birubi, and Albert, Mitchell S. ≪Pulmonary Ultrashort Echo Time 19F MR Imaging with Inhaled Fluorinated Gas Mixtures in Healthy Volunteers: Feasibility.≫ Radiology, **269**(3):pp. 903–909, 2013.

[157] Weibel, E. R. ≪What makes a good lung?≫ Swiss Medical Weekly, **139**:pp. 375–86, 2009.

[158] West, J.B. ≪Respiratory physiology: the essentials.≫ Lippincott Williams & Wilkins, 2011.

[159] McPeck, M. ≪Vibralung Acoustical Percussor: A New Paradigm in Airway Clearance Therapy.≫ Respiratory Therapy, **9**(5):pp. 45–47, 2014.

[160] Weibel, E. R. ≪Morphometry of the Human Lung.≫ Springer-Verlag Berlin Heidelberg, 1963.

[161] Ochs, M., Nyengaard, J. R., Jung, A., Knudsen, L., Voigt, M., Wahlers, T., Richter, J., and Gundersen, H. J. G. ≪The Number of Alveoli in the Human Lung.≫ American Journal of Respiratory and Critical Care Medicine, **169**(1):pp. 120–124, 2004.

[162] Weibel, E R. ≪Morphological basis of alveolar-capillary gas exchange.≫ Physiological Reviews, **53**(2):pp. 419–495, 1973.

[163] Ewald R. Weibel, William J. Federspiel, Fabienne Fryder Doffey, Connie C.W. Hsia, Martin König, Vilma Stalder Navarro, and Ruth Vock. ≪Morphometric model for pulmonary diffusing capacity I. Membrane diffusing capacity.≫ Respiration Physiology, **93**(2):pp. 125–149, 1993.

[164] Peter Gehr, Marianne Bachofen, and Ewald R. Weibel. ≪The normal human lung: ultrastructure and morphometric estimation of diffusion capacity.≫ Respiration Physiology, **32**(2):pp. 121–140, 1978.

[165] West, John B. ≪Fragility of pulmonary capillaries.≫ Journal of Applied Physiology, **115**(1):pp. 1–15, 2013.

[166] Celli, B.R., MacNee, W., Agusti, A., Anzueto, A., Berg, B., Buist, A.S., Calverley, P.M.A., Chavannes, N., Dillard, T., Fahy, B., Fein, A., Heffner, J., Lareau, S., Meek, P., Martinez, F., McNicholas, W., Muris, J., Austegard, E., Pauwels, R., Rennard, S., Rossi, A., Siafakas, N., Tiep, B., Vestbo, J., Wouters, E., and ZuWallack, R. ≪Standards for the diagnosis and treatment of patients with COPD: a summary of the ATS/ERS position paper.≫ European Respiratory Journal, **23**(6):pp. 932–946, 2004.

[167] MacIntyre, N., Crapo, R. O., Viegi, G., Johnson, D. C., van der Grinten, C. P. M., Brusasco, V., Burgos, F., Casaburi, R., Coates, A., Enright, P., Gustafsson, P., Hankinson, J., Jensen, R., McKay, R., Miller, M. R., Navajas, D., Pedersen, O. F., Pellegrino, R., and Wanger, J. ≪Standardisation of the single-breath determination of carbon monoxide uptake in the lung.≫ European Respiratory Journal, **26**(4):pp. 720–735, 2005.

[168] Roughton, F. J. W. and Forster, R. E. ≪Relative Importance of Diffusion and Chemical Reaction Rates in Determining Rate of Exchange of Gases in the Human Lung, With Special Reference to True Diffusing Capacity of Pulmonary Membrane and Volume of Blood in the Lung Capillaries.≫ Journal of Applied Physiology, **11**(2):pp. 290–302, 1957.

[169] Cleveland, Zackary I., Virgincar, Rohan S., Qi, Yi, Robertson, Scott H., Degan, Simone, and Driehuys, Bastiaan. ≪3D MRI of impaired hyperpolarized 129Xe uptake in a rat model of pulmonary fibrosis.≫ NMR in Biomedicine, **27**(12):pp. 1502–1514, 2014.

[170] Abdeen, N., Cross, A., Cron, G., White, S., Rand, T., Miller, D., and Santyr, G. ≪Measurement of xenon diffusing capacity in the rat lung by hyperpolarized 129Xe MRI and dynamic spectroscopy in a single breath-hold.≫ Magnetic Resonance in Medicine, **56**(2):pp. 255–264, 2006.

[171] Kaushik, S. Sivaram, Freeman, Matthew S., Yoon, Suk W., Liljeroth, Maria G., Stiles, Jane V., Roos, Justus E., Michael Foster, W. Sivaram, Rackley, Craig R., McAdams, H. P., and Driehuys, Bastiaan. ≪Measuring Diffusion Limitation with a Perfusion-Limited Gas - Hyperpolarized 129Xe Gas-Transfer Spectroscopy in Patients with Idiopathic Pulmonary Fibrosis.≫ Journal of Applied Physiology, **117**(6):pp. 577–585, 2014.

[172] Callaghan, P. T. ≪Principles of Nuclear Magnetic Resonance Microscopy.≫ Oxford University Press, 1993.

[173] Abragam, Anatole. ≪The Principles of Nuclear Magnetism.≫ Oxford University Press, 1961.

[174] Slichter, Charles P. ≪Principles of Magnetic Resonance (3rd Edition).≫ Springer Science & Business Media, 1990.

[175] McRobbie, Donald W, Moore, Elizabeth A, Graves, Martin J, and Prince, Martin R. ≪MRI: from Picture to Proton.≫ Cambridge University Press, 2007.

[176] Canet, D. ≪Nuclear Magnetic Resonance: Concepts and Methods.≫ John Wiley & Sons, Inc., 1996.

[177] Brown, Robert W, Cheng, Y-C Norman, Haacke, E Mark, Thompson, Michael R, and Venkatesan, Ramesh. ≪Magnetic Resonance Imaging: Physical Principles and Sequence Design.≫ John Wiley & Sons, Inc., 1999.

[178] Bernstein, Matt A., King, Kevin F., and Zhou, Xiaohong Joe. ≪Handbook of MRI Pulse Sequences.≫ Elsevier Academic Press, 2004.

[179] Levitt, M. H. ≪Spin Dynamics: Basics of Nuclear Magnetic Resonance.≫ John Wiley & Sons, Inc., 2001.

[180] Elster, A. D. ≪Questions and Answers in MRI [online].≫ Available from: http://mriquestions.com, Accessed April 2016.

[181] Traficante, Daniel D. ≪Relaxation. can t2, be longer than t1?≫ Concepts in Magnetic Resonance, **3**(3):pp. 171–177, 1991.

[182] Anet, Frank A.L., O'Leary, Daniel J., Wade, Charles G., and Johnson, Robert D. ≪Nmr relaxation by the antisymmetric component of the shielding tensor: a longer transverse than longitudinal relaxation time.≫ Chemical Physics Letters, **171**(5):pp. 401 – 405, 1990.

[183] Buckingham, A. D., Schaefer, T., and Schneider, W. G. ≪Solvent Effects in Nuclear Magnetic Resonance Spectra.≫ The Journal of Chemical Physics, **32**(4):pp. 1227–1233, 1960.

[184] Dicke, R. H. ≪Coherence in spontaneous radiation processes.≫ Physical Review Letters, **93**:pp. 99–110, 1954.

[185] Hoult, D. I. and Bhakar, B. ≪Nmr signal reception: Virtual photons and coherent spontaneous emission.≫ Concepts in Magnetic Resonance, **9**(5):pp. 277–297, 1997.

[186] Hoult, D.I. and Richards, R.E. ≪The signal-to-noise ratio of the nuclear magnetic resonance experiment.≫ Journal of Magnetic Resonance, **24**(1):pp. 71–85, 1976.

[187] Vaughan, J. T. and Griffiths, J. R. ≪RF Coils for MRI.≫ John Wiley & Sons, Inc., 2012.

[188] Middleton, Hunter, Black, Robert D., Saam, Brian, Cates, Gordon D., Cofer, Gary P., Guenther, Robert, Happer, William, Hedlund, Lawrence W., Alan Johnson, G., Juvan, Kim, and Swartz, John. ≪MR Imaging with Hyperpolarized 3He Gas.≫ Magnetic Resonance in Medicine, **33**(2):pp. 271–275, 1995.

[189] Edelstein, W. A., Glover, G. H., Hardy, C. J., and Redington, R. W. ≪The intrinsic signal-to-noise ratio in NMR imaging.≫ Magnetic Resonance in Medicine, **3**(4):pp. 604–618, 1986.

[190] Parra Robles, J., Cross, A. R., and Santyr, G. E. ≪Theoretical signal-to-noise ratio and spatial resolution dependence on the magnetic field strength for hyperpolarized noble gas magnetic resonance imaging of human lungs.≫ Medical Physics, **32**(1):pp. 221–229, 2005.

[191] McConnell, Harden M. ≪Reaction Rates by Nuclear Magnetic Resonance.≫ The Journal of Chemical Physics, **28**(3):pp. 430–431, 1958.

[192] Brigham, E. O. ≪The Fast Fourier Transform and its Applications.≫ Prentice Hall, 1988.

[193] Noll, D. C., Nishimura, D. G., and Macovski, A. ≪Homodyne detection in magnetic resonance imaging.≫ IEEE Transactions on Medical Imaging, **10**(2):pp. 154–163, 1991.

[194] Pauly, John, Le Roux, Patrick, Nishimura, Dwight, and Macovski, Albert. ≪Parameter relations for the Shinnar-Le Roux selective excitation pulse design algorithm.≫ IEEE Transactions on Medical Imaging, **10**(1):pp. 53–65, 1991.

[195] Ernst, R. R. and Anderson, W. A. ≪Application of Fourier transform spectroscopy to magnetic resonance.≫ Review of Scientific Instruments, **37**(1):pp. 93–102, 1966.

[196] Scheffler, Klaus and Hennig, Jrgen. ≪Is TrueFISP a gradient-echo or a spin-echo sequence?≫ Magnetic Resonance in Medicine, **49**(2):pp. 395–397, 2003.

[197] Stejskal, E. O. and Tanner, J. E. ≪Spin diffusion measurements: spin echoes in the presence of a time-dependent field gradient.≫ Journal of Chemical Physics, **42**(1):pp. 288–292, 1965.

[198] Krjukov, E. V., ONeill, J. D., and Owers Bradley, J. R. ≪Brute Force Polarization of 129Xe.≫ Journal of Low Temperature Physics, **140**(5-6):pp. 397–408, 2005.

[199] Comment, A., Jannin, S., Hyacinthe, J.-N., Miéville, P., Sarkar, R., Ahuja, P., Vasos, P. R., Montet, X., Lazeyras, F., Vallée, J.-P., Hautle, P., Konter, J. A., van den Brandt, B., Ansermet, J.-Ph., Gruetter, R., and Bodenhausen, G. ≪Hyperpolarizing Gases via Dynamic Nuclear Polarization and Sublimation.≫ Phys. Rev. Lett., **105**:p. 018,104, 2010.

[200] Ardenkjaer Larsen, J. H., Hansson, L., Johannesson, H., Servin, R., and Wistrand, L. ≪Method for the Production of Hyperpolarized 129Xe.≫ Patent: US8003077, 2011.

[201] Babcock, Earl, Nelson, Ian, Kadlecek, Steve, Driehuys, Bastiaan, Anderson, L. W., Hersman, F. W., and Walker, Thad G. ≪Hybrid Spin-Exchange Optical Pumping of ^3He.≫ Phys Rev Lett, **91**(12):p. 123,003, 2003.

[202] Driehuys, B., Cates, G. D., Miron, E., Sauer, K., Walter, D. K., and Happer, W. ≪High-volume production of laser-polarized Xe-129.≫ Applied Physics Letters, **69**(12):pp. 1668–1670, 1996.

[203] Ruset, I. C., Ketel, S., and Hersman, F. W. ≪Optical pumping system design for large production of hyperpolarized Xe129.≫ Phys Rev Lett, **96**(5), 2006.

[204] Cates, G. D., Benton, D. R., Gatzke, M., Happer, W., Hasson, K. C., and Newbury, N. R. ≪Laser production of large nuclear-spin polarization in frozen xenon.≫ Phys Rev Lett, **65**(20):pp. 2591–2594, 1990.

[205] Wakayama, Tetsuya, Kitamoto, Masakazu, Ueyama, Tsuyoshi, Imai, Hirohiko, Narazaki, Michiko, Kimura, Atsuomi, and Fujiwara, Hideaki. ≪Hyperpolarized 129Xe MRI of the mouse lung at a low xenon concentration using a continuous flow-type hyperpolarizing system.≫ Journal of Magnetic Resonance Imaging, **27**(4):pp. 777–784, 2008.

[206] Parnell, S. R., Deppe, M. H., Parra Robles, J., and Wild, J. M. ≪Enhancement of 129Xe polarization by off-resonant spin exchange optical pumping.≫ Journal of Applied Physics, **108**(6), 2010.

[207] Zhao, L., Mulkern, R., Tseng, C. H., Williamson, D., Patz, S., Kraft, R., Walsworth, R. L., Jolesz, F. A., and Albert, M. S. ≪Gradient-Echo Imaging Considerations for Hyperpolarized 129Xe MR.≫ Journal of Magnetic Resonance, Series B, **113**(2):pp. 179–83, 1996.

[208] Wild, J. M., Paley, M. N., Viallon, M., Schreiber, W. G., van Beek, E. J., and Griffiths, P. D. ≪k-space filtering in 2D gradient-echo breath-hold hyperpolarized 3He MRI: spatial resolution and signal-to-noise ratio considerations.≫ Magnetic Resonance in Medicine, **47**:pp. 687–95, 2002.

[209] Jameson, C. J., Jameson, A. K., and Hwang, J. K. ≪Nuclear spin relaxation by intermolecular magnetic dipole coupling in the gas phase. 129Xe in oxygen.≫ Journal of Chemical Physics, **89**(7):pp. 4074–4081, 1988.

[210] Newbury, N. R., Barton, A. S., Cates, G. D., Happer, W., and Middleton, H. ≪Gaseous 3He-3He magnetic dipolar spin relaxation.≫ Physical Review A, **48**(6):pp. 4411–4420, 1993.

[211] Torrey, H. C. ≪Chemical Shift and Relaxation of Xe-129 in Xenon Gas.≫ Phys. Rev., **130**:pp. 2306–2312, 1963.

[212] Gatzke, M., Cates, G. D., Driehuys, B., Fox, D., Happer, W., and Saam, B. ≪Extraordinarily slow nuclear spin relaxation in frozen laser-polarized 129Xe.≫ Physical Review Letters, **70**(5):pp. 690–693, 1993.

[213] Moudrakovski, I. L., Breeze, S. R., Simard, B., Ratcliffe, C. I., Ripmeester, J. A., Seideman, T., Tse, J. S., and Santyr, G. ≪Gas-phase nuclear magnetic relaxation in Xe-129 revisited.≫ Journal of Chemical Physics, **114**(5):pp. 2173–2181, 2001.

[214] Chann, B., Nelson, I. A., Anderson, L. W., Driehuys, B., and Walker, T. G. ≪129Xe-Xe Molecular Spin Relaxation.≫ Physical Review Letters, **88**(11):p. 113,201, 2002.

[215] Möller, Harald E., Cleveland, Zackary I., and Driehuys, Bastiaan. ≪Relaxation of hyperpolarized 129Xe in a deflating polymer bag.≫ Journal of Magnetic Resonance, **212**(1):pp. 109–115, 2011.

[216] Zheng, W., Cleveland, Z. I., Moller, H. E., and Driehuys, B. ≪Gradient-induced longitudinal relaxation of hyperpolarized noble gases in the fringe fields of superconducting magnets used for magnetic resonance.≫ Journal of Magnetic Resonance, **208**(2):pp. 284–90, 2011.

[217] Liner, J. C. and Weissman, Stanley. ≪Determination of the Temperature Dependence of Gaseous Diffusion Coefficients Using Gas Chromatographic Apparatus.≫ The Journal of Chemical Physics, **56**(5):pp. 2288–2290, 1972.

[218] Acosta, RH, Agulles Pedrós, L, Komin, S, Sebastiani, Daniel, Spiess, Hans Wolfgang, and Blümler, Peter. ≪Diffusion in binary gas mixtures studied by NMR of hyperpolarized gases and molecular dynamics simulations.≫ Physical Chemistry Chemical Physics, **8**:pp. 4182–4188, 2006.

[219] Tanaka, Kazuko. ≪Measurements of self-diffusion coefficients of water in pure water and in aqueous electrolyte solutions.≫ J. Chem. Soc., Faraday Trans. 1, **71**:pp. 1127–1131, 1975.

[220] Mugler, III, J. P., Mata, J. F., Wang, H-T. J., Tobias, W. A., Cates, G. D., Christopher, J. M., Missel, J. L., Reish, A. G., Ruppert, K., Brookeman, J. R., and Hagspiel, K. D. ≪The Apparent Diffusion Coefficient of 129Xe in the Lung: Preliminary Human Results.≫ Proceedings of the 12th Meeting of the International Society of Magnetic Resonance in Medicine, Kyoto, Japan, p. Abstract 769, 2004.

[221] Wild, Jim M., Fichele, Stan, Woodhouse, Neil, Paley, Martyn N.J., Swift, Andrew, Kasuboski, Larry, and van Beek, Edwin J.R. ≪Assessment and compensation of susceptibility artifacts in gradient echo MRI of hyperpolarized 3He gas.≫ Magnetic Resonance in Medicine, **50**(2):pp. 417–422, 2003.

[222] Wild, J. M., Teh, K., Woodhouse, N., Paley, M. N. J., Fichele, S., de Zanche, N., and Kasuboski, L. ≪Steady-state free precession with hyperpolarized 3He: Experiments and theory.≫ Journal of Magnetic Resonance, **183**(1):pp. 13–24, 2006.

[223] Harris, R.K. and Mann, B.E. ≪NMR and the Periodic Table.≫ Academic Press, **342**, 1978.

[224] Johnson, C. S., Grant, D. M., and Harris, R. K. ≪Encyclopedia of Nuclear Magnetic Resonance.≫ Wiley, Chichester, 1996.

[225] Kellö, V., Pyykk, P., and Sadlej, A.J. ≪Nuclear quadrupole moments of Kr and Xe from molecular data.≫ Chemical Physics Letters, **346**(1-2):pp. 155–159, 2001.

[226] Chen, X. J., Möller, H. E., Chawla, M. S., Cofer, G. P., Driehuys, B., Hedlund, L. W., Johnson, G. A., and Fitzsimons, E. G. ≪Spatially resolved measurements of hyperpolarized gas properties in the lung in vivo. Part I: Diffusion coefficient.≫ Magnetic Resonance in Medicine, **42**(4):pp. 721–728, 1999.

[227] Oros, A. M. and Shah, N. J. ≪Hyperpolarized xenon in NMR and MRI.≫ Physics in Medicine and Biology, **49**(20):pp. R105–R153, 2004.

[228] Adrian, F. J. ≪Quadrupolar Relaxation of xe^{131} in Xenon Gas.≫ Physical Review, **138**:pp. A403–A409, 1965.

[229] Stupic, K. F., Cleveland, Z. I., Pavlovskaya, G. E., and Meersmann, T. ≪Hyperpolarized 131Xe NMR spectroscopy.≫ Journal of Magnetic Resonance, **208**(1):pp. 58–69, 2011.

[230] Cherubini, A. and Bifone, A. ≪Hyperpolarised xenon in biology.≫ Progress in Nuclear Magnetic Resonance Spectroscopy, **42**(1-2):pp. 1–30, 2003.

[231] Cook, G.A. ≪Argon, helium and the rare gases.≫ Interscience New York, **2**, 1961.

[232] Clementi, E., Raimondi, D. L., and Reinhardt, W. P. ≪Atomic screening constants from SCF functions. II. Atoms with 37 to 86 electrons.≫ J Chem Phys, **47**(4):pp. 1300–1307, 1967.

[233] Eger, Edmond I. and Larson, C. Philip. ≪Anaesthetic Solubility In Blood And Tissues: Values And Significance.≫ British Journal of Anaesthesia, **36**(3):pp. 140–149, 1964.

[234] Lachmann, B., Armbruster, S., Schairer, W., Landstra, M., Trouwborst, A., Van Daal, G. J., Kusuma, A., and Erdmann, W. ≪Safety and efficacy of xenon in routine use as an inhalational anaesthetic.≫ The Lancet, **335**(8703):pp. 1413–1415, 1990.

[235] Cullen, S. C. and Gross, E. G. ≪The anesthetic properties of xenon in animals and human beings, with additional observations on krypton.≫ Science, **113**(2942):pp. 580–582, 1951.

[236] Miller, K. W., Reo, N. V., and Schoot Uiterkamp, A. J. M. ≪Xenon NMR: Chemical shifts of a general anesthetic in common solvents, proteins, and membranes.≫ Proceedings of the National Academy of Sciences of the United States of America, **78**(8 I):pp. 4946–4949, 1981.

[237] Seydoux, R., Diehl, P., Mazitov, R. K., and Jokisaari, J. ≪Chemical-Shifts in Magnetic-Resonance of the 3He Nucleus in Liquid Solvents and Comparison with Other Noble Gases.≫ Journal of Magnetic Resonance, Series A, **101**(1):pp. 78–83, 1993.

[238] Jameson, C. J., Sears, D. N., and Murad, S. ≪Molecular dynamics averaging of Xe chemical shifts in liquids.≫ Journal of Chemical Physics, **121**(19):pp. 9581–9592, 2004.

[239] Yeh, Shu-Yuan and Peterson, Richard E. ≪Solubility of carbon dioxide, krypton, and xenon in aqueous solution.≫ Journal of Pharmaceutical Sciences, **53**(7):pp. 822–824, 1964.

[240] Albert, M. S., Schepkin, V. D., and Budinger, T. F. ≪Measurement of 129Xe T1 in blood to explore the feasibility of hyperpolarized 129Xe MRI.≫ Journal of Computer Assisted Tomography, **19**(6):pp. 975–978, 1995.

[241] Ladefoged, J. and Andersen, A. M. ≪Solubility of Xenon-133 at 37C in water, saline, olive oil, liquid paraffin, solutions of albumin, and blood.≫ Physics in Medicine and Biology, **12**(3):pp. 353–358, 1967.

[242] Isbister, W. H., Schofield, P. F., and Torrance, H. B. ≪Measurement of the Solubility of xenon-133 in Blood and Human Brain.≫ Phys Med Biol, **10**:pp. 243–250, 1965.

[243] Wolber, J., McIntyre, D. J. O., Rodrigues, L. M., Carnochan, P., Griffiths, J. R., Leach, M. O., and Bifone, A. ≪In vivo hyperpolarized 129Xe NMR spectroscopy in tumors.≫ Magnetic Resonance in Medicine, **46**(3):pp. 586–591, 2001.

[244] Chen, R. Y. Z., Fan, F. C., and Kim, S. ≪Tissue-blood partition coefficient for xenon: temperature and hematocrit dependence.≫ Journal of Applied Physiology Respiratory Environmental and Exercise Physiology, **49**(2):pp. 178–183, 1980.

[245] Sakai, K., Bilek, A. M., Oteiza, E., Walsworth, R. L., Balamore, D., Jolesz, F. A., and Albert, M. S. ≪Temporal dynamics of hyperpolarized 129Xe resonances in living rats.≫ Journal of Magnetic Resonance - Series B, **111**(3):pp. 300–304, 1996.

[246] Wolber, J., Cherubini, A., Dzik Jurasz, A. S. K., Leach, M. O., and Bifone, A. ≪Spin-lattice relaxation of laser-polarized xenon in human blood.≫ Proceedings of the National Academy of Sciences of the United States of America, **96**(7):pp. 3664–3669, 1999.

[247] Wolber, J., Rowland, I. J., Leach, M. O., and Bifone, A. ≪Perfluorocarbon emulsions as intravenous delivery media for hyperpolarized xenon.≫ Magnetic Resonance in Medicine, **41**(3):pp. 442–449, 1999.

[248] Patz, Samuel, Muradian, Iga, Hrovat, Mirko I., Ruset, Iulian C., Topulos, George, Covrig, Silviu D., Frederick, Eric, Hatabu, Hiroto, Hersman, F. W., and Butler, James P. ≪Human Pulmonary Imaging and Spectroscopy with Hyperpolarized 129Xe at 0.2T.≫ Academic Radiology, **15**(6):pp. 713–727, 2008.

[249] Mugler, III, J. P., Altes, T. A., Ruset, I. C., Miller, G. W., Mata, J. F., Qing, Kun, Tsentalovich, I., Hersman, F. W., and Ruppert, K. ≪Image-based Measurement of T2* for Dissolved-Phase Xe129 in the Human Lung.≫ Proceedings of the 20th Meeting of the International Society of Magnetic Resonance in Medicine, Melbourne, Australia, p. Abstract 1347, 2012.

[250] Xu, Xiaojun, Leung, General, Norquay, Graham, Marshall, Helen, Parra Robles, Juan, and Wild, Jim M. ≪T2* Measurements Of Dissolved-Phase 129Xe In The Human Lungs at 1.5T and 3T.≫ Proceedings of the 21st Meeting of the International Society of Magnetic Resonance in Medicine, Salt Lake City, Utah, p. Abstract 4119, 2013.

[251] Xu, Xiaojun, Norquay, Graham, Parnell, Steven R., Deppe, Martin H., Ajraoui, Salma, Hashoian, Ralph, Marshall, Helen, Griffiths, Paul D., Parra Robles, Juan, and Wild, Jim M. ≪Hyperpolarized 129Xe gas lung MRI - SNR and T2* comparisons at 1.5 T and 3 T.≫ Magnetic Resonance in Medicine, **68**(6):pp. 1900–1904, 2012.

[252] Möller, H. E., Chen, X. J., Chawla, M. S., Driehuys, B., Hedlund, L. W., and Johnson, G. A. ≪Signal Dynamics in Magnetic Resonance Imaging of the Lung with Hyperpolarized Noble Gases.≫ Journal of Magnetic Resonance, **135**(1):pp. 133–143, 1998.

[253] Albert, M. S., Kacher, D. F., Balamore, D., Venkatesh, A. K., and Jolesz, F. A. ≪T1 of 129Xe in Blood and the Role of Oxygenation.≫ Journal of Magnetic Resonance, **140**(1):pp. 264–273, 1999.

[254] Albert, M. S., Balamore, D., Kacher, D. F., Venkatesh, A. K., and Jolesz, F. A. ≪Hyperpolarized 129XE T1 in oxygenated and deoxygenated blood.≫ NMR in Biomedicine, **13**(7):pp. 407–414, 2000.

[255] Norquay, Graham, Leung, General, Stewart, Neil J., Tozer, Gillian M., Wolber, Jan, and Wild, Jim M. ≪Relaxation and exchange dynamics of hyperpolarized 129Xe in human blood.≫ Magnetic Resonance in Medicine, **74**(2):pp. 303–311, 2015.

[256] Blumgart, H. L. and Weiss, S. ≪Studies on the Velocity of Blood Flow VII: the Pulmonary Circulation Time in Normal Resting Individuals.≫ Journal of Clinical Investigation, **4**(3):pp. 399–425, 1927.

[257] Swanson, Scott D., Rosen, Matthew S., Coulter, Kevin P., Welsh, Robert C., and Chupp, Timothy E. ≪Distribution and dynamics of laser-polarized 129Xe magnetization in vivo.≫ Magnetic Resonance in Medicine, **42**(6):pp. 1137–1145, 1999.

[258] Mugler, III, J. P., Miller, W. G., Meyer, C., Qing, K., Mata, J. F., Guan, S., Ruppert, K., Ruset, I., Hersman, F., and Altes, T. A. ≪Imaging of Dissolved-phase Hyperpolarized Xenon-129 in Human Kidneys.≫ Proceedings of the 23rd Meeting of the International Society of Magnetic Resonance in Medicine, Toronto, Ontario, Canada, p. Abstract: 0848, 2015.

[259] Rao, Madhwesha, Stewart, Neil J., Norquay, Graham, Griffiths, Paul D., and Wild, Jim M. ≪High resolution spectroscopy and chemical shift imaging of hyperpolarized 129Xe dissolved in the human brain in vivo at 1.5 tesla.≫ Magnetic Resonance in Medicine, p. doi:10.1002/mrm.26241, 2016.

[260] Kilian, W., Seifert, F., and Rinneberg, H. ≪Dynamic NMR Spectroscopy of Hyperpolarized 129Xe in Human Brain Analyzed by an Uptake Model.≫ Magnetic Resonance in Medicine, **51**(4):pp. 843–847, 2004.

[261] Wolber, Jan, Cherubini, Andrea, Leach, Martin O., and Bifone, Angelo. ≪Hyperpolarized 129Xe NMR as a probe for blood oxygenation.≫ Magnetic Resonance in Medicine, **43**(4):pp. 491–496, 2000.

[262] Norquay, Graham, Leung, General, Stewart, Neil J., Wolber, Jan, and Wild, Jim M. ≪129Xe chemical shift in human

blood and pulmonary blood oxygenation measurement in humans using hyperpolarized 129Xe NMR.≫ Magnetic Resonance in Medicine, p. doi:10.1002/mrm.26225, 2016.

[263] Wolber, J., Doran, S. J., Leach, M. O., and Bifone, A. ≪Measuring diffusion of xenon in solution with hyperpolarized 129 Xe NMR.≫ Chemical Physics Letters, **296**(3-4):pp. 391–396, 1998.

[264] Wolber, J., Santoro, D., Leach, M. O., and Bifone, A. ≪Diffusion of Hyperpolarized 129Xe in Biological Systems: Effects of Chemical Exchange.≫ Proceedings of the 8th Annual Meeting of the International Society for Magnetic Resonance in Medicine, Denver, Colorado, p. Abstract 754, 2000.

[265] Ruppert, K., Mata, J. F., Brookeman, J. R., Hagspiel, K. D., and Mugler, III, J. P. ≪Exploring Lung Function with Hyperpolarized 129Xe Nuclear Magnetic Resonance.≫ Magnetic Resonance in Medicine, **51**(4):pp. 676–687, 2004.

[266] Deppe, M. H. and Wild, J. M. ≪Variable flip angle schedules in bSSFP imaging of hyperpolarized noble gases.≫ Magnetic Resonance in Medicine, **67**(6):pp. 1656–1664, 2012.

[267] Imai, F., Kashiwagi, R., Imai, H., Iguchi, S., Kimura, A., and Fujiwara, H. ≪Hyperpolarized 129Xe MR imaging with balanced steady-state free precession in spontaneously breathing mouse lungs.≫ Magnetic Resonance in Medical Sciences, **10**(1):pp. 33–40, 2011.

[268] Salerno, Michael, Brookeman, James R., de Lange, Eduard E., and Mugler, John P. ≪Hyperpolarized 3He lung imaging at 0.5 and 1.5 Tesla: A study of susceptibility-induced effects.≫ Magnetic Resonance in Medicine, **53**(1):pp. 212–216, 2005.

[269] Carney, C. E., Wong, S. T. S., and Patz, S. ≪Analytical solution and verification of diffusion effect in SSFP.≫ Magnetic Resonance in Medicine, **19**(2):pp. 240–246, 1991.

[270] Hargreaves, Brian A., Vasanawala, Shreyas S., Pauly, John M., and Nishimura, Dwight G. ≪Characterization and reduction of the transient response in steady-state MR imaging.≫ Magnetic Resonance in Medicine, **46**(1):pp. 149–158, 2001.

[271] Zhao, L., Mulkern, R., Venkatesh, A. K., Gubbjartsson, H., Jolesz, F. A., and Albert, M. S. ≪Hyperpolarized 129Xe T2 and Diffusion Measurements for Fast Spin-Echo MRI.≫ Proceedings of the 6th Meeting of the International Society of Magnetic Resonance in Medicine, Sydney, Australia, p. Abstract Number: 51, 1998.

[272] Bieri, Oliver and Scheffler, Klaus. ≪Fundamentals of balanced steady state free precession MRI.≫ Journal of Magnetic Resonance Imaging, **38**(1):pp. 2–11, 2013.

[273] Norquay, G., Stewart, N. J., and Wild, J. M. ≪High 129Xe polarisation (80%) on a home-built SEOP system.≫ Proceedings of PING14: Hyperpolarised Noble Gases, Les Houches, France, p. Abstract Number: 24, 2014.

[274] Rao, Madhwesha, Robb, Fraser, and Wild, Jim M. ≪Dedicated receiver array coil for 1H lung imaging with same-breath acquisition of hyperpolarized 3He and 129Xe gas.≫ Magnetic Resonance in Medicine, **74**(1):pp. 291–299, 2015.

[275] Candes, E.J., Romberg, J., and Tao, T. ≪Robust uncertainty principles: exact signal reconstruction from highly incomplete frequency information.≫ Information Theory, IEEE Transactions on, **52**(2):pp. 489–509, 2006.

[276] Donoho, D.L. ≪Compressed sensing.≫ Information Theory, IEEE Transactions on, **52**(4):pp. 1289–1306, 2006.

[277] Lustig, M., Donoho, D., and Pauly, J. M. ≪Sparse MRI: The application of compressed sensing for rapid MR imaging.≫ Magnetic Resonance in Medicine, **58**(6):pp. 1182–1195, 2007.

[278] Ajraoui, Salma, Lee, Kuan J., Deppe, Martin H., Parnell, Steven R., Parra Robles, Juan, and Wild, Jim M. ≪Compressed Sensing In Hyperpolarized 3He Lung MRI.≫ Magnetic Resonance in Medicine, **63**(4):pp. 1059–1069, 2010.

[279] Ajraoui, S., Parra Robles, J., Marshall, H., Deppe, M. H., Clemence, M., and Wild, J. M. ≪Acquisition of 3He ventilation images, ADC, T2*and B1 maps in a single scan with compressed sensing.≫ NMR in Biomedicine, **25**(1):pp. 44–51, 2012.

[280] Qing, Kun, Altes, Talissa A., Tustison, Nicholas J., Feng, Xue, Chen, Xiao, Mata, Jaime F., Miller, G. Wilson, de Lange, Eduard E., Tobias, William A., Cates, Gordon D., Brookeman, James R., and Mugler, John P. ≪Rapid acquisition of helium-3 and proton three-dimensional image sets of the human lung in a single breath-hold using compressed sensing.≫ Magnetic Resonance in Medicine, **74**(4):pp. 1110–1115, 2015.

[281] Altes, TA, Mugler, III, J. P., Dregely, IM, Ketel, S, Ruset, IC, Hersman, FW, and Ruppert, K. ≪Hyperpolarized xenon-129 ventilation MRI: preliminary results in normal subjects and patients with lung disease.≫ Proceedings of the 18th Meeting of the International Society of Magnetic Resonance in Medicine, Stockholm, Sweden, **Abstract: 2529**, 2010.

[282] Horn, F. C., Tahir, B. A., Stewart, N. J., Collier, G. J., Norquay, G., Leung, G., Ireland, R. H., Parra Robles, J., Marshall, H., and Wild, J. M. ≪Lung ventilation volumetry with same-breath acquisition of hyperpolarized gas and

proton MRI.≫ <u>NMR in Biomedicine</u>, **27**(12):pp. 1461–1467, 2014.

[283] Whiting, N., Nikolaou, P., Eschmann, N. A., Goodson, B. M., and Barlow, M. J. ≪Interdependence of in-cell xenon density and temperature during Rb/ 129Xe spin-exchange optical pumping using VHG-narrowed laser diode arrays.≫ <u>Journal of Magnetic Resonance</u>, **208**(2):pp. 298–304, 2011.

[284] Patz, S., Hersman, F. W., Muradian, I., Hrovat, M. I., Ruset, I. C., Ketel, S., Jacobson, F., Topulos, G. P., Hatabu, H., and Butler, J. P. ≪Hyperpolarized 129Xe MRI: A viable functional lung imaging modality?≫ <u>European Journal of Radiology</u>, **64**(3):pp. 335–344, 2007.

[285] Fox, Matthew S., Ouriadov, Alexei, and Santyr, Giles E. ≪Comparison of hyperpolarized 3He and 129Xe MRI for the measurement of absolute ventilated lung volume in rats.≫ <u>Magnetic Resonance in Medicine</u>, **71**(3):pp. 1130–1136, 2014.

[286] Mata, J. F., Altes, T. A., Cai, J., Ruppert, K., Mitzner, W., Hagspiel, K. D., Patel, B., Salerno, M., Brookeman, J. R., de Lange, E. E., Tobias, W. A., Wang, H. T., Cates, G. D., and Mugler, III, J. P. ≪Evaluation of emphysema severity and progression in a rabbit model: comparison of hyperpolarized 3He and 129Xe diffusion MRI with lung morphometry.≫ <u>Journal of Applied Physiology</u>, **102**(3):pp. 1273–80, 2007.

[287] Lindsay Mathew, Andrea Evans, Alexei Ouriadov, Roya Etemad Rezai, Robert Fogel, Giles Santyr, David G. Mc-Cormack, and Grace Parraga. ≪Hyperpolarized 3He Magnetic Resonance Imaging of Chronic Obstructive Pulmonary Disease: Reproducibility at 3.0 Tesla.≫ <u>Academic Radiology</u>, **15**(10):pp. 1298 – 1311, 2008.

[288] Woodhouse, Neil, Wild, Jim M., van Beek, Edwin J.R., Hoggard, Nigel, Barker, Nicki, and Taylor, Christopher J. ≪Assessment of hyperpolarized 3He lung MRI for regional evaluation of interventional therapy: A pilot study in pediatric cystic fibrosis.≫ <u>Journal of Magnetic Resonance Imaging</u>, **30**(5):pp. 981–988, 2009.

[289] Miranda Kirby, Sarah Svenningsen, Hassaan Ahmed, Andrew Wheatley, Roya Etemad Rezai, Nigel A.M. Paterson, and Grace Parraga. ≪Quantitative Evaluation of Hyperpolarized Helium-3 Magnetic Resonance Imaging of Lung Function Variability in Cystic Fibrosis.≫ <u>Academic Radiology</u>, **18**(8):pp. 1006 – 1013, 2011.

[290] David J. Niles, Stanley J. Kruger, Bernard J. Dardzinski, Amy Harman, Nizar N. Jarjour, Marcella Ruddy, Scott K. Nagle, Christopher J. Franois, and Sean B. Fain. ≪Exercise-induced Bronchoconstriction: Reproducibility of Hyperpolarized 3He MR Imaging.≫ <u>Radiology</u>, **266**(2):pp. 618–625, 2013.

[291] Morbach, A. E., Gast, K. K., Schmiedeskamp, J., Dahmen, A., Herweling, A., Heussel, C. P., Kauczor, H. U., and Schreiber, W. G. ≪Diffusion-weighted MRI of the lung with hyperpolarized helium-3: A study of reproducibility.≫ <u>Journal of Magnetic Resonance Imaging</u>, **21**(6):pp. 765–774, 2005.

[292] Diaz, Sandra, Casselbrant, Ingrid, Piitulainen, Eeva, Pettersson, Goran, Magnusson, Peter, Peterson, Barry, Wollmer, Per, Leander, Peter, Ekberg, Olle, and Akeson, Per. ≪Hyperpolarized 3He apparent diffusion coefficient MRI of the lung: Reproducibility and volume dependency in healthy volunteers and patients with emphysema.≫ <u>Journal of Magnetic Resonance Imaging</u>, **27**(4):pp. 763–770, 2008.

[293] Parra Robles, J., Ajraoui, S., Marshall, H., Deppe, M. H., Xu, X., and Wild, J. M. ≪The influence of field strength on the apparent diffusion coefficient of 3He gas in human lungs.≫ <u>Magnetic Resonance in Medicine</u>, **67**(2):pp. 322–325, 2012.

[294] Woods, Jason C., Yablonskiy, Dmitriy A., Choong, Cliff K., Chino, Kimiaki, Pierce, John A., Hogg, James C., Bentley, John, Cooper, Joel D., Conradi, Mark S., and Macklem, Peter T. ≪Long-range diffusion of hyperpolarized 3He in explanted normal and emphysematous human lungs via magnetization tagging.≫ <u>Journal of Applied Physiology</u>, **99**(5):pp. 1992–1997, 2005.

[295] de Lange, Eduard E., Altes, Talissa A., Patrie, James T., Gaare, John D., Knake, Jeffrey J., Mugler, John P., III, and Platts Mills, Thomas A. ≪Evaluation of asthma with hyperpolarized helium-3 mri: Correlation with clinical severity and spirometry.≫ <u>Chest</u>, **130**(4):pp. 1055–1062, 2006.

[296] Kruger, Stanley J., Niles, David J., Dardzinski, Bernard, Harman, Amy, Jarjour, Nizar N., Ruddy, Marcella, Nagle, Scott K., Francois, Christopher J., Sorkness, Ronald L., Burton, Ryan M., Munoz del Rio, Alejandro, and Fain, Sean B. ≪Hyperpolarized Helium-3 MRI of exercise-induced bronchoconstriction during challenge and therapy.≫ <u>Journal of Magnetic Resonance Imaging</u>, **39**(5):pp. 1230–1237, 2014.

[297] Chan, H. F., Stewart, N. J., Parra Robles, J., Collier, G. J., and Wild, J. M. ≪3D multiple b-value ADC acquisition for whole lung morphometry with hyperpolarised gas MRIand compressed sensing.≫ <u>Proceedings of the 32nd Meeting of the European Society of Magnetic Resonance in Medicine and Biology, Edinburgh, UK</u>, p. Program Number: 135, 2015.

[298] Diaz, S., Casselbrant, I., Piitulainen, E., Magnusson, P., Peterson, B., Wollmer, P., Leander, P., Ekberg, O., and Akeson, P. ≪Validity of apparent diffusion coefficient hyperpolarized 3He-MRI using MSCT and pulmonary function

tests as references.≫ European Journal of Radiology, **71**(2):pp. 257–263, 2009.

[299] Pellegrino, R., Viegi, G., Brusasco, V., Crapo, R. O., Burgos, F., Casaburi, R., Coates, A., van der Grinten, C. P. M., Gustafsson, P., Hankinson, J., Jensen, R., Johnson, D. C., MacIntyre, N., McKay, R., Miller, M. R., Navajas, D., Pedersen, O. F., and Wanger, J. ≪Interpretative strategies for lung function tests.≫ European Respiratory Journal, **26**(5):pp. 948–968, 2005.

[300] MacIntyre, N., Crapo, R. O., Viegi, G., Johnson, D. C., van der Grinten, C. P. M., Brusasco, V., Burgos, F., Casaburi, R., Coates, A., Enright, P., Gustafsson, P., Hankinson, J., Jensen, R., McKay, R., Miller, M. R., Navajas, D., Pedersen, O. F., Pellegrino, R., and Wanger, J. ≪Standardisation of the single-breath determination of carbon monoxide uptake in the lung.≫ European Respiratory Journal, **26**(4):pp. 720–735, 2005.

[301] Hathaway, Eilish H., Tashkin, Donald P., and Simmons, Michael S. ≪Intraindividual Variability in Serial Measurements of DlCO and Alveolar Volume over One Year in Eight Healthy Subjects Using Three Independent Measuring Systems.≫ American Review of Respiratory Disease, **140**(6):pp. 1818–1822, 1989.

[302] Grace Parraga, Lindsay Mathew, Roya Etemad Rezai, David G. McCormack, and Giles E. Santyr. ≪Hyperpolarized 3He Magnetic Resonance Imaging of Ventilation Defects in Healthy Elderly Volunteers: Initial Findings at 3.0 Tesla.≫ Academic Radiology, **15**(6):pp. 776–785, 2008.

[303] Rob H. Ireland, Chris M. Bragg, Mark McJury, Neil Woodhouse, Stan Fichele, Edwin J.R. van Beek, Jim M. Wild, and Matthew Q. Hatton. ≪Feasibility of Image Registration and Intensity-Modulated Radiotherapy Planning With Hyperpolarized Helium-3 Magnetic Resonance Imaging for Non-Small-Cell Lung Cancer.≫ International Journal of Radiation Oncology Biology Physics, **68**(1):pp. 273–281, 2007.

[304] Lindsay Mathew, Andrew Wheatley, Richard Castillo, Edward Castillo, George Rodrigues, Thomas Guerrero, and Grace Parraga. ≪Hyperpolarized 3He Magnetic Resonance Imaging: Comparison with Four-dimensional X-ray Computed Tomography Imaging in Lung Cancer.≫ Academic Radiology, **19**(12):pp. 1546 – 1553, 2012.

[305] Sukstanskii, A. L. and Yablonskiy, D. A. ≪Lung morphometry with hyperpolarized 129Xe: Theoretical background.≫ Magnetic Resonance in Medicine, **67**(3):pp. 856–866, 2012.

[306] Horn, F. C., Rao, M., Stewart, N. J., Marshall, H., Parra Robles, J., and Wild, J. M. ≪Multi nuclear 3D multiple breath washout imaging with hyperpolarised 3He and 129Xe MRI.≫ European Respiratory Journal (Suppl 59), **46**, 2015.

[307] Butler, J. P., Mair, R. W., Hoffmann, D., Hrovat, M. I., Rogers, R. A., Topulos, G. P., Walsworth, R. L., and Patz, S. ≪Measuring surface-area-to-volume ratios in soft porous materials using laser-polarized xenon interphase exchange nuclear magnetic resonance.≫ Journal of Physics Condensed Matter, **14**(13):pp. L297–L304, 2002.

[308] Imai, H., Kimura, A., Iguchi, S., Hori, Y., Masuda, S., and Fujiwara, H. ≪Noninvasive detection of pulmonary tissue destruction in a mouse model of emphysema using hyperpolarized 129Xe MRS under spontaneous respiration.≫ Magnetic Resonance in Medicine, **64**(4):pp. 929–938, 2010.

[309] Månsson, S., Wolber, J., Driehuys, B., Wollmer, P., and Golman, K. ≪Characterization of diffusing capacity and perfusion of the rat lung in a lipopolysaccharide disease model using hyperpolarized 129Xe.≫ Magnetic Resonance in Medicine, **50**(6):pp. 1170–9, 2003.

[310] Freeman, Matthew S., Cleveland, Zackary I., Qi, Yi, and Driehuys, Bastiaan. ≪Enabling hyperpolarized 129Xe MR spectroscopy and imaging of pulmonary gas transfer to the red blood cells in transgenic mice expressing human hemoglobin.≫ Magnetic Resonance in Medicine, **70**(5):pp. 1192–1199, 2013.

[311] Li, Haidong, Zhang, Zhiying, Zhao, Xiuchao, Sun, Xianping, Ye, Chaohui, and Zhou, Xin. ≪Quantitative evaluation of radiation-induced lung injury with hyperpolarized xenon magnetic resonance.≫ Magnetic Resonance in Medicine, **76**(2):pp. 408–16, 2016.

[312] Gross, Thomas J. and Hunninghake, Gary W. ≪Idiopathic Pulmonary Fibrosis.≫ New England Journal of Medicine, **345**(7):pp. 517–525, 2001.

[313] Pardo, A. and Selman, M. ≪Idiopathic pulmonary fibrosis: New insights in its pathogenesis.≫ International Journal of Biochemistry and Cell Biology, **34**(12):pp. 1534–1538, 2002.

[314] Bussone, G. and Mouthon, L. ≪Interstitial lung disease in systemic sclerosis.≫ Autoimmun Rev, **10**(5):pp. 248–255, 2011.

[315] Koh, E. T., Lee, P., Gladman, D. D., and Abu Shakra, M. ≪Pulmonary hypertension in systemic sclerosis: An analysis of 17 patients.≫ British Journal of Rheumatology, **35**(10):pp. 989–993, 1996.

[316] Best, A. C., Meng, J., Lynch, A. M., Bozic, C. M., Miller, D., Grunwald, G. K., and Lynch, D. A. ≪Idiopathic pulmonary fibrosis: Physiologic tests, quantitative CT indexes, and CT visual scores as predictors of mortality.≫ Radiology, **246**(3):pp. 935–940, 2008.

[317] Leung, General, Norquay, Graham, Schulte, Rolf F., and Wild, Jim M. ≪Radiofrequency pulse design for the selective excitation of dissolved 129Xe.≫ Magnetic Resonance in Medicine, **73**(1):pp. 21–30, 2015.

[318] Crank, John. ≪The Mathematics Of Diffusion (Second Edition).≫ Oxford Science Publications, 1979.

[319] Skrok, Jan, Shehata, Monda L., Mathai, Stephen, Girgis, Reda E., Zaiman, Ari, Mudd, James O., Boyce, Danielle, Lechtzin, Noah, Lima, Joo A. C., Bluemke, David A., Hassoun, Paul M., and Vogel Claussen, Jens. ≪Pulmonary Arterial Hypertension: MR Imaging-derived First-Pass Bolus Kinetic Parameters Are Biomarkers for Pulmonary Hemodynamics, Cardiac Function, and Ventricular Remodeling.≫ Radiology, **263**(3):pp. 678–687, 2012.

[320] Gil, J., Marchevsky, A. M., and Jeanty, H. ≪Septal thickness in human lungs assessed by computerized interactive morphometry.≫ Lab Invest, **58**(4):pp. 466–72, 1988.

[321] Fåhræus, Robin and Lindqvist, Torsten. ≪The viscosity of the blood in narrow capillary tubes.≫ American Journal of Physiology, **96**(3), 1931.

[322] De Zanche, Nicola, Chhina, Navjeet, Teh, Kevin, Randell, Chris, Pruessmann, Klaas P., and Wild, Jim M. ≪Asymmetric quadrature split birdcage coil for hyperpolarized 3He lung MRI at 1.5T.≫ Magnetic Resonance in Medicine, **60**(2):pp. 431–438, 2008.

[323] Galbraith, Susan M., Lodge, Martin A., Taylor, N. Jane, Rustin, Gordon J. S., Bentzen, Sren, Stirling, J. James, and Padhani, Anwar R. ≪Reproducibility of dynamic contrast-enhanced MRI in human muscle and tumours: comparison of quantitative and semi-quantitative analysis.≫ NMR in Biomedicine, **15**(2):pp. 132–142, 2002.

[324] Bland, J Martin and Altman, Douglas G. ≪Measuring agreement in method comparison studies.≫ Statistical Methods in Medical Research, **8**(2):pp. 135–160, 1999.

[325] Savino, Carmelinda, Miele, Adriana E., Draghi, Federica, Johnson, Kenneth A., Sciara, Giuliano, Brunori, Maurizio, and Vallone, Beatrice. ≪Pattern of cavities in globins: The case of human hemoglobin.≫ Biopolymers, **91**(12):pp. 1097–1107, 2009.

[326] Hajari, A. J., Yablonskiy, D. A., Sukstanskii, A. L., Quirk, J. D., Conradi, M. S., and Woods, J. C. ≪Morphometric changes in the human pulmonary acinus during inflation.≫ Journal of Applied Physiology, **112**(6):pp. 937–943, 2012.

[327] Gläser, S., Meyer, R., Opitz, C.F., Hetzer, R., and Ewert, R. ≪Pulmonary Interstitial and Vascular Abnormalities Following Cardiac Transplantation.≫ Transplantation Proceedings, **40**(10):pp. 3585–3589, 2008.

[328] Claus Kohlhase and Helmut Maxeiner. ≪Morphometric investigation of emphysema aquosum in the elderly.≫ Forensic Science International, **134**(2):pp. 93–98, 2003.

[329] Coxson, Harvey O, Rogers, Robert M, Whittall, Kenneth P, D'yachkova, Yulia, Pare, Peter D, Sciurba, Frank C, and Hogg, James C. ≪A quantification of the lung surface area in emphysema using computed tomography.≫ American Journal of Respiratory and Critical Care Medicine, **159**(3):pp. 851–856, 1999.

[330] Miller, Martin R, Hankinson, JATS, Brusasco, V, Burgos, F, Casaburi, R, Coates, A, Crapo, R, Enright, P, Van der Grinten, CP, and Gustafsson, P. ≪Standardisation of Spirometry.≫ European Respiratory Journal, **26**(2):pp. 319–38, 2005.

[331] Sta Maria, N. and Eckmann, D. M. ≪Model predictions of gas embolism growth and reabsorption during xenon anesthesia.≫ Anesthesiology, **99**(3):pp. 638–645, 2003.

[332] Evans, AL, Busuttil, A, Gillespie, FC, and Unsworth, J. ≪The rate of clearance of xenon from rat liver sections in vitro and its significance in relation to intracellular diffusion rates.≫ Physics in Medicine and Biology, **19**(3):p. 303, 1974.

[333] Kovar, Jana, Sly, Peter D., and Willet, Karen E. ≪Postnatal alveolar development of the rabbit.≫ Journal of Applied Physiology, **93**(2):pp. 629–635, 2002.

[334] Unsworth, J. and Gillespie, F. ≪Diffusion coefficients of xenon and krypton in water from 0 C to 80 C and in biological tissues at 37 C.≫ In: Diffusion Processes: Proceedings of the Thomas Grahm Memorial Symposium, London, 1971.

[335] Mataloun, M. M. G. B., Leone, C. R., Mascaretti, R. S., Dohlnikoff, M., and Rebello, C. M. ≪Effect of postnatal malnutrition on hyperoxia-induced newborn lung development.≫ Brazilian Journal of Medical and Biological Research, **42**:pp. 606 – 613, 2009.

[336] Birks, Eric K, Mathieu Costello, Odile, Fu, Zhenxing, Tyler, Walter S, and West, John B. ≪Comparative aspects of the strength of pulmonary capillaries in rabbit, dog, and horse.≫ Respiration physiology, **97**(2):pp. 235–246, 1994.

[337] Goto, T., Suwa, K., Uezono, S., Ichinose, F., Uchiyama, M., and Morita, S. ≪The blood-gas partition coefficient of xenon may be lower than generally accepted.≫ British Journal of Anaesthesia, **80**(2):pp. 255–256, 1998.

[338] Mercer, R. R., Russell, M. L., and Crapo, J. D. ≪Alveolar septal structure in different species.≫ Journal of Applied Physiology, **77**(3):pp. 1060–1066, 1994.

[339] King Jr, T. E., Pardo, A., and Selman, M. ≪Idiopathic pulmonary fibrosis.≫ The Lancet, **378**(9807):pp. 1949–1961,

2011.

[340] West, J. B. and Dollery, C. T. ≪Distribution of blood flow and ventilation-perfusion ratio in the lung, measured with radioactive carbon dioxide.≫ Journal of Applied Physiology, **15**:pp. 405–410, 1960.

[341] Doganay, Ozkan, Wade, Trevor, Hegarty, Elaine, McKenzie, Charles, Schulte, Rolf F., and Santyr, Giles E. ≪Hyperpolarized 129Xe imaging of the rat lung using spiral IDEAL.≫ Magnetic Resonance in Medicine, **76**(2):pp. 566–576, 2016.

[342] Doganay, Ozkan, Stirrat, Elaine, McKenzie, Charles, Schulte, Rolf F., and Santyr, Giles E. ≪Quantification of regional early stage gas exchange changes using hyperpolarized 129Xe MRI in a rat model of radiation-induced lung injury.≫ Medical Physics, **43**(5):pp. 2410–2420, 2016.

[343] Ajraoui, S., Parra Robles, J., and Wild, J. M. ≪Incorporation of prior knowledge in compressed sensing for faster acquisition of hyperpolarized gas images.≫ Magnetic Resonance in Medicine, **69**(2):pp. 360–369, 2013.

[344] Wells, A U and Hirani, N. ≪Interstitial lung disease guideline.≫ Thorax, **63**(Suppl 5):pp. v1–v58, 2008.

[345] Doganay, O., Fox, Matthew S., and Santyr, G. E. ≪Measurement of Pulmonary Perfusion and Gas Exchange using Hyperpolarized 129Xe in a Rodent Model of Radiation-Induced Lung Injury.≫ Proceedings of the 22nd Annual Meeting of the International Society for Magnetic Resonance in Medicine, Milan, Italy, p. Abstract Number: 2290, 2014.

[346] Weibel, Ewald R. and Knight, Bruce W. ≪A Morphometric Study On The Thickness Of The Pulmonary Air-Blood Barrier.≫ The Journal of Cell Biology, **21**(3):pp. 367–384, 1964.

[347] Souza, C. A., Mller, N. L., Flint, J., Wright, J. L., and Churg, A. ≪Idiopathic pulmonary fibrosis: Spectrum of high-resolution CT findings.≫ American Journal of Roentgenology, **185**(6):pp. 1531–1539, 2005.

[348] Parra Robles, Juan, Vasilescu, Dragos, Hogg, James C., and Wild, Jim M. ≪Modelling of 3He gas diffusion in realistic 3D models of human acinar airways obtained from micro-CT images.≫ European Respiratory Journal (Suppl 58), **44**(Suppl 58), 2014.

[349] Fichele, S., Paley, M. N. J., Woodhouse, N., Griffiths, P. D., Van Beek, E. J. R., and Wild, J. M. ≪Investigating 3He diffusion NMR in the lungs using finite difference simulations and in vivo PGSE experiments.≫ Journal of Magnetic Resonance, **167**(1):pp. 1–11, 2004.

[350] Miller, G. W., Carl, M., Mata, J. F., Cates, G. D., and Mugler, J. P. ≪Simulations of Short-Time Diffusivity in Lung Airspaces and Implications for S/V Measurements Using Hyperpolarized-Gas MRI.≫ Medical Imaging, IEEE Transactions on, **26**(11):pp. 1456–1463, 2007.

[351] Plotkowiak, Michal, Burrowes, Kelly, Wolber, Jan, Buckley, Christopher, Davies, Robert, Gleeson, Fergus, Gavaghan, David, and Grau, Vicente. ≪Relationship between structural changes and hyperpolarized gas magnetic resonance imaging in chronic obstructive pulmonary disease using computational simulations with realistic alveolar geometry.≫ Philosophical Transactions of the Royal Society A: Mathematical, Physical and Engineering Sciences, **367**(1896):pp. 2347–2369, 2009.

[352] Rubenstein, D., Yin, W., and Frame, M. D. ≪Biofluid Mechanics: An Introduction to Fluid Mechanics, Macrocirculation, and Microcirculation.≫ Academic Press, 2011.

[353] Ebadi Amooghin, A., Sanaeepur, H., Kargari, A., and Moghadassi, A. ≪Direct determination of concentration-dependent diffusion coefficient in polymeric membranes based on the Frisch method.≫ Separation and Purification Technology, **82**:pp. 102–113, 2011.

[354] COMSOL Multiphysics. ≪Chemical engineering module model library.≫ Version 3.4, 2007.

[355] Mauroy, B. ≪Following red blood cells in a pulmonary capillary.≫ ESAIM: Proceedings, **23**:pp. 48–65, 2008.

[356] Warren, G. L., Cureton, K. J., Middendorf, W. F., Ray, C. A., and Warren, J. A. ≪Red blood cell pulmonary capillary transit time during exercise in athletes.≫ Medicine & Science in Sports & Exercise, **23**(12):pp. 1353–1361, 1991.

[357] Verleden, Stijn, Willems, Stijn, Ruttens, David, Vos, Robin, McDonough, John, Vaneylen, Annemie, Verbeken, Erik, Verschakelen, Johny, Van Raemdonck, Dirk, Rondelet, Benoît, Knoop, Christiane, Decramer, Marc, Hogg, James, Verleden, Geert, and Vanaudenaerde, Bart. ≪Structural differences in airways during chronic rejection after lung transplantation: A (micro)-CT analysis.≫ European Respiratory Journal (Suppl 56), **40**, 2014.

[358] Ruppert, Kai, Altes, Talissa A., Mata, Jaime F., Ruset, Iulian C., Hersman, F. William, and Mugler, John P. ≪Detecting pulmonary capillary blood pulsations using hyperpolarized xenon-129 chemical shift saturation recovery (CSSR) MR spectroscopy.≫ Magnetic Resonance in Medicine, **75**(4):pp. 1771–1780, 2016.

[359] Rao, M., Stewart, N. J., Norquay, G., Griffiths, P. D., and Wild, J. M. ≪Imaging the human brain with dissolved xenon MRI at 1.5T.≫ Proceedings of the 23rd Meeting of the International Society of Magnetic Resonance in Medicine, Toronto, Ontario, Canada, p. Abstract: 1254, 2015.

Chapter 11

Appendix

11.1 Publications resulting from this thesis

Book chapters

- "MRI methods for structural and functional assessment of the lungs: proton and multi-nuclear". **N. J. Stewart**, J. M. Wild. *European Respiratory Society Monograph: Chapter 1*, **70**, 1-19 (2016).

Journal articles

- "Finite Element Modeling of ^{129}Xe Diffusive Gas Exchange NMR in the Human Alveoli". **N. J. Stewart**, J. Parra-Robles, J. M. Wild. *Journal of Magnetic Resonance*, doi:10.1002/mrm.26279 (2016).

- "Reproducibility of Quantitative Indices of Lung Function and Microstructure from ^{129}Xe Chemical Shift Saturation Recovery (CSSR) MR Spectroscopy". **N. J. Stewart**, F. C. Horn, G. Norquay, et al. *Magnetic Resonance in Medicine*, doi:10.1002/mrm.26310 (2016).

- "Feasibility of Human Lung Ventilation Imaging using Highly Polarized Naturally-Abundant Xenon and Optimized 3D SSFP". **N. J. Stewart**, G. Norquay, P. D. Griffiths, J. M. Wild. *Magnetic Resonance in Medicine*, **74**(2), 346-352 (2015).

- "Experimental Validation of the Hyperpolarized ^{129}Xe Chemical Shift Saturation Recovery Technique in Healthy Volunteers and Subjects with Interstitial Lung Disease". **N. J. Stewart**, G. Leung, G. Norquay, et al. *Magnetic Resonance in Medicine*, **74**(1), 196-207 (2015).

Conference proceedings

- "Comparison of ^{3}He and ^{129}Xe MRI for Evaluation of Lung Microstructure and Ventilation in Healthy Volunteers and COPD Patients at 1.5 T". **N. J. Stewart**, H. F. Chan, G. J. Collier, et al. *In: Proceedings of the International Society for Magnetic Resonance in Medicine (ISMRM) Meeting, Singapore*, 2016. Programme number: **0979**. (Oral presentation.)

- "Methods for hyperpolarised xenon MR imaging of the human lungs and brain". **N. J. Stewart**, G. Norquay, M. R. Rao, J. M. Wild. *In: Proceedings of the Xenon / hyperpolarized noble gases in Magnetic Resonance (XeMAT) Meeting, Dresden, Germany*, 2015. Programme number: **T20**. (Oral presentation.)

- "FEM Analysis of Diffusive Exchange of Hyperpolarised ^{129}Xe in the Human Lungs using Realistic Histology-Based Geometries". **N. J. Stewart**, J. Parra-Robles, J. M. Wild. *In: Proceedings of the Xenon / hyperpolarized noble gases in Magnetic Resonance (XeMAT) Meeting, Dresden, Germany*, 2015. Programme number: **P18**. (Poster presentation.)

- "Repeatability of ^{129}Xe MR methods for quantification of interstitial thickness". **N. J. Stewart**, H. Marshall, J. M. Wild. *In: Proceedings of the European Respiratory Society (ERS) Meeting, Amsterdam, The Netherlands*, 2015. Programme number: **PA517**. (Poster presentation.)

- "Assessment of lung microstructure in ILD with ^{3}He and ^{129}Xe MRI". **N. J. Stewart**, G. Norquay, J. Parra-Robles, et al. *In: Proceedings of the European Respiratory Society (ERS) Meeting, Amsterdam, The Netherlands*, 2015. Programme number: **OA2945**. (Oral presentation.)

- "Integrated Spectroscopic Imaging (CSI) and Chemical Shift Saturation Recovery (CSSR) of Hyperpolarized ^{129}Xe in the Human Lungs". **N. J. Stewart**, J. M. Wild. *In: Proceedings of the International Society for Magnetic Resonance in Medicine (ISMRM) Meeting, Toronto, Canada*, 2015. Programme number: **1485**. (Poster presentation.)

- "^{129}Xe Dynamic Spectroscopy and Modelling: A Repeatability and Method Comparison Study". **N. J. Stewart**, H. Marshall, J. M. Wild. *In: Proceedings of the International Society for Magnetic Resonance in Medicine (ISMRM)*

Meeting, Toronto, Canada, 2015. Programme number: **1491**. (Poster presentation.)

- "Numerical Simulations of Xenon Diffusive Exchange in Human Lung Tissue and Capillaries Using Geometrical Models Based on Histology Sections". **N. J. Stewart**, J. Parra-Robles, J. M. Wild. *In: Proceedings of the International Society for Magnetic Resonance in Medicine (ISMRM) Meeting, Toronto, Canada*, 2015. Programme number: **3985**. (Poster presentation.)

- "Feasibility of Human Lung Ventilation MR Imaging Using Naturally-Abundant Xenon with Optimized 3D SSFP". **N. J. Stewart**, G. Norquay, P. Griffiths, J. M. Wild. *In: Proceedings of the International Society for Magnetic Resonance in Medicine (ISMRM) Meeting, Toronto, Canada*, 2015. Programme number: **1042**. (Oral presentation.)

- "FEM Analysis of Diffusive Exchange of Hyperpolarised ^{129}Xe in the Human Lungs using Realistic Histology-Based Geometries". **N. J. Stewart**, J. Parra-Robles, J. M. Wild. *In: Proceedings of the Insigneo Institute for in silico Medicine Showcase, Sheffield, United Kingdom*, 2015. (Poster presentation.)

- "Assessment Of Lung Microstructure In Interstitial Lung Disease With Hyperpolarised Gas MRI". **N. J. Stewart**, G. Norquay, J. Parra-Robles, et al. *In: Proceedings of the British Thoracic Society (BTS) Meeting, London, UK*, and also published in: *Thorax, 69, Supplement 2*, 2014. A192-A193. Programme number: **P273**. (Poster presentation.)

- "Feasibility of Human Lung Ventilation MR Imaging using Naturally-Abundant ^{129}Xe with Optimised 3D SSFP". **N. J. Stewart**, G. Norquay, P. D. Griffiths, J. M. Wild. *In: Proceedings of the Hyperpolarised Noble Gases (PING) Meeting, Les Houches, France*, 2014. (Oral presentation.)

- "Feasibility of high quality lung MRI with naturally-abundant hyperpolarised ^{129}Xe". **N. J. Stewart**, G. Norquay, H. Marshall, J. M. Wild. *In Proceedings of the European Respiratory Society (ERS) Meeting, Munich, Germany*, 2014. Programme number: **OA1729**. (Oral presentation.)

- "Age-dependent changes in whole-lung septal thickness measured by ^{129}Xe MRI: a comparison of healthy volunteers and subjects with ILD". **N. J. Stewart**, G. Leung, G. Norquay, et al. *In: Proceedings of the European Respiratory Society (ERS) Meeting, Munich, Germany*, 2014. Programme number: **PA550**. (Poster presentation.)

- "Human Lung MR Imaging using Naturally-Abundant ^{129}Xe with optimised 3D SSFP". **N. J. Stewart**, G. Norquay, J. M. Wild. *In: Proceedings of the British Chapter (BC) of the International Society for Magnetic Resonance in Medicine (ISMRM) Meeting, Edinburgh, United Kingdom*, 2014. (Oral presentation.)

- "Dissolved ^{129}Xe MRI - Delayed Gas Uptake Indicates Septal Thickening In Patients With Idiopathic Pulmonary Fibrosis and Systemic Sclerosis". **N. J. Stewart**, G. Leung, G. Norquay, et al. *In: Proceedings of the American Thoracic Society (ATS) Meeting, San Diego, California, USA*, 2014. Section D52: Gas Exchange in Steady State, Altitude and Exercise, **A6286**. (Poster presentation.)

- "Human Lung MR Imaging using Naturally-Abundant ^{129}Xe with optimised 3D SSFP". **N. J. Stewart**, G. Norquay, J. M. Wild. *In: Proceedings of the European Cooperation in Science and Technology (COST) EUROHYPERPOL Meeting, Zurich, Switzerland*, 2014. Working group: WG4. (Oral presentation.)

- "Gas Exchange in Interstitial Lung Disease with Hyperpolarised ^{129}Xe". **N. J. Stewart**, G. Leung, G. Norquay, et al. *In: Proceedings of the Sheffield Lung and Pulmonary Vascular MR Imaging Meeting, Sheffield, UK*, 2014. (Oral presentation.)

- "Dissolved Hyperpolarised ^{129}Xe MR as a Probe of Lung Function in IPF and SSc". **N. J. Stewart**, G. Leung, G. Norquay, et al. *In: Proceedings of the International Society for Magnetic Resonance in Medicine (ISMRM) Meeting, Milan, Italy*, 2014. Programme number: **0775**. (Oral presentation.)

- "Dissolved ^{129}Xe Lung MRI - Delayed Gas Uptake Indicates Septal Thickening In Patients With Interstitial Lung Disease". **N. J. Stewart**, G. Leung, G. Norquay, et al. *In: Proceedings of the British Chapter (BC) of the International Society for Magnetic Resonance in Medicine (ISMRM) Meeting, York, United Kingdom*, 2013. Programme number: **P6**. (Poster presentation.)

- "Evaluation of Alveolar Septal Thickening in IPF Subjects with Hyperpolarised ^{129}Xe CSSR". **N. J. Stewart**, G. Leung, G. Norquay, et al. *In: Proceedings of the International Workshop for Pulmonary Functional Imaging (IWPFI) Meeting, Madison, Wisconsin, USA*, 2013. (Oral presentation.)

11.2 Other co-authored publications

Journal articles

- "Multiple Breath Washout of Hyperpolarized ^{129}Xe and ^{3}He in Human Lungs with Three-dimensional Balanced Steady-state Free-precession Imaging". F. C. Horn, M. Rao, **N. J. Stewart**, J. M. Wild. *Magnetic Resonance in Medicine*, doi:10.1002/mrm.26319 (2016).

- "Whole lung morphometry with 3D multiple b-value hyperpolarized gas MRI and compressed sensing". H-F. Chan, **N. J. Stewart**, J. Parra-Robles, G. Collier, J. M. Wild. *Magnetic Resonance in Medicine*, doi:10.1002/mrm.26279 (2016).

- "High resolution spectroscopy and chemical shift imaging of hyperpolarized ^{129}Xe dissolved in the human brain in vivo at 1.5 tesla". M. Rao, **N. J. Stewart**, G. Norquay, P. D. Griffiths, J. M. Wild. *Magnetic Resonance in Medicine*, doi:10.1002/mrm.26241 (2016).

- "^{129}Xe chemical shift in human blood and pulmonary blood oxygenation measurement in humans using hyperpolarized ^{129}Xe NMR". G. Norquay, G. Leung, **N. J. Stewart**, J. Wolber, J. M. Wild. *Magnetic Resonance in Medicine*, doi:10.1002/mrm.26225 (2016).

- "Observation of cardiogenic flow oscillations in healthy subjects with hyperpolarized ^{3}He MRI". G. J. Collier, H. Marshall, M. Rao, **N. J. Stewart**, D. Capener, J. M. Wild. *Journal of Applied Physiology*, **119** (9), 1007-1014 (2015).

- "Relaxation and exchange dynamics of hyperpolarized ^{129}Xe in human blood". G. Norquay, G. Leung, **N. J. Stewart**, et al. *Magnetic Resonance in Medicine*, **74**, 303-311 (2015).

- "Lung ventilation volumetry with same-breath acquisition of hyperpolarized gas and proton MRI". F. C. Horn, B. A. Tahir, **N. J. Stewart**, et al. *NMR In Biomedicine*, **27**, 1461-7 (2014).

Conference proceedings

- "3D Multi-Parametric Acquisition of ^{3}He Lung Ventilation Images, Lung Diffusion Morphometry and T_2^* Maps with Compressed Sensing". H-F. Chan, **N. J. Stewart**, G. Collier, J. M. Wild. *In: Proceedings of the International Society for Magnetic Resonance in Medicine (ISMRM) Meeting, Singapore*, 2016. Programme number: **2928**. (Poster presentation.)

- "Accurate T_1 Mapping in Patients with Pulmonary Hypertension and Age Matched Volunteers Using Synthetic Image Based Registration". L. C. Saunders, **N. J. Stewart**, C. Hammerton, et al. *In: Proceedings of the International Society for Magnetic Resonance in Medicine (ISMRM) Meeting, Singapore*, 2016. Programme number: **0460**. (Oral & Poster presentation.)

- "Hyperpolarized ^{13}C-Urea MRI for the Assessment of the Urea Gradient in the Porcine Kidney". E. Hansen, **N. J. Stewart**, J. M. Wild, H. Stødkilde-Jørgensen, C. Laustsen. *In: Proceedings of the International Society for Magnetic Resonance in Medicine (ISMRM) Meeting, Singapore*, 2016. Programme number: **0666**. (Oral presentation.)

- "MR of Hyperpolarized Xe-129 Dissolved in the Human Brain at 1.5 T and 3.0 T". M. R. Rao, **N. J. Stewart**, G. Norquay, P. D. Griffiths, J. M. Wild. *In: Proceedings of the International Society for Magnetic Resonance in Medicine (ISMRM) Meeting, Singapore*, 2016. Programme number: **0722**. (Oral & Poster presentation.)

- "Native Myocardial T_1 Correlates with Right Ventricular Mass and Invasive Catheter Measurement in Patients with Pulmonary Hypertension". L. C. Saunders, **N. J. Stewart**, C. Hammerton, et al. *In: Proceedings of the International Society for Magnetic Resonance in Medicine (ISMRM) Meeting, Singapore*, 2016. Programme number: **3157**. (Poster presentation.)

- "Whole Lung Morphometry with Hyperpolarised ^{3}He Gas Diffusion MRI - 3D Multiple B-Value Acquisition and Compressed Sensing". H-F. Chan, **N. J. Stewart**, J. Parra-Robles, G. Collier, J. M. Wild. *In: Proceedings of the International Society for Magnetic Resonance in Medicine (ISMRM) Meeting, Singapore*, 2016. Programme number: **2925**. (Poster presentation.)

- "Relationship between brain and pulmonary function studied by hyperpolarized ^{129}Xe MRI/MRS". A. Shimokawa, H. Matsumoto, Y. Yamauchi, S. Hodono, S. Okumura, **N. J. Stewart**, H. Imai, H. Fujiwara, A. Kimura. *In: Proceedings of the combined Asia Oceania Workshop of Pulmonary Functional Imaging (AOWPFI) and Japanese Society of Pulmonary Functional Imaging (JSPFI) Meeting, Awaji, Japan*, 2015. Programme number: **P3-4-3**. (Poster presentation.)

- "MR imaging and spectroscopy of human brain with hyperpolarized ^{129}Xe at 1.5 T". M. R. Rao, **N. J. Stewart**, G. Norquay, P. D. Griffiths, J. M. Wild. *In: Proceedings of the Xenon / hyperpolarized noble gases in Magnetic Resonance (XeMAT) Meeting, Dresden, Germany*, 2015. Programme number: **T10**. (Oral presentation.)

- "Pulmonary oxygenation determination using hyperpolarised ^{129}Xe NMR". G. Norquay, **N. J. Stewart**, J. M. Wild. *In: Proceedings of the Xenon / hyperpolarized noble gases in Magnetic Resonance (XeMAT) Meeting, Dresden, Germany*, 2015. Programme number: **T17**. (Oral presentation.)

- "Correlations of functional multi-nuclear MR imaging indices with pulmonary function tests in the assessment of idiopathic pulmonary fibrosis". N. D. Weatherley, H. Marshall, **N. J. Stewart**, et al. *In: Proceedings of the British Thoracic Society (BTS) Meeting, London, United Kingdom*, 2015. (Poster presentation.)

- "MR imaging and spectroscopy of human brain with hyperpolarized ^{129}Xe at 1.5 T". M. R. Rao, **N. J. Stewart**, G. Norquay, J. M. Wild. *In: Proceedings of the European Society for Magnetic Resonance in Medicine and Biology (ESMRMB) Meeting, Edinburgh, United Kingdom*, 2015. (Oral presentation.)

- "Accurate T_1 mapping using automated image registration in patients with pulmonary hypertension and healthy volunteers". L. C. Hutchison, C. Hammerton, **N. J. Stewart**, et al. *In: Proceedings of the European Society for Magnetic Resonance in Medicine and Biology (ESMRMB) Meeting, Edinburgh, United Kingdom*, 2015. (Poster presentation.)

- "3D multiple b-value ADC acquisition for whole lung morphometry with hyperpolarised gas MRIand compressed sensing". H-F. Chan, **N. J. Stewart**, J. Parra-Robles, G. Collier, J. M. Wild. *In: Proceedings of the European Society for Magnetic Resonance in Medicine and Biology (ESMRMB) Meeting, Edinburgh, United Kingdom*, 2015. (Oral presentation.)

- "Hyperpolarised gas MRI — a pathway to clinical diagnostic imaging". J. M. Wild, L. Smith, F. Horn, G. Collier, A. Swift, **N. J. Stewart**, M. Rao, G. Norquay, D. Hughes, K. Ugonna, H. Marshall. *In: Proceedings of the International Workshop for Pulmonary Functional Imaging (IWPFI) Meeting, Edinburgh, United Kingdom*, 2015. (Oral presentation.)

- "Preliminary investigations of lung structure-function with multi-nuclear MR imaging and pulmonary function tests in idiopathic pulmonary fibrosis". N. D. Weatherley, H. Marshall, **N. J. Stewart**, et al. *In: Proceedings of the International Workshop for Pulmonary Functional Imaging (IWPFI) Meeting, Edinburgh, United Kingdom*, 2015. (Oral presentation.)

- "Myocardial T_1 mapping MRI in patients with PH and age-matched healthy volunteers". L. Hutchison, **N. J. Stewart**, P. Hughes, et al. *In: Proceedings of the European Respiratory Society (ERS) Meeting, Amsterdam, The Netherlands*, 2015. Programme number: **PA2466**. (Poster presentation.)

- "Hyperpolarised gas MR lung imaging — Breaks through to clinical practice". J. M. Wild, L. Smith, F. Horn, G. Collier, A. Swift, **N. J. Stewart**, M. Rao, G. Norquay, D. Hughes, K. Ugonna, H. Marshall. *In: Proceedings of the European Respiratory Society (ERS) Meeting, Amsterdam, The Netherlands*, 2015. Programme number: **OA4992**. (Oral presentation.)

- "Multi nuclear 3D multiple breath washout imaging with hyperpolarised ^{3}He and ^{129}Xe MRI". F. Horn, M. R. Rao, **N. J. Stewart**, et al. *In: Proceedings of the European Respiratory Society (ERS) Meeting, Amsterdam, The Netherlands*, 2015. Programme number: **PA3752**. (Poster presentation.)

- "Quantitative T_1 Mapping and Oxygen Enhanced MRI in Patients with Interstitial Lung Disease". K. Hart, H. Marshall, **N. J. Stewart**, et al. *In: Proceedings of the International Society for Magnetic Resonance in Medicine (ISMRM) Meeting, Toronto, Canada*, 2015. Programme number: **1451**. (Poster presentation.)

- "In Vivo Dynamic Measurement of Pulmonary Blood Oxygenation and Cardiac Output Using Hyperpolarised ^{129}Xe".

G. Norquay, **N. J. Stewart**, J. M. Wild. *In: Proceedings of the International Society for Magnetic Resonance in Medicine (ISMRM) Meeting, Toronto, Canada*, 2015. Programme number: **1485**. (Poster presentation.)

- "Approaching the Theoretical Limit for ^{129}Xe Hyperpolarisation with Continuous-Flow Spin-Exchange Optical Pumping". G. Norquay, **N. J. Stewart**, J. M. Wild. *In: Proceedings of the International Society for Magnetic Resonance in Medicine (ISMRM) Meeting, Toronto, Canada*, 2015. Programme number: **1505**. (Poster presentation.)

- "Multi Nuclear 3D Multiple Breath Washout Imaging with ^{3}He and ^{129}Xe Using a Dual Tuned Coil". F. C. Horn, M. R. Rao, **N. J. Stewart**, et al. *In: Proceedings of the International Society for Magnetic Resonance in Medicine (ISMRM) Meeting, Toronto, Canada*, 2015. Programme number: **1500**. (Poster presentation.)

- "Quantification of Perfusion and Xenon-Transport Across the Blood-Brain Barrier in Humans with Hyperpolarized ^{129}Xe Brain MR at 1.5T". M. R. Rao, **N. J. Stewart**, G. Norquay, J. M. Wild. *In: Proceedings of the International Society for Magnetic Resonance in Medicine (ISMRM) Meeting, Toronto, Canada*, 2015. Programme number: **1445**. (Poster presentation.)

- "RF Instrumentation for Same-Breath Triple-Nuclear Lung MR Imaging of ^{1}H and Hyperpolarized ^{3}He and ^{129}Xe at 1.5 T". M. R. Rao, J. Parra-Robles, H. Marshall, **N. J. Stewart**, G. Collier, J. M. Wild. *In: Proceedings of the International Society for Magnetic Resonance in Medicine (ISMRM) Meeting, Toronto, Canada*, 2015. Programme number: **1812**. (Poster presentation.)

- "Imaging the Human Brain with Dissolved Xenon MRI at 1.5 T". M. R. Rao, **N. J. Stewart**, G. Norquay, P. Griffiths, J. M. Wild. *In: Proceedings of the International Society for Magnetic Resonance in Medicine (ISMRM) Meeting, Toronto, Canada*, 2015. Programme number: **1254**. (Poster presentation.)

- "Spectroscopy of Dissolved ^{129}Xe in the Human Brain at 1.5 T". M. R. Rao, **N. J. Stewart**, G. Norquay, J. M. Wild. *In: Proceedings of the Hyperpolarised Noble Gases (PING) Meeting, Les Houches, France*, 2014. (Oral presentation.)

- "^{129}Xe Chemical Shift and Spin-Lattice Relaxation Dependence on Blood Oxygenation". G. Norquay, G. Leung, **N. J. Stewart**, J. M. Wild. *In: Proceedings of the Hyperpolarised Noble Gases (PING) Meeting, Les Houches, France*, 2014. (Oral presentation.)

- "High ^{129}Xe Polarisation (80%) on a Home-Built SEOP System". G. Norquay, **N. J. Stewart**, J. M. Wild. *In: Proceedings of the Hyperpolarised Noble Gases (PING) Meeting, Les Houches, France*, 2014. (Poster presentation.)

- "Spectroscopy of Dissolved ^{129}Xe in the Human Brain at 1.5 T". M. R. Rao, **N. J. Stewart**, G. Norquay, J. M. Wild. *In: Proceedings of the British Chapter (BC) of the International Society for Magnetic Resonance in Medicine (ISMRM) Meeting, Edinburgh, United Kingdom*, 2014. (Poster presentation.)

- "Quantitative lung T_1 mapping and oxygen enhanced MRI in IPF". K. Hart, H. Marshall, **N. J. Stewart**, et al. *In Proceedings of the European Respiratory Society (ERS) Meeting, Munich, Germany*, 2014. Programme number: **OA1727**. (Oral presentation.)

- "Spectroscopy of Dissolved ^{129}Xe in Human Brain at 1.5 T". M. R. Rao, **N. J. Stewart**, G. Norquay, J. M. Wild. *In: Proceedings of the European Cooperation in Science and Technology (COST) EUROHYPERPOL Meeting, Zurich, Switzerland*, 2014. Working group: WG4. (Oral presentation.)

- "Revisiting the ^{129}Xe Relaxation Rate in Human Blood and Quantifying the Relaxivity of Deoxyhaemoglobin in the Presence of ^{129}Xe". G. Norquay, G. Leung, **N. J. Stewart**, et al. *In: Proceedings of the International Society for Magnetic Resonance in Medicine (ISMRM) Meeting, Milan, Italy*, 2014. Programme number: **2292**. (Poster presentation.)

- "Spectroscopy of Dissolved ^{129}Xe in Human Brain at 1.5 T". M. R. Rao, **N. J. Stewart**, G. Norquay, J. M. Wild. *In: Proceedings of the International Society for Magnetic Resonance in Medicine (ISMRM) Meeting, Milan, Italy*, 2014. Programme number: **3532**. (Poster presentation.)